NASA/CP-1999-209691/VOL1/PT1

1997 NASA High-Speed Research Program Aerodynamic Performance Workshop

Volume I—Configuration Aerodynamics

Edited by
Daniel G. Baize
Langley Research Center, Hampton, Virginia

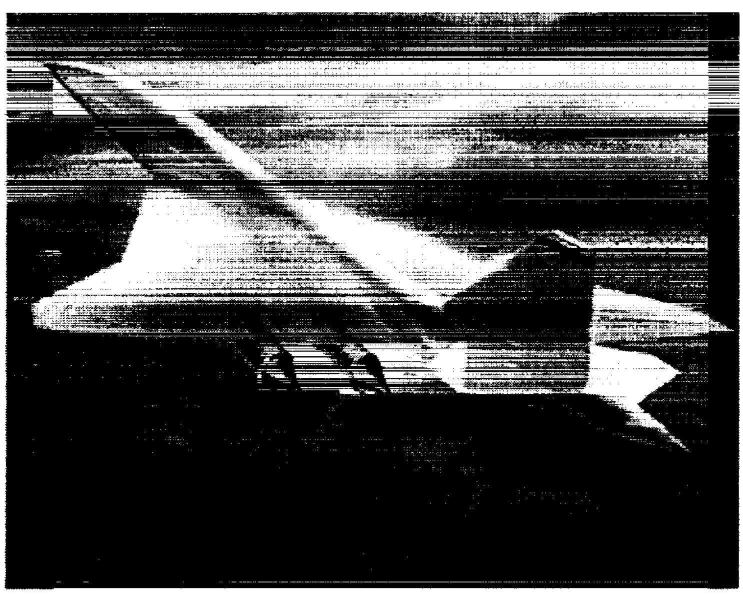

December 1999

The NASA STI Program Office . . . in Profile

Since its founding, NASA has been dedicated to the advancement of aeronautics and space science. The NASA Scientific and Technical Information (STI) Program Office plays a key part in helping NASA maintain this important role.

The NASA STI Program Office is operated by Langley Research Center, the lead center for NASA's scientific and technical information. The NASA STI Program Office provides access to the NASA STI Database, the largest collection of aeronautical and space science STI in the world. The Program Office is also NASA's institutional mechanism for disseminating the results of its research and development activities. These results are published by NASA in the NASA STI Report Series, which includes the following report types:

- TECHNICAL PUBLICATION. Reports of completed research or a major significant phase of research that present the results of NASA programs and include extensive data or theoretical analysis. Includes compilations of significant scientific and technical data and information deemed to be of continuing reference value. NASA counterpart of peer-reviewed formal professional papers, but having less stringent limitations on manuscript length and extent of graphic presentations.
- TECHNICAL MEMORANDUM. Scientific and technical findings that are preliminary or of specialized interest, e.g., quick release reports, working papers, and bibliographies that contain minimal annotation. Does not contain extensive analysis.
- CONTRACTOR REPORT. Scientific and technical findings by NASA-sponsored contractors and grantees.
- CONFERENCE PUBLICATION. Collected papers from scientific and technical conferences, symposia, seminars, or other meetings sponsored or co-sponsored by NASA.
- SPECIAL PUBLICATION. Scientific, technical, or historical information from NASA programs, projects, and missions, often concerned with subjects having substantial public interest.
- TECHNICAL TRANSLATION. English-language translations of foreign scientific and technical material pertinent to NASA's mission.

Specialized services that complement the STI Program Office's diverse offerings include creating custom thesauri, building customized databases, organizing and publishing research results . . . even providing videos.

For more information about the NASA STI Program Office, see the following:

- Access the NASA STI Program Home Page at ***http://www.sti.nasa.gov***
- Email your question via the Internet to help@sti.nasa.gov
- Fax your question to the NASA STI Help Desk at (301) 621-0134
- Telephone the NASA STI Help Desk at (301) 621-0390
- Write to:
  NASA STI Help Desk
  NASA Center for AeroSpace Information
  7121 Standard Drive
  Hanover, MD 21076-1320

NASA/CP-1999-209691/VOL1/PT1

1997 NASA High-Speed Research Program Aerodynamic Performance Workshop

Volume I—Configuration Aerodynamics

Edited by
Daniel G. Baize
Langley Research Center, Hampton, Virginia

Proceedings of a workshop held at
Langley Research Center,
Hampton, Virginia
February 25–28, 1997

National Aeronautics and
Space Administration

Langley Research Center
Hampton, Virginia 23681-2199

December 1999

Available from:

NASA Center for AeroSpace Information (CASI)
7121 Standard Drive
Hanover, MD 21076-1320
(301) 621-0390

National Technical Information Service (NTIS)
5285 Port Royal Road
Springfield, VA 22161-2171
(703) 605-6000

PREFACE

The High-Speed Research Program and NASA Langley Research Center sponsored the NASA High-Speed Research Program Aerodynamic Performance Workshop on February 25–28, 1997. The workshop was designed to bring together NASA and industry High-Speed Civil Transport (HSCT) Aerodynamic Performance technology development participants in areas of Configuration Aerodynamics (transonic and supersonic cruise drag prediction and minimization), High-Lift, Flight Controls, Supersonic Laminar Flow Control, and Sonic Boom Prediction. The workshop objectives were to (1) report the progress and status of HSCT aerodynamic performance technology development; (2) disseminate this technology within the appropriate technical communities; and (3) promote synergy among the scientist and engineers working HSCT aerodynamics. In particular, single- and multi-point optimized HSCT configurations and HSCT high-lift system performance predictions were presented along with executive summarizes for all the Aerodynamic Performance technology areas.

The workshop was organized in three sessions as follows:

Session I	Plenary Session
Session II	Independent Session
Session III	Executive Summaries

The proceedings are published in two volumes:

Volume I, Parts 1 and 2	Configuration Aerodynamics
Volume II	High Lift

Conference Chairmen: Daniel G. Baize and Robert L. Calloway
NASA Langley Research Center

CONTENTS

Volume I, Part 2—Configuration Aerodynamics

Volume II—High Lift

Adams, Jr.
William M.
NASA Langley Research Center
Mail Stop 489
Hampton VA 23681-0001
Ph. 757-864-4013
fax 757-864-7795
eMail: w.m.adams@larc.nasa.gov

Agrawal
Shreekant
McDonnell Douglas Aerospace Co.
Mail Code 71-35
2401 E. Wardlow Road
Long Beach CA 90807-5309
Ph. 562-593-3436
fax 562-593-7593
eMail: agrawal@mdta.mdc.com

Allen
Jerry M.
NASA Langley Research Center
Mail Stop 499
Hampton VA 23681-0001
Ph. 757-864-5592
fax 757-864-4869
eMail: j.m.allen@larc.nasa.gov

Anders
Scott G.
NASA Langley Research Center
Mail Stop 170
Hampton VA 23681-0001
Ph. 757-864-8044
fax 757-864-8801
eMail: s.g.anders@larc.nasa.gov

Anderson
W. Kyle
NASA Langley Research Center
Mail Stop 128
Hampton VA 23681-0001
Ph. 757-864-2164
fax 757-864-8816
eMail: w.k.anderson@larc.nasa.gov

Antani
Tony
McDonnell Douglas Aerospace Co.
Mail Code 71-35
2401 E Wardlow Road
Long Beach CA 90807-5309
Ph. 562-593-3920
fax 562-593-7593
eMail: C362247@mdcpo05.lb.mdc.com

Applin
Zac
NASA Langley Research Center
Mail Stop 286
Hampton VA 23681-0001
Ph. 757-864-5062
fax 757-864-8192
eMail: z.t.applin@larc.nasa.gov

Arslan
Alan
McDonnell Douglas Aerospace Co.
Mail Code 71-35
2401 E. Wardlow Road
Long Beach CA 90807-5309
Ph. 562-593-8535
fax 562-593-7593
eMail: aea@indigo1.mdc.com

Bailey
F. Alan
The Boeing Company
Mail Stop 6H-FK
P.O. Box 3707
Seattle WA 98124-2207
Ph. 206-965-2699
fax 206-234-4543
eMail: frazier.a.bailey@boeing.com

Bailey
Mel
Lockheed Engineering & Sciences Co
NASA Langley Research Center
Mail Stop 389
Hampton VA 23681-0001
Ph. 757-864-4030
fax 757-864-7795
email: m.l.bailey@larc.nasa.gov

Bailey
Randall
Calspan Advanced Tech Center
P.O. Box 400
4455 Genesee Street
Buffalo NY 14225-0400
Ph. 716-631-6939
fax 716-631-6990
eMail: bailey@calspan.com

Baize
Dan
NASA Langley Research Center
Mail stop 119
Hampton VA 23681-0001
Ph. 757-864-1071
fax 757-864-8852
eMail: d.g.baize@larc.nasa.gov

Ball
Doug
The Boeing Company
Mail Stop 6H-FK
P.O. Box 3707
Seattle WA 98124-2207
Ph. 206-965-2151
fax 206-234-4543
eMail: baldnb00@ccmail.ca.boeing.com

Barrett
Mike
Honeywell Inc.
MS: MN65-2810
3660 Technology Drive
Minneapolis MN 55418
Ph. 612-951-7286
fax 612-951-7438
eMail: mike_barrett@htc.honeywell.com

Belcastro
Christine
NASA Langley Research Center
Mail Stop 161
Hampton VA 23681-0001
Ph. 757-864-4035
fax 757-864-7795
eMail:christine.m.belcastro@larc.nasa.go

Bencze
Dan
NASA Ames Research Center
Mail Stop 227-6
Moffett Field CA 94035-1000
Ph. 415-604-6618
fax 415-604-0737
eMail: dbencze@mail.arc.nasa.gov

Bengston
Robert
Pratt & Whitney
Mail Stop 165-21
400 Main St.
East Eartford CT 06108
Ph. 860-565-2080
fax 860-565-0123
eMail: bengtsrj@pweh.com

Bharadvaj
Bala
McDonnell Douglas Aerospace Co.
Mail Code 71-35
2401 E Wardlow Road
Long Beach CA 90807-5309
Ph. 562-593-3514
fax 562-982-7787
eMail: c336381@mail.mdc.com

Borland
Chris
The Boeing Company
Mail Stop 6H-FK
P.O. Box 3707
Seattle WA 98124-2207
Ph. 206-965-0336
fax 206-234-4543
eMail: christopher.j.borland@boeing.com

Bunin
Bruce
McDonnell Douglas Aerospace Co.
Mail Code 71-30
2401 E. Wardlow Road
Long Beach CA 90807-5309
Ph. 562-593-0629
fax 562-982-7383
eMail: bunin@mdta.mdc.com

Buning
Pieter G.
NASA Langley Research Center
Mail Stop 280
Hampton VA 23681-0001
Ph. 757-864-3093
fax 757-864-8195
eMail: p.g.buning@larc.nasa.gov

Burner
Alpheus W.
NASA Langley Research Center
Mail Stop 236
Hampton VA 23681-0001
Ph. 757-864-4635
fax 757-864-7607
eMail: a.w.burner@larc.nasa.gov

Buttrill
Carey
NASA Langley Research Center
Mail Stop 132
Hampton VA 23681-0001
Ph. 757-864-4016
fax 757-864-7795
eMail: c.s.buttrill@larc.nasa.gov

Calloway
Robert
NASA Langley Research Center
Mail Stop 119
Hampton VA 23681-0001
Ph. 757-864-2960
fax 757-864-8852
eMail: r.l.calloway@larc.nasa.gov

Camache
Peter
McDonnell Douglas Aerospace Co.
Mail Code 71-30
2401 E. Wardlow Road
Long Beach CA 90807-5309
Ph. 562-593-7012
fax 562-982-7787
eMail: camacho@mdta.mdc.com

Campbell
Brian A.
NASA Langley Research Center
Mail Stop 286
Hampton VA 23681-0001
Ph. 757-864-5069
fax 757-864-8192
eMail: b.a.campbell@larc.nasa.gov

Campbell
James F.
NASA Langley Research Center
Mail Stop 499
Hampton VA 23681-0001
Ph. 757-864-2866
fax 757-864-8469
eMail: j.f.campbell@larc.nasa.gov

Campbell
Richard L.
NASA Langley Research Center
Mail Stop 499
Hampton VA 23681-0001
Ph. 757-864-2872
fax 757-864-8469
eMail: r.l.campbell@larc.nasa.gov

Capone
Fran J.
NASA Langley Research Center
Mail Stop 280
Hampton VA 23681-0001
Ph. 757-864-3004
fax 757-864-8195
eMail: f.j.capone@larc.nasa.gov

Cappuccio
Mina
NASA Ames Research Center
Mail Stop 227-6
Moffett Field CA 94035-1000
Ph. 415-604-1313
fax 415-604-0737
eMail: mcappuccio@mail.arc.nasa.gov

Chaney
Steve R.
The Boeing Company
Mail Stop 6H-FK
P.O. Box 3707
Seattle WA 98124-2207
Ph. 206-237-2878
fax 206-234-4543
eMail:

Chang
Bor-Chin
Drexel University
Dept. Mechanical Engineering
Philadelphia PA 19104
Ph. 215-895-1790
fax 215-895-1478
eMail: bchang@coe.drexel.edu

Chen
Allen W.
The Boeing Company
Mail Stop 6H-FK
P.O. Box 3707
Seattle WA 98124-2207
Ph. 206-965-3490
fax 206-234-4543
eMail: awc@hsctaero.ca.boeing.com

Cheung
Samson
McDonnell Douglas Aerospace Co.
Mail Code 71-35
2401 E. Wardlow Road
Long Beach CA 90807-5309
Ph. 562-593-9025
fax 562-593-7593
eMail: shc@indigo1.mdc.com

Christhilf
David M.
Lockheed Engineering & Sciences Co.
NASA Langley Research Center
Mail Stop 389
Hampton VA 23681-00
Ph. 757-864-4029
fax 757-864-8838
eMail: d.m.christhilf@larc.nasa.gov

Chu
Julio
NASA Langley Research Center
Mail Stop 248
Hampton VA 23681-0001
Ph. 757-864-5136
fax 757-864-3553
eMail: j.chu@larc.nasa.gov

Clark
Roger
McDonnell Douglas Aerospace Co.
Mail Code 71-35
2401 E Wardlow Road
Long Beach CA 90807-5309
Ph. 562-982-5334
fax 562-593-7593
eMail: c08375@mdcpo17.lb.mdc.com

Cliff
Susan
NASA Ames Research Center
Mail Stop 227-6
Moffett Field A 94035-1000
Ph. 415-604-3907
fax 415-604-0737
eMail: cliff@ra-iris.arc.nasa.gov

Coen
Peter
NASA Langley Research Center
Mail Stop 248
Hampton VA 23681-0001
Ph. 757-864-5991
fax 757-864-3553
eMail: p.g.coen@larc.nasa.gov

Conner
Roy S.
The Boeing Company
Mail Stop 6H-FK
P.O. Box 3707
Seattle WA 98124-2207
Ph. 206-965-3774
fax 206-234-4543
eMail: rsc7463@hsctaero.ca.boeing.com

Cuthbertson
R. D.
The Boeing Company
Mail Stop 6H-FR
P.O. Box 3707
Seattle WA 98124-2207
Ph. 206-237-7594
fax 206-234-4543
eMail: robert.d.cuthbertson@boeing.com

Darden
Christine
NASA Langley Research Center
Mail Stop 119
Hampton VA 23681-0001
Ph. 757-864-5258
fax 757-864-8852
eMail: c.m.darden@larc.nasa.gov

Deere
Karen A.
NASA Langley Research Center
Mail Stop 280
Hampton VA 23681-0001
Ph. 757-864-8986
fax 757-864-8195
eMail: k.a.deere@larc.nasa.gov

DeLoach
Richard
NASA Langley Research Center
Mail Stop 236
Hampton VA 23681-0001
Ph. 757-864-4657
fax 757-864-7607
eMail: r.deloach@larc.nasa.gov

Derry
Steve
NASA Langley Research Center
Mail Stop 125B
Hampton VA 23681-0001
Ph. 757-864-7412
fax 757-864-8837
eMail: s.d.derry@larc.nasa.gov

Domack
Christopher S.
Lockheed Engineering & Sciences Co.
NASA Langley Research Center
Mail Stop 248
Hampton VA 23681-0001
Ph. 757-864-6504
fax 757-864-3553
eMail: domack@avd00.larc.nasa.gov

Duffy
Keith S.
The Boeing Company
Mail Stop 6H-FA
P.O. Box 3707
Seattle WA 98124-2207
Ph. 206-965-0116
fax 206-234-4543
eMail: keith@brazil.ca.boeing.com

Ebner
N. Keith
The Boeing Company
Mail Stop 6H-FK
P.O. Box 3707
Seattle WA 98124-2207
Ph. 206-965-0198
fax 206-234-4543
eMail: keith.ebner@boeing.com

Elgersma
Mike
Honeywell Inc.
MS: MN 65-2810
3660 Technology Drive
Minneapolis MN 55418
Ph. 612-951-7208
fax 612-951-7438
eMail: mike_elgersma@htc.honeywell.com

Erickson
Gary E.
NASA Langley Research Center
Mail Stop 413
Hampton VA 23681-0001
Ph. 757-864-2886
fax 757-864-8095
eMail: g.e.erickson@larc.nasa.gov

Fan
Xuetong
ASE Technologies Inc.
Suite 203
4015 Exeuctive Park Drive
Cincinnati OH 45241
Ph. 513-563-8855
fax 513-563-8865
eMail: fan@mars.asetach.com

Feifel
Winfried M.
The Boeing Company
Mail Stop 6H-FK
P.O. Box 3707
Seattle WA 98124-2207
Ph. 206-965-0561
fax 206-234-4543
eMail:

Fenbert
James W.
NASA Langley Research Center
Mail Stop 248
Hampton VA 23681-0001
Ph. 864-5973
fax
eMail: j.w.fenbert@larc.nasa.gov

Funk
Joan G.
NASA Langley Research Center
Mail Stop 119
Hampton VA 23681-0001
Ph. 757-864-3092
fax 757-864-8852
eMail: j.g.funk@larc.nasa.gov

Garg
Sanjay
NASA Lewis Research Center
Mail Stop 77-1
21000 Brookpark Road
Cleveland OH 44135
Ph. 216-433-2685
fax 216-433-8643
eMail: sanjay.garg@lerc.nasa.gov

Ghaffari
F.
NASA Langley Research Center
Mail Stop 499
Hampton VA 23681-0001
Ph. 757-864-2856
fax 757-864-8469
eMail: f.ghaffari@larc.nasa.gov

Giesy
Dan
Lockheed Engineering & Sciences Co.
NASA Langley Research Center
Mail Stop 389
Hampton VA 23681-0001
Ph. 757-864-4006
fax 757-864-8838
eMail: d.p.giesy@larc.nasa.gov

Gilbert
Bill
NASA Langley Research Center
Mail Stop 119
Hampton VA 23681-0001
Ph. 757-864-6392
fax 757-864-8852
eMail: w.p.gilbert@larc.nasa.gov

Glaab
Louis
Lockheed Engineering & Sciences Co.
NASA Langley Research Center
Mail Stop 343
Hampton VA 23681-0001
Ph. 757-864-1159
fax 757-864-7722
eMail: l.j.glaab@larc.nasa.gov

Goldberg
Perry
McDonnell Douglas Aerospace Co.
Mail Code 71-35
2401 E. Wardlow Road
Long Beach CA 90807-5309
Ph. 562-982-2126
fax 562-593-7593
eMail: goldbet@citm.mdc.com

Gracey
Chris
NASA Langley Research Center
Mail Stop 161
Hampton VA 23681-0001
Ph. 757-864-4019
fax 757-864-7795
eMail: c.gracey@larc.nasa.gov

Green
Lawrence L.
NASA Langley Research Center
Mail Stop 159
Hampton VA 23681-0002
Ph. 757-864-2228
fax 757-864-9713
eMail: l.l.green@larc.nasa.gov

Gregory
Irene
NASA Langley Research Center
Mail Stop 132
Hampton VA 23681-0001
Ph. 757-864-4075
fax 757-864-7795
eMail: i.m.gregory@larc.nasa.gov

Greiner
Glenn P.
George Washington University
NASA Langley Research Center
Mail Stop 132
Hampton VA 23681-0001
Ph. 757-864-4086
fax 757-864-7795
eMail: g.p.greiner@larc.nasa.gov

Griffiths
Robert C.
The Boeing Company
Mail Stop 6H-FK
P.O. Box 3707
Seattle WA 98124-2207
Ph. 206-965-3465
fax 206-234-4543
eMail: robert.c.griffiths@boeing.com

Gumbert
Clyde R.
NASA Langley Research Center
Mail Stop 159
Hampton VA 23681-0001
Ph. 757-864-2221
fax 757-864-9713
eMail: c.r.gumbert@larc.nasa.gov

Hager
James
McDonnell Douglas Aerospace Co.
Mail Code 71-35
2401 E. Wardlow Road
Long Beach CA 90807-5309
Ph. 562-982-9217
fax 562-593-7593
eMail: joh@indigo1.mdc.com

Hahne
Dave
NASA Langley Research Center
Mail Stop 153
Hampton VA 23681-0001
Ph. 757-864-1162
fax 757-864-7722
eMail: d.e.hahne@larc.nasa.gov

Halberg
Eric N.
Naval Postgraduate School
Mail Code 31
Halligan Hall
Monterey CA 93940
Ph. 408-656-5040
fax 408-656-2313
eMail: hallberg@aa.nps.navy.mil

Hamner
Marvine P.
McDonnell Douglas Aerospace Co.
Mail Code S1022272
P.O. Box 516
St Louis MO 63166-0516
Ph. 314-233-1600
fax 314-777-2984
eMail: mph@indigo1.mdc.com

Hartwich
Peter M.
McDonnell Douglas Aerospace Co.
Mail Code 71-35
2401 E. Wardlow Road
Long Beach CA 90807-4418
Ph. 562-593-2965
fax 562-593-7593
eMail: pmh@indigo1.mdc.com

Henderson
Dennis K.
McDonnell Douglas Aerospace Co.
Mail Code 71-35
2401 E Wardlow Road
Long Beach CA 90807-5309
Ph. 562-982-9269
fax 562-593-7593
eMail: dhenderson@c17m.mdc.com

Hickey
Paul K.
ASE Technologies, Inc.
Suite 203
4015 Executive Park Drive
Cincinnati OH 45241
Ph. 513-563-8855
fax 513-563-8865
eMail: phickey@asetech.com

Hines
Dick
Pratt & Whitney
Mail Stop 165-22
400 Main St.
East Hartford CT 06108
Ph. 860-565-7239
fax 860-565-0168
eMail: hinesrw@pwfl.com

Jackson
Bruce
NASA Langley Research Center
Mail Stop 132
Hampton VA 23681-0001
Ph. 757-864-4060
fax 757-864-7795
eMail: e.b.jackson@larc.nasa.gov

Jackson
Mike
Honeywell Inc.
MS: MN 65-2810
3660 Technology Drive
Minneapolis MN 55418
Ph. 612-951-7748
fax 612-951-7438
eMail: mike_jackson@htc.honeywell.com

Jager
Merle L.
McDonnell Douglas Aerospace Co.
Mail Code 71-30
2401 E. Wardlow Road
Long Beach CA 90807-5309
Ph. 562-593-4003
fax 562-982-7787
eMail: C391818@mdcpo10.lb.mdc.com

Joshi
Suresh
NASA Langley Research Center
Mail Stop 132
Hampton VA 23681-0001
Ph. 757-964-6608
fax 757-864-7795
eMail: s.m.joshi@larc.nasa.gov

Joslin
Ron
NASA Langley Research Center
Mail Stop 170
Hampton VA 23681-0001
Ph. 757-864-2234
fax 757-864-8801
eMail: r.d.joslin@larc.nasa.gov

Kaminer
Issac I.
Naval Postgraduate School
Mail Code AA/KA
Monterey CA 93943
Ph. 408-656-5040
fax 408-656-2313
eMail: kaminer@aa.nps.navy.mil

Kandula
Max
Dynacs Engineering Co., Inc.
Building 3, Suite B
258 S.W. 43rd
Renton WA 98055
Ph. 206-251-8692
fax 206-251-9564
eMail: kandula@vm.nas.gov

Kemmerly
Guy T.
NASA Langley Research Centr
Mail Stop 286
Hampton VA 23681-0001
Ph. 757-864-5070
fax 757-864-8192
eMail: g.t.kemmerly@larc.nasa.gov

Kennelly
Robert A.
NASA Ames Research Center
Mail Stop 227-6
Moffett Field CA 94035-1000
Ph. 415-604-5860
fax 415-604-0737
eMail: rakennelly@mail.arc.nasa.gov

Kinard
Tom A.
Lockheed Martin
86 South Cobb Drive
Mail Code 0685
Marietta GA 30063-0685
Ph. 770-494-8588
fax 770-494-3055
eMail: kinard@mar.lmco.com

Klopter
Goetz H.
MCAT, Inc.
NASA Ames Research Center
Mail Stop 258-1
Moffett Field CA 94035-1000
Ph. 415-604-3993
fax 415-604-2238
eMail: klopter@nas.nasa.gov

Kobayashi
Takahisa
NASA Lewis Research Center
Mail Stop 77-1
21000 Brookpark Road
Cleveland OH 44135-3191
Ph. 216-433-3739
fax 216-433-8643
eMail: tak@lerc.nasa.gov

Krause
Fred
General Electric
Mail Drop T34
1 Neumann Way
Cincinnati OH 45215-1988
Ph. 513-552-4279
fax 513-552-4350
eMail: fred.h.krause@ae.ge.com

Krist
Steven E.
NASA Langley Research Center
Mail Stop 280
Hampton VA 23681-0001
Ph. 757-864-3046
fax
eMail: s.e.krist@larc.nasa.gov

Kubiatko
Paul
McDonnell Douglas Aerospace Co.
Mail Code 71-35
2401 E. Wardlow Road
Long Beach CA 90807-5309
Ph. 562-982-7850
fax 562-593-7593
eMail: kubiatko@mdta.mdc.com

Kulfan
Bob
The Boeing Company
Mail Stop 6H-FK
P.O. Box 3707
Seattle WA 98124-2207
Ph. 206-965-3779
fax 206-234-4543
eMail: robert.m.kulfan@boeing.com

Kwatny
Harry
Drexel University
Dept Mechanical Engineering
Philadelphia PA 19104
Ph. 215-895-2356
fax 215-895-1478
eMail: hkawtny@coe.drexel.edu

Lawrence
Scott
NASA Ames Research Center
Mail Stop T27-B-2
Moffett Field CA 94035-1000
Ph. 415-604-4050
fax 415-604-1095
eMail: lawrence@nas.nasa.gov

Leavitt
Larry
NASA Langley Research Center
Mail Stop 280
Hampton VA 23681-0001
Ph. 757-864-3017
fax 757-864-8195
eMail: l.d.leavitt@larc.nasa.gov

Lessard
Victor R.
VIGYAN
30 Research Drive
Hampton VA 23666-1325
Ph. 757-864-5072
eMail: v.r.lessard@larc.nasa.gov.

Lessard
Wendy
NASA Langley Research Center
Mail Stop 286
Hampton VA 23681-0001
Ph. 757-864-1165
fax 757-864-8192
eMail: w.b.lessard@larc.nasa.gov

Light
Bruce A.
The Boeing Company
Mail Stop 6H-FP
P.O. Box 3707
Seattle WA 98124-2207
Ph. 206-965-1934
fax 206-234-4543
eMail:

Lin
Kyong
NASA Langley Research Center
Mail Stop 161
Hampton VA 23681-0001
Ph. 757-864-4342
fax 757-864-7797
eMail: k.b.lim@larc.nasa.gov

Liu
Tianshu
High Technology Corporation
28 Research Drive
Hampton VA 23666
Ph. 757-865-6766
eMail: tianshu@htc.tech.com

Ludas
Kevin
McDonnell Douglas Aerospace Co.
Mail Code 71-30
2401 E Wardlow Road
Long Beach CA 90807-5309
Ph. 562-593-2889
fax 562-982-7383
eMail: ludas@mdta.mdc.com

Lund
David W.
The Boeing Company
Mail Stop 6H-FK
P.O. Box 3707
Seattle WA 98124-2207
Ph. 206-965-2151
fax 206-234-4543
eMail: david.w.lund@boeing.com

MacKinnon
Malcolm I.K.
The Boeing Company
Mail Stop 6H-FM
P.O. Box 3707
Seattle WA 98124-2207
Ph. 206-237-0339
fax 206-234-4543
eMail: malcolm.i.mackinnon@boeing.com

MacWilkinson
Derek G.
McDonnell Douglas Aerospace Co.
Mail Code 71-30
2401 E. Wardlow Road
Long Beach CA 90807-5309
Ph. 562-496-8723
fax 562-982-7383
eMail: dmacw@mdta.mdc.com

Maddalon
Dal V.
NASA Langley Research Center
Mail Stop 170
Hampton VA 23681-0001
Ph. 757-864-1909
fax 757-864-8801
eMail: d.v.maddalon@larc.nasa.gov

Martin
Grant L.
McDonnell Douglas Aerospace Co.
Mail Code 71-35
2401 E. Wardlow Road
Long Beach CA 90807-5309
Ph. 562-593-0040
fax 562-593-7593
eMail: glm@indigo1.mdc.com

McMillin
S. Naomi
NASA Langley Research Center
Mail Stop 499
Hampton VA 23681-0001
Ph. 757-864-5581
fax 757-864-8469
eMail: s.n.mcmillin@larc.nasa.gov

McMinn
Dana
NASA Langley Research Center
Mail Stop 132
Hampton VA 23681-0001
Ph. 757-864-4069
fax 757-864-7795
eMail: j.d.mcminn@larc.nasa.gov

Mejia
Kevin K.
The Boeing Company
Mail Stop 6H-FK
P.O. Box 3707
Seattle WA 98124-2207
Ph. 206-965-3773
fax 206-234-4543
eMail: devin.m.mejia@boeing.com

Meredith
Paul T.
The Boeing Company
Mail Stop 6H-FK
P.O. Box 3707
Seattle WA 98124
Ph. 206-965-3468
fax 206-234-4543
eMail: paul.t.meredith@ca.boeing.com

Morgenstern
John
McDonnell Douglas Aerospace Co.
Mail Code 71-30
2401 E Wardlow Road
Long Beach CA 90807-5309
Ph. 562-982-9276
fax 562-982-7787
eMail: morgenstern@mdta.mdc.com

Morris
Martin J.
McDonnell Douglas Aerospace Co.
Mail Code 106-7126
P.O. Box 516
St. Louis MO 63166-0516
Ph. 314-232-6939
fax 314-777-1328
eMail: mmorris@mdc.com

Mortlock
Alan
McDonnell Douglas Aerospace Co.
Mail Code 71-30
2401 E Wardlow Road
Long Beach CA 90807-5309
Ph. 562-593-3937
fax 562-982-7787
eMail: mortlock@mdta.mdc.com

Narducci
Robert
McDonnell Douglas Aerospace Co.
Mail Code 71-35
2401 E. Wardlow Road
Long Beach CA 90807-5309
Ph. 562-593-0171
fax 562-593-7593
eMail: rpn@indigo1.mdc.com

Nelms, Jr.
Pres
NASA Ames Research Center
Mail Stop 237-2
Moffett Field CA 94035-1000
Ph. 415-604-6093
fax 415-604-6990
eMail: p_nelms@qmgate.arc.nasa.gov

Nelson
Chester P.
The Boeing Company
Mail Stop 6H-FK
P.O. Box 3707
Seattle WA 98124-2207
Ph. 206-965-5514
fax 206-234-4543
eMail: chester.p.nelson@boeing.com

Newman
Brett
Old Dominion University
Ph. 757-683-3720
fax 757-683-3200

Owens
Lewis
NASA Langley Research Center
Mail Stop 286
Hampton VA 23681-0001
Ph. 757-864-5127
fax 757-864-8192
eMail: l.r.owens@larc.nasa.gov

Ozoroski
L. P.
NASA Langley Research Center
Mail Stop 248
Hampton VA 23681-0001
Ph. 757-864-5992
fax 757-864-3553
eMail: l.p.ozoroski@larc.nasa.gov

Pao
S. Paul
NASA Langley Research Center
Mail Stop 280
Hampton VA 23681-0001
Ph. 757-864-3044
fax 757-864-8195
eMail: s.p.pao@larc.nasa.gov

Patton
Robert E.
The Boeing Company
Mail Stop 6H-FK
P.O. Box 3707
Seattle WA 98124-2207
Ph. 206-965-1425
fax 206-234-4543
eMail: robert.e.patton@boeing.com

Peavey
Charles C.
Northrop Grumman Corp.
Mail Code 9B52/GK
8900 E. Washington Blvd.
Pico Rivera CA 90660
Ph. 562-948-8937
fax 562-948-8068
eMail: cpeavey@world.northgrum.com

Pittman
James L.
NASA Langley Research Center
Mail Stop 395
Hampton VA 23681-0001
Ph. 757-864-1361
fax 757-864-8193
eMail:

Polito
Ryan C.
McDonnell Douglas Aerospace Co.
Mail Code 71-35
2401 E. Wardlow Road
Long Beach CA 90807-5309
Ph. 562-593-0048
fax 562-593-7593
eMail: rp@indigo1.mdc.com

Popernack, Jr.
Thomas G.
NASA Langley Research Center
Mail Stop 267
Hampton VA 23681-0001
Ph. 757-864-5163
fax
eMail: t.g.popernack.jr@larc.nasa.gov

Pototzky
Anthony S.
NASA Langley Research Center
Mail Stop 389
Hampton VA 23681-0001
Ph. 757-864-2827
fax 757-864-8838
eMail: a.s.pototzky@larc.nasa.gov

Powell
Art
McDonnell Douglas Aerospace Co.
Mail Code 71-35
2401 E. Wardlow Road
Long Beach CA 90807-5309
Ph. 562-593-3225
fax 562-593-7593
eMail: C306624@mdcpo11.lb.md.com

Proffitt
Melissa
Lockheed Engineering and Sciences Co.
NASA Langley Research Center
Mail Stop 389
Hampton VA 23681-0001
Ph. 757-864-4024
fax 757-864-7795
eMail: m.s.proffitt@larc.nasa.gov

Radeztsky
Ronald
High Technology Corporation
28 Research Drive
Hampton VA 23666
Ph. 757-865-0818
fax 757-865-6766
eMail: ron@htc.tech.com

Raney
David
NASA Langley Research Center
Mail Stop 489
Hampton VA 23681-0001
Ph. 757-864-4033
fax 757-864-7795
eMail: d.l.raney@larc.nasa.gov

Ray
James K.
The Boeing Company
Mail Stop 6H-FA
P.O. Box 3707
Seattle WA 98124-2207
Ph. 206-965-1997
fax 206-234-4543
eMail: james.k.ray@.boeing.com

Reuther
James
RIACS
NASA Ames Research Center
Mail Stop 227-6
Moffett Field CA 94035-1000
Ph. 415-604-1516
fax 415-604-0737
eMail: reuther@ra.iris-arc.nasa.gov

Ricketts
Rodney H.
NASA Langley Research Center
Mail Stop 119
Hampton VA 23681-0001
Ph. 757-864-1209
fax 757-864-8852
eMail: r.h.ricketts@larc.nasa.gov

Rimlinger
Mark J.
Sterling Software, Inc.
NASA Ames Research Center
Mail Stop 227-6
Moffett Field CA 94035-1000
Ph. 757-864=5944
fax 757-864-0737
eMail: rimlinge@ra-iris.arc.nasa.gov

Rivers
Melissa B.
NASA Langley Research Center
Mail Stop 499
Hampton VA 23681-0001
Ph. 757-864-5161
fax 757-864-7892
eMail: m.b.rivers@larc.nasa.gov

Rivers
Rob
NASA Langley Research Center
Mail Stop 132
Hampton VA 23681-0001
Ph. 757-864-3917
fax 757-864-8549
eMail: r.a.rivers@larc.nasa.gov

Roberts
Thomas W.
NASA Langley Research Center
Mail Stop 128
Hampton VA 23681-0001
Ph. 757-864-6804
fax 757-864-8166
eMail: t.w.roberts@larc.nasa.gov

Rossitto
Ken
McDonnell Douglas Aerospace Co.
Mail Code 36-41
2401 E Wardlow Road
Long Beach CA 90807-5309
Ph. 562-593-3870
fax 562-593-7593
eMail: rossitto@mdta.mdc.com

Saladino
Anthony J.
Dynacs Engineering Co., Inc.
Building 3, Suite B
258 S.W. 43rd Street
Renton WA 98055
Ph. 206-251-8692
fax 206-251-9564
eMail: saladino@indyl.dynacsgen.com

Sawyer
Wallace C.
NASA Langley Research Center
Mail Stop 119
Hampton VA 23681-0001
Ph 757-864-2267
fax 757-864-8852
Email: w.c.sawyer@larc.nasa.gov

Scott
Michael
NASA Langley Research Center
Mail Stop 132
Hampton VA 23681-0001
Ph. 757-864-6618
fax 757-864-7795
eMail: michael.allen.scott@larc.nasa.gov

Shaw
Joe
NASA Lewis Research Center
Mail Stop 60-2
21000 Brookpark Road
Cleveland OH 44135-3191
Ph. 216-977-7135
fax 216-977-7133
eMail: robert.j.shaw@lerc.nasa.gov

Shields
Bill
Lockheed Engineering & Sciences Co.
NASA Langley Research Center
Mail Stop 248
Hampton VA 23681-0001
Ph. 757-864-5958
fax 757-864-5958
eMail: c.w.shields@larc.nasa.gov

Siclari
Michael J.
Northrop Grumman Corp.
Mail Stop KO8-14
South Oyster Bay Road
Bethpage NY 11714
Ph. 516-575-8067
fax 516-346-2937
eMail: siclari@gateway.grumman.com

Smith
Brian
NASA Ames Research Center
Mail Stop 247-2
Moffett Field CA 94035-3191
Ph. 415-604-6669
fax 415-604-3489
eMail: bsmith@mail.arc.nasa.gov

Snyder
Phil
NASA Ames Research Center
Mail Stop 237-2
Moffett Field CA 94035-1000
Ph. 415-604-4592
fax 415-604-6990
eMail: p.t.snyder@mail.arc.gov

Sundaram
Pichuraman
McDonnell Douglas Aerospace Co.
Mail Code 71-35
2401 E. Wardlow Road
Long Beach CA 90807-5309
Ph. 562-496-9787
fax 562-593-7593
ps@indigo1.mdc.com

Tamrat
Befecadu
Boeing North American Inc.
Mail Code Sk12
2600 Westminster Blvd.
Seal Beach CA 90740
Ph. 310-797-4948
fax 310-797-4854
eMail: bftamrat@naa.boeing.com

Thomas
James L.
NASA Langley Research Center
Mail Stop 128
Hampton VA 23681-0001
Ph. 757-864-2163
fax 757-864-8816
eMail: j.l.thomas@larc.nasa.gov

Thomas
Scott D.
Sterling Software, Inc.
NASA Ames Research Center
Mail Stop 237-2
Moffett Field CA 94035-1000
Ph. 415-604-6387
fax 415-604-6990
eMail: thomas@nas.nasa.gov.

Troha
William A.
NASA Lewis Research Center
Mail Stop 86-1
21000 Brookpark Road
Cleveland OH 44135-3191
Ph. 216-433-3195
fax 216-433-6624
eMail: william.a.troha@lerc.nasa.gov

Unger
Eric R.
McDonnell Douglas Aerospace Co.
Mail Code 71-35
2401 E. Wardlow Road
Long Beach CA 90807-5309
Ph. 562-593-3037
fax 562-593-7593
eMail: c386821@hc1038.mdc.com

Vasquez
Moises
George Washington University
NASA Langley Research Center
Mail Stop 286
Hampton VA 23681-0001
Ph.
Fax
eMail: vasquez@ab80.larc.nasa.gov

Vatsa
Veer N.
NASA Langley Research Center
Mail Stop 128
Hampton VA 23681-0001
Ph. 757-864-2236
fax 757-864-8816
eMail: v.n.valsa@larc.nasa.gov

Viars
Philip
General Electric
Mail Drop T34
1 Neumann Way
Cincinnati OH 45215-1988
Ph. 513-552-4132
fax 513-552-4350
eMail: Philip.Viars@ae.ge.com

Wahls
Richard A.
NASA Langley Research Center
Mail Stop 499
Hampton VA 23681-0001
Ph. 757-864-5108
fax 757-864-8469
eMail: r.awahls@larc.nasa.gov

Wallace
Hoyt
McDonnell Douglas Aerospace Co.
Mail Code S270-2370
P.O. Box 516
St Louis MO 53166-0516
Ph. 314-233-7712
fax 314-234-7210
eMail: hwallace@mdc.com

Walsh
Michael J.
NASA Langley Research Center
Mail Stop 170
Hampton VA 23681-0001
Ph. 757-864-5542
fax 757-864-7897
eMail: m.j.walsh@larc.nasa.gov

Wechsler
Jim
McDonnell Douglas Aerospace Co.
Mail Code 71-35
2401 E. Wardlow Road
Long Beach CA 90807-5309
Ph. 562-496-7627
fax 562-982-7787
eMail: jwex@mdta.mdc.com

Westra
Bryan W.
Northrop Grumman Corp.
Mail Code 9B52/GK
8900 E. Washington Blvd.
Pico Rivera CA 90660
Ph. 562-948-7560
fax 562-948-8068
eMail: bwestra@world.northgrum.com

Whitehead
Allen H. Jr.
NASA Langley Research Center
Mail Stop 119
Hampton VA 23681-0001
Ph. 757-864-7800
fax 757-864-8852
eMail: allen.h.whitehead@larc.nasa.gov

Wilhite
Alan W.
NASA Langley Research Center
Mail Stop 119
Hampton VA 23681-0001
Ph. 757-864-2982
fax 757-864-8852
eMail: a.w.wilhite@larc.nasa.gov

Williams
Todd
McDonnell Douglas Aerospace Co.
Mail Code 71-12
2401 E. Wardlow Road
Long Beach CA 90807-5309
Ph. 562-496-8795
fax 562-496-9244
eMail: twilliams@mdta.mdc.com

Wilson
Doug
The Boeing Company
Mail Stop 6H-FK
P.O. Box 3707
Seattle WA 98124-2207
Ph. 206-965-3458
fax 206-234-4543
eMail: douglas.l.wilson@boeing.com

Wittenberg
K. Robyn
The Boeing Company
Mail Stop 6H-FK
P.O. Box 3707
Seattle WA 98124-2207
Ph. 206-965-1091
fax 206-234-4543
eMail:

Woan
Chung-Jin
Boeing North American, Inc.
Mail Code SK07
P.O. Box 3644
Seal Beach CA 90740-7644
Ph.
fax
eMail

Wood
Rick
NASA Langley Research Center
Mail Stop 499
Hampton VA 23681-0001
Ph. 757-864-6174
fax 757-864-8469
eMail:

Wyatt
Greg
The Boeing Company
Mail Stop 6H-FK
P.O. Box 3707
Seattle WA 98124-2207
Ph. 206-965-3466
fax 206-234-4543
eMail: douglas.l.wilson@boeing.com

Yaghmaee
Sasan S.
The Boeing Company
Mail Stop 6H-FK
P.O. Box 3707
Seattle WA 98124-2207
Ph. 206-965-3777
fax 206-234-4543
eMail: sasan.yagmaee@boeing.com

Yaros
Steven
NASA Langley Research Center
Mail Stop 286
Hampton VA 23681-0001
Ph. 757-864-3050
fax 757-864-8192
eMail: s.f.yaros@larc.nasa.gov

Yeh
David T.
McDonnell Douglas Aerospace Co.
Mail Code 71-35
2401 E. Wardlow Road
Long Beach CA 90807-5309
Ph. 562-496-9113
fax 562-593-7593
eMail: dty@indigo1.mdc.com

Zuniga
Fanny
NASA Ames Research Center
Mail Stop 247-2
Moffett Field CA 94035-1000
Ph. 415-604-2017
fax 415-604-3489
eMail: fzuniga@mail.arc.nasa.gov

Overview of MDC Configuration Aerodynamics Activities

Shreekant Agrawal

McDonnell Douglas Corporation
Long Beach, California

NASA/Industry HSR Aerodynamics Performance Workshop
February 25-28, 1997
NASA Langley Research Center, Hampton, VA

Funded Subtasks to MDC Under PCD II (FY96)

WBS	Subtask Description
4.3.1.1	Nonlinear Rigid and Aeroelastic Analysis Methods
4.3.1.1.1	Rigid Full Configuration Force and Moments
	Valid. of Structured Multizone Method (Supersonic)
	Parallel Processing (CFL3D)
4.3.1.1.2	Inviscid Aeroelastic Analysis
	Implement/Valid. nonlinear Aeroelastic Flow Solver
	Grid Perturbation Scheme for Multizone Grids
4.3.1.2	Aerodynamic Design Optimization Capability
4.3.1.2.1	Nonlinear Cruise Point Design
	Wing Camber/Twist, Fuselage Camber Optim.
	Wing Thickness/Body Shape Optimization
	Viscous Optimization
	Adjoint/ADIFOR Methods
	Geometry Parameterization
	Integrated W/B/N/D Optimization
	Trim Drag Optimization
	Wind-Tunnel Test Support (LaRC NFW Design)

Funded Subtasks to MDC Under PCD II (Cont'd)

WBS	Subtask Description
4.3.1.3	Nacelle/Diverter Design and Airframe Integration
4.3.1.3.1	Assess. of Inlet Flowfield Constraints and Nacelle Integ.
	TCA Assessment
	Nacelle Orientation
4.3.1.3.3	Nacelle/Diverter Design and Integration
	Nacelle/Diverter Shaping
	2-D Nozzle Boattail Drag Study
	Propulsion-Induced Test Program Definition
4.3.1.4	Technology Concept Assessment
4.3.1.4.1	Initial Aerodynamic Performance
	Experimental TCA Evaluation
4.3.1.4.2	Initial Stability and Control Assessment
	Support Baseline Configuration Testing
	Initial Tech Concept S&C Database Development
	Reference H Carryover Test Support
	Alternate Controls Report
	Reference H Assessment Closeout

MDC HSR Configuration Aerodynamics Team

Shreekant Agrawal	Principal Investigator, CFD/Optimization Methods
Tony Antani	Aerodynamics Project Manager/Advisory Role
Alan Arslan	Aeroelastics/CFD Analyses for PAI
Samson H. Cheung	CFD Analysis/Optimization Methods
James O. Hager	CFD Analysis/Optimization Methods
Peter M. Hartwich	Grid Perturbation/Geometry Representation
Dennis Henderson	Stability and Control Studies
Paul Kubiatko	Stability and Control Studies
Geojoe Kuruvila	CFD Analyses/Optimization Methods
Grant Martin	M2.4-7A Opt5 W.T. Data Analysis/CFD Analysis
Todd E. Magee	CFD/W.T. Test Support
Robert P. Narducci	CFD/Optimization Methods/W.T Data Analysis
Michael G. Novean	W.T. Test Support/Data Analysis
Patrick E. Rodi	W.T. Test Support/Data Analysis
Chih Fang Shieh	PAI/Nozzle Boattail Drag Studies
P. Sundaram	PAI/Nozzle Boattail Drag Studies/Parallelization
Eric R. Unger	CFD Analysis/Optimization Methods
Hoyt Wallace	PIE/Nozzle Boattail Drag Studies

Subcontractors:

Lockheed Martin	Stability and Control Studies
Eagle Aeronautics, Inc.	CFD Analysis/Optimization Methods

Enhancements of CFL3Dhp Parallel code and its HSR Applications

P. Sundaram

Mike Novean

Samson Cheung

HSR Aerodynamic Performance Workshop

NASA Langley, February 25-28, 1997

Abstract

This paper presents the recent progress made and the results obtained in the area of parallel computing for the CFD analysis of large HSR configurations. The code used for the present study is CFL3Dhp, a coarse-grain parallel version of the MDC Configuration Aerodynamics group work-horse Euler/Navier-Stokes analysis and nonlinear design code, CFL3D. The original parallelization of the code was carried out by Computer Sciences Corporation under contract from NASA LaRC. The parallel version of the code uses MPI as the message passing language and can be used in a heterogeneous distributed computing environment. Several enhancements to the code have been made at MDC including the addition of a full restart capability as well as making it more user friendly.

The successful application of the code on a parallel platform, the IBM SP-2 system for several HSCT configurations are demonstrated. Also, the application of the code on other shared memory platforms such as Cray C-90 and the J-90 cluster are also highlighted. The results obtained show the promise of using this code for large CFD problems in HSCT analysis and design with rapid turn-around.

Outline

The objectives of this parallelization study is presented followed by a brief historical perspective of the earlier parallel system architectures and the programming environment. Following this, we provide a brief description of the CFL3Dhp code and the improvements that have been made recently. We also describe the pre-processing utilities that have been written to enable a friendly transition of users from a serial to the parallel environment. Next, several application for the TCA configuration analysis using the CFL3Dhp code are presented. Finally, the conclusions and future parallelization plan are described.

Outline

- Objectives
- Parallel platforms and environments
- CFL3Dhp code description
- Pre-processors for CFL3Dhp
- Enhancements to CFL3Dhp
- CFL3Dhp applications
- Conclusions and future work

Objectives

The primary objective of the present study is to reduce the cycle time of large aerodynamic analysis and design problems making use of the progress in the computer hardware and software technologies. In this context, several questions pertaining to why the parallel computing is beneficial are answered. Also, these objectives are directed towards the technology goals needed for the HSCT detailed design phase.

Objectives

- Solve large CFD problems
  - full configuration grids have > 7 million grid points
- Rapid turn-around times
  - W/B/N/D Navier-Stokes / full configuration Euler polar in one day
- Perform nonlinear design with hundreds of design variables
- Efficient use of the available computer resources
- Develop software for emerging large parallel systems for HSR applications

Parallel Platforms and Environments

Prior to describing the present day parallel environment, it is instructive to have an overall understanding of the evolution of the various parallel hardware architectures and their programming environment in the last few years. Some of these systems consisted of the SIMD architectures wherein tens of thousands of simple and inexpensive processors with small local memory were connected together in a hypercube, mesh, or toroidal interconnection networks. The distributed memory MIMD architecture systems had less number of processors and communicated with each other using message passing.

Some of these systems are still in existence and are being used for many applications including CFD. Several others, although very promising with raw CPU power, could not deliver the equivalent of the large shared memory vector processors of the Cray class on real numerical schemes and hence disappeared. In addition, the need for parallel programming ease, scalability, and portability of the parallel codes were the primary reasons for the demise of these wonderful systems.

This chart shows the various NAS parallel systems available and the resources availble under the HSR and HPCCP projects.

Parallel Platforms and Environments

NAS Cray C-90 (vonneumann)	NAS IBM SP-2 (babbage and poseidon)	NAS J-90 Cluster (Newton)	Workstation Cluster
16 CPUs, 8 GBytes Memory 15 GFlops	Up to 200 nodes, 24 GBytes Memory 30 GFlops	24 nodes, 4 GBytes Memory 6 GFlops	unknown
Mulitasking	Message Passing	Mulitasking and Message Passing	Message Passing
Poor turn around	Good turn around	Good turn around	unknown

Multitasking on Shared Memory Vector Supercomputers

The Cray vector supercomputers have provided several systems as a contribution to the parallel architectures. The parallel programming in these systems are primarily through multitasking. However, the parallelization is at loop level and so the parallel efficiency is limited by the conditional "if" blocks inside the loops. Software utilities for parallelization of serial codes can be readily accomplished through *autotasking*; although only a limited spped-up can be realized. For the CFL3D serial code, the *autotasking* speed-up is very poor. Additional hand coding of some of the loops brought the best speed-up to nearly 3.8 for the utilization of 16 processors. It is possible to improve it slightly by additional macrotasking.

Multitasking is the only way that processor memory > 300 Mw can be utilized on the C-90. This approach is taken for the nozzle boattail computations that require a memory of 360 Mw on C-90.

Multitasking on C-90

- Loop level task distribution amongst the processors
  - autotasking helps to extract simple loop level multitasking
  - more loop level task distribution needed to improve speedup
- Parallel efficiency dependent on the system load
  - runs more efficiently with higher priority for multitasking
- Limited speed-ups on multitasked serial codes
  - NAS charging policy helps to alleviate this problem slightly
- Multitasked CFL3D runs poorly (~3.8 / 16 CPUs) on C-90
  - Nearly 20% penalty in CPU time charges

Distributed Computing for CFD

The lessons learnt from the failure of several parallel system architectures identified that message passing is the most practical way for inter-processor communication. The push for software standardization of the parallel programming environment (pvm and MPI) by the HPCCP project resulted in the success of distributed computing. Also, the continuous increase in the processor speed of the workstations and the network hardware bandwidth increases through FDDi and HiPPI hardware, again thanks to HPCCP, enabled the decentralization of CPU power from large and expensive vector supercomputers to clusters. Thus, today's realistic and efficient parallel computing environment was born. Also, the distributed platforms can include heterogeneous computers.

Today's CFD codes are written for multiblock grids and it is natural to extract parallelism in the code through block-to-node mapping. For processor load balancing, a simple static load balancing can itself significantly improve the parallel efficiency.

Distributed Computing for CFD

- Distributed computing environment is most suitable for CFD
- Workstation clusters have a lot of CPU power
- Coarse grain parallel programs are easy to write
- PVM and MPI are platform independent
- Grids are mapped to different nodes for task distribution
- Static load balancing is adequate and easy to achieve

CFL3Dhp Code Description

NASA LaRC initiated the development of a parallel version of the Euler/Navier-Stokes code, CFL3D. CSC developed the early version of the CFL3Dhp code during the middle of 1996. We, at MDC obtained the code and worked on it to render it as a powerful analysis and design tool. The code had several desirable features listed below, but needed testing for realistic grid sizes. The details of the various efforts to use it as a routine analysis tool is described in the following.

CFL3Dhp Code Description

- Euler/Navier-Stokes solver from NASA Langley
- Parallel version of CFL3D suitable for distributed computing - original version by CSC
- Coarse grain parallelism with minimal code modifications
- Host controls the node processors for task distribution
- MPI used for message passing
- Grid blocks mapped to the available number of nodes
- Supports heterogeneous architectures

CFL3Dhp Enhancements

In the process of testing the early version of the code, several changes were made. The most important one is the incorporation of a full multigrid restart capability. Also, minimum distance calculations are included in the main program instead of doing it in the pre-processor. Our experience suggests that the minimum distance calculation by a single node is quite tedious, particularly for the Baldwin-Barth turbulence model.

CFL3Dhp Enhancements

- Full restart capability
- Turbulence models with directed distance calculation by individual processors
- Load balancing by redistributing grid blocks to nodes
- Full compatibility with CFL3D v4.1 including bug fixes

Grid Splitting Strategy

Grids have to be split for task distribution to various nodes. The strategy followed to split the W/B sinlge-block grid is shown below. The same splitter utility can also split any block in a multiblock grid.

Grid Splitting Strategy for CFL3Dhp

TCA wing/body Navier–Stokes grid, 1.5 Million Grid points

- **Original grid was 97x241x65 single zone grid**
- **Split using a splitting code**
  - can cycle over i,j,k as needed
  - output as plot3d file
- **Generate twelve (12) 17x121x65 blocks for best load balancing**
  - split 6 times out the span (i–direction)
  - split twice around the chord (j–direction)

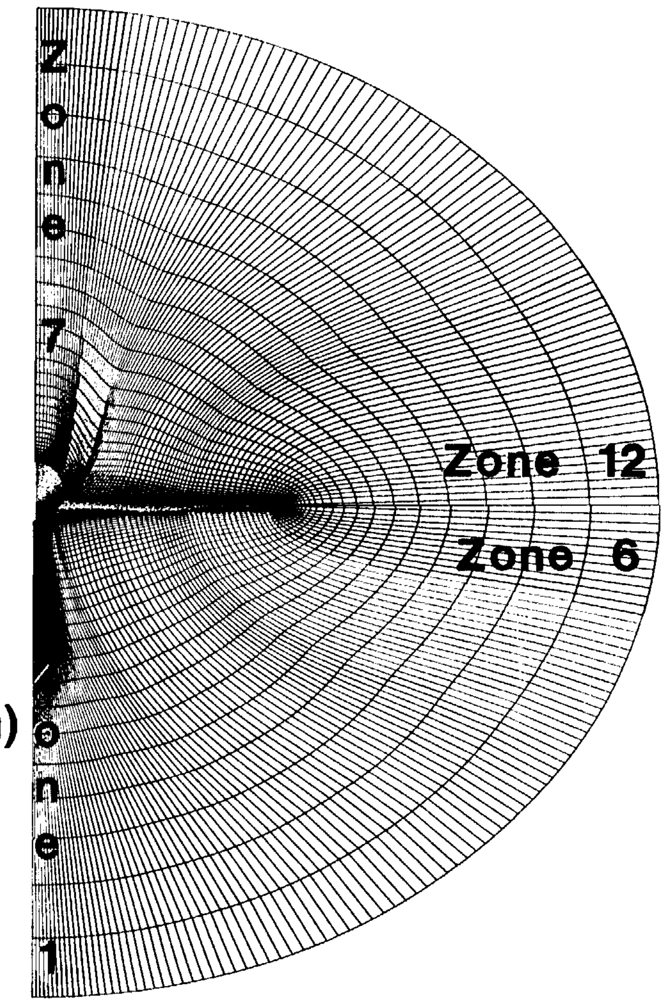

+x direction view of split sample grid

MN 2/17/97
/CA_WORKSHOP/splitgridslide.sho

Load Balancing

Load balancing is performed by combining the various blocks together so that the maximum number of grid points per processor does not exceed a value limited by the processor memory constraints (e.g.,, for CFL3Dhp, the per processor grid points for Baldwin-Lomax turbulence models should be < 200,000.) This process of combining the blocks is carried out for different number of total processors to be used and the best load for a particular combination is chosen.

Load Balancing

- Split single-block grids for load balancing
- Split multiblock grids according to processor memory limitations
- Map multiple blocks to a node based on the task load
- For the given number of nodes for execution, the block-to-node mapping is optimal

Load Balancing of a Multiblock TCA W/B/N/D Grid

This chart shows the load distribution of the 31-block split grid with a predetermined per processor grid size of around 150,000 points (due to processor memory limitations).of the original 22-block TCA baseline W/B/N/D Euler grid. It can be seen that simple block-to-processor mapping yields very poor load distribution amongst the processors. The load balancing software described above combines the blocks for improving the load distribution. Note that the recommended number of nodes is 23 which increases the parallel efficiency by 25%.

Load Distribution for the TCA W/B/N/D Euler Grid

Original Grid Load

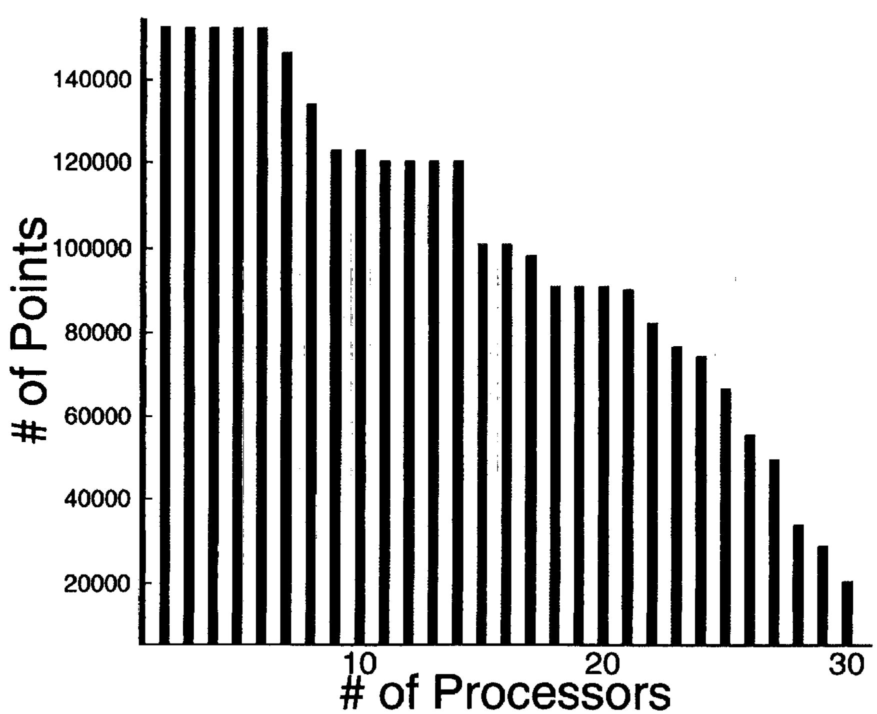

Load Balanced Distribution

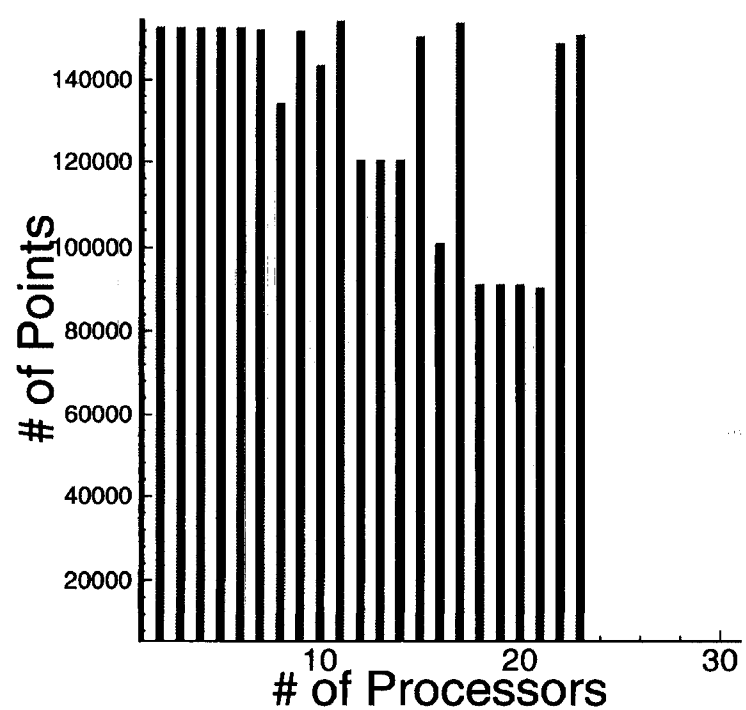

CFL3Dhp Input File Preparation

The input file for CFL3Dhp is similar to its serial version counterpart. However, since the blocks are split, the input file preparation has to be carefully redone. Also, since the blocks that contain non point-matched surfaces are sometimes split, there is an additional complexity in the input file preparation. In addition, this has to be done routinely and automatically to be useful. Since we already have a utility (*precflinp*) to automatically prepare the CFL3D input file at MDC, additional block splitting related modifications to the input file is also included.

CFL3Dhp Input File Preparation

- As in CFL3D, the CFL3Dhp inputs include a grid, flow conditions and boundary conditions input, and grid patch interpolation coefficients
- *precflinp* prepares the basic input file for both CFL3D and ronnie patch interpolation programs
- *precflinp-hp* reads the above input file and prepares the CFL3Dhp input files for the split-block grid automatically

CFL3Dhp Applications on the IBM SP-2

Thus far, several cases of the TCA configuration analysis have been performed on the IBM SP-2. These are designed to not only compare the accuracy of the parallel version of the code but also to test the various aspects of thecode's capabilities. Initially, the TCA W/B configuration is considered to evaluate both the solution accuracy as well as the parallel efficiency of the code. This is followed by the grid sensitivity study for the TCA W/B configuration which indicated the scalability of the problem size whci shows that the program is scalable (within the per processor memory limitations) with respect to per processor load. This study also indicated that for point-matched grid split grids, nearly 200,000 grid points can be mapped to a single SP-2 processor without any degradation of processor performance.

Additional runs to demonstrate the capability to perform routine computations with fast turn-around times such as the W/B Navier-Stokes drag polar for M=1.8 and is given. All these computations have one-to-one patch surfaces between adjacent blocks. The next case is the CFL3Dhp code used for non-point-matched grids for the TCA W/B/E configuration. Additional computations for more complex geometries including TCA W/B/N/D and full configuration analysis using CFL3Dhp are underway.

CFL3Dhp Applications on the IBM SP-2

- TCA W/B Navier-Stokes supersonic cruise analysis
  - accuracy and scalability study for 12 and 16 nodes
- Grid sensitivity study for TCA W/B grids
  - problem size scalability for 12 nodes
- TCA W/B Navier-Stokes analysis for $M_\infty = 1.8$
- 21-block patched grid TCA W/B/E Euler solutions
- TCA W/B/E Navier-Stokes solutions

Residual History (Cray C-90 vs. IBM SP-2)

This chart shows the residual convergence history for the 12-block TCA baseline W/B grid. The 12-block grid was obtained by splitting the original single-block grid using the splitting program and automatically modifying the single-block CFL3D input program suitable for multiblock grid. Note that the convergence histories are not identical between the two systems, Cray C-90 and IBM SP-2. This is due to the difference in the numerical precision of the two systems (C-90 uses 64-bit arithmetic while the IBM SP-2 uses 32-bit arithmetic and operates in double precision). This implies that the IBM SP-2 solutions should run for more iterations for the same level of convergence compared to C-90. The significant random disturbance coming from the block boundaries in the C-90 solutions are less noticeable for the solution obtained on IBM SP-2.

Another important result shown in the chart below are the CPU times for C-90 and 12 and 16 node IBM SP-2. The results show that the speed-up is approximately linear and that nearly 10.5 SP-2 nodes have the same sustained power as the single processor Cray C-90.

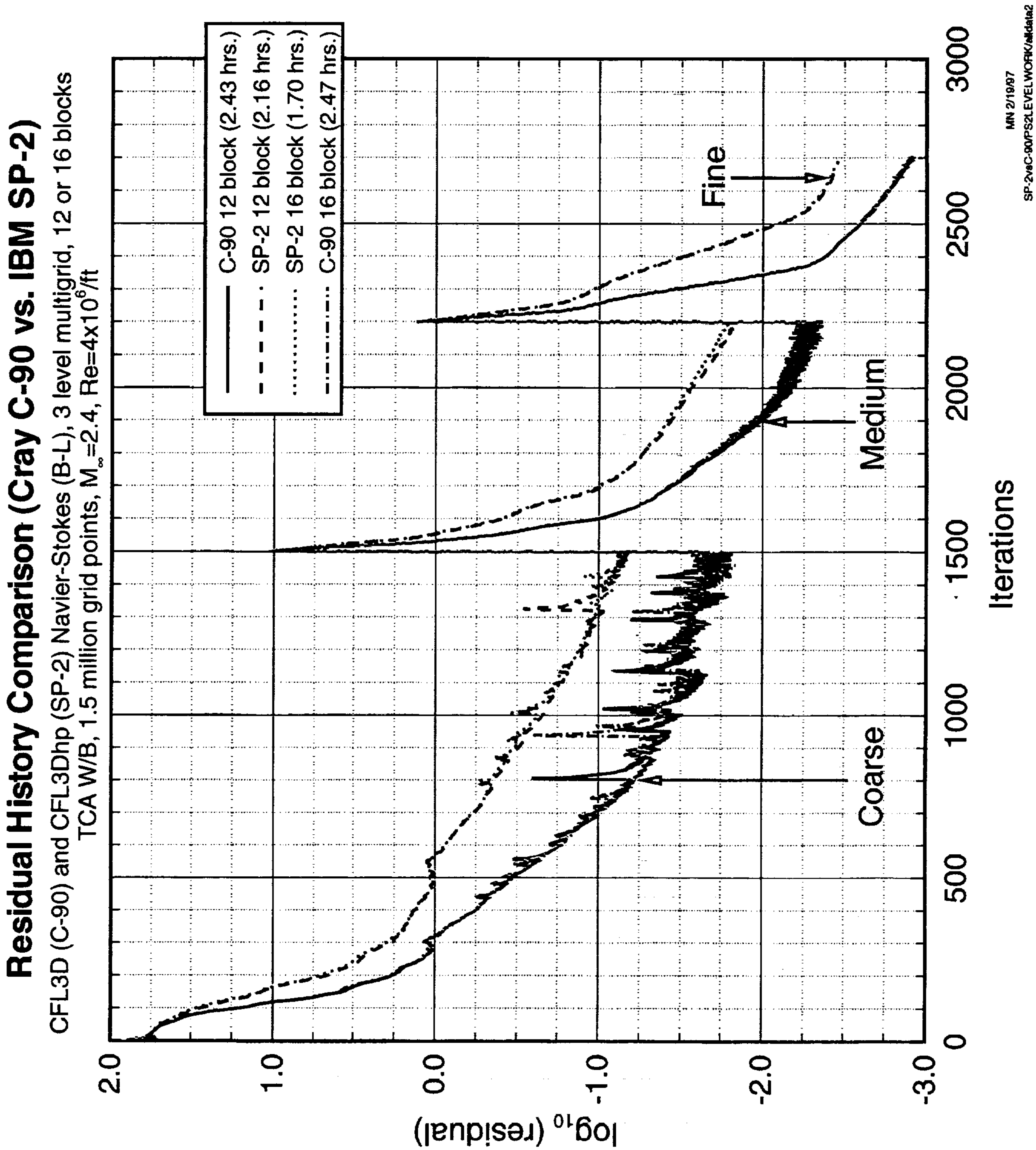

Residual History Comparison (Cray C-90 vs. IBM SP-2)
CFL3D (C-90) and CFL3Dhp (SP-2) Navier-Stokes (B-L), 3 level multigrid, 12 or 16 blocks
TCA W/B, 1.5 million grid points, M∞=2.4, Re=4x10^6/ft
C-90 12 block (2.43 hrs.)
SP-2 12 block (2.16 hrs.)
SP-2 16 block (1.70 hrs.)
C-90 16 block (2.47 hrs.)
Coarse
Medium
Fine
log10 (residual)
Iterations
2.0
1.0
0.0
-1.0
-2.0
-3.0
0
500
1000
1500
2000
2500
3000
MN 2/19/97
SP-2vsC-90/PS2LEVELWORK/alldata2

Drag Convergence History (Cray C-90 vs. IBM SP-2)

This chart compares the drag convergence history obtained from the C-90 with that of the IBM SP-2 parallel system. It can be seen that the drag values obtained from the two solutions are different only by 0.1 counts for the same number of iterations. Converging the IBM SP-2 solutions further to the same level of residual values as the C-90 would yield identical drag values.

Drag Convergence Comparison (Cray C-90 vs. IBM SP-2)

CFL3D (C-90) and CFL3Dhp (SP-2), Navier-Stokes (B-L), 3 level multigrid, 12 or 16 blocks
TCA W/B, 1.5 million grid points, M_∞=2.4, Re=4x10^6/ft

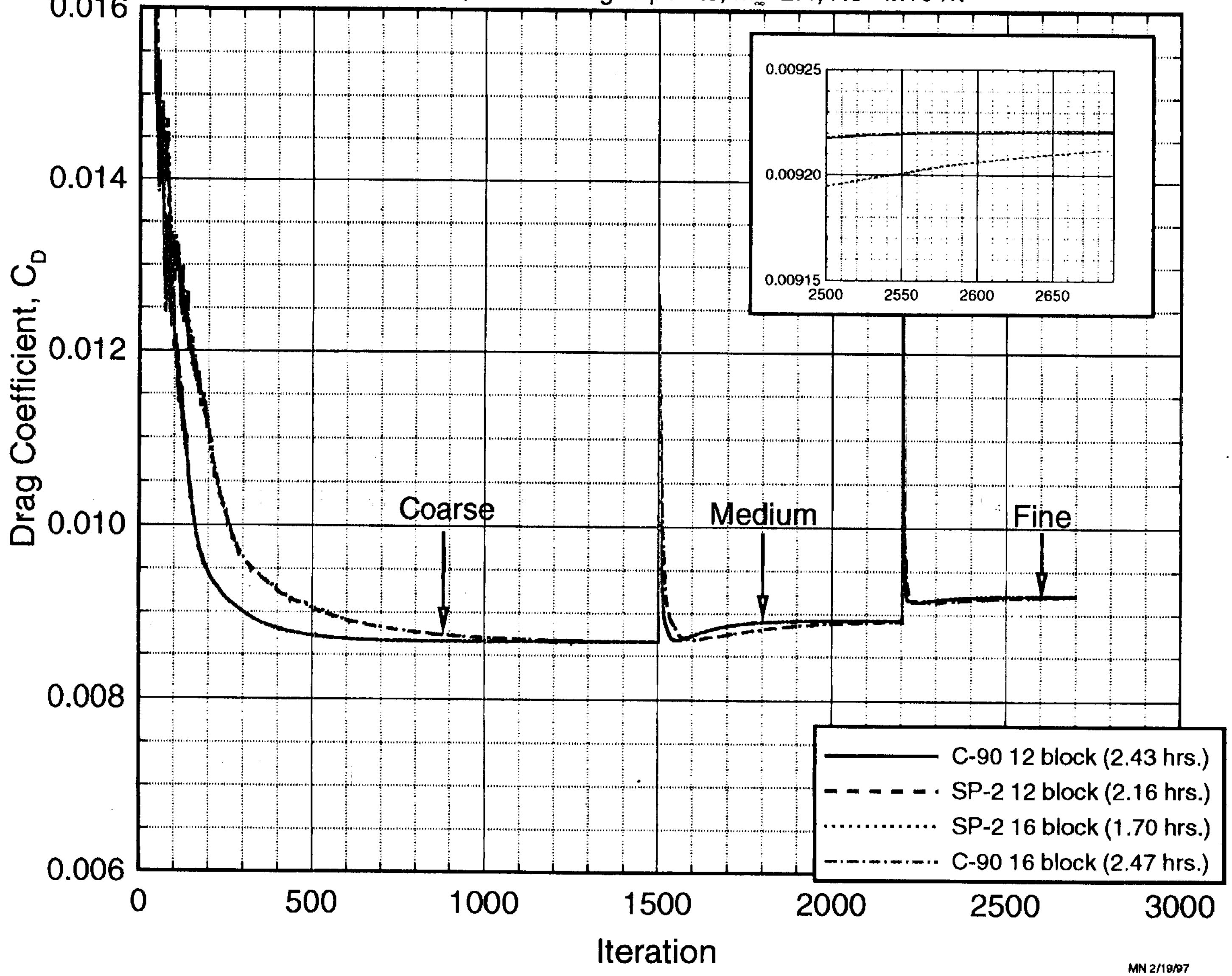

Pressure Drag Polar for the TCA W/B/E Configuration

Next step in the analysis complexity is the inclusion of the non-point-matched patched grid surfaces. The chosen geometry for this analysis is the TCA W/B/E configuration. The original 12-block grid with 3.1 million grid points has been split to 21-blocks for CFL3Dhp Euler analysis on the IBM SP-2. The pressure drag polar obtained from this analysis is given below. The force comparison with the Cray C-90 results show once again excellent agreement.

Pressure Drag Coefficients (C_{Dp}) for the TCA W/B/E Configuration
CFL3D Euler, M_∞=2.4

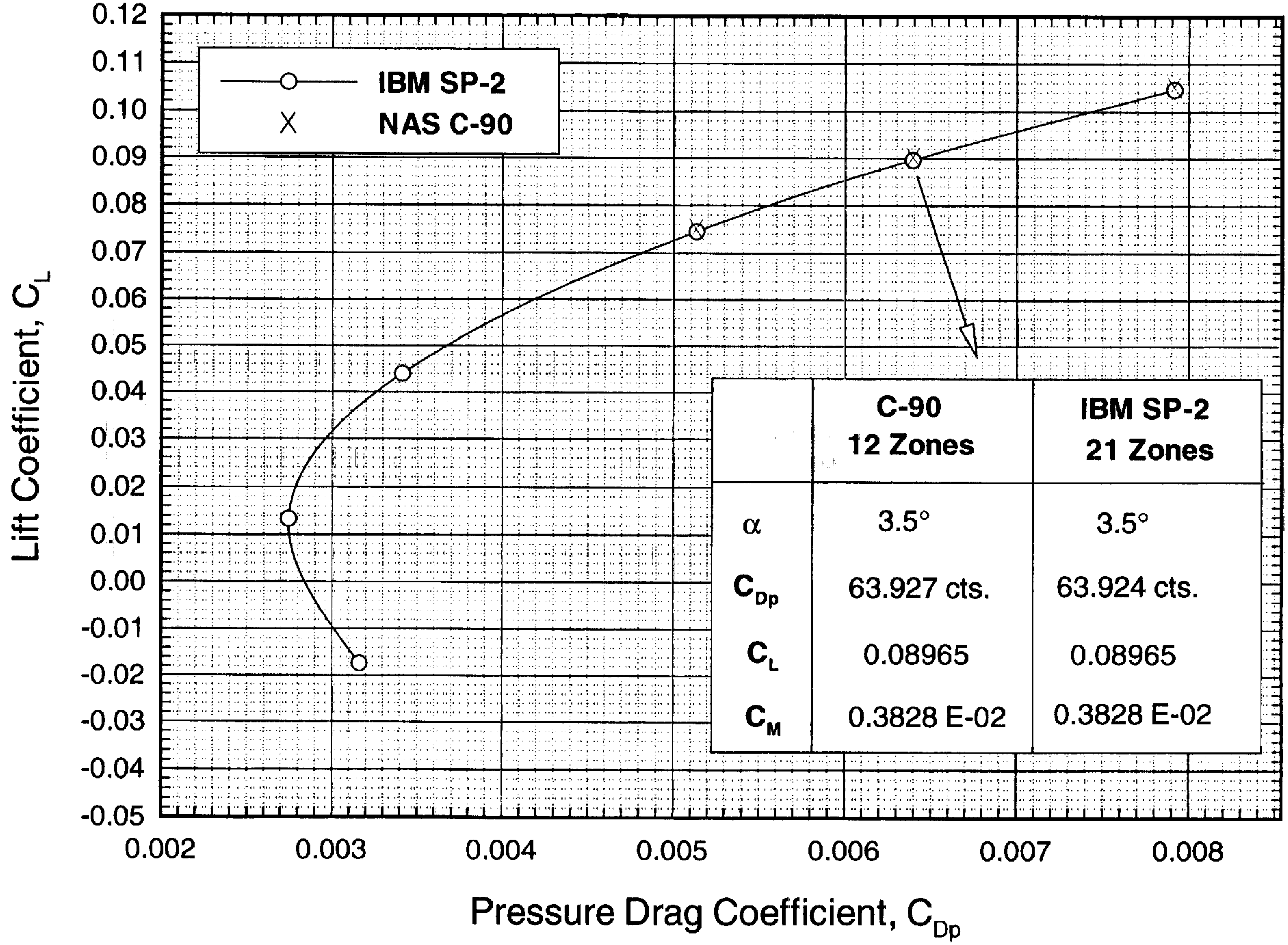

CFL3D Navier-Stokes Grid Refinement Study

The grid sensitivity to increasing grid sizes from the baseline grid size of 97x241x65 has been used to evaluate the CFL3Dhp scalability related information in addition to the primary objective of the aerodynamic reasons. Each grid has the same near-wall clustering criterion in the normal direction. This chart shows the variation of the various aerodynamic forces with respect to the change in the grid points in the normal direction. The grid size in the normal direction has been varied from the baseline value of 65 points to 77 and 85 successively. The grids have been split in the same fashion as the baseline grid.

The results show that the baseline grid is adequate for the accurate prediction of all forces at the supersonic cruise condition. The CPU time comparisons of the three solutions using CFL3Dhp shows a linear scaling.

CFL3D Navier-Stokes Grid Refinement Study

TCA W/B Configuration, M_∞=2.4, Re=6.36x10^6, α=3.518°

Solution Performed on IBM SP-2

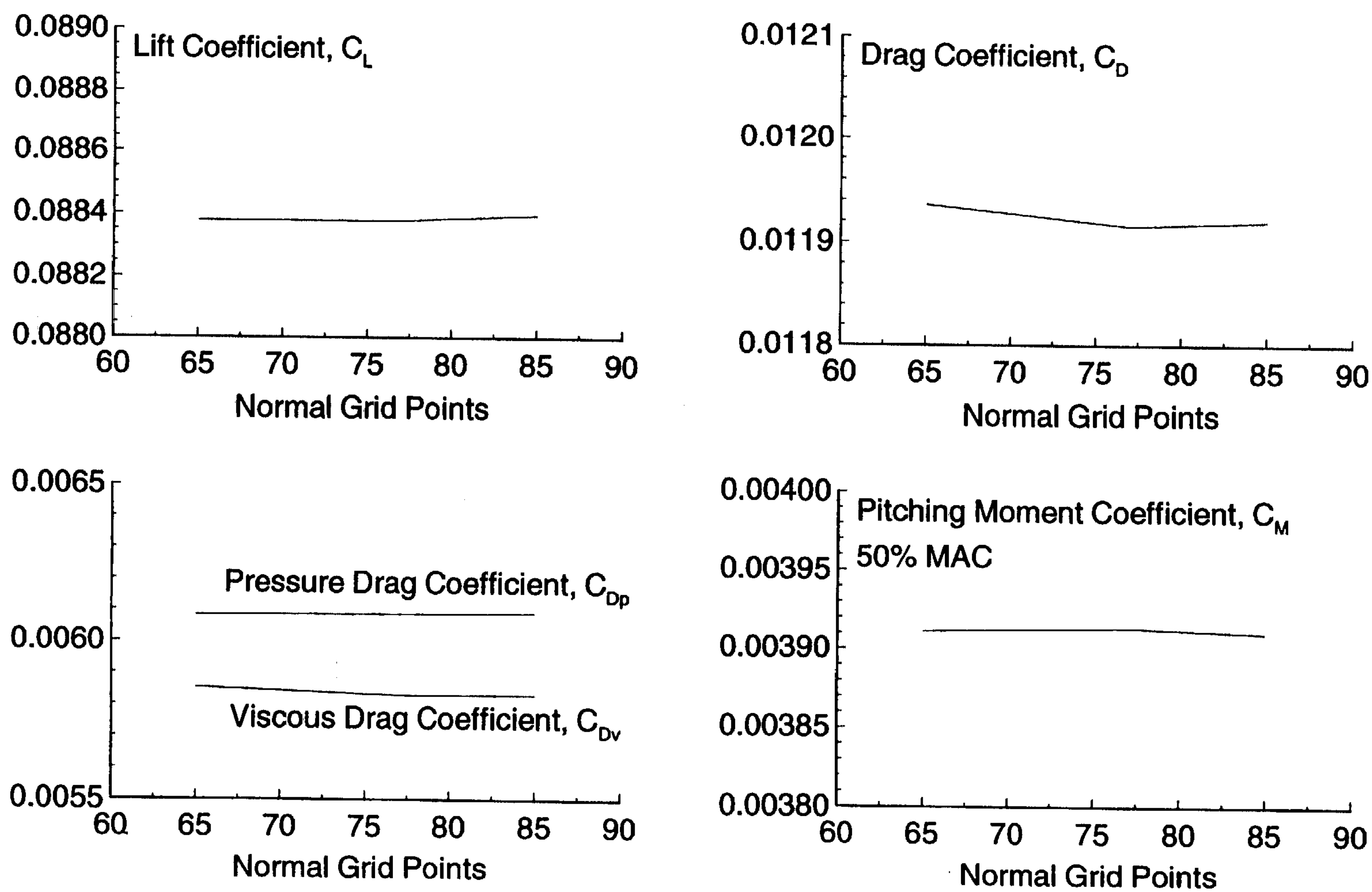

Predicted Drag Polar for the TCA

The TCA W/B drag polar at M = 1.8 obtained using CFL3Dhp on the IBM SP-2 has been included in this chart along with other results. The entire polar was obtained in a single 12-node run for 9 hrs. of wall clock time. The solutions were successively restarted beginning from the cruise angle-of-attack of 3.518 solution. It is important to note that the parallel code performs well even at large angles-of-attack at which the serial code on Cray C-90 could not converge.

Predicted Drag Polar for the TCA Wing/Body Configuration

CFL3Dhp Navier-Stokes solution, M_∞=2.1, Re=4x10^6/ft

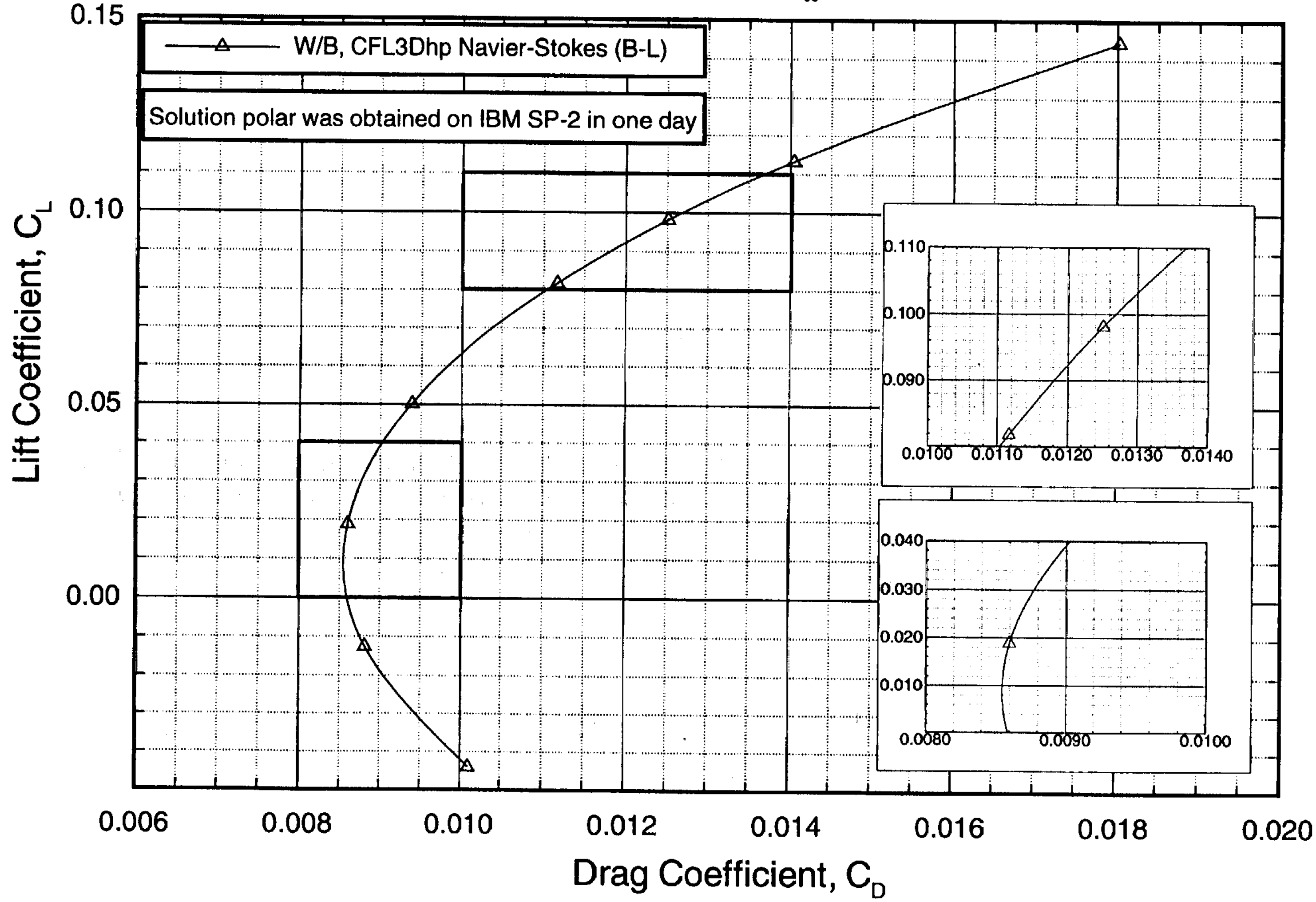

MN 2/19/87
CA-WORKSHOP/plrinday.ps

Conclusions and Future Work

CFL3Dhp has been successfully applied for various CFD analysis in HSCT. The results are accurate and the turn-around time is good. The code is being applied for full configuration analysis and soon a full configuration polar a day will be possible. Efforts are underway to incorporate the CFL3Dhp analysis code in the MDC nonlinear optimization environment.

Conclusions and Future Work

Conclusions

- CFL3Dhp has been proven to be an efficient and a validated parallel Euler/N-S solver for routine W/B and W/B/E CFD analysis
- Nearly 10.5 nodes produce the CPU power of a C-90 processor
- A W/B Navier-Stokes polar a day is a reality now

Future Work

- Combine CFL3Dhp with the MDA nonlinear optimization code, MDO3Dhp for W/B optimization
- Incorporate the aeroelastic analysis capability in CFL3Dhp

Full Configuration Force and Moment Calculations using Multiblock CFL3D on HSCT Configurations

Grant L. Martin and Robert P. Narducci
McDonnell Douglas Corporation
Long Beach, California 90807-5309

During the past year, the McDonnell Douglas Corporation (MDC) has made large strides in Computational Fluid Dynamics (CFD) analysis of increasingly complex HSCT configurations using both serial and parallel computational platforms. While tools for grid generation and analysis on serial computers have remained relatively unchanged, a new gridding strategy has been employed to obtain Navier-Stokes analyses of HSCT configurations which include the wing, body, nacelles, diverters, and empennage. Additionally, with the promising efficiency of parallel machines, MDC has contributed to the development of CFL3Dhp, a parallel version of CFL3D for the IBM SP-2.

Presented herein are full configuration Euler and Navier-Stokes solutions obtained using CFL3D on the NAS C-90 and IBM SP-2. With the objectives of validating CFL3D for supersonic cruise calculations on several platforms, CFD results for the Reference H and Technology Concept Airplane (TCA) configurations are presented in a build-up fashion. The build-up fashion entails analyzing the simplest of configuration first, the wing/body (W/B) followed by the additional complexity of the empennage (W/B/E), then nacelles and diverters (W/B/N/D), and finally the entire configuration (W/B/N/D/E). A thorough build-up has been performed on the Reference H configuration, while the TCA build-up work is still in progress. To assist in the validation, a number of comparisons are made to available experimental data from the NASA Langley Unitary Plan Wind Tunnel (UPWT).

Full Configuration Force and Moment Calculations using Mulitblock CFL3D on HSCT Configurations

Grant L. Martin & Robert P. Narducci

McDonnell Douglas Corportation
Long Beach, California

NASA/Industry HSR
Configuration Aerodynamics Workshop
February 25-28, 1997
NASA Langley Research Center, Hampton, VA

Outline

In this report, we investigate flow over full configuration (W/B/N/D/E) HSCT configurations using CFL3D, the work-horse code for analysis and design of HSCT configurations at the MDC. After the motivation and objectives have been established, descriptions of the flow analysis tools and platforms used to run the codes are given. In a build up fashion, force and moment predictions are presented for the Reference H and TCA configurations. Both Euler and Navier-Stokes solutions are presented, however due to limited availability of resources, Navier-Stokes solutions are computed for selected cases. In each presentation of results for the Reference H and TCA configurations, a description of the geometry is given, followed by a description of the grids. The results include W/B, W/B/E, W/B/N/D, and W/B/N/D/E for the Reference H configuration and W/B, W/B/E, and W/B/N/D for the current Technology Concept Aircraft (TCA). The report closes with important conclusions on the capability of supersonic cruise analysis of full configuration force and moment predictions.

Outline

- Objectives
- Description of flow analysis and platforms
- Reference H build-up calculations
  - Geometry description
  - Grids
  - Presentation of solutions
- TCA build-up calculations
  - Geometry description
  - Grids
  - Presentation of solutions
- Summary and conclusions

Objectives

As the HSR program advances, greater detail and more complexity are incorporated into the HSCT configurations. For the program to continue to be successful, good engineering judgment based on accurate analysis of these configurations must be made. Thus, it becomes important to validate the analysis tools used for the increasingly complex configurations. There are three main objectives of this work. The first is to demonstrate the feasibility of the computation; the second is to assess the quality of the performance predictions; and the third is to gain an understanding of the aerodynamic performance impact due to the addition of components such as the nacelles and empennage.

Objectives

- Demonstrate the feasibility of full configuration (W/B/N/D/E) computations
- Assess the accuracy of full configuration force and moment predictions
- Understand the effects of the addition of various components on HSCT configurations

Flow Analysis and Platforms

The flow solver used in this study is CFL3D. Version 4.1 was used on the Cray C-90 and J-90 computers and a parallel version of CFL3D was used on the IBM SP-2. Though the Cray J-90 is a parallel machine, it was exercised in the serial mode only. CFL3D uses a structured, multiblock, upwind scheme to solve either the Euler or Navier-Stokes equations. Convective terms were differenced using Roe flux difference splitting. A variety of turbulence models are available including Baldwin-Lomax (with and without Degani-Schiff), Baldwin-Barth, Spalart-Almaras, and k-ω. In this work, the Baldwin-Lomax and Baldwin-Barth turbulence models are used. A number of convergence accelerators are programmed in CFL3D to reduce CPU time. Here, grid sequencing and multigrid are actively used.

The Euler drag predictions are supplemented with skin-friction estimates from flat-plate theory. Here, Clutter charts are used to compute a skin-friction coefficient for each component of the HSCT configuration. Skin-friction drag is then calculated from

$$C_{Dv} = \frac{\sum_i C_{f,i} S_{wet,i}}{S_{ref}}$$

where form, interference, and excrescence factors are assumed to be 1.

Flow Analysis and Platforms

- CFL3D Flow Solver:
  - Version 4.1 on Cray C-90 and J-90 cluster (J-90 exercised in the serial mode only)
  - CFL3D (parallel) version on IBM SP-2
  - Skin friction bug removed for all calculations
  - Features used:
    - Grid sequencing & multigrid convergence acceleration
    - Roe flux difference splitting
    - Baldwin-Lomax and Baldwin-Barth turbulence models
- Clutter charts used for skin-friction drag estimates to complement Euler drag predictions

Reference H Build-up

In the first section of this paper, full configuration prediction validation is attempted using the 1.675%-scale Reference H modular controls model. The model was tested in a variety of configurations allowing for a build-up approach to CFL3D validation of an HSCT W/B/N/D/E configuration. The geometries of interest include wing and body with the extended aft end, flow-through nacelles, horizontal stabilizers and vertical tail. Comparisons between CFD and experiment are done at a common Mach number, M_∞=2.1, for the configurations of interest, W/B/E, W/B/N/D, and W/B/N/D/E. Here, configurations designated with E (*i.e.*, W/B/E and W/B/N/D/E) include both the horizontal stabilizer and vertical tail. All configurations include the extended aft end. The electronic definition of this geometry was not available to the HSR community. Thus, the CFD geometry was obtained by scaling the 2.7% Reference H model to define the wing and body. The cylindrical aft end and placement of the horizontal and vertical tails was constructed from scratch using a model drawing as a guide. The aft end was faired to the W/B definition using a best-guess approximation to the true model geometry.

Reference H Build-up

- Reference H geometry & grids
  - Nonavailability of electronic geometry file
  - Re-scaled 2.7% Ref. H model geometry & supplemented with aft end constructed from scratch using model drawings
- Reference H force and moment build-up
  - $M_{\infty}=2.1$, $Re=3x10^6/ft$
  - Euler solutions for W/B, W/B/N/D, W/B/E, & W/B/N/D/E
  - Navier-Stokes solutions for W/B & W/B/E
- Empennage and nacelle/diverter drag increments

1.675%-Scale HSR Reference H Modular Controls Model Extended Aft Body with Tails

NASA Langley Unitary Plan Wind Tunnel, Section #1

A view of the 1.675%-scale Reference H modular controls model in the NASA Langley UPWT is shown in the figure below. The Reference H modular controls model was tested in the NASA Langley 4-ft Unitary Plan Wind Tunnel (UPWT), test section #1, from February 6 to March 30, 1996. During the wind-tunnel entry, designated as test 1812, the model was tested at M_∞=1.65, 1.8, and 2.1. Additional data for higher supersonic Mach numbers and transonic Mach numbers were obtained in other tests at Langley UPWT section #2 and 16-ft Transonic facility. A total of 82 configurations were tested during entry 1812 including combinations of outboard leading-edge flaps, trailing-edge flaps, spoiler slot deflectors, horizontal stabilizer, vertical tail, flow-through nacelles and blocked nacelles.

1.675% Scale HSR Reference H Modular Controls Model Extended Aft Body with Tails

NASA Langley Unitary Plan Wind Tunnel, Section #1

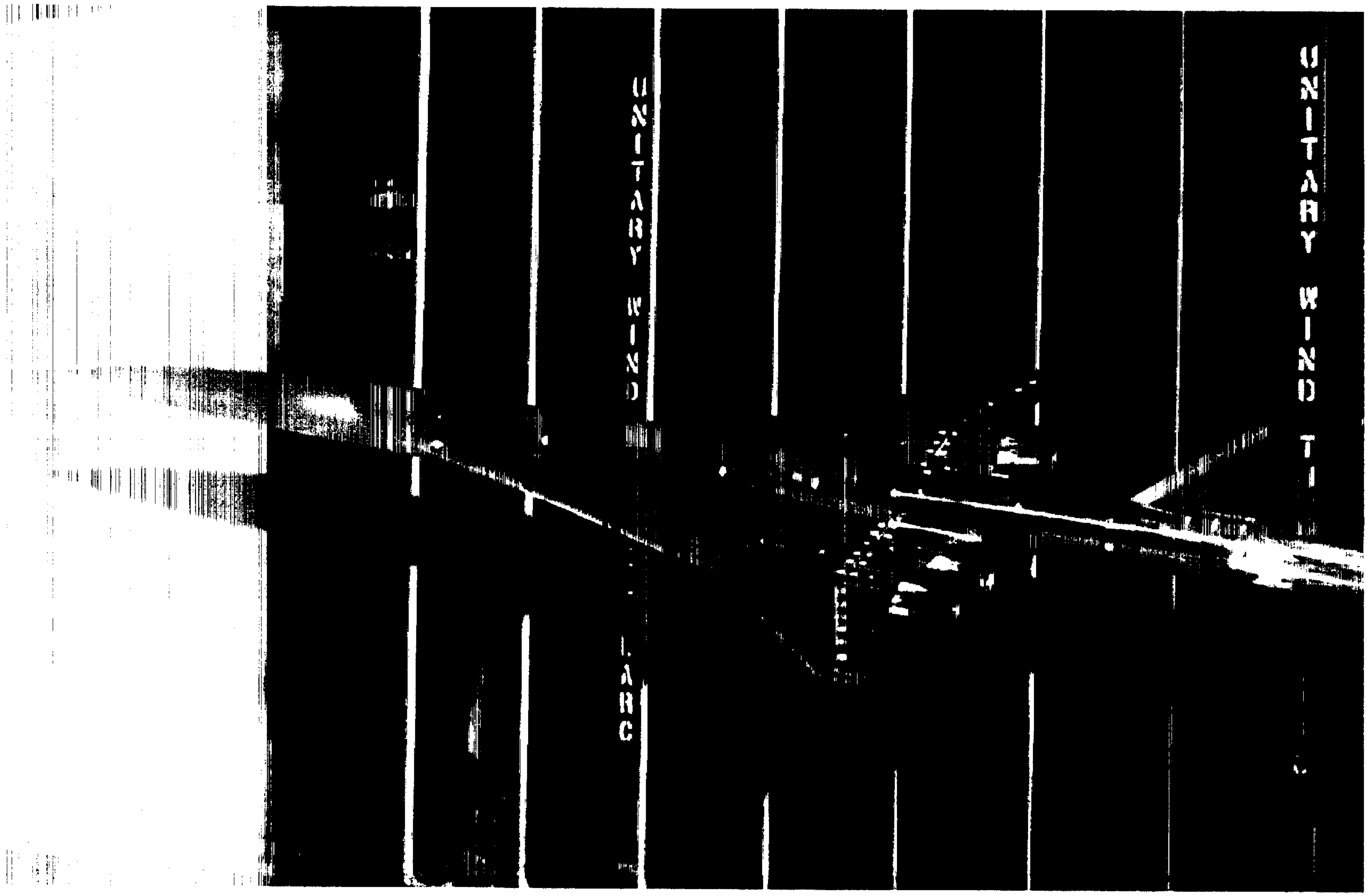

W/B and W/B/E Supersonic Grids
1.675% Reference H Modular Controls Model

The Reference H W/B supersonic Euler grid has a C-O topology with 93 spanwise points, 241 axial points and 41 normal points. This grid served as the foundation to make all other grids. The W/B/E grids are created by breaking the W/B grid at the trailing edge of the wing. The C-O topology covering the wing and body is unmodified. Using an H-O topology, the aft end was re-gridded in two zones; one zone covers the lower empennage and another covers the upper empennage. The total number of points in the W/B/E Euler grid is 1.5 million.

The W/B and W/B/E Navier-Stokes grids are built from the corresponding Euler grids with additional planes clustered near the surface to obtain a y^+ of approximately 1.5. The dimensions of the W/B Navier-Stokes grid is 93x241x57. The total number of points in the W/B/E Navier-stokes grid is 2.3 million. The W/B/E Navier-Stokes grid is shown below.

Ref. H W/B/E Supersonic Navier–Stokes Grid

1.675% Modular Wind–Tunnel Model, Cylindrical Aft End

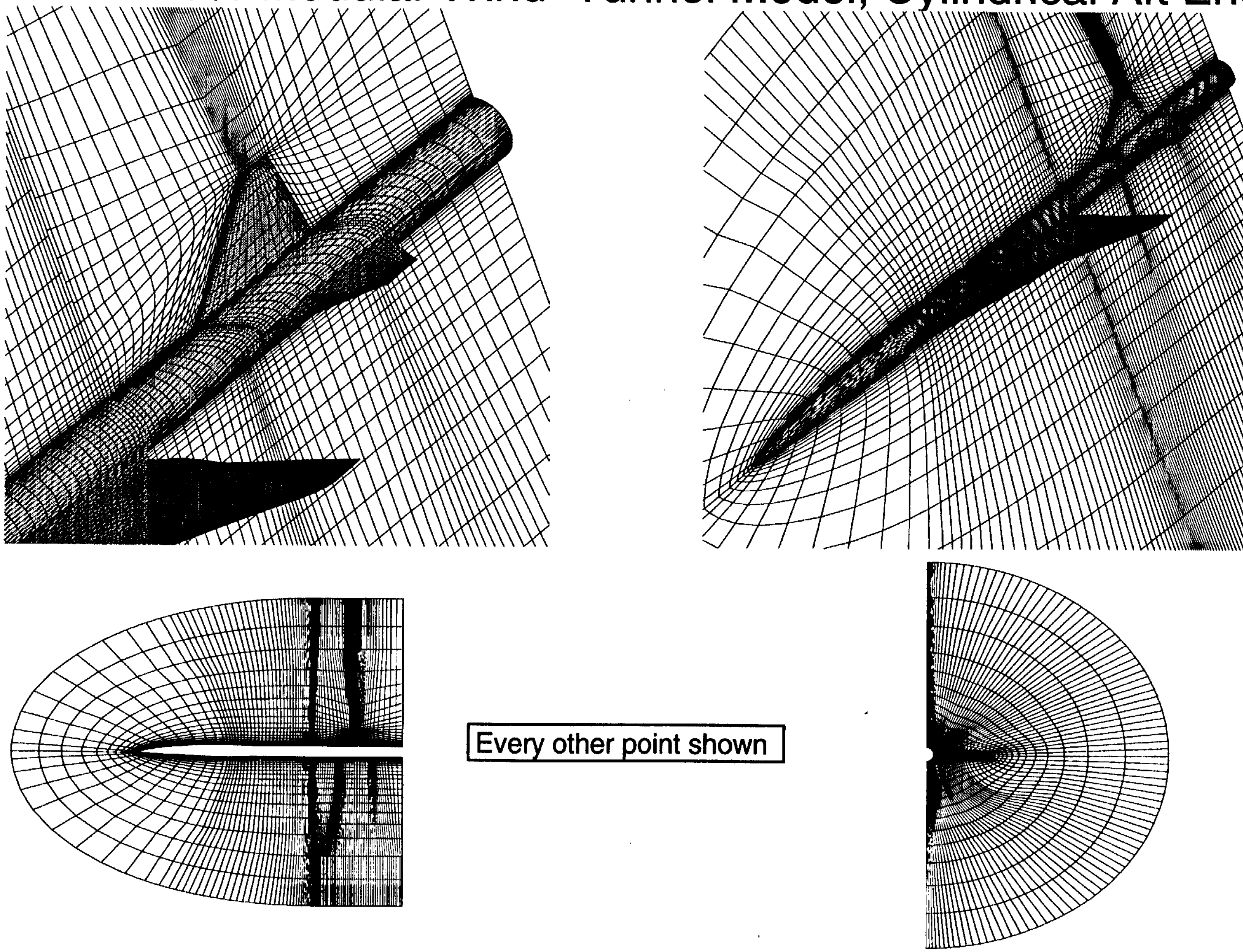

W/B/N/D and W/B/N/DE Supersonic Euler Grids 1.675% Reference H Modular Controls Model

It was discovered some time after the W/B/E Navier-Stokes solutions were obtained that similar zonal breaks at the trailing edge of the wing for W/B/N/D and W/B/N/D/E calculations can cause convergence difficulties, particularly if the grids are to be clustered for Navier-Stokes computations. Also in the upper zone, skewing was introduced to cluster the leading edges of the vertical and horizontal tails with the same axial grid lines. The grid strategy thus employed for the Euler W/B/N/D and W/B/N/D/E configurations was designed to eliminate the skewing and potential convergence problems at the wing trailing edge. The W/B/N/D and W/B/N/D/E grids are identical except for the zones which make up the empennage. The W/B/N/D grid is made up of 23 zones and 2.4 million points. The two zones covering the aft end of the geometry was replaced with three zones for the W/B/N/D/E calculations. Thus, there are 24 zones and 2.7 million grid points in the W/B/N/D/E grid. A view of the aft end of the W/B/N/D/E grid is shown below. The different colored surfaces represent different zones.

Ref. H Full Configuration Supersonic Euler Grid

1.675% Modular Wind–Tunnel Model, W/B/N/D/E Configuration

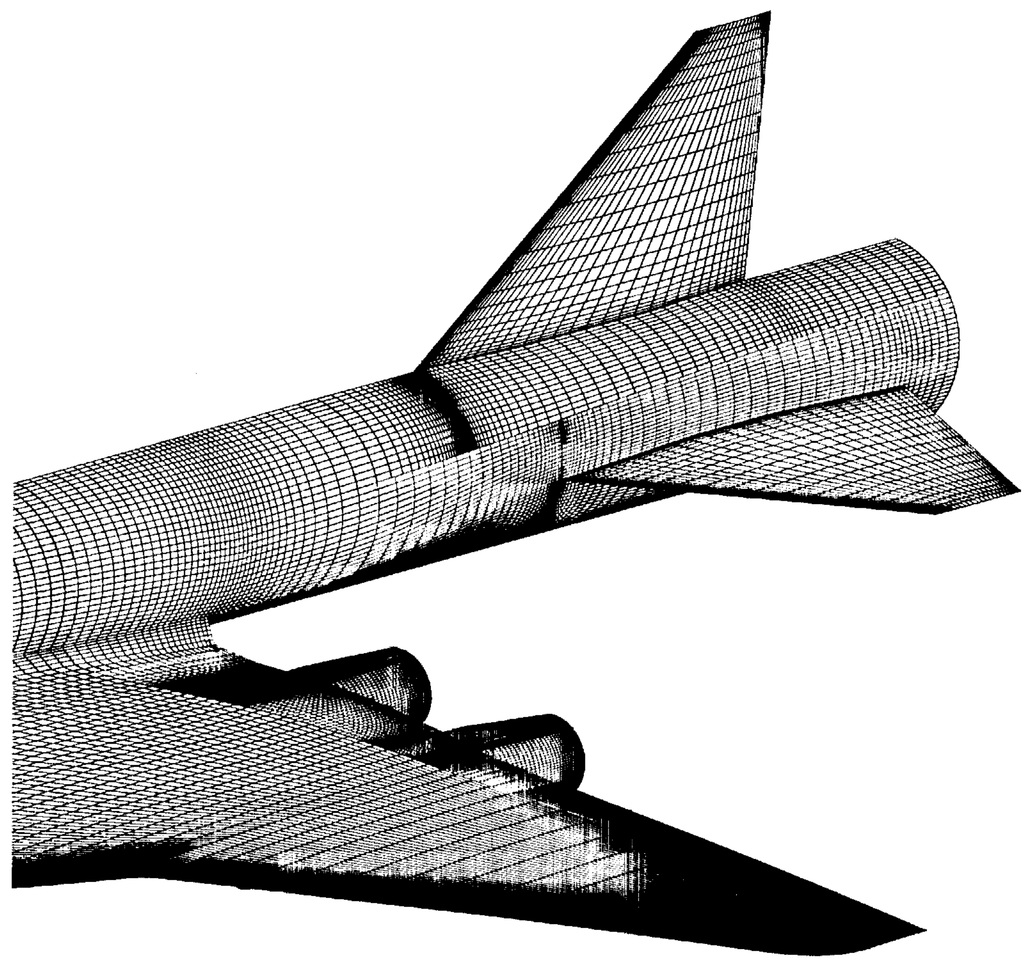

W/B/N/D and W/B/N/DE Supersonic Euler Grids - Near Nacelles 1.675% Reference H Modular Controls Model

The figure above shows the surface grid in the nacelle region of the W/B/N/D and W/B/N/D/E grids. As before, the colors indicate different zones. Three zones surround each nacelle and diverter and two zones make up the inner core flow-through region. The 10 zones which encompass the inboard and outboard nacelles have 1.26 million points, or approximately 47% of the total W/B/N/D/E grid.

Ref. H Full Configuration Supersonic Euler Grid

1.675% Modular Wind–Tunnel Model, W/B/N/D/E Configuration

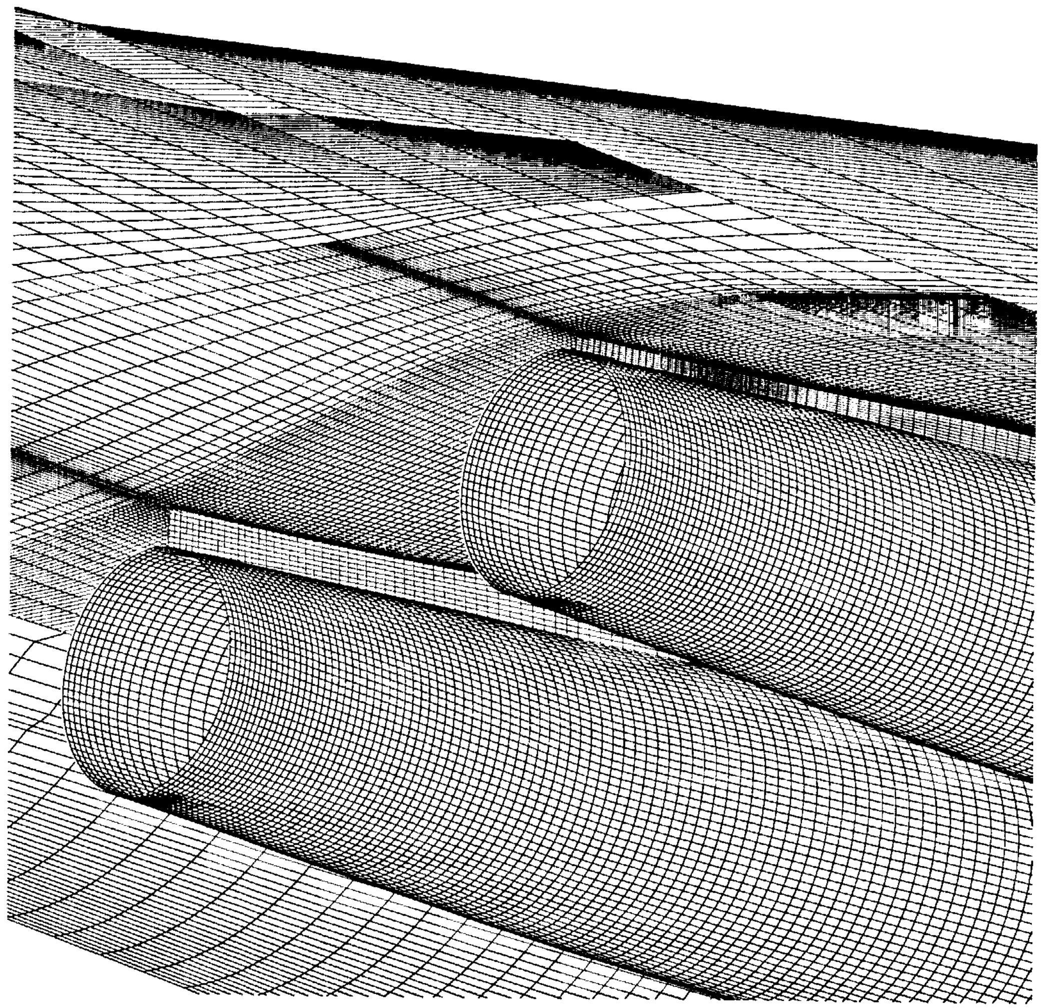

Comparison of Predicted and Experimental Lift Curves
1.675% Reference H Modular Controls Model

CFL3D & Langley UPWT 1812, M_∞=2.1, Re=3x10^6/ft

The Euler lift predictions are compared to the experimental data in the figure above. Experimental data are shown with square symbols and splined together for clarity. The CFD results are presented as solid lines with a color corresponding to the appropriate experimental run. Generally, the comparisons are good, however there is a slight over-prediction in the lift curve slope, which is most apparent in the W/B/N/D/E calculations. The addition of nacelles translates the curves so that the configuration experiences more lift at a given angle-of-attack. The addition of the empennage rotates the curves with additional lift coming from the horizontal tail at larger angles-of-attack.

Comparison of Predicted and Experimental Lift Curves
1.675% Reference H Modular Controls Model

CFL3D & Langley UPWT 1812, M_∞=2.1, Re=3×10^6/ft

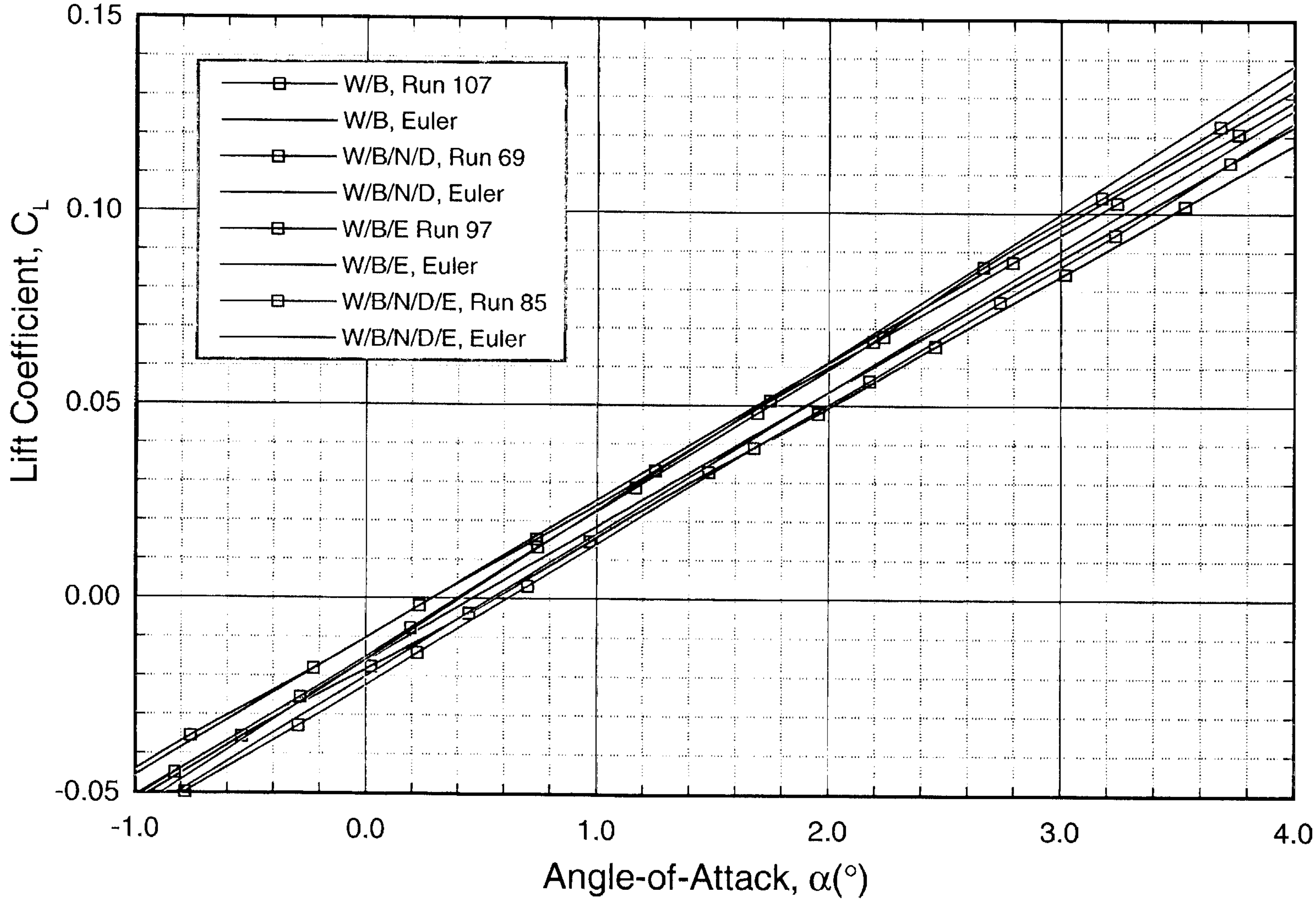

Comparison of Predicted and Experimental Drag Polars
1.675% Reference H Modular Controls Model

CFL3D & Langley UPWT 1812, $M_{\infty}=2.1$, $Re=3x10^6/ft$

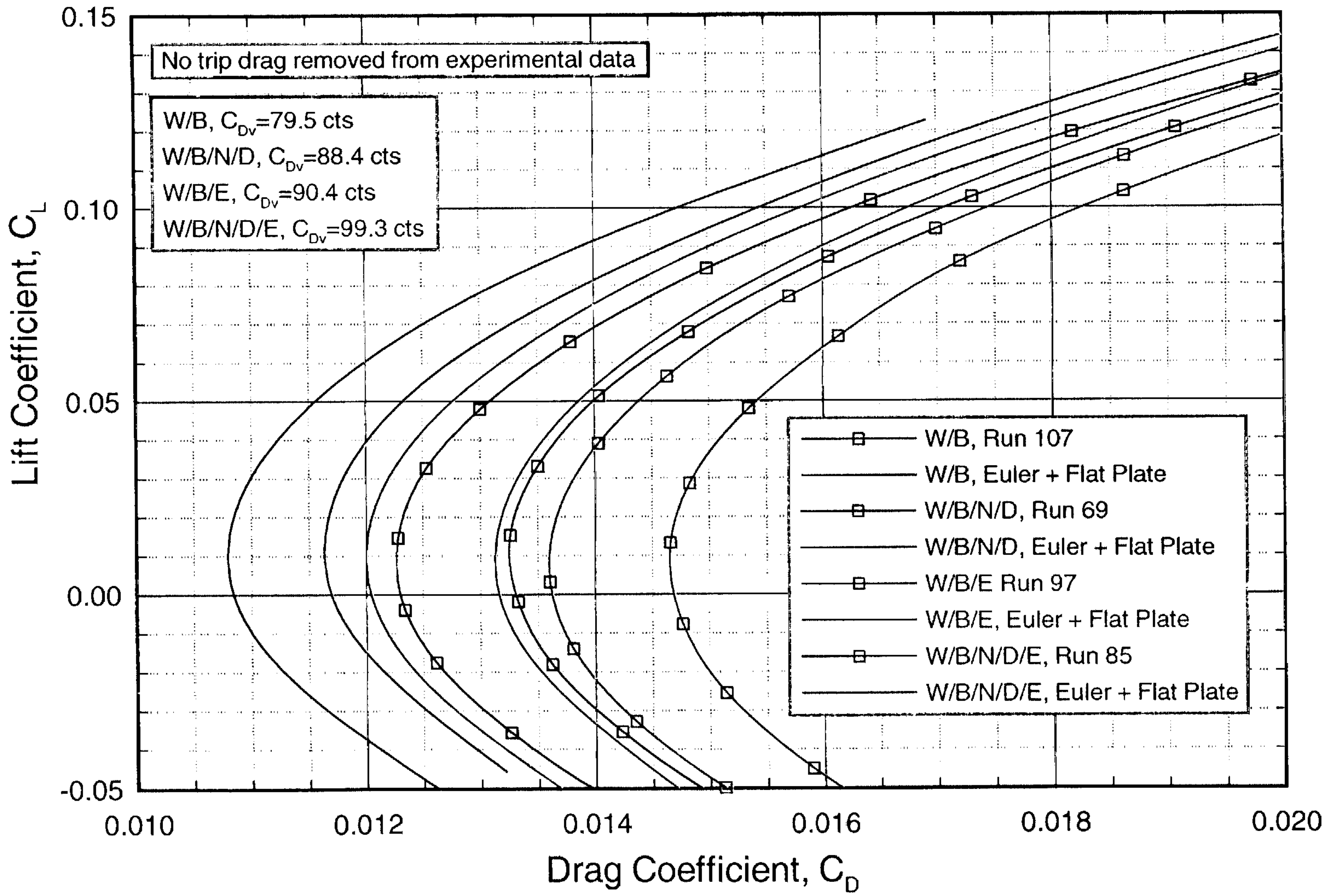

Comparison of Predicted and Experimental Drag Polars
1.675% Reference H Modular Controls Model

CFL3D & Langley UPWT 1812, M_∞=2.1, Re=3x10^6/ft

This figure shows the drag comparison which falls short of our expectations. Euler predictions complemented by flat plate viscous drag under-predicted the experimental data by approximately 16 counts for each configuration analyzed. Historically, CFL3D Euler analyses complemented with flat plate skin friction have agreed very well with experimental data for HSCT W/B and W/B/N/D configurations. Thus, it was surprising to see the large discrepancy in this case. The fact that all configurations are consistently 16 counts off suggests that the CFD geometry and wind-tunnel geometry differ in some component common to all configurations. A quality assessment report on the model has yet to be issued. Another possibility is that the wind-tunnel data has been improperly reduced.

The nacelle internal duct is not intended to have any contribution to the forces and moments. Thus, W/B/N/D and W/B/N/D/E force calculations do not include integration of pressure or viscous terms from inside the nacelles. A flat plate estimate of the skin friction of the duct has been removed from the wind-tunnel data. Thus, a slight inconsistency is introduced as the pressure forces acting inside the nacelles of the wind-tunnel model are not accounted for in the CFD solutions. It is thought that this cannot account for more than 1 count of discrepancy.

While no attempt was made to estimate trip drag on the experimental model, this effect is thought to be on the order of 3 to 4 counts. The modular control model is inherently "dirty" with many cracks resulting from the fit of model parts (flaps, etc.). Nevertheless, it is doubtful that this could account for much of the difference between the CFD and experiment.

Comparison of Predicted and Experimental Lift-to-Drag Ratio
1.675% Reference H Modular Controls Model

CFL3D & Langley UPWT 1812, M_∞=2.1, Re=3x10^6/ft

The lift-to-drag ratio curves are presented here for all configurations. Euler results, complemented with flat-plate viscous drag estimates, are in poor agreement with the experimental data since the drag is under-predicted.

Comparison of Predicted and Experimental Lift-to-Drag Ratio
1.675% Reference H Modular Controls Model
CFL3D & Langley UPWT 1812, M_∞=2.1, Re=$3x10^6$/ft

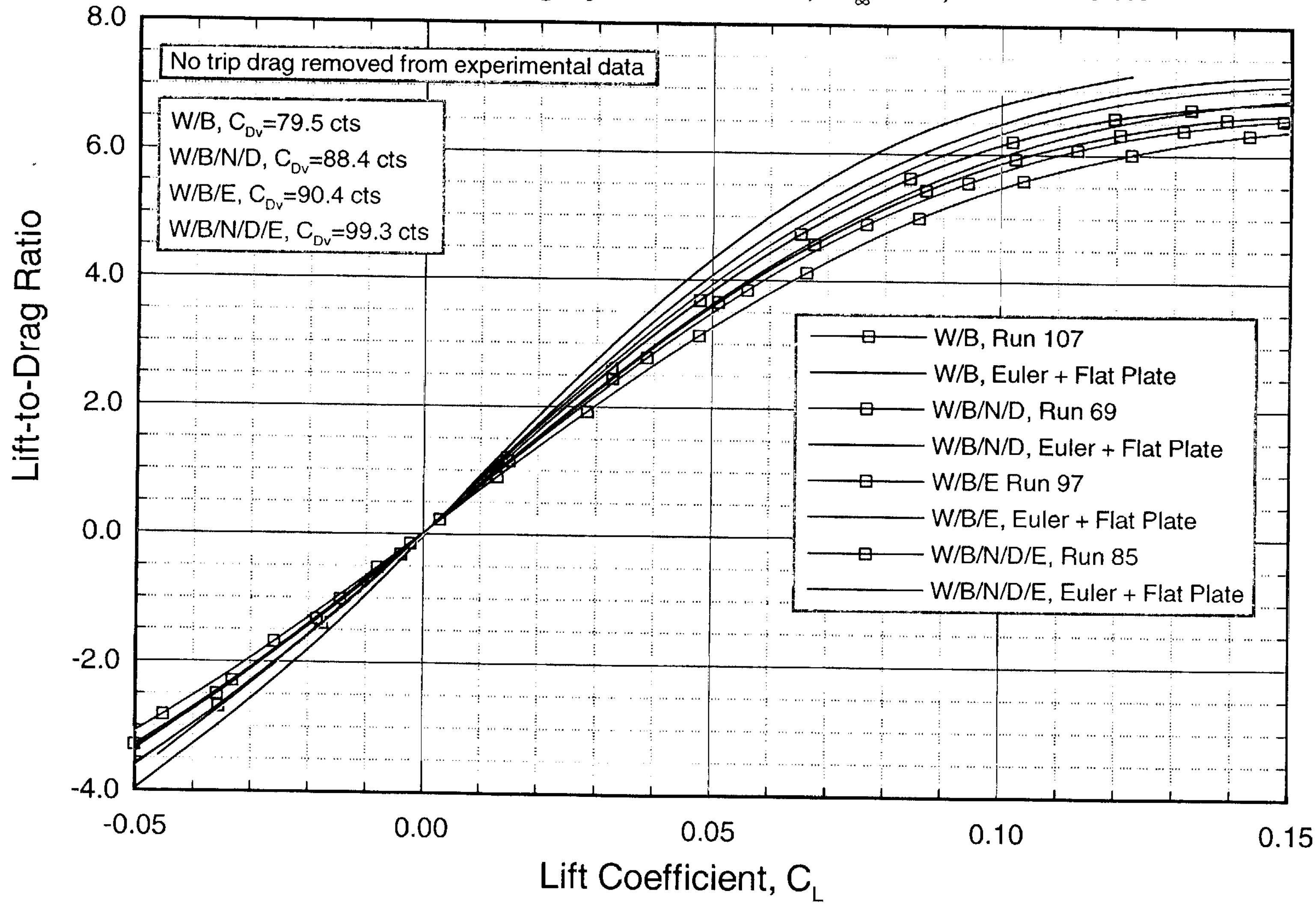

Comparison of Predicted and Experimental Pitching Moments
1.675% Reference H Modular Controls Model

CFL3D & Langley UPWT 1812, M_∞=2.1, Re=3x10^6/ft

Historically it has been difficult for CFD to accurately predict pitching moment. Presented here are Euler predictions for W/B, W/B/E, W/B/N/D and W/B/N/D/E compared to experimental data. No correction for viscosity has been attempted. Despite a poor prediction in drag, the pitching moment is in good agreement. Drag plays a minor role in the pitching moment calculations compared to the lift. As the magnitude in lift increases, the difference between experiment and CFD gets larger.

Comparison of Predicted and Experimental Pitching Moments
1.675% Reference H Modular Controls Model

CFL3D & Langley UPWT 1812, M_∞=2.1, Re=$3x10^6$/ft

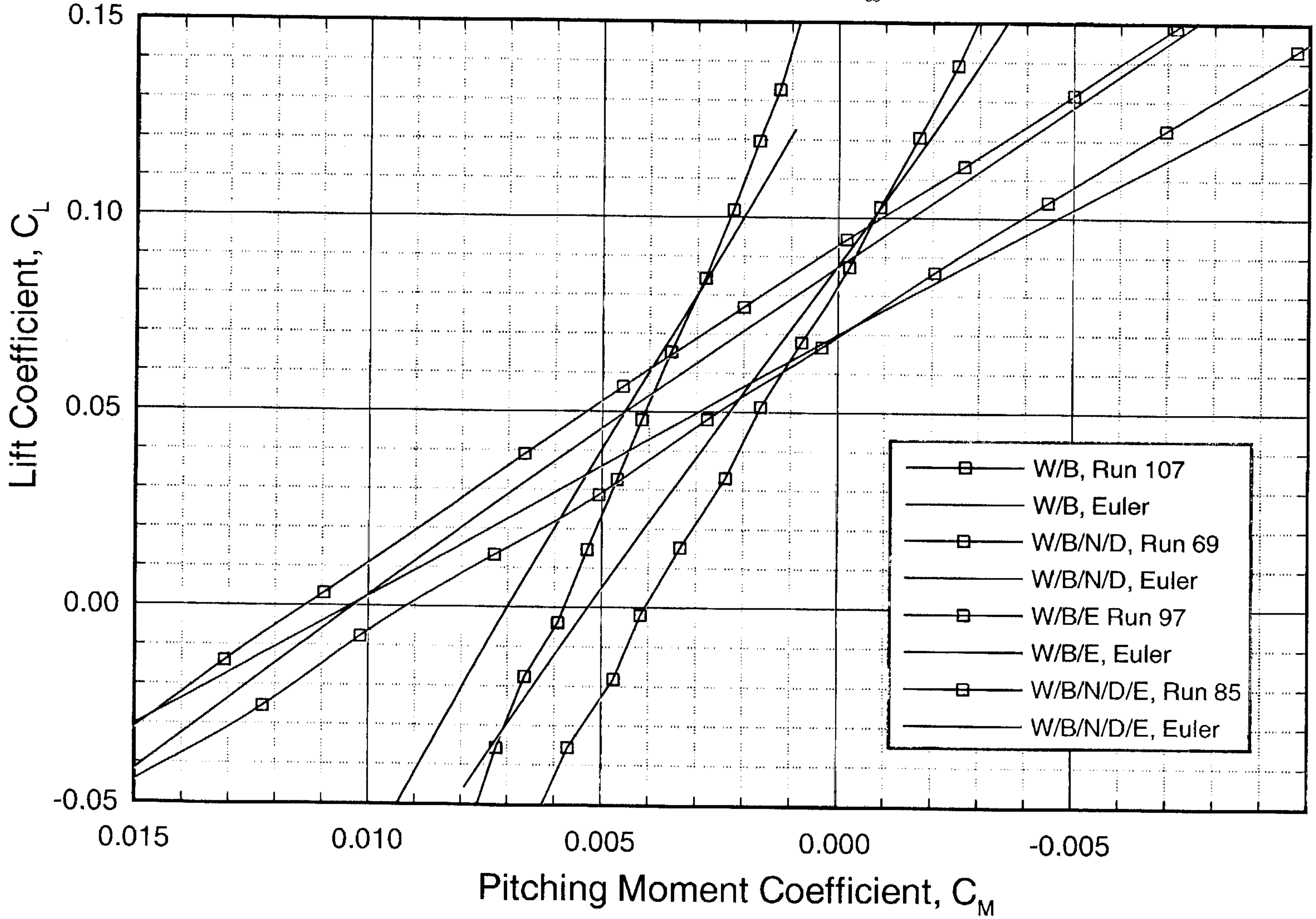

Comparison of Predicted and Experimental Drag Polars
1.675% Reference H Modular Controls Model

CFL3D & Langley UPWT 1812, $M_{\infty}=2.1$, $Re=3x10^6/ft$

Presented below are Navier-Stokes solutions for the W/B and W/B/E configurations only. Limited resources has prevented the computation of Navier-Stokes solution for the more complex configurations. However, these calculations are planned in the near future. The Baldwin-Lomax turbulence model was chosen for the W/B calculation since it has predicted force well for other HSCT configuration. For the W/B/E configuration, accurate modeling of the wake becomes a larger issue since it directly interacts with the horizontal stabilizer. For this reason, a number of turbulence models will be experimented with. To date, only the Baldwin-Lomax and Baldwin-Barth models have been used.

Agreement between the Navier-Stokes simulations and experiment, like the Euler comparisons shown earlier, is poor. The W/B configuration, analyzed using the Baldwin-Lomax turbulence model under-predicts the drag by nearly 16 counts throughout the polar. This, at least, is consistent with Euler and flat plate predictions. Previous W/B Navier-Stokes predictions have been very reliable, enforcing the theory that the CFD geometry and the wind-tunnel model may differ significantly or that the wind-tunnel data has been improperly reduced. Likewise, the Navier-Stokes solutions of the W/B/E configuration under-predicted the experimental drag levels. Here, Baldwin-Lomax and Baldwin-Barth turbulence models were used in the simulations. The two turbulence models predict similar pressure drag contributions but show a three count difference in skin-friction drag. Overall, the Baldwin-Barth is closest to the data showing an 8 count under-prediction. Unfortunately, with the uncertainty in predicting even the W/B drag, it is difficult to draw any conclusions concerning the effectiveness of the turbulence models.

Comparison of Predicted and Experimental Drag Polars
1.675% Reference H Modular Controls Model

CFL3D & Langley UPWT 1812, M_∞=2.1, Re=3×10^6/ft

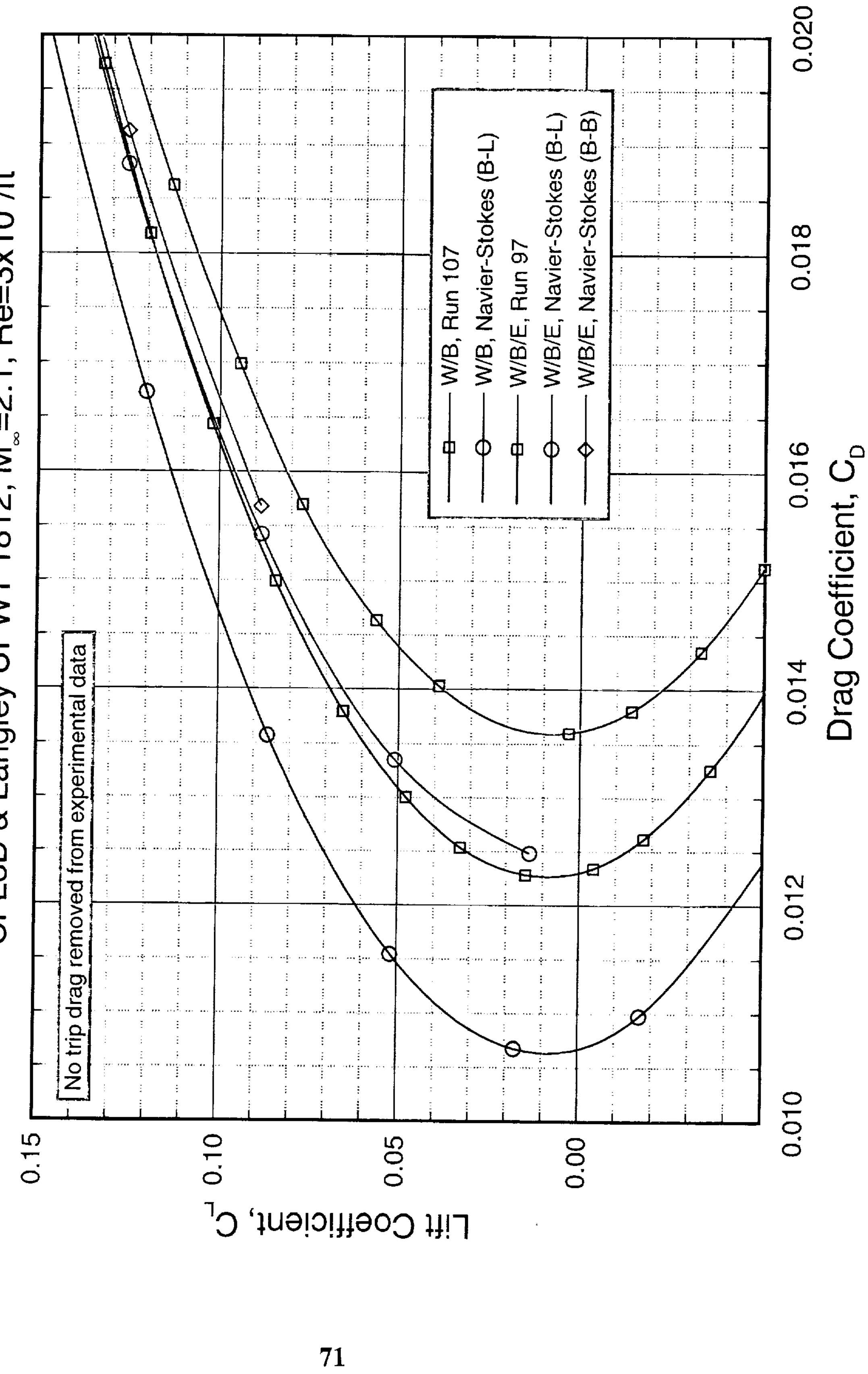

Comparison of Predicted and Experimental Drag Polars
2.7% Reference H, W/B Model

CFL3D, TLNS3D, & Ames 9x7 Tunnel, M_∞=2.4, Re_c=7x10^6

As seen in the previous chart, the CFL3D Navier-Stokes under-predicted the experimental data for the 1.675% Reference H modular controls model by approximately 16 counts for the W/B configuration. The chart below shows earlier calculations done on the 2.7% Reference H W/B configuration. These results were presented in Task No. 37 (Reference: CRAD-9103-TR-0235). Here we see Navier-Stokes solution accurately predicts drag throughout the polar at Mach 2.4.

Comparison of N-S CFD and Experimental Results: C_L vs. C_D

2.7% Ref. H Wing/Body, $M_\infty=2.4$, $Re_c=7\times10^6$

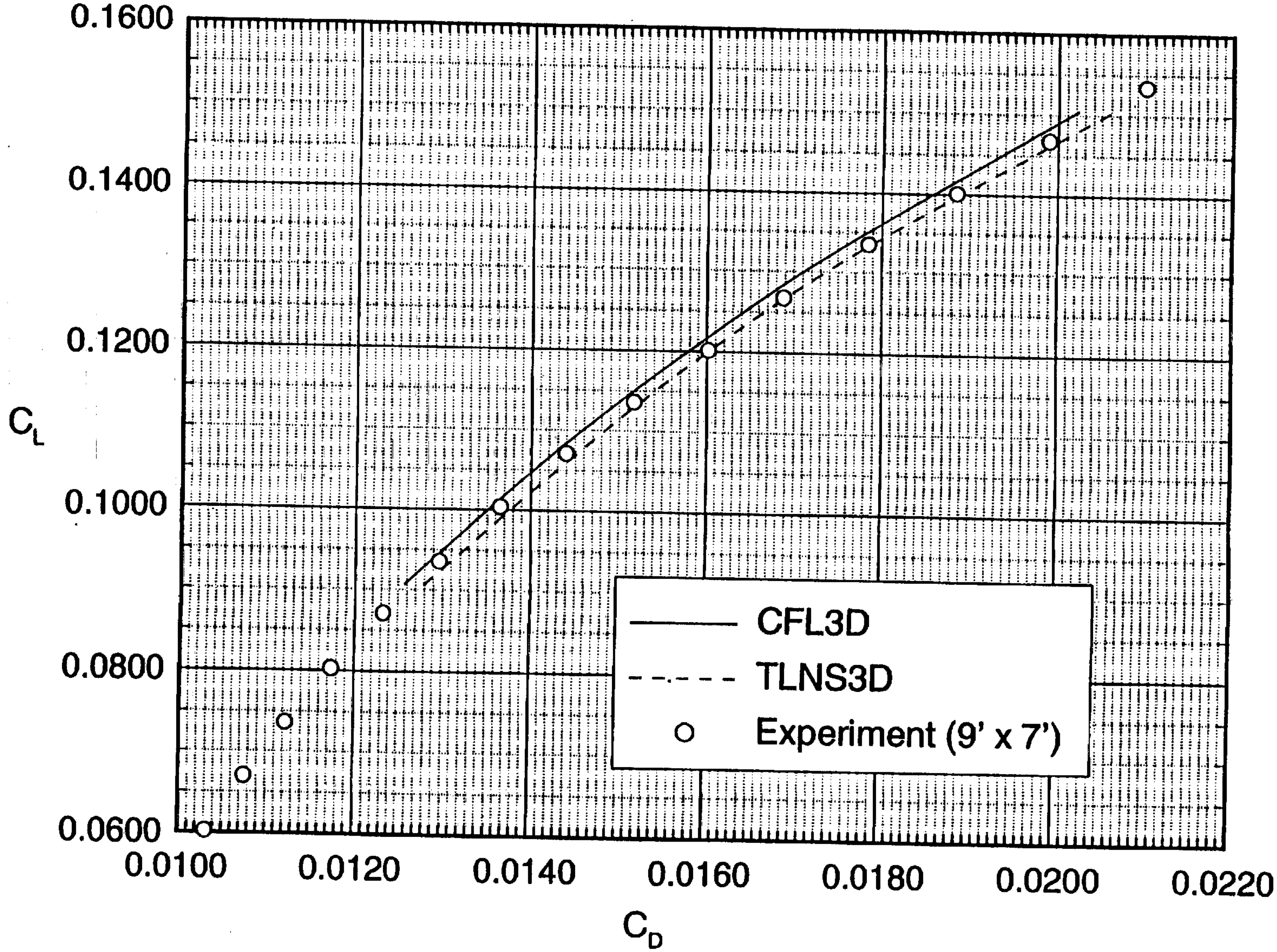

Nacelle/Diverter and Empennage Effect on Drag
1.675% Reference H Modular Controls Model

CFL3D & Langley UPWT 1812, M_∞=2.1, at C_L=0.12, Re=$3x10^6$/ft

This chart shows the drag build-up near the cruise C_L at M_∞=2.1 for the full configuration Reference H modular controls model referenced to the W/B configuration with the extended aft end. The first group of colored bars represents the drag increment due to the addition of horizontal and vertical tail surfaces; the next group represents the increment due to nacelles and diverters; the final group is the combined effect of the nacelles, diverters, and empennage. The increments are obtained by comparing data of similar type, so that the experimental increments are obtained by subtracting experimental drag data for each configuration, Euler increments are obtained by subtracting Euler drag data, etc. Although overall drag levels predicted by CFL3D were significantly under-predicted, the drag increments for each component are in good agreement between the experiment and the Euler solutions. CFD Euler and experiment show about 11 counts of drag due to the horizontal and vertical tails and 8 counts due to nacelles and diverters. At this condition, the drag increments appear additive, as the increment for nacelle, diverter, and tail surfaces is approximately 19 counts. Disappointedly, the Navier-Stokes predicted increments were further from experiment than the Euler. A possibility for this may be in the turbulence modeling especially in the wake region.

Component Drag Increments

1.675% Reference H Modular Controls Model

CFL3D & Langley UPWT 1812, M_∞=2.1, C_L=0.12, Re=3×10^6/ft

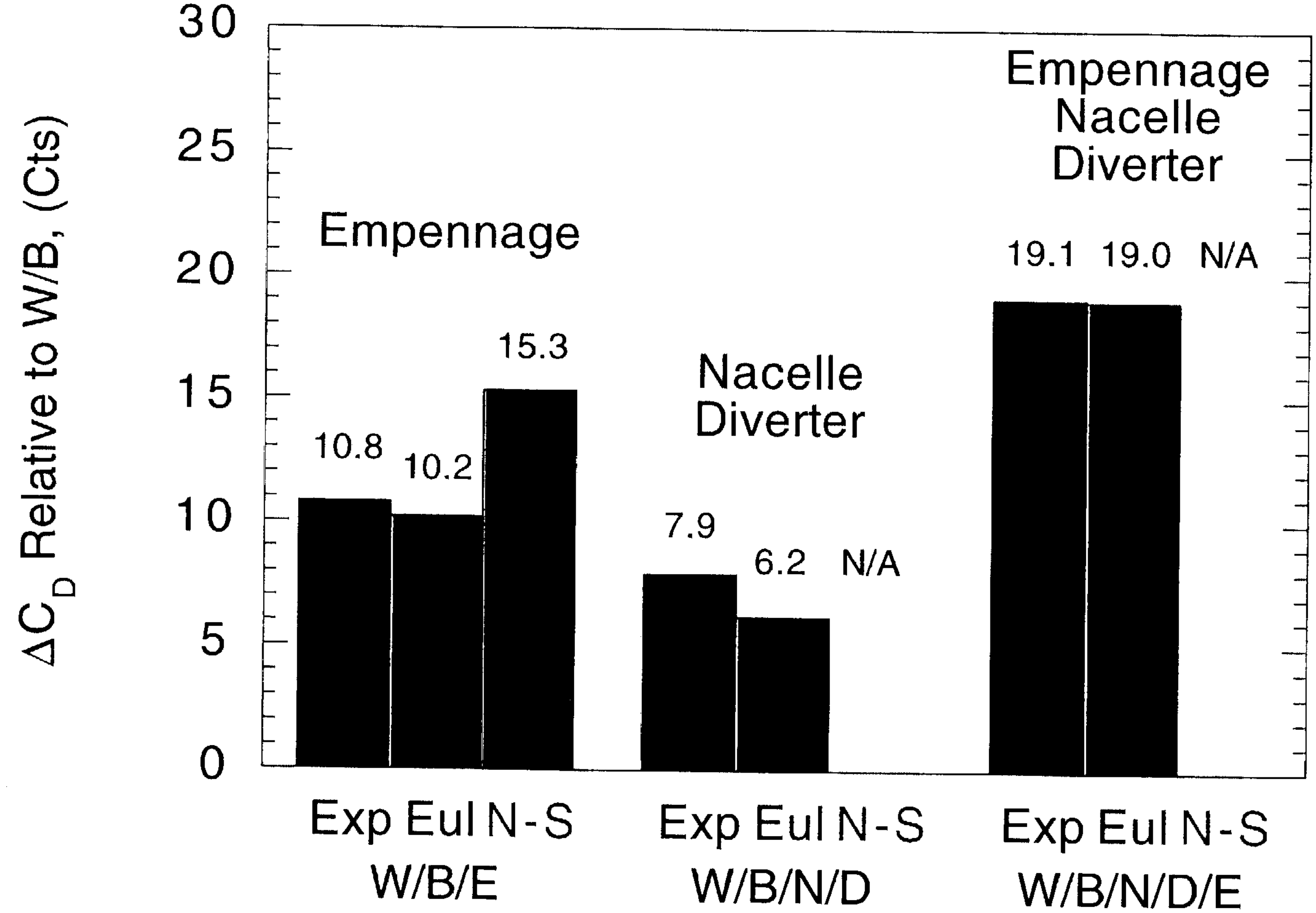

Empennage Effect on Pitching Moment
1.675% Reference H Modular Controls Model

CFL3D & Langley UPWT 1812, M_∞=2.1, at C_L=0.12, Re=3×10^6/ft

The figure below shows the effect of the empennage on the pitching moment for the predicted and experimental results. The measured, Euler, and Navier-Stokes predictions of the empennage effect on pitching moment for the W/B configuration is approximately -0.0050 at a C_L=0.12. This number is obtained in two ways. The first is to compare the pitching moment of the W/B configuration with the W/B/E; the second is to compare the pitching moments of the W/B/N/D with the W/B/N/D/E.

Component Pitching Moment Increments

1.675% Reference H Modular Controls Model

CFL3D & Langley UPWT 1812, M_∞=2.1, C_L=0.12, Re=3x10^6/ft

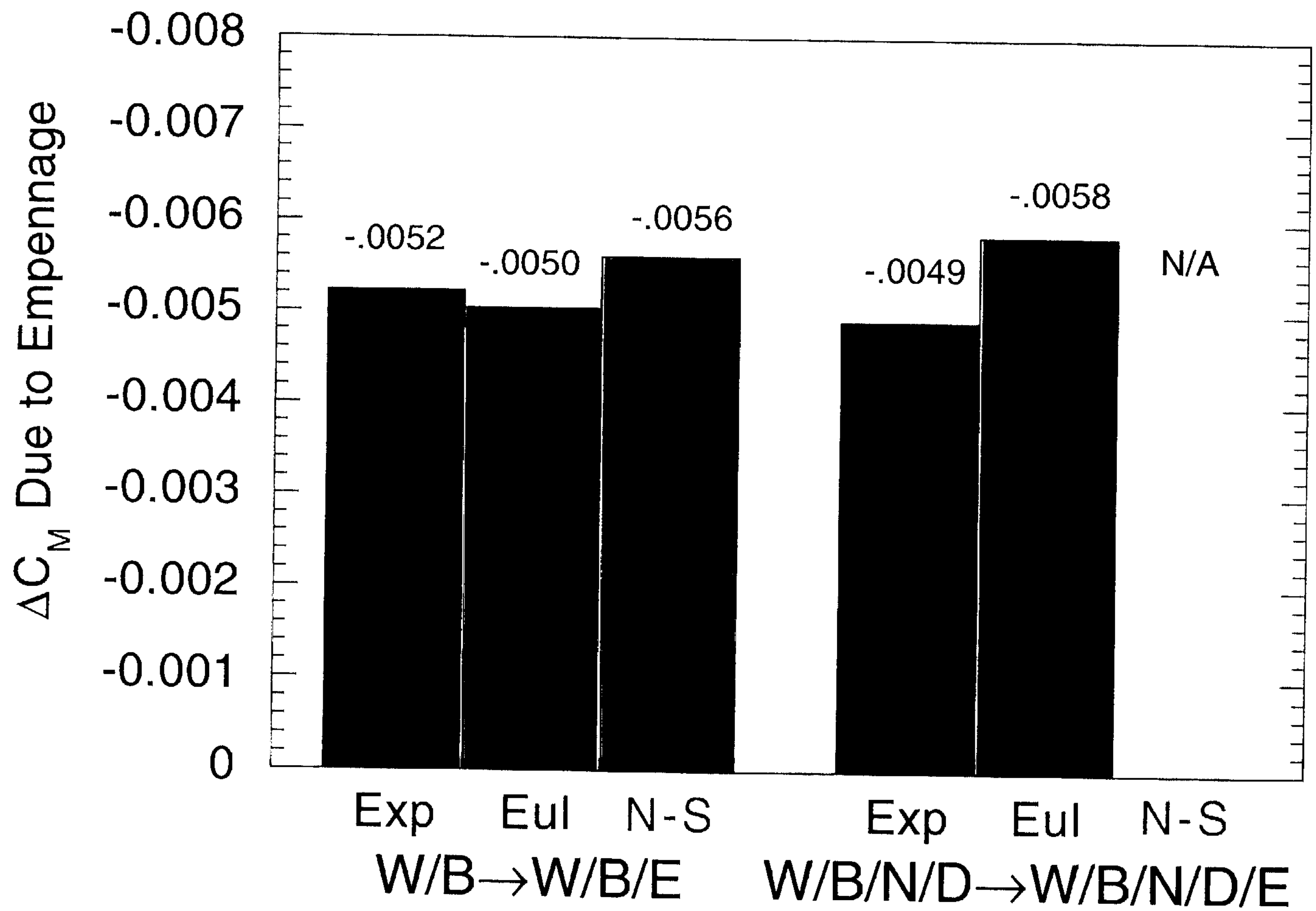

HSR Technology Concept Airplane (TCA)

The TCA build-up will be presented with the W/B and W/B/N/D solutions first, followed by the TCA W/B/E. The W/B and W/B/N/D have a truncated aft fuselage and the W/B/E has the closed aft body.

TCA Build-Up

- TCA W/B and W/B/N/D solutions
  - sting aftbody
  - comparisons with wind-tunnel data
- TCA W/B/E solutions
  - closed aftbody

TCA W/B/E Grid Structure, $i_H=0^\circ$
12 Zones, 3.1 Million Grid Points

The grid structure for the TCA W/B/E with closed fuselage aft body is shown below. The W/B/E grid was created from the W/B/N/D Euler grid. This strategy was taken in part to decrease the overall gridding effort leading up to the full configuration, W/B/N/D/E. The nacelle blocks were taken out from the W/B/N/D grid and replaced by a singular rectangular block, hence giving a W/B/E grid. The nacelle blocks can easily replace this rectangular "plug", giving a full configuration grid within minutes. The open aft body of the W/B/N/D grid was closed to create a real configuration.

The empennage is enclosed by 3 blocks. Both the horizontal and vertical tails have 45 chordwise grid lines and 25 spanwise out to the tip. Since the horizontal and vertical tails start at different streamwise locations, and clustering is needed at the leading edge of both, the decision was made to create two blocks that use a Ronnie patch instead of having one block with skewness in the grid lines. This can be seen in the lower left window in the following chart.

HSR Technology Concept Airplane (TCA) W/B/E, $i_H=0°$
12 Zones, 3.1 Million Grid Points

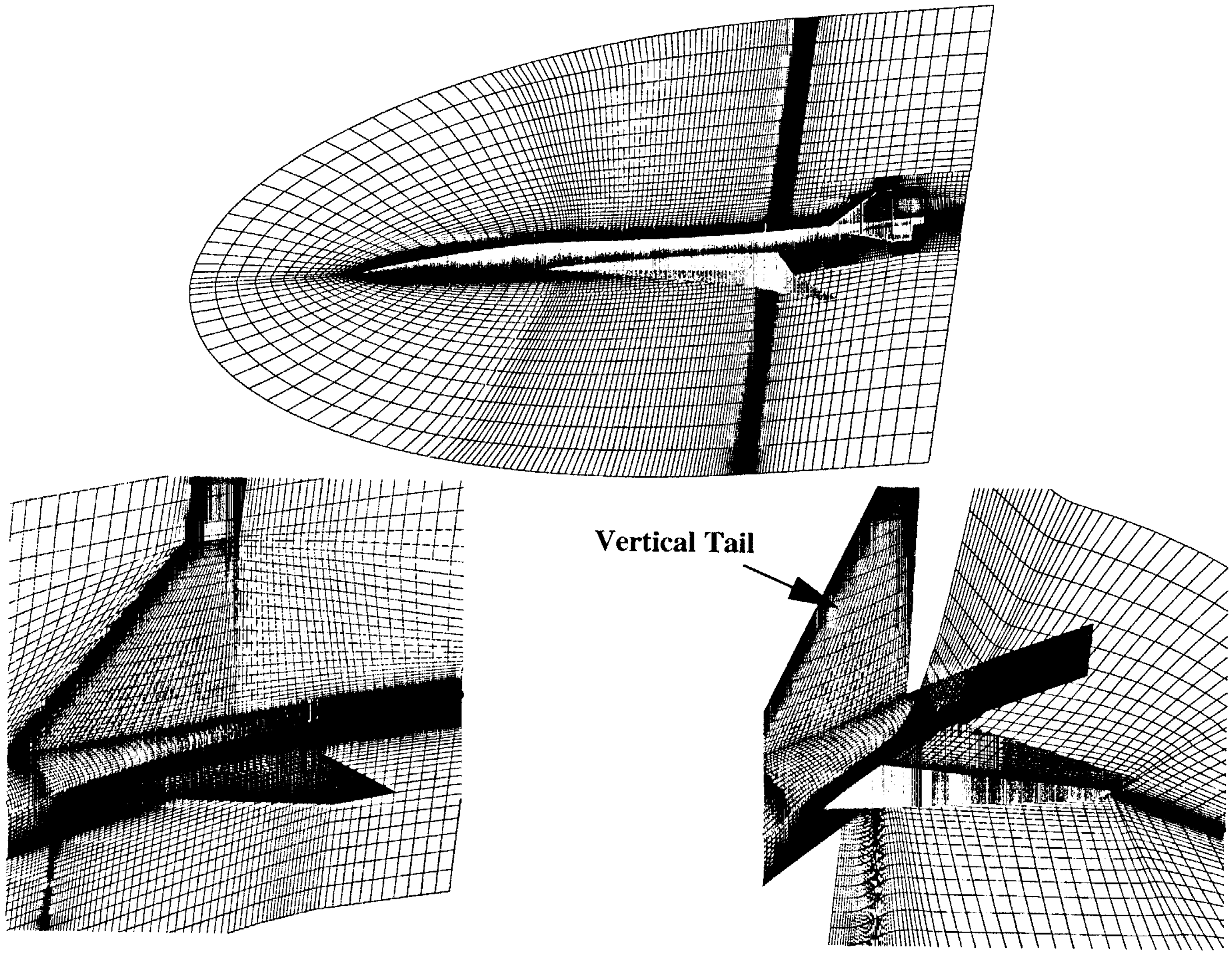

Comparison of Predicted and Experimental Lift Curves
1.675% TCA Model, W/B Configuration

CFL3D & Langley UPWT 1671, M_{∞}=2.4, Re=4x10^6/ft

The following chart shows a comparison between the CFL3D Euler and Navier-Stokes predictions to experimental measurements for the W/B configuration. Both Euler and Navier-Stokes results slightly over-estimate the lift curve slope in relation to the test data. At a constant lift coefficient of C_L=0.1, the Euler solution under-estimated the required angle-of-attack by 0.2° and the Navier-Stokes solution under-estimates the required angle-of-attack by 0.05°.

Comparison of Predicted and Experimental Lift Curves
TCA Wing/Body Configuration

Langley Test 1671, UPWT-2, M_∞=2.4, Re=4×10^6/ft

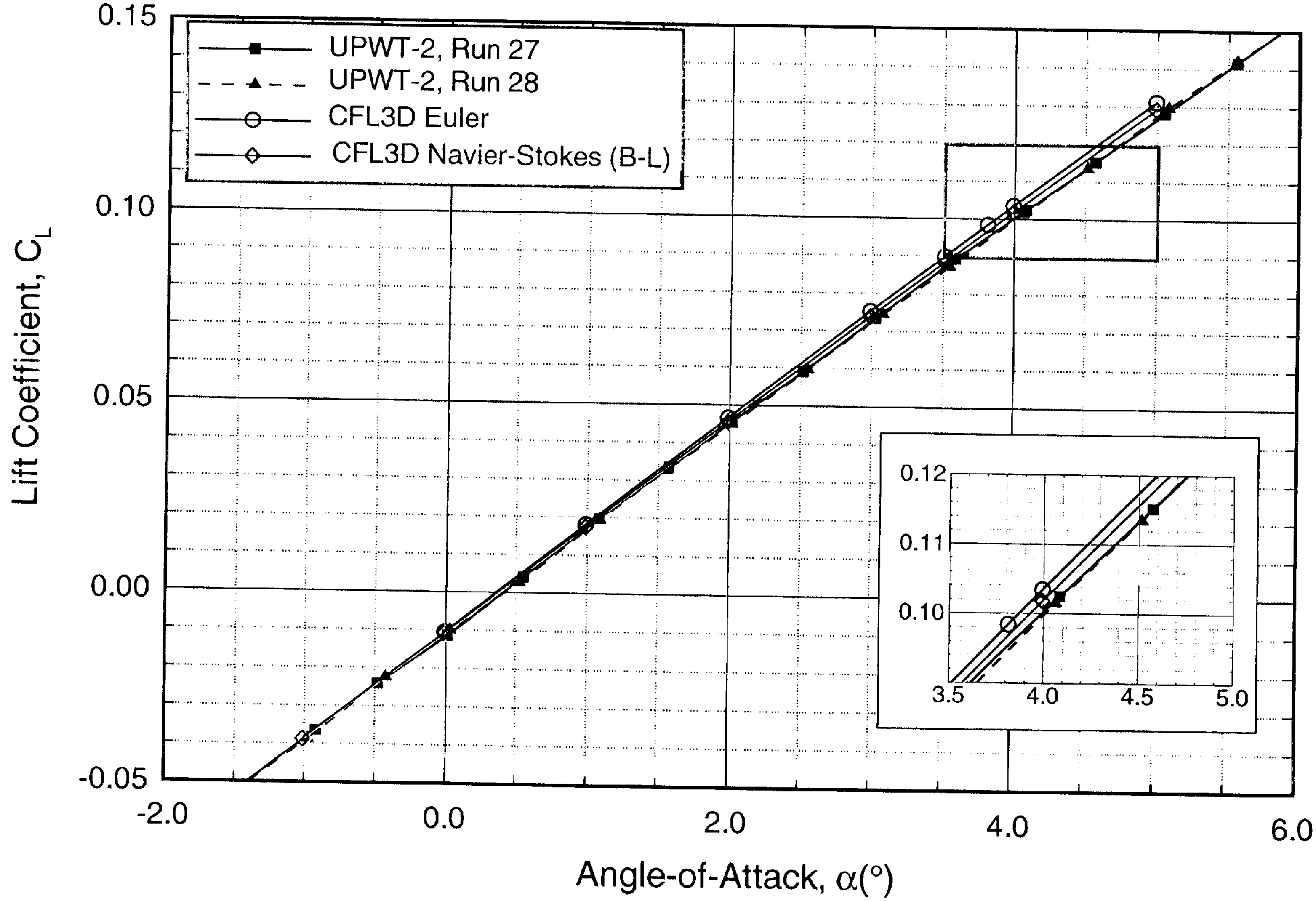

GLM 2/13/97

Comparison of Predicted and Experimental Drag Polars
1.675% TCA Model, W/B Configuration

CFL3D & Langley UPWT 1671, M_∞=2.4, Re=4x10^6/ft

The predicted drag polars at M_∞=2.4 are compared to the test data below. A flat plate skin-friction drag estimate of 61.06 counts has been added to the Euler calculations. The Euler results over-predict the drag at the minimum drag condition while the Navier-Stokes results have good agreement. The Euler and Navier-Stokes over-estimate the drag value at C_L=0.1 by approximately 4.5 and 3.0 counts, respectively. A trip drag estimate varying with C_L and ranging from 2 to 4.5 counts has been removed from the wind-tunnel data. The uncertainty in the trip drag estimate is approximately 2 counts.

Comparison of Predicted and Experimental Drag Polars
TCA Wing/Body Configuration

Langley Test 1671, UPWT-2, M_∞=2.4, Re=4x10^6/ft, Trip Drag Removed

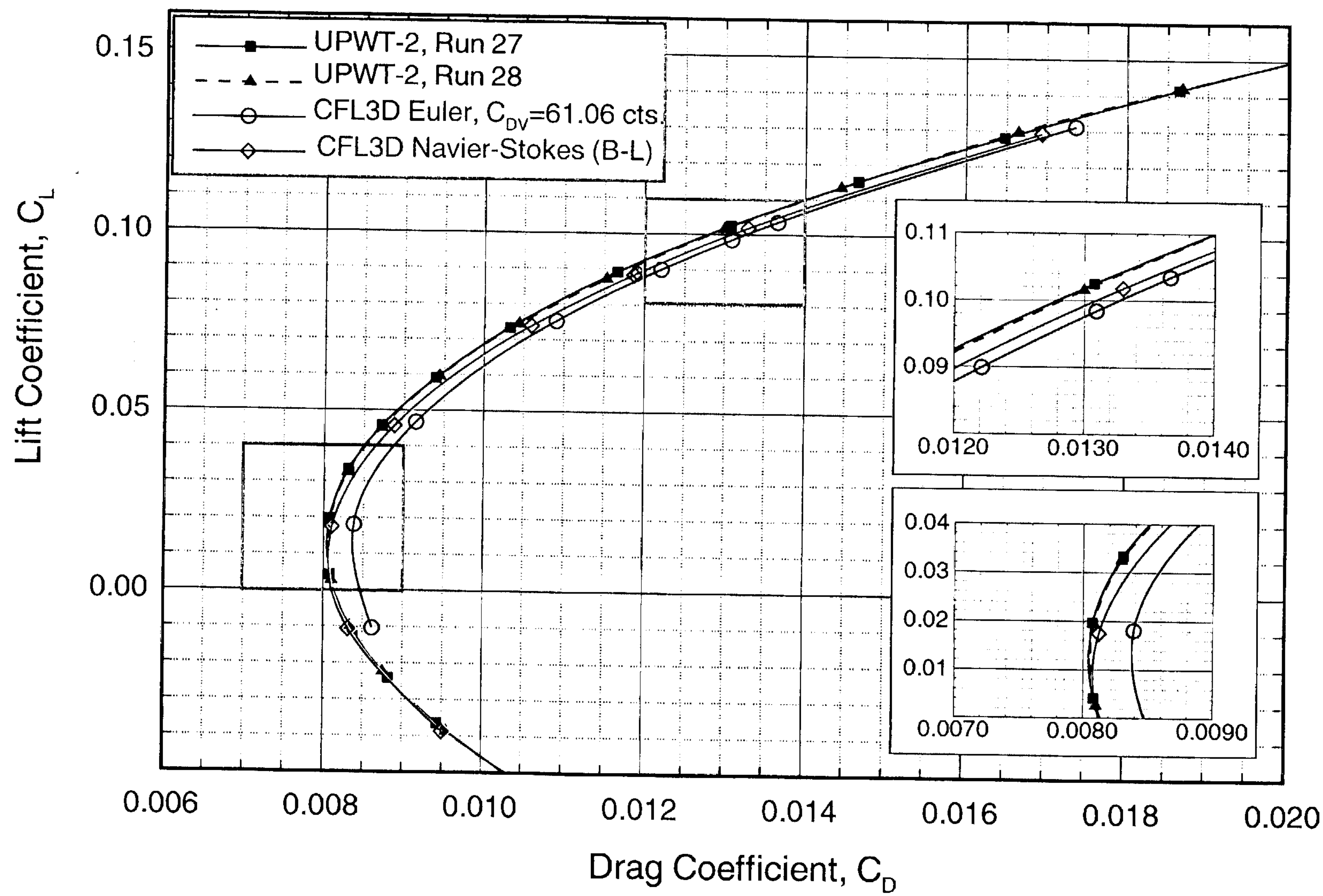

GLM 2/13/97

Comparison of Predicted and Experimental L/D Ratios
1.675% TCA Model, W/B Configuration

CFL3D & Langley UPWT 1671, M_∞=2.4, Re=4x10^6/ft

The following presents lift-to-drag ratio comparisons between the CFL3D Euler and Navier-Stokes predictions to experimental measurements. Due to the over-estimation in drag by the computational results, the predicted lift-to-drag ratios are slightly lower than the test data. The measured L/D_{max} is approximately 7.85 while the Euler and Navier-Stokes results are approximately 7.6 and 7.7, respectively. As described previously, trip drag has been removed from the test data.

Comparison of Predicted and Experimental Lift-to-Drag Ratios
TCA Wing/Body Configuration

Langley Test 1671, UPWT-2, M_∞=2.4, Re=4x10^6/ft, Trip Drag Removed

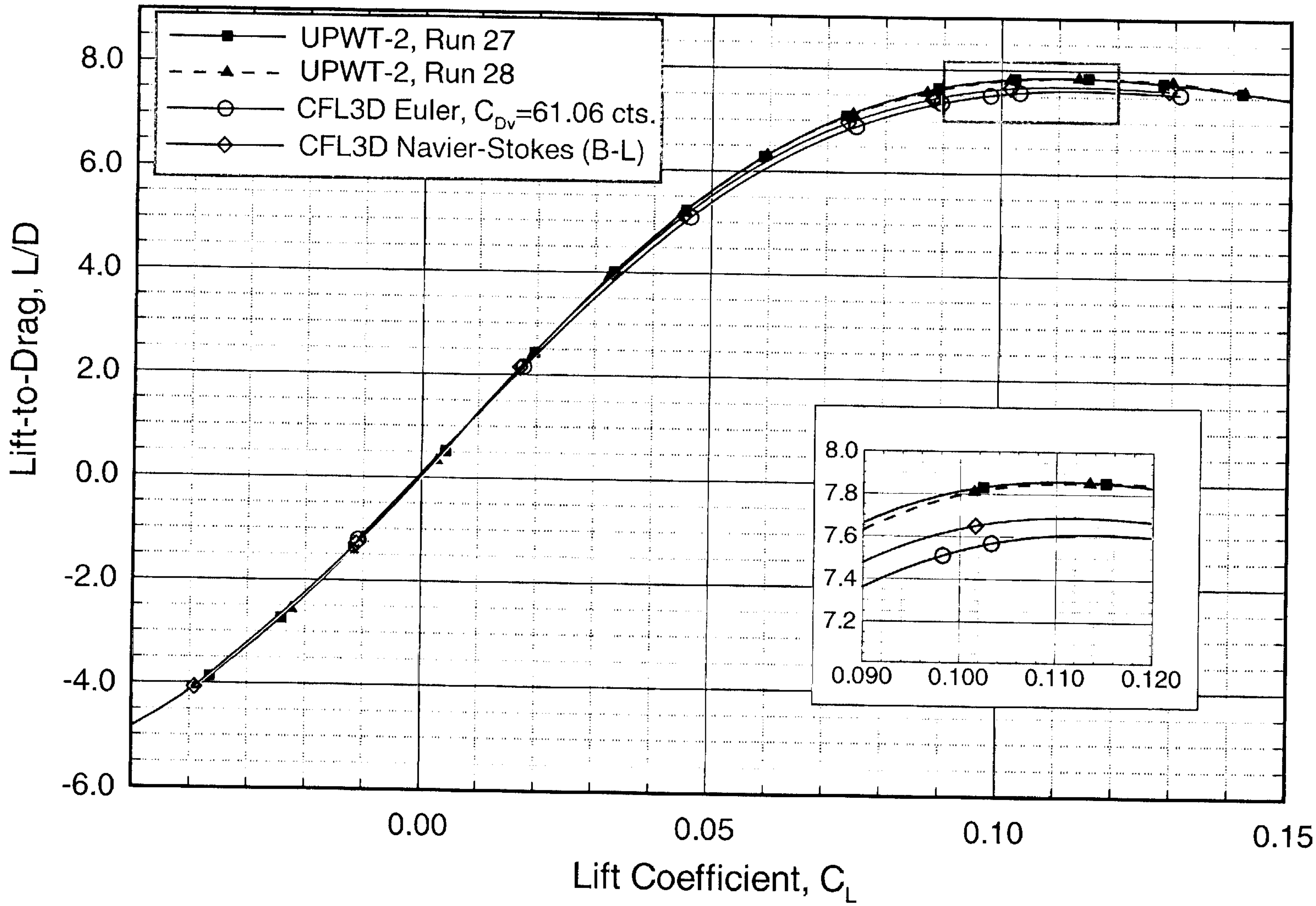

GLM 2/13/97

Comparison of Predicted and Experimental Pitching Moments
1.675% TCA Model, W/B Configuration

CFL3D & Langley UPWT 1671, M_∞=2.4, Re=4x10^6/ft

The W/B pitching moment curve shows a stable configuration up to the cruise condition. The CFL3D Euler and Navier-Stokes predictions give lower ($\partial C_m/\partial C_L$) values compared to the experimental data.

Comparison of Predicted and Experimental Pitching Moments
TCA Wing/Body Configuration

Langley Test 1671, UPWT-2, M_∞=2.4, Re=$4x10^6$/ft

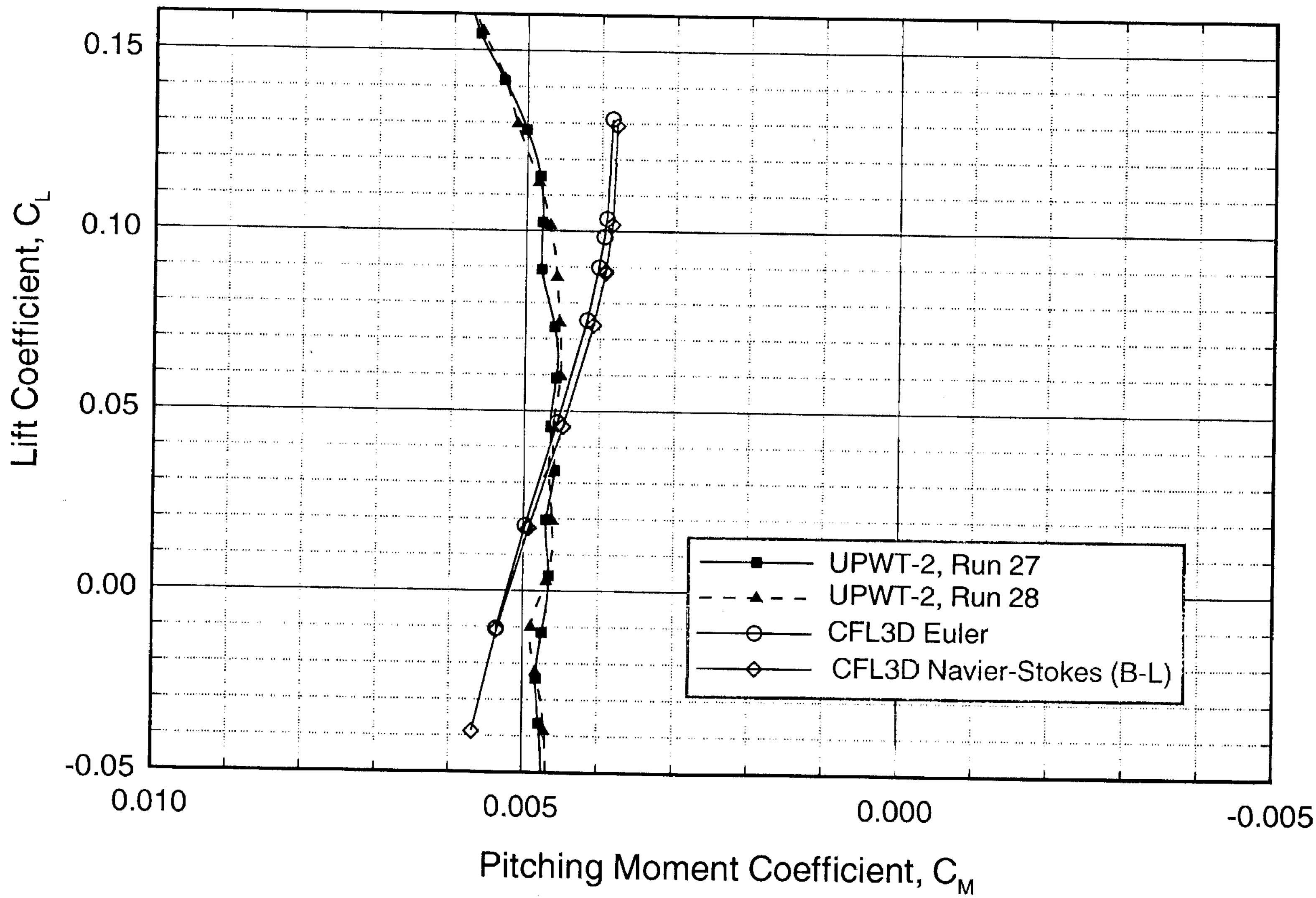

GLM 2/13/97

Comparison of Predicted and Experimental Lift Curves 1.675% TCA Model, W/B/N/D Configuration

CFL3D & Langley UPWT 1671, M_∞=2.4, Re=4x10^6/ft

The Euler and Navier-Stokes solutions computed using CFL3D predict a slightly higher lift-curve slope than the lift-curve slope from the wind-tunnel test. At the constant lift-coefficient of C_L=0.1, the Euler and Navier-Stokes results under-estimate the required angle-of-attack by approximately 0.1°.

Comparison of Predicted and Experimental Lift Curves
TCA Wing/Body/Nacelle/Diverter Configuration

Langley Test 1671, UPWT-2, M_{∞}=2.4, Re=4×10^6/ft

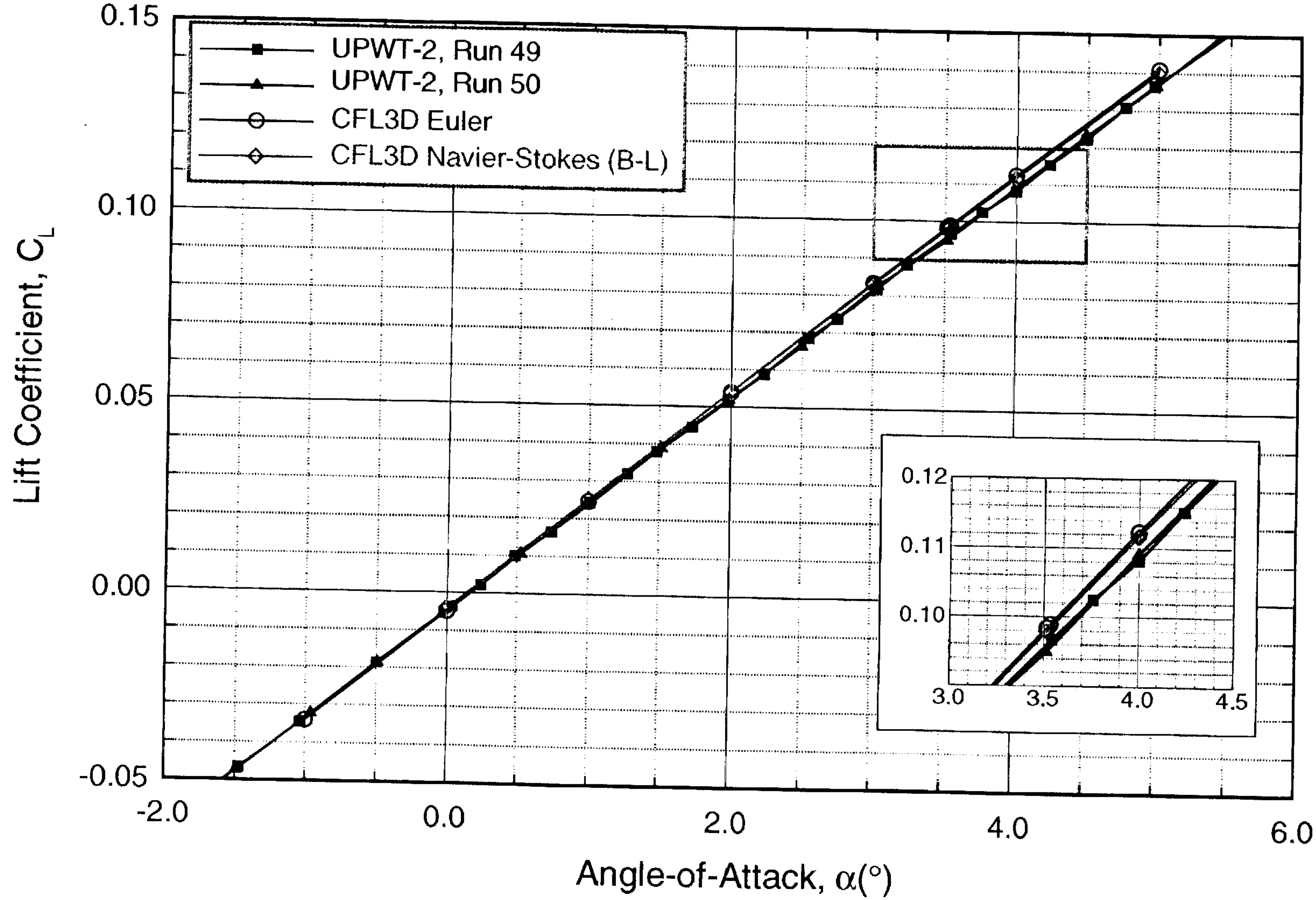

MN 2/13/97

Comparison of Predicted and Experimental Drag Polars
1.675% TCA Model, W/B/N/D Configuration

CFL3D & Langley UPWT 1671, M_∞=2.4, Re=4x10^6/ft

The Mach 2.4 Euler and Navier-Stokes-based drag predictions using CFL3D are compared to the test data below. The experimental data has the appropriate trip drag removed at each lift coefficient. A flat plate skin-friction drag estimate of 70.2 counts has been added to the Euler calculations. Both Euler and Navier-Stokes predicted higher drag values at minimum drag , C_{Dmin}. At C_L=0.1 , the Euler and Navier-Stokes solutions over-estimate the drag by approximately 3 and 2 counts, respectively. A trip drag estimate varying with C_L and ranging from 3 to nearly 7 counts has been removed from the wind-tunnel data. The uncertainty in the trip drag estimate is approximately 3 counts.

Comparison of Predicted and Experimental Drag Polars
TCA Wing/Body/Nacelle/Diverter Configuration

Langley Test 1671, UPWT-2, M_∞=2.4, Re=4x10^6/ft, Trip Drag Removed

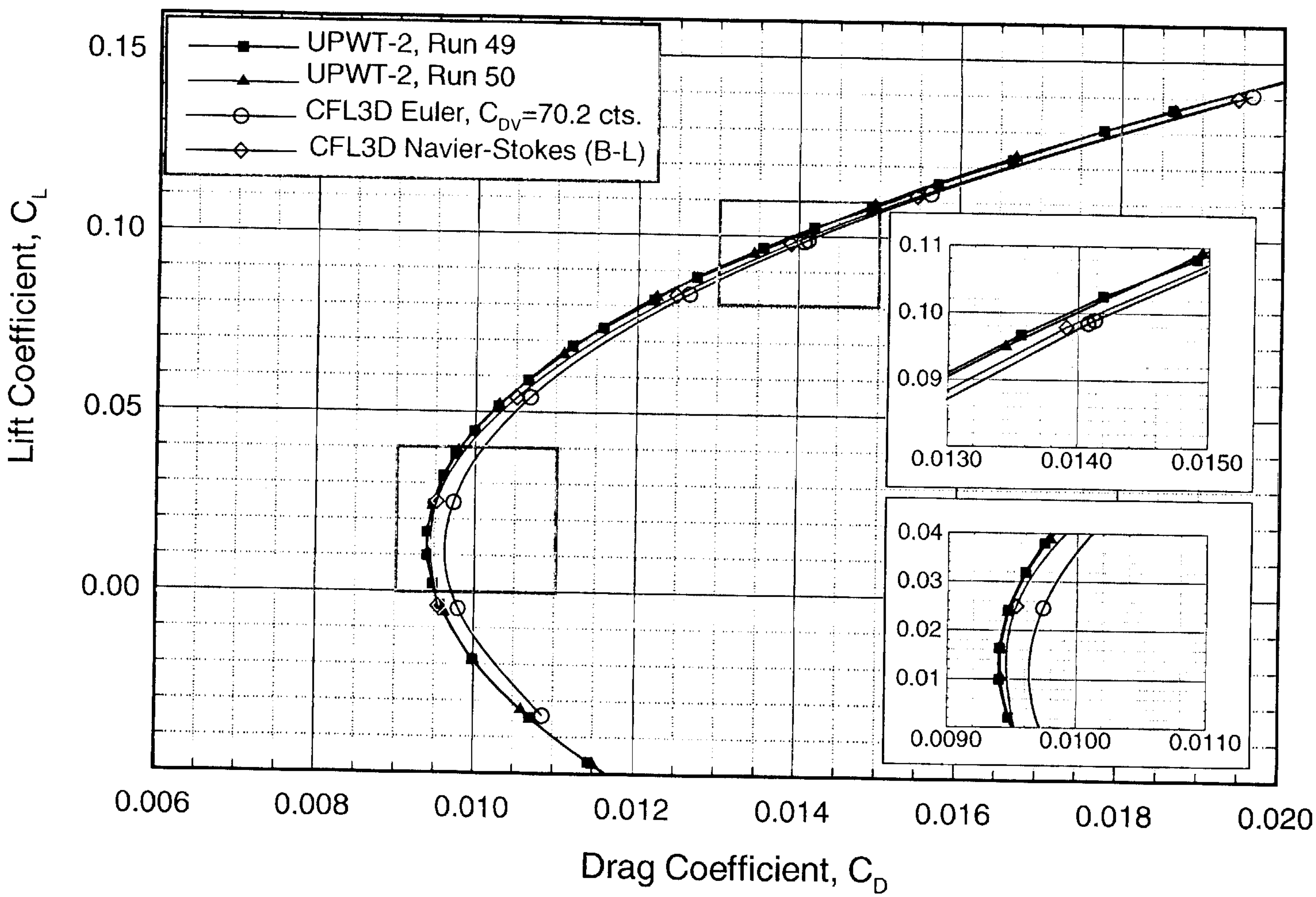

MN 2/13/97

Comparison of Predicted and Experimental L/D Curves
1.675% TCA Model, W/B/N/D Configuration

CFL3D & Langley UPWT 1671, M_{∞}=2.4, Re=4x10^6/ft

The following presents lift-to-drag ratio comparisons between the CFL3D Euler and Navier-Stokes predictions to experimental measurements. Due to the over-estimation in drag by the computational results, the predicted lift-to-drag ratios are slightly lower than the test data. The measured L/D_{max} is approximately 7.35 while the Euler and Navier-Stokes results are approximately 7.25 and 7.36, respectively. As described previously, trip drag has been removed from the test data.

Comparison of Predicted and Experimental Lift-to-Drag Ratios
TCA Wing/Body/Nacelle/Diverter Configuration

Langley Test 1671, UPWT-2, M_∞=2.4, Re=4x10^6/ft, Trip Drag Removed

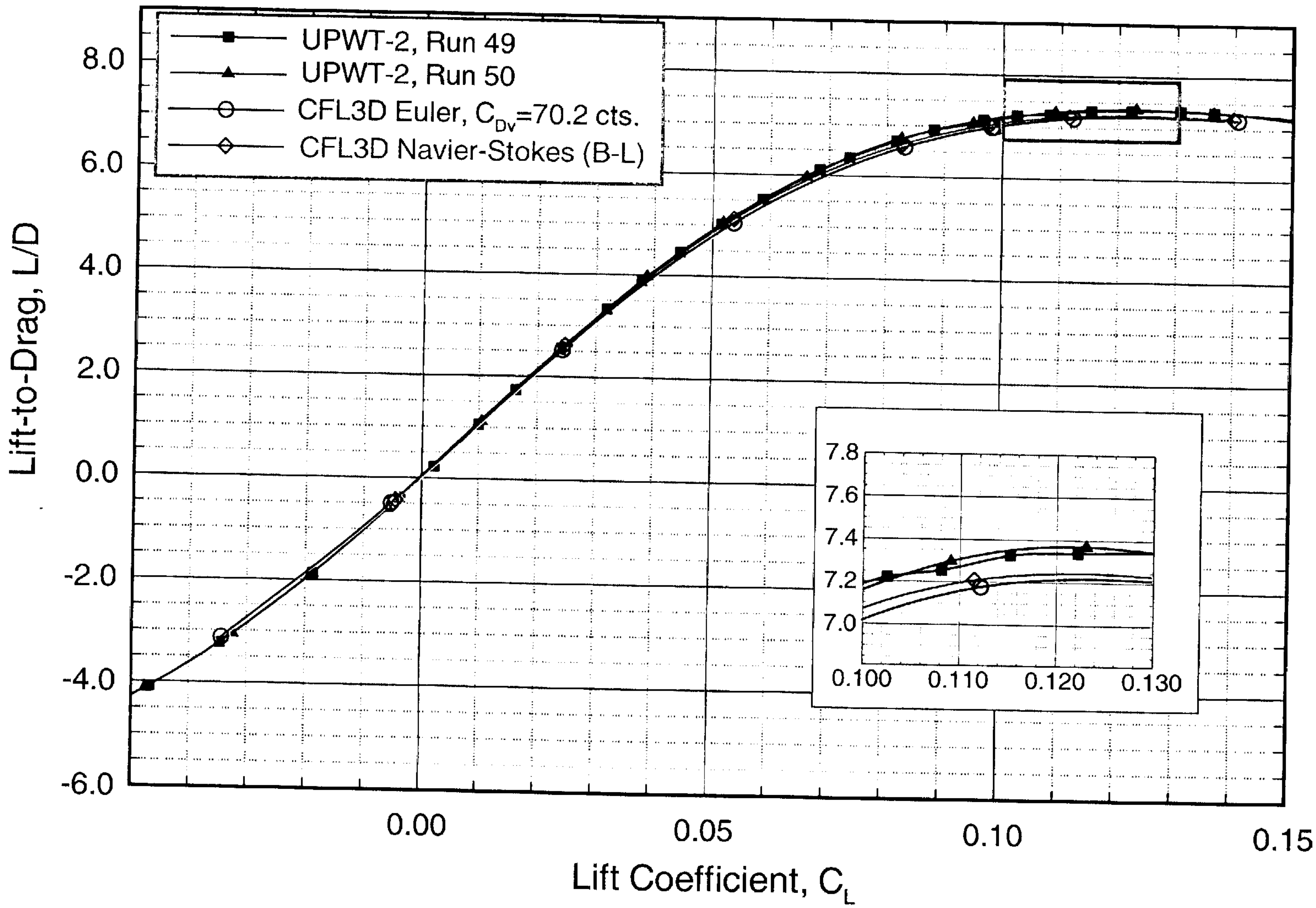

MN 2/13/97

Comparison of Predicted and Experimental Pitching Moments
1.675% TCA Model, W/B/N/D Configuration

CFL3D & Langley UPWT 1671, M_∞=2.4, Re=4x10^6/ft

The W/B/N/D moment curve shows a stable configuration up to the cruise condition. As seen in the W/B case the CFL3D Euler and Navier-Stokes predictions give lower ($\partial C_m/\partial C_L$) values compared to the experimental data.

Comparison of Predicted and Experimental Pitching Moments
TCA Wing/Body/Nacelle/Diverter Configuration

Langley Test 1671, UPWT-2, M_∞=2.4, Re=4x10^6/ft

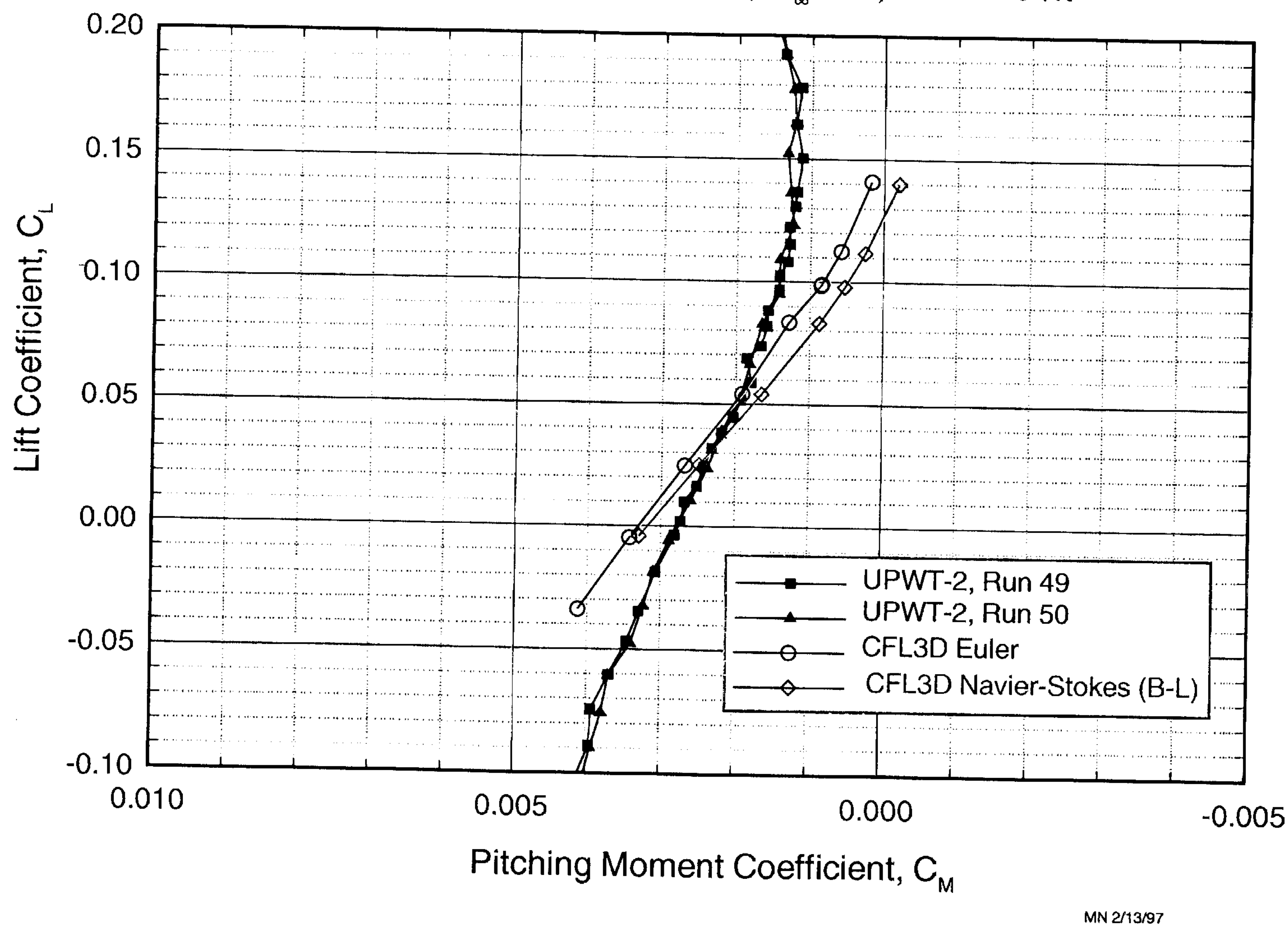

Predicted Nacelle Installation Drag

M_∞ 2.4, C_L=0.1, Re=$4x10^6$/ft.

The predicted nacelle drag increment is compared to the measured drag below. The drag values seen below are in units of drag counts. Though the absolute drag levels of the Euler and Navier-Stokes predictions were high, the increment is predicted well.

Predicted Nacelle Installation Drag

M_∞=2.4, C_L=0.1, R_e=4x10^6/ft.

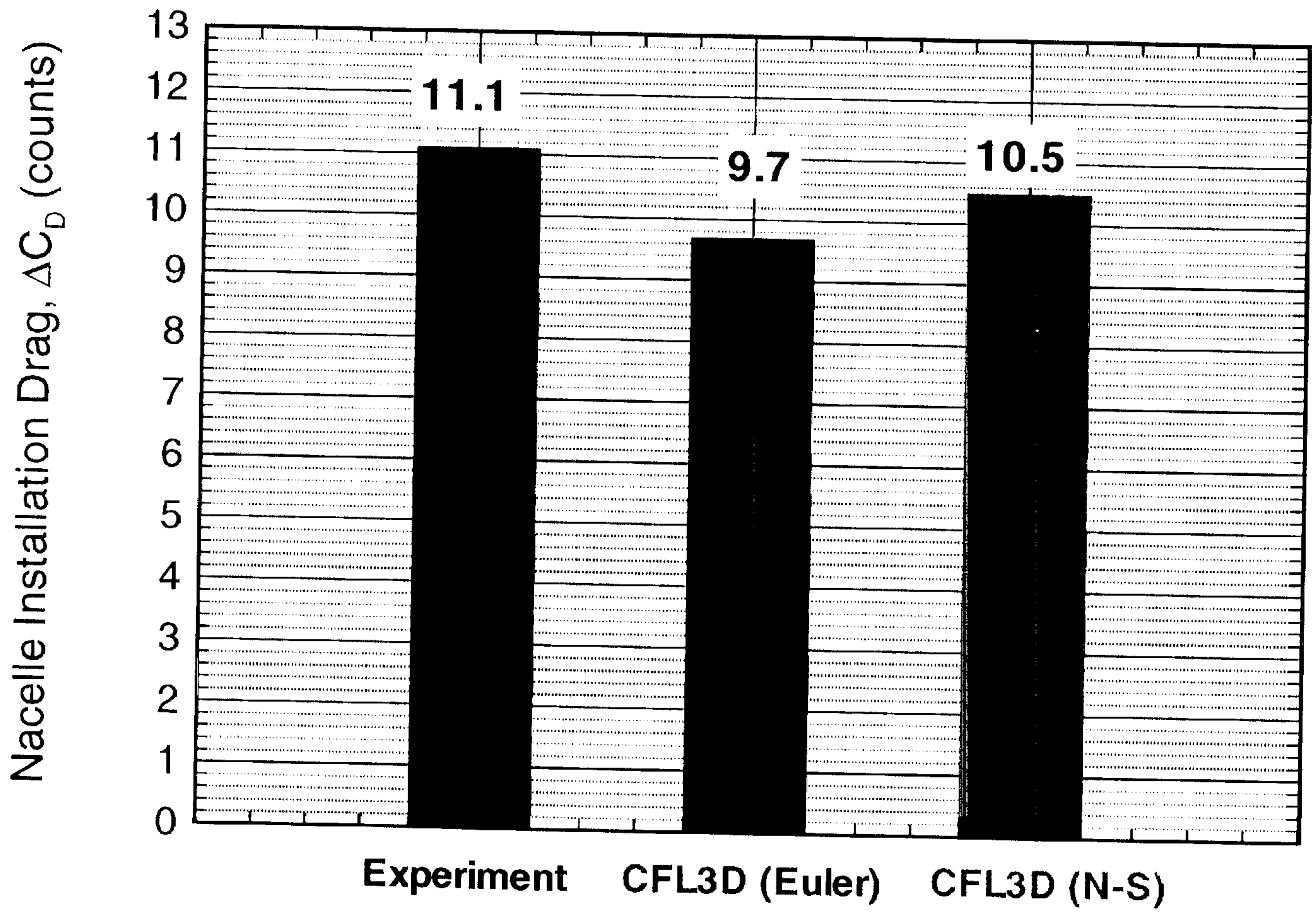

Lift Coefficients for the TCA W/B/E Configuration CFL3D Euler, M_∞=2.4

The figure below shows the TCA W/B/E lift coefficients with horizontal tail settings of -5°, 0°, and +2°. At an angle-of-attack of 3.5°, the TCA W/B/E with horizontal tail setting of +2° has approximately 5.6% higher C_L than the 0° horizontal tail setting.

Lift Coefficients for the TCA Wing/Body/Empennage Configuration
CFL3D Euler, M_∞=2.4

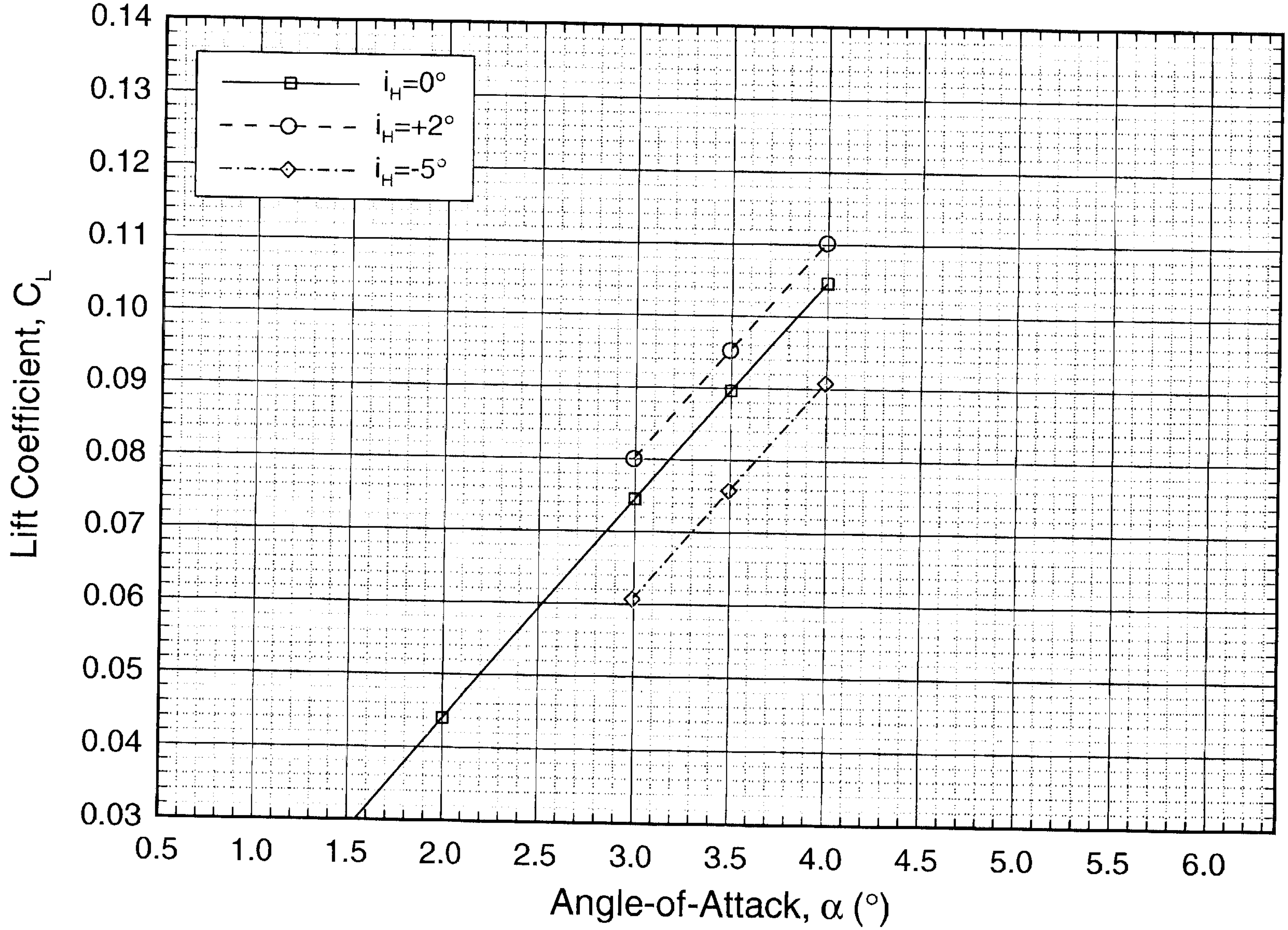

Pressure Drag Coefficients (C_{D_P}) for the TCA W/B/E Configuration CFL3D Euler, M_∞=2.4

The figure shows the TCA W/B/E pressure-drag coefficients with horizontal tail settings of -5°, 0°, and +2°. The W/B/E with the +2° horizontal tail setting has approximately 2 counts less C_{D_P} than the 0° horizontal tail case at a C_L of 0.1. These calculations were performed with a closed fuselage aft body.

Pressure Drag Coefficients (C_{Dp}) for the TCA W/B/E Configuration
CFL3D Euler, M_∞=2.4

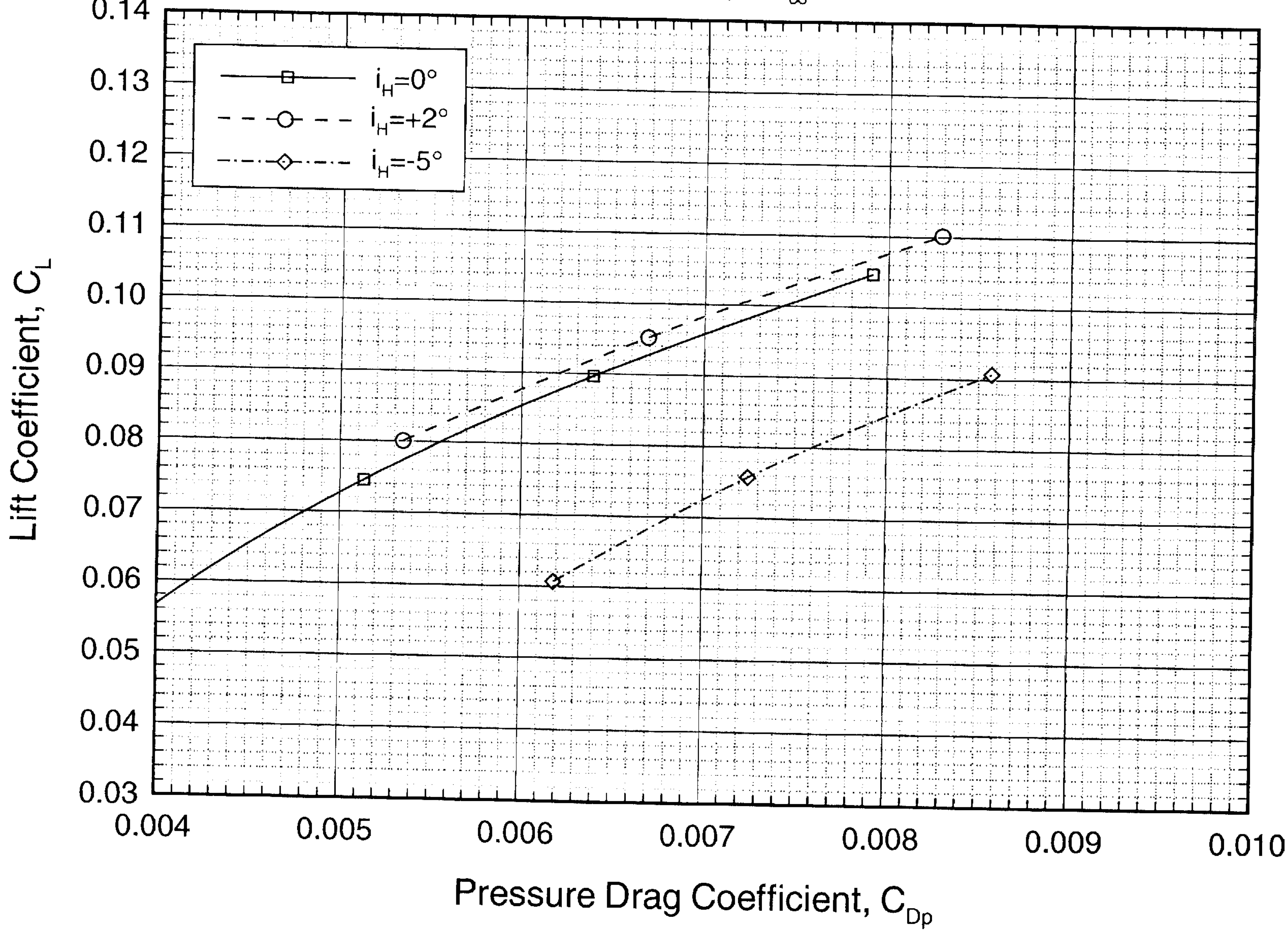

Pitching Moments for the TCA W/B/E Configuration CFL3D Euler, M_∞=2.4

Seen below is the pitching moments for the TCA W/B/E configuration. The +2° horizontal tail setting produces an overall more negative (nose-down) pitching moment for the configuration while i_H=-5° produces a more positive (nose-up) pitching moment. Results from these solutions will be used in a trim drag optimization study.

Pitching Moment for the TCA Wing/Body/Empennage Configuration
CFL3D Euler, M_∞=2.4

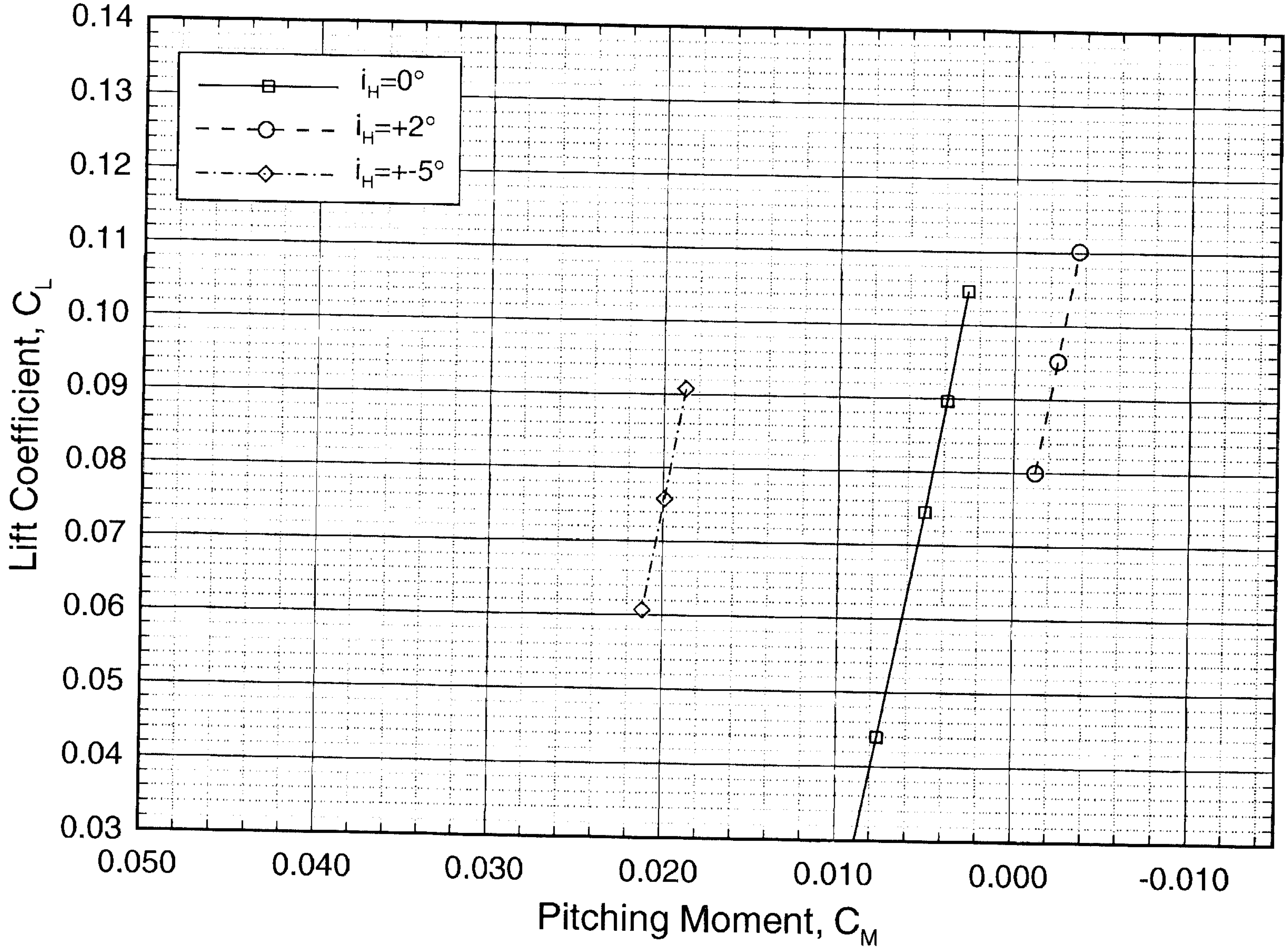

Pressure Contours on the TCA Empennage
CFL3D Euler, M_∞=2.4

The pressure contours on the TCA empennage for all three horizontal tail settings at alpha = 3.5° are shown below. The -5° horizontal tail setting shows a much stronger leading-edge shock compare to the 0° and +2° cases. The horizontal tail leading-edge shock interaction with the aft end of the fuselage is also seen.

Pressure Contours on HSR Technology Concept Airplane (TCA) W/B/E
CFL3D Euler, 12 Zones, 3.1 Million Grid Points
M_∞=2.4, α= 3.5°

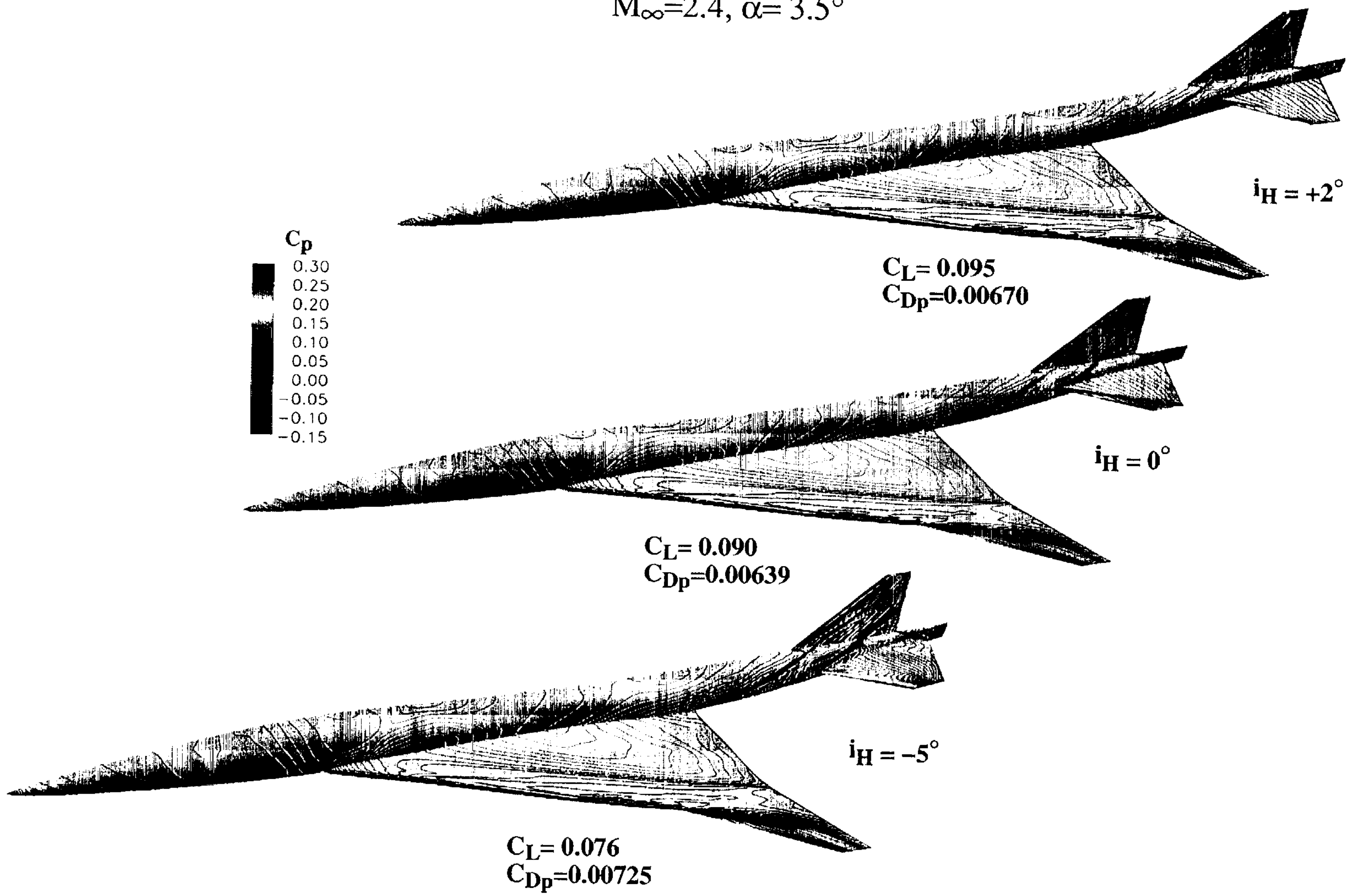

Pressure Contours on the TCA Empennage
CFL3D Euler, $M_{\infty}=2.4$

The pressure contours on the TCA empennage for all three horizontal tail settings at alpha = 3.5° are shown below with the corresponding pressure drag value (C_{Dp}). The W/B/E with the +2° horizontal tail setting has approximately 2 counts less C_{Dp} than the 0° horizontal tail case at a C_L of 0.1.

Pressure Contours on HSR Technology Concept Airplane (TCA) Empennage
CFL3D Euler, 12 Zones, 3.1 Million Grid Points
M_∞=2.4, α= 3.5°

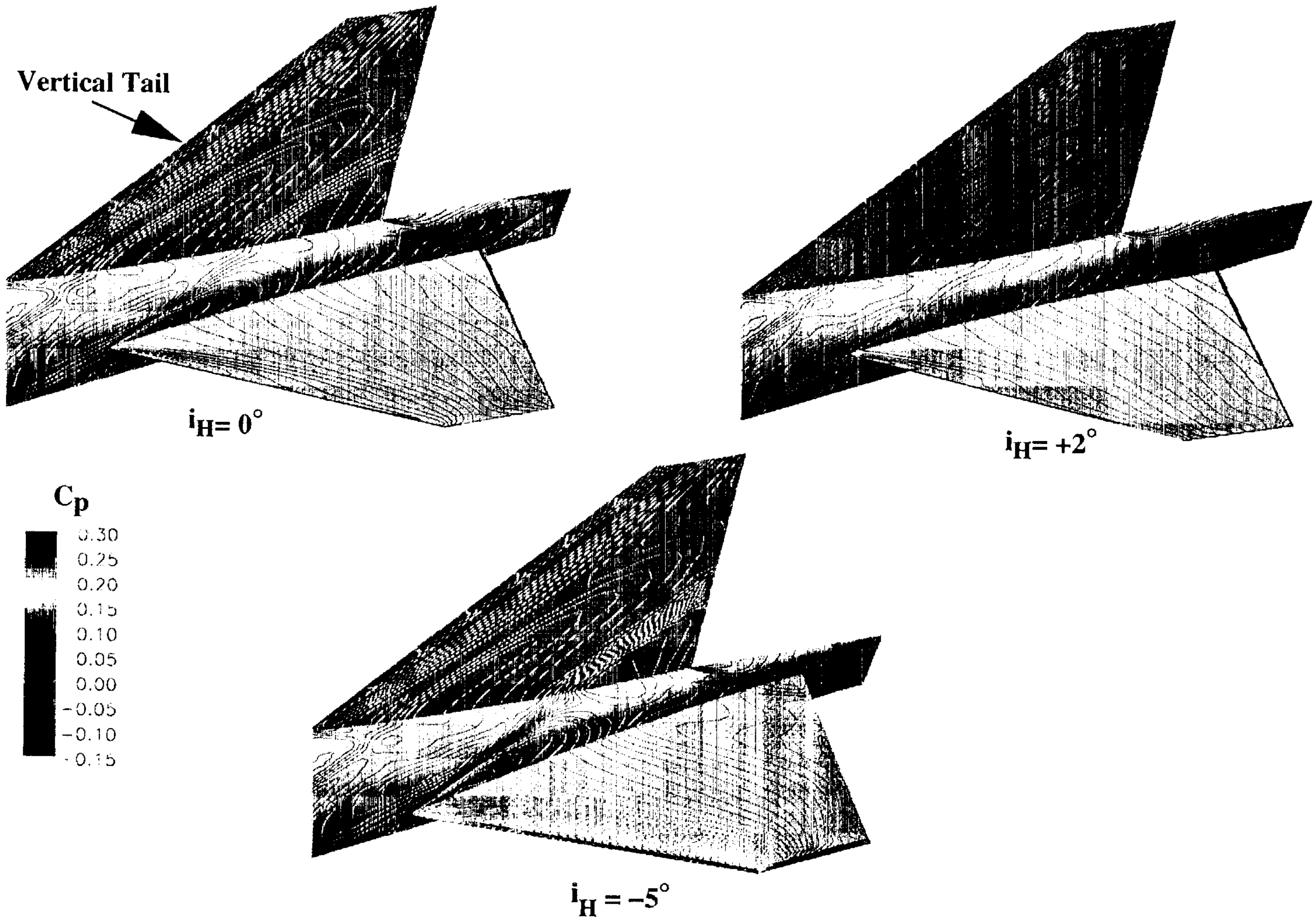

Computer Resources Used for Calculations on Various Configurations at Supersonic Conditions

One of the objectives of this task was to assess the feasibility of full-configuration force and moment calculations. The above table is a summary of the required memory and CPU time to run a single solution for all configurations presented herein. A number of platforms were used to make the computations. In each case the CPU requirement is based on convergence of lift and drag to five significant digits. The Cray C-90 is a well established computer and CPU requirements are not expected to diminish in the future. The IBM SP-2 and J-90 are newer machines and software modifications to take advantage of the hardware architectures can be expected to reduce the CPU requirements.

Computer Resources Used for Calculations on Various Configurations at Supersonic Conditions

Config.	Solution Type	Turb. Model	Grid Size (Millions)	Platform	CPU Time (hrs)	Memory Req. (Mw)
W/B	Euler	N/A	0.9	C-90	1.5	40
W/B	N-S	B-L	1.5	J-90	10	68
W/B/E	Euler	N/A	1.5	C-90	2	58
W/B/E	Euler	N/A	3.1	SP-2	1.5	85
W/B/E	N-S	B-L	2.2	C-90	4	91
W/B/E	N-S	B-B	2.2	C-90	8	104
W/B/N/D	Euler	N/A	2.4	C-90	3.5	85
W/B/N/D	N-S	B-L	6.0	C-90	16	212
W/B/N/D/E	Euler	N/A	2.6	C-90	3.5	90

Summary and Conclusions

The flow over two full configuration (W/B/N/D/E) HSCT configurations were analyzed using CFL3D. Although the drag levels predicted by CFL3D were significantly under-predicted for the Reference H configuration, the drag increment for each component are in good agreement between the experiment and the Euler solutions. The Navier-Stokes component increment predictions were further from the experimental data than the Euler results. Further investigations will be done to find a turbulence model which captures the wake region flow characteristics. Thus far, the TCA W/B and W/B/N/D CFL3D results are very encouraging. The Navier-Stokes W/B/N/D predictions over-estimated the experimental data by 2 counts. This agreement is extremely important in order to validate the analysis tools used for the complex configurations.

Summary & Conclusions

- Ref. H CFL3D results under-estimate drag but Euler component build-up is reasonable
- Ref. H CFD geometry and wind-tunnel model may differ significantly
- Good agreement between CFD Navier-Stokes and wind-tunnel for TCA W/B and W/B/N/D
- TCA full configuration analysis is underway

Supersonic Cruise Point Design Optimization of TCA

Eric R. Unger
Robert P. Narducci
James O. Hager
Geojoe Kuruvila
Peter M. Hartwich
Shreekant Agrawal

McDonnell Douglas Corporation
Long Beach, California 90807-5309

Since July of 1996, McDonnell Douglas (along with other teams from NASA Ames and Boeing Commercial Aircraft Group), has been working on a second series of optimizations for the TCA configuration. The approach used at MDC was conservative in terms of acceptable geometric qualities that were allowed to appear in the final Cycle 2 design. The hope was that any final outcome would be more robust and raise the least amount of uncertainties from other technology disciplines. The downside of this approach was the inability to fully maximize the possible L/D gains within the given time and within these strict geometric guidelines.

This paper presents an overview of MDC's final Cycle 2 configuration. First, a brief introduction and highlights of the new design are given along with some geometric details. Second, a look at the configuration's overall performance and pressure field details will be given. Next, some details of the design constraints that were used during optimization will be described. And finally, the paper will close with a summary of the Cycle 2 configuration and a look ahead to the immediate future.

Supersonic Cruise Point Design Optimization of TCA

Eric R. Unger
Robert P. Narducci
James O. Hager
Geojoe Kuruvila
Peter M. Hartwich
Shreekant Agrawal

McDonnell Douglas
Long Beach, California

1997 AP Workshop
February 25, 1997

Contents

Listed below are the contents of the paper to be discussed.

Contents

- Introduction to the Cycle 2 design
- OML characteristics
- Aerodynamic performance and section cuts
- Constraint evaluation
- Summary
- Future directions

TCA Nonlinear Point Design Optimization Cycle 2

In July 1996 the HSR Configuration Aerodynamics (CA) Nonlinear Point-Design Optimization PDR took place. The intention was to select a model for wind-tunnel testing to meet the Nonlinear Point-Design milestone. However, none of the designs by the three participants (NASA Ames, Boeing, and McDonnell Douglas Corp.) were deemed mature enough to proceed with model construction. Therefore, a decision was made to perform a second cycle of the study and hold a new PDR in January '97. The participants of the new cycle were the same as before with each group using their own design and analysis tools and a common set of constraints (as was the case in the first cycle). In the end, the final Cycle 2 Configurations from each of the participants were quite different from one another.

TCA Nonlinear Point Design Optimization Cycle 2

- Initial (cycle 1) PDR was held in July 1996
- Program initiated after cycle 1 results were deemed immature
- Participants included NASA Ames, Boeing, and McDonnell Douglas
  - Each used different analysis and optimization codes along with different overall philosophies toward optimization and design
  - Each satisfied a common set of design constraints
  - Three very different final outcomes

Design Tools

Listed below are the design tools that were used in the creation of the TCA Cycle 2 design. For the most part, the MDO3D code was used to perform the optimization on this configuration. This is a finite-difference based, fully constrained design code utilizing CFL3D for analysis and DOT for the shape optimization of the wing and fuselage. For a small portion of the effort, the NASA Ames SYN87 adjoint-based design code was utilized for some wing twist and camber optimization. It should be noted that the optimization was frequently halted for various smoothing and clean-up procedures.

Design Tools

- MDO3D (CFL3D/DOT) finite-difference-based, fully constrained design code was used for the majority of wing and fuselage optimization
- SYN87 (FLO87/NPSOL) adjoint-based design code from NASA Ames was used for initial wing camber and twist optimization
- Frequent application of smoothing routines to clean-up geometry

TCA Cycle 2 Highlights

The philosophy used to create the MDC TCA Cycle 2 design was very different from those of the other participants. The goal was to minimize the supersonic cruise drag as much as possible while maintaining the smoothness and relatively flat features of the TCA Baseline design. Along with these goals was a similar desire to generate a configuration that would achieve its benefits with very smooth pressure distributions and good leading-edge suction that would be beneficial at off-design conditions as well.

With these goals in mind, the MDC TCA Cycle 2 design was created. This configuration is very smooth with well-behaved pressure distributions and good leading-edge suction. The configuration also maintains a good portion of its improvement over a very large portion of the drag polar. A beneficial outcome of this philosophy also resulted in significant volume increases in the fuselage (2.7%), the wing (4.3%), and the fuel volume (7.4%). Even with all of these volume increases and smoothness requirements, the configuration still achieved a 3.9 count reduction in the supersonic cruise drag at a C_L of 0.10.

TCA Cycle 2 Highlights

- Aerodynamically conservative design
  - Smooth wing surface
  - Smooth well-behaved pressure distributions with good leading-edge suction
  - Good off-design performance
- Significant volume increases over baseline TCA
  - 2.7% increase in fuselage volume
  - 4.3% increase in wing volume
  - 7.4% increase in fuel volume

The TCA Cycle 2 Shaded Images

The next two slides show shaded images of the MDC Cycle 2 Configuration. On this first isometric view, note the marked smoothness of the lower surface of the wing and the substantial thickness of the inboard wing. Also noticeable in this view is the gentle curving upward of the trailing edge of the wing near the wing/body intersection. This curving region only extends forward to approximately the 3/4 chord although it does encompass the rear spar. Additional geometric features can also be spotted on the fuselage where the cross-sectional area near the leading edge of the wing/body intersection has been increased.

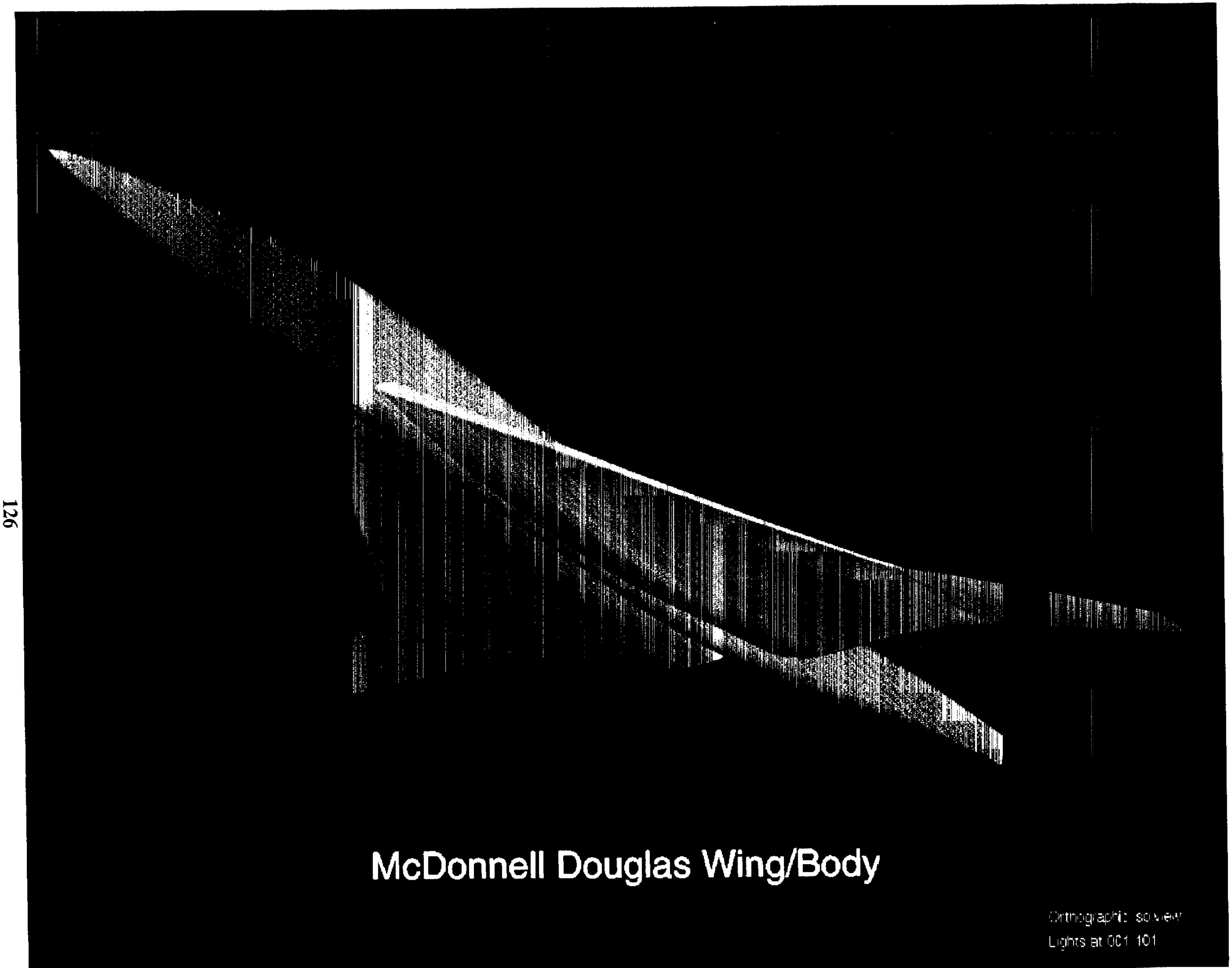
McDonnell Douglas Wing/Body
Orthographic isoview
Lights at 001 101

The TCA Cycle 2 Shaded Images (cont.)

This shaded image shows the front view of the TCA Cycle 2 Configuration. Noteworthy on this view is the overall flatness of the TCA Cycle 2 design.

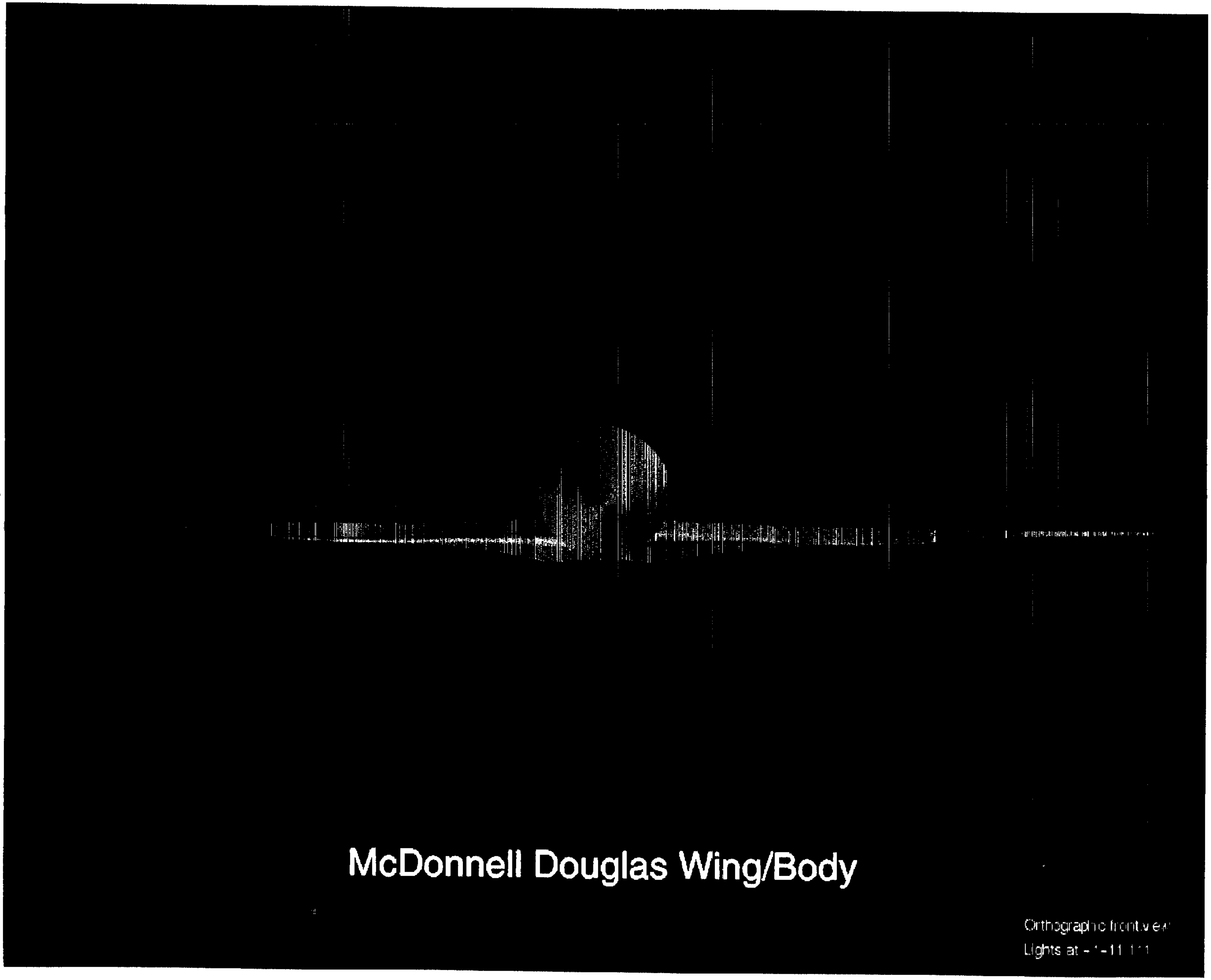
McDonnell Douglas Wing/Body
Orthographic front view

Waterline Contours for the Baseline TCA Configuration

The next two slides show waterline contours for the TCA Baseline and Cycle 2 designs. In these plots, the Z-component (waterline) of the upper and lower wing surfaces is used to contour the planform. Such plots are useful in evaluating the smoothness of a configuration where erratic or rapid color changes could indicate a non-smooth design.

Shown first is the TCA Baseline configuration. Note that there are no abrupt changes (except at the leading-edge break) in the contours and that the lines are smooth.

Waterline Contours for Baseline TCA

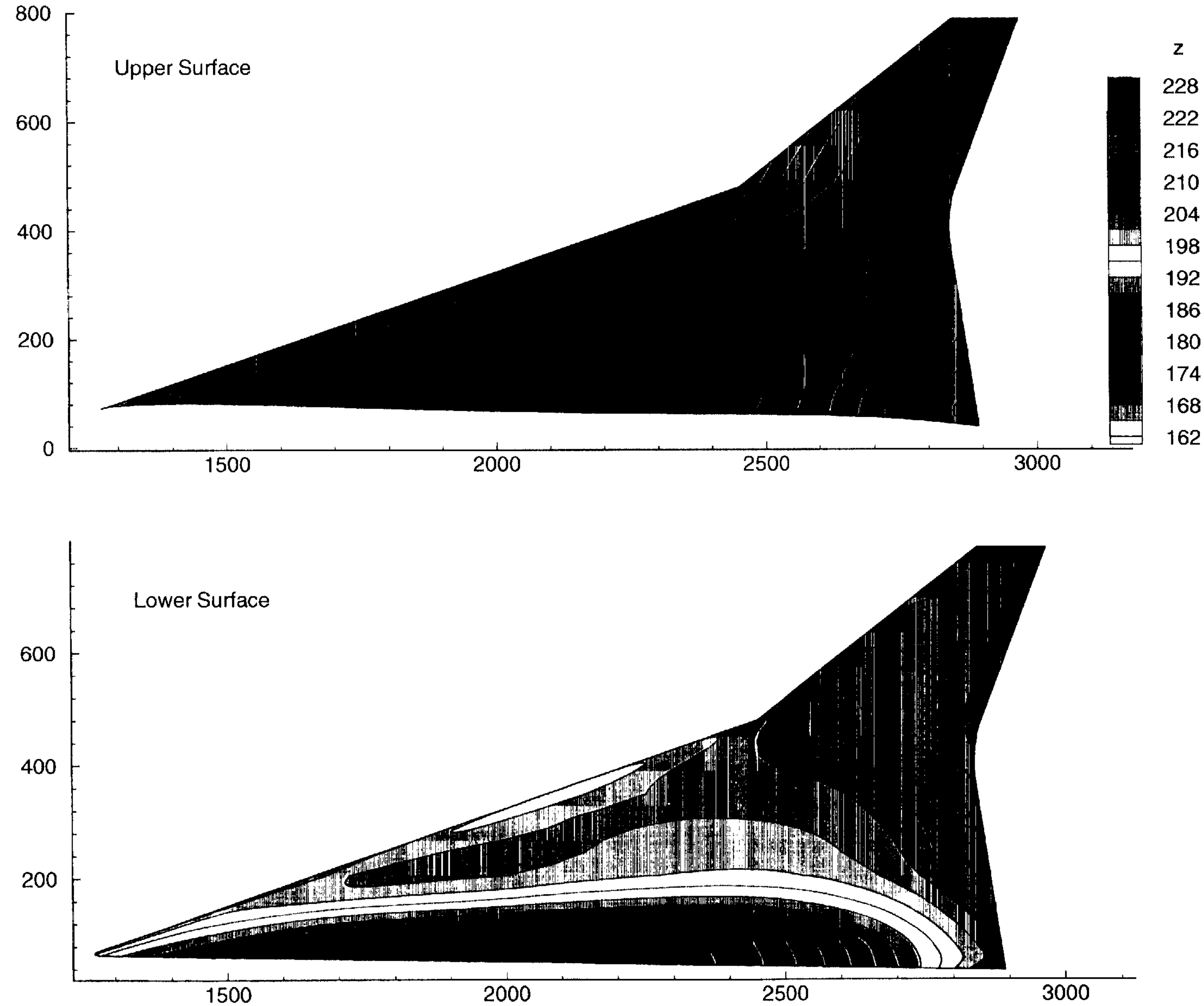

gk, 970127

Waterline Contours for the TCA Cycle 2 Configuration

Shown next is the waterline plot for the TCA Cycle 2 Configuration. Note again that there are no erratic contour changes and that the lines are fairly smooth indicating a smooth design.

Waterline Contours for Optimized TCA Cycle 2

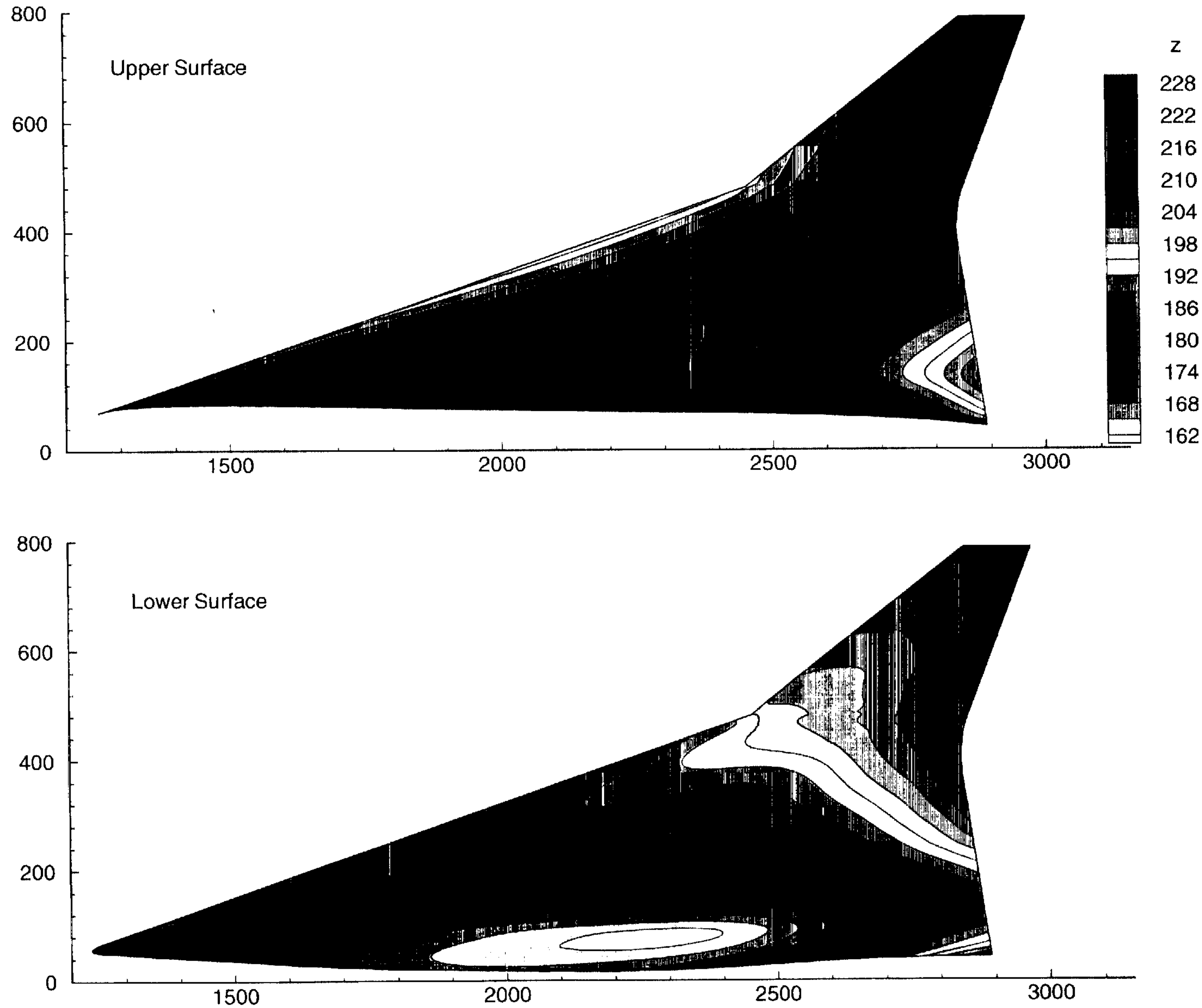

gk, 970126

Wing Twist Distribution

Illustrated below is a comparison of the Baseline and Cycle 2 twist distributions. The Cycle 2 design shows a marked increase in twist near the body over the baseline configuration (good for shifting wing loading inboard) and a general twist reduction elsewhere. Note that while the figure shows a slight twist increase of the wing tip, the Cycle 2 design has about 0.1 deg less α at cruise which eliminates this undesirable trait.

Wing Twist Distribution

Baseline and Cycle 2 TCA Configurations

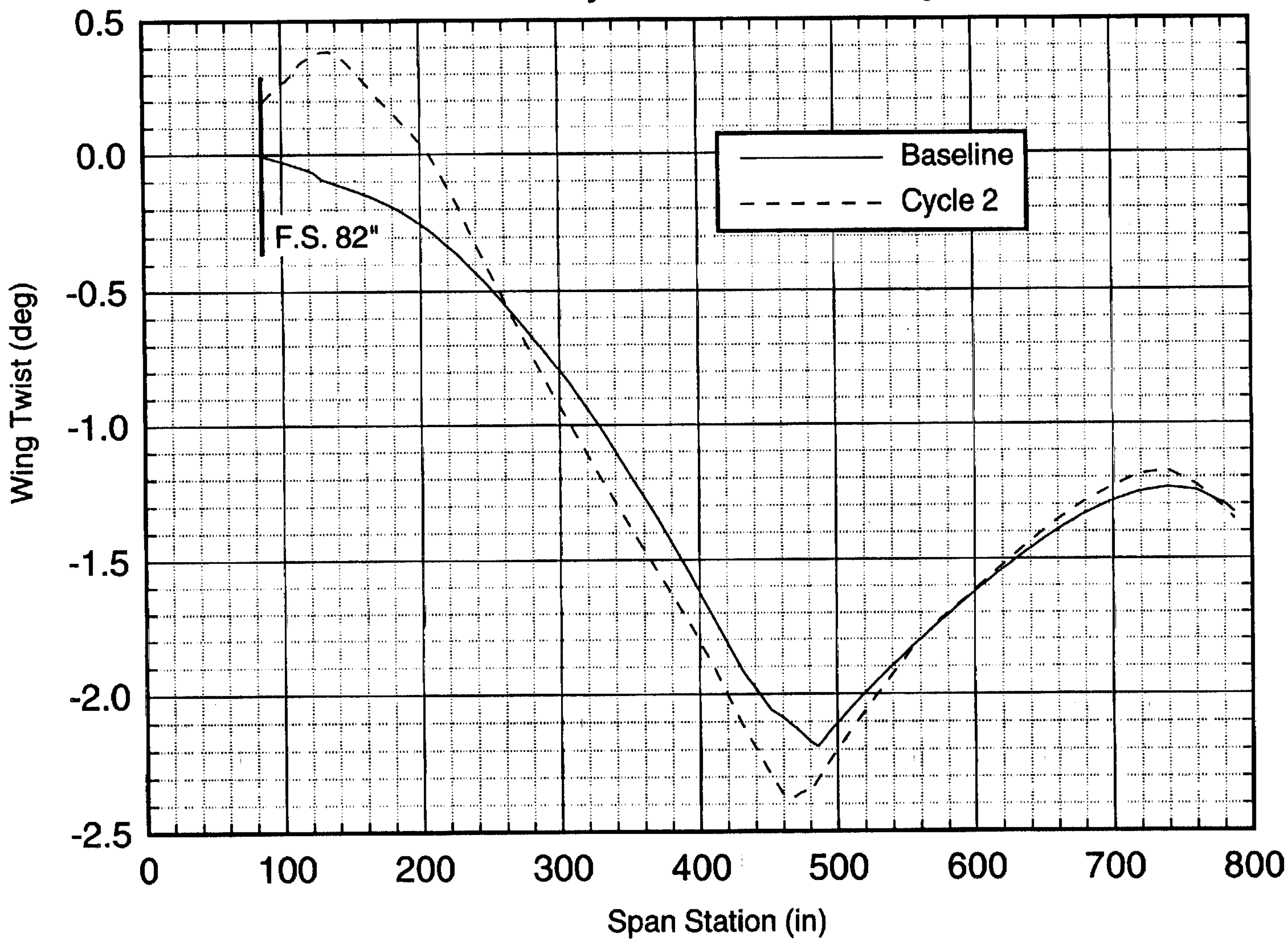

TCA Baseline and Cycle 2 Camber Distributions

Shown below are the camber distributions for the TCA Baseline and Cycle 2 configurations at six different span stations. Note that except for the inner most station, and immediately after the break, the camber distribution of the Cycle 2 design is not radically different from the baseline. In general, the Cycle 2 configuration seems to exhibit a slight increase in overall camber.

Camber Distribution
Baseline and Cycle 2 TCA Configurations

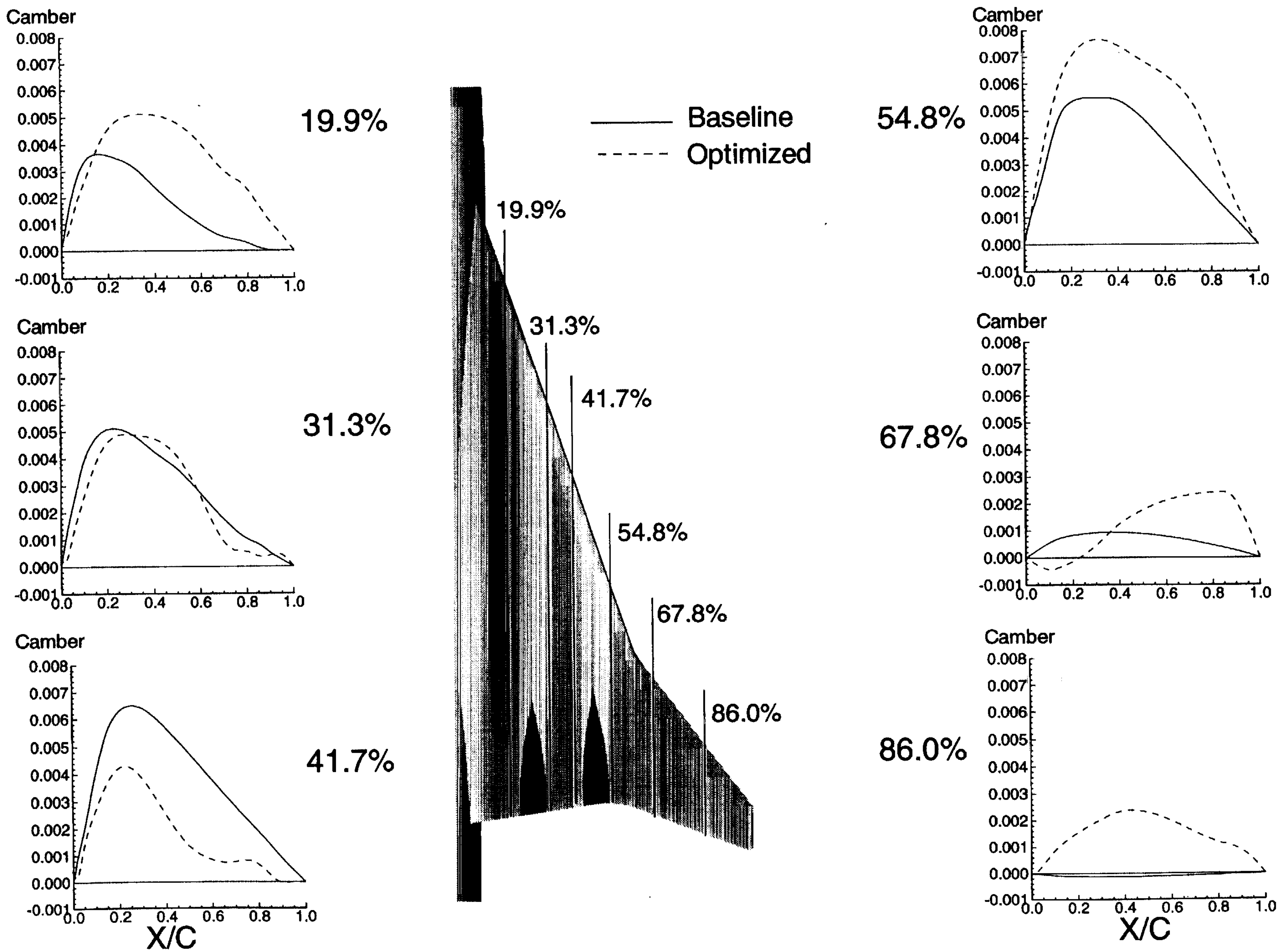

TCA Baseline and Cycle 2 Fuselage Camber Lines

Illustrated below is a comparison of the Baseline and Cycle 2 fuselage camber lines. Other than a slight rotation of the camberline, the Cycle 2 configuration does not exhibit any large modifications to the baseline.

TCA Fuselage Camber Lines

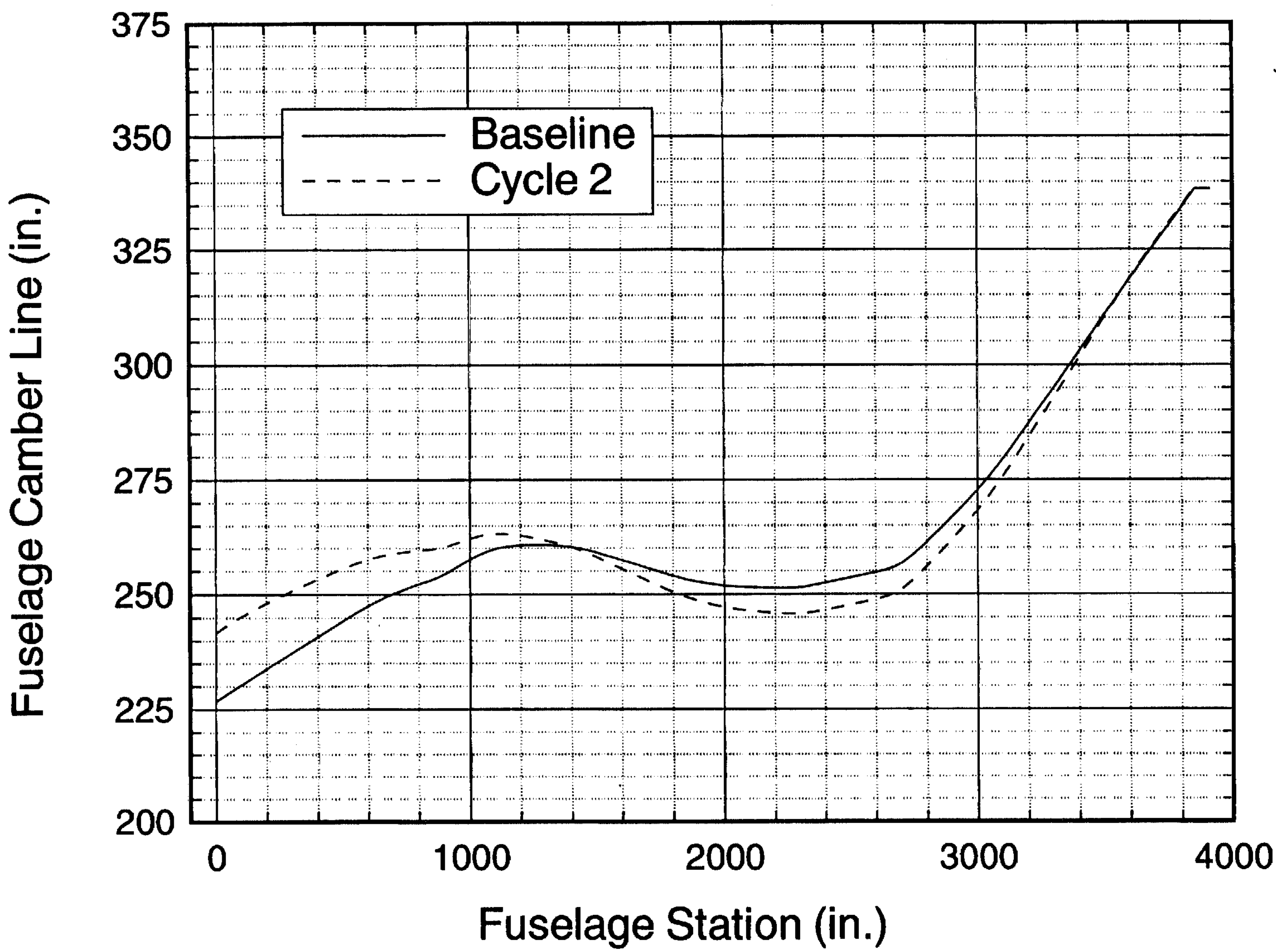

JOH 1-17-97

Baseline and Cycle 2 Maximum Thickness-to-Chord Ratio Distributions

Illustrated below is a comparison of the Baseline and Cycle 2 maximum thickness-to-chord ratio distributions. The Cycle 2 design shows a marked increase in t/c over most all of the inboard wing panel and a slight increase on the outboard panel. This inboard thickness increase is what is responsible for the 7.4% fuel volume increase. It is also possible that a great deal of this volume increase could likely be traded for further drag reductions.

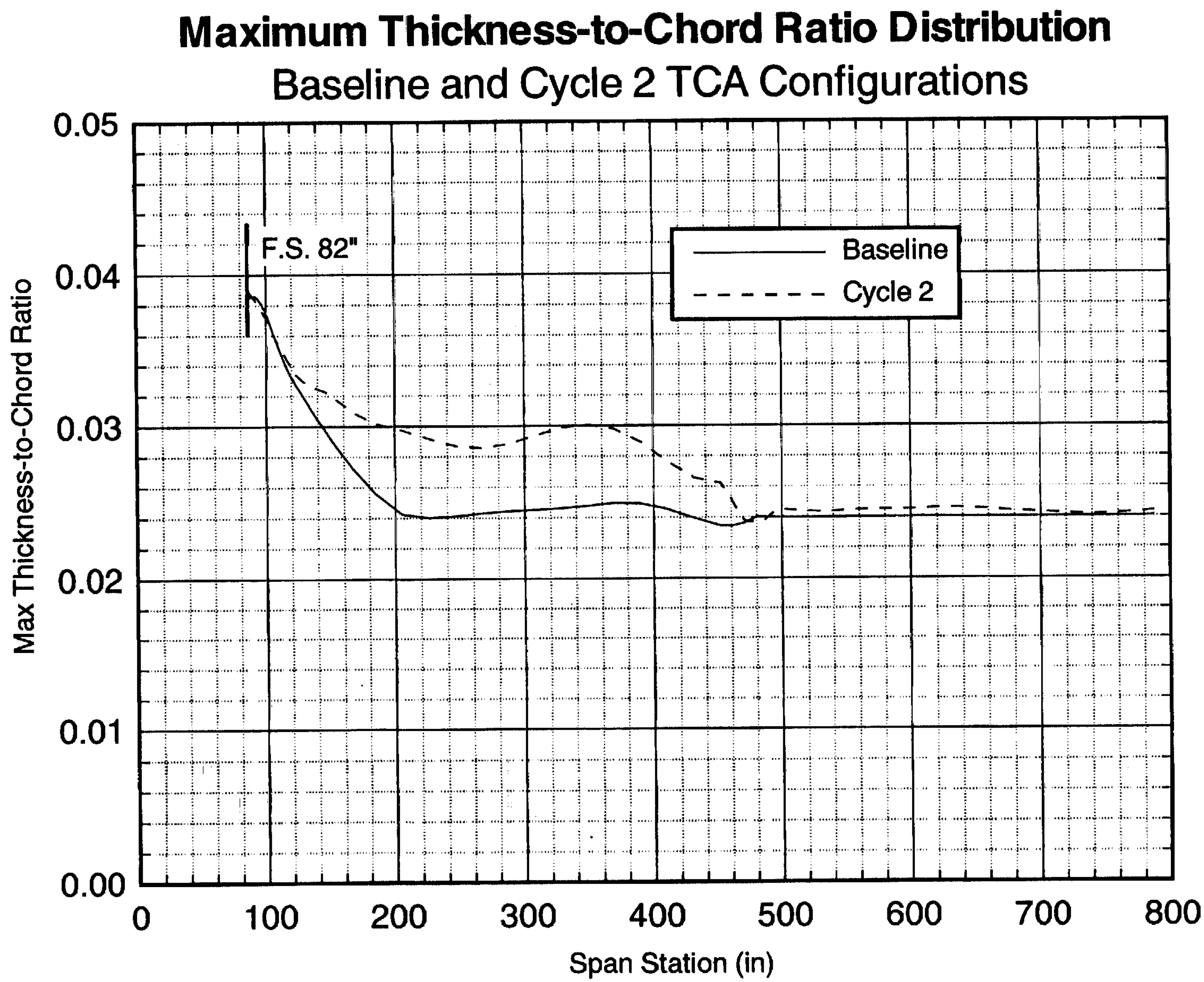
Maximum Thickness-to-Chord Ratio Distribution
Baseline and Cycle 2 TCA Configurations
F.S. 82"
Baseline
Cycle 2
Max Thickness-to-Chord Ratio
0.05
0.04
0.03
0.02
0.01
0.00
0
100
200
300
400
500
600
700
800
Span Station (in)

TCA Baseline and Cycle 2 Fuselage Cross-Sectional Area Distributions

Illustrated below is a comparison of the Baseline and Cycle 2 fuselage cross-sectional area distributions. Here, we see an increase in the Cycle 2 area in the middle portion of the fuselage with the largest increases at about 1200". This location corresponds to the leading edge of the wing/body intersection.

TCA Fuselage Cross-Sectional Area Distributions

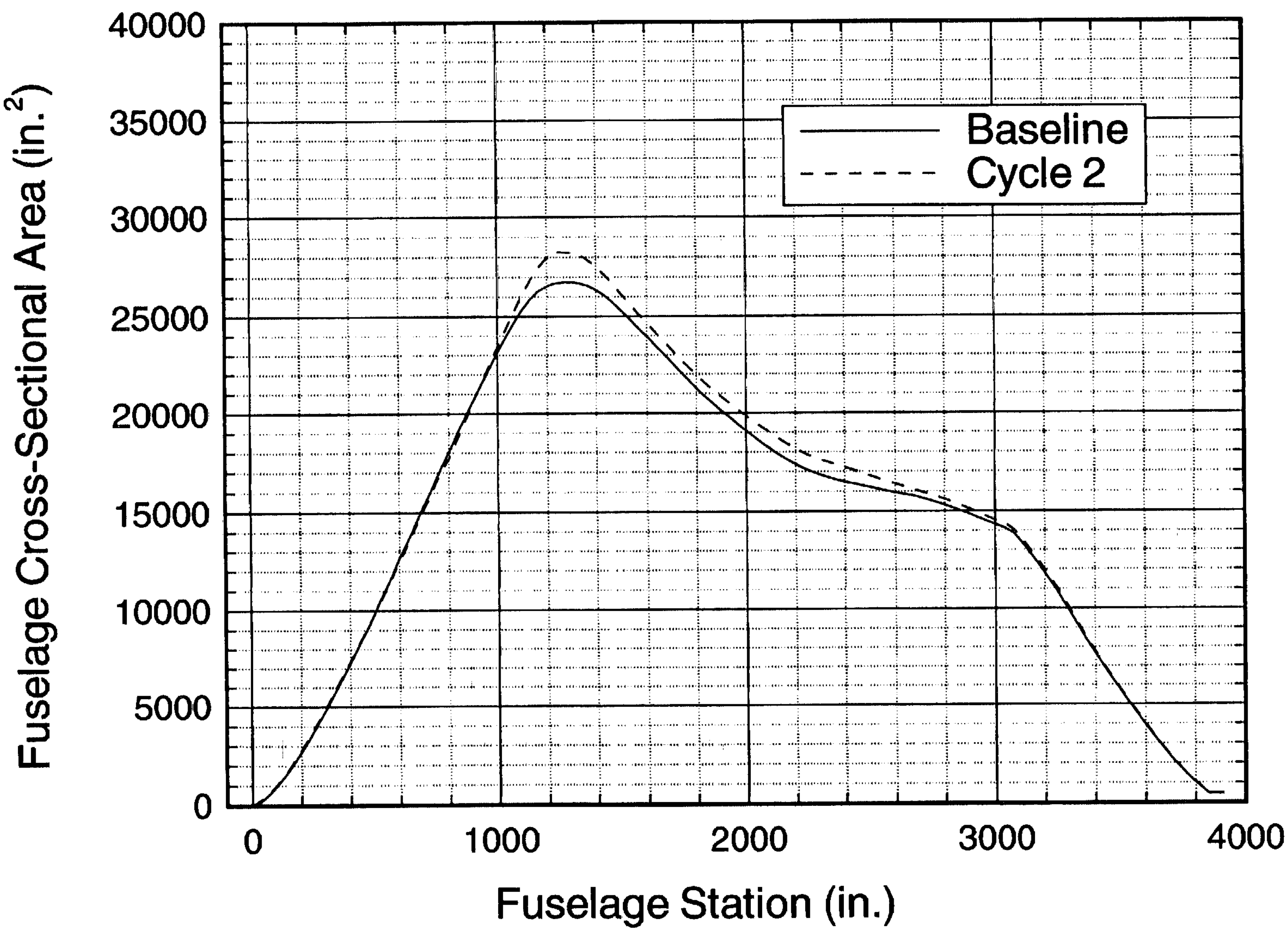

JOH 1-17-97

TCA Baseline and Cycle 2 Wing/Body Cross-Sectional Area Distributions

Illustrated below is a comparison of the Baseline and Cycle 2 normal (M=1.0) wing/body cross-sectional area distributions. This plot shows the area build-up for the wing/body configuration which is critical for wave drag considerations. Abrupt changes in area tend to increase drag and should be avoided. As shown in this figure, we can see that the Cycle 2 configuration has smoothed out the area where the wing and the body first meet, leading to some explanation for the fuselage volume increases in this region. Due to the frozen planform restrictions, virtually nothing could be done for the wing trailing-edge region (note that the presence of the nacelles will help in this region).

TCA Cross-Sectional Area Distributions

(Wing/Body transition is based on the grid)

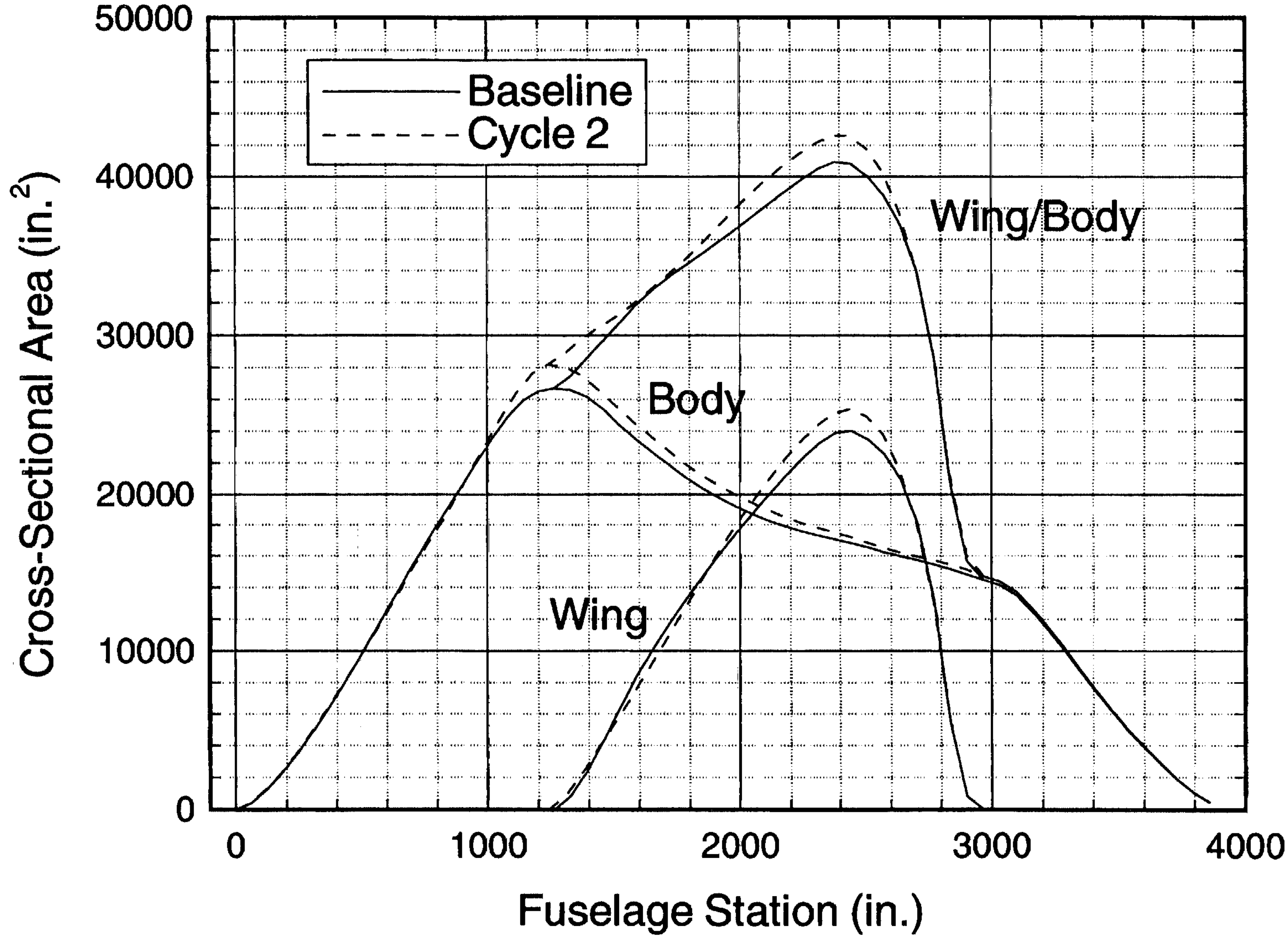

JOH 1-17-97

TCA Baseline and Cycle 2 W/B/N/D Lift Comparisons

Lift curves from CFL3D Navier-Stokes analysis of the TCA Baseline and Cycle 2 wing/body/nacelle/diverter configurations are shown. As with all the previous optimization studies, the slope of the lift curve is larger for the optimized configuration. It is believed the increase of leading-edge suction for the optimized configuration is responsible for this phenomenon.

Lift for the TCA W/B/N/D Configurations

CFL3D, Navier-Stokes (Baldwin-Lomax), $M_{\infty}=2.4$, $Re_c=6.36x10^6$

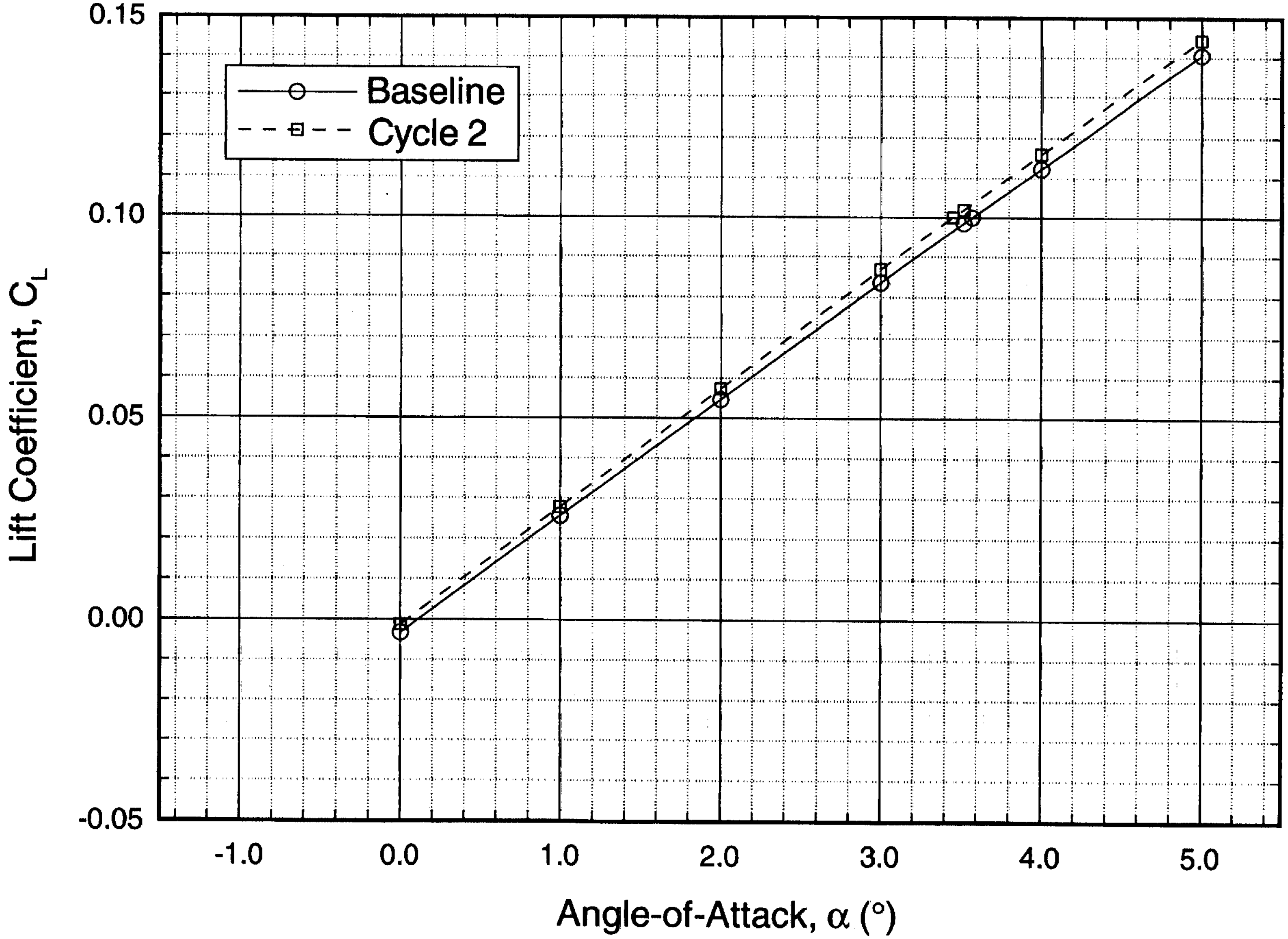

JOH 1-27-97

TCA Baseline and Cycle 2 W/B/N/D Drag Polar Comparisons

Drag polars from CFL3D Navier-Stokes analysis of the TCA Baseline and Cycle 2 wing/body/nacelle/diverter configurations are shown. The cycle 2 design shows a 3.9 count reduction in drag at the evaluation C_L of 0.10. The pressure drag reduction at this condition was about 3.7 counts and the friction drag reduction was about 0.2 counts. Although not illustrated, it is important to note that Euler analysis of these same two configurations yielded only a 3.5 count drag reduction at the same conditions. This result is not too surprising due to the well behaved nature of the pressure distributions.

Drag Polars for the TCA W/B/N/D Configurations

CFL3D, Navier-Stokes (Baldwin-Lomax), M_∞=2.4, Re_c=6.36x10^6

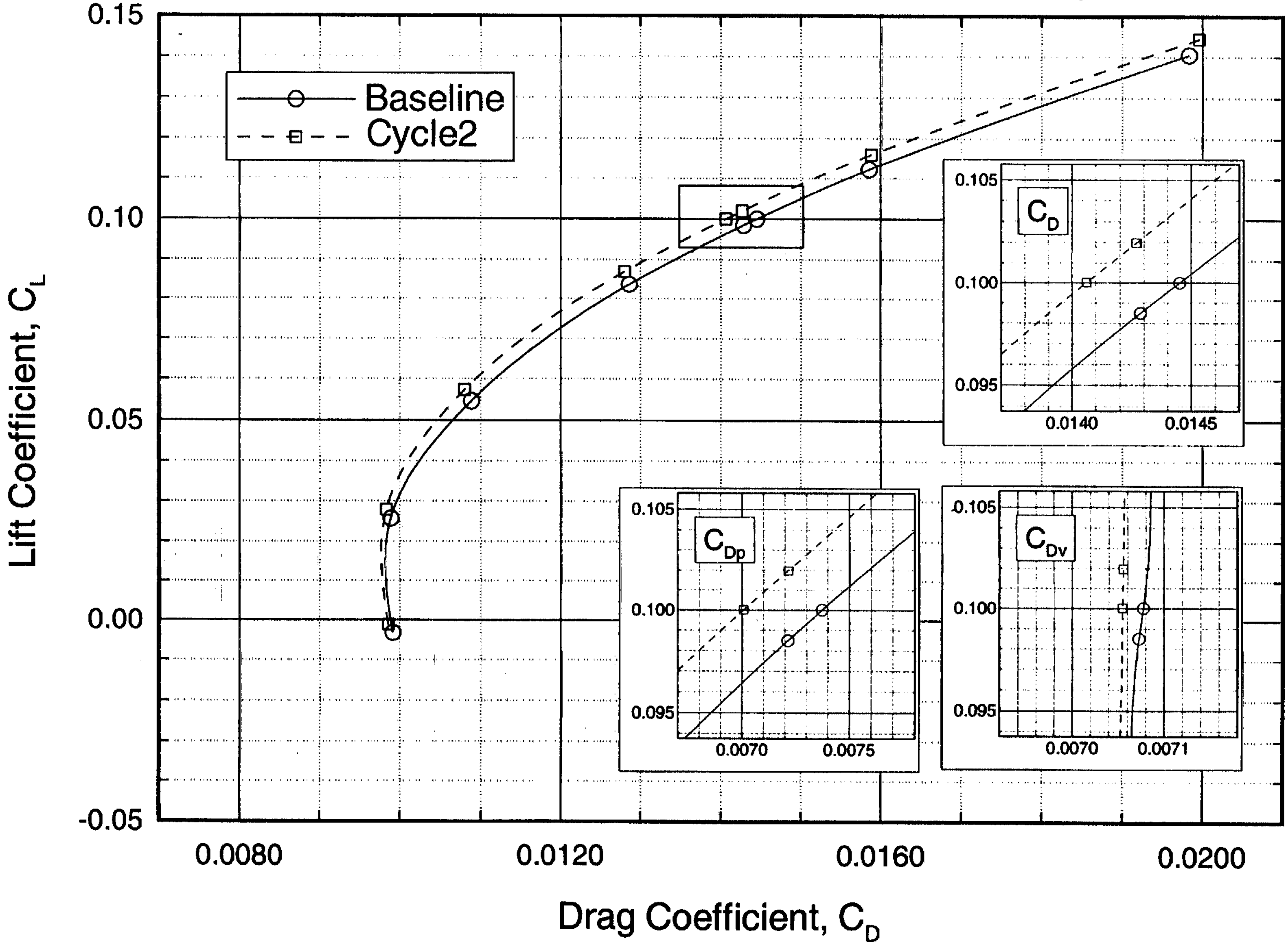

JOH 2-19-97

TCA Baseline and Cycle 2 W/B/N/D Pitching Moment Coefficient Comparisons

Pitching moment coefficients from CFL3D Navier-Stokes analysis of the TCA Baseline and Cycle 2 wing/body/nacelle/diverter configurations are shown. Here, we see only a slight nose-up change in the pitching moment coefficient in the cycle 2 configuration (note the expanded scale).

Pitching Moment for the TCA W/B/N/D Configurations

CFL3D, N-S (B-L), M_∞=2.4, Re_c=6.36x10^6, Moment about 50% MAC

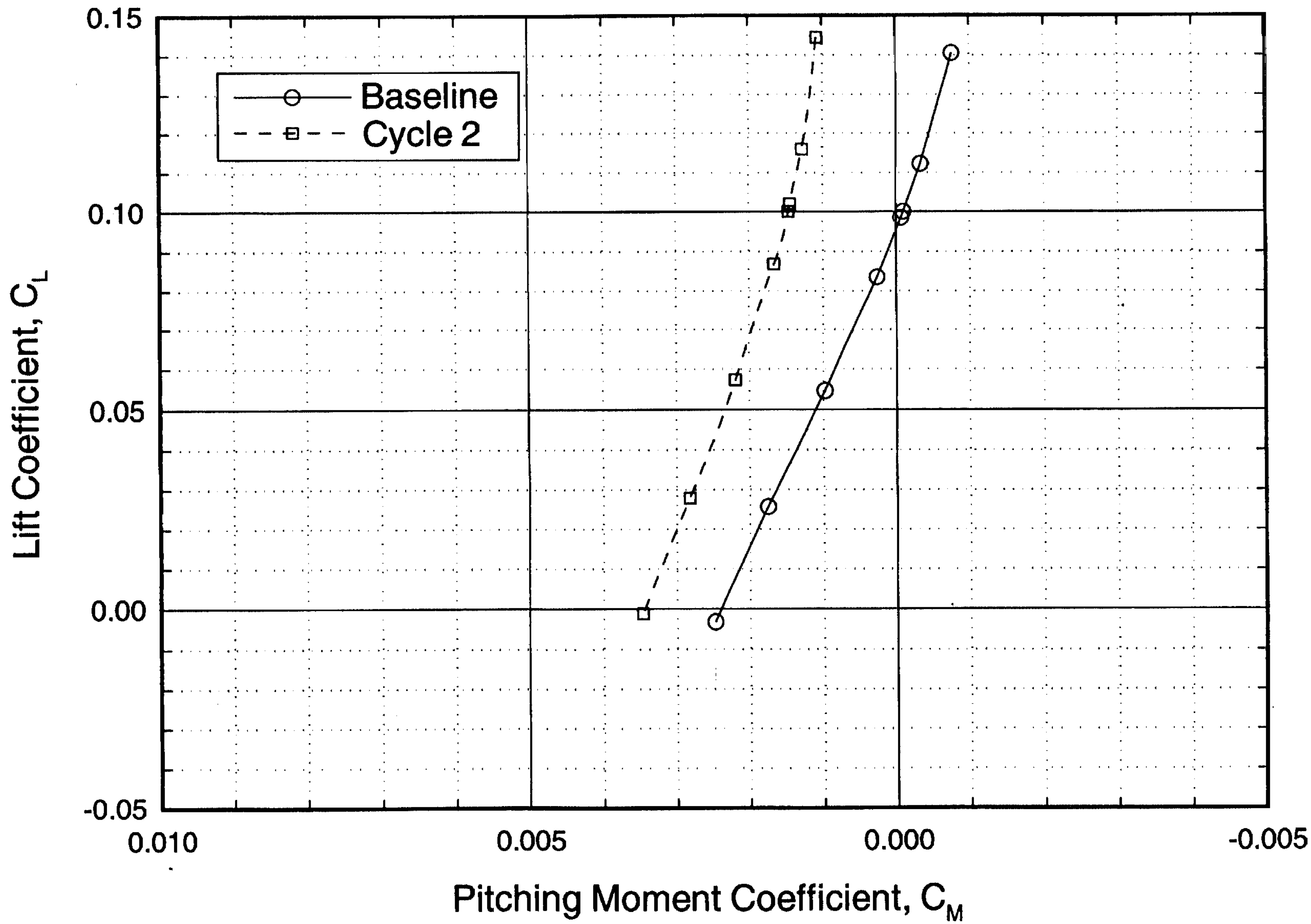

JOH 1-27-97

TCA Baseline W/B/N/D Pressure Distributions

The next two slides show surface pressure distributions (CFL3D N-S) for the TCA Baseline and Cycle 2 configurations at the evaluation condition. The slide below shows in general how the baseline configuration has a fairly smooth pressure variation with only a very slight compression wave on the upper surface. Note that the diverters generate relatively strong shocks.

TCA W/B/N/D Pressure Distributions

CFL3D, N–S (B–L), M_∞=2.4, C_L=0.10 (α=3.57°), Re_c=6.36x10^6

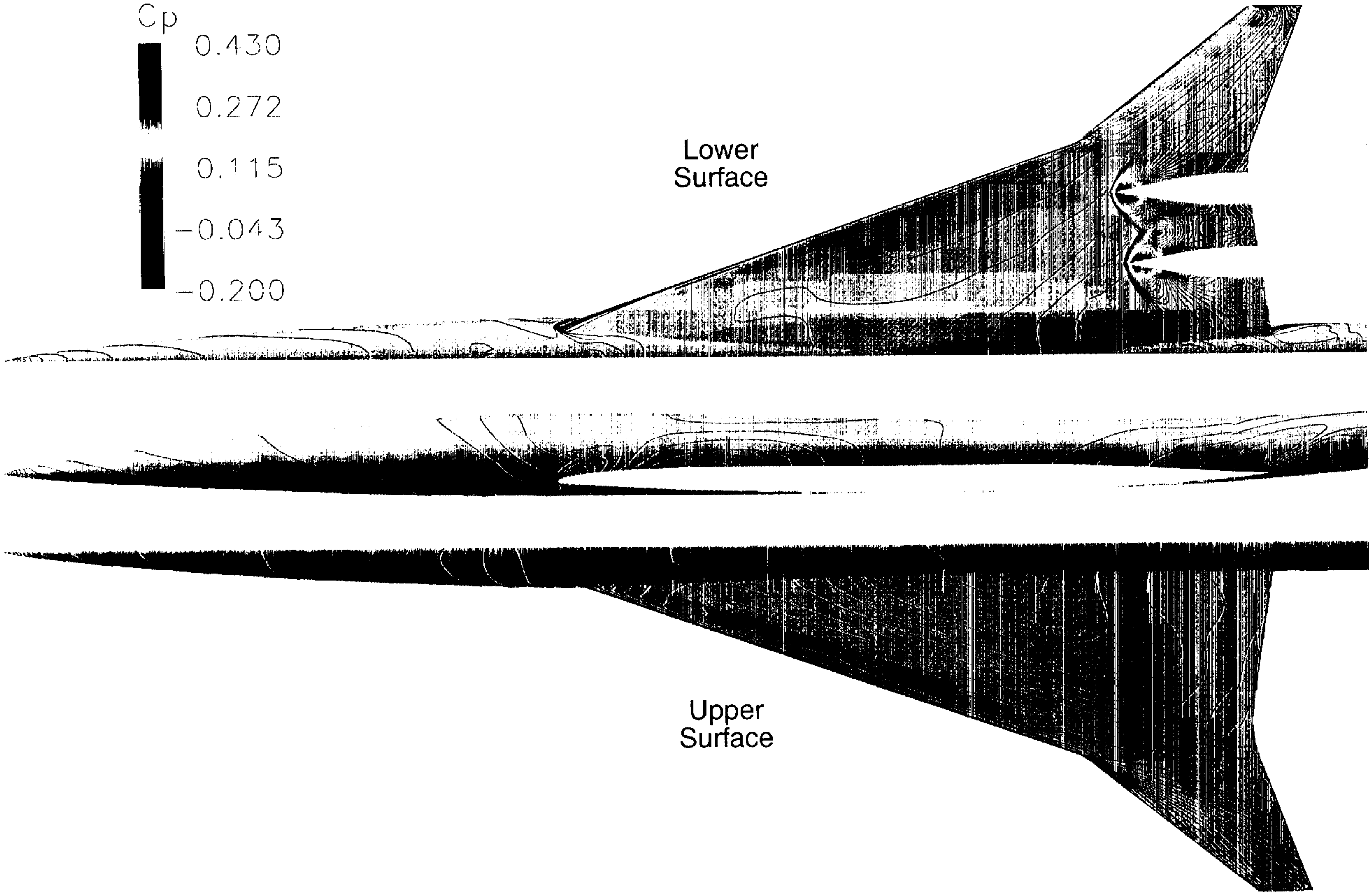

JOH 2-11-97

TCA Cycle 2 W/B/N/D Pressure Distributions

This slide shows the pressure distributions for the Cycle 2 design. Note that on this configuration, the upper surface leading-edge pressure is reduced (leading-edge suction) and that the shock strength of the the inboard diverter is slightly reduced. Also note that the pressure variations are still smooth and that the upper surface compression wave is somewhat reduced.

TCA Cycle 2 W/B/N/D Pressure Distributions

CFL3D, N–S (B–L), M_∞=2.4, C_L=0.10 (α=3.45°), Re_c=6.36x10^6

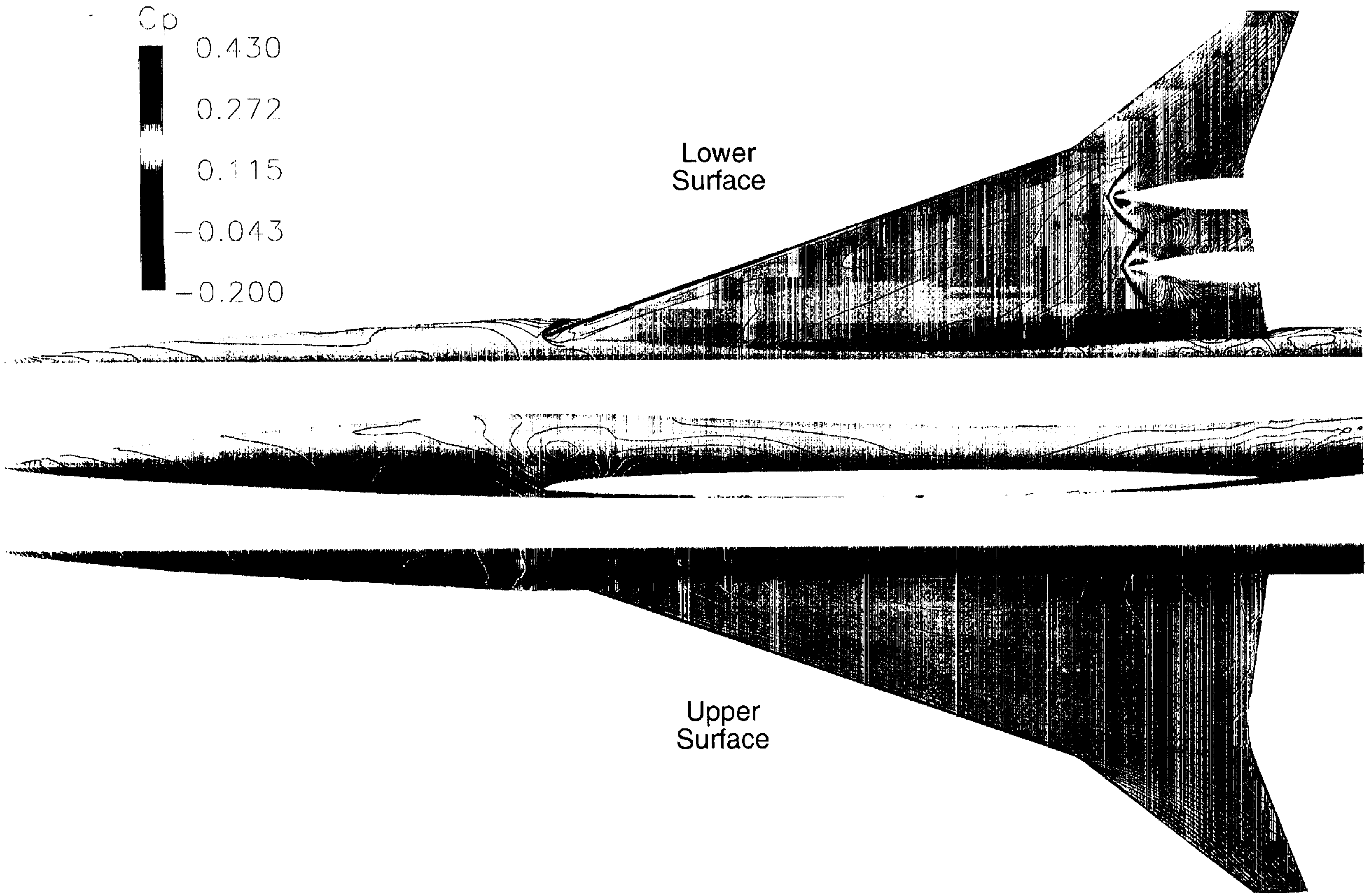

JOH 2–11–97

Component Drag for the TCA Baseline and Cycle 2 Wing/Body/Nacelle/Diverter Configurations

A total drag breakdown for the TCA Baseline and Cycle 2 configurations is shown. Such a breakdown is useful to understand where the optimization process made improvements and design trade-offs. As indicated in the slide, the optimizer removed 4.7 counts of drag from the wing alone and, as we typically see during optimization, the body gained about 1.9 counts of drag. This is clearly a trade-off where fuselage performance was sacrificed to further improve the wing. This is an illustration of how important it is to optimize the wing and fuselage simultaneously. Also shown in this slide is the fact that the drag on both diverters and nacelles is virtually unchanged.

Component Drag for the Baseline and Cycle 2 TCA W/B/N/D Configurations

CFL3D, Navier-Stokes (B-L), M_∞=2.4, C_L=0.10, Re_c=6.36x10^6

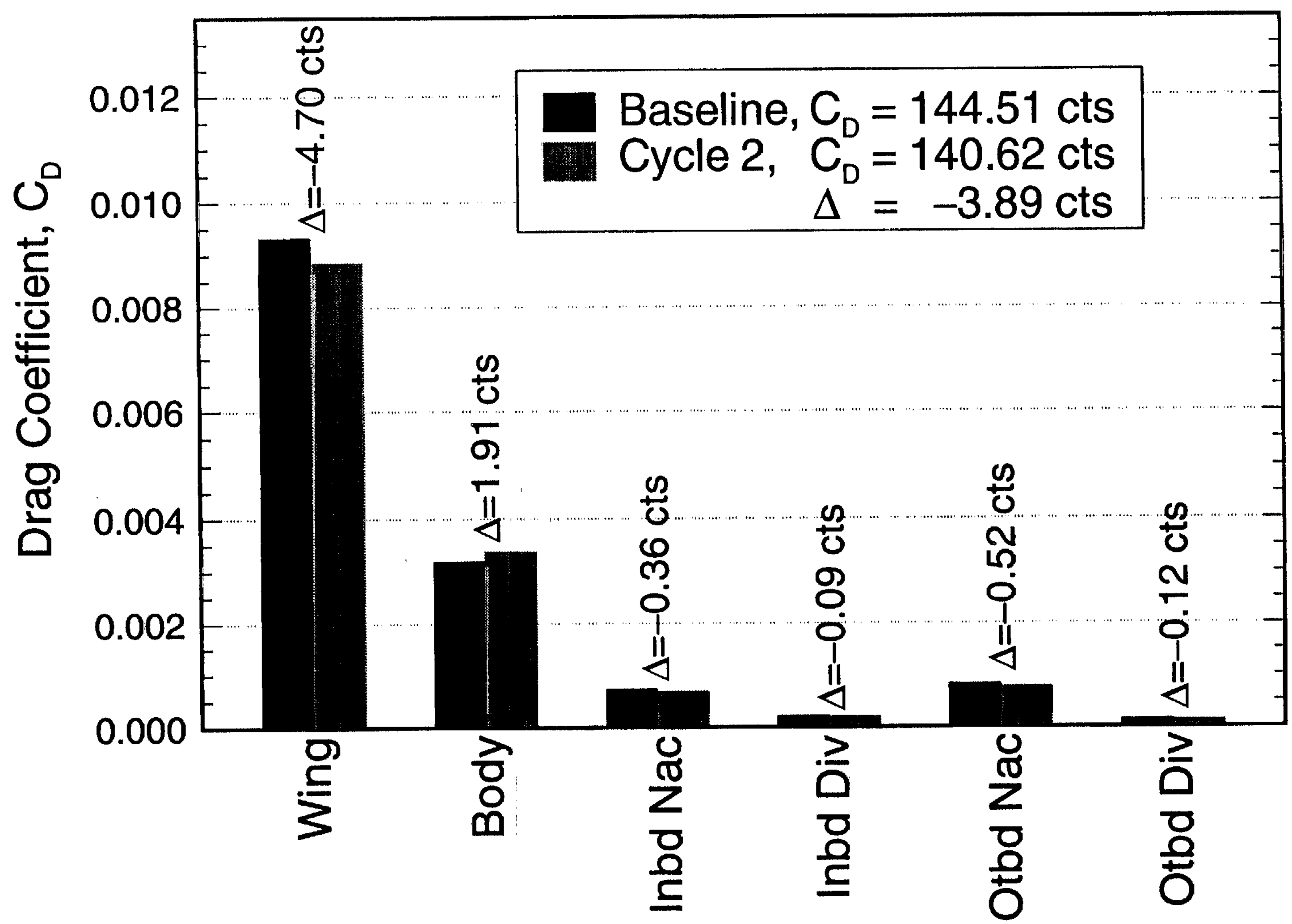

JOH 2-19-97

TCA Baseline and Cycle 2 Pressure Coefficient and Airfoil Cut Comparisons

The next four slides show comparisons of the TCA Baseline and Cycle 2 chordwise pressure coefficients and airfoil variations. Note that throughout these plots the pressures are all quite smooth and well-behaved. The first of these cuts (below), is at a wing semi-span of 19.9%. At this station, we can see that optimization has significantly increased leading-edge suction and has slightly increased aft loading. The shock strength and position from the inboard diverter and nacelle appears only slightly changed. Looking at the airfoil cut, it's clear that the thickness of this section has been increased along with the camber.

TCA Baseline and Optimized Configurations

Span Station 156 (19.9% Semi-span)

CFL3D Navier-Stokes (Baldwin-Lomax), 1.675% W/B/N/D Configuration, M_∞=2.4, α=3.518°, Re_c=6.36x10^6

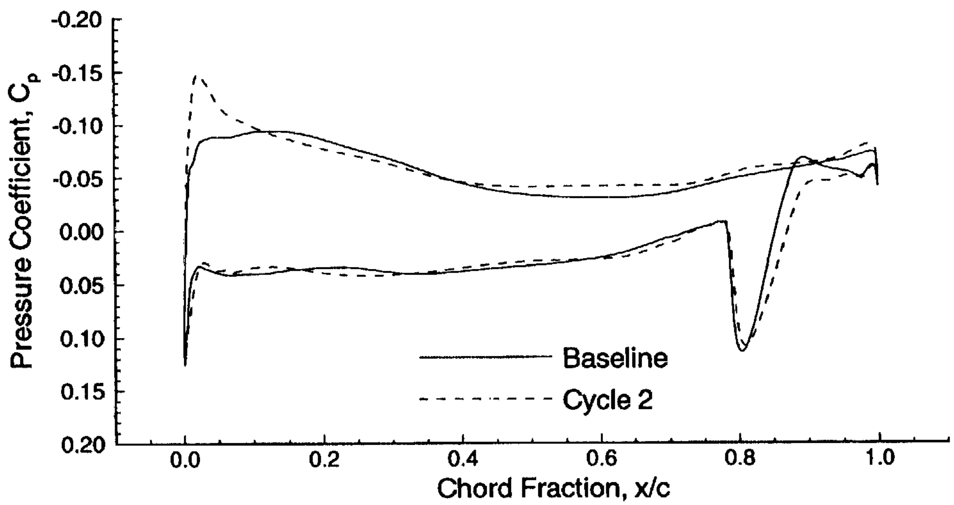

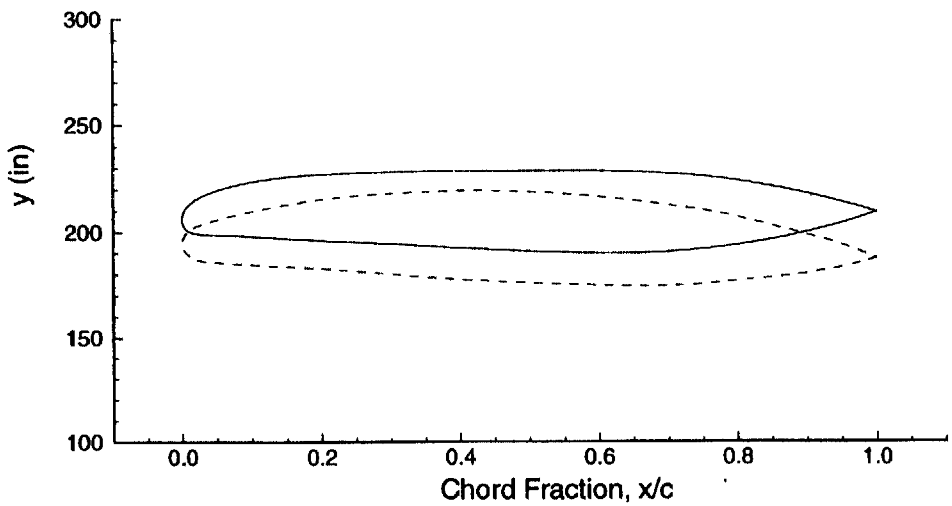

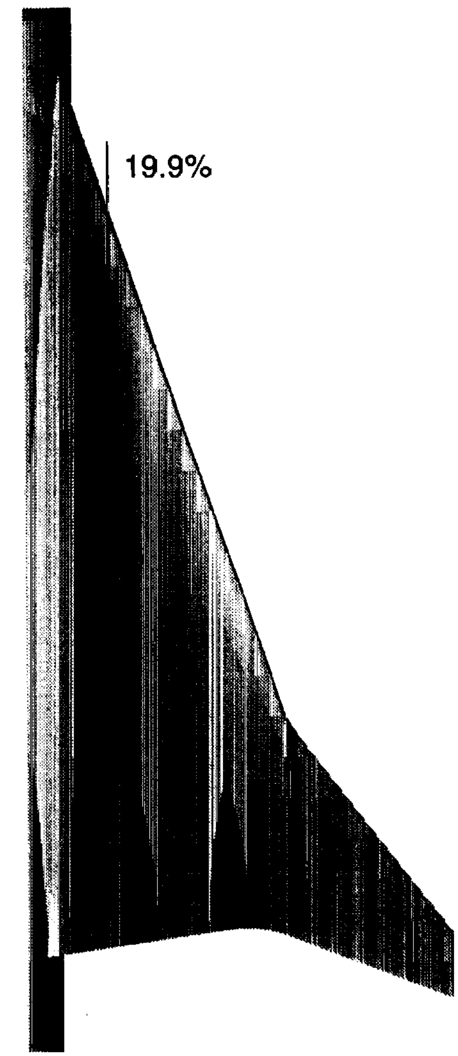

TCA Baseline and Cycle 2 Pressure Coefficient and Airfoil Cut Comparisons (cont.)

This slide shows the pressure and airfoil variations at a wing semi-span of 32.6%. Once again, there is an increase of leading-edge suction although the aft-loading remains unchanged here. At this cut, the shock strength of the inboard diverter has been reduced and the position is same. Again, significant wing area has been added but some slight thinning at the wing trailing edge occurs.

TCA Baseline and Optimized Configurations

Span Station 256 (32.6% Semi-span)

CFL3D Navier-Stokes (Baldwin-Lomax), 1.675% W/B/N/D Configuration, M_∞=2.4, α=3.518°, Re_c=6.36x10^6

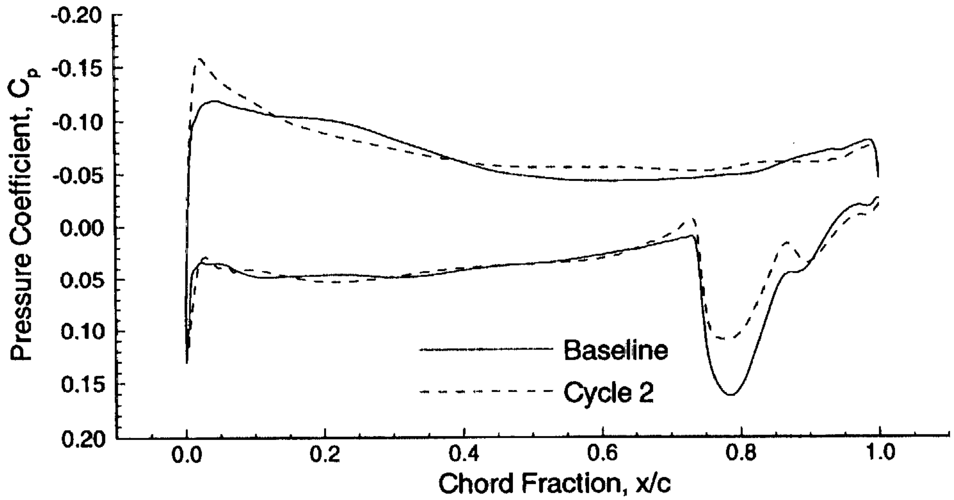

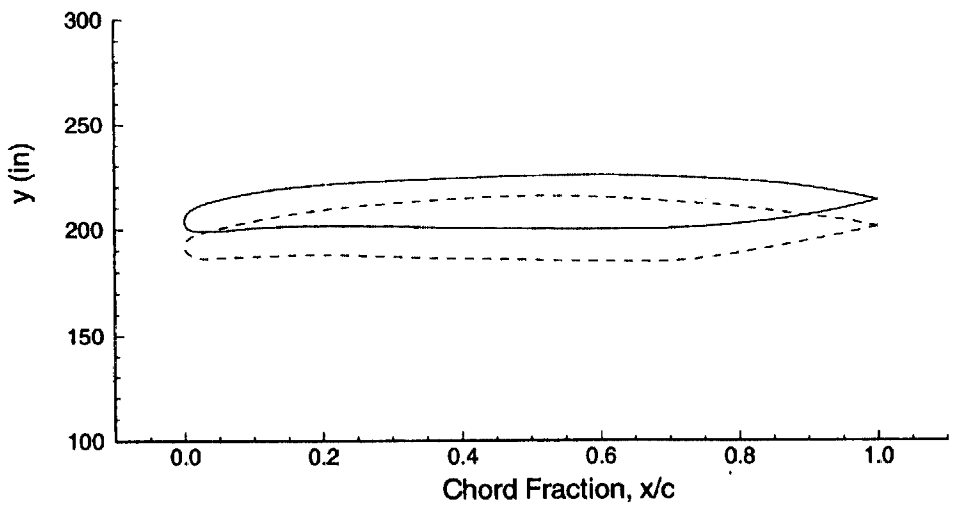

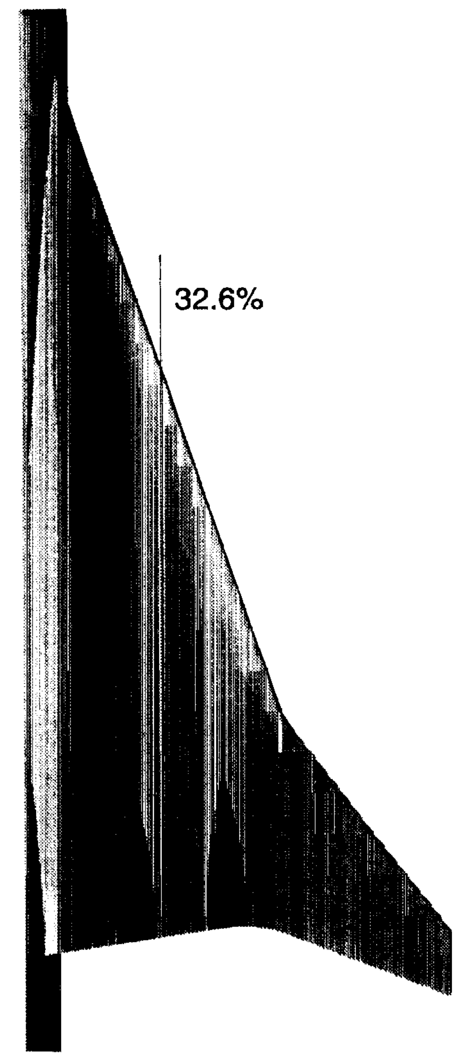

TCA Baseline and Cycle 2 Pressure Coefficient and Airfoil Cut Comparisons (cont.)

This slide shows the pressure and airfoil variations at a wing semi-span of 41.3%. Once again, there is an increase of leading-edge suction but in this case the aft loading appears to be reduced. At this cut, the shock strength of the outboard diverter has been unchanged but has been moved slightly aft. This cut also demonstrates a prominent double shock pattern. Again, significant wing area has been added, especially in the middle of the airfoil.

TCA Baseline and Optimized Configurations

Span Station 325 (41.3% Semi-span)

CFL3D Navier-Stokes (Baldwin-Lomax), 1.675% W/B/N/D Configuration, M_∞=2.4, α=3.518°, Re_c=6.36x10^6

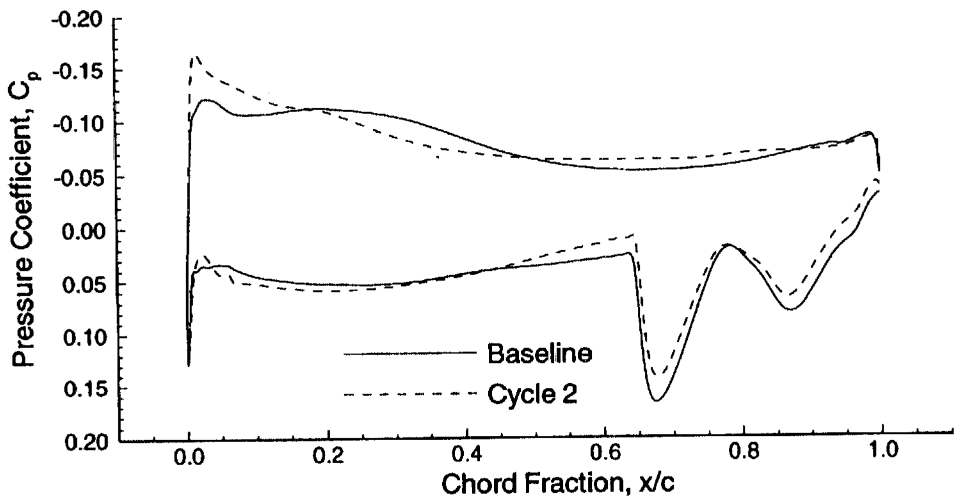

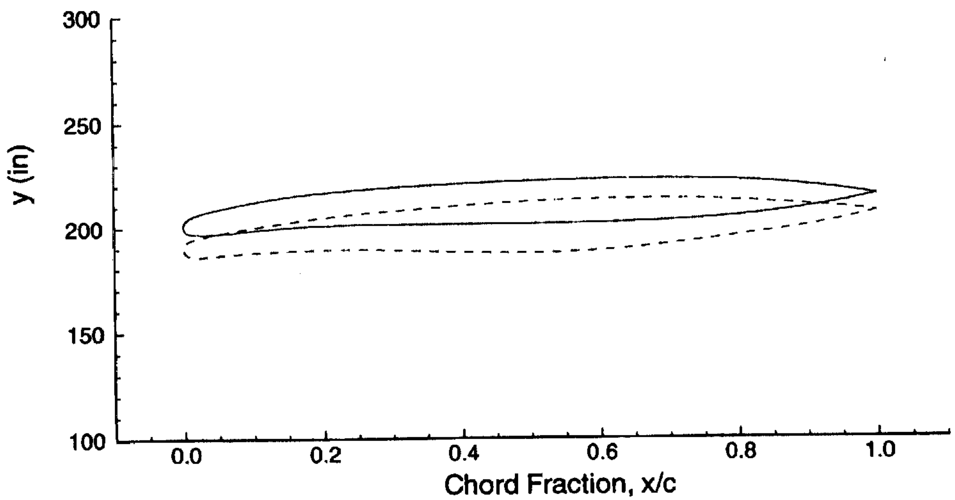

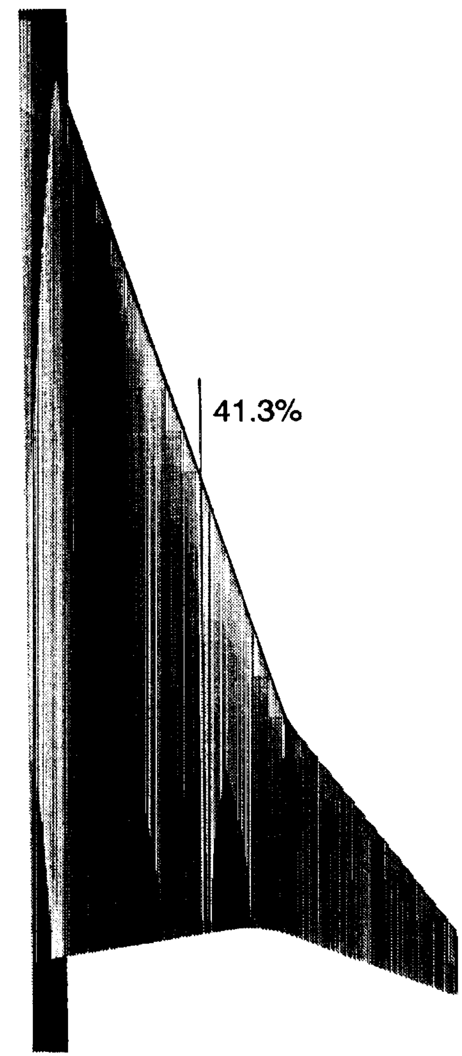

TCA Baseline and Cycle 2 Pressure Coefficient and Airfoil Cut Comparisons (cont.)

This slide shows the pressure and airfoil variations at a wing semi-span of 67.9%, an example of a sharp outboard panel. In this example, the loading at the leading edge has been increased with contribution from the upper and lower surfaces. In addition, the aft loading has increased and the mild pressure increase from the outboard nacelle/diverter appears to have been eliminated. For this cut, airfoil modifications appear minimal.

TCA Baseline and Optimized Configurations

Span Station 535 (67.9% Semi-span)

CFL3D Navier-Stokes (Baldwin-Lomax), 1.675% W/B/N/D Configuration, M_∞=2.4, α=3.518°, Re_c=6.36x10^6

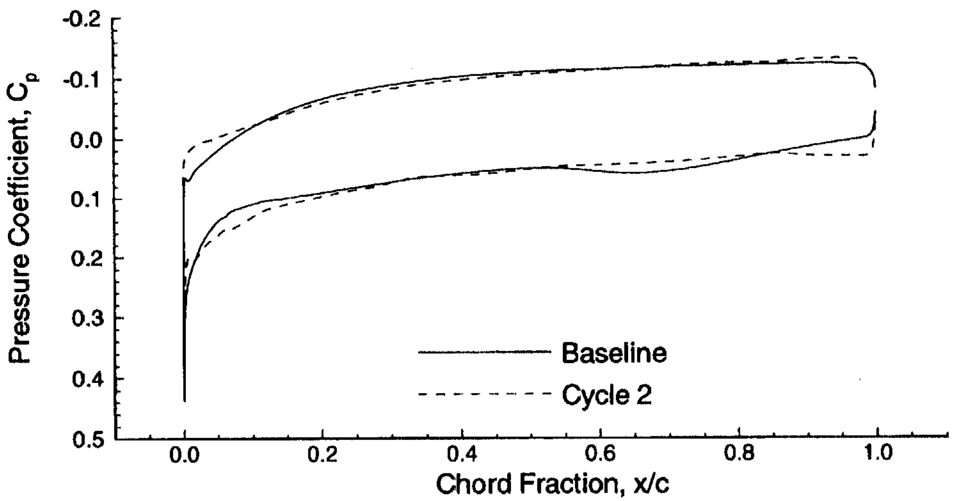

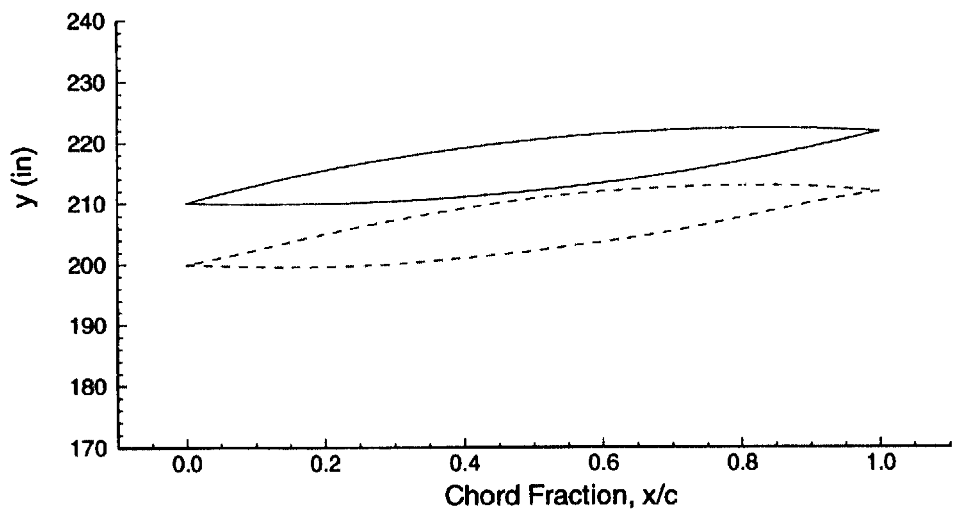

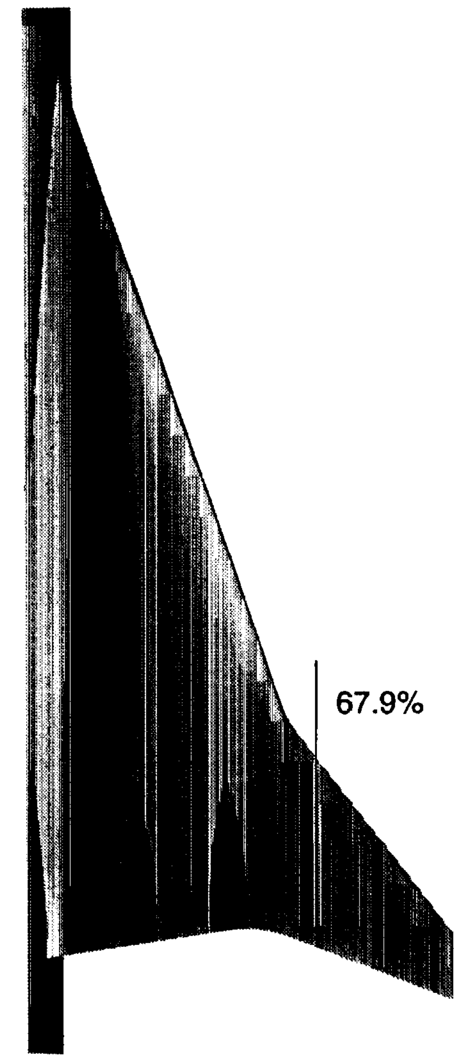

Wing Constraints

Listed below is a complete table of the wing constraints used during this optimization. Not specifically listed is a mid-spar constraint (the front spar of the wing structural box) that MDC added to further enhance the smoothness of the final design. This new constraint also prevented a `digging-out' of wing volume just outboard of the landing-gear bay. Where it is applicable, the table lists the design constraint values and the values achieved by the Cycle 2 design. Note that in cases were there are slight constraint violations, analyses were done to measure what the drag impact would be to satisfy the constraint in question. To fully satisfy all the violated constraints, the penalty was calculated to be 0.1 count (see the following chart as an illustration of this process).

Wing Constraints

Number	Description	Design Value	Constraint Value	Satisfied?	Drag Impact	Comment
W1	Front Spar Thickness	*	*	N	0.04 cts	Max violation near break
W2	Rear Spar Thickness	*	*	N	<0.05 cts	Max violation @ span station 167
W3	In-spar Thickness			Y		
W4	Landing Gear Bay Clearance	*	*	Y		
W5	Leading-edge Bluntness	*	*	N	0.01 cts	Evaluated thickness 6" aft of LE; Violation @ break
W6	Trailing-edge Closure Angle	3.8°	≥5°	N	0.00 cts	Max violation @ break
W7	Wing Fuel Volume	10,390	≥9674 cu ft	Y		7.4% increase in fuel volume
W8	Floor Location Above Wing Upper Surface	9.6"	≥9.4"	Y		F.S. 2459-2669 (systems)
W9	Floor Location Above Wing Box	6.9"	≥7"	Y		F.S. 2066-2166 (systems)
W10	Wing Upper Surface Above Floor	-9.2"	≤7.0"	Y		F.S. 1804 (door)
W11	Wing Corner Points			Y		
W12	Wing Leading-edge Intersection	Not a constraint				
W13	Wing Trailing-edge Intersection	Not a constraint				

* see figures

Front Spar (W1) Sensitivity Study

This chart shows the process that was used to determine the penalty for fully satisfying a given constraint, in this case the leading-edge spar thickness. As one can see in the lower left-hand figure, the front spar thickness on the Cycle 2 design violates the given constraint thickness in the immediate vicinity of the wing break. This violation was due mostly to an improperly applied smoothing technique that did not maintain the sharp thickness transition at the break. The figure at the upper left-hand side shows an example of the required airfoil modifications that were locally applied to the cycle 2 configuration. The upper right-hand plot shows the drag impact (about 0.04 counts) of modifying all the airfoils necessary to fully satisfy the front spar constraint.

Front Spar Thickness (W1) Sensitivity Study

- Objective was to find sensitivity of drag performance with small modifications to leading-edge spar thickness
- Upper and lower surface was modified between LE and 50% chord to activate LE spar thickness constraint over entire span

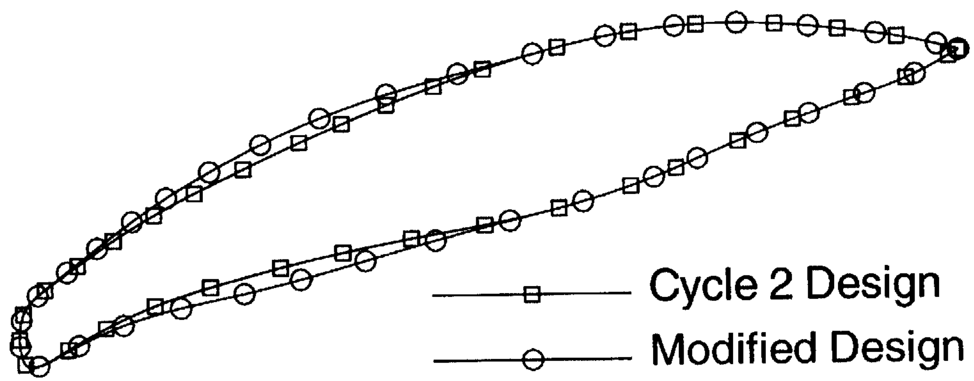

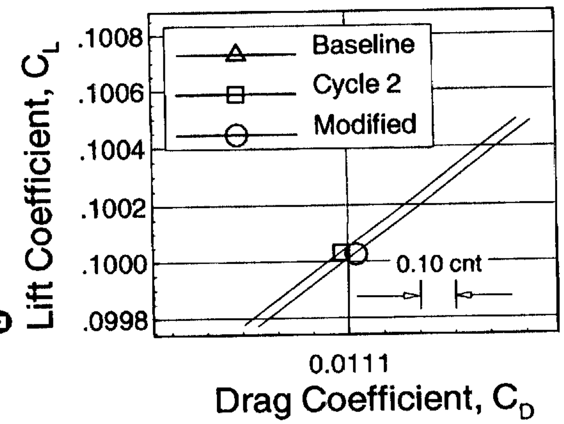

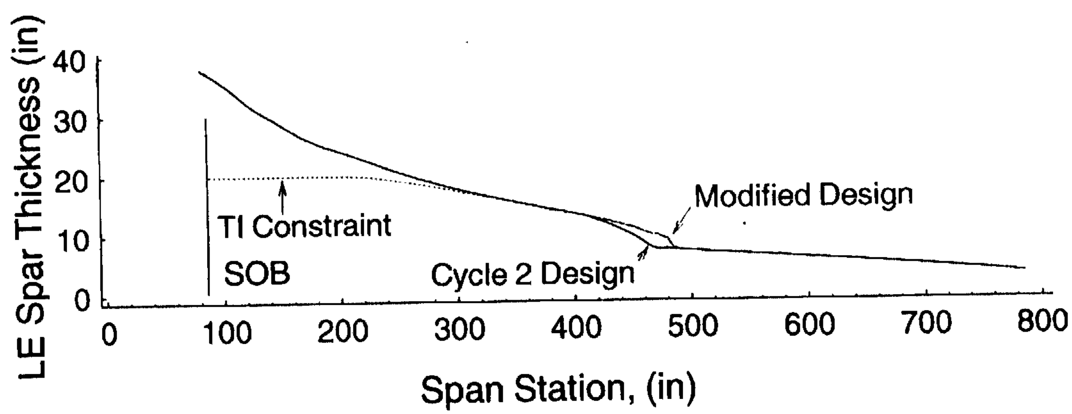

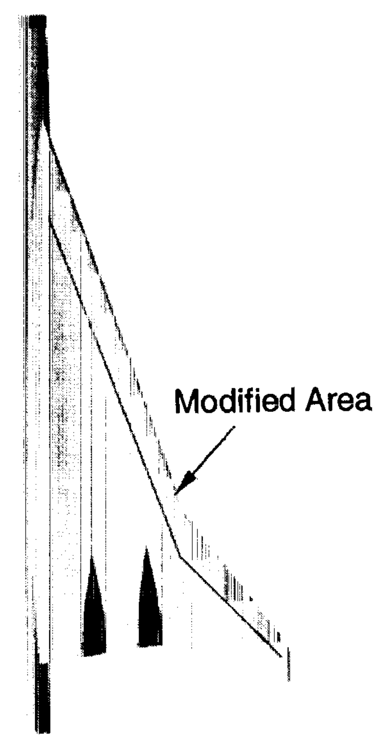

TCA Cycle 2 Landing-Gear Bay Layout

This figure shows a graphical representation of the landing-gear bay placement on the Cycle 2 design. This constraint was particularly difficult to deal with and as is shown there is no extra room for the bay. To fit the bay, it was pitched up approximately 1 deg and rolled about 7 deg with respect to the baseline configuration.

TCA Cycle 2 Landing-Gear Bay Layout

(Gear Bay Shown in Red)

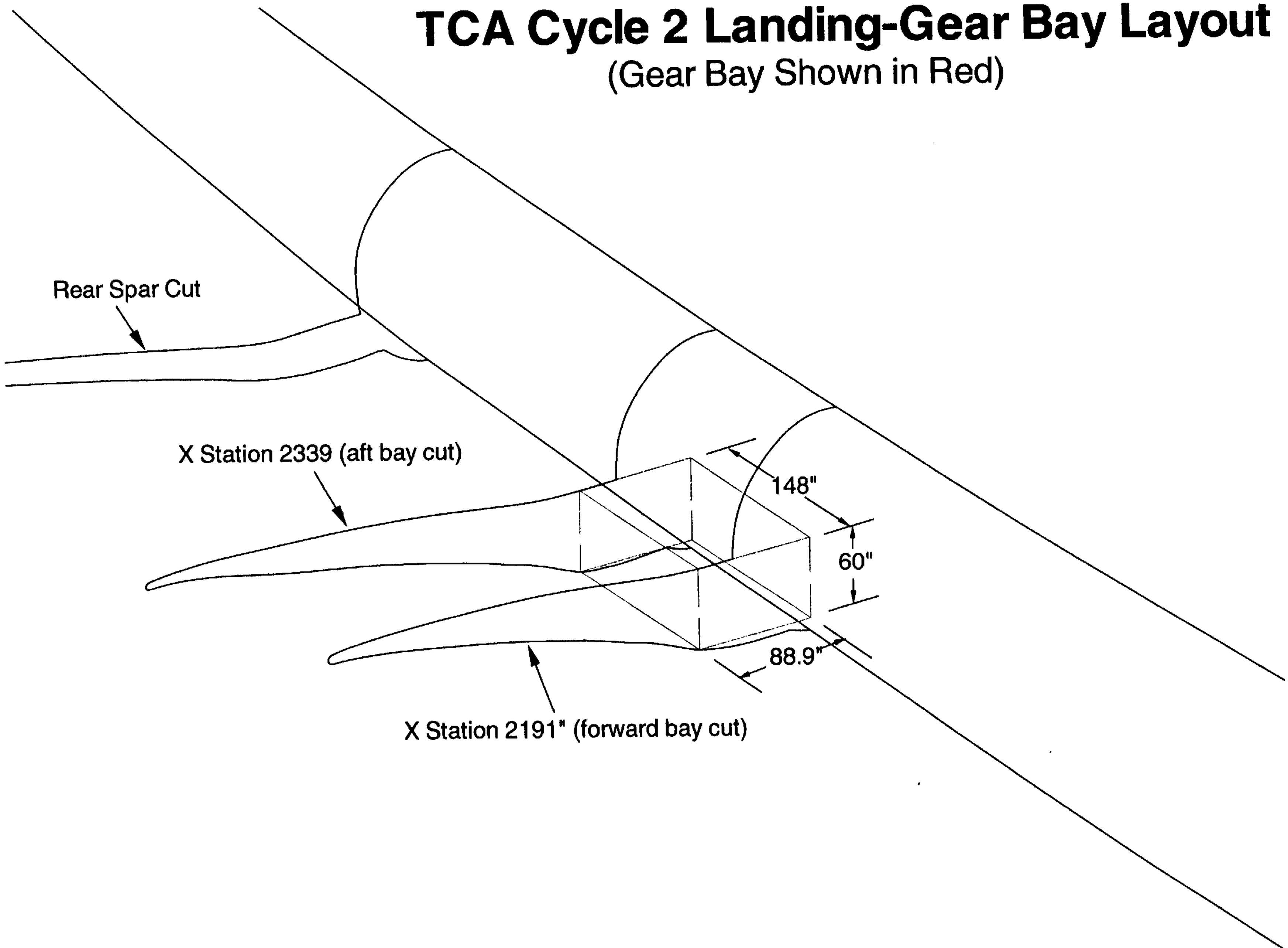

TCA Cycle 2 Fuel Volume Layout

This figure shows a graphical representation of the fuel volume layout on the Cycle 2 design. The planform dimensions of the volume are exactly the same as the baseline configuration. Recall that the significant increase in the inboard wing thickness has led to a 7.4% increase in fuel volume.

TCA Cycle 2 Fuel Volume Layout

(Fuel Volume Shown in Red)

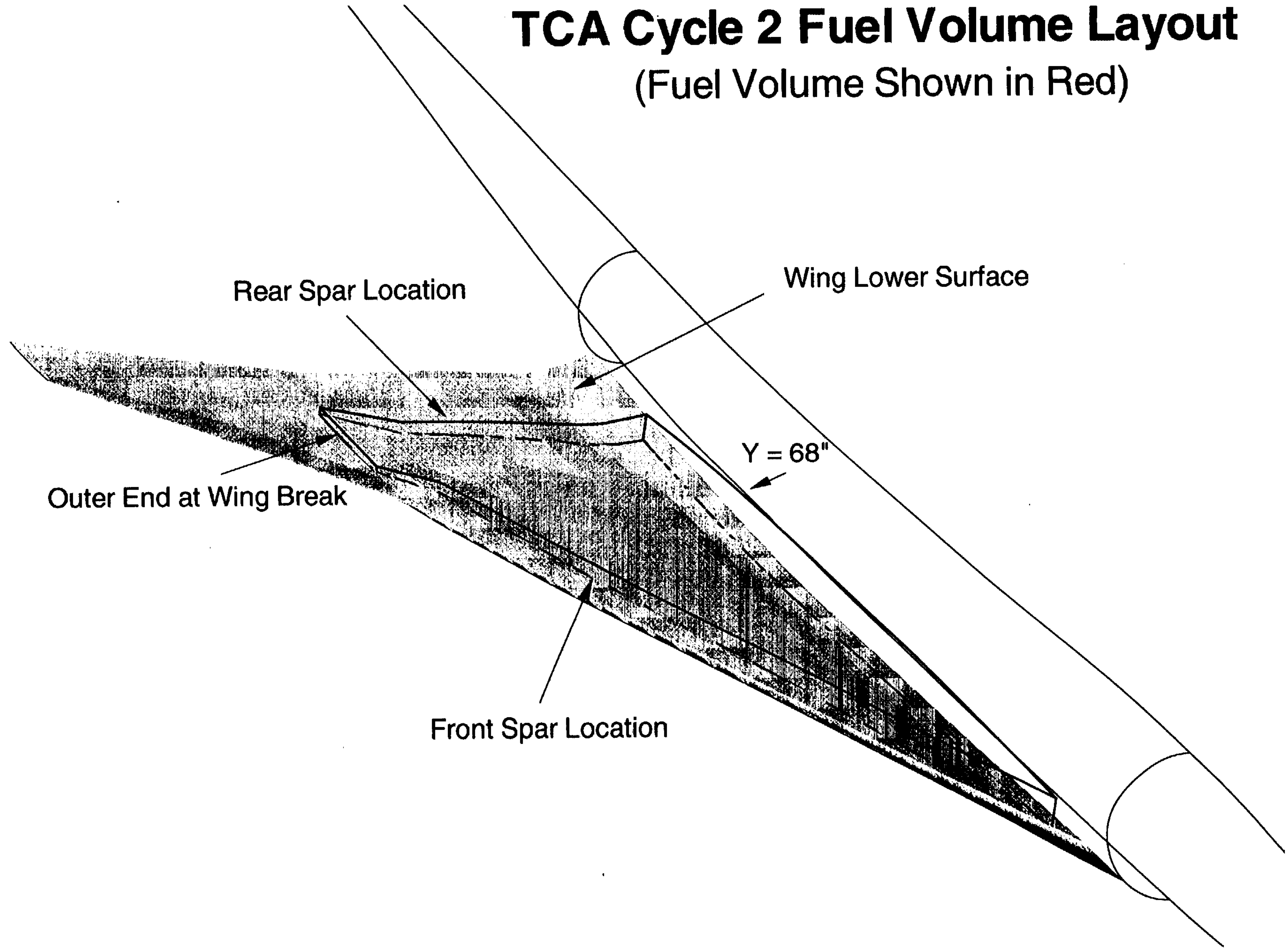

Fuselage Constraints

This slide (and the subsequent 2 slides) shows a table of the fuselage constraints. The complete list includes about 60 important constraints for optimization with the fuselage. A graphical presentation that helps to interpret some of the above table follows. As before, the constraint design value is shown where appropriate, along with the realized values of the Cycle 2 configuration.

Body Constraints

Number	Description	Design Value	Constraint Value	Satisfied ?	Drag Impact	Comment
B1	Body Length	3912"	=3912"	Y		
B2	Area @ Pilot's Eye	51.2 sq ft	≥49 sq ft	Y		Imposed at F.S. = 400
B3	First Class Enclosure					Imposed at F.S. 780 - 1040
	Aisle Height	99.4"	≥92.0"	Y		
	Head Clearance	90.1"	≥80.9"	Y		
	Seat Clearance	73.6"	≥67.6"	Y		
	Foot Clearance	64.5"	≥60.9"	Y		
B4	Nose Landing Gear Bay Enclosure	55.6"	≥55.7"	Y		Imposed at F.S. 820 - 900
B5	Business Class Enclosure					Imposed at F.S. 1190 - 1730
	Aisle Height	107."	≥92.0"	Y		
	Head Clearance	90.5"	≥90.5"	Y		
	Seat Clearance	83.8"	≥80.3"	Y		
	Foot Clearance	80.6"	≥72.1"	Y		
	Cargo Upper	75.1"	≥71.8"	Y		
	Cargo Lower	71.2"	≥71.1"	Y		
B6	Economy Class Enclosure					
	Aisle Height	92.0"	≥92.0"	Y		Imposed at F.S. 500 - 3600
	Head Clearance	79.7"	≥79.7"	Y		
	Seat Clearance	68.6"	≥67.2"	Y		
	Foot Clearance	58.5"	≥57.9"	Y		

Fuselage Constraints (cont.)

Fuselage constraint table (cont.)

Body Constraints

Number	Description	Design Value	Constraint Value	Satisfied ?	Drag Impact	Comment
B7	Radius of Curvature	47"<r<300"	30"<r<500"	Y		Imposed at F.S. 500 - 3600
B8	Keel @ Rear Spar	12.4"	≥6.0"	Y		Imposed at F.S. 2669
B9	Floor Segment F.S. Positions					
	Control Point #1	676	=676	Y		Not changed
	Control Point #2	1065	1065<x<1107	Y		Not changed
	Control Point #3	1788	1788<x<1820	Y		Not changed
	Control Point #4	2688	2524<x<2688	Y		Not changed
	Control Point #5	3200	=3200	Y		Not changed
B10	Cabin Floor Attitude					Evaluated at AOA = 3.035° (CL=0.088)
	Segment #1	2.4°	-3.5°≤a≤3.5°	Y		
	Segment #2	3.5°	-3.5°≤a≤3.5°	Y		
	Segment #3	3.1°	-3.5°≤a≤3.5°	Y		
	Segment #4	1.2°	-3.5°≤a≤3.5°	Y		
B11	Change in Floor Angle					
	Segment #1 to segment #2	-1.2°	-2.0°≤a≤2.0°	Y		
	Segment #2 to segment #3	0.5°	-2.0°≤a≤2.0°	Y		
	Segment #3 to segment #4	1.9°	-2.0°≤a≤2.0°	Y		

Fuselage Constraints (cont.)

Fuselage constraint table (cont.)

Body Constraints

Number	Description	Design Value	Constraint Value	Satisfied ?	Drag Impact	Comment
B12	Empennage Carry Through					
	Theta = -90°	43.9"	≥43.6"	Y		Imposed at F.S. 3540
	Theta = -59°	44.0"	≥43.7"	Y		Imposed at F.S. 3540
	Theta = -40°	40.5"	≥40.5"	Y		Imposed at F.S. 3540
	Theta = -0°	32.9"	≥32.6"	Y		Imposed at F.S. 3540
	Theta = 40°	40.5"	≥40.5"	Y		Imposed at F.S. 3540
	Theta = 59°	44.0"	≥43.7"	Y		Imposed at F.S. 3540
	Theta = 90°	43.9"	≥43.6"	Y		Imposed at F.S. 3540
	Theta = -90°	42.3"	≥42.1"	Y		Imposed at F.S. 3570
	Theta = -59°	42.2"	≥42.1"	Y		Imposed at F.S. 3570
	Theta = -40°	37.6"	≥37.4"	Y		Imposed at F.S. 3570
	Theta = -0°	30.3"	≥30.0"	Y		Imposed at F.S. 3570
	Theta = 40°	37.6"	≥37.4"	Y		Imposed at F.S. 3570
	Theta = 59°	42.3"	≥42.1"	Y		Imposed at F.S. 3570
	Theta = 90°	42.3"	≥42.1"	Y		Imposed at F.S. 3570

TCA Cycle 2 Fuselage Side View with Constraints

This fuselage side view gives a graphical representation of some of the previously listed fuselage constraints. It is most useful for visualizing deck placement and structural box carry-through.

TCA Cycle 2 Fuselage Side View With Constraints

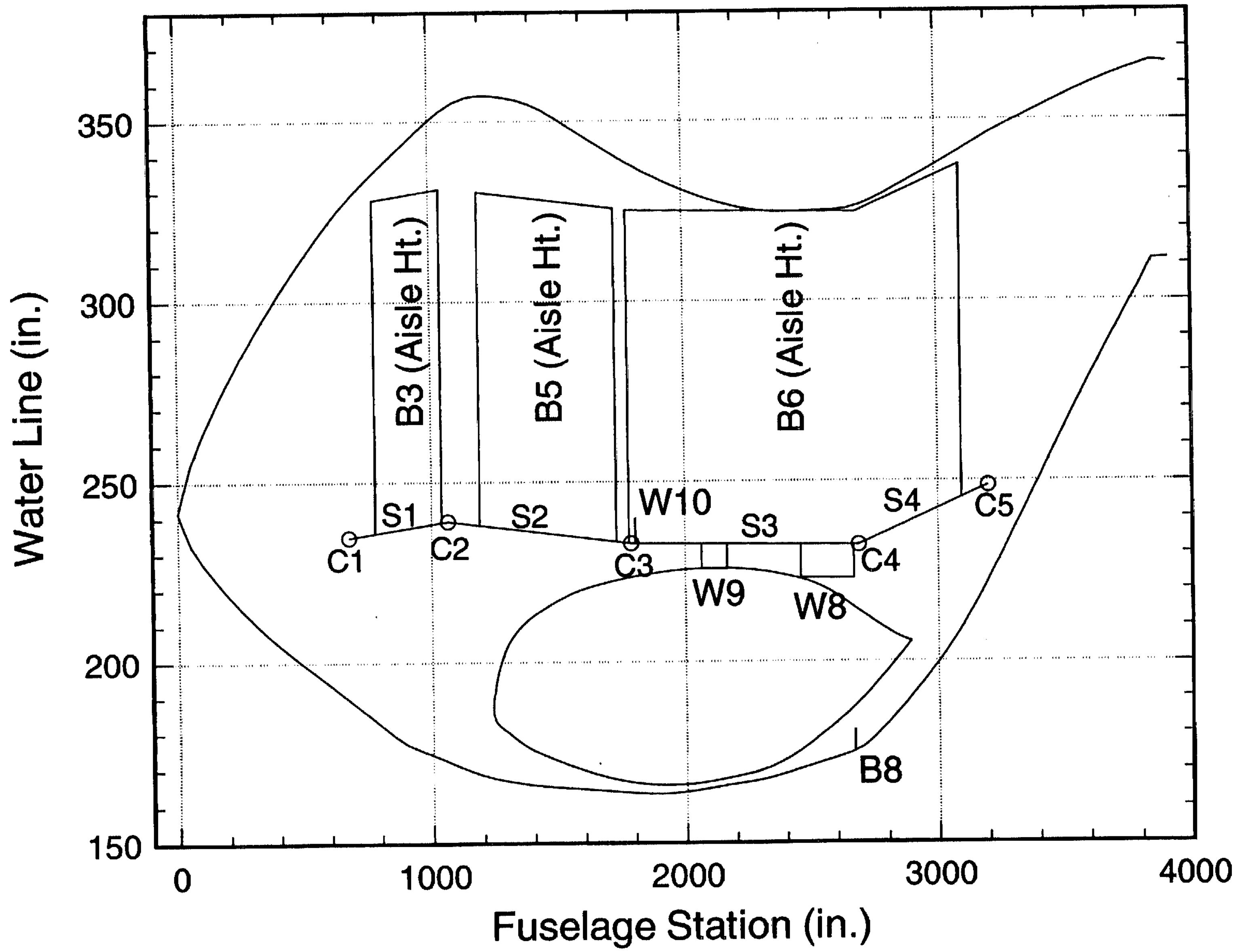

JOH 1-27-97

TCA Fuselage Cross-Sections with Constraints

This slide gives a graphical representation of the fuselage cross-sectional area constraints at various fuselage cuts. It also illustrates optimization modifications to the fuselage at the different stations. The changes are most notable at the fuselage station of 1202", where the fuselage has been flattened to some extent. This station also roughly corresponds to the location where the wing first intersects. Note that at the last fuselage station (FS 3076") the area constraints are critical.

TCA Fuselage Cross-Sections With Constraints

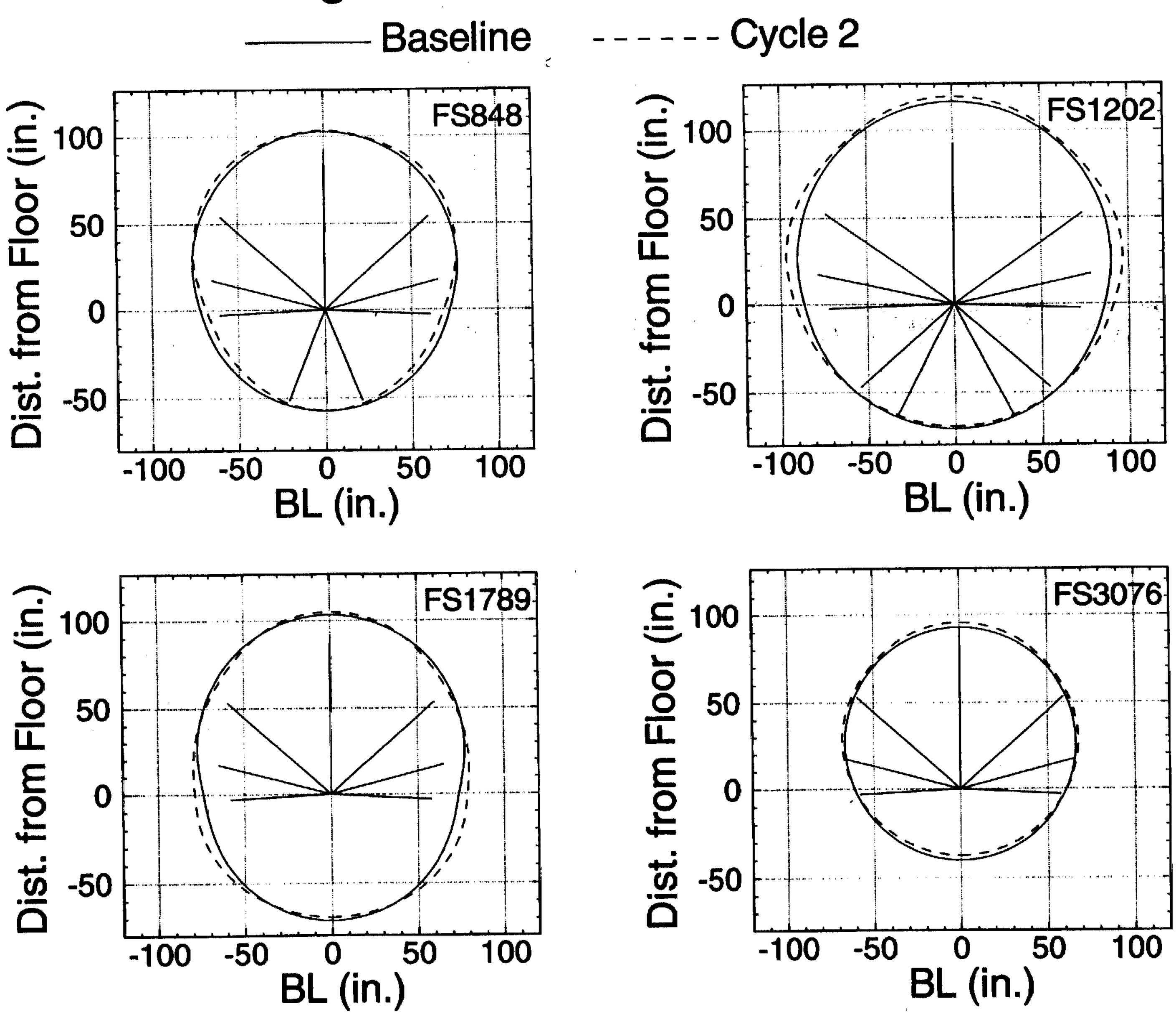

JOH 2-19-97

Cycle 2 Summary

These next two slides give a summary of the information presented in this paper. The MDC Cycle 2 configuration reduced drag (W/B/N/D N-S) by 3.9 counts at the evaluation condition ($C_L = 0.10$) while increasing volume by 2.7% for the fuselage and 4.3% for the wing (and 7.4% for the fuel volume). There were only minor constraint violations on the wing which when fully satisfied, only cost a 0.10 count drag penalty. To ensure a smoother final design, an additional spar constraint was added to the constraint list.

Cycle 2 Summary

- W/B/N/D Drag reduced 3.9 cts. (CFL3D Navier-Stokes with Baldwin-Lomax turbulence model)
- Fuselage volume increased ~2.7% (10,500 ft^3)
- Wing volume increased ~4.3% (4900 ft^3)
- Minor wing constraint violations; less than 0.1 ct penalty to satisfy
- Additional spar constraint enforced to reduce waviness

Cycle 2 Summary (cont.)

Here, at MDC, we still feel that with further optimization of this low-risk design we can still achieve further improvements. In closing, the MDC Cycle 2 design is a well-behaved configuration which should hold no surprises in its performance under various conditions. In addition, it has drag reductions and some significant usable volume increases.

Cycle 2 Summary (con'd)

- Drag can still be reduced with further optimization
- Low risk, very smooth design with aerodynamically desirable features:
  - Good leading-edge flow characteristics
  - No flow separation
  - Reduced shock strength in nacelle region
  - Smooth pressure distributions with no abrupt pressure oscillations
  - Straight streamlines

Future Directions

We have many near-term activities to further enhance our optimization studies. However, we still believe it is important to not allow many radical geometry changes in the configuration. Again, we feel that the configuration presented here can be further improved upon without harming many of its redeeming features. Some of these areas of activity include an implementation of ADIFOR derivatives to increase optimization accuracy, and the use of full configuration optimization to allow for the improved tailoring of shocks from the nacelles and diverters.

Future Directions

- MDC design philosophy is to proceed slowly through the design space with tight move limits. With current tools Cycle 2 design can still be improved
- Addition of ADIFOR derivatives shows promise to increase the accuracy of the gradients
- Addition of multiblock W/B/N/D design capability to allow tailoring of shocks from the nacelles and diverters

Improvements to the MDC Nonlinear Aerodynamic Design Tools

James O. Hager, Peter M. Hartwich, Eric R. Unger,
Geojoe Kuruvila, Robert P. Narducci, and Shreekant Agrawal
McDonnell Douglas Corporation
Long Beach, California 90807-5309

Nonlinear aerodynamic optimization is considered a key technology required to develop a High Speed Civil Transport (HSCT). Within the High Speed Research (HSR) program, McDonnell Douglas is developing nonlinear optimization tools to be able to support the launch of an HSCT program at the end of HSR II. This paper presents recent improvements to the tools.

The first set of improvements were made to be able to optimize the Technology Concept Aircraft (TCA). The TCA presented some grid-generation issues because it is a true low-wing configuration. In addition, several constraints were required to maintain a realistic design.

Second, the geometry modeling capability was improved to move toward full-configuration modeling. Empennage effects have been modeled, and wing/body/flaps configurations can be modeled. Efforts were also made to produce and improve tools required for integrated wing/body/nacelle/ diverter modeling.

Third, alternate gradient evaluation techniques are being examined to replace the finite-difference calculations currently being used. ADIFOR was applied to CFL3D and demonstrated for a 100+ design-variable problem. Also, an adjoint module is being created for TLNS3D.

Finally, a transition is being made to a modular design environment to facilitate improvements and the addition of new codes.

Improvements to the MDC Nonlinear Aerodynamic Design Tools

MCDONNELL DOUGLAS

HSCT

James O. Hager, Peter M. Hartwich,
Eric R. Unger, Geojoe Kuruvila, Robert P. Narducci,
and Shreekant Agrawal

HSR AP Workshop
NASA Langley, 25-28 February 1997

MDC HSR Nonlinear Design Optimization Capability

The philosophy used to develop the McDonnell Douglas HSR nonlinear design optimization capability is shown by the five general thrusts shown in the figure.

It was developed to support three design challenges: 1) cruise-point design, 2) transonic-flap optimization, and 3) multi-point design.

The optimization capability must be affordable. First, the results must be accurate: the results predicted by the optimization must be realized through analysis and testing. Also, the process must be efficient and robust to reduce the turnaround time and guarantee a good result every time. In addition, a modular structure facilitates improvements and can reduce computer resources.

Geometry modeling influences the accuracy and efficiency of a design. Wing/body (W/B) analysis is the least expensive but cannot capture the important effects of the nacelles and diverters (N/D). W/B analysis with nacelle-effects can be used to model the N/D effects with minimal expense. W/B/N/D analysis is considerably more expensive but is more representative of the complete aircraft. Naturally, a full configuration, including tails and flaps, is desired to have the highest accuracy.

The physics modeled by the flow solver also influences the accuracy and efficiency of a design. Currently, the physics modeled by the Euler equations are considered the lowest level of fidelity that are desirable for HSCT design. The physics modeled by the Navier-Stokes equations are probably required for an optimum N/D installation.

In addition, the tool must be able to enhance the design process of a realistic configuration. This requires a large design space with practical constraints. A general patched-grid capability will allow flexibility for complex geometries.

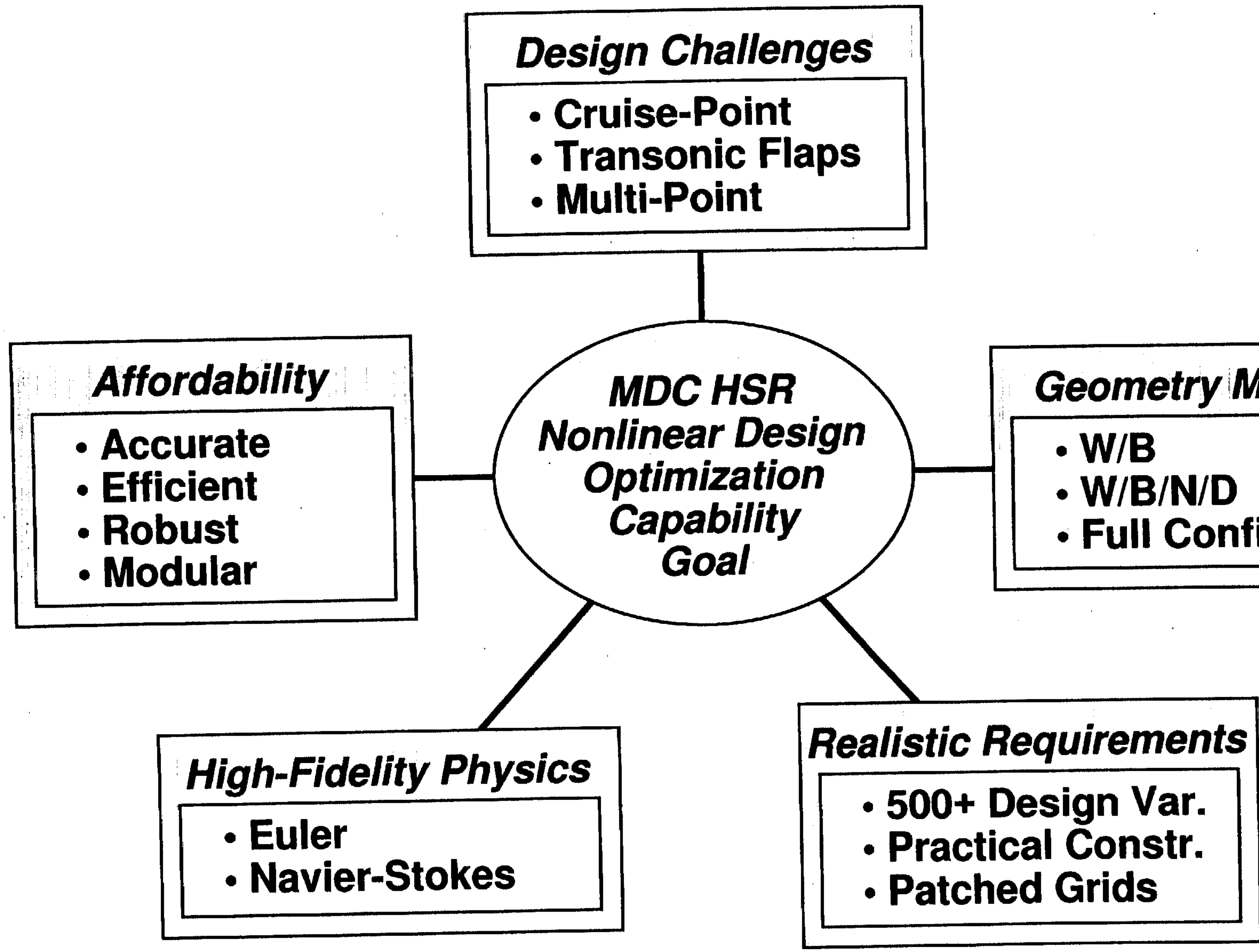
Design Challenges
• Cruise-Point
• Transonic Flaps
• Multi-Point
Affordability
• Accurate
• Efficient
• Robust
• Modular
MDC HSR
Nonlinear Design
Optimization
Capability
Goal
Geometry Model
• W/B
• W/B/N/D
• Full Config.
High-Fidelity Physics
• Euler
• Navier-Stokes
Realistic Requirements
• 500+ Design Var.
• Practical Constr.
• Patched Grids

JOH, 2-23-97

Items Addressed (Since Start of FY96)

The previous chart describes the long-term goal for the MDC nonlinear design optimization capability to be achieved by the end of HSR II. Since the start of FY96, four major items were addressed to move closer to the goal.

The general design capability was enhanced in order to move from M2.4-7A optimization to TCA optimization.

The geometry modeling capability was enhanced to move from W/B with nacelle-effects to: 1) include empennage effects, 2) model a W/B/F (flaps) configuration , and 3) initiate integrated W/B/N/D modeling.

The gradient evaluation capability is being enhanced by moving from finite-difference calculations to alternate methods.

Finally, a move was made to a modular design environment.

Items Addressed
(Since Start of FY96)

- General design capability
  - M2.4-7A optimization → TCA optimization
- Geometry modeling capability
  - W/B with nacelle effects → Empennage, flaps, W/B/N/D
- Gradient evaluation capability
  - Finite-difference → Alternate methods
- Modular design environment

Tasks Performed (Outline)

This figure lists the major tasks performed to support the four items in the previous chart, and also serves as the outline for the presentation.

Tasks Performed
(Outline)

- Design capability
  - Handle TCA-type W/B junction
  - Design variables and constraints
- Geometry capability
  - Empennage effects
  - W/B/F modeling
  - W/B/N/D modeling
- Alternate gradient capability
  - ADIFOR for CFL3D
  - Adjoint TLNS3D

Improved Design Capability:
Handle TCA-type W/B Junction

Before TCA optimization could begin, a basic grid-generation problem had to be solved. The QGRID grid generation routines were developed for a mid-wing configuration where there is a distinct part of the fuselage between the wing and the symmetry plane. The TCA, however, is a low-wing configuration where there are regions where there is no fuselage below the wing. QGRID was improved to automatically split the wing to create a "fuselage."

Improved Design Capability: Handle TCA-Type W/B Junction

- QGRID designed for mid-wing configuration

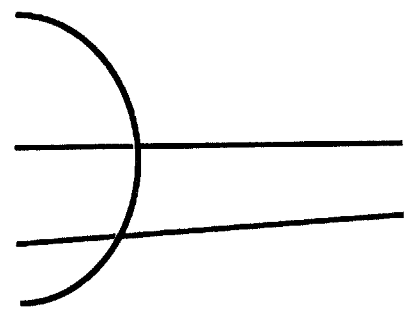

- TCA has low-wing configuration

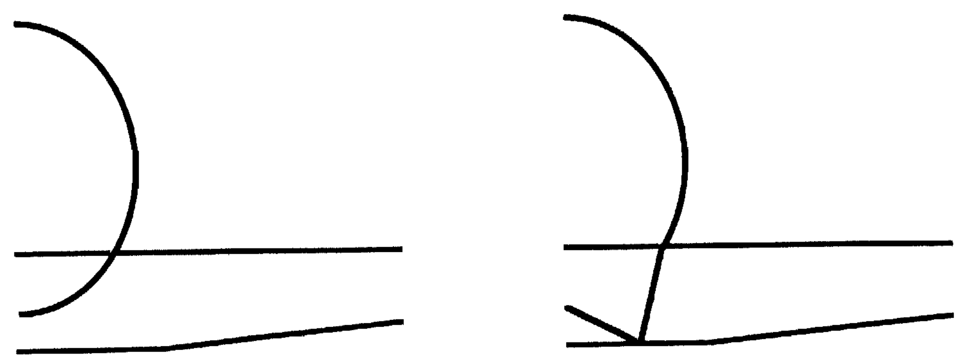

JOH, 2-22-97

Improved Design Capability:
Design Variables

Two types of design variables were modified. The wing sinusoidal shape functions can now be applied over a limited chordwise range. Also, the fuselage cross-sectional area design variables can be applied over a limited fuselage range. These two improvements increase the design space by allowing local perturbations to be created with a single variable instead of a combination of global variables.

A new design variables were added. First, wing can now twist about an arbitrary line. This capability was added so that twist could be applied about the rear spar to prevent spanwise perturbations in the spar due to wing twist. Also, angle-of-attack was added to allow the incidence of the entire configuration to change to maintain lift.

Improved Design Capability: Design Variables

- Modifications
  - Wing sinusoidal shape functions can be applied over a limited chordwise range
  - Fuselage cross-sectional area DVs can be applied over a limited fuselage range
- New variables
  - Wing twist about an arbitrary line (e.g., the rear spar)
  - Angle of attack

Improved Design Capability: Constraints

Several new constraints were added to support the TCA optimization and are shown in the chart. The cross-sectional shape enclosure constraint was improved by adding a variant that is active over a range of fuselage stations.

Improved Design Capability: Constraints

- Wing constraints added for TCA optimization
  - Fuel volume
  - Landing-gear bay enclosure
  - Trailing-edge closure angle
- Fuselage constraints added for TCA optimization
  - Improved cross-sectional shape enclosure
  - Radius of curvature
  - Keel clearance at rear spar
  - Change in deck angle

Improved Geometry Capability: Empennage Effects

In order to perform a full-configuration optimization, the entire geometry must be modeled and the configuration must remain in steady flight. The latter means that the configuration must remain trimmed. As a first step to optimize while considering trim drag, a simple empennage-effects model was created.

The procedure is to analyze the tails-off geometry (W/B, W/B with nacelle-effects, or W/B/N/D) to obtain the analysis values of lift, drag, and pitching-moment ($C_{L,anal}$, $C_{D,anal}$, and $C_{M,anal}$). The configuration is then trimmed in pitching-moment by solving for the proper tail deflection to maintain $C_{M,w/E}$. The tail deflection is then used to increment the analysis lift and drag to obtain the empennage-effects lift and drag ($C_{L,w/E}$, $C_{D,w/E}$). $C_{L,w/E}$, $C_{D,w/E}$ are then used for the objective and constraint evaluation.

Improved Geometry Capability: Empennage Effects

Analysis Geometry

↓

Flow Solver

Evaluate

$C_{L,anal}$, $C_{D,anal}$, $C_{M,anal}$

↓

Empennage Effects

Trim (maintain $C_{M,w/E}$: calc δ):

$$C_{M,w/E} = C_{M,anal} + \Delta C_{M,\delta=0} + \partial C_M/\partial\delta \; \delta$$

Update C_L and C_D for this tail deflection:

$$C_{L,w/E} = C_{L,anal} + \Delta C_{L,\delta=0} + \partial C_L/\partial\delta \; \delta$$

$$C_{D,w/E} = C_{D,anal} + \Delta C_{D,\delta=0} + \partial C_D/\partial\delta \; \delta + \partial^2 C_D/\partial\delta^2 \; \delta^2/2$$

↓

$C_{L,w/E}$, $C_{D,w/E}$, $C_{M,w/E}$

JOH, 2-22-97

Improved Geometry Capability: Wing/Body/Flap Modeling

Work was recently completed to model a wing/body/flap configuration. The flap-deflection and grid-generation capability was obtained from the MDC HSR High-Lift group and a sample grid is shown. These modules, and CFL3D, were tied together with a modular optimization tool to perform transonic flap optimization.

Flap Optimization Grid

Single Block, C–O Topology, 145x33x91

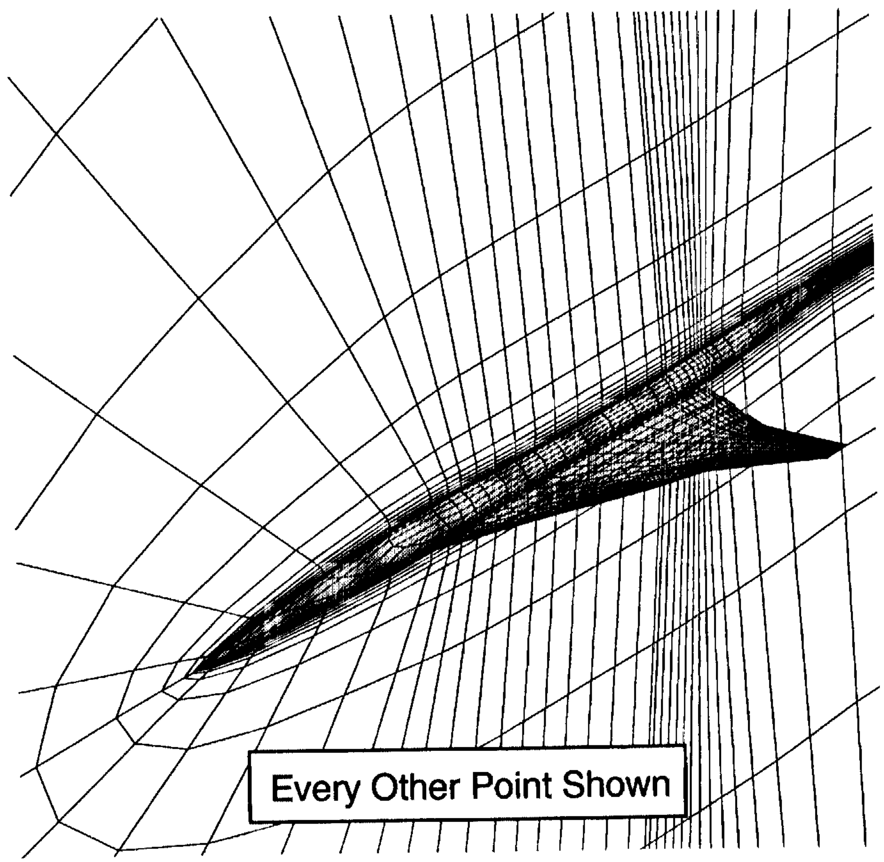

Inboard L.E. Flap: 8°
Outboard L.E. Flap: 8°

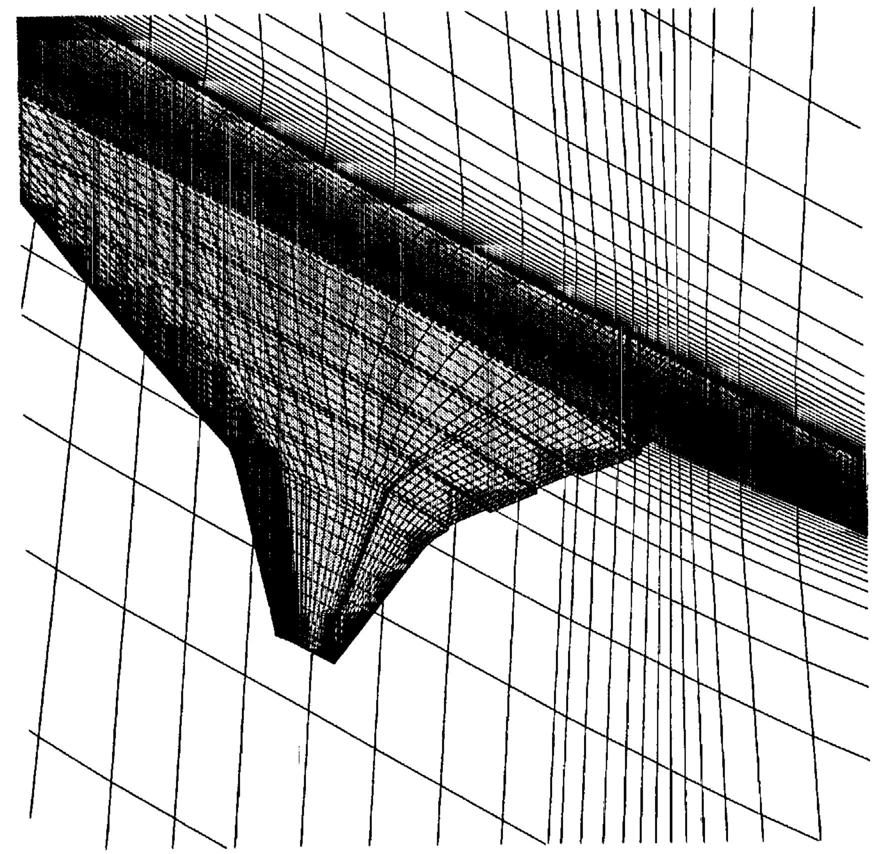

Inboard T.E. Flap: 3°
Middle T.E. Flap: 3°
Outboard T.E. Flap: 3°

Improved Geometry Capability: Integrated W/B/N/D Modeling

This chart outlines the procedure that will be used to perform integrated W/B/N/D modeling. The next several charts will fill in some of the details.

Improved Geometry Capability: Integrated W/B/N/D Modeling

- N/D reintegration
- W/B/N/D surface grid regeneration
- W/B/N/D volume grid perturbation (FlexMesh)

Improved Geometry Capability: Nacelle/Diverter Reintegration

In prior design studies, the nacelles and diverters were by hand reinstalled into wings whose shape and position had changed during an aerodynamic shape optimization process. This was a time consuming and a costly labor intensive process. This motivated this activity which aimed to speed up the nacelle/diverter (N/D) reintegration process by automating the process.

This automated N/D reintegration process is designed to maintain a pre-defined shape of the nacelle. Input from MDC's Technical Integration (TI) group was solicited to ensure consistency of the proposed N/D reintegration procedure with their practices.

Improved Geometry Capability: Nacelle/Diverter Reintegration

MCDONNELL DOUGLAS

HSCT

- Reduce design cycle time
  - replace labor intensive manual process
- Constraints:
  - maintain baseline nacelle shape
  - consistency with MDC TI practice

Baseline Nacelle/Diverter Reintegrated to a New Wing Geometry

This slide gives a demonstration of the nacelle/diverter (N/D) re-integration routine. The baseline N/D has been re-integrated into a new wing geometry. The steps involved are: 1) translation and rotation to make the N/D follow the wing; 2) intersection of the diverter with the wing; and 3) regeneration of the surface grids of the diverter and diverter top. The translation and rotation are performed to retain a constant-span location of the nacelle at the wing trailing edge as well as a given diverter leading edge height.

Baseline Nacelle/Diverter Reintegrated to a New Wing Geometry

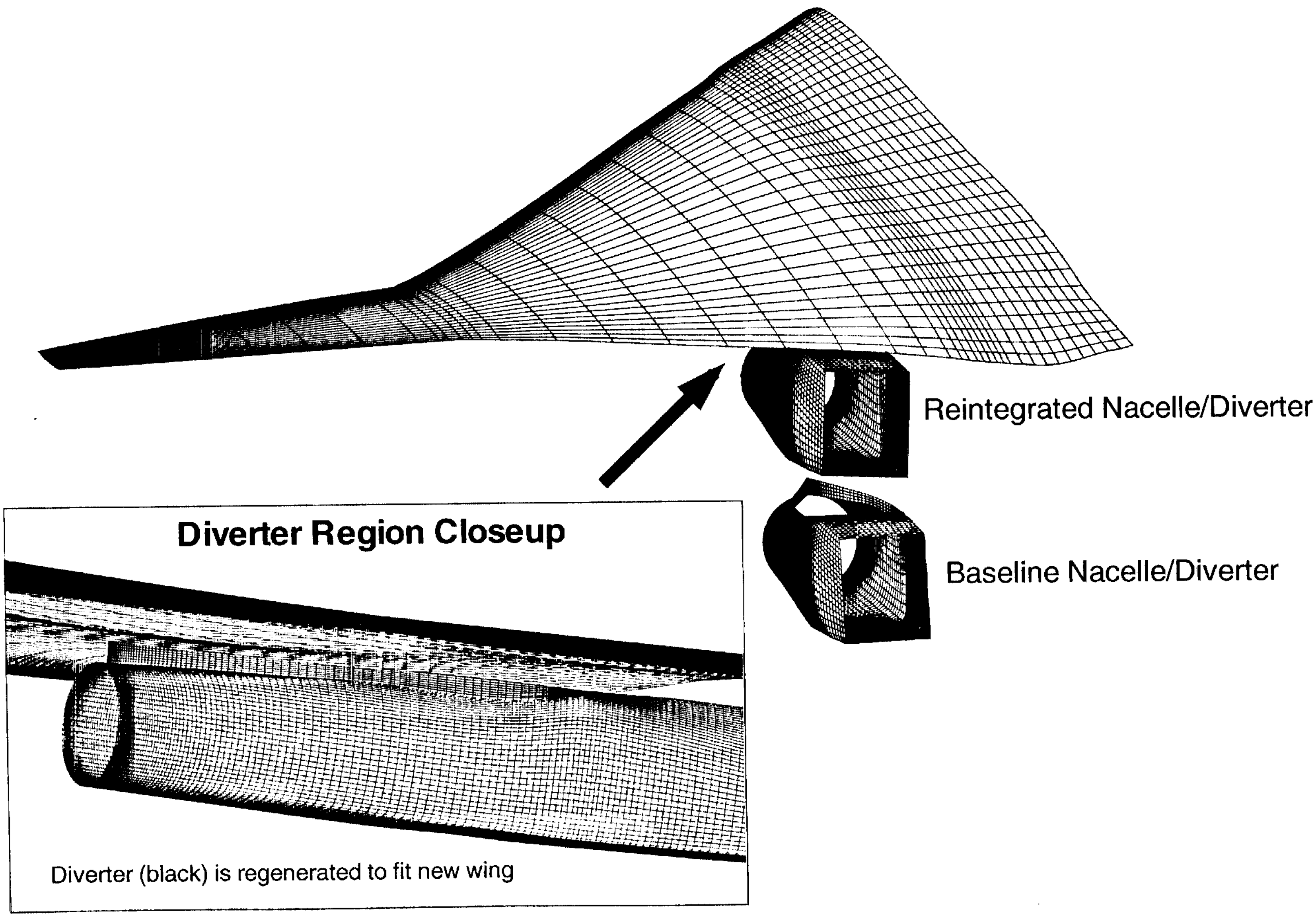

Improved Geometry Capability:
Automatic W/B/N/D Surface Grid Generation

Originally, it was planned to use an existing grid perturbation tool , NASA Langley's CSCMDO, for perturbing W/B/N/D surface grids and to integrate this capability into a script-driven grid generation module. This approach was dropped in favor of using mostly hard-wired surface grid generation modules and coupling them with MDC's FlexMesh volume grid perturbation method. This approach, while less flexible than the script-driven process, is much less complicated to develop.

This would also remove two problems encountered in using CSCMDO. First, CSCMDO requires a rather detailed input stream which takes time and expertise to set up. Second, MDC has only access to the executable of CSCMDO. This paces MDC's needs for future adjustments or expansions of W/B/N/D surface grid generation capabilities with the schedule of the CSCMDO developers.

Improved Geometry Capability: Automatic W/B/N/D Surface Grid Generation

MCDONNELL DOUGLAS

HSCT

- Reduce complexity of integration within MDO3D
- Avoid dependency on CSCMDO
  - input driven software
  - executable only available

Automatic W/B/N/D Surface Grid Generation

A existing body surface patch is mapped into a (u,v) parameter space. The updated definition of the body geometry (as a result of the shape optimization process) is then mapped using bilinear splines into that parameter space.

The work on this automated process is about 70 percent complete at this time. The surface grid patches in this figure illustrates which portions of the surface grid can presently be generated by the integrated surface grid generation module.

Automatic Wing/Body/Nacelle/Diverter Surface Grid Generation

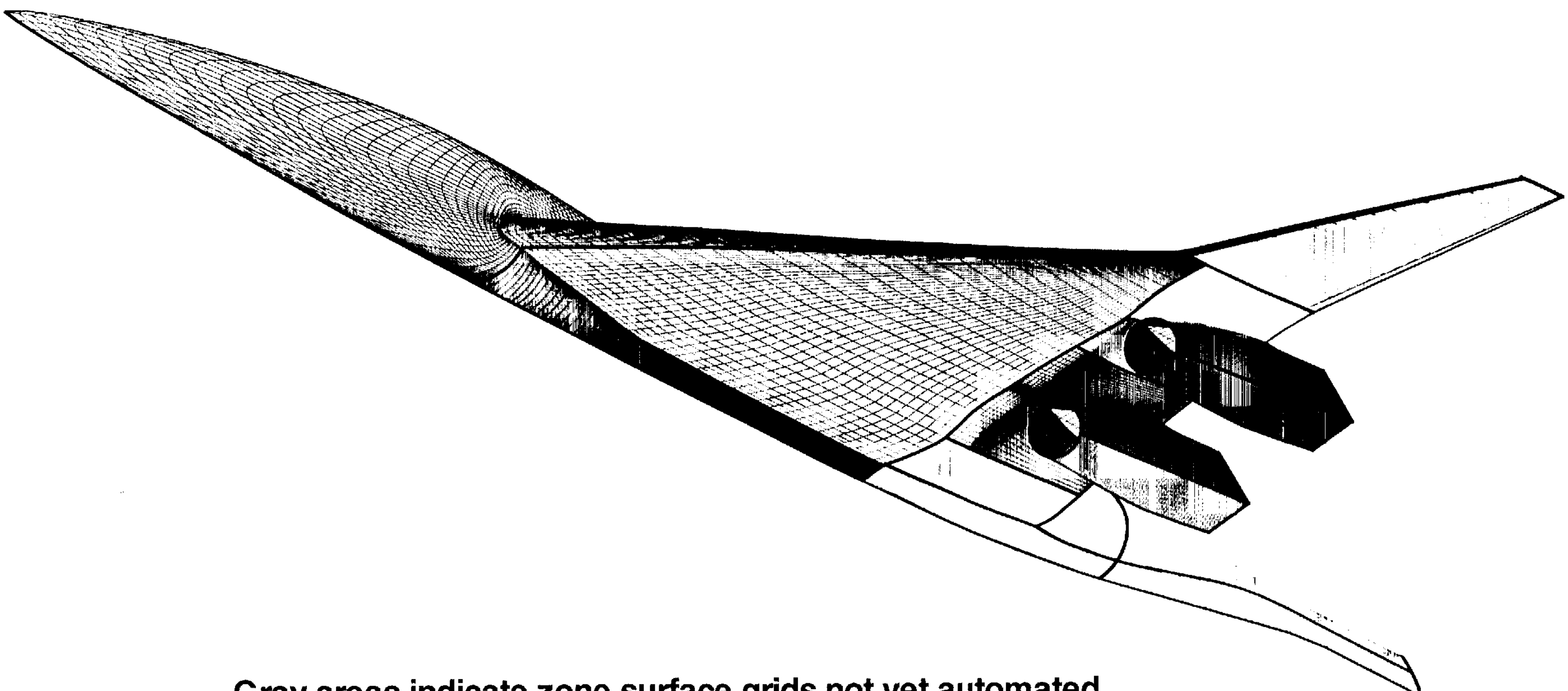

Gray areas indicate zone surface grids not yet automated

Improved Geometry Capability: W/B/N/D Volume Grid Perturbation (FlexMesh)

Body conforming computational grids need to be continuously adjusted to changes in airframe geometries during an aerodynamic shape optimization process. One existing computational tool (i.e., CSCMDO) requires a skilled person-in-the-loop who sets up input decks for complex multiblock patched grids. Human labor is much more expensive than computer expenditures. Also, MDC has only access to the executable of this software which requires to mesh MDC's needs for code development with the schedules of CSCMDO's developers.

Another volume grid perturbation method, WARP3D, is claimed to provide a high level of automation. However, this tool is limited to handle multiblock grids with point-matched (as opposed to patched or point-mismatched) grid block interfaces. Also, WARP3D is highly integrated into the Euler solver FLO87, the flow solver in the SYN87 design tool. Not only does MDC's shape design tool, MDO3D, presently rely on CFL3D as the flow solver, but generally a grid volume grid perturbation tool should as much as possible be a stand-alone utility that could be coupled with other flows solvers as well.

Thus, development of a stand-alone, automated grid perturbation scheme has been pursued.

Improved Geometry Capability: W/B/N/D Volume Grid Perturbation (FlexMesh)

MCDONNELL DOUGLAS

HSCT

- Methodology needs to be suitable for multiblock patched grids
- User-independent approach is preferred
- Flexibility/extendibility of method requires access to source code

Improved Geometry Capability:
W/B/N/D Volume Grid Perturbation (FlexMesh)

Key in the development of an automated grid perturbation method for use on multiblock patched grids is to make the grid block boundaries transparent to the computer tool. This is achieved by 1) basing the relationship between a master (or surface) node and its slave nodes on minimum distance, and by 2) storing the grid information in one-dimensional arrays. The one-dimensional data structure permits a grid point to be identified by a single (address) number. Thus, a slave is associated with its master by storing the slave's address into the master's address.

The slave points are associated with vertices of subgrids in the grid block faces. The subgrid structure 1) aides the preservation of smoothness in perturbed grid planes; 2) improve the computational efficiency of the grid perturbation process; and 3) still helps to maintain point-matched grid block interfaces.

There are two different classes of master nodes: those along the perimeter of a surface patch and those lying inside such a patch. Master/slave couplings for the latter require that master and slave coincide. All other slave nodes are coupled to master points along the perimeter of a surface patch. This two-tier system avoids spikes in perturbed grid block interfaces due to slaves that pop out of plane because they connect to master nodes inside a solid-body patch.

Improved Geometry Capability: W/B/N/D Volume Grid Perturbation (FlexMesh)

MCDONNELL DOUGLAS HSCT

- Transparency of grid block boundaries
  - master/slave coupling based on minimum distance
  - memory management uses indirect addressing
  - subgrids in grid block faces for efficiency and grid quality
- Two-tier system for group master nodes
  - master and slave nodes are identical within a solid surface patch
  - off-body slave nodes are connected to master nodes along the perimeter of a solid-surface patch

Improved Geometry Capability: W/B/N/D Volume Grid Perturbation (FlexMesh)

After a change in the surface geometry, the displacement of the master point, scaled with a decay function, is applied to their respective slave nodes. The decay function is essentially a Gaussian distribution with the ratio of the distance between slave and master to the magnitude of the displacement vector as the exponential argument. The decay function ensures the integrity of the grid in the presence of multiple deforming surfaces.

The displacements of the vertices of these subgrids are propagated throughout the entire grid by using a three-tiered transfinite interpolation (TFI) technique. First, the displacements are applied to nodes along the edges of the subgrids. Then, the displacement of the nodes along the perimeter of the subgrids are interpolated into the interior of these subgrids. Finally, the displacements in the subgrids are interpolated into the interior domain of each grid block.

The interpolations are performed in physical space rather than the customary parameter space. Thus, the distribution of the perturbations in the interior of the grid reflect the grid stretching of the baseline grid.

Improved Geometry Capability: FlexMesh - Cont'd

- Slaves follow movements of their masters
  - scaling using a Gaussian distribution function preserves integrity of grids with multiple solid surfaces
- Transfinite interpolation propagates displacements of vertices
  - first to nodes along the edges of subgrids
  - then to nodes in the interior of the subgrids
  - finally to the nodes in the interior of each grid block

Multiblock Grid Perturbation Demonstration
Maintenance of Point-Matched Block Interfaces

This figure illustrates one aspect of an application of the grid perturbation scheme to a 28-block patched grid over the 1404 IMT wing/body/nacelle/diverter configuration. This grid, suitable for computing Euler solutions, consists of more than 2.6 million grid points and more than 100,000 surface nodes.

The two details at the bottom of this figure show the surface grids of three grid blocks that come to lie abut to the physical plane indicated in the top part of this composite figure. There are one grid block to the upstream side of this physical plane and two grid blocks to its downstream side. Compared to the baseline configuration, the wing is mounted higher and at an increased incidence to the fuselage for the optimized configuration. This figure demonstrates how the subgrid structure used by the grid perturbation scheme ensures that this point-matched quality of the baseline grid is retained during the perturbation process. Maintenance of the point-matched quality is reflected by the perfect overplotting of the grid lines and by the continuity of grid lines transversing the block edges.

Multiblock Grid Perturbation Demonstration

Maintenance of Point-Matched Block Interfaces

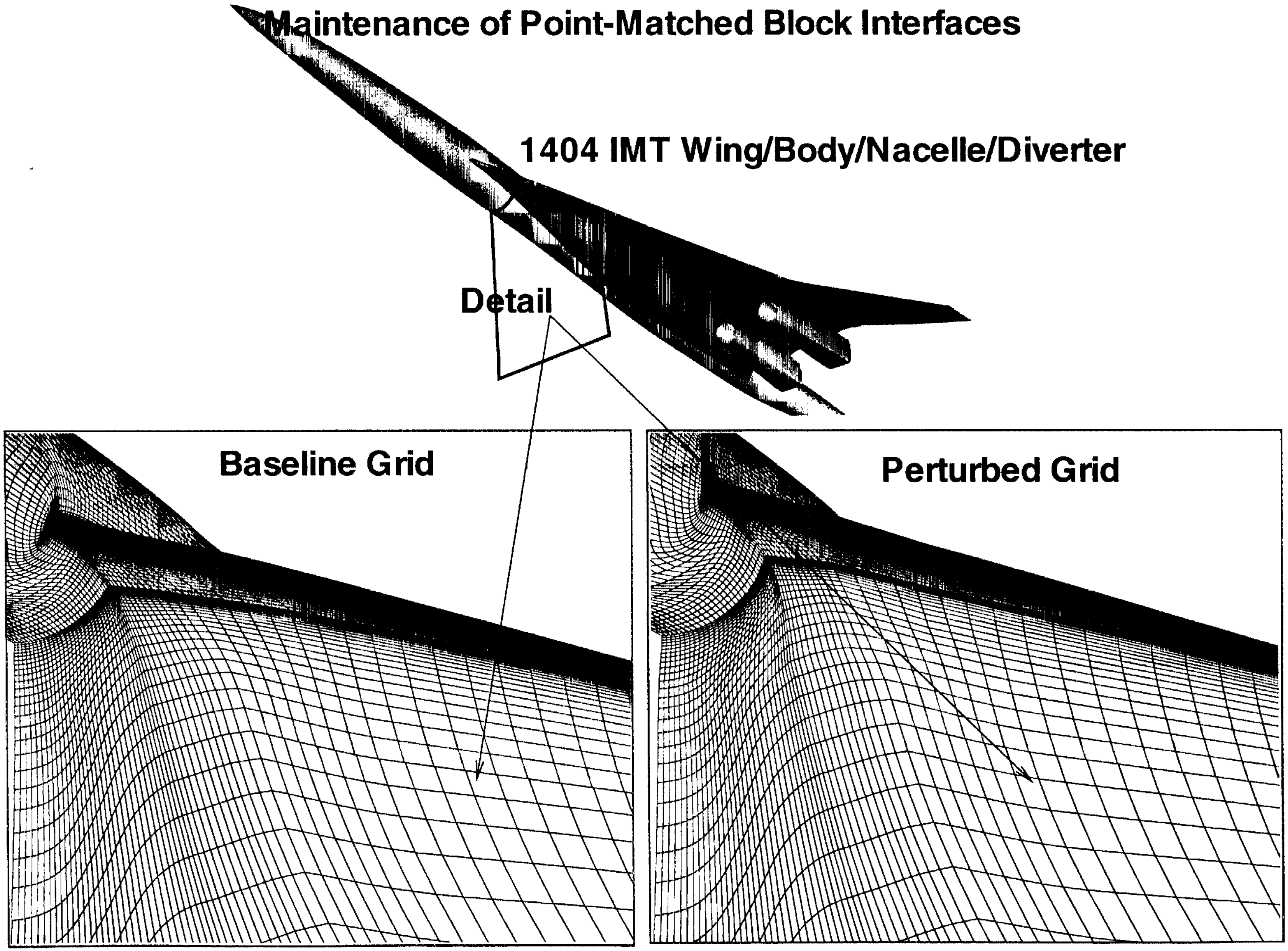

Multiblock Grid Perturbation Demonstration

Integrity of Grid in the Presence of Multiple Body Surfaces

This figure illustrates another aspect of an application of the grid perturbation scheme to a 28-block patched grid over the 1404 IMT wing/body/nacelle/diverter configuration. This grid, suitable for computing Euler solutions, consists of more than 2.6 million grid points and more than 100,000 surface nodes.

The two bottom details in this figure show cross-sectional grids in a physical plane outlined in the top portion of this figure. This physical plane lies under the wing and inboard of the inboard nacelle/diverter combination. The cross-sectional grids belong to two grid blocks which share a point-matched interface. Going from the baseline to the optimized geometry, the shape of the lower wing surface has changed and the nacelle has been lowered, leading to a taller diverter. This figure illustrates how scaling the movement of the "slave" nodes with a decay function preserves the integrity of the grid in the presence of multiple solid surfaces.

Multiblock Grid Perturbation Demonstration

Integrity of Grid in the Presence of Multiple Body Surfaces

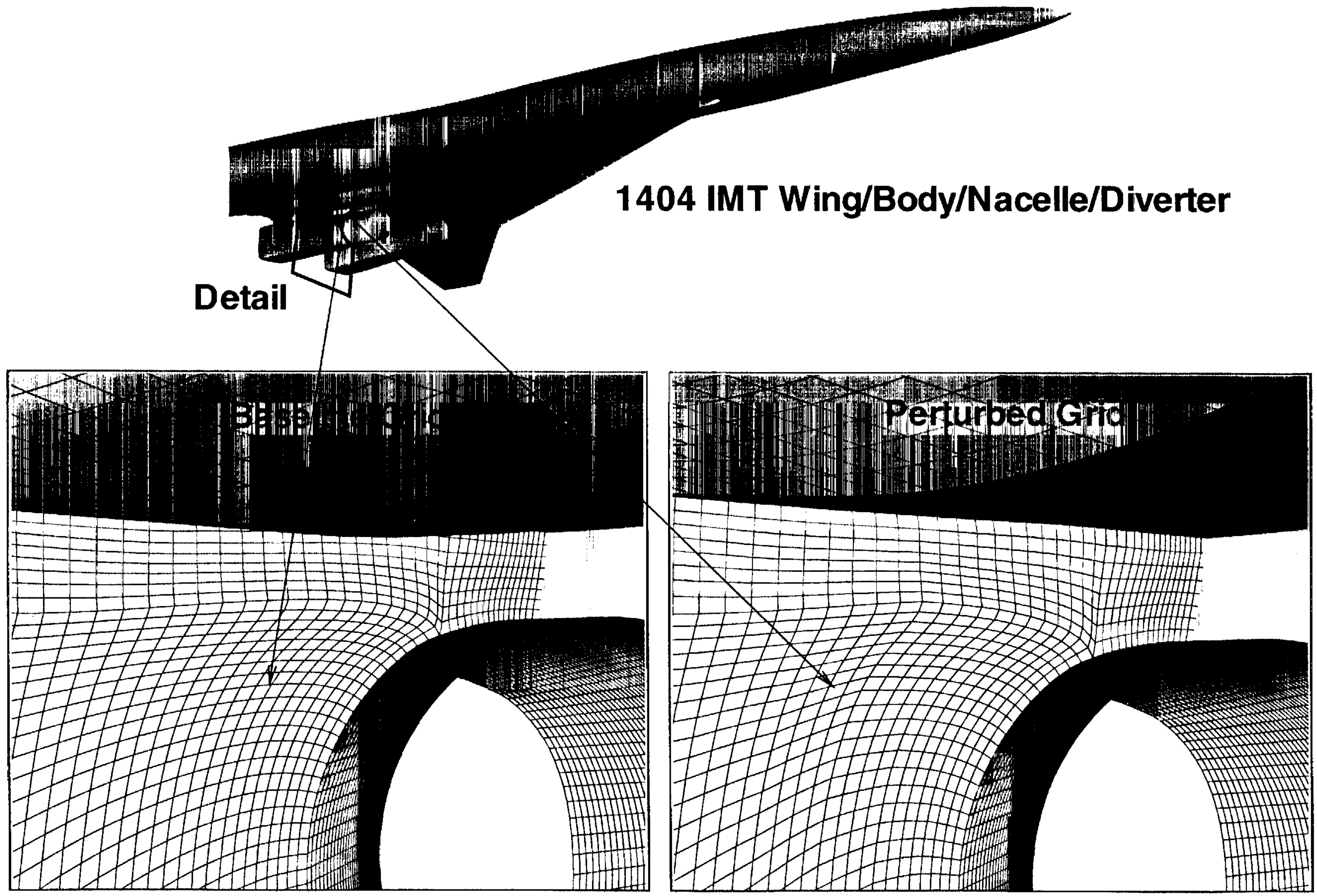

Automated Surface-Grid Regeneration

Another feature in the grid perturbation method pertains to a surface-grid regeneration capability. A new surface grid is often generated with some external utility. Such utilities were found to occasionally generate surface grids with grid stretchings quite different from that of the baseline grid. As sketched below, the consequence of this incompatibility is the introduction of considerable grid skewness. This is to be explained as follows. The vertices of subgrids follow the displacement of the "masters." The coordinates of nodes between non-"master" subgrid vertices are computed from interpolation using subgrid vertex information only. Thus, there is no information about possible changes in the grid spacing along the solid-body contour.

This disconnect between surface and field points is remedied by redistributing the surface grid such that it restores the relative spacing of the original surface grid. This is accomplished by "moving" the surface nodes along grid lines whose shape is computed from piecewise defined polynomials conforming to a perturbed surface shape.

Improved Geometry Capability: Automated Surface-Grid Regeneration

MCDONNELL DOUGLAS

HSCT

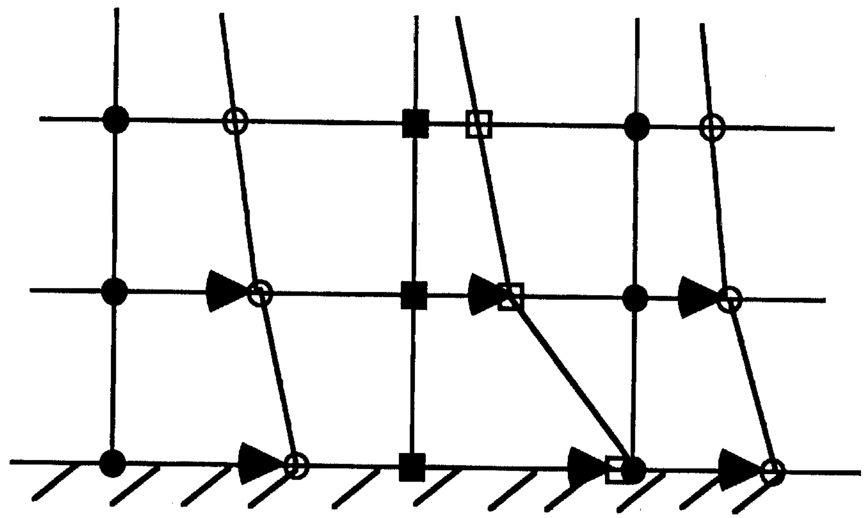

○ ● vertices of sub grids

□ ■ "non-slave" grid points

● ■ baseline grid

○ □ perturbed grid

Automated Surface Grid Projection

This figure demonstrates the need for a surface-grid perturbation capability. The center part of this figure shows the TCA Opt3 W/B configuration, an intermediate nonlinear TCA design, along with part of the grid in the plane of symmetry. The upper and lower details in this figure show how one of the families of grid lines connects to the surface grid of the fuselage. For illustration purposes, only every other grid line in the radial direction in the plane of symmetry is plotted. Ideally, the grid lines in the plane of symmetry that emanate form the fuselage are orthogonal to the body surface. One quite drastically deviates from this ideal if the fuselage surface grid is used as provided. Redistributing the surface grid restores the degree of orthogonality to levels found in the baseline grid over this W/B configuration.

Automated Surface Grid Projection

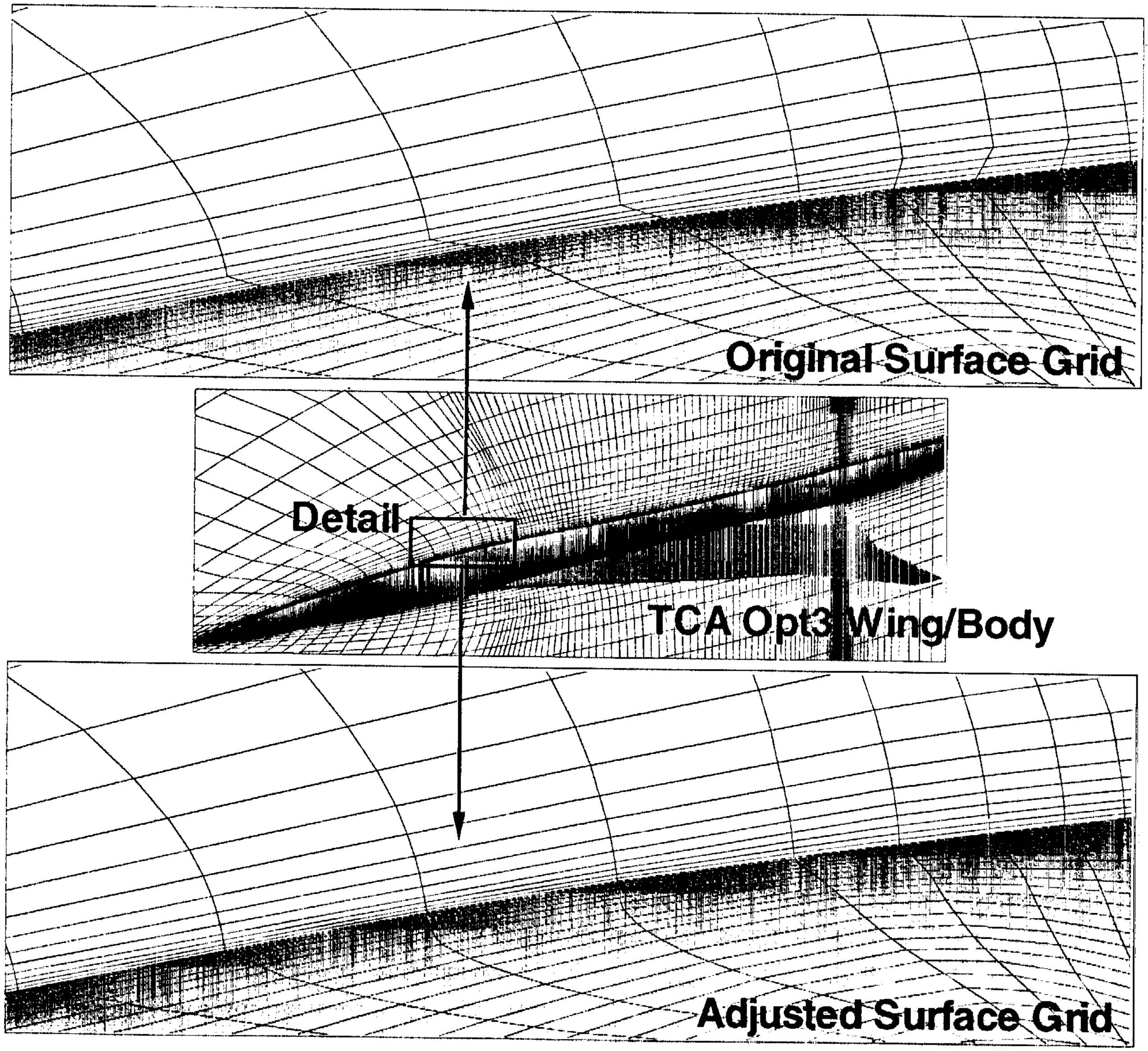

Efficiency of FlexMesh

After having demonstrated the effectiveness of the multiblock grid perturbation method, the issue of efficiency still needs to be addressed. The table below lists some statistics for the applications of the grid perturbation scheme as previously presented in this section. The timings are given for a Cray C-90 computer used in single processor mode. In judging the performance of FlexMesh, keep in mind that it produces these results in a highly automated fashion without requiring hours or even days of expensive intervention of a skilled user. Also note that the connectivity information is computed only once for any given baseline grid. The actual perturbation process, even of large patched multiblock grids over the HSCT wing/body/nacelle/diverter configurations requires only a few seconds of computing time.

Great strides have been made in reducing the memory requirements for FlexMesh. From previous memory penalties in excess of 125 percent, FlexMesh currently requires only about 50 percent more memory than the baseline Euler/Navier-Stokes solver CFL3D, presently the flow solver of choice in MDO3D.

Improved Geometry Capability: Efficiency of FlexMesh

MCDONNELL DOUGLAS

HSCT

Application	TCA Opt3	1404 IMT	TCA Opt7
Geometry	W/B	W/B/N/D	W/B/N/D
No. of Grid Blocks	1	28	19
No. of Nodes	928,814	2,676,496	3,139,091
No. of Surface Nodes	18,927	102,059	108,676
Generation of Connectivity Information*	4.6 secs	237.1 secs	175.9 secs
Grid Adjustment*	5.9 secs	18.1 secs	20.4 secs
Memory in MWs (CFL3D/FlexMesh)	61 (40/21)	151 (96/55)	173 (105/68)

*timings are for Cray C-90 computer, single processor

Alternate Gradient Capability

An alternate gradient capability is being developed to overcome the limitations of finite-difference-based gradient calculations. In particular, the accuracy of finite-difference calculations is dependent on the step size, and the CPU-time grows linearly with the number of design variables.

The first alternate method is ADIFOR for CFL3D. This method was chosen for the improved accuracy.

The second alternate method is an adjoint module for TLNS3D. This method was chosen for the improved efficiency and the potential for improved accuracy.

Alternate Gradient Capability

MCDONNELL DOUGLAS — HSCT

- Limitations of finite-difference calculations
  - Accuracy dependent on step size
  - CPU time grows linearly with number of DVs
- Alternate sensitivity evaluation
  - ADIFOR for CFL3D $\Rightarrow$ Improved accuracy
  - Adjoint TLNS3D $\Rightarrow$ Improved efficiency (and accuracy?)

Alternate Gradient Capability: ADIFOR for CFL3D

ADIFOR (Automatic DIfferentiation of FORTRAN) is attractive because it will produce very accurate gradients by differentiating an analysis tool. In addition, it can be applied to any code, including both Euler and Navier-Stokes codes. ADIFOR can be applied in a black-box mode to an analysis code, but the resulting sensitivity code will be very inefficient and too memory-inetnsive for any practical design application.

In order to obtain a more efficient sensitivity code, ADIFOR was applied in an ADII (Automatic Differentiation in Incremental Iterative) form. In this approach, ADIFOR is applied only to sections of the code relevant to the sensitivity analysis. Further gains in efficiency are achieved by processing only the inviscid or Euler variant of CFL3D, version 4.1, and by restoring parts of the code after applying the ADIFOR process to allow Fortran compilers to optimize the executable comparably to CFL3D baseline code. While improved, the code still requires large computer memory and CPU time to evaluate sensitivities for a large number of design variables simultaneously. An easy way to reduce this requirement is to run the code in parallel with each processor evaluating the sensitivity of a small number of design variables.

Alternate Gradient Capability: ADIFOR for CFL3D

- ADIFOR (Automatic DIfferentiation of FORTRAN)
  - Provides accurate derivatives
  - Applicable to any code (Euler/N-S)
- Demonstrate feasibility of ADIFOR for a design problem with a realistic number of design variables*
- Procedure
  - Automatic DIfferentiation in Incremental Iterative (ADII) to CFL3D, v4.1, (Euler): CFL3D.ADII
  - Reduce CPU time by running in parallel

*This work was performed by Prof. A. Taylor and Dr. A. Oloso through Eagle Aeronautics, Inc., Newport News, VA.

CFL3D.ADII - Efficiency

A benchmark test involving 5 design variables was formulated for the M2.4-7A wing/ body configuration was formulated. Analyses as well as sensitivity information was computed with the baseline CFL3D and with the CFL3D.ADII. In case of running the baseline CFL3D code, the sensitivities were calculated by applying finite differences to repeated flowfield solutions.

It appears that CFL3D.ADII produces analysis and sensitivities in about twice the computing time required for using the baseline CFL3D code and evaluate the sensitivities from finite-differences. To put matters in perspective, previous ADIFOR-ed versions of CFL3D were an order of magnitude slower than using finite-differences for the sensitivities and repeated flowfield solution from the baseline CFL3D code.

CFL3D.ADII's memory requirements still scale with the number of design variables. On the one hand , this is much better than what has been experienced in previous applications of automatic differentiation to CFL3D, but still is too high for using CFL3D.ADII in practical design applications on Cray-type machines.

Alternate Gradient Capability: CFL3D.ADII - Efficiency

MCDONNELL DOUGLAS — HSCT

- Benchmark
  - CFL3D, version 4.1 (Euler)
  - CFL3D.ADII
  - 5 design variables
  - Cray Y-MP, single processor

	Baseline CFL3D	CFL3D.ADII
T (= CPU time/cycle/node)	18.3 μsecs	188.5 μsecs
T / design variable	18.3 μsecs	37.7 μsecs
Memory	10 MWs	59 Mws

CFL3D.ADII - Accuracy

For the same benchmark test discussed in the previous chart, this table gives the ratios of the sensitivities as computed with automatic differentiation (labeled ADII) and with finite differences (identified with the subscript FD).

The difference between the two approaches lies less in the values for the sensitivities themselves than in the way they were computed. It is wellknown that finite-difference sensitivities can be as good as the, by definition, highly accurate ADIFOR sensitivities. However, the ADIFOR sensitivity information is produced in a hands off fashion whereas the accuracy of finite-difference sensitivities can be very much a function of the experience of the user.

Alternate Gradient Capability: CFL3D.ADII - Accuracy

MCDONNELL DOUGLAS

HSCT

- Benchmark
  - CFL3D, version 4.1 + finite-differences for sensitivities
  - CFL3D.ADII
  - 5 design variables

Design Variable	$\frac{\nabla C_{L,ADII}}{\nabla C_{L,FD}}$	$\frac{\nabla C_{D,ADII}}{\nabla C_{D,FD}}$	$\frac{\nabla C_{M,ADII}}{\nabla C_{M,FD}}$
1	1.0008	1.0119	0.9531
2	1.0000	1.0000	1.0000
3	0.9927	0.9896	1.0031
4	1.0023	1.0002	0.9954
5	0.9990	1.0025	1.0022

Alternate Gradient Capability: CFL3D.ADII - Design Demonstration

Emphasis was put on demonstrating that CFL3D.ADII with a realistic number of design variables can be used in nonlinear aerodynamic design at acceptable cost. Thus it sufficed to put a rather basic design methodology together and port it to the IBM SP-2 parallel computer at NAS.

The M2.4-7A HSCT wing/body configuration was chosen for these design exercises because a robust grid regeneration tool, MDC's QGRID, could be provided to Eagle Aeronautics. At the time these activities commenced, QGRID could not yet handle the wing/fuselage intersection of the TCA configuration (see above).

It was stipulated that more than 100 design variables were to be used in this demonstration project. Much leeway was given concerning the constraints. This explains the choice of constraints by Eagle Aeronautics.

Alternate Gradient Capability: CFL3D.ADII - Design Demonstration

MCDONNELL DOUGLAS HSCT

- Demonstration of CFL3D.ADII for a design problem with realistic number of design variables
  - M2.4-7A HSCT wing/body configuration
  - grid sensitivities through ADIFOR for QGRID
  - Computational grid with 210,177 nodes
  - >100 design variables (twist, thickness, and camber)
  - constraints: lift, root bending moment, and max. twist

Alternate Gradient Capability: CFL3D.ADII - Design Demonstration

The first design was successful in achieving the computational performance goal, but the resulting design was somewhat impractical due to a lack of thickness constraints; the wing just became unrealistically thin. The second design was used as a sanity check to make sure that CFL3D.ADII can produce an aerodynamically acceptable design

The computational expenditure for these designs on an IBM SP-2 parallel processing computer is also provided. Each processor of this computer was use to simultaneously provide a flow analysis and sensitivity information for one design variable.

Alternate Gradient Capability: CFL3D.ADII - Design Demonstration

- Design #1
  - 108 design variables (thickness, camber, twist)
  - 2 design cycles
  - 7.2 counts of drag reduction
- Design #2
  - 60 design variables (camber, twist)
  - 5 design cycles
  - 1.2 counts of drag reduction
- IBM-SP2
  - # of processors = # of design variables
  - about 12 hours CPU time/design cycle

Alternate Gradient Calculation: MDO3D/CFL3D.ADII Coupling

A first step has been made to incorporate an alternate gradient calculation capability into MDO3D by loosely coupling CFL3D.ADII. In this procedure, MDO3D performs the standard finite-difference calculations, but produces grid sensitivity data instead of the aerodynamic-coefficient sensitivity data. Then, CFL3D.ADII calculates the aerodynamic-coefficient sensitivity data. Then, MDO3D reads the aerodynamic-coefficient sensitivity data and performs the 1-D search.

Alternate Gradient Calculation: MDO3D/CFL3D.ADII Coupling

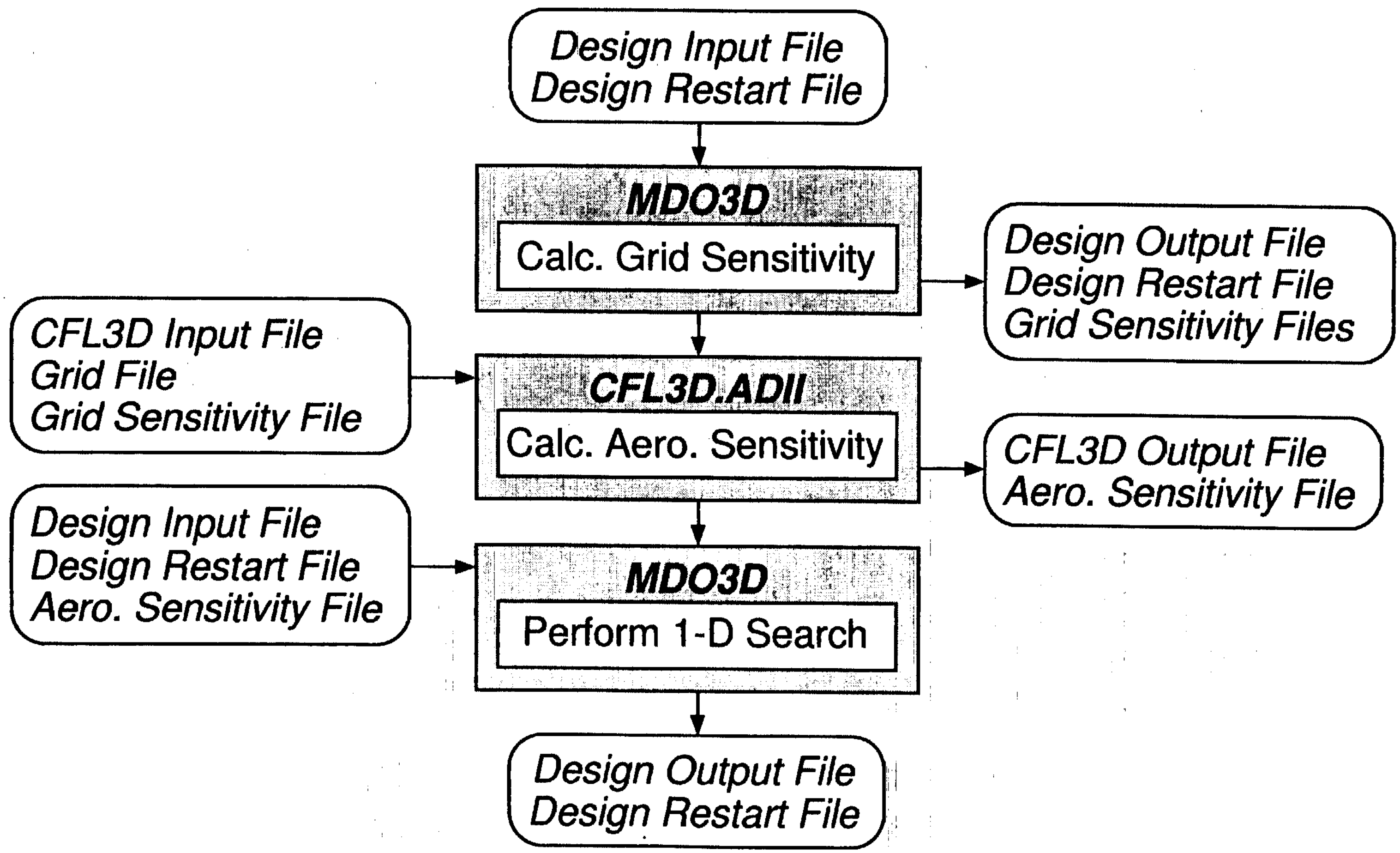

JOH, 2-22-97

TCA Wing Twist Sensitivity

A single wing twist design variable was used to compare the aerodynamic sensitivities predicted by finite-difference calculations in MDO3D and automatically differentiated calculations in CFL3D.ADII. The twist was applied about the rear spar with the maximum displacement at the wing LE break, with the perturbation lofted from the gear bay to the tip. The finite-difference-based and CFL3D.ADII-based sensitivities are comparable. A 0.05° perturbation was used for the calculations, and a 2° perturbation is shown in the figure.

TCA Wing Twist Sensitivity

- Twist about the rear spar
- Max. displacement at LE break
- Lofted from gear bay to tip

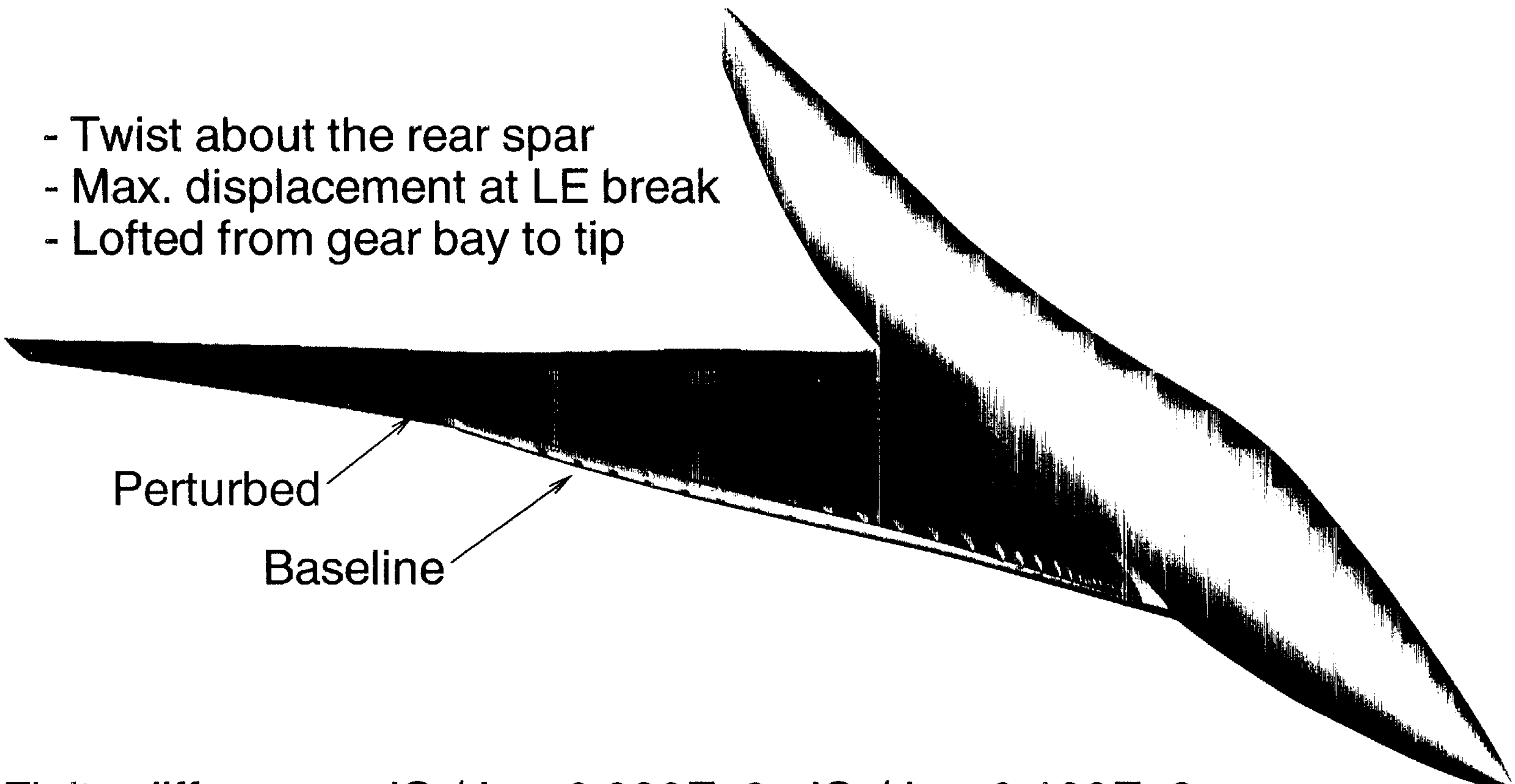

Finite-difference: $dC_L/dv = 0.930E{-}3$, $dC_D/dv = 0.100E{-}3$

CFL3D.ADII: $dC_L/dv = 0.936E{-}3$, $dC_D/dv = 0.101E{-}3$

JOH, 2-18-97

Adjoint TLNS3D

The emphasis in assessing an adjoint approach for evaluating gradients is put on efficiency since the CPU time is (relatively) independent of the number of design variables. While being capable of producing accurate gradients, adjoint methods depend on the suitability of the computational grid for both flow and gradient evaluation. Thus, adjoint methods are not by default as accurate as, for instance, an ADIFOR-based approach.

The adjoint method requires solving the standard flow equations (analysis module), solving the corresponding adjoint equations for the adjoint variables (adjoint module), and obtaining the gradients (gradient module).

The adjoint method is formulated for the flow solver TLSN3D because it employs differencing techniques for which corresponding adjoint modules are easier to generate than for so-called upwind codes such CFL3D.

Alternate Gradient Capability: Adjoint TLNS3D

- Advantages
  - CPU time(relatively) independent of number of DV's
  - Accuracy determined by grid-quality
- Formulation

Analysis module: $R = 0$ (TLNS3D-Euler)

Adjoint module: $$\left(\frac{\partial R}{\partial U}\right)^T \lambda + \frac{\partial F}{\partial U} = 0$$

Gradient module: $$\frac{dF}{db} = \left[\left(\frac{\partial R}{\partial X}\right)^T \lambda + \frac{\partial F}{\partial X}\right]\frac{\partial X}{\partial b}$$

$R\,(U,X)$: Euler equations; $F\,(U,X)$: Cost function;

$\lambda\,(U,X)$: Adjoint variables; $U\,(X)$: Flow variables;

$X\,(b)$: Grid; b : Design variables

Summary

Several major additions were made to the MDO3D design code. The grid generation capability was improved to support the TCA optimization where there is no distinct fuselage near the symmetry plane. Also, the design space was increased by adding design variables (NACA 5-series airfoil definition) and modifying the application of other design variables (wing sinusoidal functions and fuselage cross-sectional area functions). Numerous additional constraints were added to support the TCA optimization.

Much progress has been made in expanding the geometry capabilities in MDC's nonlinear design tools. Empennage effects can now be modeled. An automated flap modeling capability permits optimization of transonic flap settings. Several utilities for (re-)generating surface and volume grids for W/B/N/D configurations make a nonlinear optimization of such integrated configurations imminent.

Work is continuing to demonstrate alternate gradient evaluation techniques such as CFL3D.ADII and an adjoint formulation for TLSN3D.

Summary

- Improved design capability
- Improved geometry capability
  - Empennage effects
  - W/B/F modeling
  - Integrated W/B/N/D modeling (in progress)
- Alternate gradient capability
  - ADIFOR for CFL3D (in progress)
  - Adjoint TLNS3D (in progress)

Future Work

The implementation of the geometric modeling capability for use with an integrated optimization of W/B/N/D HSCT configurations needs to be completed, tested, and updated as needed.

The work on the alternate gradient capabilities has to be driven to a point where decisions can be made which way to proceed.

The transonic flap optimization capability is crucial in meeting an upcoming milestone in the HSR Phase II program. It will also form a cornerstone in future multipoint design exercises.

MDC's design capabilities grow faster than the available computer resources. To scale back the computing requirements while still increasing the design capabilities, MDO3D will be converted to a modular (script-driven) environment.

Future Work

MCDONNELL DOUGLAS HSCT

- W/B/N/D modeling
- Alternate gradient capability
  - ADIFOR for CFL3D: Improve efficiency
  - Adjoint TLNS3D: Complete development
- Transonic flap optimization
- Multi-point optimization
- Convert MDO3D to modular environment

TCA Nacelle Installation Assessment and Design Studies

Alan Arslan
P. Sundaram
Chih-Fang Shieh

HSR Aerodynamic Performance Workshop
NASA Langley, February 25-28, 1997

Abstract

This paper presents the computational investigation of the PAI related study in which the primary objective is to assess and then reduce the installation drag of the nacelles for the TCA configuration at the supersonic cruise condition of $M_\infty = 2.4$, $C_L=0.1$

As a first step in reducing the nacelle installation drag, it is necessary to assess the baseline installation. This assessment refers to interference and installation drag assessments, as well as flowfield assessment, at both flight ($Re_c = 212$ million) and wind-tunnel ($Re_c = 6.36$ million) conditions. An analysis of the inlet flowfield quality is necessary to assess alignment.

After satisfying inlet constraints by aligning the inlets with the local flowfield, the drag is reassessed. An assessment of the boundary layer height at the diverter leading edge suggests a height reduction for the inboard diverter. Finally, diverter and nacelle shape modifications were attempted with limited success.

Outline

The primary objective of this effort is to assess and then reduce the installation drag of the nacelles for the TCA configuration at the supersonic cruise condition of $M_{\infty}= 2.4$, $C_L=0.1$.

Before undertaking nacelle/diverter shaping studies, it is necessary to assess the installation drag of the TCA baseline configuration at cruise conditions. Therefore, it is necessary to assess the baseline performance at cruise for the wing/body, isolated nacelle, and wing/body/nacelle/diverter configurations. Once the installation assessment is complete, nacelle inlet alignment is conducted to improve the inlet flow quality. The study also showed that the inboard diverter leading-edge height can be reduced considerably. Nacelle cambering in both planform and sideview are tried to reduce the installation drag of the TCA W/B/N/D configuration and a diverter/nacelle shaping methodology is presented.

Outline

- **Objectives:**
  - —Assess the nacelle/diverter installation on the TCA Baseline configuration
  - —Modify nacelles/diverters to improve aero. performance at the cruise condition
- **Baseline assessment**
  - – Nacelle Installation drag assessment at cruise ($M_\infty = 2.4$, $C_L = 0.1$)
    - W/B
    - W/B/N/D
    - Isolated Nacelles
  - – Inlet flow quality determination
- **Nacelle alignment and design studies**
  - – Baseline nacelle/diverter alignment for improved inlet flow quality
  - – Boundary layer height assessment
  - – Nacelle/diverter camber modifications

Drag Polars for the TCA W/B Configuration

CFL3D Euler and N-S (Re_c= 6.36 million) solutions for the TCA W/B and W/B/N/D configurations were shown in another paper. In this paper, to avoid redundancy the emphasis is more on the full-scale Reynolds number solutions.

A standard C-O topology Euler W/B grid (93x241x41) was clustered so as to maintain y^+ of 1.5 at the wing trailing-edge for a Reynolds number of 212 million to obtain the Navier-Stokes grid. The Euler cells in the body normal direction that were contained within twice the boundary layer height at the trailing edge were packed with an extra 24 cells.

At C_L = 0.1, the CFL3D W/B N-S solution at the flight Reynolds number of Re_c = 212 million shows about one count less drag than the Euler pressure drag combined with the flat-plate skin-friction estimate. However, at the C_{Dmin} point, the drag difference is around 2 to 3 counts.

Drag Polars for the TCA Wing/Body Configuration
(CFL3D, M_∞=2.4, Re_c=212 x10^6)

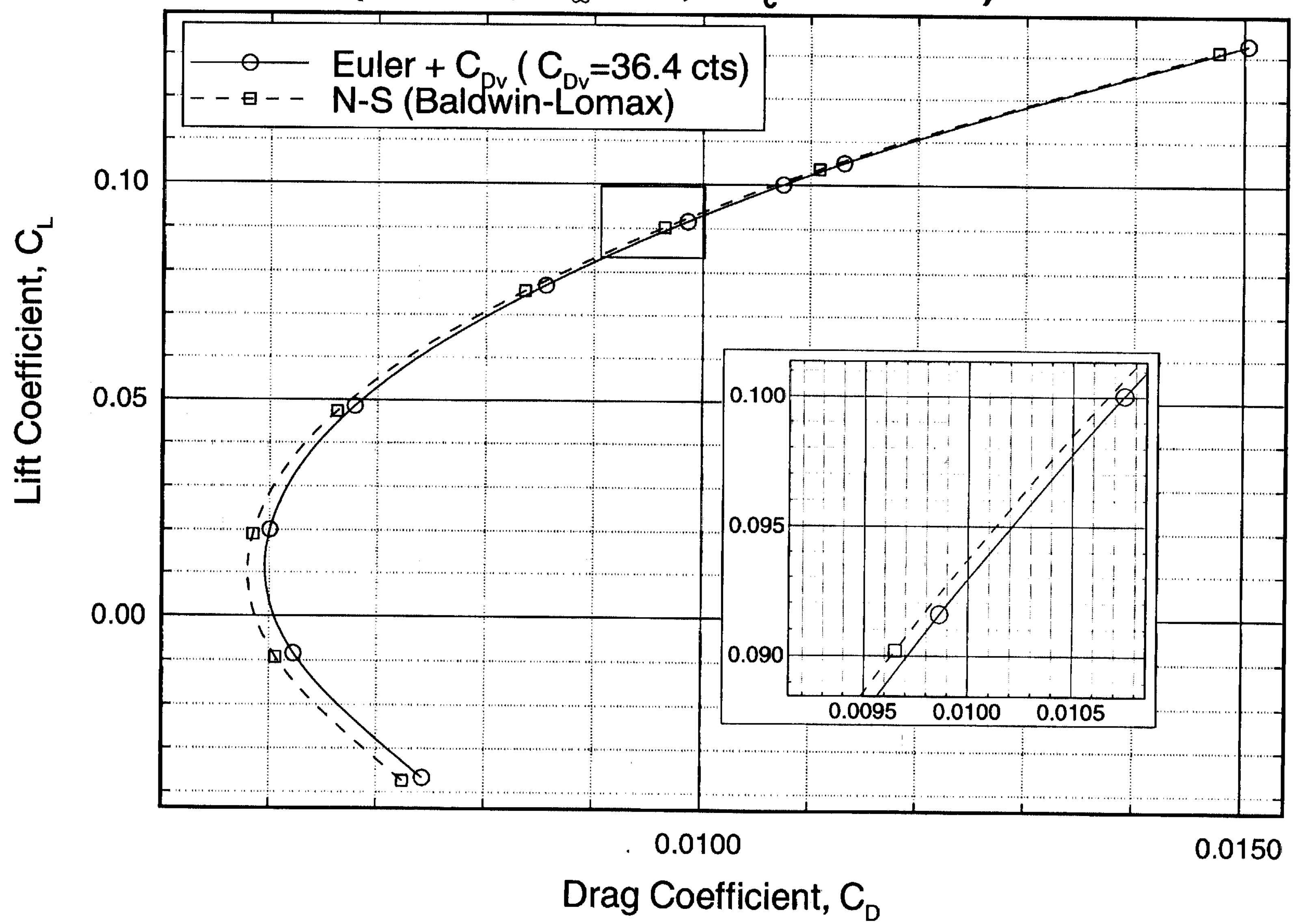

Wing/Body/Nacelle/Diverter Navier-Stokes Grid Topology for the TCA Baseline Configuration (Wing/Body Blocks)

Here, the same approach as the wing/body was difficult to adopt for the Navier-Stokes clustering since 8 Euler cells were dictated by the diverter height. On the other hand, and for consistency with the W/B and isolated nacelle clustering, three constantly spaced cells at solid surfaces with a y^+ of 1.5 at the wing trailing-edge were chosen for N-S clustering.

Earlier W/B/N/D grid blockings showed convergence problems for three basic reasons. Block mismatch of the nacelle outer blocks with the W/B blocks in the normal direction, block mismatch of the nacelle outer blocks with the core blocks in the viscous direction, and block mismatches in high gradient areas such as wakes. Point-matching in areas of large gradients proved to be the solution to most problems. Moving block boundaries away from regions of large gradients was an even better precautionary measure. The resulting W/B/N/D patched grid comprised of 19 blocks with about 6 million points.

Only the grids relevant to the W/B portion of the configuration are shown here. The wing/body surface, shown in blue, is patched with the diverter top surface in green. This green surface contains the wing trailing edge and is point-matched with all blocks relevant to the nacelles/diverters and point-mismatched with the fuselage/wake (red) surface coming from the original W/B grid.

Wing/Body/Nacelle/Diverter Navier–Stokes Topology for the Baseline TCA Configuration (19 Blocks, 6.01 Million Grid Points, Wing/Body Blocks)

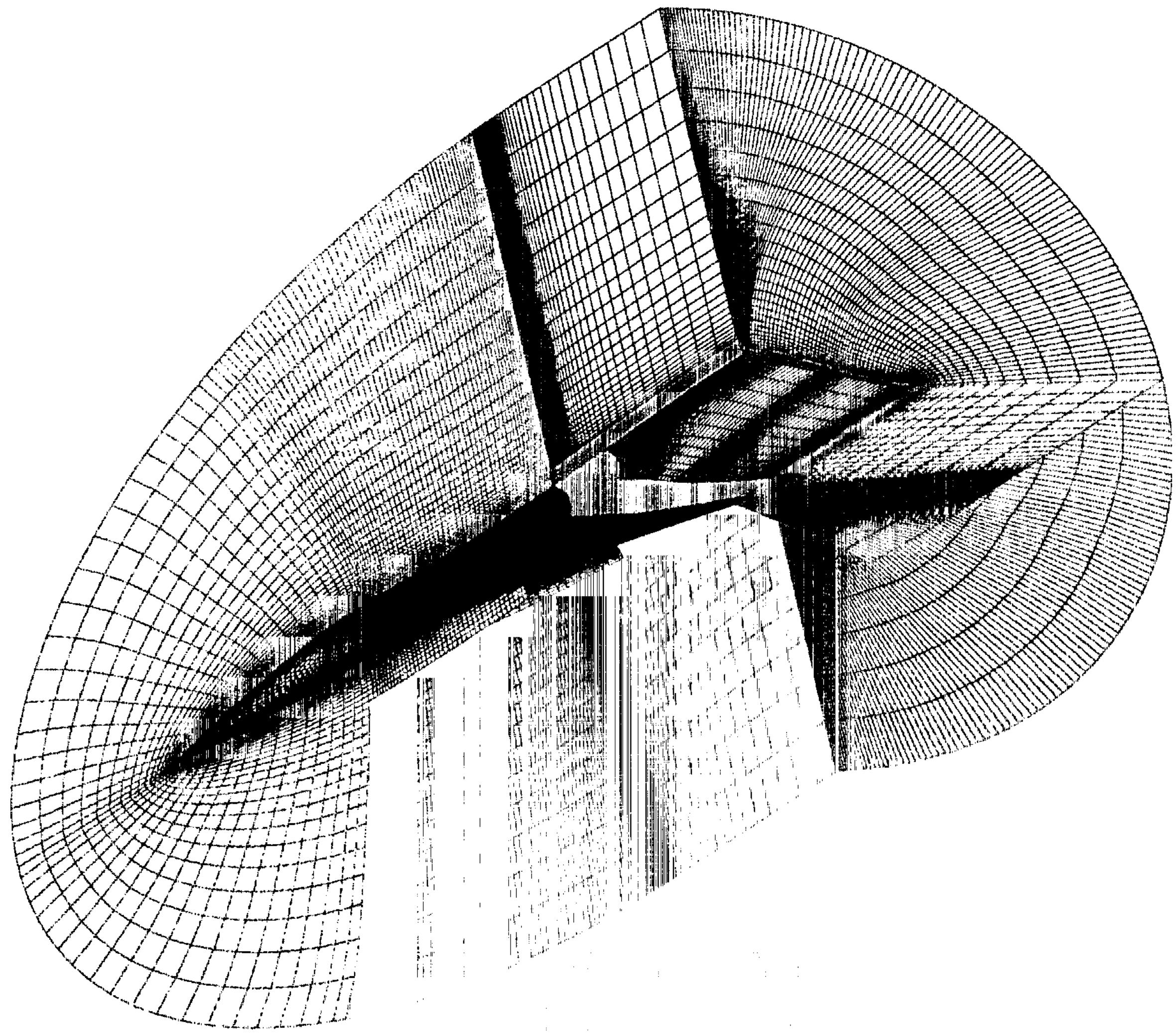

Wing/Body/Nacelle/Diverter Navier-Stokes Topology for the Baseline TCA Configuration (Nacelle_Back Blocks)

Axial cuts of the volume grid at the wing trailing-edge location are shown. The point-matching of the nacelle outer blocks with the core, and the preservation of spacing continuity required clustering about the nacelles' upper corner, where the diverters are located which results in the clustering in the field observed in the chart.

Wing/Body/Nacelle/Diverter Navier–Stokes Topology for the Baseline TCA Configuration (19 Blocks, 6.01 Million Grid Points, Nacelle_Back Blocks)

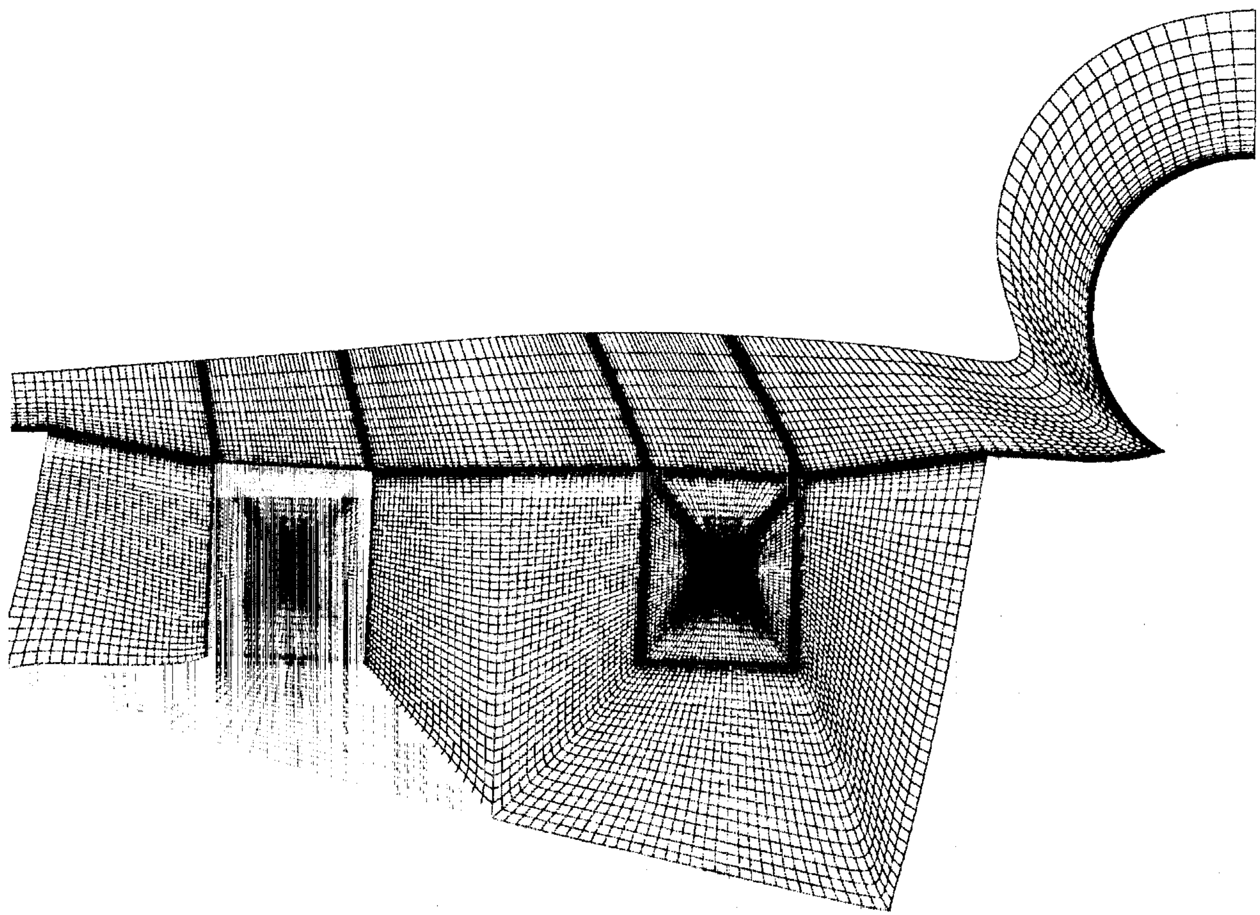

Drag Polars for the TCA Baseline W/B/N/D Configuration

As in the W/B case, the drag polars for Euler and N-S agree fairly well. Here, unlike the W/B solution, the N-S polar shows about 0.5 counts of increased drag at a C_L of 0.1. However, around the minimum drag point, the trends agree with those of the W/B.

Drag Polars for the Wing/Body/Nacelle/Diverter TCA Baseline Configuration (CFL3D, M_∞=2.4, Re_c=212 x10^6)

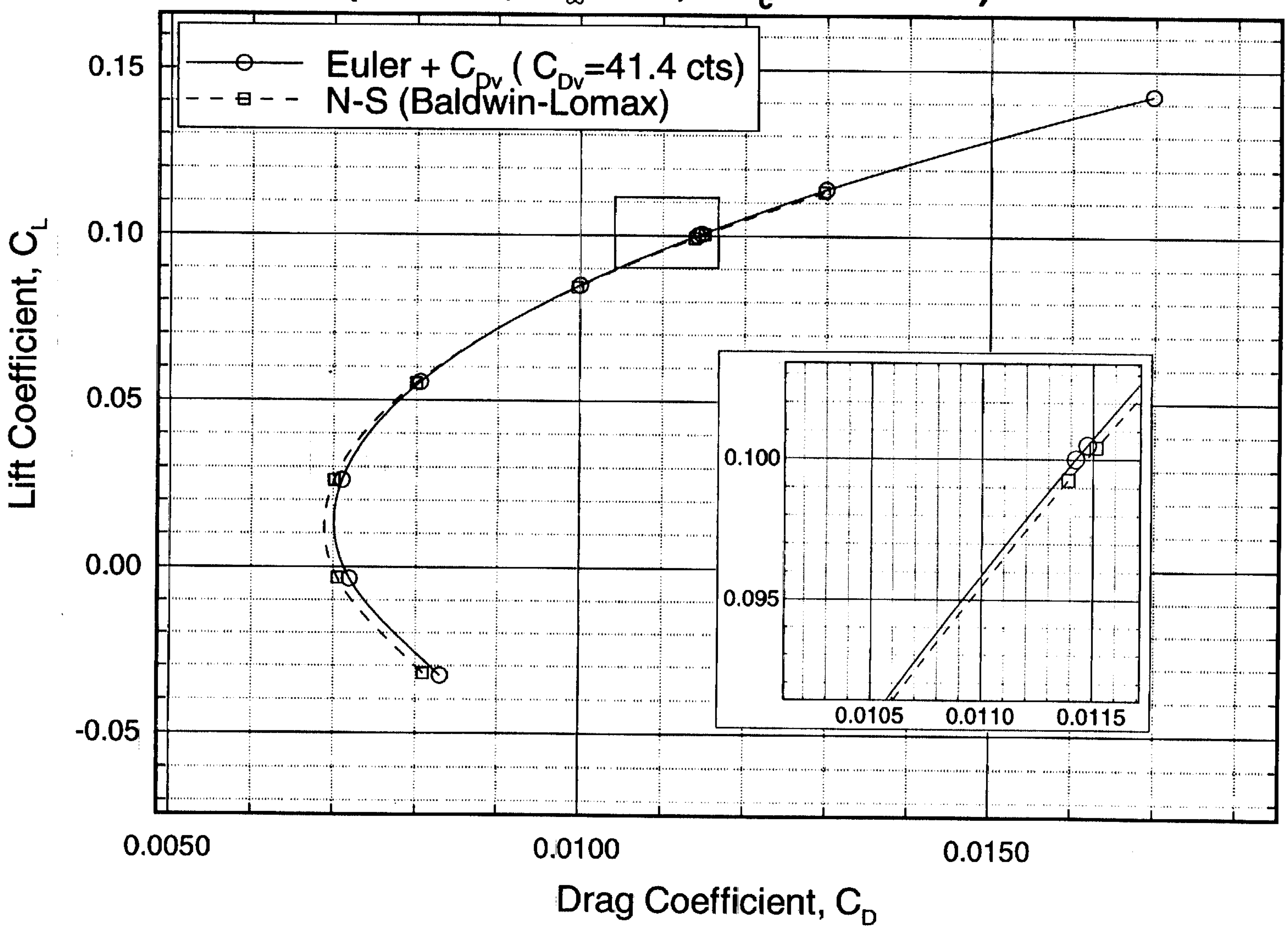

Drag Polars for the Baseline TCA W/B and W/B/N/D Configurations

The installation drag (at $C_L = 0.1$) is nearly 8 counts for the N-S analysis at full-scale Reynolds number. This increment is about one count higher than the one estimated by Euler with flat plate skin-friction estimates shown in a different paper.

Drag Polars for the Wing/Body/Nacelle/Diverter and Wing/Body Baseline TCA Configurations (CFL3D Navier-Stokes, M_∞=2.4, Re_c=212 x10^6, Baldwin-Lomax)

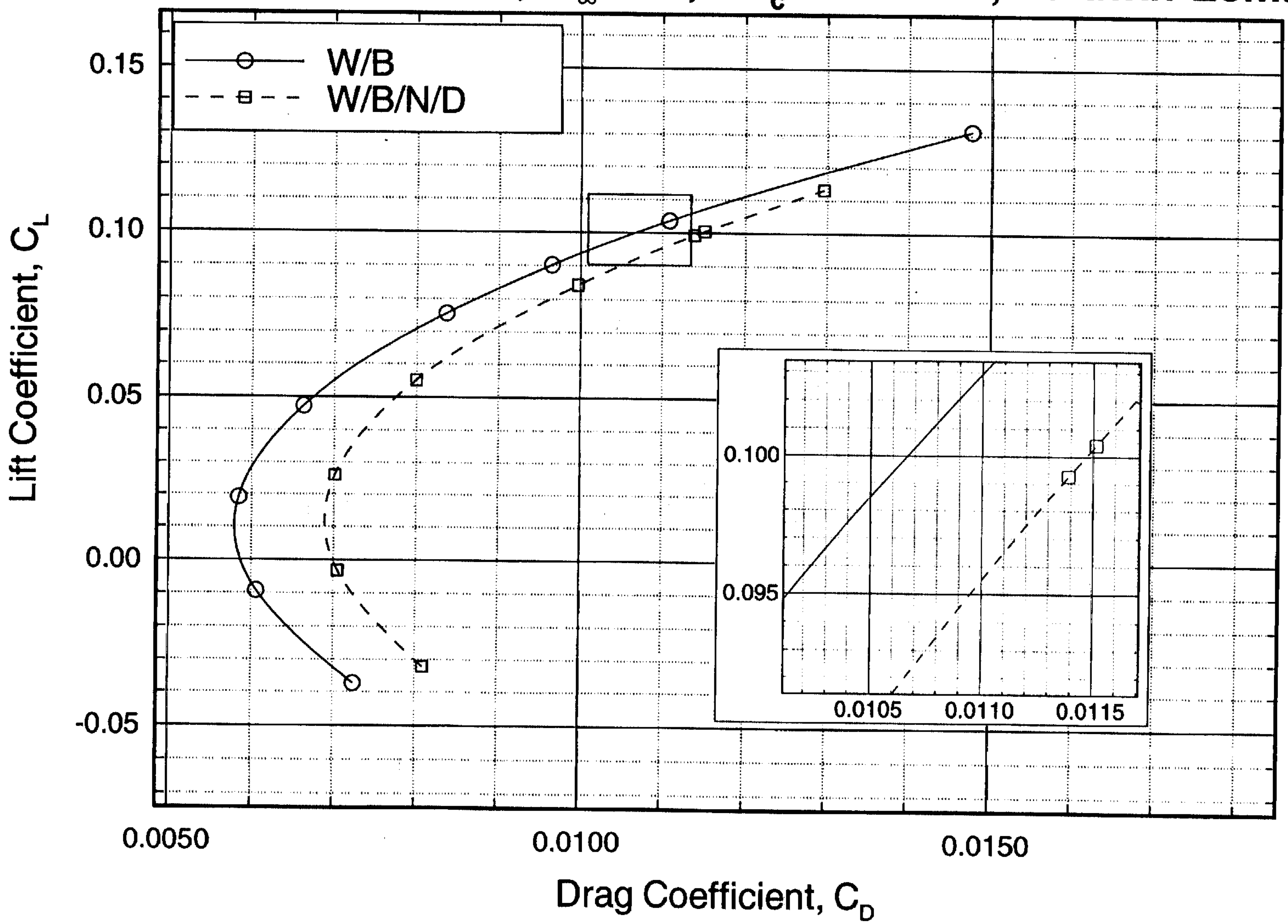

Pressure Distributions for the TCA Baseline W/B/N/D Configuration

Small differences are observed on the wing upper surface as well as regions away from strong interactions. Euler predicted nacelle/diverter shocks and expansions are stronger and further aft than those of the Navier-Stokes solutions.

It is worthy to note that the triple shock pattern observed from Euler would typically give more pressure drag than the double shock pattern observed from N-S. In other words, one would expect the N-S solution to yield a smaller installation pressure drag than the Euler solution.

Pressure Distributions for the Baseline TCA W/B/N/D Configuration

CFL3D, M_∞=2.4, α=3.518°, Re_c=212x10^6

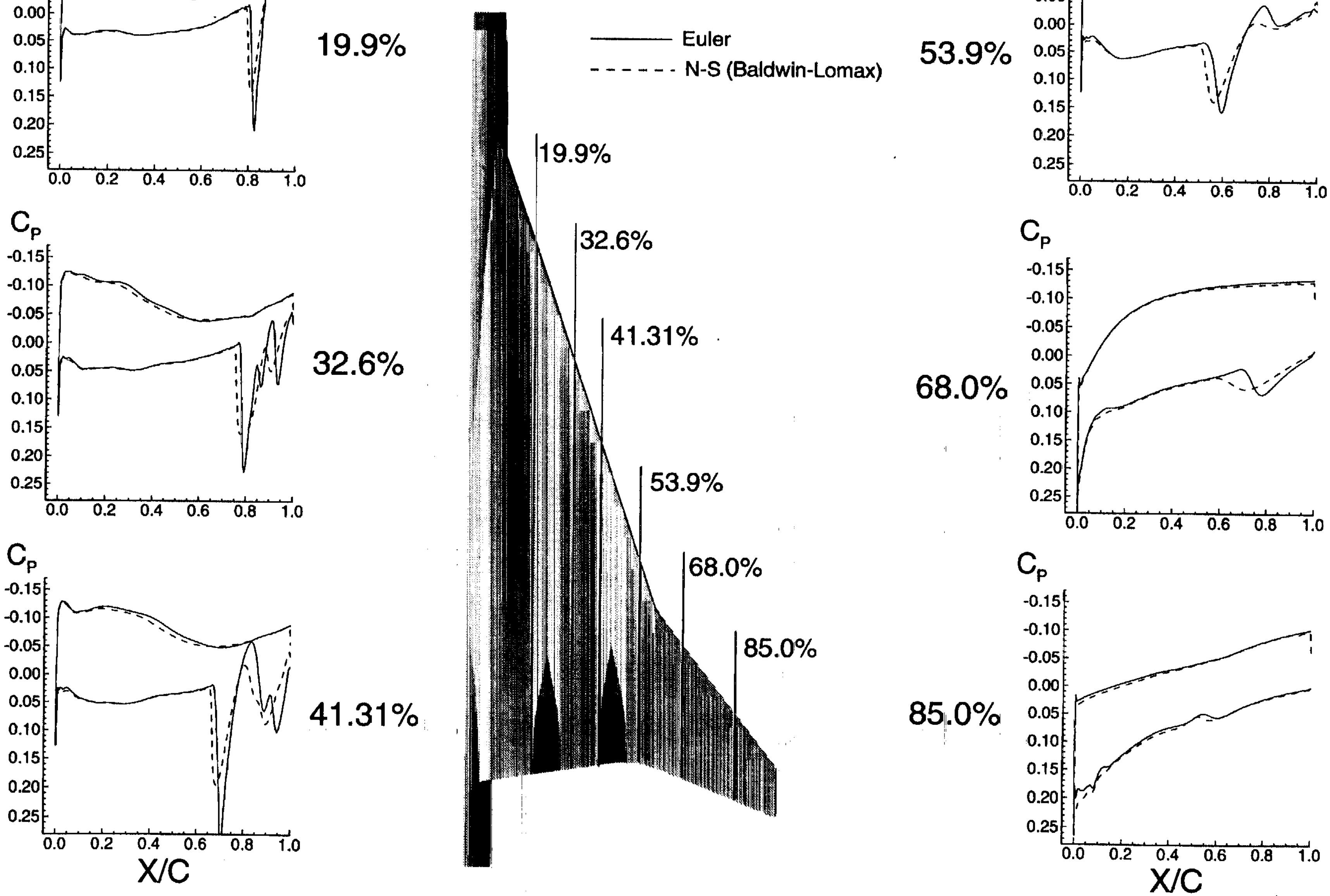

Lower Surface Pressure Contours for the Baseline W/B/N/D TCA Configuration

The N-S shocks are much blunter than those shown by the Euler solution. Consequently, the interactions inside the channel region would change.

In addition to a significant smearing of shocks observed from the N-S solution, the shocks are further weakened by the strong diverter or nacelle shoulder expansions.

Lower Surface Pressure Contours for the Baseline Wing/Body/Nacelle/Diverter TCA Configuration
CFL3D, $M_\infty = 2.4$, $\alpha = 3.518°$, $Re_c = 212 \times 10^6$

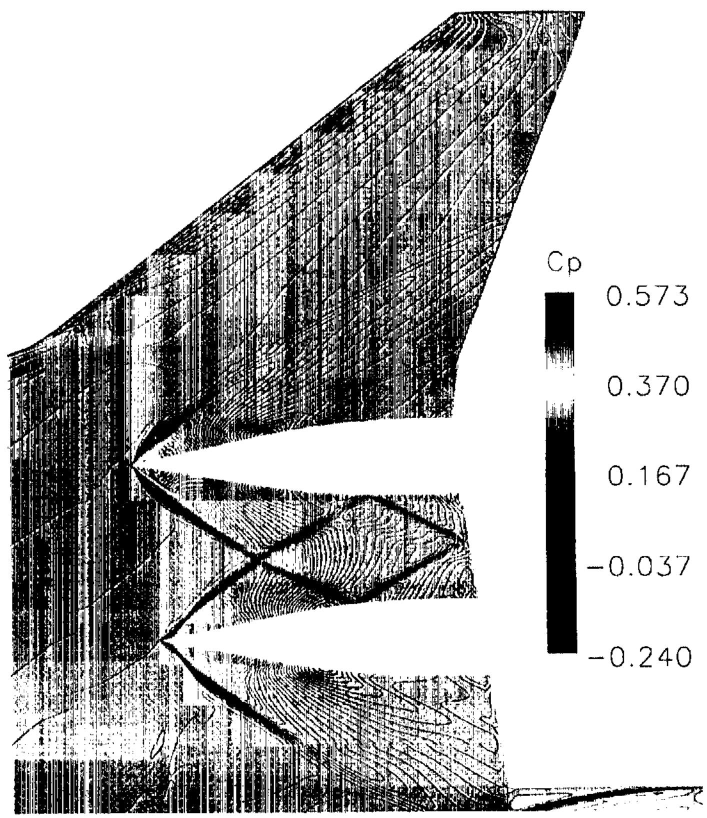

Euler

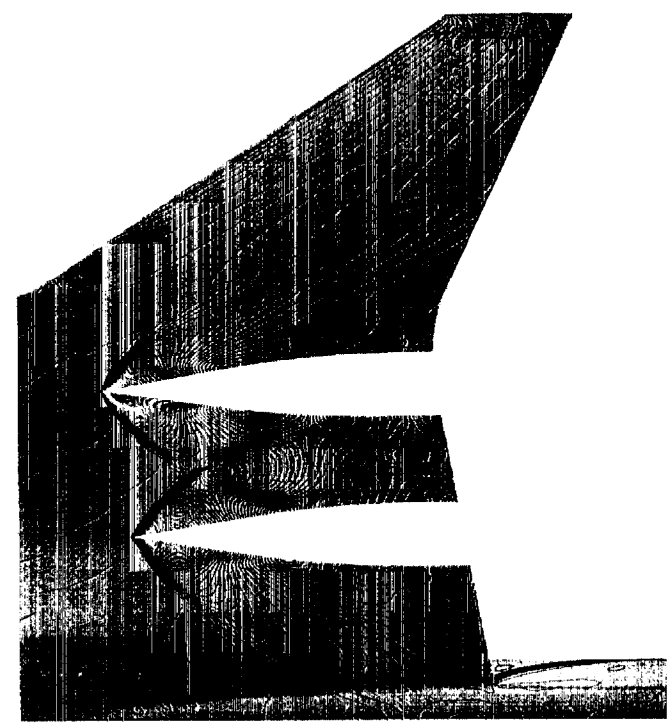

N–S (Baldwin–Lomax)

Mach Contours for the TCA Isolated Inboard Nacelle CFL3D N-S Solution

The inboard nacelle was selected for all isolated simulations. In order to obtain accurate pressure drag values for the interference/installation drag assessment, the nacelle had to be aligned with the flowfield No major gradients are observed around the inlet portion of the nacelles. The contours for the N-S solution at Re_c=212 show the same overall behavior as the Euler solutions, except for the presence of a boundary layer around solid surfaces. However, the side view does show the presence of a strong expansion associated with the presence of a base.

Mach Contours for the TCA Isolated Inboard Nacelle, Side and Top Views with Inlet Aligned with Freestream, CFL3D N-S Solution, $M_\infty = 2.4$, $Re_c = 212 \times 10^6$ (3 Block H-O Grid, Baldwin-Lomax)

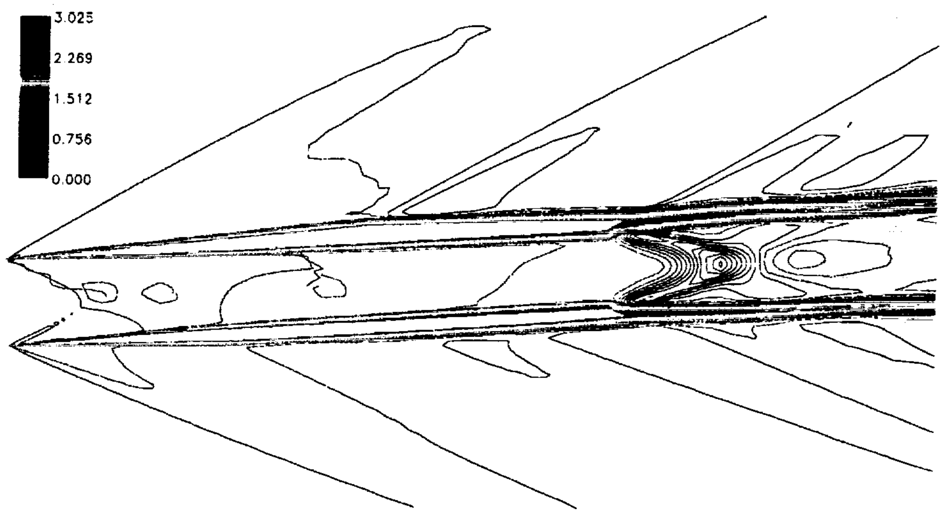

Side View

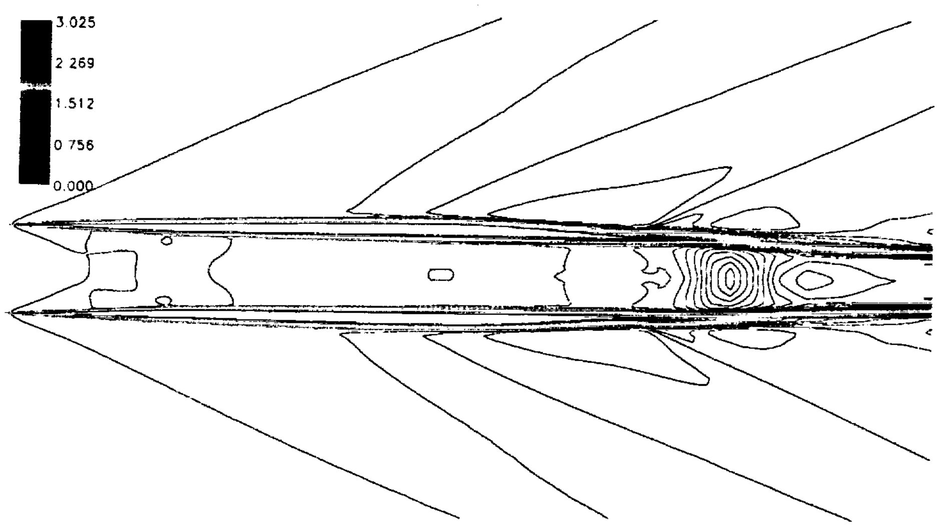

Top View

Pressure Drag Breakdown for the TCA Configuration
M = 2.4, C_L = 0.1

This chart shows the pressure drag for the various components, W/B, W/B/N/D, and the 4 isolated nacelles, of the TCA configuration. The bar chart includes side-by-side results obtained from CFL3D Euler, N-S at wind-tunnel Reynolds number, and N-S at full-scale Reynolds number.

The pressure drag obtained for the four isolated nacelles is identical for all analyses. However, for the W/B configuration, the N-S analysis at the wind-tunnel Reynolds number shows about 2.46 counts more pressure drag than the Euler analysis while the full-scale Reynolds number N-S simulation shows only a 1.34 count increase over the Euler case. Similarly, for the W/B/N/D configuration the wind-tunnel Reynolds number N-S analysis shows a 1.19 count increment over Euler while the full-scale Reynolds number N-S simulation shows about 0.44 counts. It can be seen from this chart that the Reynolds number effect on pressure drag varies with the TCA component that is considered.

Pressure Drag Breakdown for the TCA Configuration

$C_L = 0.1,\ M_\infty = 2.4$

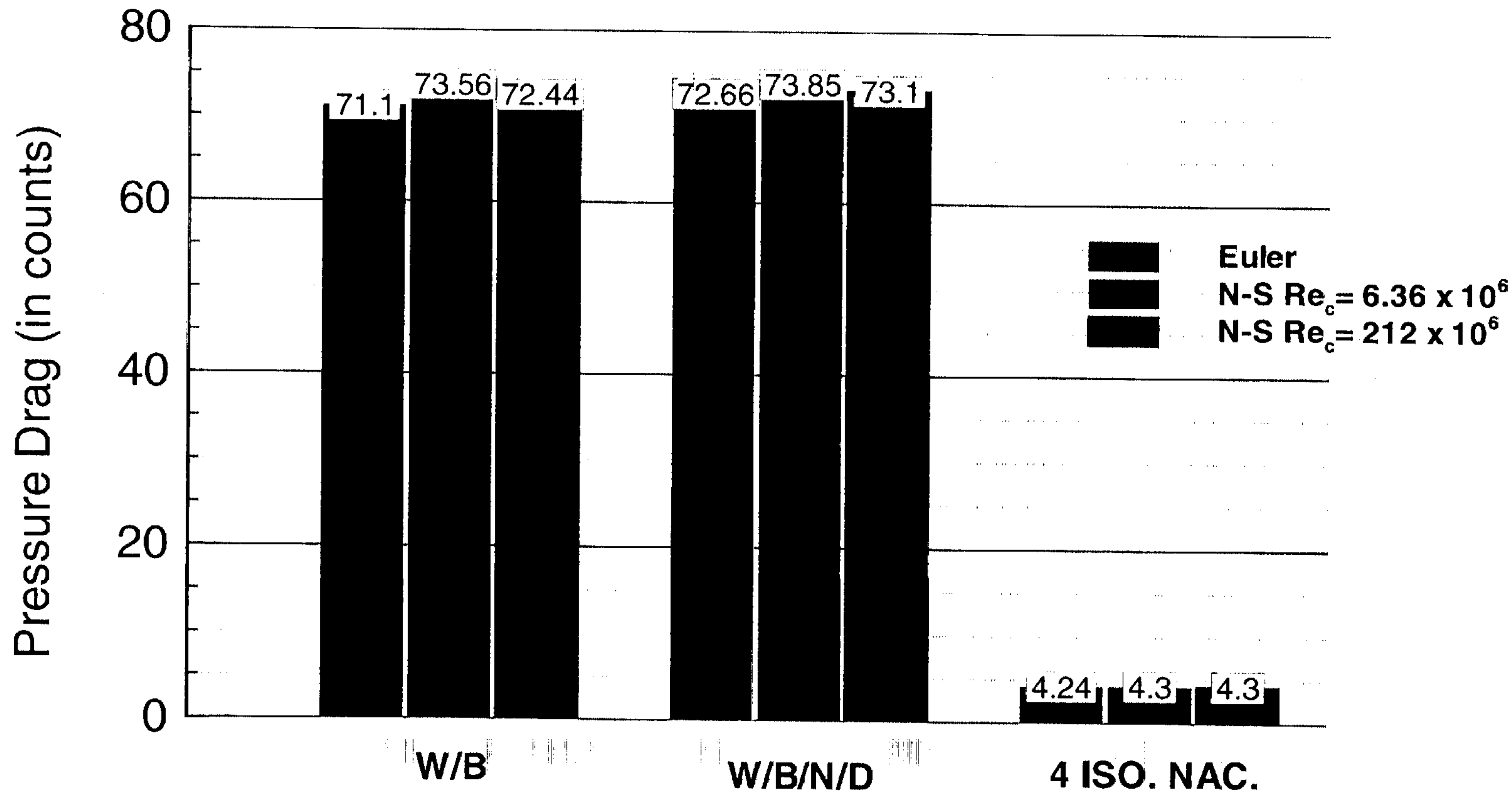

Skin-Friction Drag Breakdown for the TCA Configuration
$M = 2.4$, $C_L = 0.1$

This chart shows the viscous drag for the various components, W/B, W/B/N/D, and the 4 isolated nacelles, of the TCA configuration. The bar chart includes side-by-side results obtained from flat plate skin-friction estimates and N-S analyses viscous drag. The top chart corresponds to the wind-tunnel Reynolds number results while the bottom chart corresponds to those for the full-scale Reynolds number.

For the W/B configuration, the N-S viscous drag component is about 3.1 counts lower than the flat-plate estimates for Re_c= 6.36 million and 1.82 counts lower for Re_c= 212 million. For the W/B/N/D configuration, that difference is reduced to 1.76 counts for the wind-tunnel Reynolds number and 0.1 counts for the full-scale Reynolds number. For the four isolated nacelles, the agreement between N-S viscous drag and flat-plate skin-friction estimates is excellent. It can be seen from this chart that the difference between flat-plate skin-friction estimates and N-S viscous drag decreases with Reynolds number. Also, a higher discrepancy with flat-plate is observed for the W/B configurations.

Skin-Friction Drag Breakdown for the TCA Configuration

$C_L = 0.1,\ M_\infty = 2.4$

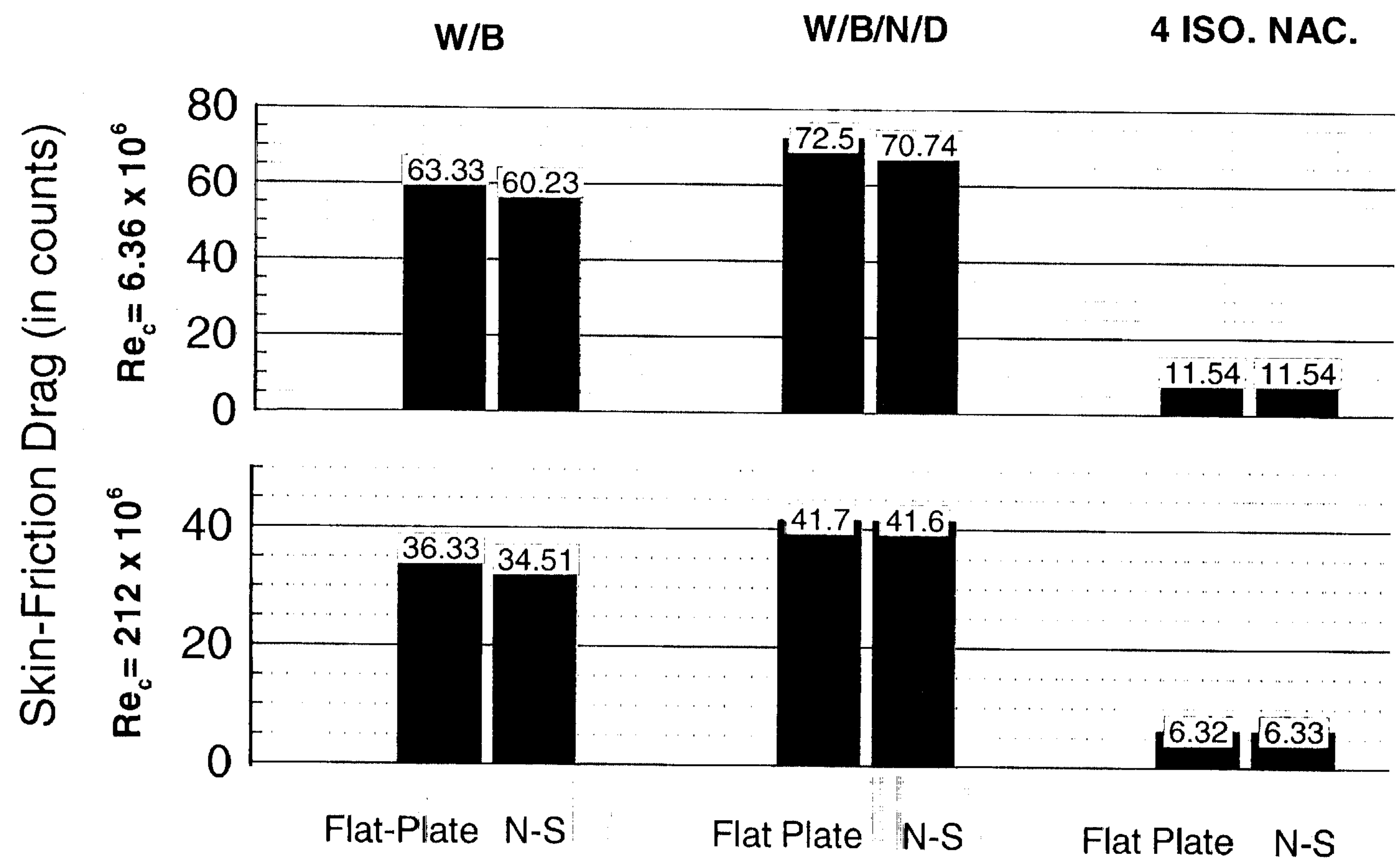

Nacelle Installation Drag for the TCA Configuration

This bar chart compares the installation pressure and total drag for the TCA W/B/N/D configuration at both the wind-tunnel as well as the flight Reynolds numbers.

The installation total drag of the N-S analyses agreeswithin one count for the full-scale Reynolds number and within 0.1 count for the wind-tunnel Reynolds number with Euler+flat plate estimates. The latter agreement is no longer valid when looking at the pressure installation drag which yields to the fact that viscous effects have a significant contribution on pressure installation drag.

Nacelle Installation Drag for the TCA Configuration

$C_L = 0.1, M_\infty = 2.4$

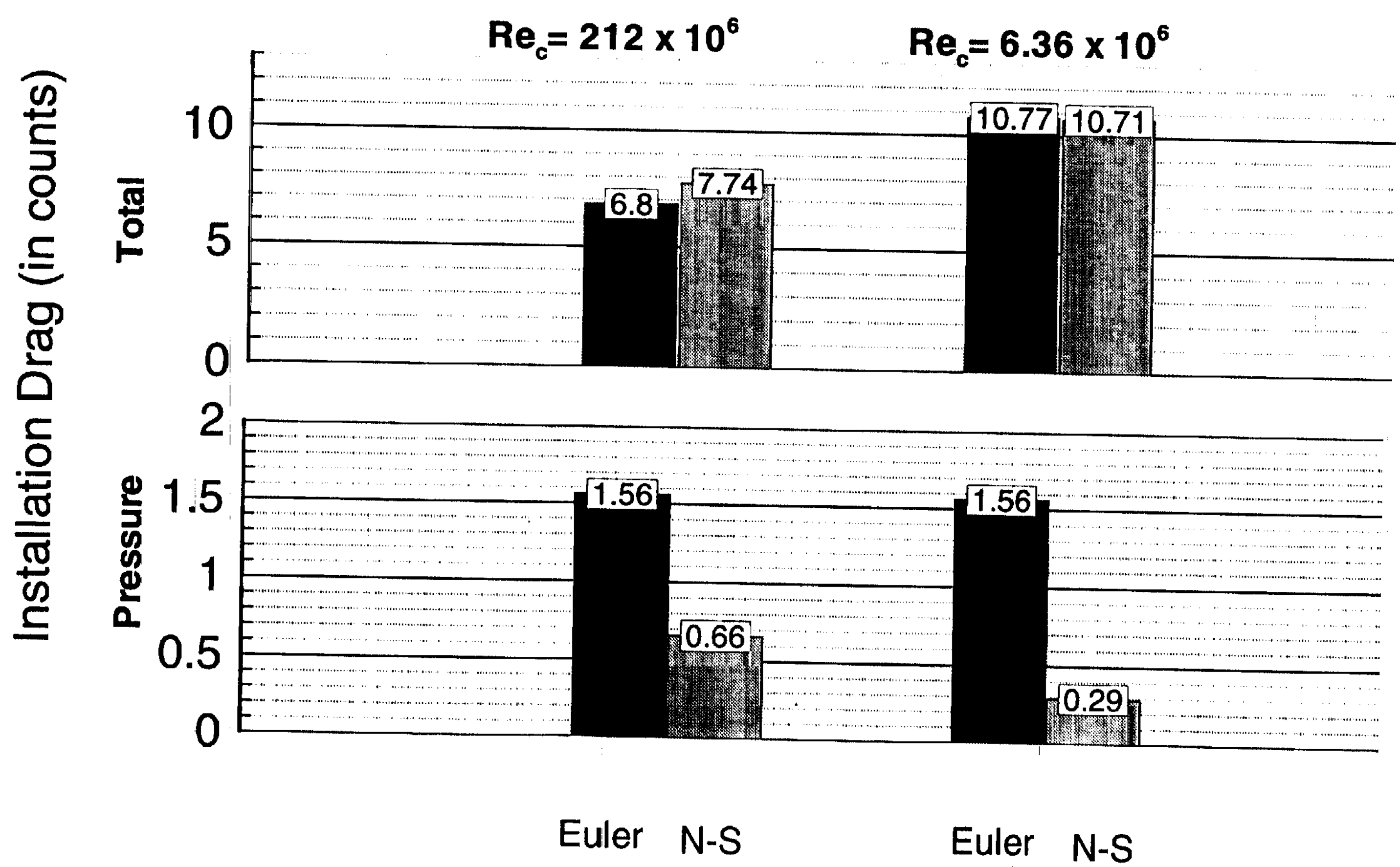

Nacelle Interference Drag for the TCA Configuration

The favorable interference due to the nacelles installed on the TCA W/B configuration is shown in this chart for both the wind-tunnel and flight Reynolds number cases.

Nacelle Interference Drag for the TCA Configuration

$C_L = 0.1$, $M_\infty = 2.4$

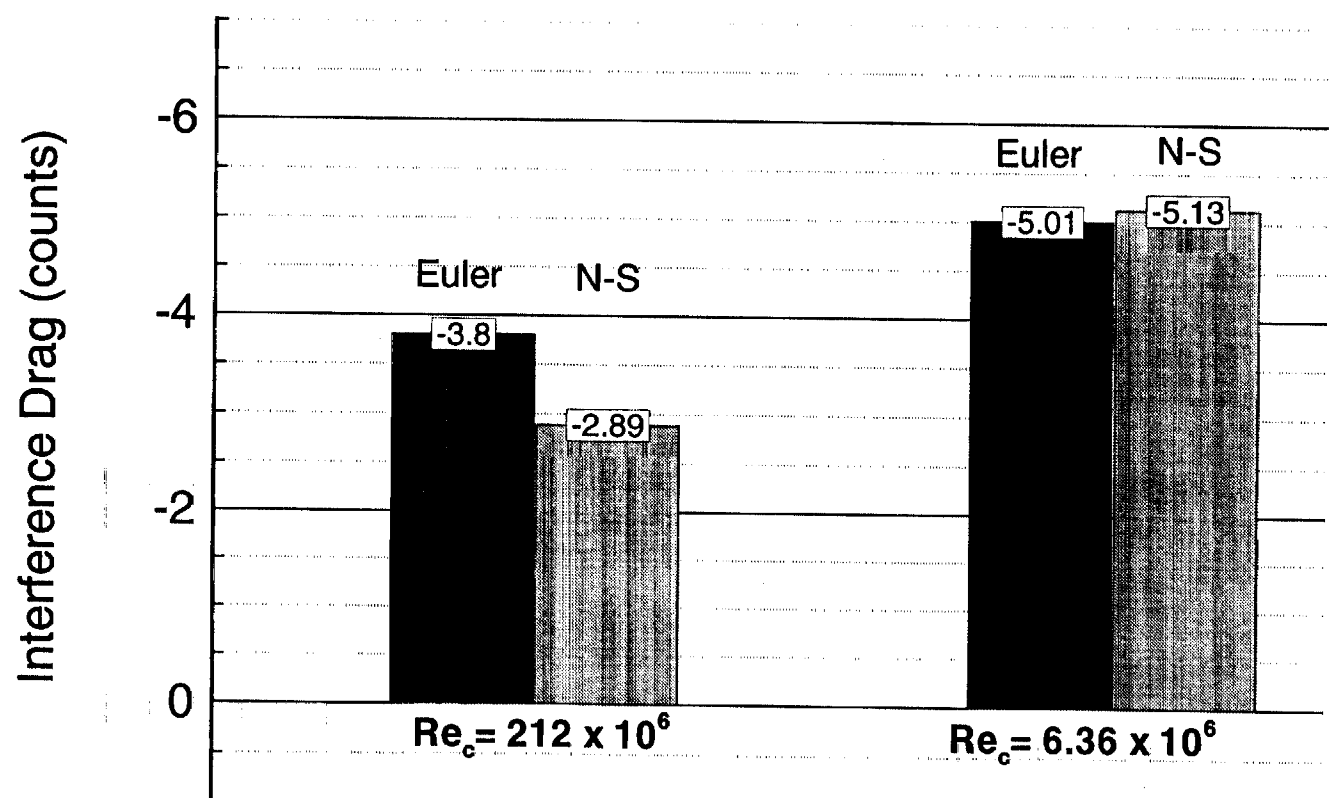

Comparisons of Nacelle Inlet Mach Number Distributions
TCA W/B/N/D Configuration

This chart shows the Mach number distributions at the inlet face of the TCA baseline W/B/N/D configuration. Once again, both the CFL3D Euler and Navier-Stokes results are used to obtain these contours. It can be seen that the inboard nacelle Euler contours show more non-uniformity which is improved for the Navier-Stokes results. Slight differences in the Mach number variations are also seen in the Euler and Navier-Stokes results for the outboard nacelle inlet face. This implies that the TCA baseline nacelles need alignment.

Comparisons of Nacelle Inlet Mach Number Distributions
TCA W/B/N/D Configuration
(CFL3D Analyses, M_∞=2.4, α=3.5°)

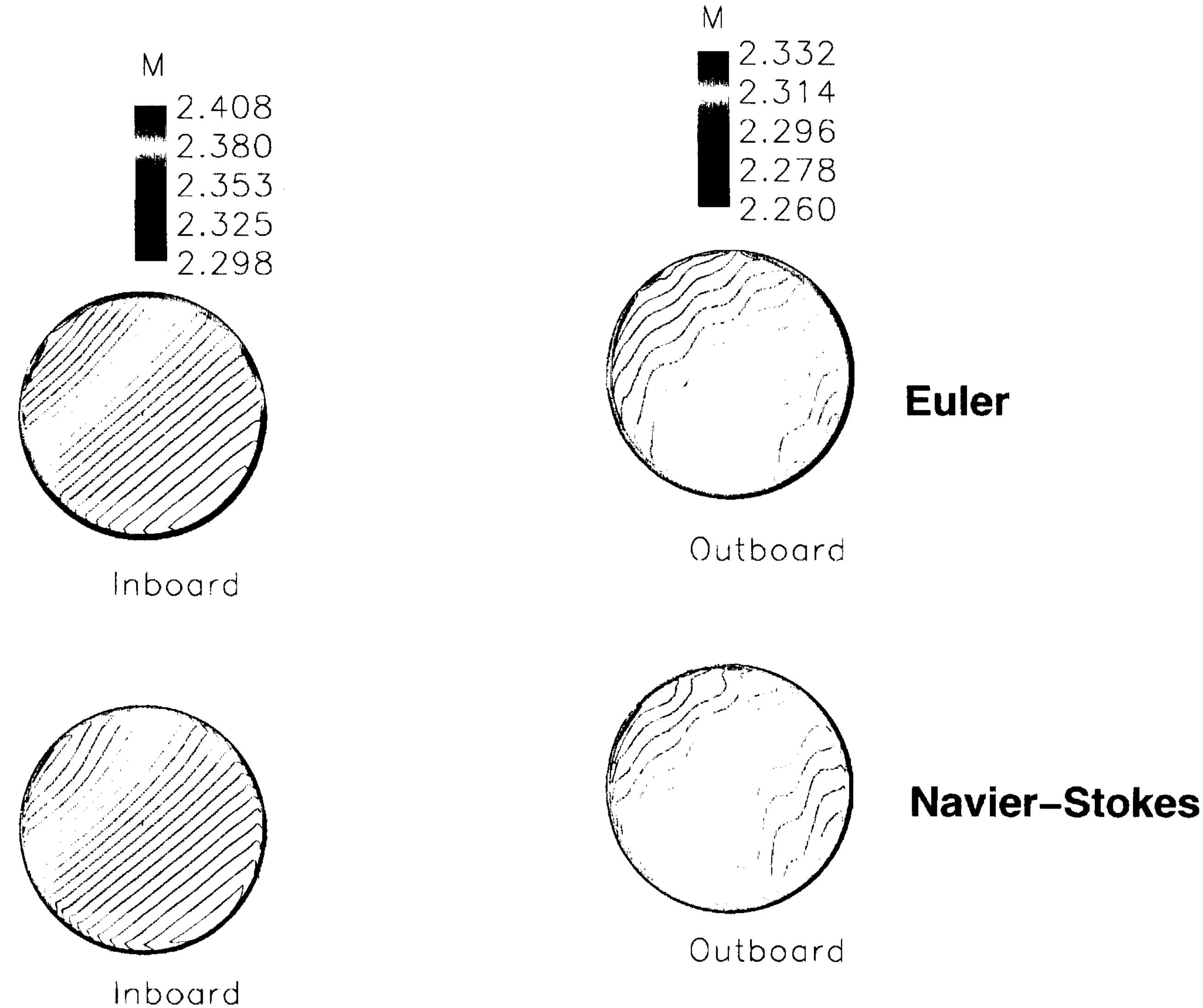

Inlet Flow Angle Variations (w.r.t. the angle at the inlet center) TCA W/B/N/D Configurations

The flow angle variations at the nacelle inlet face of the TCA baseline configuration are shown in the form of deviations from the inlet face centerline. The contours are obtained from the CFL3D Euler and Navier-Stokes results at the flight Reynolds number. Very little difference in the inlet flow variation contours can observed from these contour plots.

Inlet Flow Angle Variations (w.r.t. to the angle at the inlet center)
TCA W/B/N/D Configuration
(CFL3D Analyses, M_∞=2.4, α=3.5°)

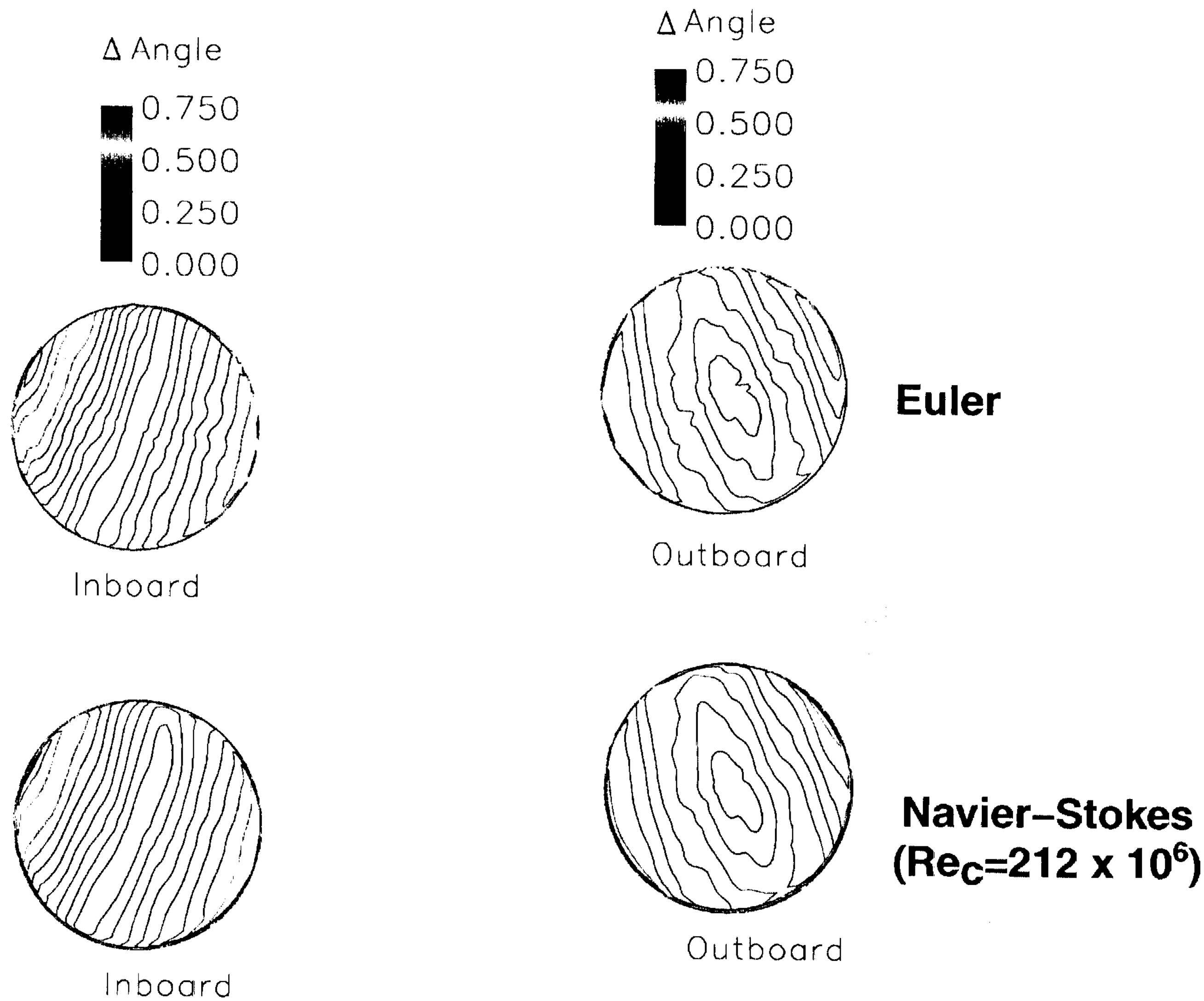

Nacelles and Diverters Alignment Assessment for the Baseline Wing/Body/Nacelle/Diverter TCA Configuration CFL3D Euler M = 2.4, $\alpha = 3.5^o$

The nacelle inlet flow angle and Mach number distributions qualitatively show that the TCA baseline nacelles need alignment in both pitch and yaw. To exactly quantify this and then correct it, the alignment assessment is undertaken.

To calculate the inlet flow angle variations at the inlet face, the geometric angularities as well as the flow angularities for the TCA baseline W/B/N/D configuration have been obtained from the CFL3D analyses. The inlet flow variations are calculated at the nacelle inlet face. Only misalignments of more than 0.3^o were considered.

This chart shows the outcome of the TCA alignment assessment investigation. Since the difference between the alignment calculated using the CFL3D Euler and Navier-Stokes results are not significant, as observed in earlier studies, only the Euler analysis is used. Since the Mach number and flow angularity distributions were done at the nacelles inlet faces, it was more convenient to perform all the analyses on the W/B/N/D configuration. The Table in this chart gives both the geometric as well as the flow angles computed for the inlet face as well as the diverter. The difference calculated from the local geometric and the local flow angle is the deviation from the alignment.

Nacelles and Diverters Alignment Assessment for the Baseline Wing/Body/Nacelle/Diverter TCA Configuration

CFL3D Euler, $M_\infty = 2.4$, $\alpha = 3.5°$

	Inb. Nac.		Outb. Nac.		Inb. Div.		Outb. Div.	
	Pitch Down	Toe In	Pitch Down	Toe In	Pitch Down	Toe In	Pitch Down	Toe In
Geom Ang.	2.19°	0.44°	0.8°	1.44°	-	0.46°	-	1.47°
Flow Ang.	0.91°	0.53°	0.88°	2.82°	-	0.14°	-	3.45°
Rotation for Alignment	-1.28°	-	-	1.38°	-	-	-	1.98°

Alignment of Nacelles/Diverters

The chart below shows the approach and procedure for the alignment of nacelles/diverters. Note that geometry shaping is necessary for alignment in order to maintain a smooth merging of nacelles and diverters at the wing trailing edge.

Alignment of Nacelles/Diverters

- Baseline TCA nacelles/divertters were misaligned in pitch and yaw
- Reshape nacelles and diverters to align the inlet face with the local flowfield
  - Preserve the diverter height, nozzle base height, and nozzle thrust angle
  - Ensure a smooth merging of nacelles and diverters at the wing trailing edge

Lower Surface Pressure Contours for the TCA W/B/N/D Configuration Before and After Nacelle/Diverter Alignment

As mentioned in a previous slide, the outboard diverter leading-edge shock is more symmetric for the aligned case.

When looking at the inboard panel of the outboard diverter, a secondary shock/expansion is observed right before the shock reflection. After alignment, this secondary shock becomes more significant and points to a premature expansion (in other words, an expansion that takes place too far forward and ends with a stronger shock).

Lower Surface Pressure Contours for the Wing/Body/Nacelle/Diverter TCA Configuration Before and After Nacelle/Diverter Alignment CFL3D Euler , $M_{\infty} = 2.4, \alpha = 3.5°$

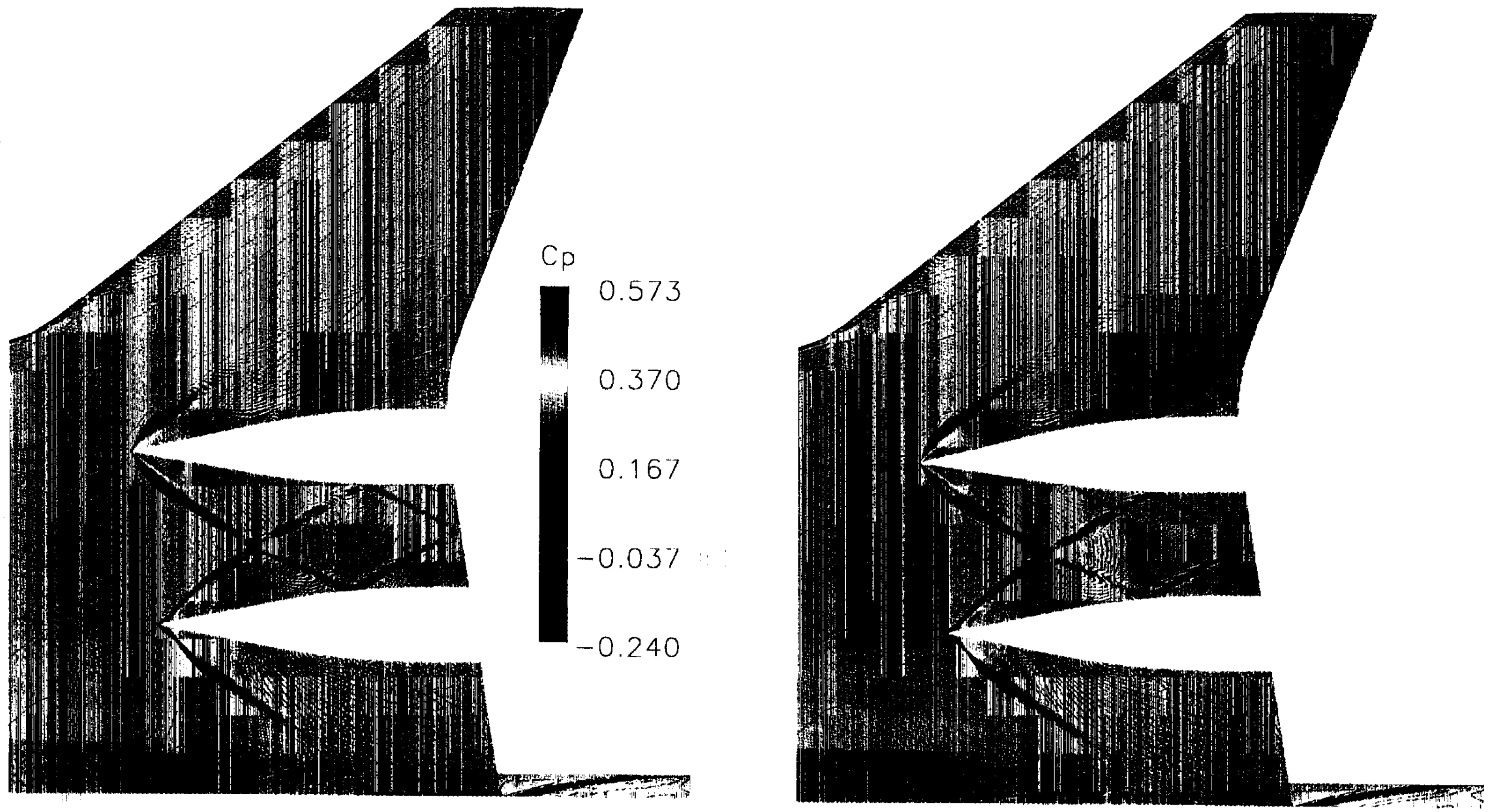

Baseline

Aligned

Comparison of Boundary Layer Profiles from W/B and W/B/N/D (Inboard Nacelle)

In one of our attempts to align the inlet center with the flowfield for the inboard nacelle, a pitch-up rotation with respect to a station 150 inches dowstream of the inlet location resulted in a diverter leading-edge height reduction and an associated 0.5 count drag benefit. Consequently, it was decided to take a closer look at the boundary layer profiles and their corresponding heights.

The profile obtained from the W/B N-S solution at the inboard leading-edge location is very similar to that of the W/B/N/D solution in spite of differences in grid clustering strategies. Even though different portions of the boundary layer see different relative grid clustering, the overall observed boundary- layer height is the same.

Comparison of Boundary Layer Profiles from W/B and W/B/N/D CFL3D N–S solutions, Baldwin–Lomax Turbulence Model
$\alpha = 3.518°$, $M_\infty = 2.4$, $Re_c = 212 \times 10^6$

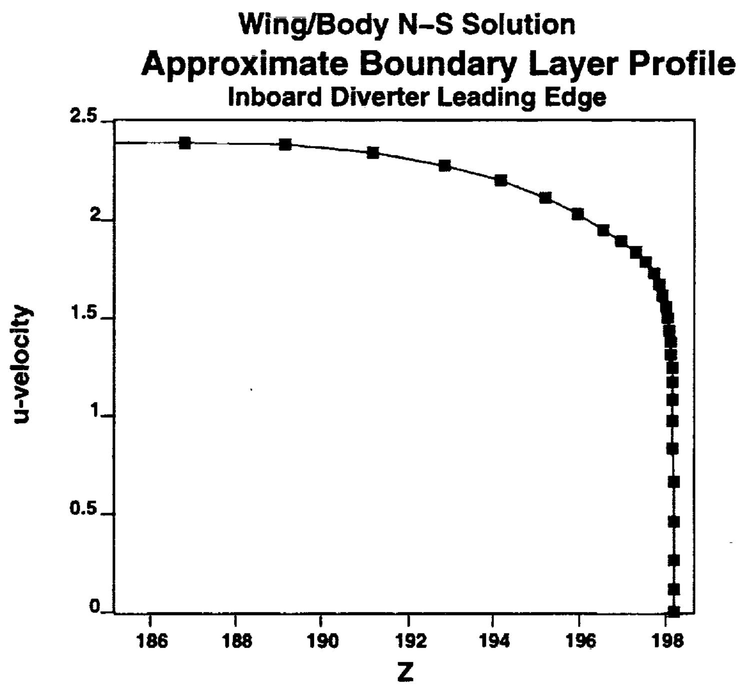

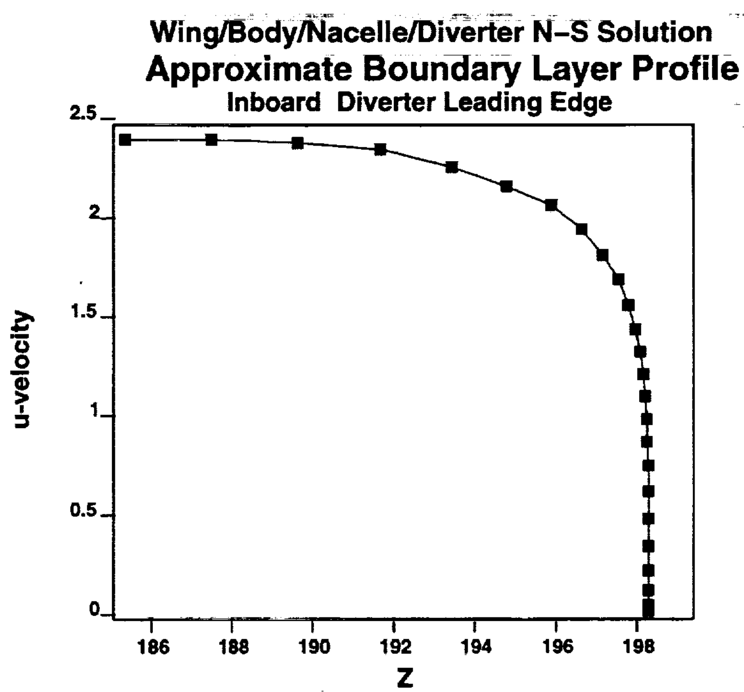

Estimated Boundary Layer Heights

The boundary layer heights estimated from both W/B and W/B/N/D solutions agree with each other and with heights obtained from BL3D, a 3-D boundary layer code. The W/B N-S solutions using the Baldwin-Barth turbulence model also gives the same boundary layer heights.

The table below shows a comparison of boundary layer heights at the diverter leading-edge locations. The baseline TCA geometric diverter leading-edge heights agree quite well with the height criterion. However, N-S calculations show a smaller boundary layer height and the difference between the baseline diverter height and the N-S boundary layer height is almost three inches for the inboard diverter.

Euler analyses of the aligned configuration with reduced inboard diverter height indicate a drag benefit of 0.3 counts at a given lift.

Estimated Boundary Layer Heights at Diverter Leading-Edge Locations on the TCA Baseline Configuration

CFL3D Navier-Stokes, $M_\infty = 2.4$, $\alpha = 3.5^\circ$, $Re_c = 212 \times 10^6$

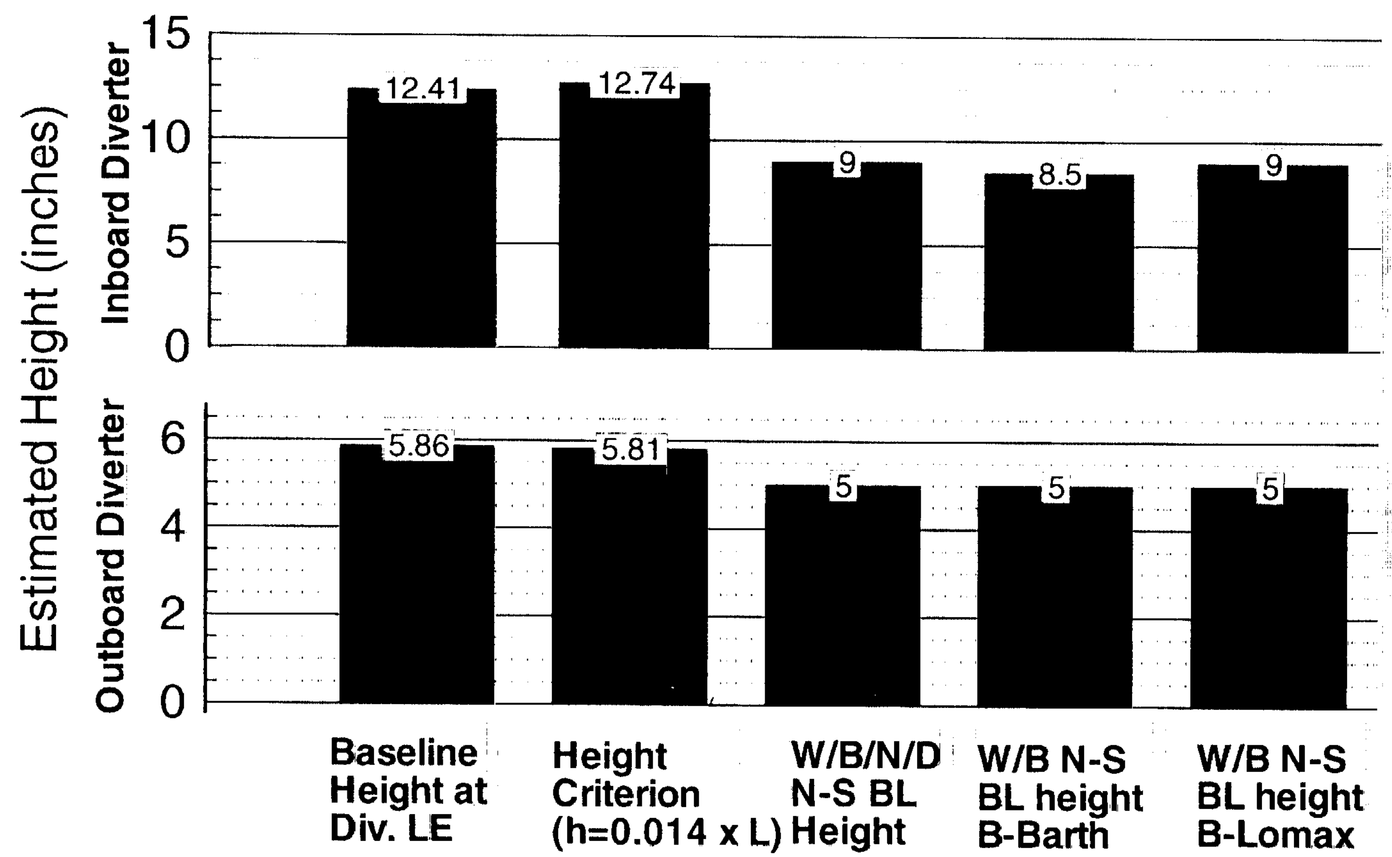

Nacelle/Diverter Modification Study

Next, we consider the nacelle/diverter modifications for both alignment and aerodynamic performance improvement of the installation. The charts below show the various results of the nacelle alignment and other shape modification study that were performed. All the modifications were done manually, although the principles and procedures applied can be extended to nonlinear optimization. Given that the nacelles and diverters merge at the wing trailing edge, and since cambering the nacelle centerlines will make the intersection of the merged nacelles/diverters difficult, the procedure to change camber had to use modifications to the external surface of the relevant geometries.

Diverters were modified by rotation of a portion of the geometry with respect to its leading-edge and cubic fairing of the remaining portion. On the other hand, nacelles were modified by applying design shape functions, similar to the ones used in wing optimization, to the nacelle surface grids.

Nacelle/Diverter Modification Study

- Diverter LE shape and camber modifications

  Div1 Case1: 1 deg. toe-out of inboard diverter with smooth blending at 30″ from LE.

  Div1 Case2: Same as above with blending at 150″ from LE.

- Nacelle camber modification (both planform and side view cambers) to lower the installation drag

  Nac1 Case1: Inboard bump applied on the inboard nacelle at wing TE location.

  Nac1 Case2: Same as above with the resulting maximum thickness moved forward.

Diverter Cambering Procedure for the TCA
Div1 Case1

This figure shows a planform view of the diverter/wing intersection. The inboard diverter (called Div1) was chosen to be modified. The square drawn on the upper portion of the figure indicates the section where the diverter modification is to be done.

The first zoom box indicates a one degree rigid body rotation of the selected section. The last box indicates that a cubic fairing, from the diverter leading edge to the 30 location, is done after the toe-out rotation of the diverter.

Diverter Cambering Procedure for the TCA
Div1 Case1: -1 deg. Toe-In Case, Modification
30" Downstream from the Diverter Leading-Edge

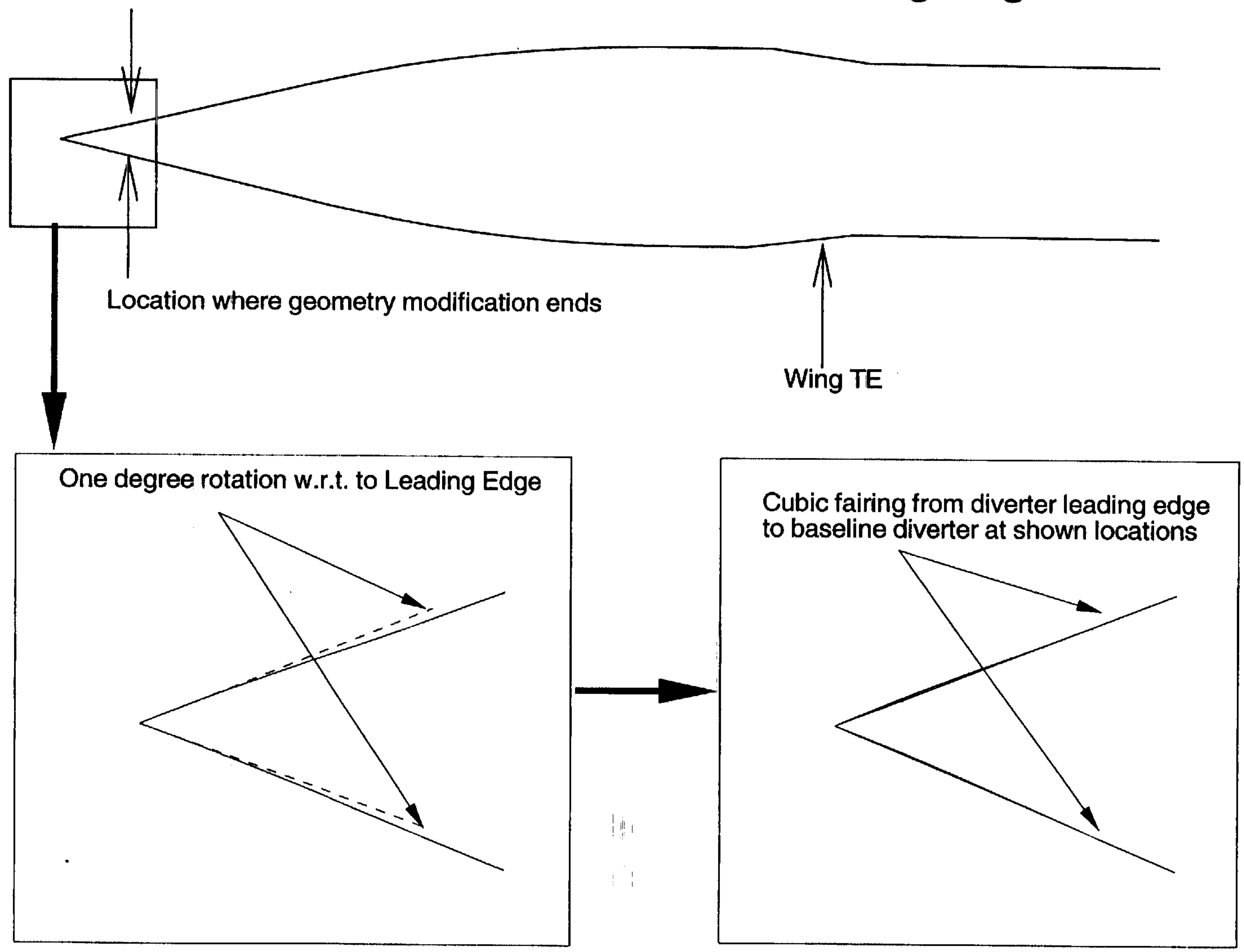

Inboard Nacelle Cambering Results for the Aligned TCA W/B/N/D Configuration

All the results were obtained using CFL3D Euler at cruise conditions. The four cases shown on the table below are:

Div1 Case1: 1 deg. toe-out of inboard diverter with smooth blending at 30″ from LE.

Div1 Case2: Same as above with blending at 150″ from LE.

Nac1 Case1: Inboard bump applied on the inboard nacelle at wing TE location.

Nac1 Case2: Same as above with the resulting maximum thickness moved forward.

Compared to the baseline, all camber cases have shown drag levels that are approximately 1/2 a count lower. However, when compared with the aligned case, none of the cambered geometries have shown any drag improvement.

When examining the diverter cambering results, it seems like toeing-in the inboard diverter can only increase the drag.

No significant difference was found for both nacelle cambering cases, larger modifications are perhaps needed. With such a low installation drag penalty, a one count improvement is quite optimistic, given the constraints.

Inboard Nacelle Cambering Results for the Aligned TCA W/B/N/D Configuration

CFL3D Euler, $M_\infty = 2.4$, $C_L = 0.1$

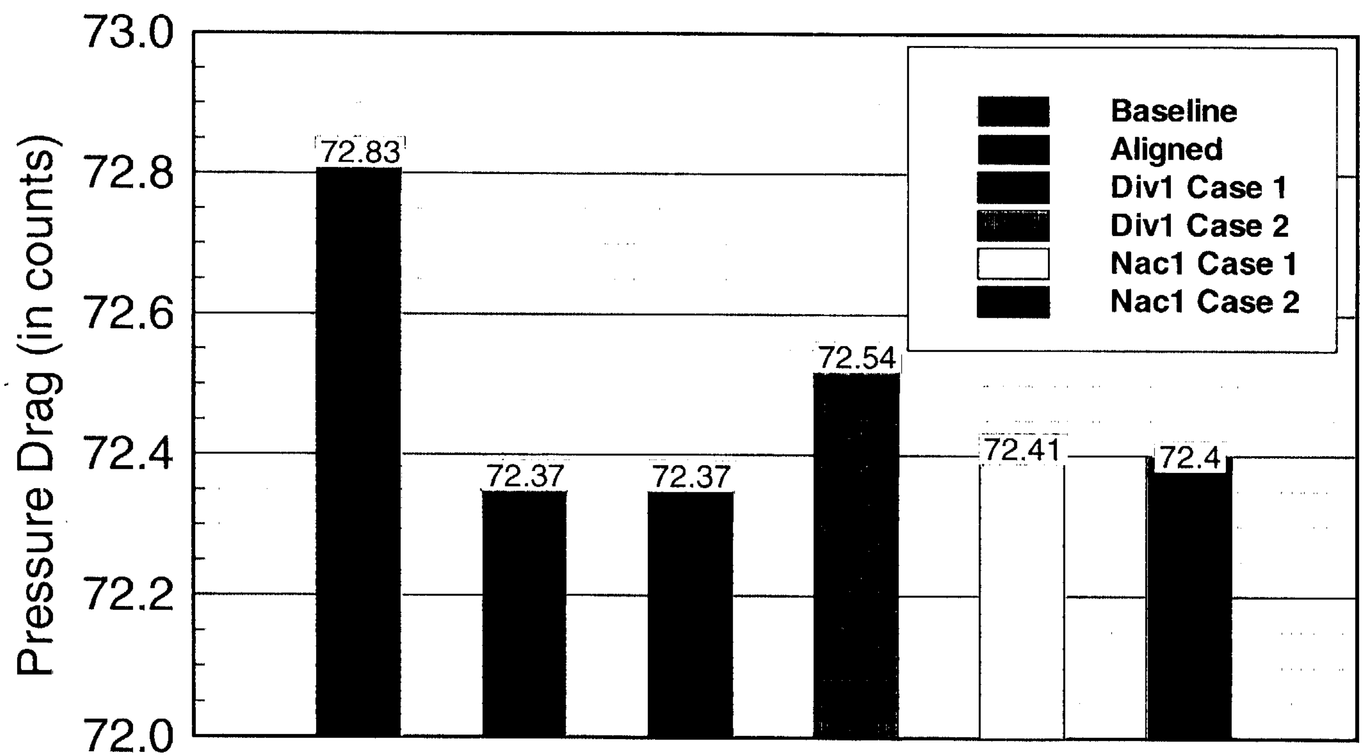

Conclusion and Work in Progress

The highlights of the TCA baseline assessment study are given in the chart below. In summary, the TCA baseline assessment and nacelle installation studies have been completed for both the flight and wind-tunnel Reynolds numbers. After anlyses of the inlet flowfield quality, nacelle alignment was evaluated. Consequently, inlet alignment was undertaken and a Boundary-Layer height investigation was intiated. More work is underway in the area of nacelle and diverter cambering.

Conclusions and Work in Progress

- Results show that the nacelles have been integrated without any significant pressure drag increase
- Viscosity reduces the installation pressure drag by one count
- TCA baseline did not satisfy the inlet flow alignment constraints
- Nacelles/diverters have been realigned to improve inlet flow field which yielded 0.45 counts drag reduction
- Inboard diverter LE indicate possibility of a 3 in. reduction in height
- Results from nacelle and diverter shape modifications showed negligible drag benefits so far

Isolated and Installed Nozzle Boattail Drag Studies

Hoyt Wallace
P. Sundaram
Alan E. Arslan
Chih Fang Shieh

HSR Aerodynamic Performance Workshop
NASA Langley, February 25-28, 1997

Abstract

As part of the FY95 transonic nozzle boattail drag study for the Reference H configuration, the McDonnell Douglas (MDC) task included the axisymmetric nozzle assessment while Northrop Grumman (NGC) studied the 2-D nozzle geometry. The 2-D nozzle was a simulation of the baseline nozzle as of March 1995, while the axisymmetric nozzle was the equivalent body of revolution. Boattail settings representing transonic operation (i.e., small exit area) and the wide-open, supersonic reference nozzle were analyzed.

During the course of the investigation, significant difficulties were experienced and hence the results of the axisymmetric supersonic nozzle geometry could not be obtained. As a result, the study was continued (although with minimal effort) this past year to complete the axisymmetric nozzle geometry.

A new grid was generated with a modified topology, first for the installed axisymmetric supersonic nozzle configuration and later for the axisymmetric transonic nozzle (solution repeated for consistency) configuration. After successfully obtaining the CFL3D Navier-Stokes results for the axisymmetric installed nozzle geometry at $M_\infty = 0.9$, the study was continued for the 2-D installed transonic nozzle configuration as well, to ensure consistency in the comparison of the axisymmetric and 2-D nozzle results. Solutions for the four isolated nacelles have been obtained at both Mach 0.9 and 1.10. The solutions for the installed axisymmetric supersonic nozzle configuration at Mach 1.10 and for the 2-D installed transonic nozzle configuration at either Mach 0.9 or Mach 1.10 have not been obtained as of this writing. However, the results to date indicated the following: (1) the drag of the isolated axisymmetric transonic nozzle was slightly less that that of the 2-D nozzle at both Mach 0.9 and 1.10; (2) the interference drag for both the axisymmetric and 2-D nacelles are nearly identical at Mach 0.90.

Outline

The various topics included in the presentation are given below

Outline

- Objectives
- Background
- Axisymmetric isolated and installed nozzles
- 2-D isolated nozzle CFD solutions
- 2-D installed CFL3D solutions -work in progress
- Comparison of Drag Increments from CFD and Wind Tunnel Tests
- Comparison of CFD and IMS Drag Increments

Objective

The objective of this study was to evaluate several recently completed or on-going efforts to predict or measure the installed drag of nozzles at transonic speeds on a representative HSCT configuration. Particular emphasis was also placed on evaluation of the difference in installed drag for axisymmetric and 2-D nozzles. At least three methods are being used in the HSR program for for obtaining nozzle drag: (1) empirical techniques based on linear theory, such as the Integral Mean Slope (IMS) method; (2) wind tunnel testing of isolated nacelles and full configurations; and (3) computational fluid dynamics (CFD) with Navier-Stokes flow solvers.

Objective

- To assess the isoalted and installed boattail drag of axisymmetric and 2-D nozzle geometries at transonic speeds

Approach

- Navier-Stokes solutions are used to assess the Reference H nozzle boattail drag at transonic speeds. The solutions were obtained using the CFL3D flow solver with the Baldwin-Barth turbulence model at $Re_c = 40x10^6$ for $M_\infty = 0.9$ and 1.1.

Approach

- Obtain CFL3D Navier-Stokes solutions for the Reference H isolated and installed nozzles with simulated power effects
  - $Re_c = 40 \times 10^6$
  - $M_\infty = 0.9$ and 1.1
  - Baldwin-Barth turbulence model

Background

The NASA-industry team has sponsored several studies in the last two years to address the installed boattail drag issues. In the fall of 1994 some of the methods being used to estimate propulsion drag increments showed that the boattail drag of candidate nozzles could be as much as 25 to 40% of the subsonic cruise drag. The empirical IMS method, originally developed for fighter aircraft, was updated (under McDonnell Douglas IRAD) to be applicable to the HSCT. The updated IMS method (known as "95 IMS") is now being used to predict throttle-dependent boattail drag for all installed engine performance decks. The CA ITD Team sponsored an ambitious CFD study to evaluate the interference and installed drag of 2-D and axisymmetric nozzles. The CA team also authorized wind tunnel testing at NASA-Langley to evaluate the installation drag of axisymmetric and 2-D nacelles (at flow-through pressures) and the drag of isolated, powered nozzles at transonic speeds.

Background

- CFD study initiated in early 1995 to evaluate installed, transonic drag of axisymmetric and 2-D nozzles
- Wind-tunnel tests to obtain nacelle installation drag for 2-D and axisymmetric reference (flow-through) nacelles conducted by NASA-LaRC in 1996 at transonic and supersonic speeds
- Wind-tunnel tests by NASA-LaRC in 1996 to obtain isolated nozzle drag for 2-D transonic nozzles 16-T
- Empirical techniques (e.g., the Integral Mean Slope method) were refined in 1995 for application to HSCT

Nozzle Boattail CFD Study

The CFD study was initiated in early 1995 to evaluate the installation of the "Best DSM" 2-D nozzle on the Ref. H configuration. Also the axisymmetric equivalent of the nacelle of the 2-D nozzle was also to be evaluated. The axi equivalent nozzle was selected instead of an actual axi design to allow the team to evaluate the axi vs. 2-D drag issue without the confounding effects of different area distributions between the axi and 2-D nacelles.

The initial results of the study were reported at the CA Workshop in February 1996. These results indicated an unexpectedly large, favorable interference drag benefit for the axisymmetric nozzle at both 0.90 and 1.10 Mach numbers. It was decided to re-grid and rerun the axi cases at Mach 0.90 and to have McDonnell Douglas run the transonic 2-D nozzle configurations as a cross-code check case. This present report will present the status of this subsequent effort.

Nozzle Boattail CFD Study

- Evaluated the “Best DSM” (as of February 1995) and its axi Equivalent Nacelle on the Ref. H
- 1995 work split
  - 2-D Configurations: Boeing & Northrop-Grumman.
  - Axi Configurations: McDonnell Douglas
  - NASA LaRC to verify the two results
- Initial results indicated favorable interference drag benefits for the axi nozzle
- Discrepancies in computed drag values by the different participants

Recent Wind Tunnel Tests

Four nacelles were built and tested on the 1.7% scale Ref. H model to evaluate the installation drag of axi and 2-D nozzles. In addition to the two nacelles being evaluated in the CFD study, models of a realistic axi design, the axisymmetric-tilt-chute (ATC) nozzle, and a newer 2-D design, the fixed-chute nozzle (FCN) were also built. Due to the limitations of the existing, small-scale wind tunnel model, these nacelles cannot be tested with high pressure air to simulate a realistic jet plume. The model can only be tested in the flow-through mode. Only the supersonic cruise nozzle external geometry was built as the exit area of the transonic nozzle is too small to pass a realistic inlet flow rate.

The nozzles tested on the isolated nacelle were built at approximately 8% scale so that a correctly scaled internal nozzle geometry and jet could be simulated. These nozzles are parametric variations of the FCN design of May 1995.

Additional information on these tests can be obtained from Francis Capone of NASA-LaRC.

Recent Wind-Tunnel Tests to Evaluate Nozzle Drag

- Installed - 1.7% Ref. H Modular Model
  - Supersonic - Mach 2.4
    - Two entries in the LaRC UPWT in 1996
    - Four nacelles evaluated
      - best DSM and FCN
      - ATC and axi equivalent of best DSM
  - Transonic -Mach 0.80 to 1.20
    - LaRC 16-foot tunnel in June 1996
    - Best DSM and axi equivalent of best DSM
- Isolated - Mach 0.60 to 1.20
  - Several (14+) 2-D nozzles representative of transonic flight for HSCT tested in April 1996

Comparison of Predicted and Measured Drag Polars

The experimental drag polar of the NASA LaRC transonic test of the Reference H W/B configuration is compared here with the CFL3D Navier-Stokes computed results. The CFD solution has been computed at $Re_c = 40 \times 10^6$. This has been corrected to the wind-tunnel Reynolds number using a flat plate correction. The results show that the predicted results are in close agreement with the experimental data at $M = 0.9$.

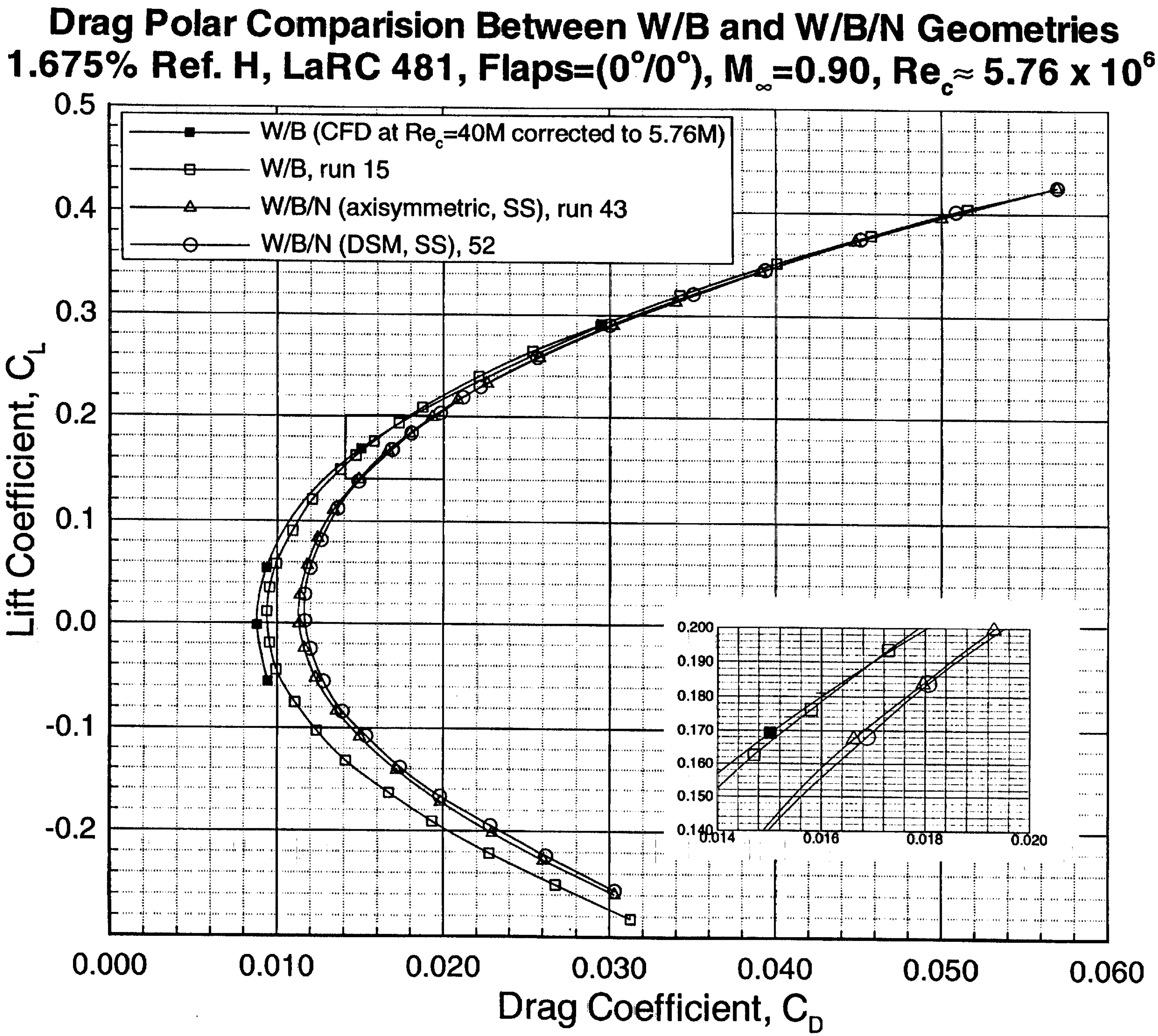
Drag Polar Comparision Between W/B and W/B/N Geometries
1.675% Ref. H, LaRC 481, Flaps=(0°/0°), M_∞=0.90, $Re_c \approx 5.76 \times 10^6$
W/B (CFD at Re_c=40M corrected to 5.76M)
W/B, run 15
W/B/N (axisymmetric, SS), run 43
W/B/N (DSM, SS), 52
Lift Coefficient, C_L
Drag Coefficient, C_D
0.5
0.4
0.3
0.2
0.1
0.0
-0.1
-0.2
0.000
0.010
0.020
0.030
0.040
0.050
0.060
0.200
0.190
0.180
0.170
0.160
0.150
0.140
0.014
0.016
0.018
0.020

Convergence Histories for the Ref. H Installed Axisymmetric Supersonic Nozzle Configuration

The W/B/N/D Navier-Stokes grid consisted of nearly 7.2 million grid points. The memory requirement was nearly 310 Mw on the NAS Cray C-90 system. The runs were made on a special queue set up by NAS due to the increased memory requirement. The runs took nearly 100 CPU hours on the C-90. As can be seen, the residual as well as lift and drag convergence are very good.

Convergence Histories for the Ref. H Installed Supersonic Nozzle Configuration

CFL3D N-S, M_∞=0.90, α=4.0°, Baldwin-Barth Turbulence Model, Re_c= 40 x 10^6

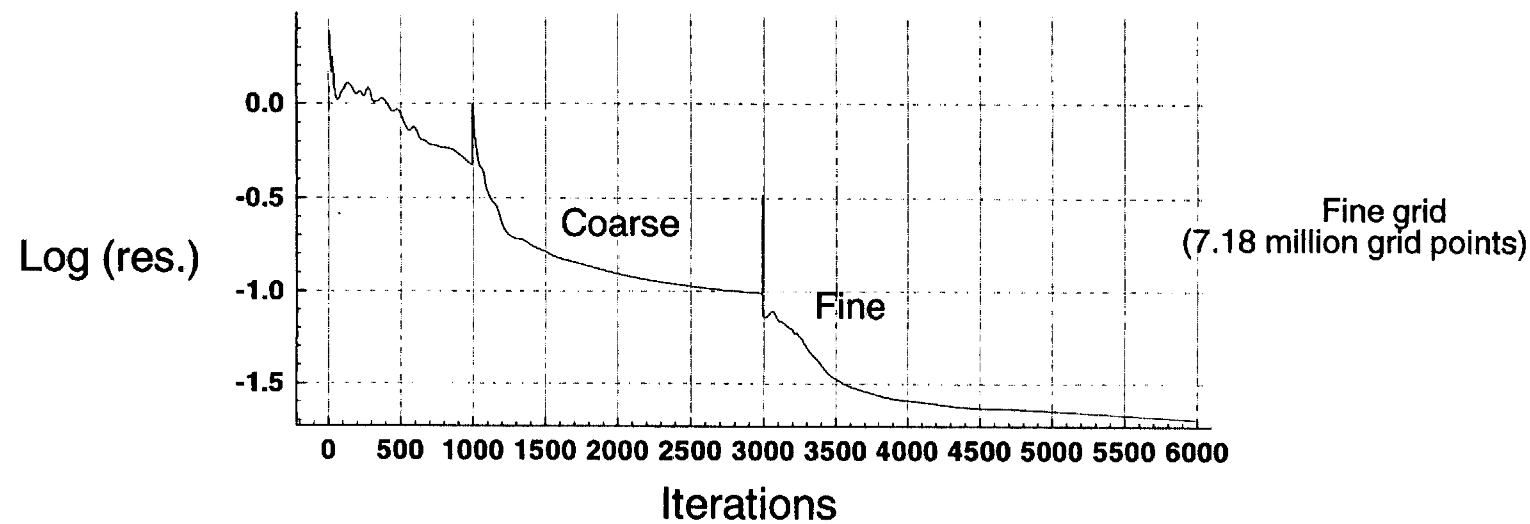

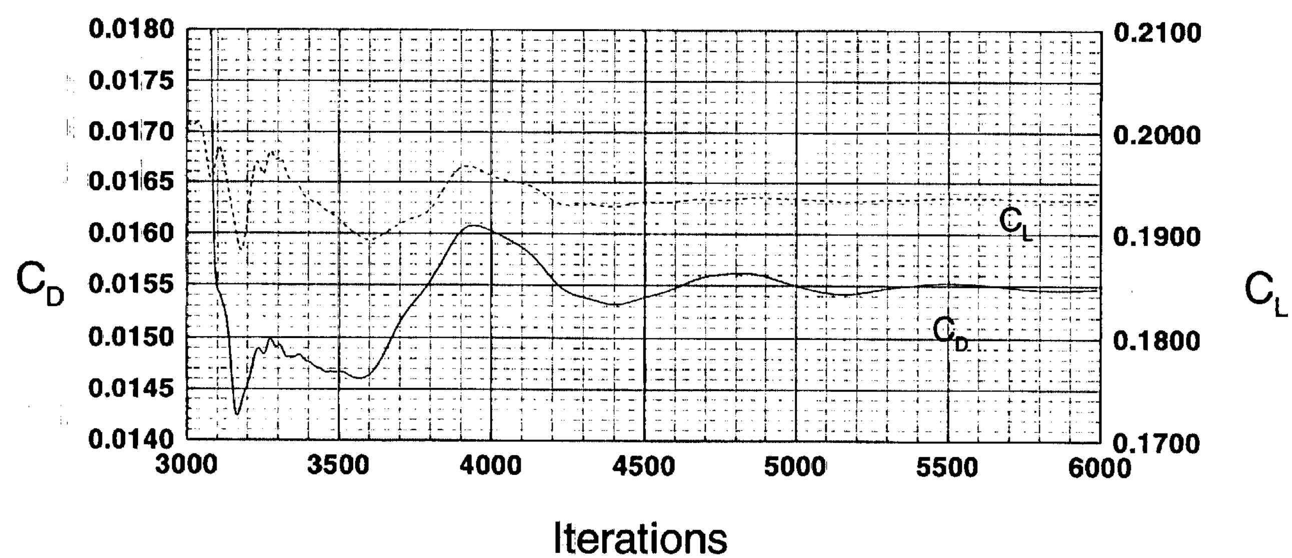

Convergence Histories for the Ref. H Installed Axisymmetric Transonic Nozzle Configuration

Although the CFL3D Navier-Stokes results of this geometry were already obtained during FY95, they were recomputed here due to the fact that the grid topology for the reference configuration computations were quite different from what was originally used in the transonic configuration. The grid for this configuration was obtained by perturbing the supersonic configuration grid using the CSCMDO software.

The W/B/N/D Navier-Stokes grid consisted of nearly 7.18 million grid points. The memory requirement was nearly 310 Mw on the NAS Cray C-90 system. These runs were also made on the special queue setup by NAS due to the increased memory requirement. The transonic nozzle solution was started from the converged fine grid solutions of the supersonic nozzle setting. The runs took nearly 60 CPU hours on the C-90. As can be seen, the residual as well as lift and drag convergence is very good.

Convergence Histories for the Ref. H Installed Transonic Nozzle Configuration

CFL3D Navier-Stokes, $M_{\infty}=0.90$, $\alpha=4.0^{\circ}$, Baldwin-Barth Turbulence Model, $Re_c = 40 \times 10^6$

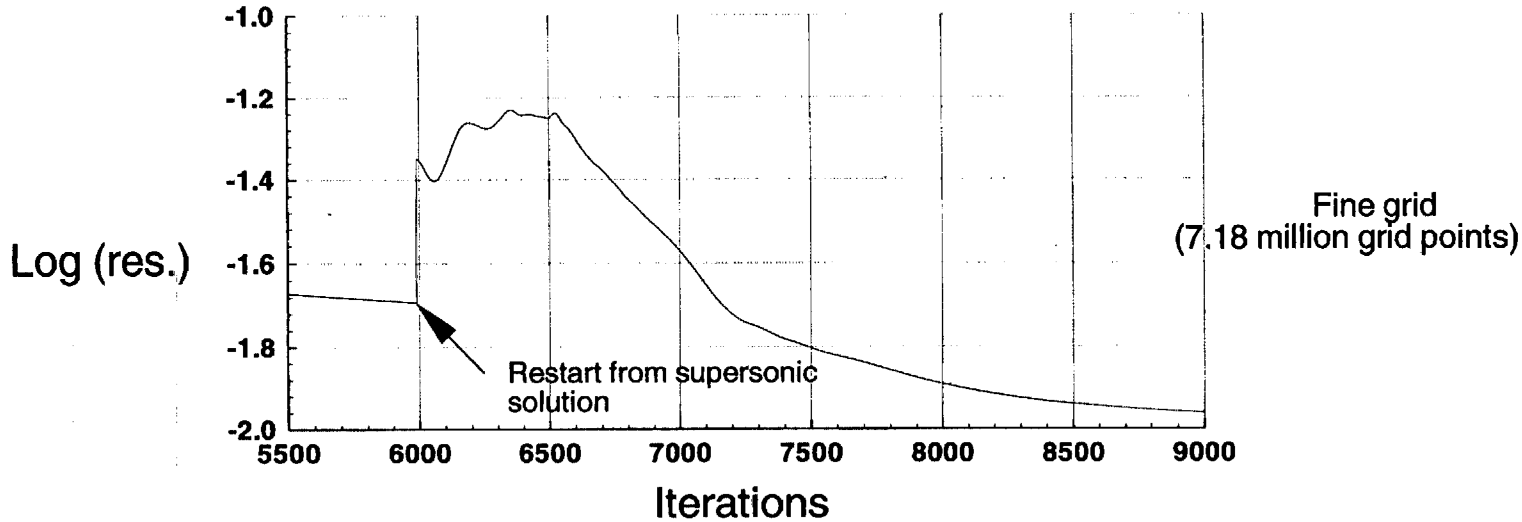

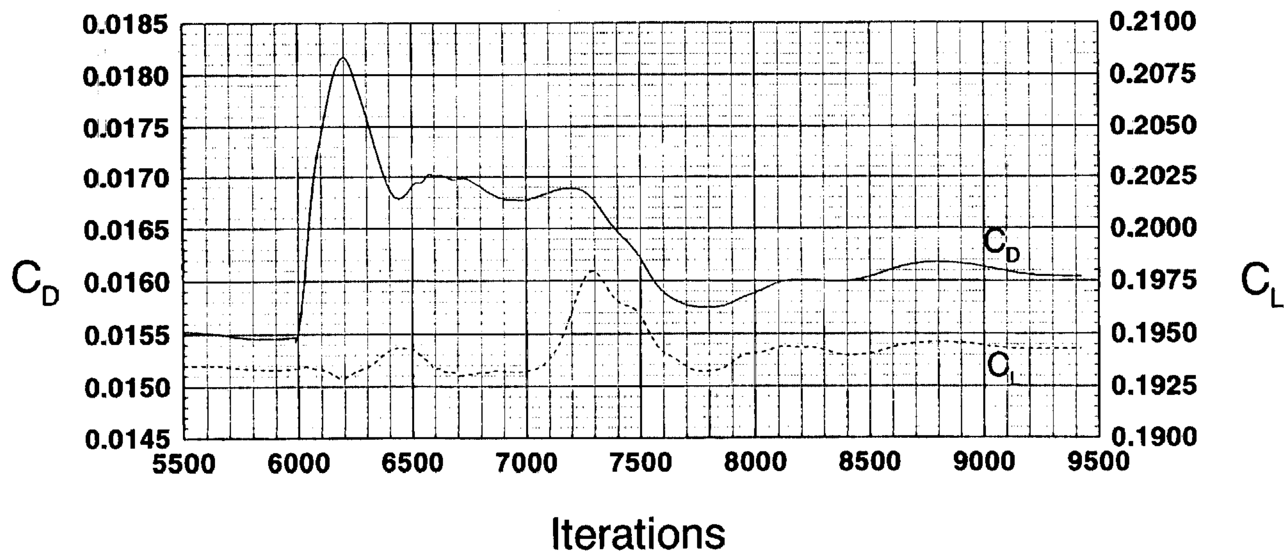

Upper Surface Pressure Contours for the Installed Axisymmetric Nozzles

The upper surface pressure contour comparison for the installed configuration at the transonic and supersonic nozzle settings at a free stream Mach number of 0.9 is shown. The wing upper surface pressures show very little difference between the two cases. However, the pressure contours in the nozzle region are significantly different. The pressure oscillation found on the transonic nozzle configuration is completely missing for the supersonic setting. The high pressure region in the aft end of the nozzle boattail region is responsible for a thrust component that is absent in the supersonic setting. This aspect could nullify some of the shock losses that are prevalent in the boattail region of the transonic nozzle setting.

Upper Surface Pressure Distributions
Reference H Installed Axisymmetric Nozzle Configurations
$M_\infty = 0.9$, $\alpha = 4.0°$, $Re_c = 40 \times 10^6$, CFL3D N–S, Baldwin–Barth Turbulence Model

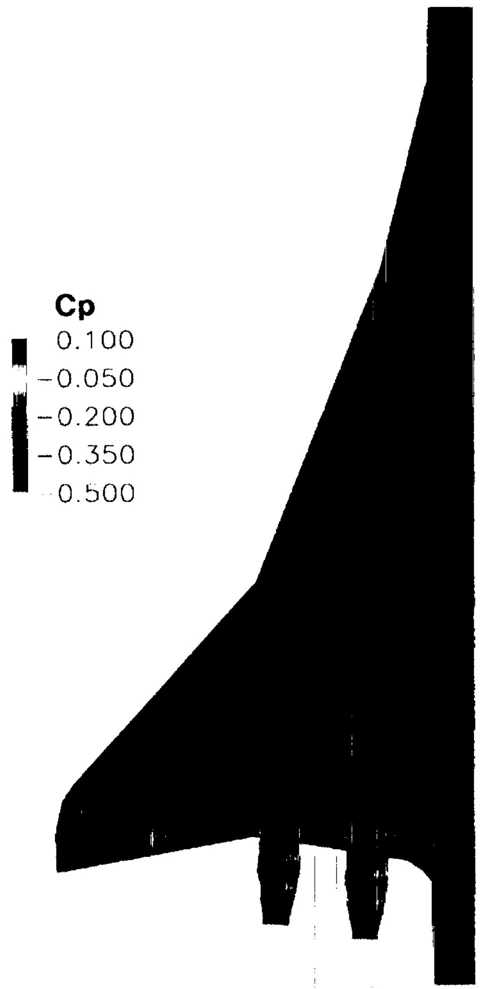

Transonic Nozzle Configuration

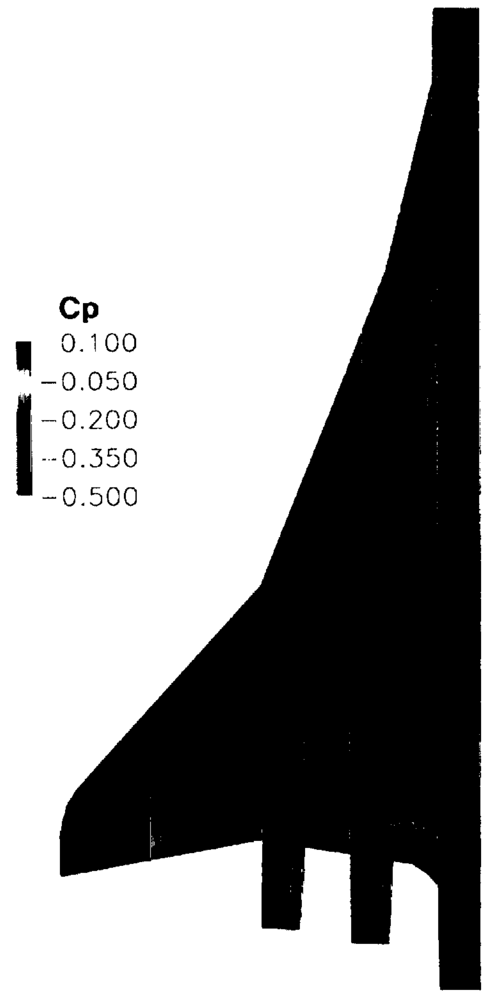

Supersonic Nozzle Configuration

Lower Surface Pressure Contours for the Installed Axisymmetric Nozzles

Both supersonic and transonic installed nozzle configurations display the same behavior in the diverter channel region. High pressures are observed near the leading edges of both diverters, followed by expansions terminated with a normal shock further downstream before the wing trailing edge. However, the supersonic nozzle case seems to have a stronger shock (between the two nacelles) that is slightly upstream compared to the installed transonic nozzle configuration.

Reference H Lower Surface Pressure Contours for the Installed Axisymmetric Nozzle Configuration at Both Supersonic and Transonic Settings
($M_\infty = 0.9$, $\alpha = 4.0°$, $Re_c = 40 \times 10^6$, CFL3D N–S, Baldwin–Barth Turbulence Model)

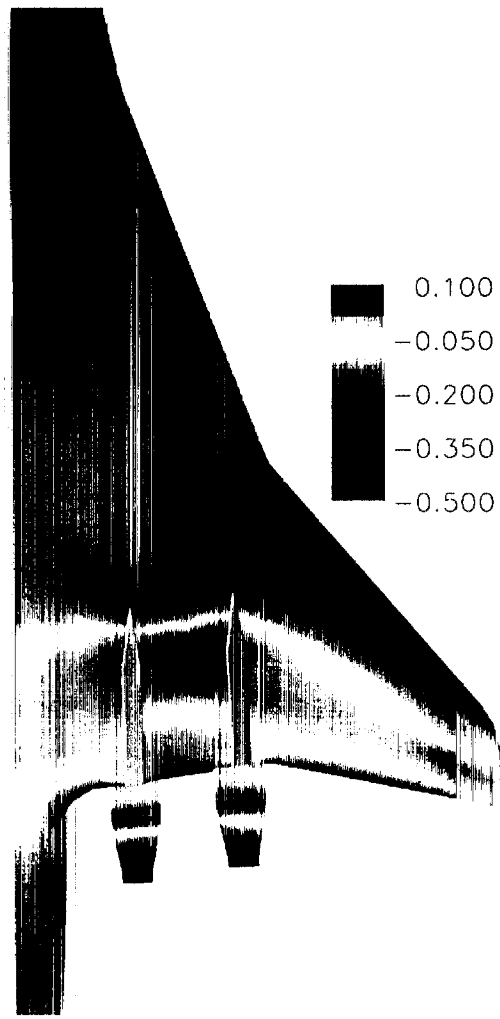

Transonic Nozzle Configuration

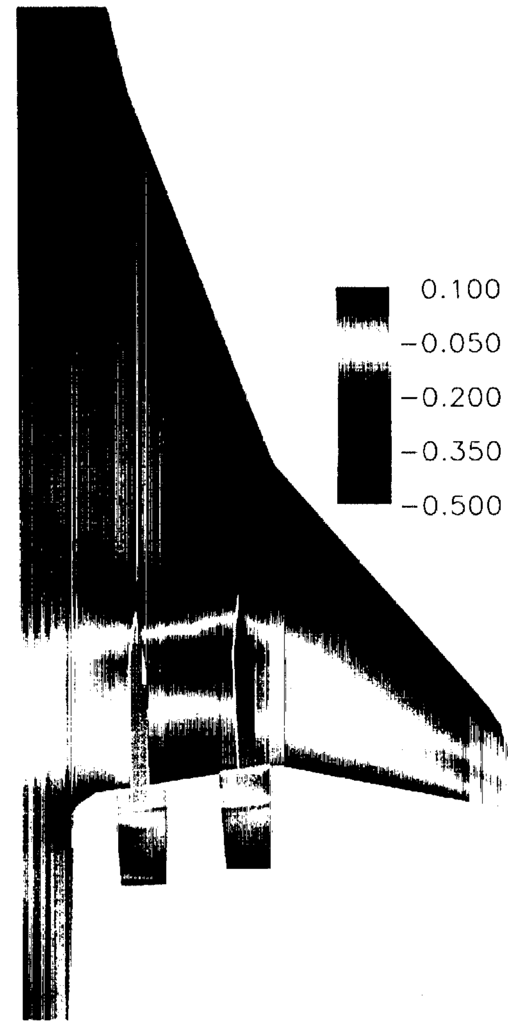

Supersonic Nozzle Configuration

Mach Contours (Horizontal Cuts) with surface C_p Distribution for the Reference H with both Transonic and Supersonic Nozzle Configurations

Here, the same comments as in the previous charts are still applicable. In addition, for the installed transonic nozzle configuration, Mach cuts indicate the presence of a shock at the beginning of the boattail closure of both nozzles.

Mach Contours (Horizontal Cuts) with Surface Cp Distribution for the Reference H with both Transonic and Supersonic Nozzle Configurations

($M_\infty = 0.9$, $\alpha = 4.0°$, $Re_c = 40 \times 10^6$, CFL3D N–S, Baldwin–Barth Turbulence Model)

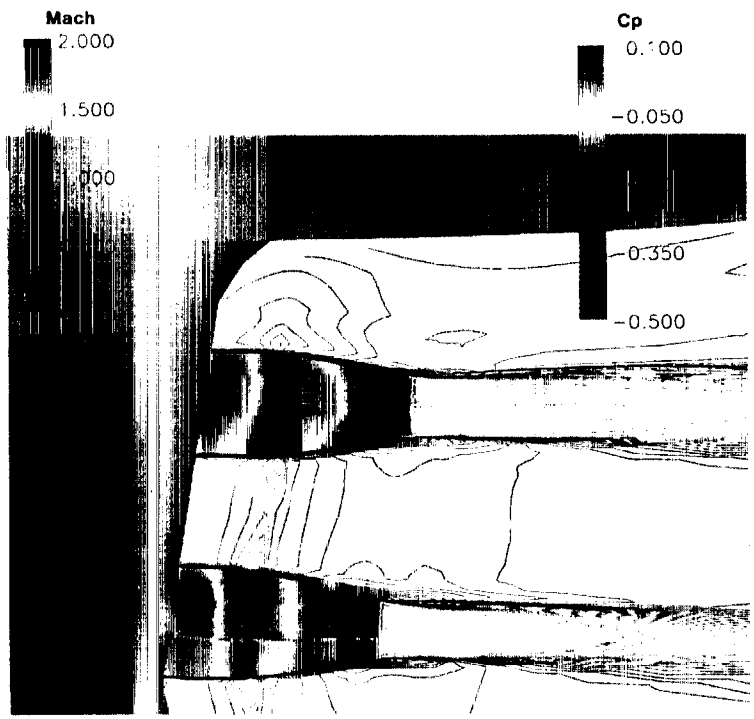

Transonic Nozzle Configuration

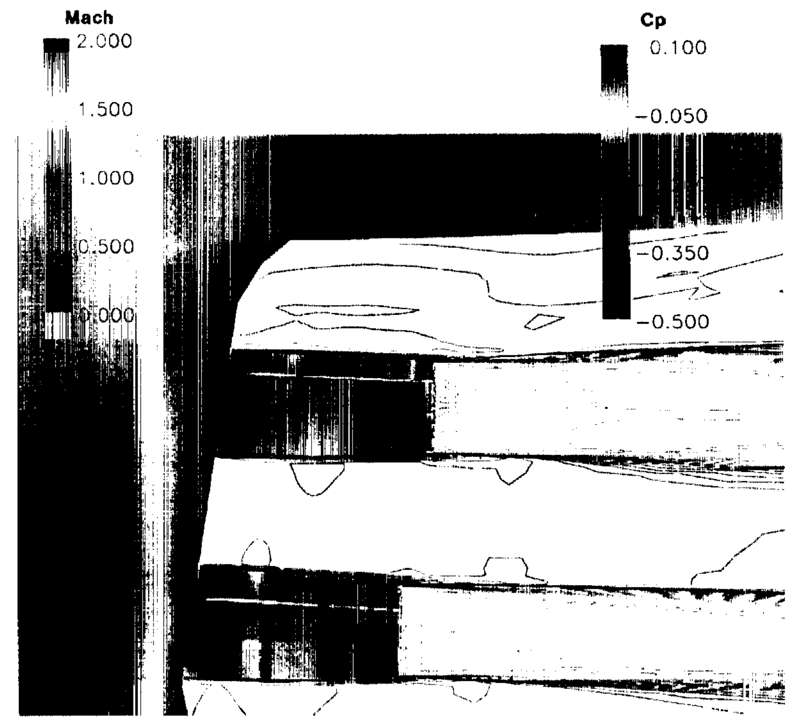

Supersonic Nozzle Configuration

C_p Distributions for Reference H Installed Axisymmetric Nozzle Configurations

Shown here are the surface C_p's on all viscous surfaces as well as the vertical pressure cuts in the field near the boattail region of each nacelle.

The supersonic nozzle configuration shows very mild local shock/expansion systems in the boattail region while the transonic nozzle setting exhibits a strong expansion/shock system on the nacelle lower surface, particularly for the outboard nacelle. On the other hand, and unlike the isolated transonic boattail configuration, the upper surface of the installed transonic nozzle does not show any major shock, as seen from the pressure cuts.

Finally, the more drastic shock structure observed for the transonic configuration is responsible for the increased drag shown later.

Cp Distributions for Reference H Installed Axisymmetric Nozzle Configurations

$M_\infty = 0.9$, $\alpha = 4.0°$, $Re_c = 40 \times 10^6$, CFL3D N–S, Baldwin–Barth Turbulence Model

Transonic Nozzle Configuration

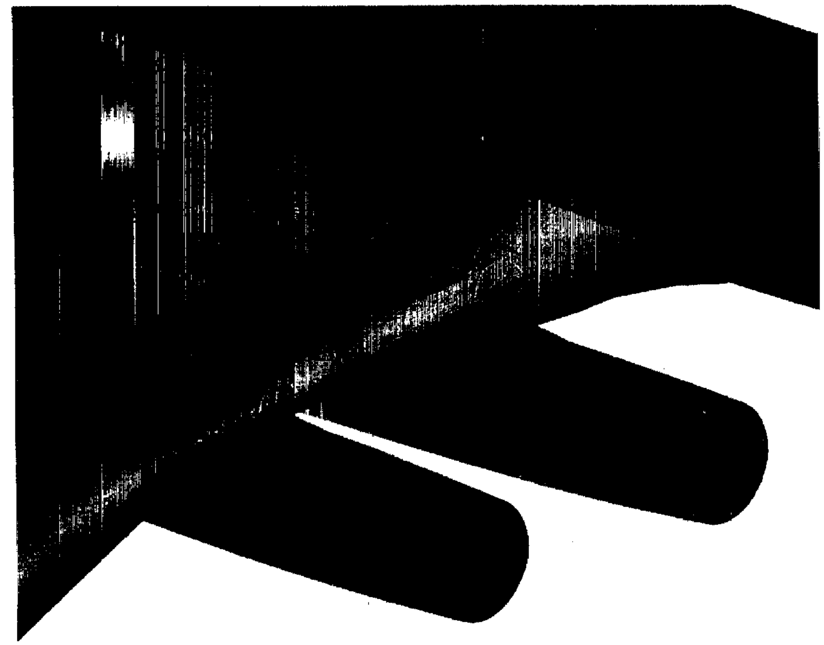

Supersonic Nozzle Configuration

Isolated 2-D/Transonic Nozzle Boattail

The computed surface flow patterns are shown for free stream Mach number of 0.9 and Reynolds number (based on the Ref. H mean aerodynamic chord) of 40 million.

The figure shows that the flow is separated over the entire upper flap surface. However, the flow at the lower flap surface is separated at the flap hinge line and reattached a short distance downstream of the hinge line, and then separated again near the nozzle exit. The asymmetric flow pattern is due to the fact there is some nacelle camber. The symbols C_{Dp}, C_{Dv}, and C_{DT} denote the pressure, the surface skin friction, and the total drag, respectively.

Isolated Ref. H 2D/Transonic Nozzle Boattail Configuration
Computed Surface Oil–Flow Pattern

(CFL3D Baldwin–Barth, M_∞=0.9, Re_C=40x10^6; 12–zones, 1.5 million grid points)

α=0°,NPR=5.0, NTR=3.262

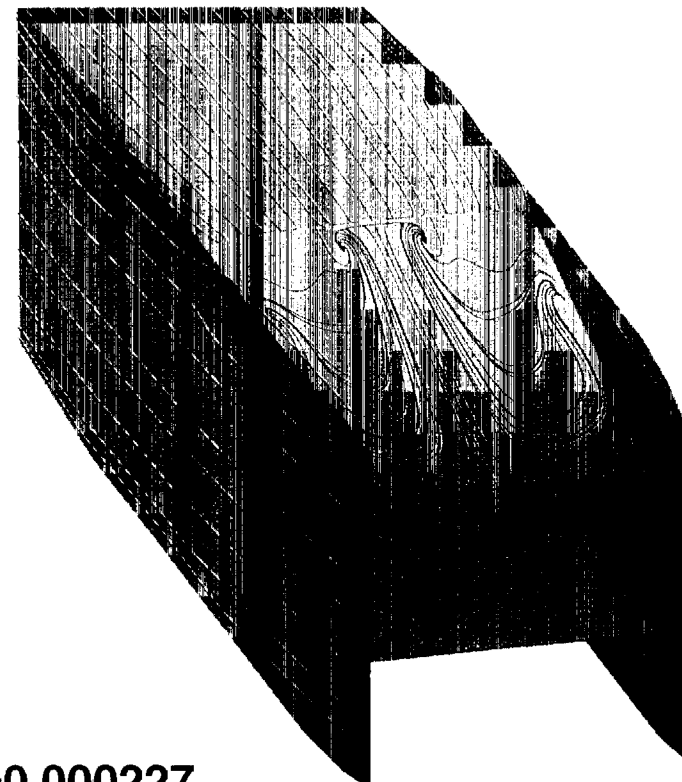

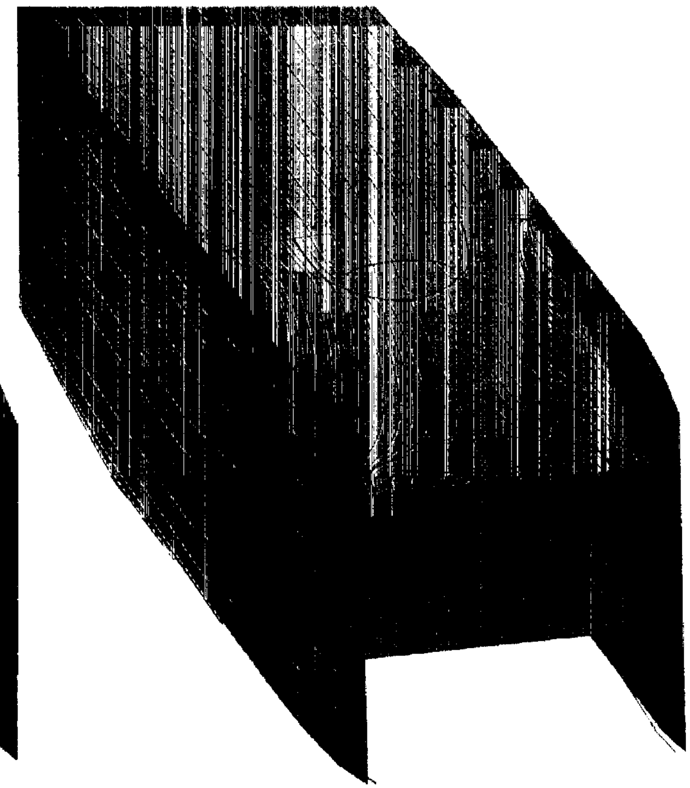

C_{Dp}=0.000227
C_{Dv}=0.000207
C_{DT}=0.000434

Upper Flap
Flap angle =14°

Lower Flap
Flap angle = 12°

Isolated 2-D/Transonic Nozzle Boattail

The computed surface flow patterns are shown for free stream Mach number of 1.1, and Reynolds number (based on the Ref. H mean aerodynamic chord) of 40 million.

The figure shows that the flow stays attached up to somewhat upstream of the nozzle exit on both of the upper and lower flap surfaces. Unlike the $M_\infty = 0.9$ case, the flow patterns are nearly symmetric on the upper and lower flap surfaces. The symbols C_{Dp}, C_{Dv}, and C_{DT} denote the pressure, the surface skin friction, and the total drag, respectively.

Isolated Ref. H 2D/Transonic Nozzle Boattail Configuration Computed Surface Oil–Flow Pattern

(CFL3D Baldwin–Barth, M_∞=1.1, Re_c=40x10^6; 3–zones, 3 million grid points)

α=0°,NPR=5.0, NTR=3.055

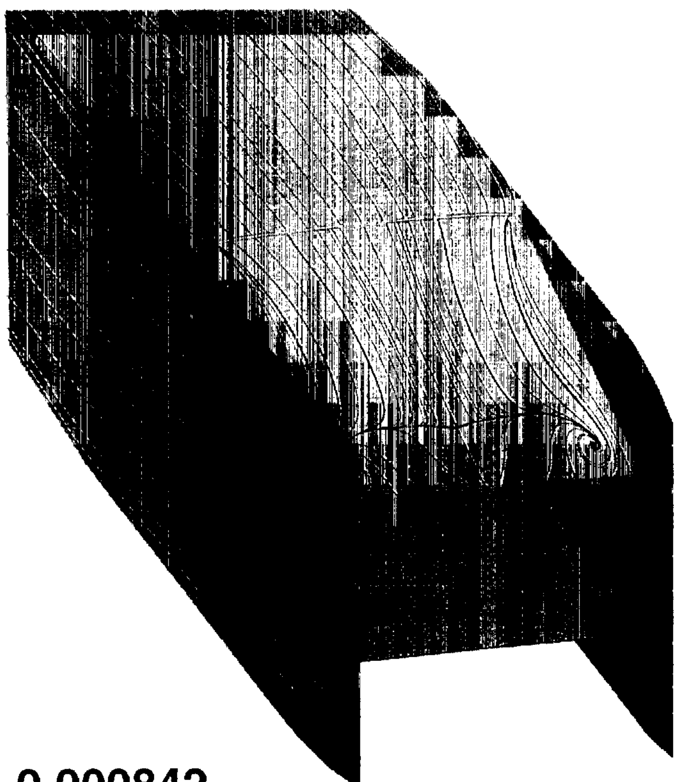

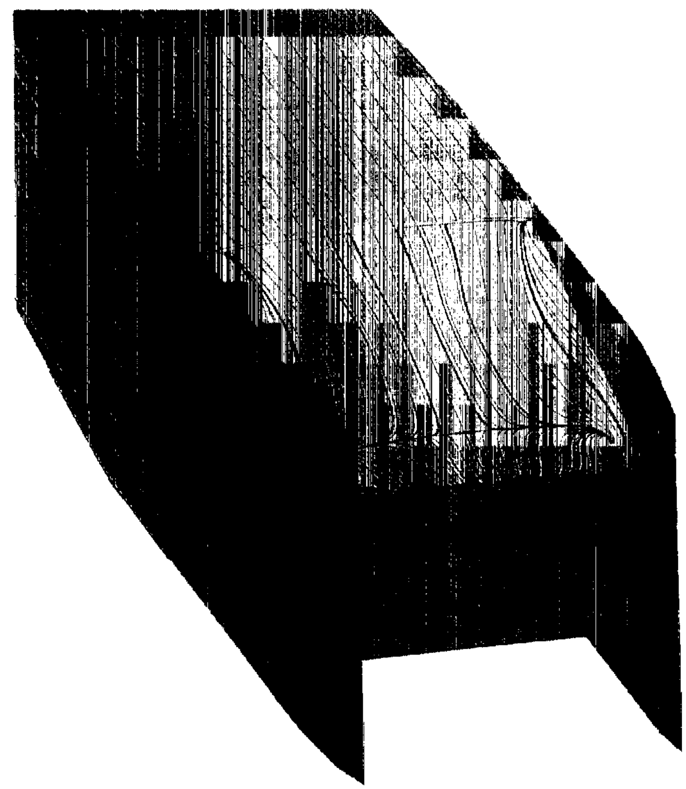

C_{Dp}=0.000842
C_{Dv}=0.000210
C_{DT}=0.001052

Upper Flap
Flap angle = 14°

Lower Flap
Flap angle = 12°

Isolated 2-D/Transonic Nozzle Boattail Cp Distributions

The C_p distributions at the top, side, and bottom centerlines are shown for $M_\infty = 0.9$. Shock waves near the hinge line (x/L=0.0) of the deflected flap surfaces are evident; L denotes the flap length. Due to the nacelle cambering, the upper flap and the lower flap angles are 14 and 12 degrees, respectively. Flow separation on the entire upper flap surface has been observed from the surface flow patterns, which will be shown later.

Isolated Ref. H 2D/Transonic Nozzle Boattail Configuration Computed Cp Distributions

(CFL3D Baldwin–Barth, Re_c=40x10^6; 12–zones, 1.5 million grid points)

α=0°,NPR=5.0, M_∞=0.9, NTR=3.262

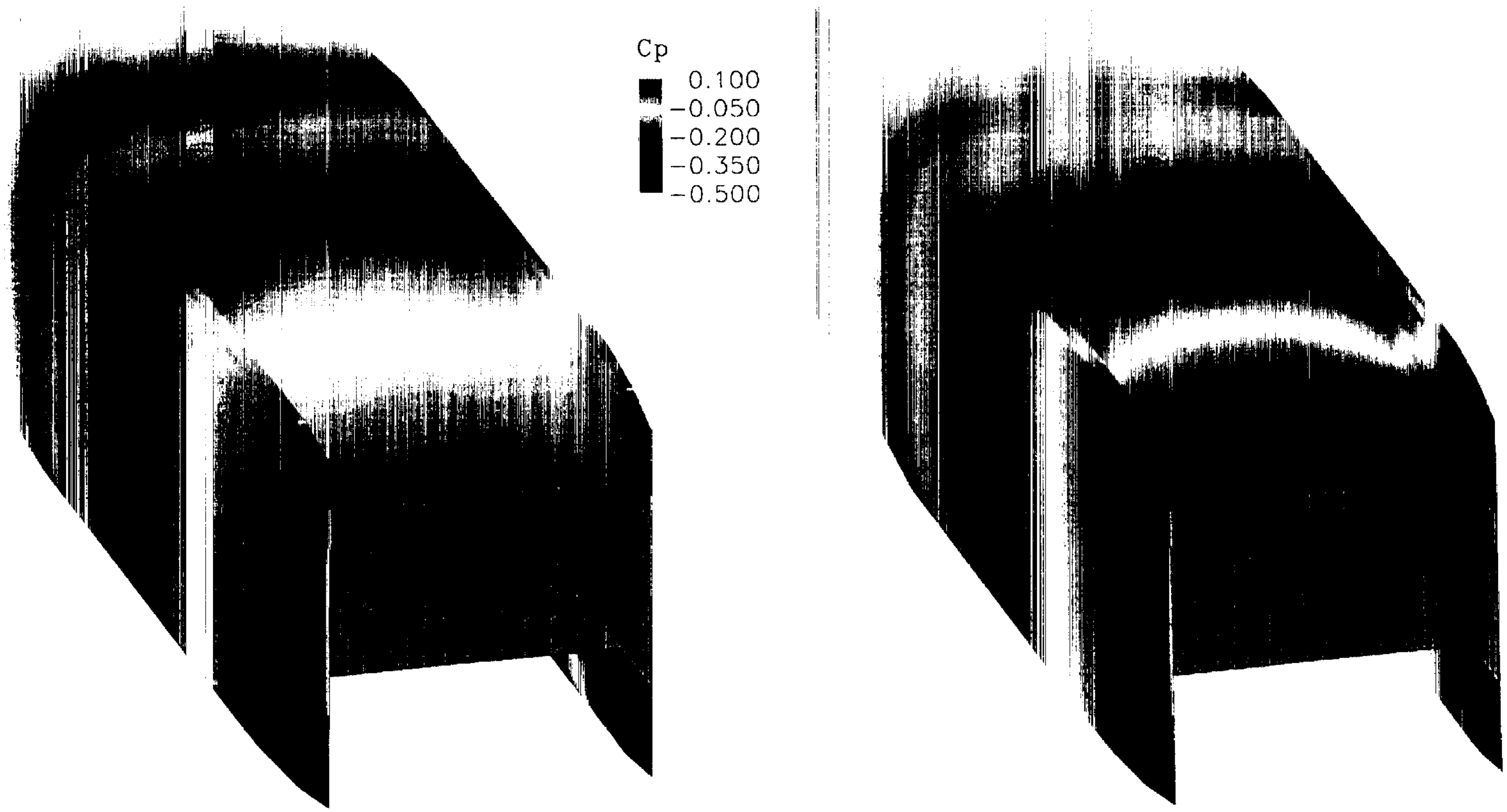

Upper Flap
Flap Angle = 14°

Lower Flap
Flap Angle = 12°

Isolated 2-D/Supersonic Nozzle Boattail

The computed surface flow patterns are shown for free stream Mach numbers of 0.9 and 1.1, and Reynolds number (based on the Ref. H mean aerodynamic chord) of 40 million.

The figure shows that the flow stays attached on the entire flap surfaces except at the corners of the flap hinge line. Similar to the 2-D/transonic $M_\infty = 1.1$ case, the flow patterns on the upper and lower flaps are nearly symmetric and, therefore, only the upper surface patterns are shown. The symbols C_{Dp}, C_{Dv}, and C_{DT} denote the pressure, the surface skin friction, and the total drag, respectively.

Isolated Ref. H 2D/Supersonic Nozzle Boattail Configuration Computed Surface Oil–Flow Pattern

(CFL3D Baldwin–Barth, Re_C=40x10^6; 12–zones, 1.5 million grid points)

α=0°,NPR=5.0, NTR=3.262 (M_∞=0.9); NTR=3.055 (M_∞=1.1)

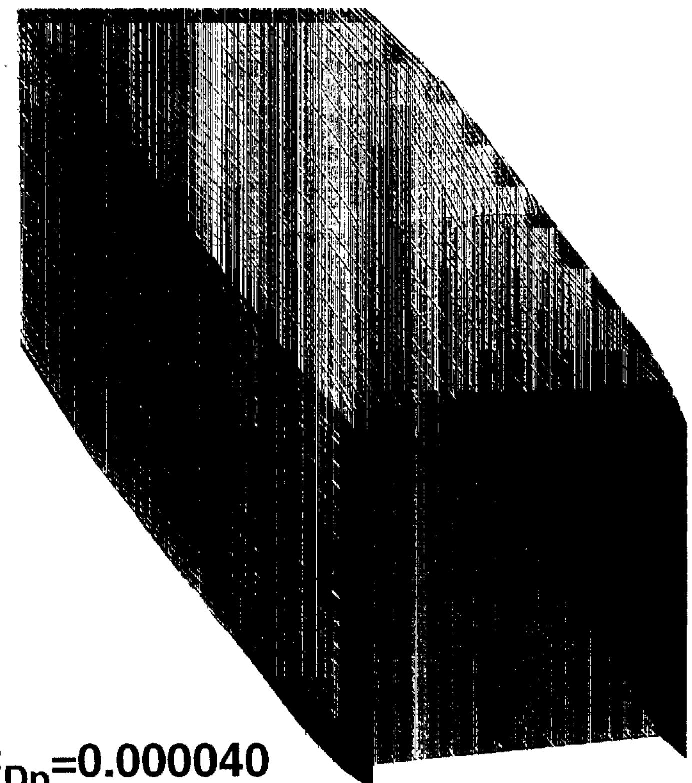

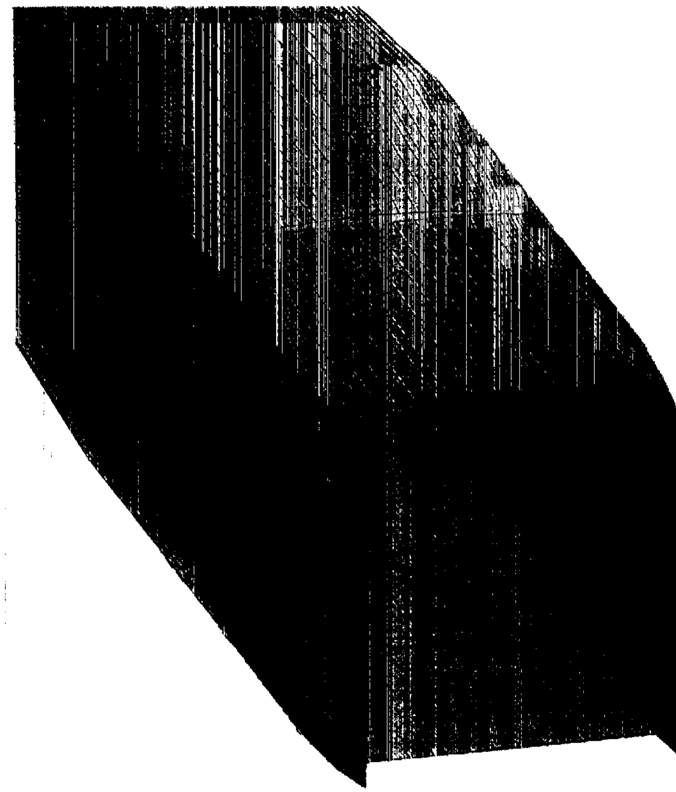

Grid Structure for the Reference H Installed 2-D Nozzle

This chart shows the grid structure for the installed 2-D nozzle configuration. Considerable point-matching and removal of block boundaries has resulted in a 8.33 million grid point patched grid.

Grid Structure for the Reference H Installed 2–D Nozzle Configuration at the Transonic Setting

(37 blocks, 8.33 million gridpoints, back–view)

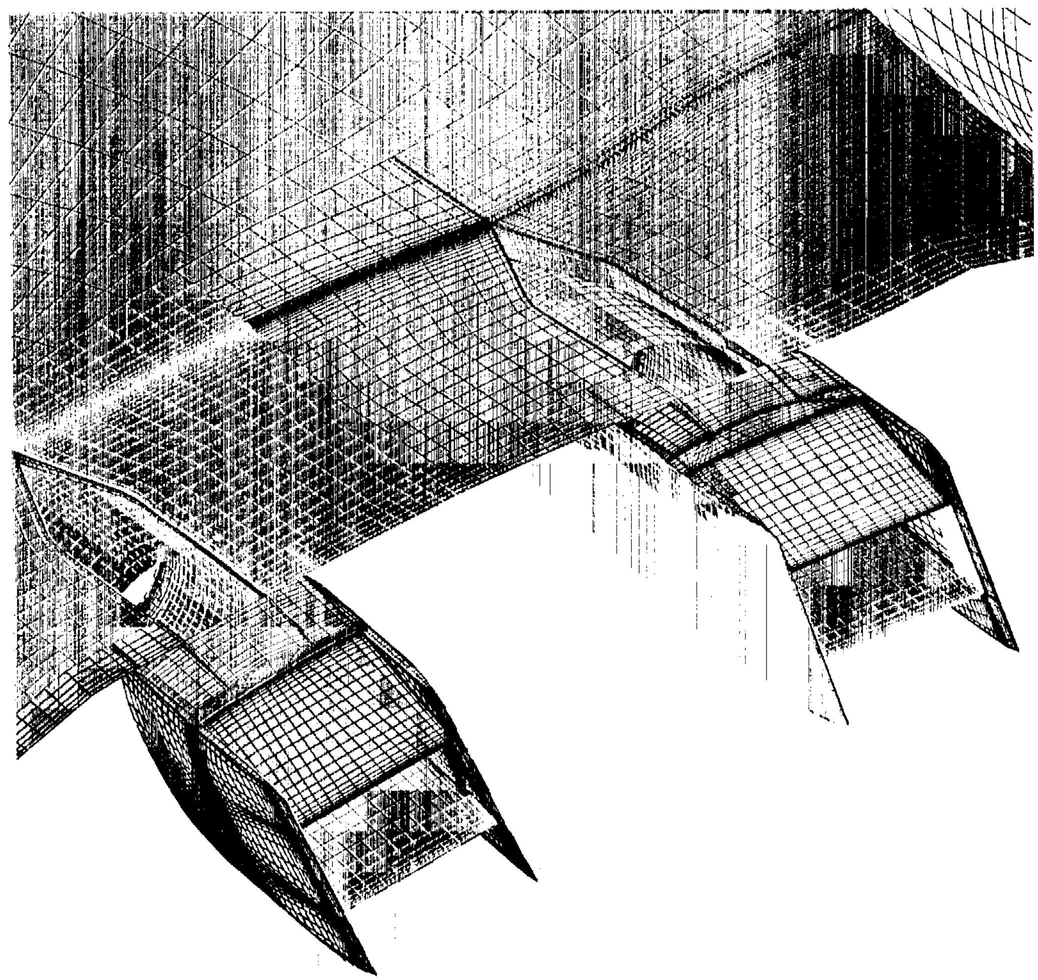

Cp Distribution for the Installed Reference H 2-D Transonic Nozzle Configuration

The installed 2-D nozzle boattail grid generated has been used to obtain the CFL3D Navier-Stokes solution using Baldwin-Barth turbulence model. The large memory requirements of 360 Mw mandated the use of the multitask version of the code. At the time of reporting, the solutions are not converged. However, because of the fact that fine grid solutions have advanced sufficiently, it is proper to look at the flow features and understand the details.

The pressure distribution on the wing upper surface together with the nozzle upper flap region are shown in this chart. It can be seen that the flow field is similar to the axisymmetric nozzle configuration shown in an earlier chart. Also, the upper flap pressures are similar to the isolated 2-D nozzle pressures in the flap region.

Cp Distribution for the Installed Reference H 2D Transonic Nozzle Configuration

$M_\infty = 0.9$, $\alpha = 4.0°$, $Re_c = 40 \times 10^6$, CFL3D N–S, Baldwin–Barth Turbulence Model

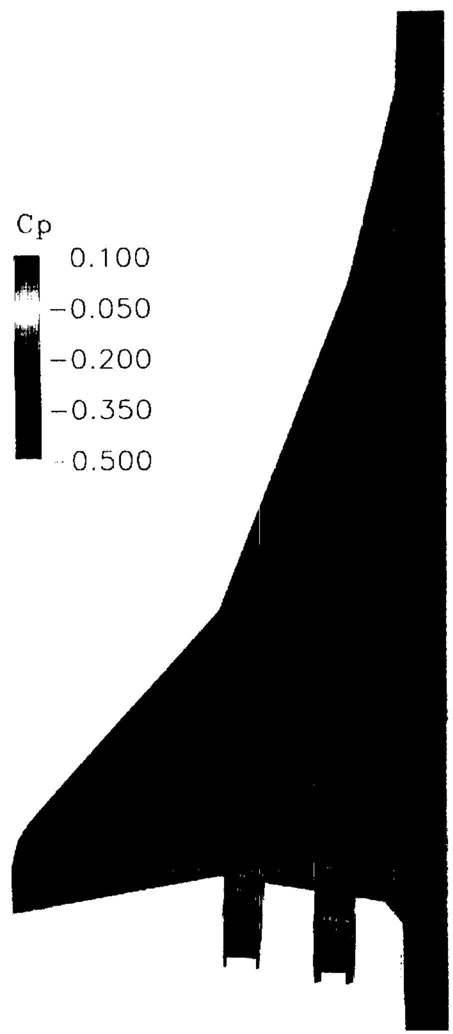

Top View

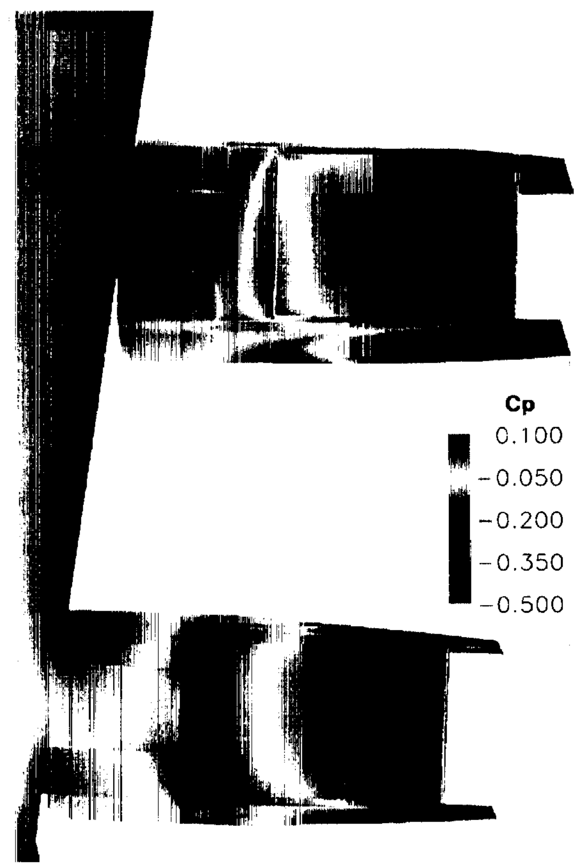

Zoom View

Surface Cp Distribution

This chart shows the surface pressure distribution on the wing lower surface as well as the nozzle lower flap regions for the installed 2-D transonic nozzle. Also shown are the surface streamlines on the lower flap surface of the inboard and outboard nozzles. The inboard nozzle flap region surface streamlines have some regions of separation and reattachment which are similar to the isolated nacelle lower flap surface streamlines shown earlier. However, the outboard nozzle flap region has significant extent of large flow separation.

Surface Cp Distribution
Installed Reference H 2–D Transonic Nozzle Configuration
$M_\infty = 0.9$, $\alpha = 4.0°$, $Re_c = 40 \times 10^6$, CFL3D N–S, Baldwin–Barth Turbulence Model

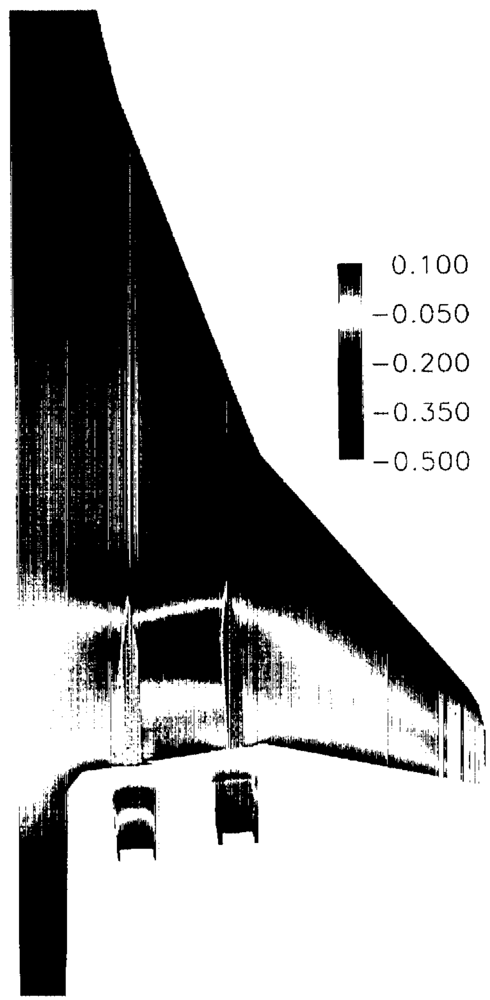

Bottom View

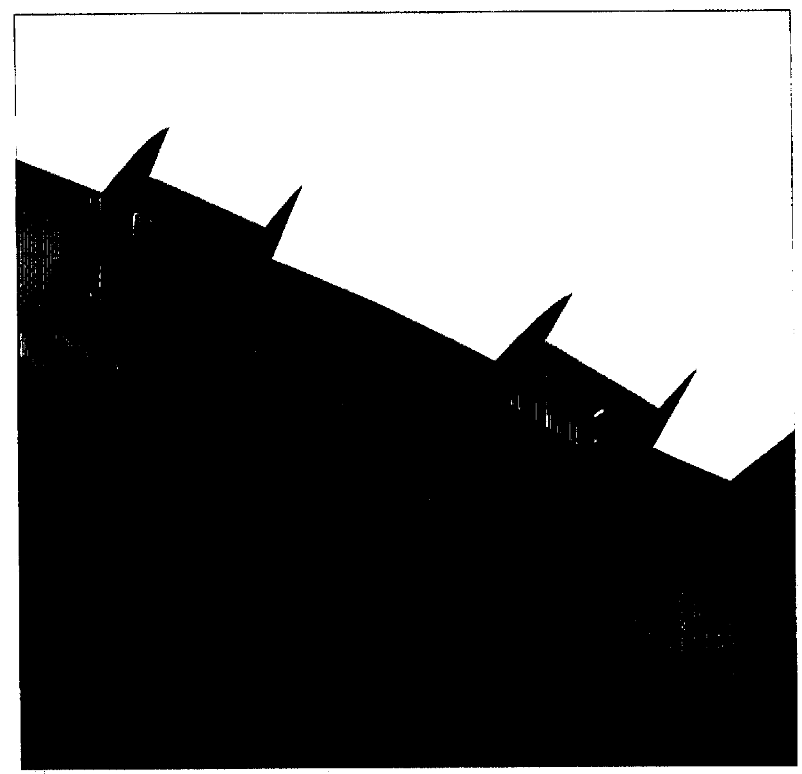

Nozzle Zoom View

Axi and 2-D Isolated Drag Comparisons at Mach 0.9

At Mach 0.90, both IMS and the CFD codes predicted that the pressure drag of the isolated 2-D nozzle would be about 5 drag counts than that of its equivalent axi shape. In general the drag measured in the wind tunnel test was slightly lower than that predicted by IMS. These comparisons will be shown later in this report.

Axi and 2-D Isolated Nozzle Drag Comparisons

Boattail and Sidewall Pressure Drag

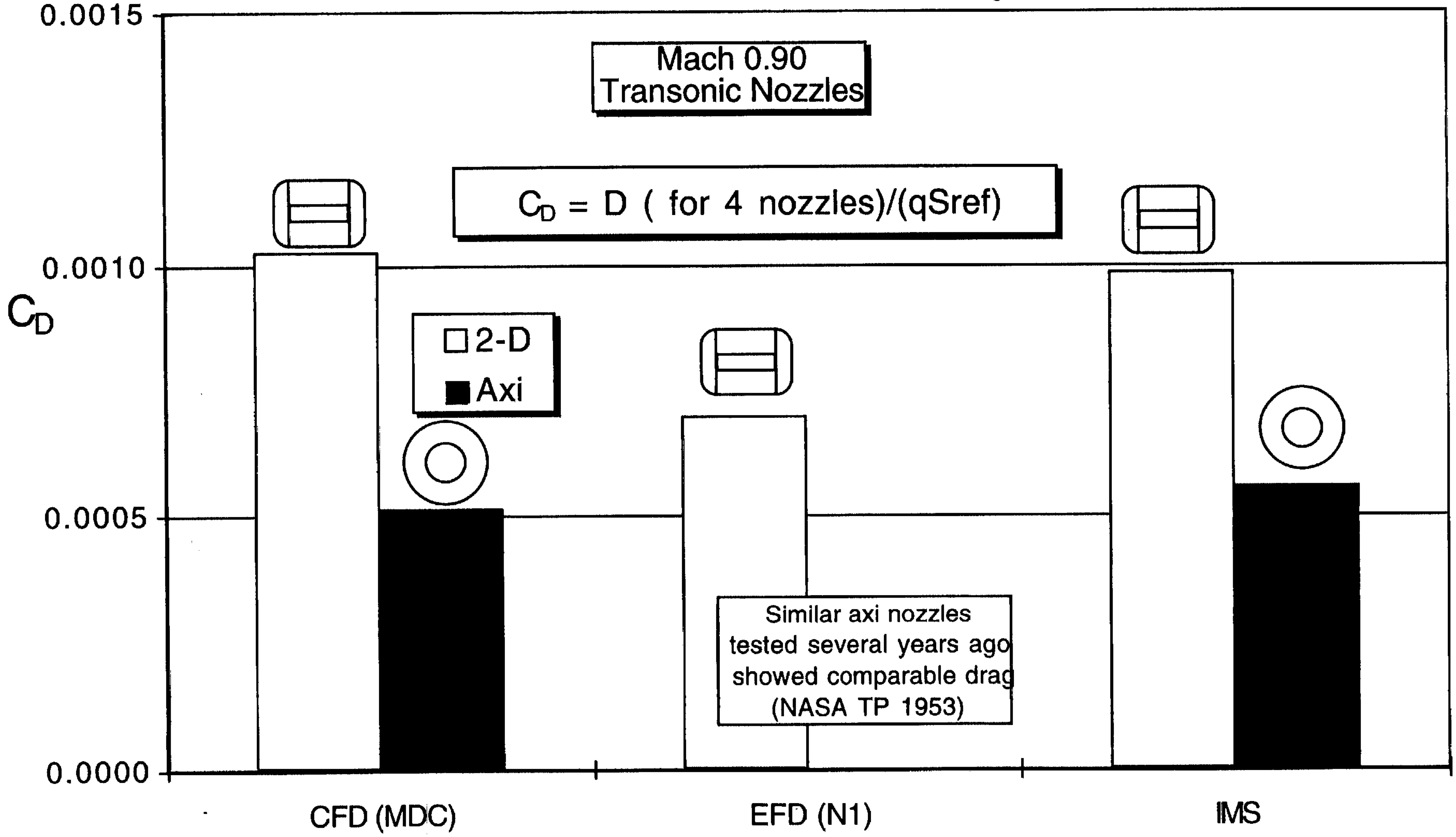

Axi and 2-D Isolated Drag at Mach 1.10

The drag of the 2-D nozzle was also higher than that of the axi nozzle at Mach 1.10.

Axi and 2D Nozzle Drag Comparisons

Boattail and Sidewall Pressure Drag

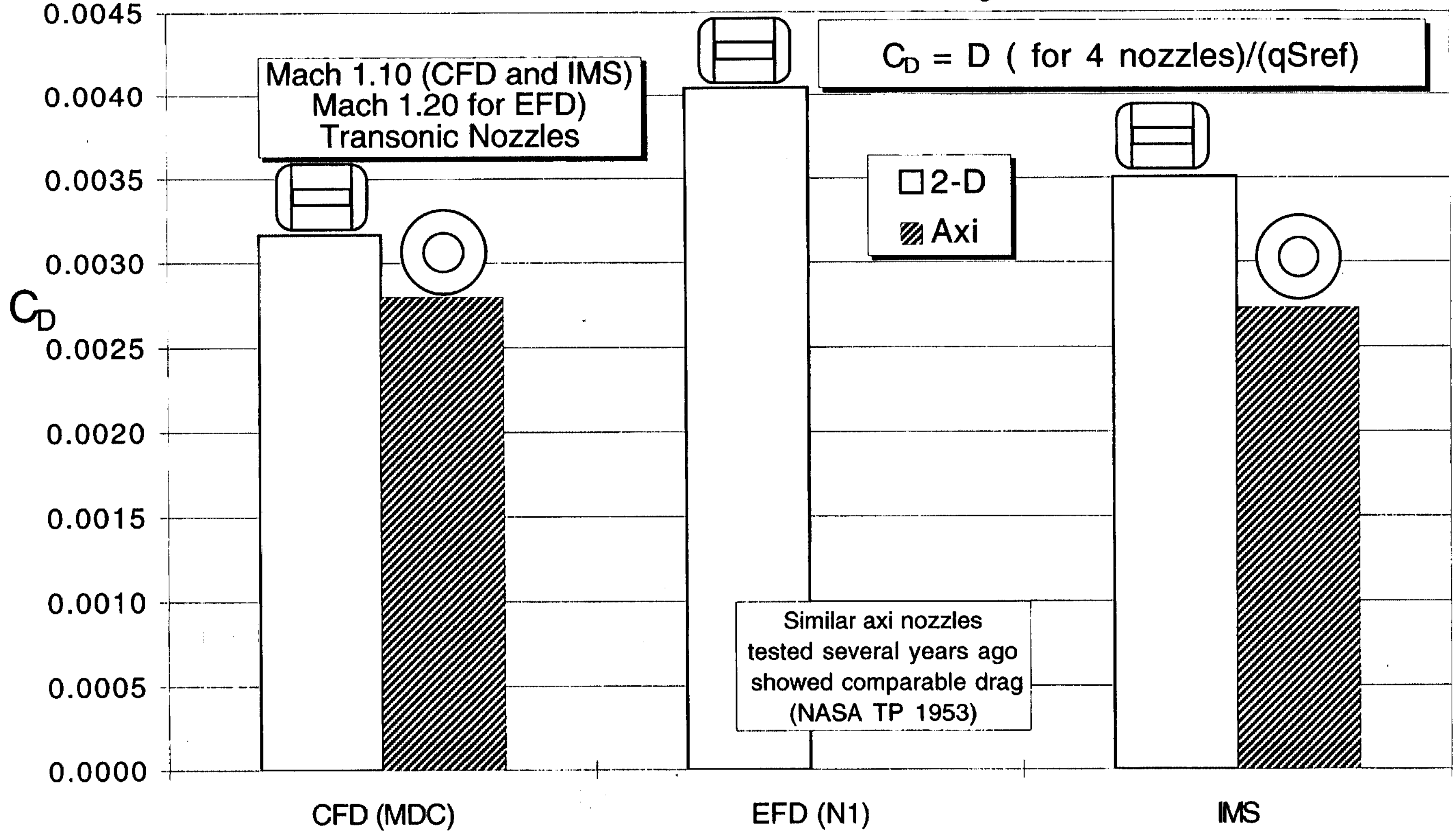

Configuration Aerodynamics Workshop, 25 February 1997

Axi Isolated Drag at Mach 0.90 and 1.10 - Supersonic Geometry

The drag of the axi reference nozzle was very low, as expected, since the boattail angle and aft projected area are small compared to the transonic nozzles. The drag of the 2-D reference nozzles is similar.

CFD and IMS Nozzle Drag Comparisons

Boattail and Sidewall Pressure Drag

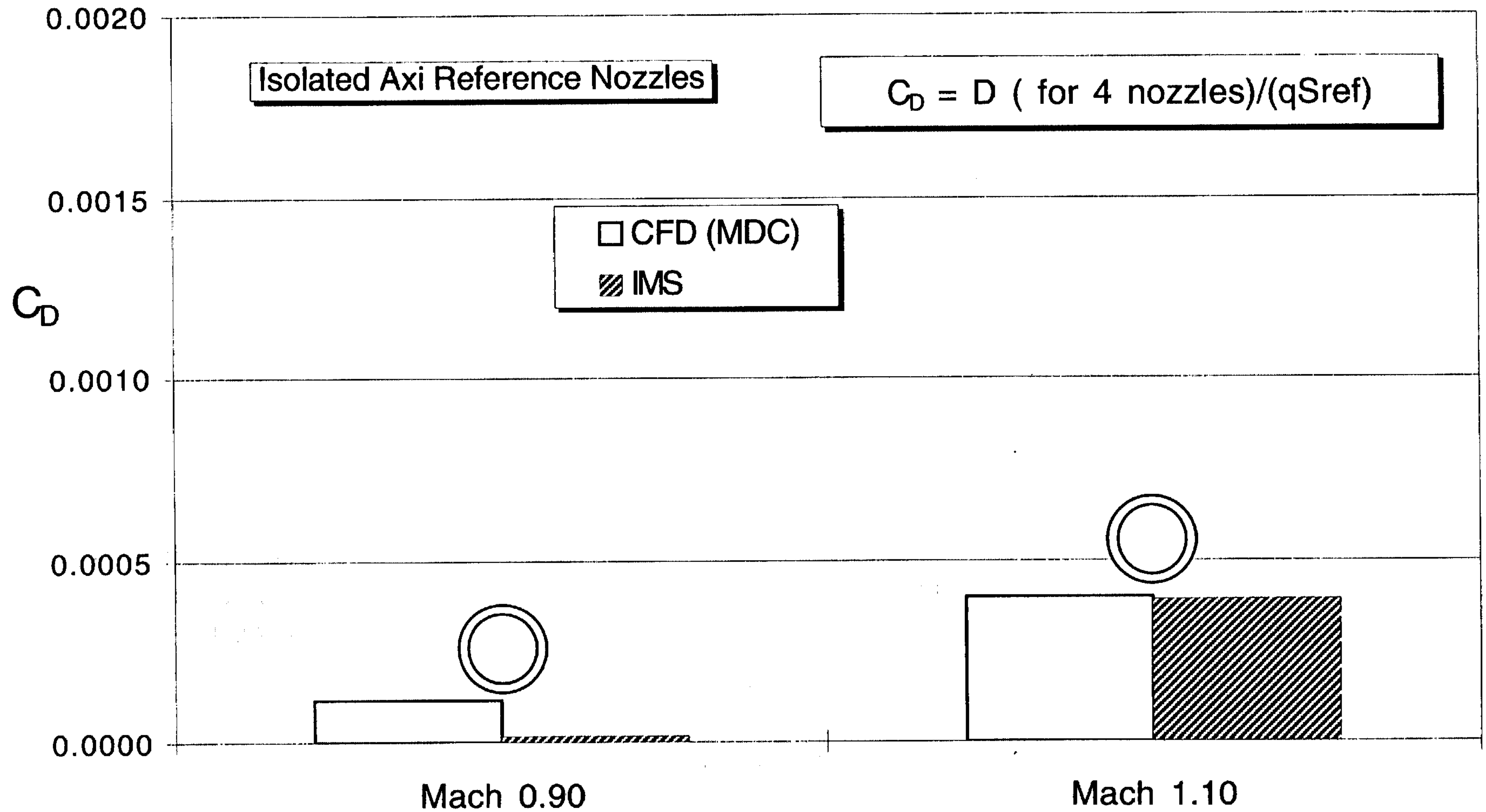

Configuration Aerodynamics Workshop, 25 February 1997

Comparison of CFD Codes for the Isolated 2-D Nozzle Drag

The cross-check for the CFD codes was obtained for the 2-D transonic, isolated nacelles. The drag predicted by CFL3D is about 4 drag counts lower than that of GCNSfv at both Mach numbers.

Nozzle Drag Comparisons between the CFD Codes

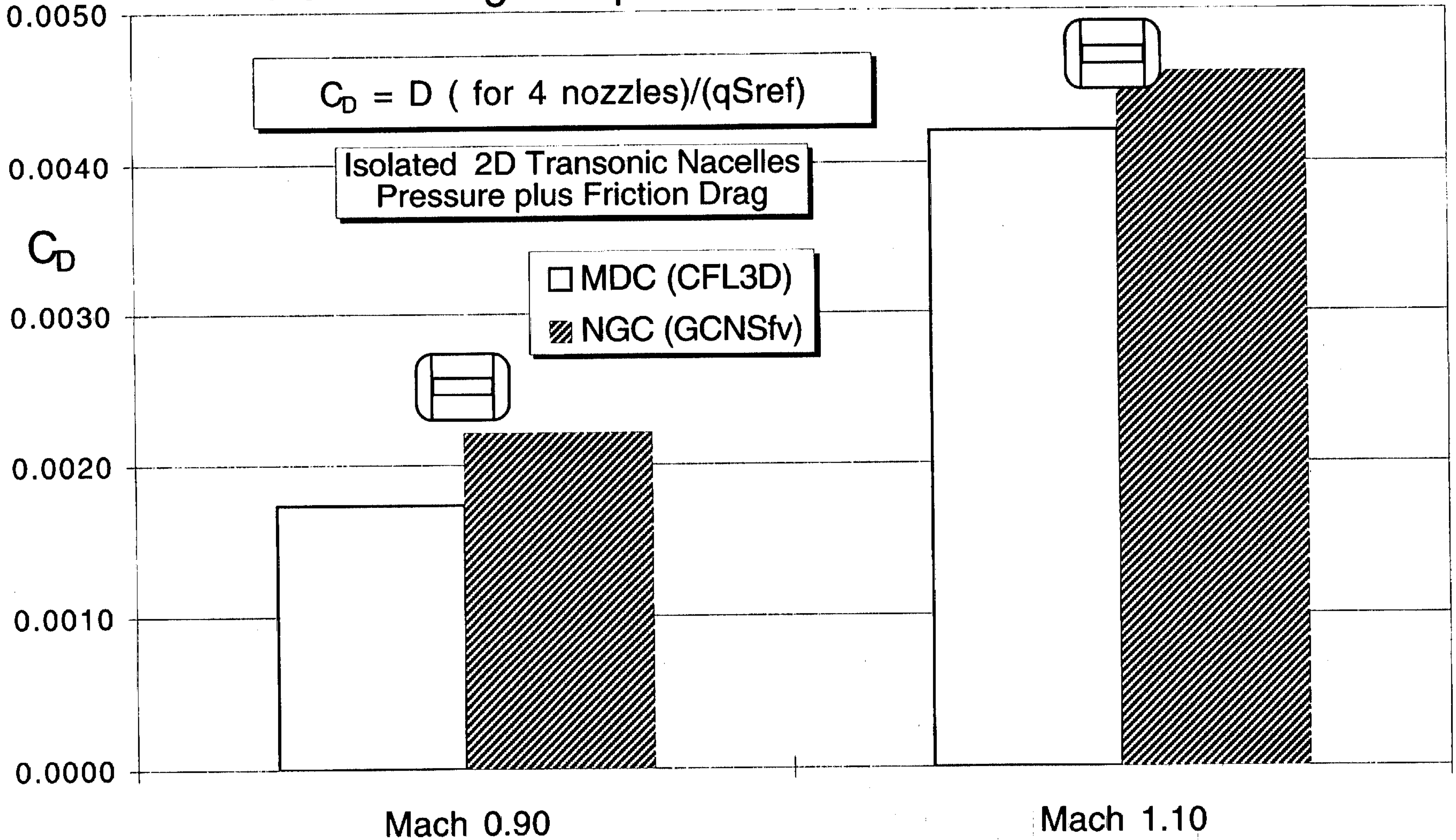

Nacelle Installation Increments, Mach 0.90

Solutions for the full configurations were generally obtained at angles of attack of 2, 4, and 6°. All comparisons at Mach 0.90 are at a constant lift coefficient of 0.190; all comparisons at Mach 1.10 are at a lift coefficient of 0.206. The results were curve-fit with C_D versus C_L^2 and then interpolated to obtain the values that are shown in the following charts. The results for Mach 0.90 are shown above.

Nacelle Installation Increments, 2-D, Mach 0.90

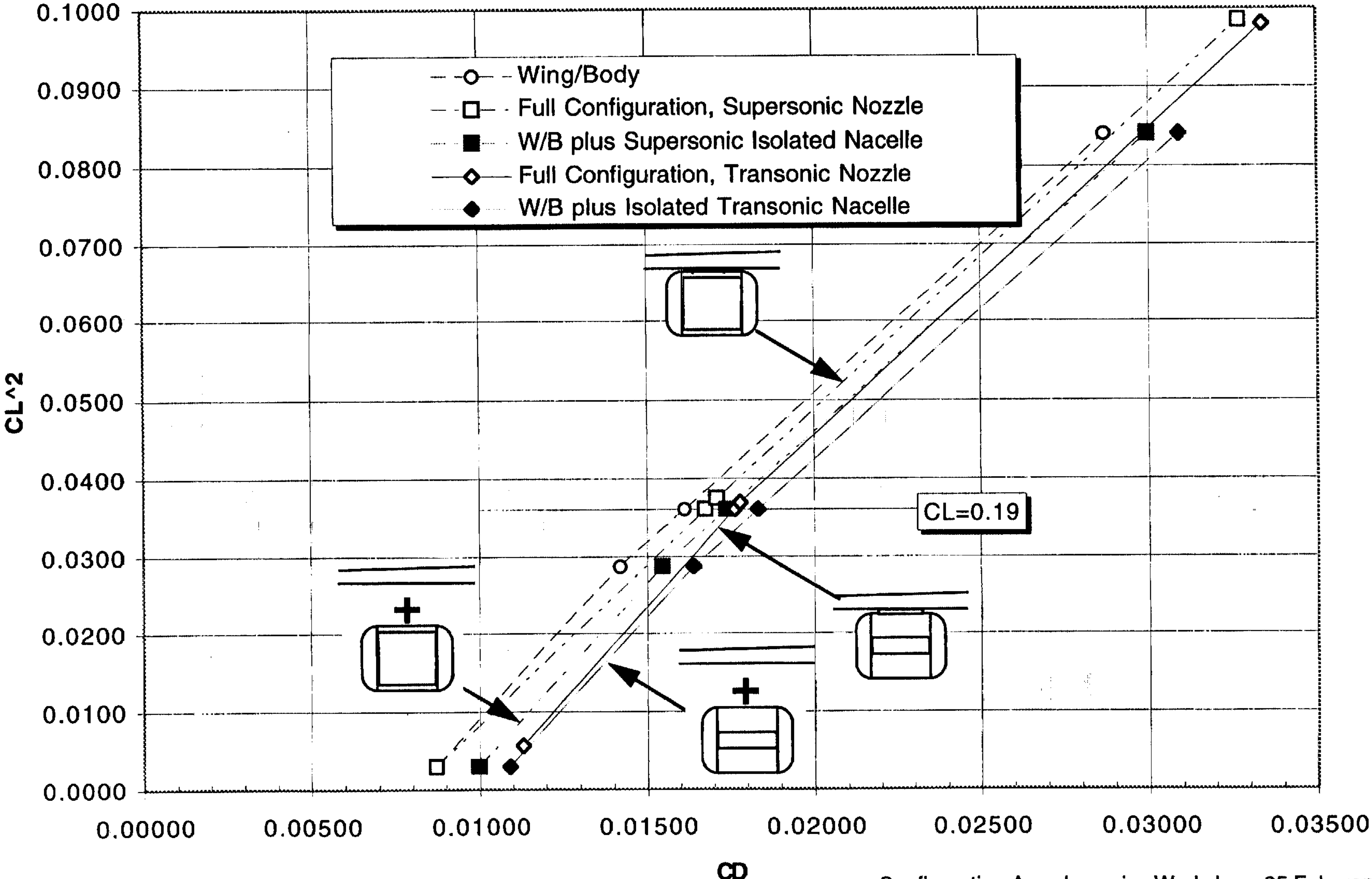

Configuration Aerodynamics Workshop, 25 February 1997

Axi and 2-D Nacelle Interference Drag Comparisons

The interference drag for both the axi and 2-D nozzles was favorable and nearly identical at Mach 0.90. The initial results shown earlier in 1996 indicated that the interference drag for the axi nozzle was about 10 drag counts more favorable than that of the 2-D nozzle. However, the results recently obtained with the refined grid for the axi nozzles indicates that the interference drag is the same for each nozzle type. The results from the wind tunnel test also indicate little difference between the two nozzles. The cause for the smaller amount of interference drag seen on the wind tunnel model is not yet understood. It could be associated with the jet simulation and the truncated fuselage of the wind tunnel model

Axi and 2-D Nacelle Interference Drag Comparisons

Mach 0.90, $C_L = 0.190$

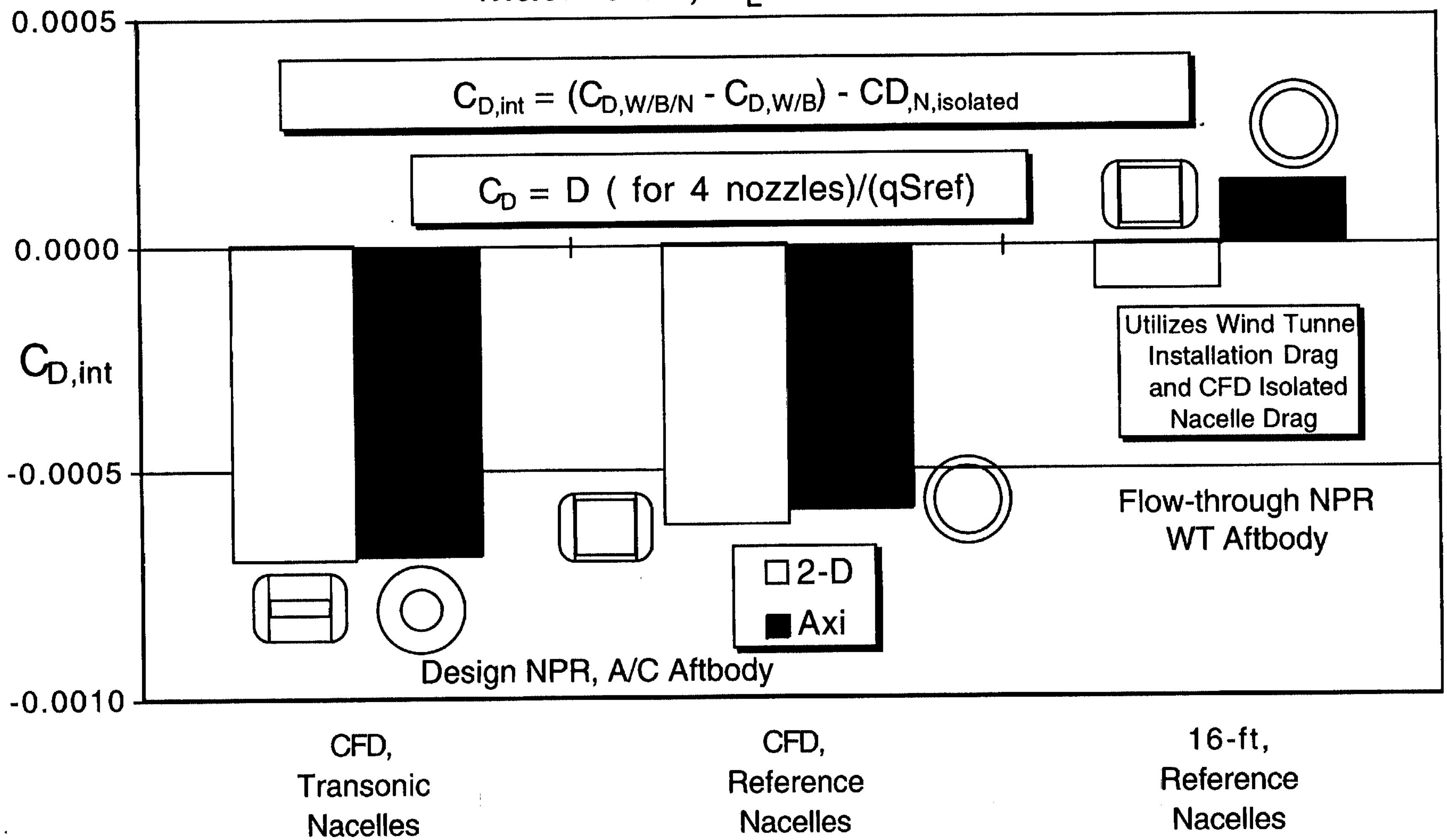

Configuration Aerodynamics Workshop, 25 February 1997

Nacelle Interference Drag Comparisons

The interference drag for both the axi and 2-D nozzles at Mach 1.10 was favorable and of greater magnitude than the interference drag seen at Mach 0.90. These results are essentially the same as the initial results presented earlier in 1996. These results, using the 1995 solution for the installed axisymmetric nozzle, indicate that the interference drag for the axi nozzle may be about 8 drag counts more favorable than that of the 2-D nozzle. It is planned to obtain solutions for the transonic and supersonic axi nozzles at Mach 1.10 with the refined grid. We anticipate that the interference drag for the axisymmeric nacelle may be about the same as that of the 2-D nacelles. The results from the wind tunnel test indicate little difference between the two nozzles. The cause for the smaller amount of interference drag seen on the wind tunnel model is not yet understood. It could be associated with the jet simulation and the truncated fuselage of the wind tunnel model.

Axi and 2D Nacelle Interference Drag Comparisons

Mach 1.10, $C_L = 0.206$

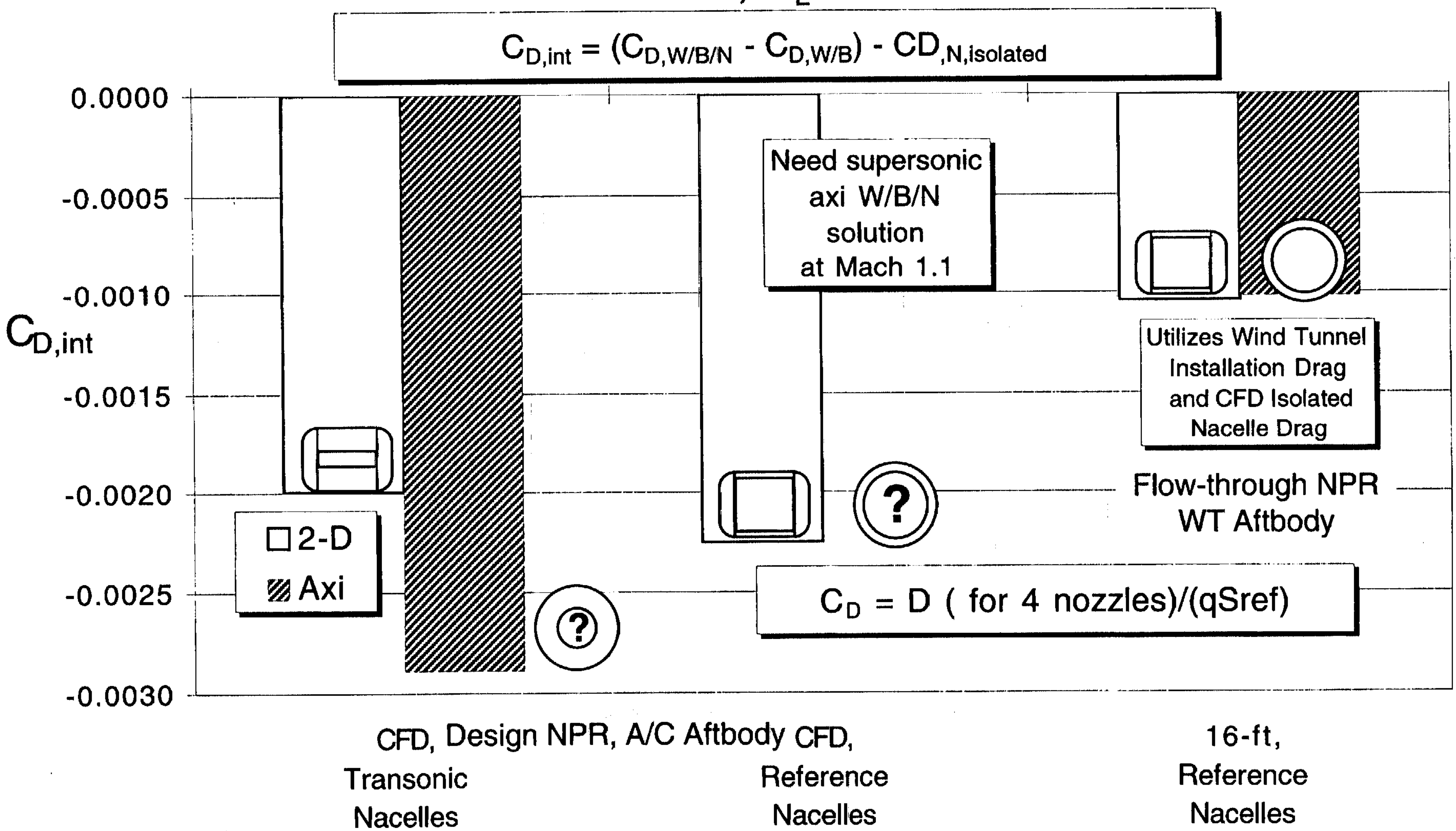

Configuration Aerodynamics Workshop, 25 February 1997

Nacelle Interference Increments, 2-D - Axi

The differences in the interference drag between the 2-D and axi nozzles indicate that aircraft performance studies should be based on similar values at Mach 0.90. At Mach 1.10, the favorable interference increment for the axi is at most 8 drag counts; it may be zero.

Nacelle Interference Increments, 2-D - Axi

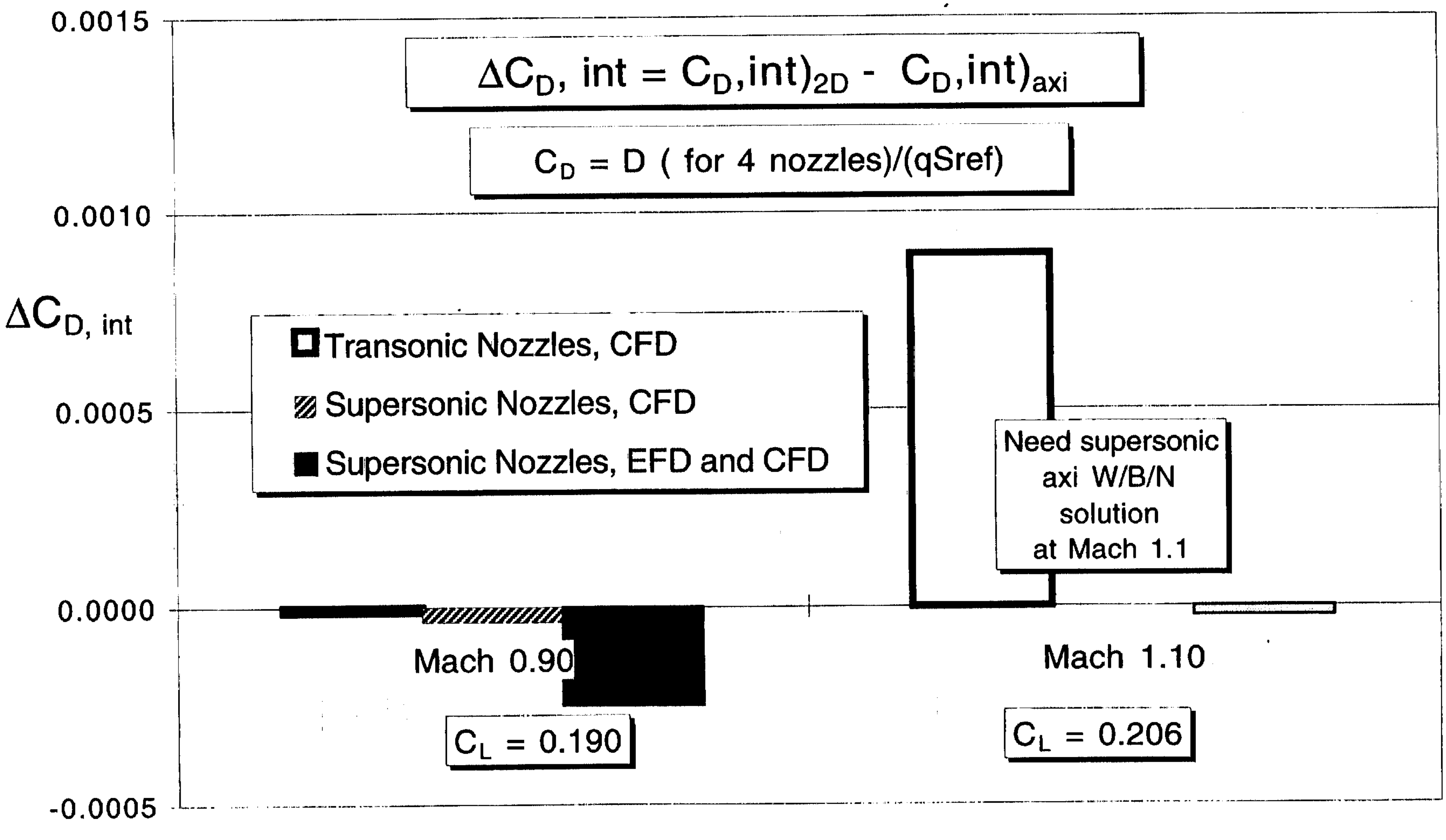

Configuration Aerodynamics Workshop, 25 February 1997

CFD and IMS Jet Effects Drag Comparisons, $M_\infty = 0.9$

The jet effects drag increments at Mach 0.90 also indicate similar levels of interference, as there is little difference between the increment obtained from the full configuration, the isolated nacelles, or even the simple IMS prediction.

CFD and IMS Jet Effects Drag Comparisons

$\Delta C_D = C_D$, transonic nozzle - C_D, reference nozzle

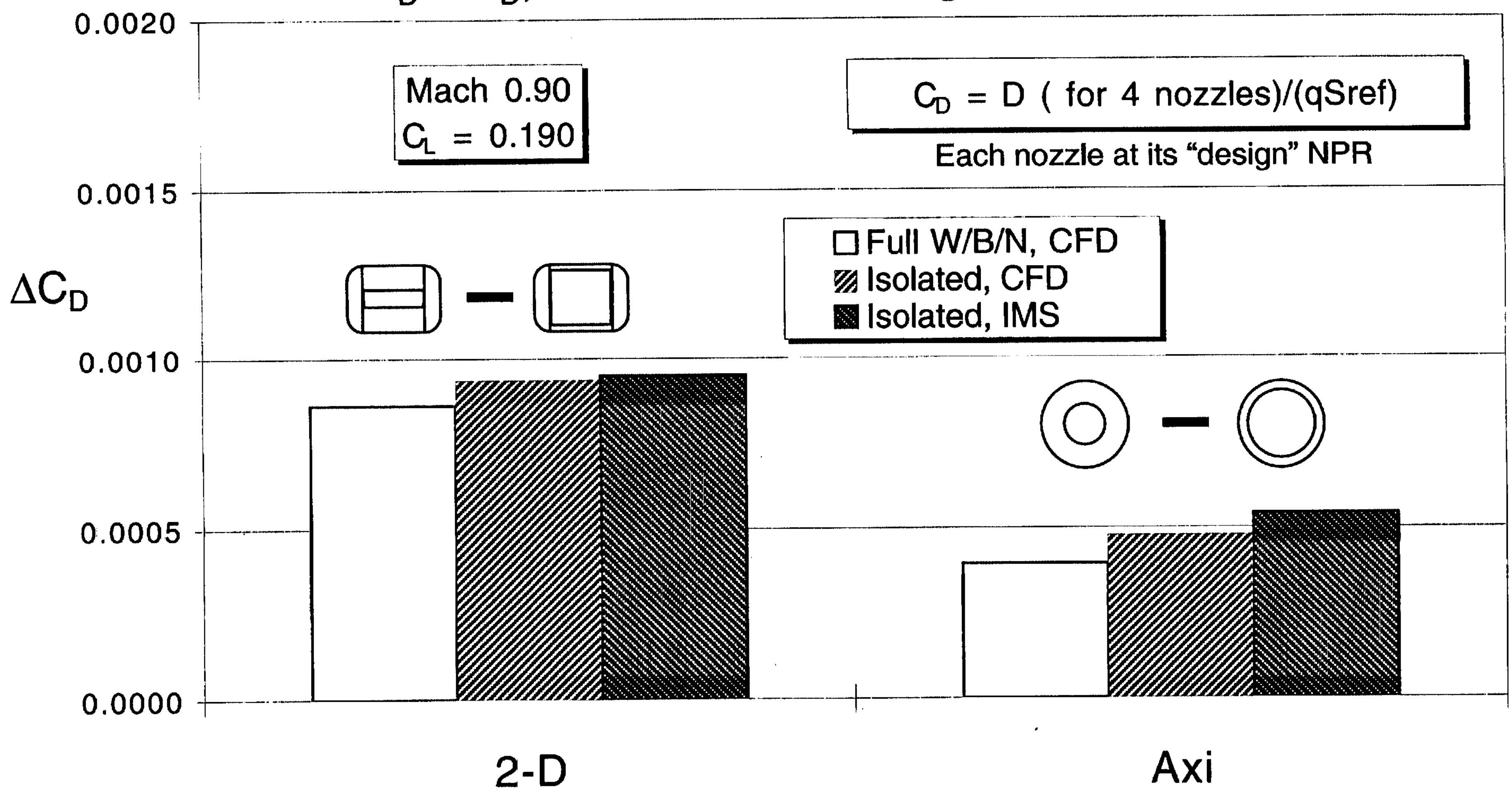

Configuration Aerodynamics Workshop, 25 February 1997

CFD and IMS Jet Effects Drag Comparisons, $M_\infty = 1.1$

The jet effects drag increments at Mach 1.10 also indicate similar levels of interference, as there is little difference between the increment obtained from the full configuration, the isolated nacelles, or even the simple IMS prediction. Note that a solution for the axi reference nozzle at Mach 1.10 is required to complete the evaluation.

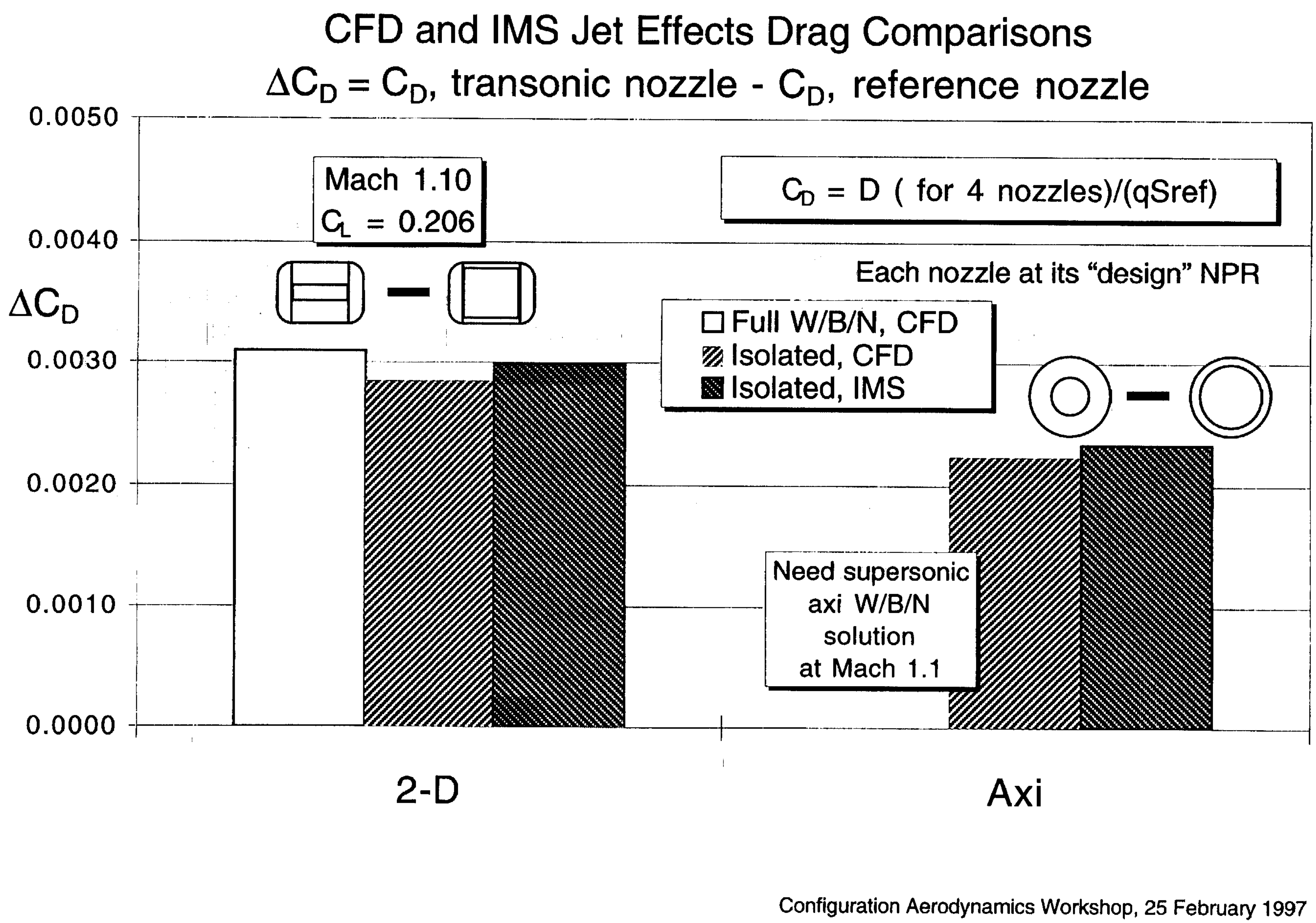

CFD and IMS Jet Effects Drag Comparisons
$\Delta C_D = C_D$, transonic nozzle - C_D, reference nozzle
0.0050
0.0040
0.0030
0.0020
0.0010
0.0000
ΔC_D
Mach 1.10
C_L = 0.206
C_D = D (for 4 nozzles)/(qSref)
Each nozzle at its "design" NPR
Full W/B/N, CFD
Isolated, CFD
Isolated, IMS
Need supersonic
axi W/B/N
solution
at Mach 1.1
2-D
Axi
Configuration Aerodynamics Workshop, 25 February 1997

2-D Fixed Chute Nozzle and Axi Tilt Chute Nozzle at Subsonic Cruise

All of the comparisons between axisymmetric and 2-D nozzles shown in the preceding charts are for the "Best DSM" 2-D nozzle and its axisymmetric equivalent body. Thus, area distributions and projected areas for the axi nozzle would be identical to those of the 2-D nozzle. The intent of the investigation was to evaluate the effect of shape on installed drag. There would, of course, be differences in the geometry of actual nozzle designs. An evaluation of the installed performance of representative 2-D and axisymmetric nozzles is currently being conducted as part of the CPC propulsion system integration studies. The features of these nozzles are illustrated below. The axisymmetric nozzle is longer than the 2-D nozzle to accommodate the acoustic liners. However, none of this additional length can be used to reduce the boattail angle (and IMS) at subsonic or transonic operating conditions. The results of this evaluation are scheduled to be presented at the CPC triannual meeting on 12 March 1997, at Cleveland.

2-D Fixed Chute Nozzle and Axi Tilt Chute Nozzle at Subsonic Cruise

2-D FCN (SAR = 2.9)

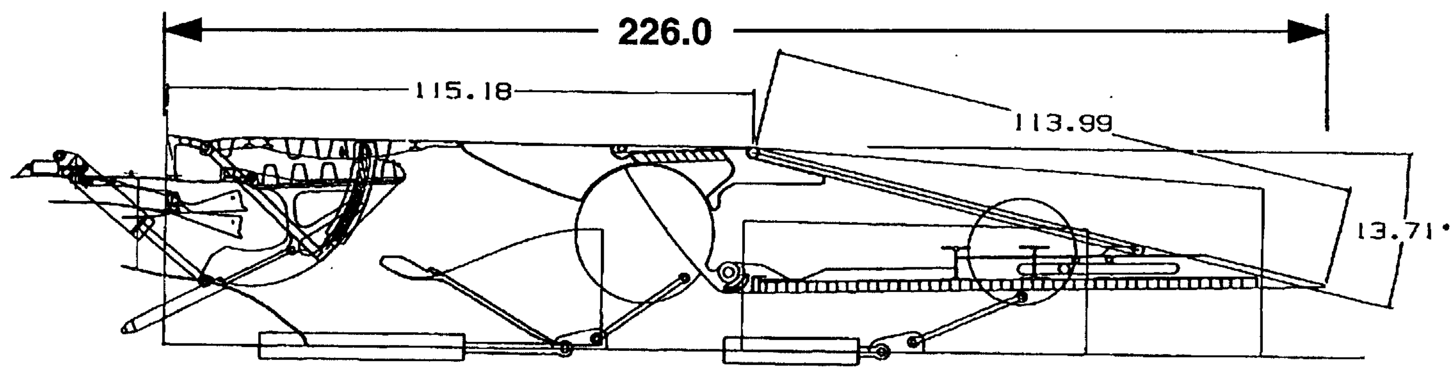

ATC Nozzle (SAR = 3.1)

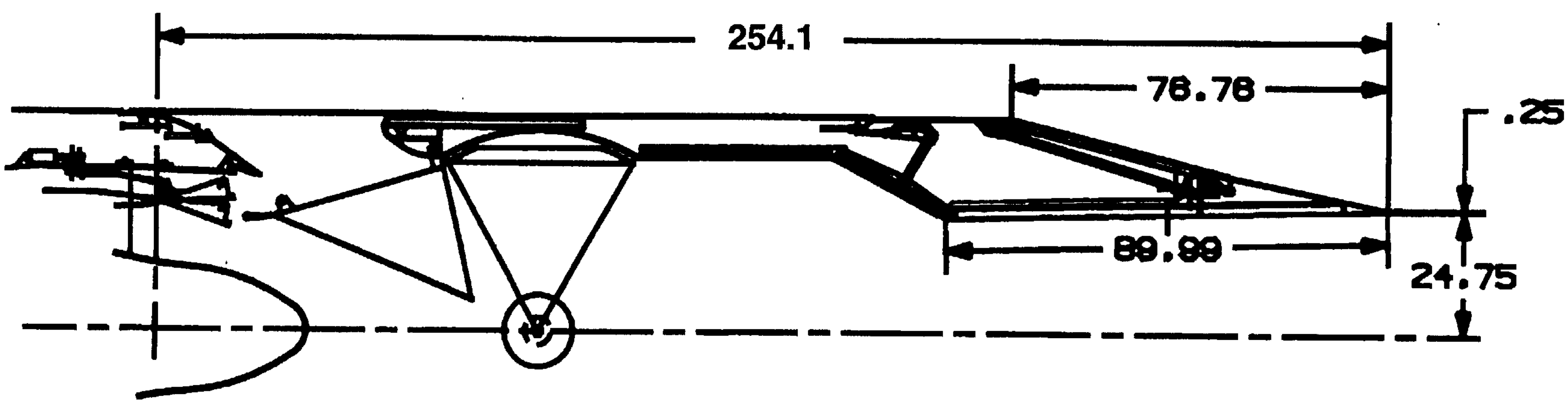

ATC and FCN Comparison (3770.69 cycle)

A comparison of the nozzle design parameters for the current generation axi and 2-D nozzles for the HSR program are summarized. Note that the longer boattail flaps of the 2-D FCN provide a lower value of IMS (and thus a lower average boattail pressure coefficient) than that of the axisymmetric ATC nozzle at transonic conditions. However, the smaller maximum area of the ATC may offset the effect of the longer boattail flap of the 2-D nozzle.

ATC and FCN Comparison (3770.69 cycle)

Parameter		ATC	FCN	Benefit to?
Source	units	Chris Culbertson	GE96-099-N	
Fixed				
SAR		3.1	2.9	
Length	in	254	226	2-D
Hmax	in	87.2	81.48	
Max Width	in	87.2	71.17	
Amax	sq in	5,972	6,823	Axi
Rmax, eq (eq. axi)	in	43.6	46.60	Axi
Subsonic Cruise				
A9 at sub cruise	sq in	1,924.4	1,907.3	
Lext flap @ sub cruise	in	76.76	113.99	
β at sub cruise	deg	13.6	13.71	
Lext flap / Dmax, eq		0.88	1.22	2-D
IMS at sub cruise		0.793	0.665	2-D
Projected area at sub cruise	sq in	4,048	4,916	Axi
A9/Amax at sub cruise		0.322	0.280	Axi
Supersonic Cruise (Reference Nozzle)				
A9 at super cruise	sq in	4,448.5	4,472.3	
IMS at super cruise		0.290	0.298	
Projected area at super cruise	sq in	1,523	2,351	Axi
A9/Amax at super cruise		0.745	0.655	Axi
Nozzle Length	in	252.3	223.7	
Nozzle Surface area, external	sq ft	467	458	2-D

Nozzle Drag Comparison between 2-D FCN and ATC Nozzles

At subsonic cruise, the IMS method predicts slightly higher drag for the ATC than for the FCN. However, at all other conditions, the axi nozzle is predicted to have a pressure drag advantage. There should be little difference in skin friction drag between the two nozzles.

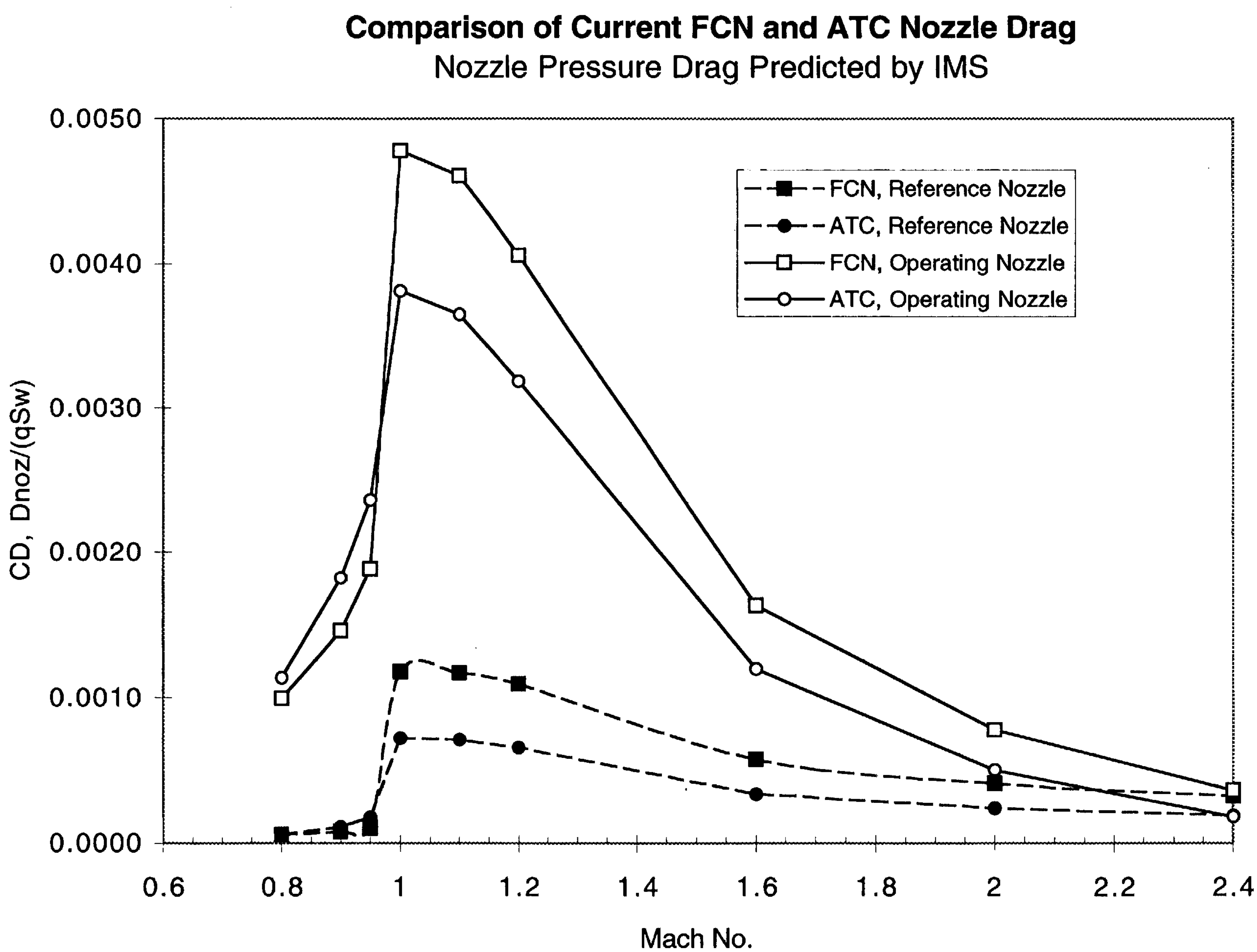

Configuration Aerodynamics Workshop, 25 February 1997

Installed Transonic Nozzle Drag
Status and Current Observations as of 25 February 1997

The study is not yet complete, but there are important observations to be made.

Installed Transonic Nozzle Drag
Status and Current Observations as of 25 February 1997

- Interference drag due to the nacelle/nozzle/diverter installation:
  - Need to reconcile differences between CFD and wind tunnel data
  - Need to complete remaining CFD cases
  - There is little difference between axi and 2-D nozzle interference drag increments at Mach 0.90 or Mach 1.10

- The IMS correlations need to be updated to reflect the parametric data from the NASA - Langley 16-Ft Transonic Tunnel Test 477
  - Shoulder radius effects
  - Sidewall fence effects
  - Jet effects (off-design NPR)

- There is only a small advantage for an <u>isolated</u> axi nozzle if:
  - the boattail flaps are sufficiently long to keep the boattail angles less than $\approx 12°$
  - the maximum nacelle area for the 2-D nozzle is similar to that of the axi (most of the drag differences are due to area or volume, not nozzle shape)

Uncertainties in HSCT Cruise Drag Prediction

Shreekant Agrawal, Michael G.B. Novean, Geojoe Kuruvila, and Robert P. Narducci
McDonnell Douglas Corporation
Long Beach, California 90807-5309

Within the High Speed Research (HSR) program, NASA and Industry are jointly developing various technologies so that the U.S. Industry has the capability to launch the High Speed Civil Transport (HSCT) aircraft development in early 2000. One of the primary objectives of the HSR program is to be able to predict the cruise aerodynamic performance of the HSCT configurations with a sufficiently high confidence level that will aide Industry in the decision to proceed with the development of the aircraft and guarantee its performance to its airline customers.

This paper addresses the current status in the prediction of drag at primarily the supersonic cruise Mach number (M = 2.4), however, drag at the transonic cruise Mach number (M = 0.9) is also presented, wherever appropriate. The thrust of this paper is the uncertainty (or the confidence level) in drag prediction. Use is made of the available experimental, linear and nonlinear computational, and empirical database to the McDonnell Douglas Corporation (MDC). In some cases, there is sufficient database; in some other cases, there is very little database; and yet in some other cases, there is none available. However, an attempt is made to see where we stand today in the cruise drag prediction, although it is difficult to determine uncertainty levels in all the elements contributing to drag. Please note that the uncertainty levels discussed here are the views of the researchers at MDC only, and they may not represent those at other organizations.

Uncertainties in HSCT Cruise Drag Prediction

Shreekant Agrawal
Michael G.B. Novean
Geojoe Kuruvila
Robert P. Narducci

McDonnell Douglas Corporation
Long Beach, California

NASA/Industry HSR Aerodynamics Performance Workshop
February 25-28, 1997
NASA Langley Research Center, Hampton, VA

What is Uncertainty?

The definition of uncertainty is defined as the lack of certainty or confidence level.

What is Uncertainty?

- Lack of certainty (confidence level)
- Not having sure knowledge

Contributing Factors in HSCT Cruise Performance Prediction

There are many factors that need to be considered in the aerodynamic performance prediction. Lift, drag, and pitching moment predictions for the entire vehicle are the main challenges. Usually the database is not available for the entire vehicle, hence a build-up from available data is performed. In such build-ups, one needs to consider the various components of the vehicle geometry as well as effects of Reynolds number, aeroelastics, and various excrescences. Additionally, predictive computational tools need to be validated for accuracy. Not to mention, the wind-tunnel test data and corrections in the test data need to be accurate.

The items with an asterisk (*) indicate those to be addressed in this paper.

Contributing Factors in HSCT Cruise Performance Prediction

- Drag (pressure and viscous) *
- Trip drag *
- Pressure distribution *
- Nacelle installation effects *
- Nozzle boattail drag *
- Fuselage aftbody closure drag
- Excrescence drag
- Wind-tunnel data corrections
- ...

- Lift
- Pitching moment
- Empennage effects/trim drag
- Aeroelastic effects *
- Reynolds number effects *
- Flap deflection effects
- Inlet bleed, bypass, spillage effects
- Advanced computational methods
- ...

* Discussed in this paper

Outline

An outline of the presentation is shown. Uncertainties in only the drag prediction will be discussed first. Then, overall uncertainties in drag prediction will be followed by the drag build-up for the HSR Technology Concept Airplane (TCA) configuration. Finally, the conclusions will be summarized.

Outline

- Uncertainty in prediction (primarily at $M = 2.4$) of
  - Drag (total, pressure, viscous)
  - Trip drag
  - Pressure distributions
  - Nacelle installation drag
  - Isolated nozzle boattail drag
  - Aeroelastic effects
  - Reynolds number effects
- Overall uncertainties in drag prediction
- TCA full configuration drag build-up
- Summary and conclusions

Comparison of Predicted and Experimental Drag Polars TCA Wing/Body and Wing/Body/Nacelle/Diverter Configurations

The predicted drag polars for both configurations at $M_\infty=2.4$ are compared to the experimental data in this figure. A trip drag correction that varies with angle-of-attack (this will be explained later in the paper) has been applied to the experimental data. For the Euler calculations, viscous skin-friction drag penalties of 61.06 counts and 70.2 counts have been applied to the wing/body and wing/body/nacelle/diverter configurations, respectively. For both configurations, the Navier-Stokes solutions slightly over-predict the drag at the minimum drag condition. In the Euler solution, the over prediction at minimum drag is just over two counts for the wing/body/nacelle/diverter configuration and around three counts for the wing/body configuration. At cruise, the Navier-Stokes predictions are roughly three counts too high for both configurations while the Euler predictions are approximately 5.0 counts too high for the wing/body configuration and 4.0 counts too high for the wing/body/nacelle/diverter configuration.

Comparison of Predicted and Experimental Drag Polars
TCA Wing/Body and Wing/Body/Nacelle/Diverter Configurations

Langley Test 1671, UPWT-2, M_∞=2.4, Re_c=6.36x10^6, Trip Drag Removed

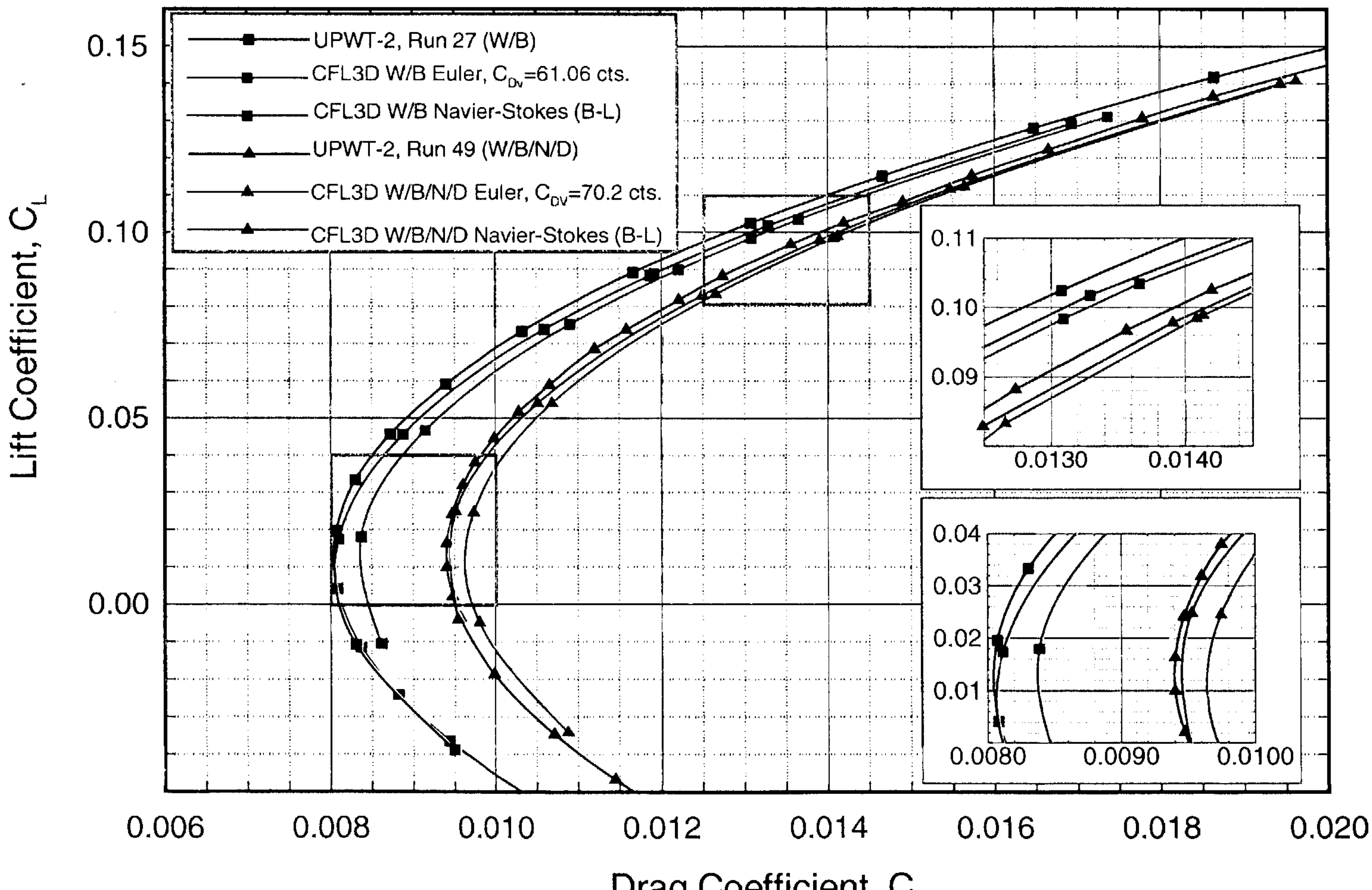

MN 2/13/97

Trip Drag Assessment

Supersonic wind-tunnel conditions are such that the flow over HSCT models is inherently part laminar and part turbulent. In order to more accurately simulate the large regions of turbulent flow present at flight conditions, thin circular disks are used to trip the boundary layer. These disks are placed along the upper and lower wing surfaces, around the inner and outer surfaces of the nacelles, and around the fuselage forebody. The trips, while effective in tripping the boundary layer, change the configuration of the model and hence affect the drag polar. Here, we attempt to estimate the impact on drag incurred due to the presence of transition disks. The objective of this assessment is to estimate a correction to be applied to the drag measurements so that the drag data represents a fully turbulent boundary layer flow (beyond a set transition line determined by the placement of the disks). The assessment is made using W/B data. The estimate for the W/B/N/D configuration is made by multiplying 1.5 to the W/B correction. This represents the number of additional disks required on the W/B/N/D configuration for tripping the boundary layer on the nacelles.

Procedures to determine the drag associated with transition disks continue to be an area of interest to the HSR community. Efforts are continuing in this field but data repeatability and inability to conduct tests at sufficiently high Reynolds numbers to transition the boundary layer without disks makes the assessment a formidable task. The procedure described below represents the current understanding to assess trip drag behavior:

1.) Obtain lift and drag data for several disk heights, insuring that each disk height transitions the boundary layer at the appropriate location.
2.) Average the drag polars over all repeated runs for each trip height. Each individual run is carefully fitted and then averaged to obtain one representative polar for each trip height. The fit must be of extremely high fidelity; errors on the order of tenths of a count in the fit can lead to a several count error in the trip drag.
3.) Plot drag versus trip height at constant lift for the entire range of lift. An extrapolation of this data to a trip height of zero will yield the drag of the TCA model with a fully turbulent boundary layer (beyond a set transition line) without the effects of the trip dots. The trip drag correction to the data is the difference between the drag at the given height and the extrapolated value at a trip height of zero.

Trip Drag Assessment

- Problem:
  - Current supersonic wind tunnels do not produce fully turbulent flow, hence trips are required
- Objective:
  - Assess the drag impact due to the presence of transition trips
- Procedure:
  - Obtain drag polars for several trip heights, each tripping the flow
  - Plot drag versus trip height, k, at constant lift
  - Extrapolate data at k=0
- Assumptions:
  - Each trip height transitions the flow at the same location

Trip Drag Assessment Procedure

In step 3 of the procedure outline previously, the method of extrapolation to a zero trip height has been a topic of much debate within the HSR community. Arguments have been made supporting a quadratic fit of the form

$$C_D = C_0 + C_1 k^2, \tag{1}$$

where k is the trip height and C_0 and C_1 are the curve fit coefficients. Likewise, arguments have been made supporting a linear fit of the form

$$C_D = C_0 + C_1 k. \tag{2}$$

It has been suggested that the function ought to behave as (1) below some critical trip height, k_{cr}, and above which the dependence is as (2). Regardless, one must remember that extrapolation is very dangerous

> "... the dangers of extrapolation cannot be over emphasized: An interpolating function, which is perforce an extrapolating function, will typically go berserk when the argument x is outside the range of tabulated values by more than the typical spacing of tabulated points."[1]

Here the typical spacing of our data is 0.002" and the distance of our extrapolation is 6 times this! The argument of which extrapolation polynomial to use may be secondary if one considers the large errors that are produced from the extrapolation.

Any source of error will be magnified in the extrapolation. Sources of error come from the variance of the trip heights and the uncertainty of the drag data. During HSR tunnel tests, the variance of the trip heights is typically ±0.00025". The uncertainty in the drag data is with ±0.25 cts.

With the current set of data available, it seems reasonable to assume that the trip drag correction will be banded between the estimates obtained using the extrapolation polynomials (1) and (2). For this reason and for lack of additional data, the trip drag estimate is obtained using an average of the extrapolating polynomials. Only with large numbers of repeat runs and trip heights can the errors of extrapolation be significantly reduced.

1.) Press, W.H., Teukolsky, S.A., Vetterling, W.T., and Flannery,B.P., Numerical Recipes in FORTRAN; the Art of Scientific Computing, Cambridge University Press, New York, 1992.

Trip Drag Assessment Procedure

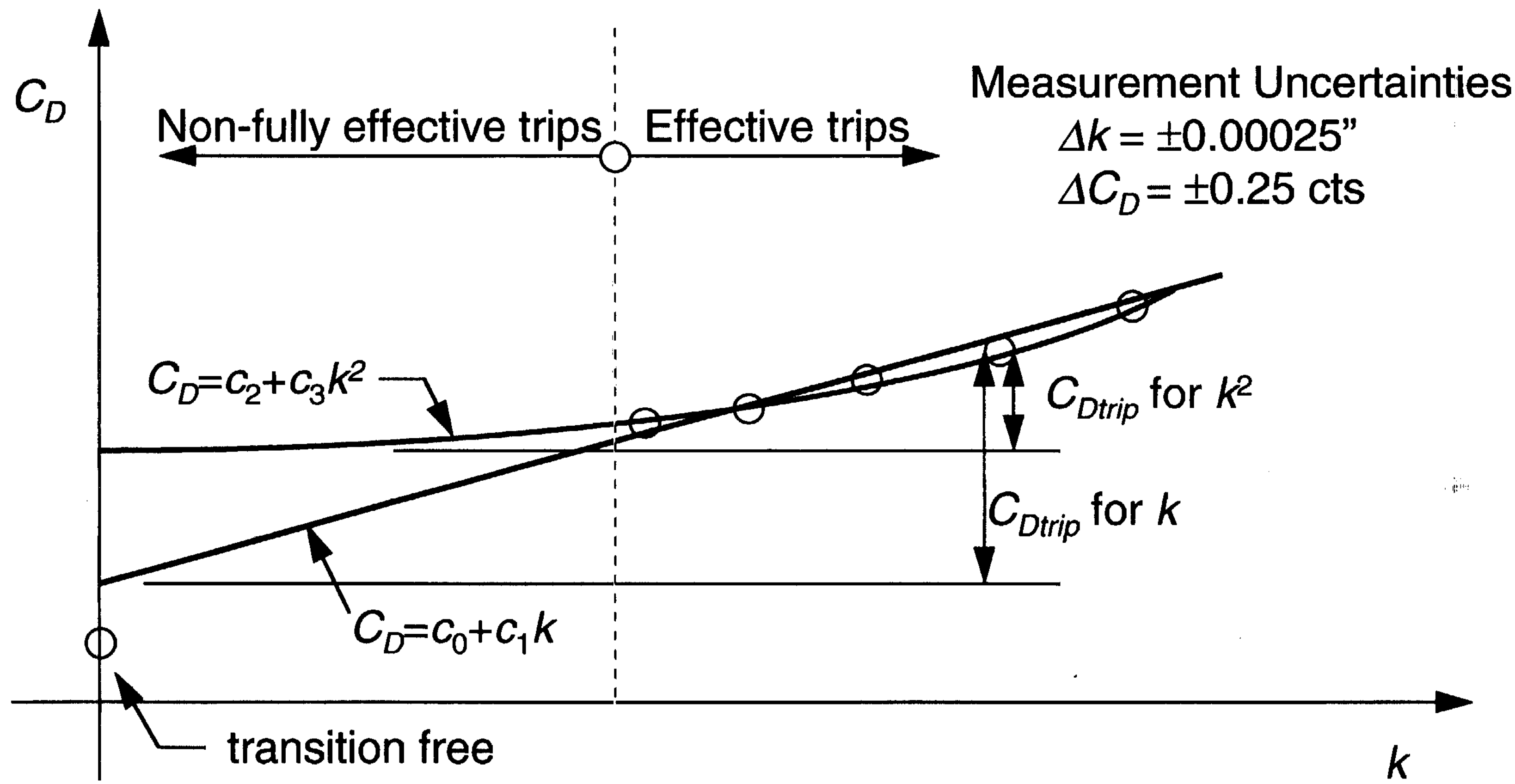

Uncertainty in Trip Drag Measurement

By way of the Method of Equal Effects, whereby we assume the source of error from uncertainties in the trip height and drag measurement are equal, the total error can be estimated by

$$\Delta C_{D\,trip} = \sum_i \left| \frac{\partial f}{\partial c_i} \Delta c_i \right| + \left| \frac{\partial f}{\partial k} \Delta k \right|, \tag{3}$$

where f is the polynomial extrapolation function, and c_i are its coefficients obtained from a least-squares fit to the drag data. The uncertainties in the evaluation of these coefficients can be estimated, again by using the Method of Equal Effects, with

$$\Delta c_i = \left| \frac{\partial g}{\partial k_1} \Delta k_1 \right| + \left| \frac{\partial g}{\partial k_2} \Delta k_2 \right| + \left| \frac{\partial g}{\partial k_3} \Delta k_3 \right| + \left| \frac{\partial g}{\partial C_{D_1}} \Delta C_{D_1} \right| + \left| \frac{\partial g}{\partial C_{D_2}} \Delta C_{D_2} \right| + \left| \frac{\partial g}{\partial C_{D_3}} \Delta C_{D_3} \right|,$$

where g is the mathematical process to determine the coefficients, which in principle can be expressed as

$$c_i = g(k_1, k_2, k_3, C_{D_1}, C_{D_2}, C_{D_3}).$$

Here, we see the dependence on the uncertainties in the trip height and drag measurements.

Uncertainty in Trip Drag Measurement

Assume $C_{Dtrip}=f(c_i,k_1)$. The uncertainty in $C_{D\,trip}$ can be estimated as

$$\Delta C_{D\,trip} = \sum_i \left|\frac{\partial f}{\partial c_i}\Delta c_i\right| + \left|\frac{\partial f}{\partial k}\Delta k\right|.$$

c_i are coefficients, obtained in a least-squares fit,

$$c_i = g(k_1, k_2, k_3, C_{D1}, C_{D2}, C_{D3})$$

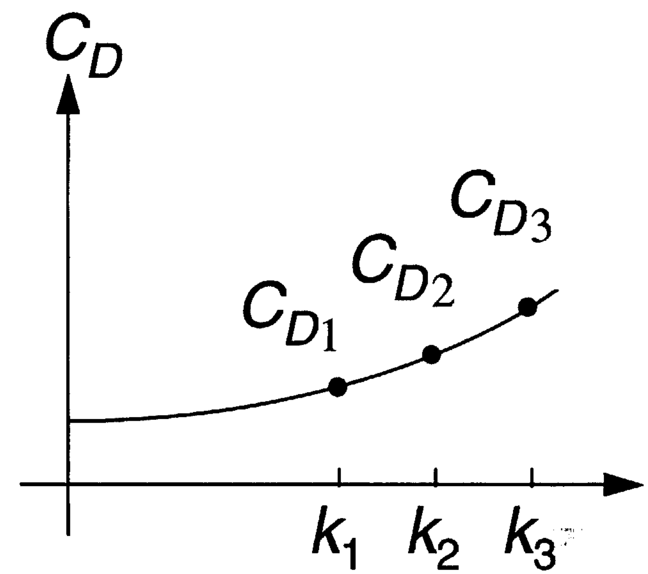

Its uncertainty can be estimated as

$$\Delta c_i = \left|\frac{\partial g}{\partial k_1}\Delta k_1\right| + \left|\frac{\partial g}{\partial k_2}\Delta k_2\right| + \left|\frac{\partial g}{\partial k_3}\Delta k_3\right| + \left|\frac{\partial g}{\partial C_{D1}}\Delta C_{D1}\right| + \left|\frac{\partial g}{\partial C_{D2}}\Delta C_{D2}\right| + \left|\frac{\partial g}{\partial C_{D3}}\Delta C_{D3}\right|$$

Trip Drag Study, Drag Polars
1.675% TCA Baseline Model, W/B Configuration

The drag polars shown below represent all the data used in the determination of the trip drag for the TCA W/B configuration at the M_∞=2.4 condition during UPWT section 2, test 1671. The various colors used in the plot represent different trip heights tested, including the transition free runs. The curve fit applied to the runs is shown in black. The polars are essentially quadratic, however higher order polynomials are needed to fit the data accurately. Between a C_L of -0.1 and 0.12, a fifth-order polynomial was used to fit the data. A second interpolating polynomial of order three was used for C_L values greater than 0.12. Each experimental run was fitted independently. The black line through the data points represents an average to all the data of a particular trip height. As can be seen in the expanded views of the polar near minimum drag and just above cruise, the fits lie within the scatter of the data.

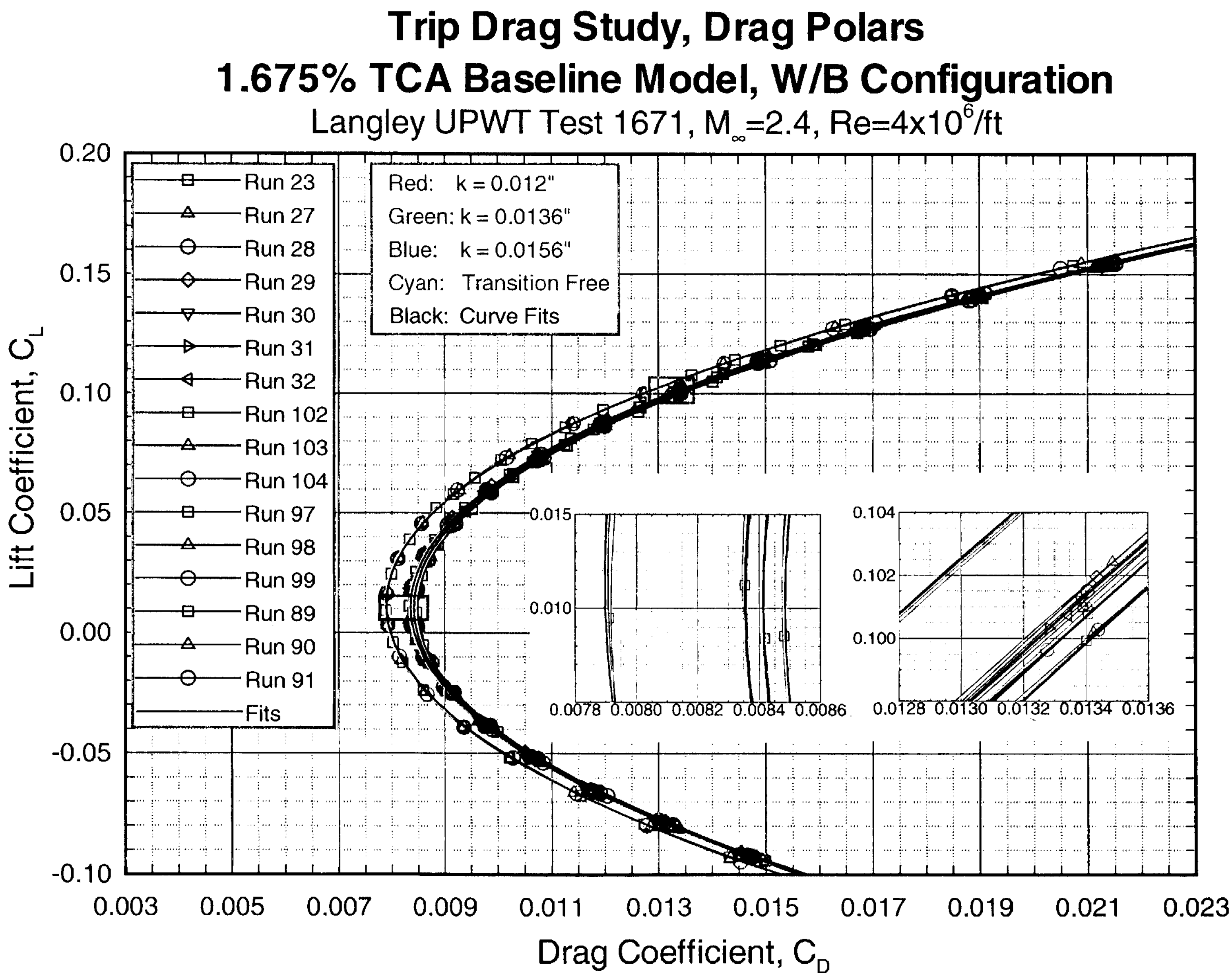

Trip Drag Study, Drag Polars
1.675% TCA Baseline Model, W/B Configuration
Langley UPWT Test 1671, M∞=2.4, Re=4x10^6/ft
Run 23
Run 27
Run 28
Run 29
Run 30
Run 31
Run 32
Run 102
Run 103
Run 104
Run 97
Run 98
Run 99
Run 89
Run 90
Run 91
Fits
Red: k = 0.012"
Green: k = 0.0136"
Blue: k = 0.0156"
Cyan: Transition Free
Black: Curve Fits
Lift Coefficient, CL
Drag Coefficient, CD
0.20
0.15
0.10
0.05
0.00
-0.05
-0.10
0.003
0.005
0.007
0.009
0.011
0.013
0.015
0.017
0.019
0.021
0.023
0.015
0.010
0.0078 0.0080 0.0082 0.0084 0.0086
0.104
0.102
0.100
0.0128 0.0130 0.0132 0.0134 0.0136

Trip Drag Study, Extrapolation to k=0"
1.675% TCA Baseline Model, W/B Configuration

The figure below shows the fitted drag data obtained from the previous plot as a function of trip height at four representative values of C_L. Included on the plot is the transition free data. The extrapolation to a trip height of zero is performed using both the linear and quadratic polynomials. The linear fit at the higher C_L drops below the transition free data points at k=0" suggesting that the extrapolation is inaccurate. Physically, this would mean a turbulent boundary layer produces less drag on the TCA than a partially turbulent/partially laminar one. Yet one can expect this when the extrapolation is highly sensitive to errors.

Trip Drag Study, Extrapolation to k=0"

1.675% TCA Baseline Model, W/B Configuration

Langley UPWT Test 1671, M_∞=2.4, Re=4x10^6/ft

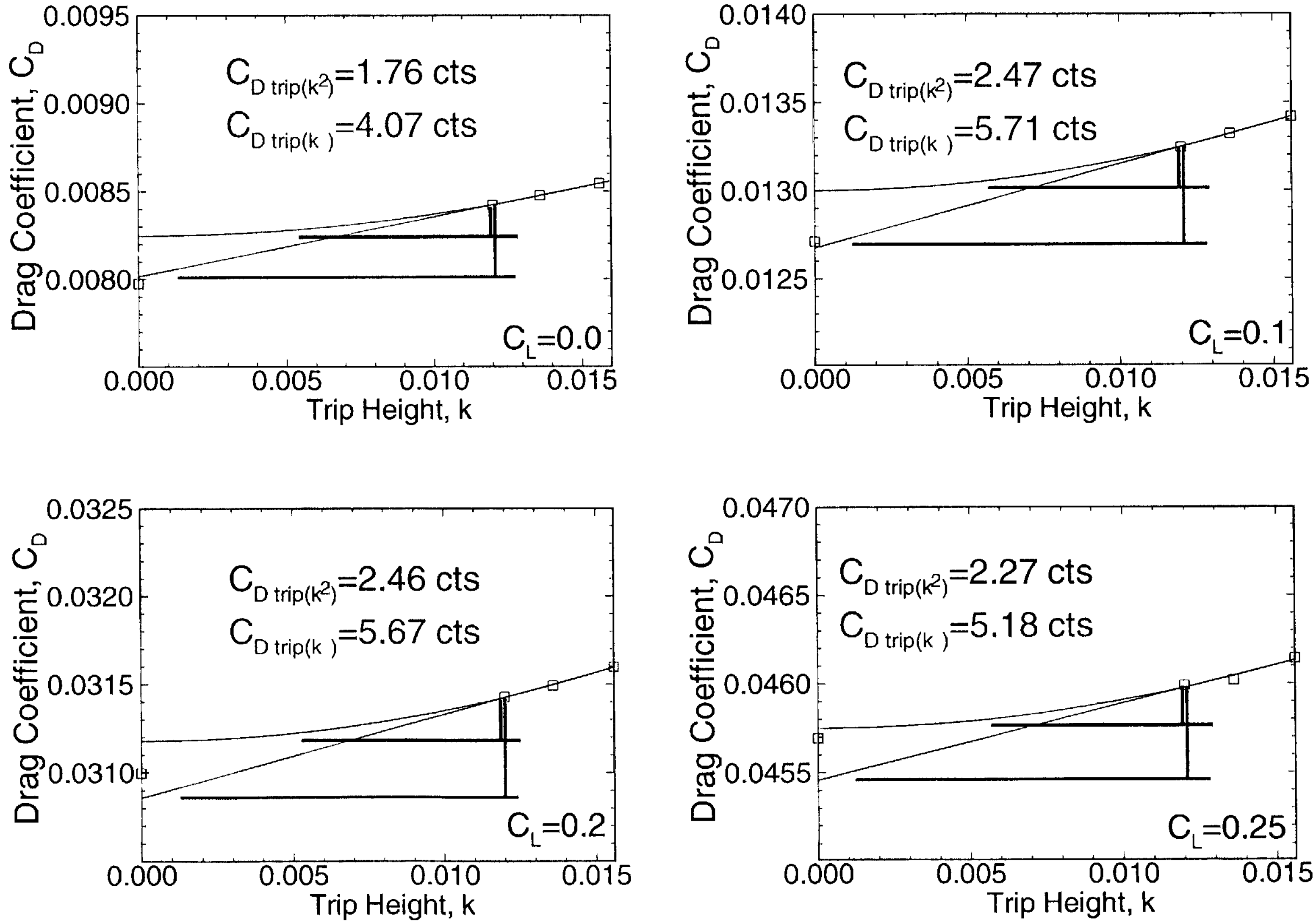

Trip Drag for k=0.012"
1.675% TCA Baseline Model

Shown below is the trip drag associated with k=0.012" computed using the linear and quadratic extrapolating polynomials, and an average of the two. In the legend, those marked with a "k^2" represent the quadratic extrapolation; those marked with a "k" represent a linear extrapolation. For lack of additional data, we assume that the nominal trip drag associated with a given trip height lies somewhere between the lines marked with like color. Without doing a costly trip study on the nacelles, we assume that the trip drag associated with the W/B/N/D configuration is merely 1.5 times that of the W/B, knowing that there are 50% more trip disks on the W/B/N/D configuration.

Trip Drag for k=0.012"
1.675% TCA Baseline Model
Langley UPWT Test 1671, M_∞=2.4, Re=4×10^6/ft

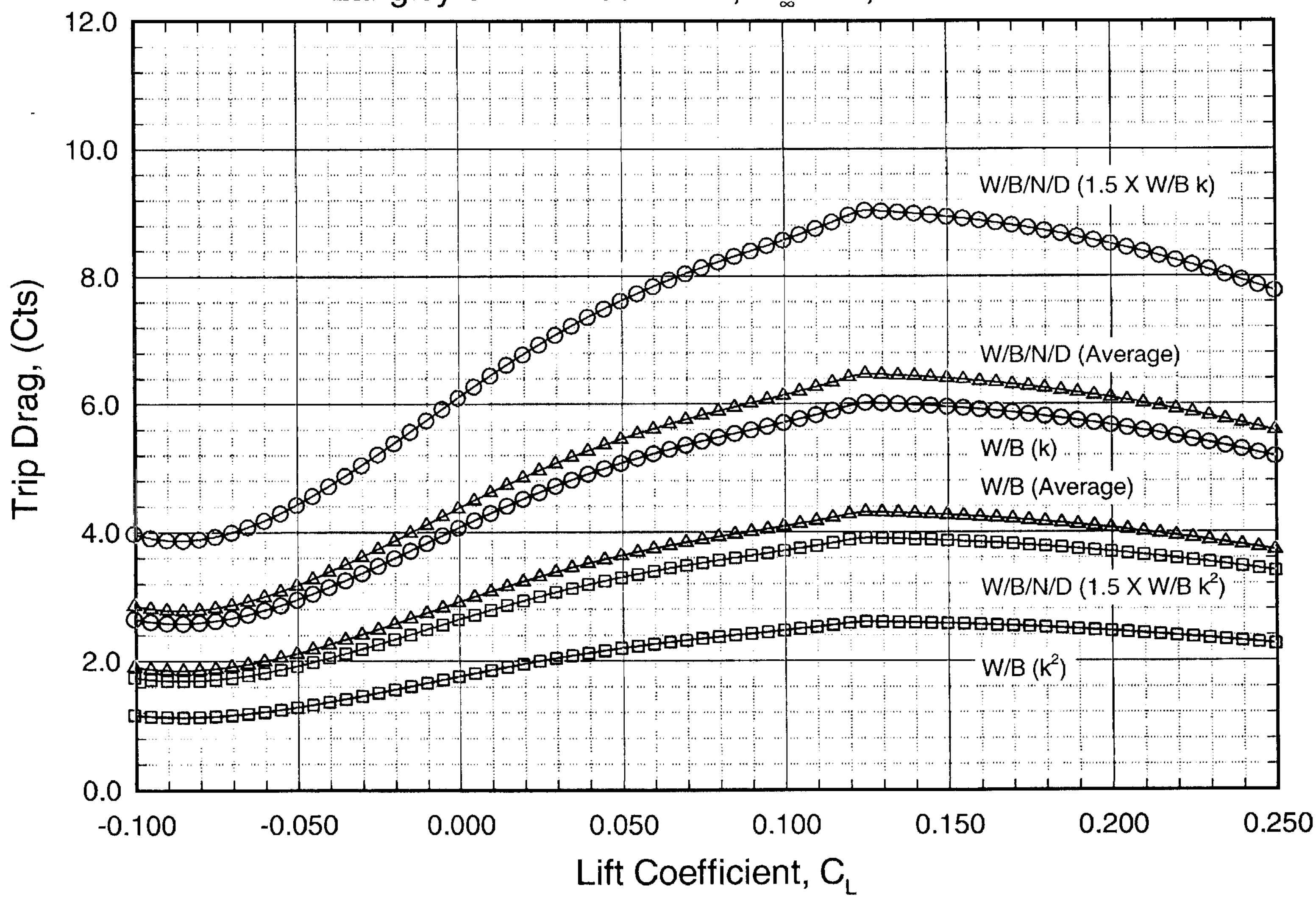

Uncertainty in Trip Drag Estimation
1.675% TCA Baseline Model, W/B Configuration

Using the Method of Equal Effects outlined earlier, a sample calculation of the uncertainty in the trip drag calculation is presented below. Given the variance in transition disk heights and the uncertainty in drag measurements, the total uncertainty in the trip drag correction is computed for flight conditions of M_∞=2.4, and C_L=0.1 and for k=0.012". Using both linear and quadratic extrapolating polynomials, we find for the W/B:

$$\Delta C_D = 5.7 \pm 2.6 \quad \text{for linear fit}$$

$$\Delta C_D = 2.5 \pm 1.2 \quad \text{for quadratic fit}$$

and for W/B/N/D

$$\Delta C_D = 8.6 \pm 3.9 \quad \text{for linear fit}$$

$$\Delta C_D = 3.7 \pm 1.8 \quad \text{for quadratic fit}$$

We see the quadratic fit is not as vulnerable to errors incurred in the measurements, nevertheless the uncertainty is near 50%.

Uncertainty in Trip Drag Estimation

Flight Conditions: $M_\infty = 2.4$

$C_L = 0.1$

$Re = 4 \times 10^6$/ft

Given: $\Delta C_D = \pm 0.25$ cts,

$\Delta k = \pm 0.00025$"

$k = 0.012$"

Linear Fit (k)

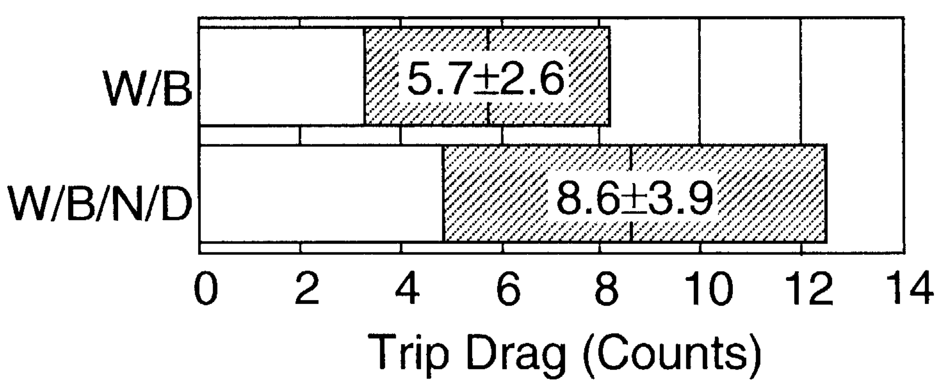

Quadratic Fit (k^2)

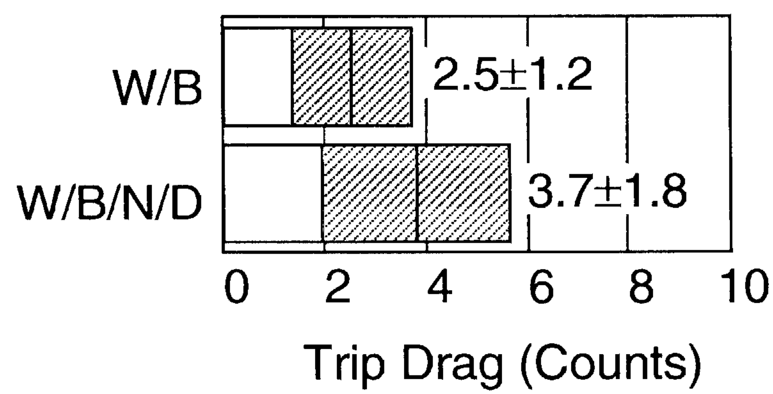

Uncertainties can be reduced by:

- Increasing the number of trip heights tested
- Increasing the number of repeat runs at a specific k (*i.e.*, reduce ΔC_D)

Pressure Distributions for the TCA Wing/Body Configuration

Again, the predicted and measured pressure distributions at six streamwise wing stations are compared in the following figure at the cruise angle-of-attack at M_∞=2.4. Both numerical schemes (Euler and Navier-Stokes) predict the pressure distributions quite well. The Navier-Stokes solution is slightly superior to the Euler solution in certain regions such as on the upper surface of the wing, inboard close to the fuselage. The experimental data also appears to contain some points which are likely incorrect, probably due to blockage of the pressure tap or connecting pressure tubing.

Pressure Distributions for the TCA Wing/Body Configuration
UPWT 1671, CFL3D Euler and Navier-Stokes

Baldwin-Lomax Turbulence Model, $Re_c = 6.36 \times 10^6$

$M_\infty = 2.4$, $\alpha = 3.5^\circ$

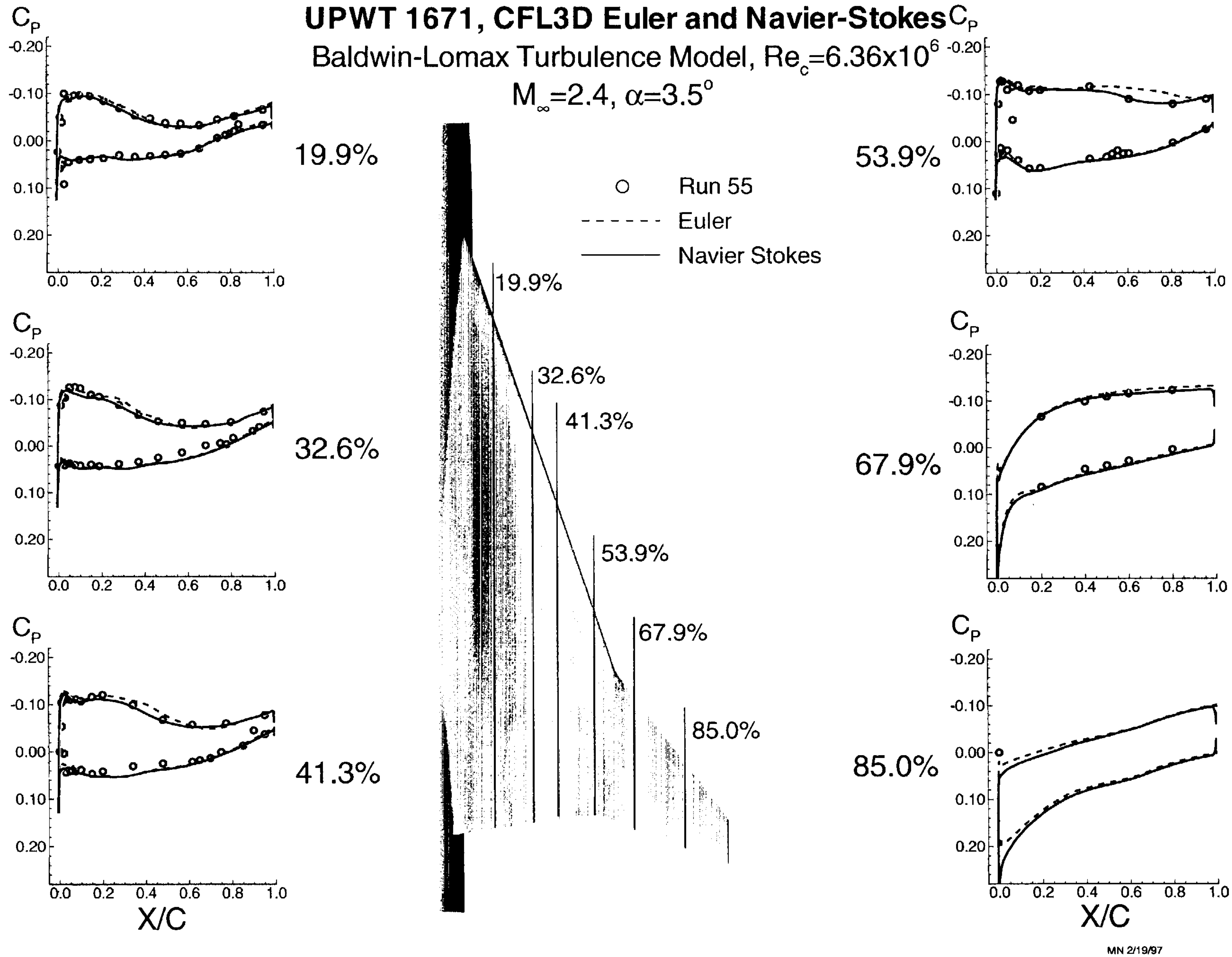

Pressure Distributions for the Ref. H Wing/Body Configuration

Pressure distributions from Navier-Stokes solutions using Baldwin-Lomax turbulence model are compared with experimental data from the NASA Ames 9'x7' wind tunnel for $M_\infty = 2.4$, $\alpha = 4.4°$ and $Re_C = 7$ million. Two CFD solution were obtained, one using CFL3D and the other using TLNS3D. Both these solutions agree very well with the experimental data. From these comparison, it is reasonable to say that we can predict the pressure distribution and, consequently, the pressure drag very well using CFD.

Comparison of Pressure Distributions for the Baseline Ref. H Wing/Body Configuration, N-S Solutions

M_∞=2.4, α=4.4°, Re_c=7x10^6

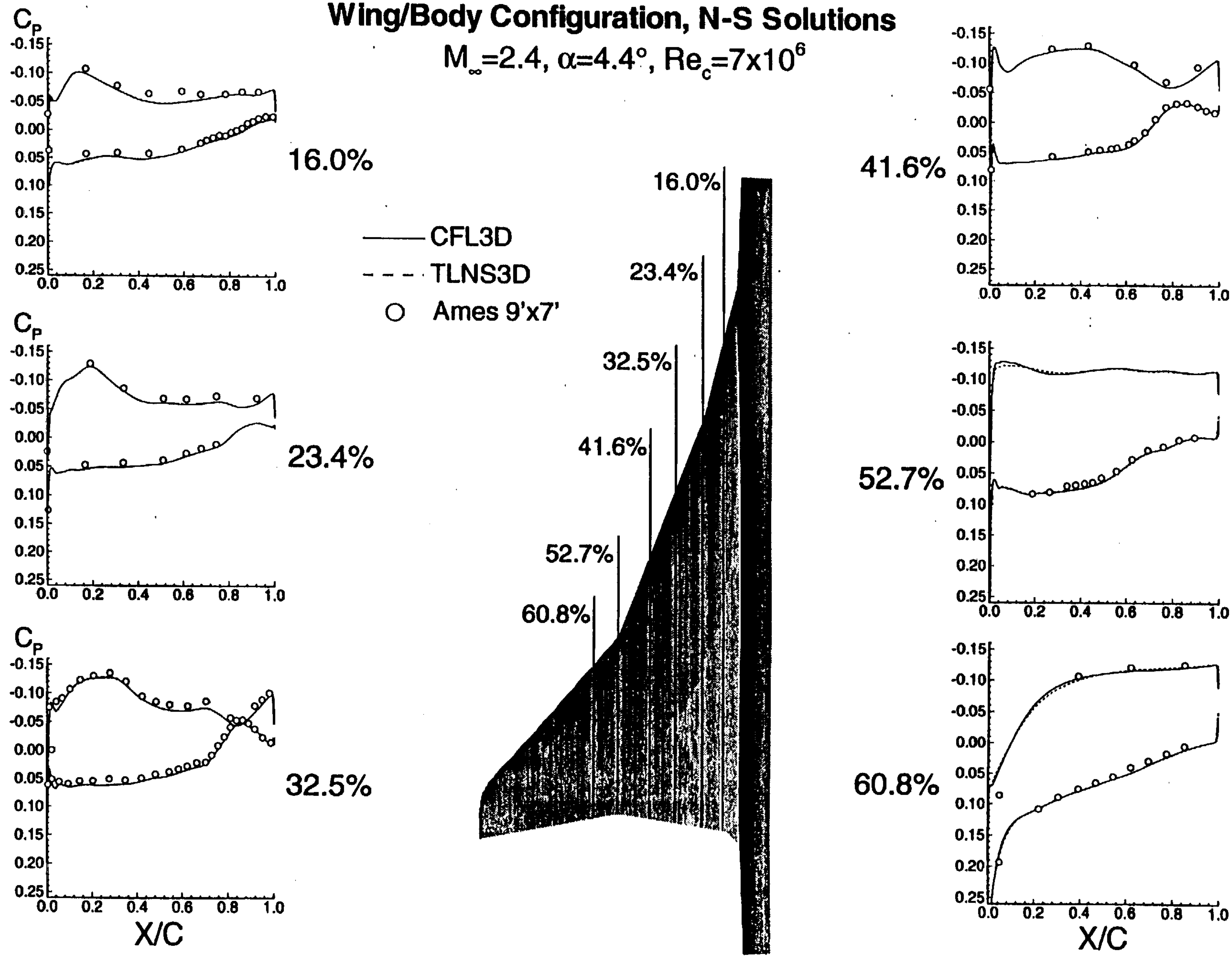

Pressure Distributions for the TCA Wing/Body/Nacelle/Diverter Configuration: Experimental Data, Euler, and Navier-Stokes

The predicted and measured pressure distributions at the six spanwise wing stations are compared in the following figure at the cruise angle of attack at M_∞=2.4. As seen in the wing/body comparison, both numerical schemes (Euler and Navier-Stokes) predict the pressure distributions quite well. The Navier-Stokes solution is slightly superior to the Euler solution particularly in the prediction of shock wave strength and location on the wing lower surface between the nacelles. At the 32.6% spanwise location, there are a pair of stray data points near the shock which appear to be incorrect. These unusual readings at these tap locations were seen at other angles-of-attack as well. Overall, it can be concluded that the Navier-Stokes solution do a very good job of capturing the flow physics. The diverter shocks are very crisp and agree well with the experimentally predicted shock strengths. Likewise, subsequent expansions and reflected shocks are nicely predicted as well.

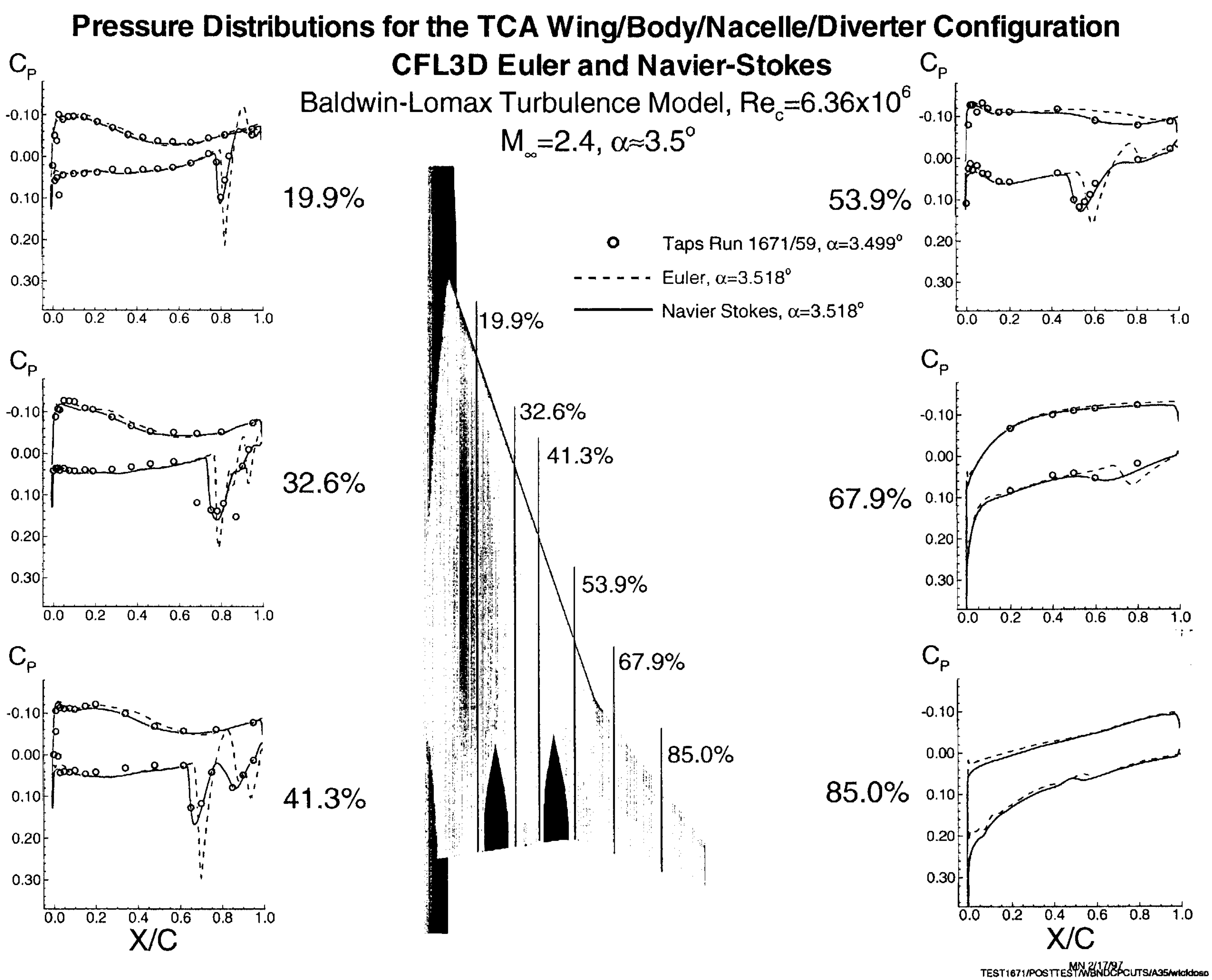

Pressure Distributions for the TCA Wing/Body/Nacelle/Diverter Configuration
CFL3D Euler and Navier-Stokes
Baldwin-Lomax Turbulence Model, Re_c=6.36x10^6
M_∞=2.4, α≈3.5°
Taps Run 1671/59, α=3.499°
Euler, α=3.518°
Navier Stokes, α=3.518°
19.9%
32.6%
41.3%
53.9%
67.9%
85.0%
C_P
X/C
MN 2/17/97
TEST1671/POSTTEST/WBNDCPCUTS/A35/wlcldoso

Pressure Distributions for the Ref. H Wing/Body/Nacelle/Diverter Configuration: Experimental Data and Navier-Stokes

Again, the comparison is excellent as seen for the TCA wing/body/nacelle/diverter case. These comparisons give a very warm feeling that Navier-Stokes based CFD codes can predict pressures, hence pressure drag quite well.

Comparison of Pressure Distributions for the Baseline Ref. H Wing/Body/Nacelle/Diverter Configuration

$M_\infty=2.4$, $\alpha=4.1°$, $Re_c=7\times10^6$

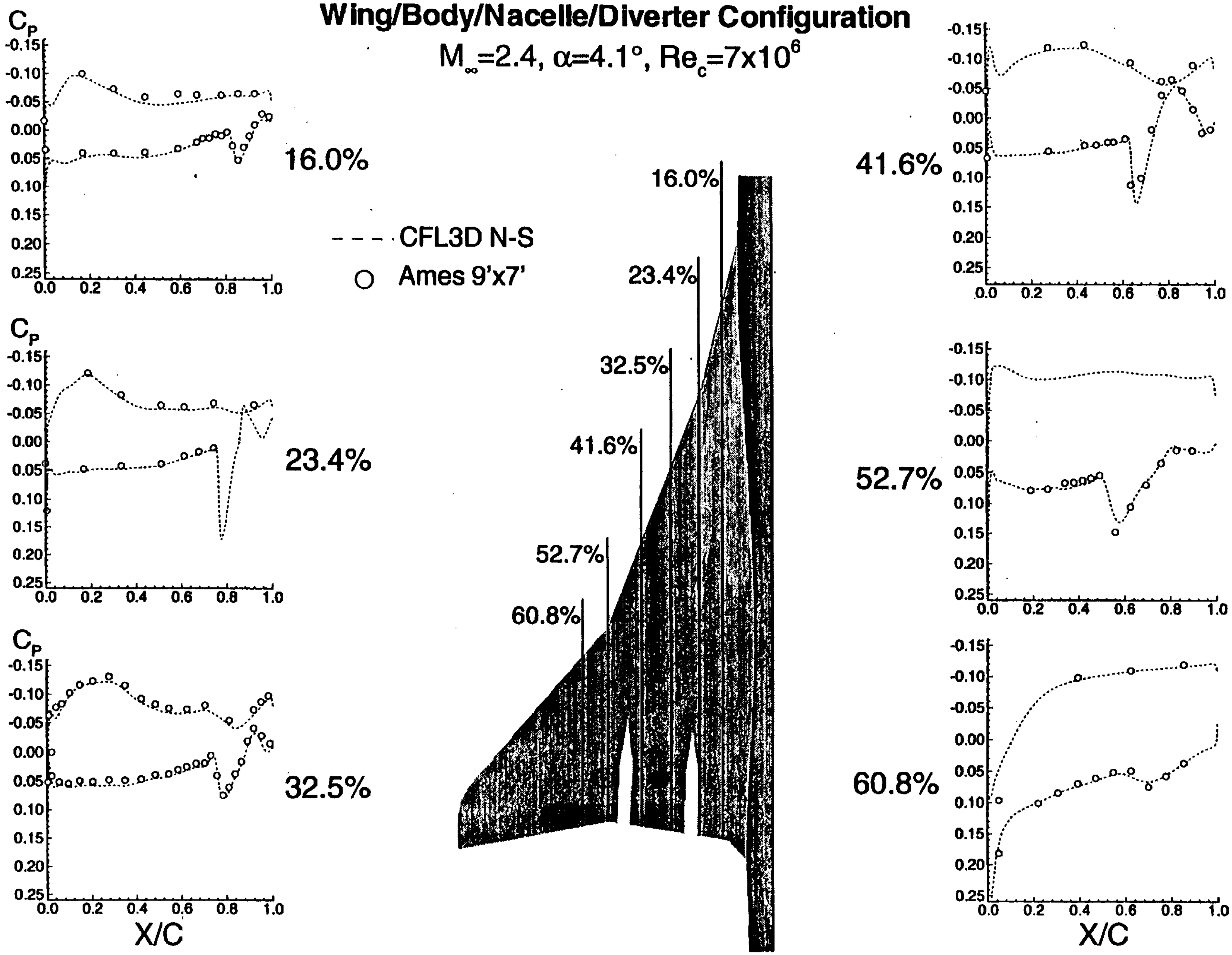

Pressure Drag at Supersonic Condition

The pressure drag values predicted by CFL3D and TLNS3D Navier-Stokes solutions using Baldwin-Lomax, for 2.7% Ref. H wing/body configuration, are presented. At M_∞=2.4, Re_c=7x10^6 and C_L=0.1, the pressure drag values are nearly identical.

TLNS3D and CFL3D uses different types of discretization to solve the Navier-Stokes equations. But the close agreement of the pressure drag values gives us the confidence to say that either code is good to predict the pressure drag.

Pressure Drag at Supersonic Condition

Navier-Stokes (Baldwin-Lomax), $M_\infty = 2.4$, $C_L = 0.1$

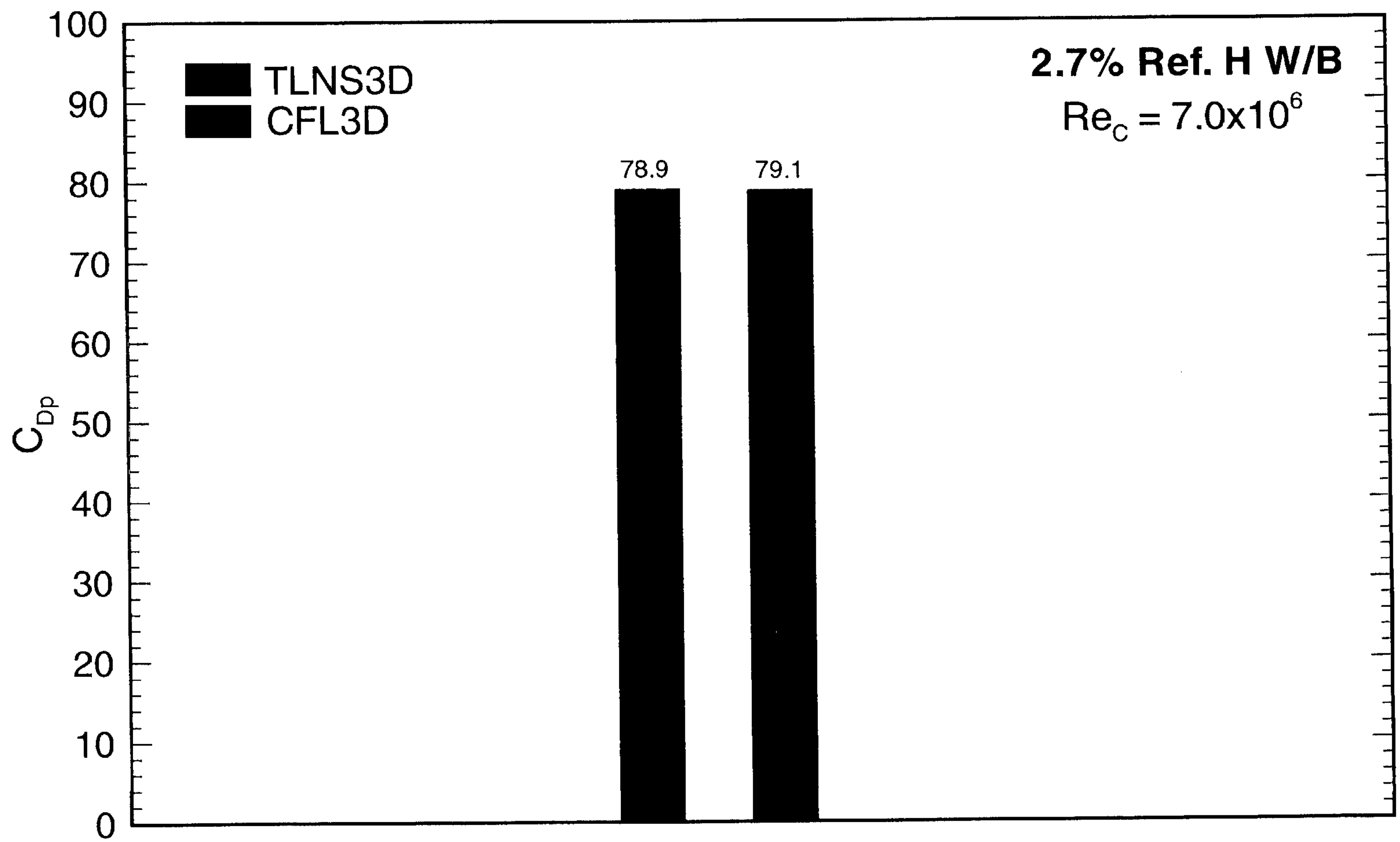

gk970221

Skin-friction Drag for TCA W/B, Isolated Nacelle and W/B/N/D

Skin-friction drag, obtained using several methods, for the TCA wing/body, nacelles, and wing/body/nacelle/diverter configurations at $M_\infty=2.4$ and $C_L=0.1$ are compared. Note that the nacelles were analyzed at $\alpha=0°$. The blue bar represents the best estimate of the skin-friction drag component of the experimental data. This was obtained by subtracting the skin-friction drag obtained from CFD analysis from the corrected experimental drag. Since we have high confidence in the pressure drag predicted by CFD, this approach is considered to be reasonable. Skin-friction drag obtained from CFL3D Navier-Stokes calculations using Baldwin-Lomax turbulence model is shown in red. The remaining two bars indicate the skin-friction drag obtained using two equivalent flat-plate methods, namely, the Van Driest II formulation (in green) and the Sommer-Short formulation (in purple). Van Driest II formulation is used widely at MDC while BCAG prefers the Sommer-Short formulation.

For the TCA wing/body configuration, at $Re_c=6.36x10^6$, there is significant uncertainty in the data. There is about a 6 count difference between the highest and the lowest values. For the wing/body/nacelle/diverter configuration, this difference is less, about 3.5 counts, but still significant. For the isolated nacelle, however, there is very good agreement between CFD and flat-plate estimates (there is no experimental data). This may be due to the flow being relatively benign in this case.

At the flight condition ($Re_c=212x10^6$), the maximum difference between the CFD and flat-plate skin-friction drag estimates is 1.8 counts for the wing/body configuration and 1.4 counts for the wing/body/nacelle/diverter configuration.

Skin-friction Drag for TCA W/B, Isolated Nacelle and W/B/N/D

$M_\infty = 2.4, C_L = 0.1$

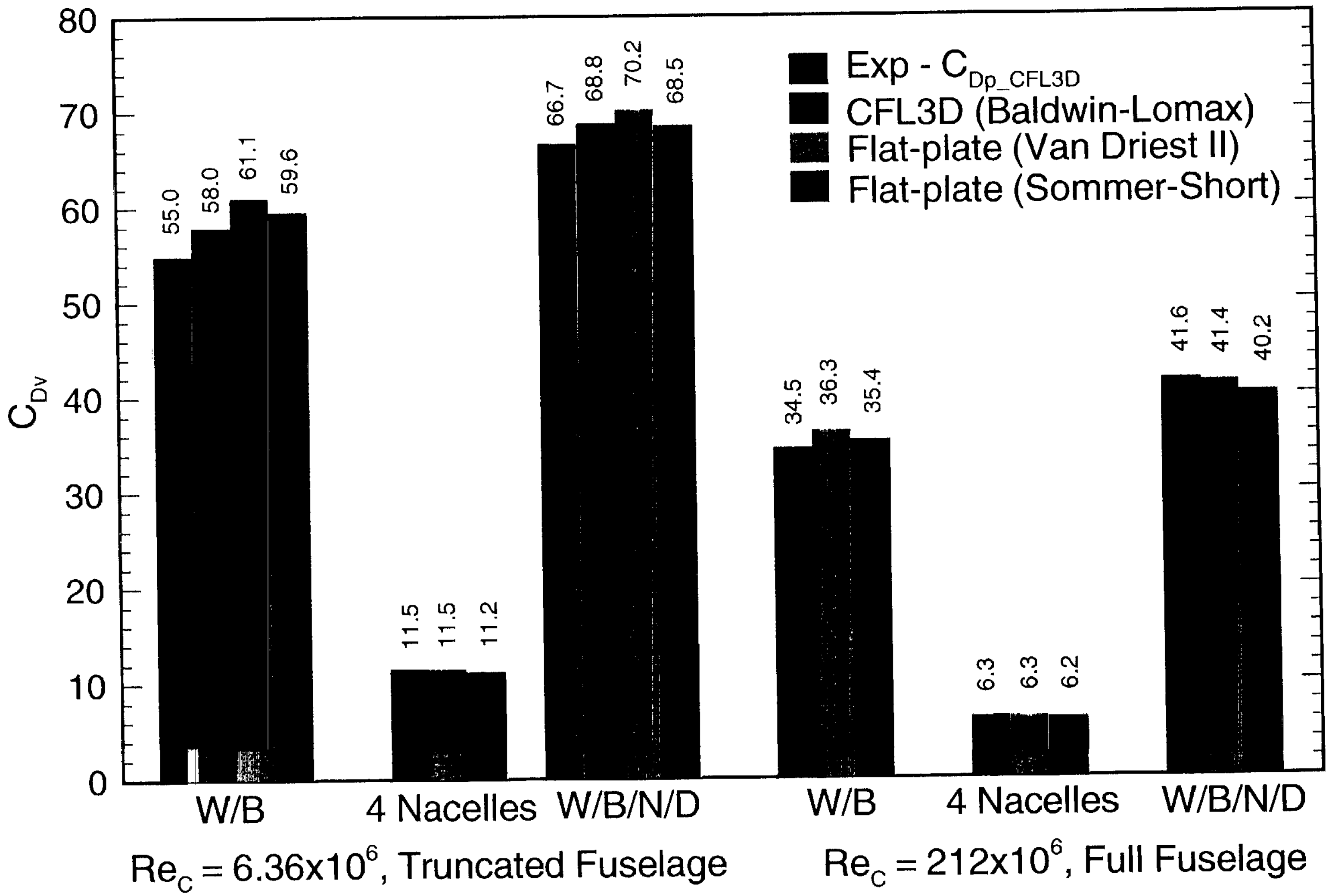

gk970221

Skin-friction Drag for 2.2% Ref. H Wing/Body Configuration

Skin-friction drag, obtained using several methods, for the 2.2% Ref. H wing/body configuration at M_∞=0.9 and C_L=0.18, for Reynolds numbers ranging from 10 to 80 million, are compared. The blue bar represents the best estimate of the skin-friction drag component of the experimental data. This was obtained by subtracting the skin-friction drag obtained from CFD analysis from the corrected experimental drag. Since we have high confidence in the pressure drag predicted by CFD, this approach is considered reasonable. Skin-friction drag obtained from TLNS3D Navier-Stokes calculations using Baldwin-Lomax turbulence model is shown in red. The remaining two bars indicate the skin-friction drag obtained using two equivalent flat-plate methods, namely, the Van Driest II formulation (in green) and the Sommer-Short formulation (in purple). Van Driest II formula is widely used by MDC while BCAG prefers the Sommer-Short formula.

The differences in skin-friction drag between the highest and lowest values are 6 counts at $Re_c=10.3 \times 10^6$, 4.5 counts at $Re_c=30 \times 10^6$ and 5.3 counts at $Re_c=80 \times 10^6$. Also note that the two equivalent flat-plate methods predict identical skin-friction drag at this Mach number.

Skin-friction Drag for 2.2% Ref. H Wing/Body Configuration

$M_\infty = 0.9$, $C_L = 0.18$

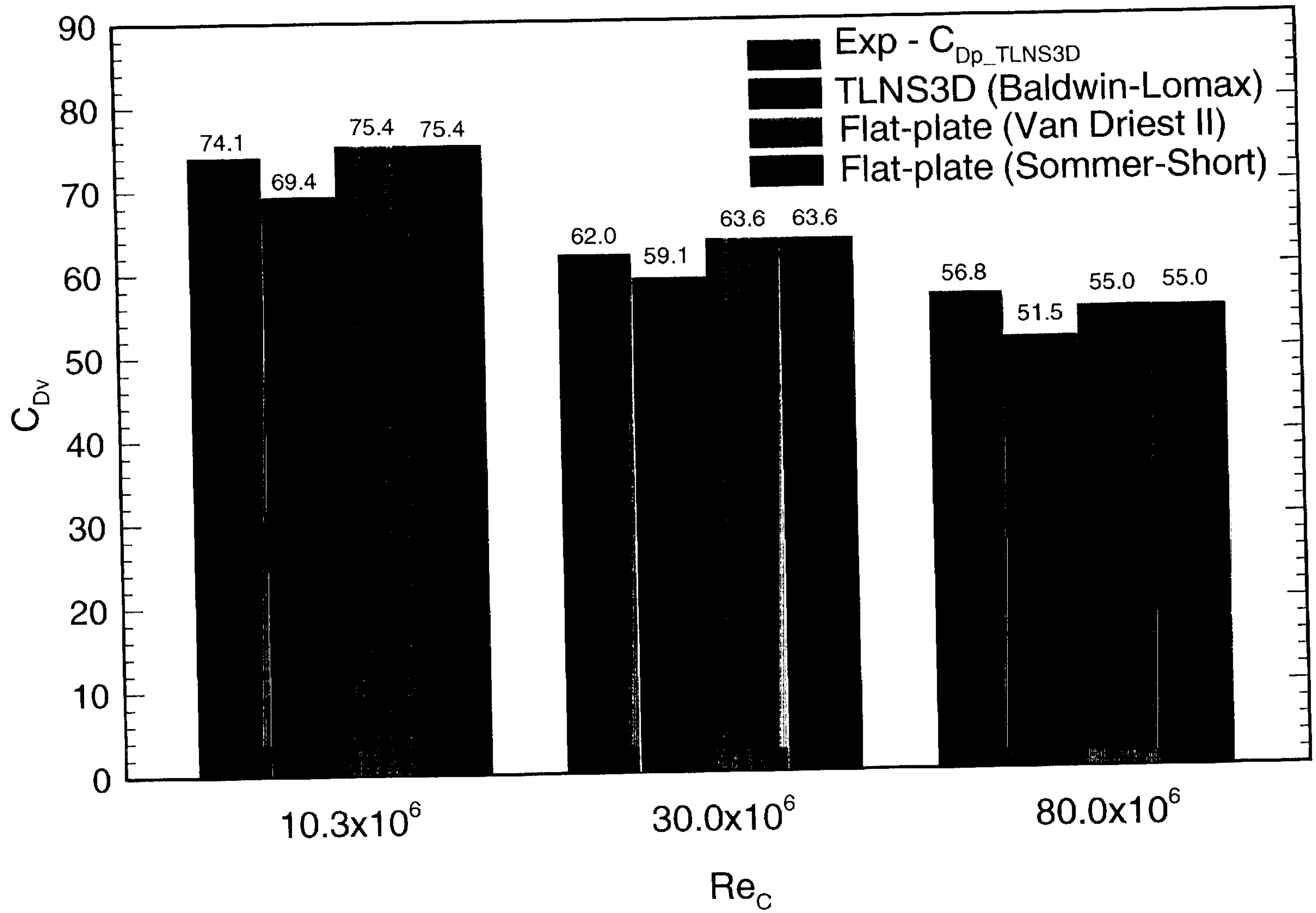

gk970221

Prediction of Nacelle Installation Drag

Experimental and computed nacelle installation drag are presented for ref. H and TCA configurations. Near the minimum drag condition, only the computed results are shown. As can be observed, near minimum drag condition, the variability is 1.4 counts. Near the cruise condition, however, the variability is two counts.

Prediction of Nacelle Installation Drag

CFL3D & Experiment, M_∞=2.4

1.7% TCA (Re$_c$=6.36x10^6)
2.7% Ref. H (Re$_c$=7x10^6)

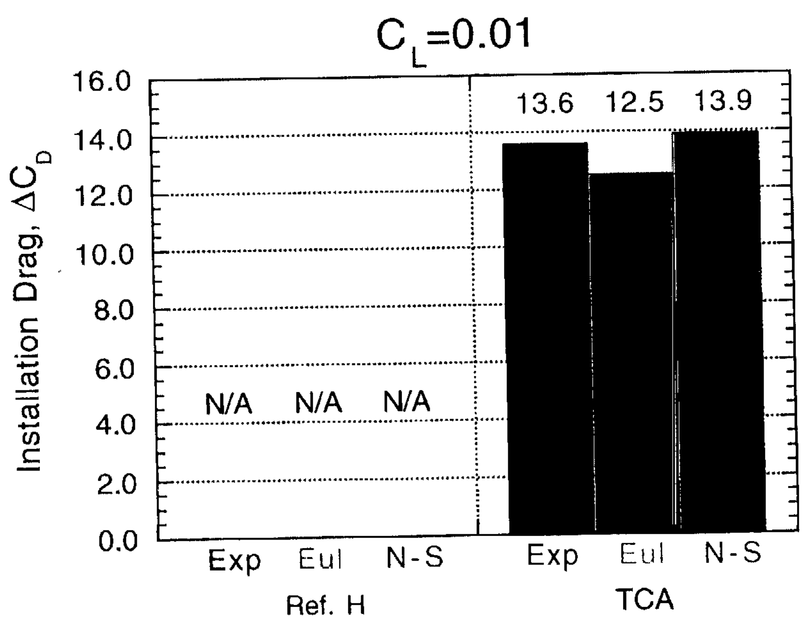

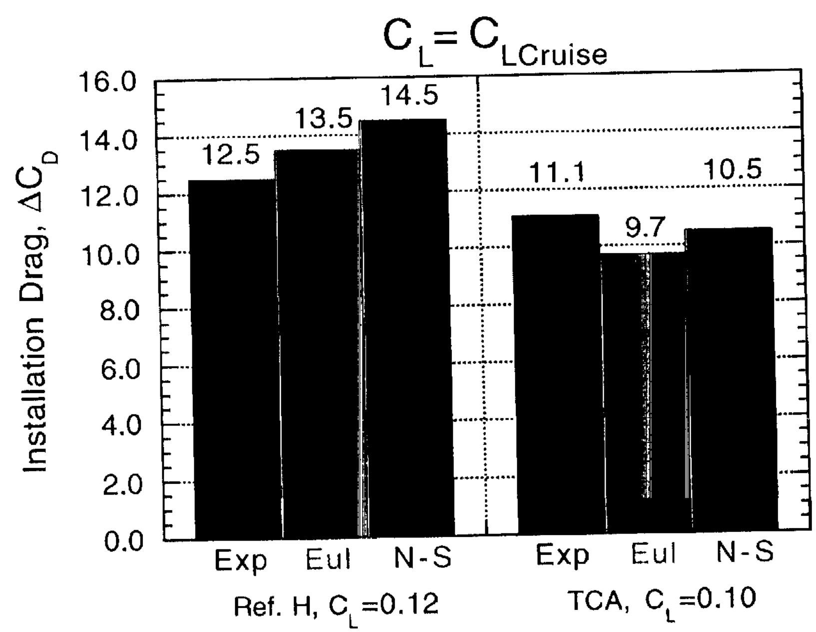

Prediction of Isolated Nozzle Boattail Drag

Boattail drag values for the isolated Ref. H axisymmetric and 2-D nozzles are compared. Results from three different methods are shown. The MDC results were obtained using the CFL3D (Baldwin-Barth turbulence model), while the Northrop-Grumman (NGC) results were obtained using another Navier-Stokes solver (2-equation Menter's turbulence model). The IMS (Integrated Mean Slope) method is based on empirical database. As shown in the figure, the uncertainty in predicting isolated nozzle boattail drag is about 2 counts.

Uncertainty in Predicting Nozzle Boattail Drag

- Isolated Ref. H Axisymmetric and 2-D Nozzles

$$C_{D\ boattail} = C_{D\ trans} - C_{D\ super}$$

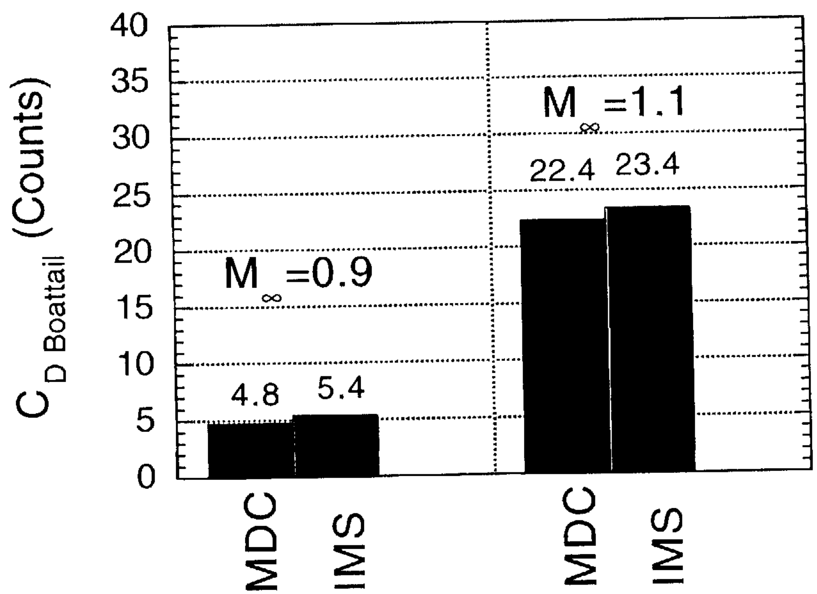

Axisymmetric

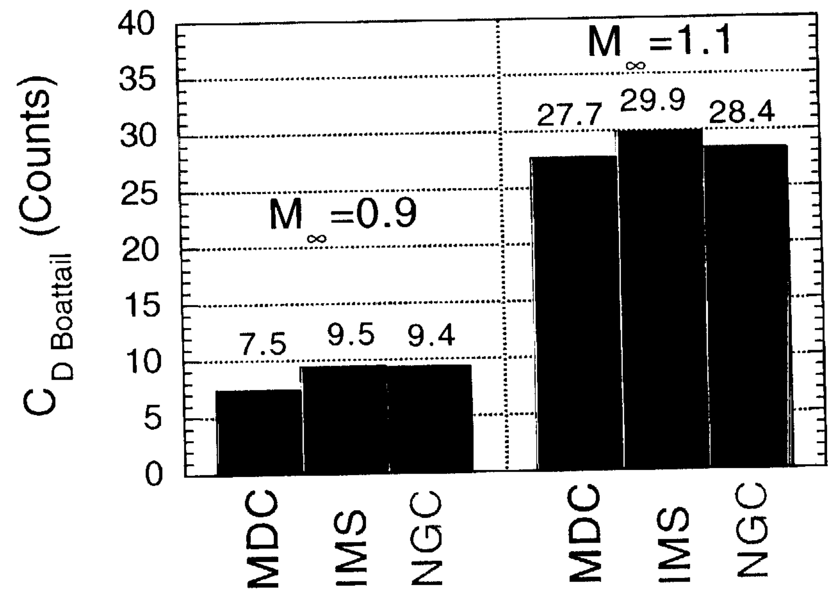

2-D

Geometries of the Rigid and Flexible Opt 5 Model Corresponding to the Measured Structural Deflections at $\alpha=4°$

During the testing of the Opt5 model in the NASA Langley UPWT, model deformation data (wing twist and bending) at the 84.5% and 96.1% semi-span stations were acquired. These data indicated that the model, although assumed rigid for CFD purposes, was undergoing deformation under the aerodynamic loads. The CFD grids were then perturbed to agree with the model deformation data that was acquired in the UPWT by imposing the twist and bending data upon the grid and linearly fairing these deformation values through the other grid points. Since no deformation data was acquired on the inboard wing panel, it was assumed to remain rigid. The following figure shows the differences between the "flexible model" grid and the "rigid model" grid.

Geometries of the Rigid and Flexible Opt5 Model Corresponding to the Measured Structural Deflections at $\alpha = 4^\circ$

M_∞=2.4, Re=4x10^6/ft

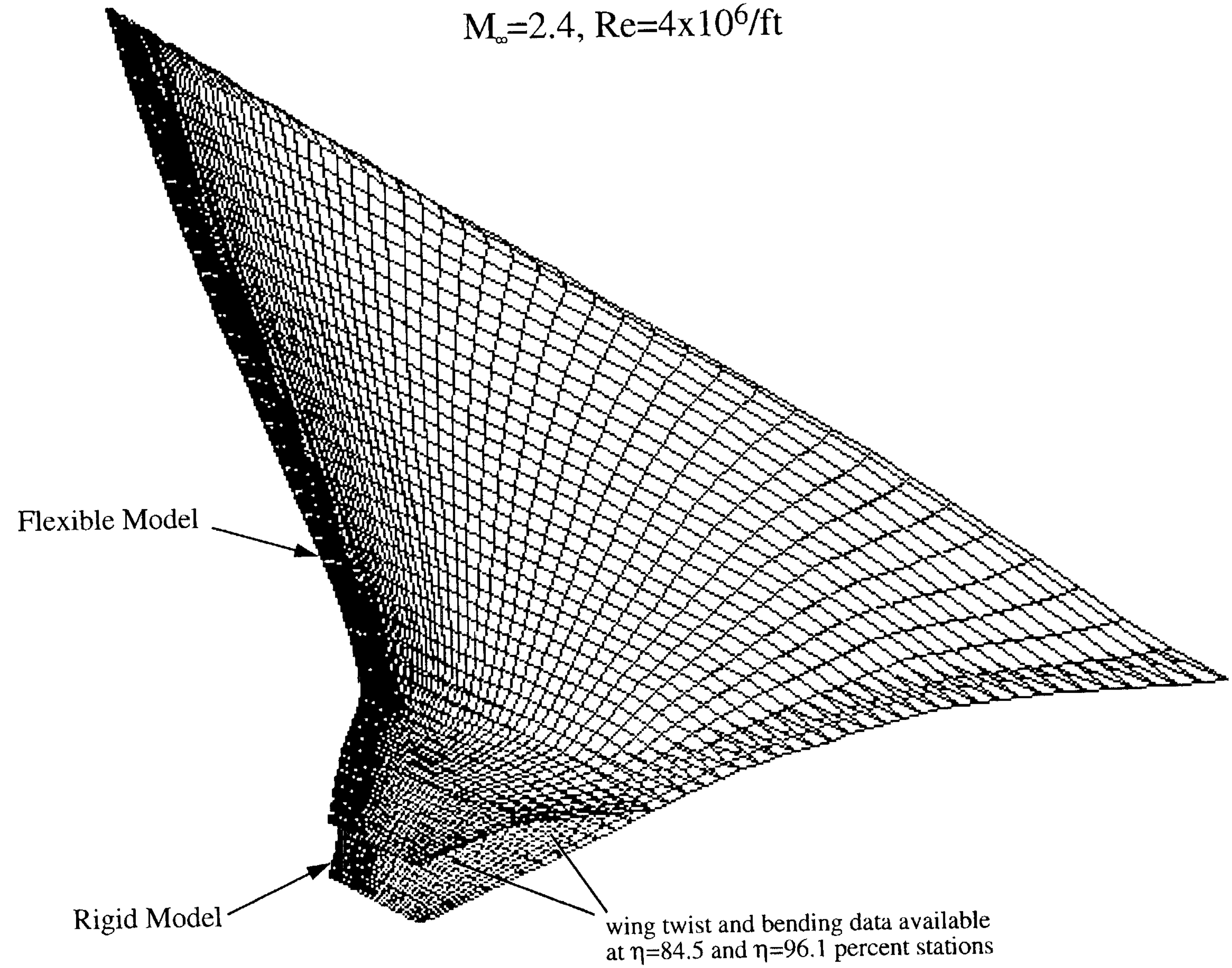

Aeroelastic Study Drag Polars
M2.4-7A Opt 5 1.675% Model, Wing/Body Configuration

The following figure presents the numerically predicted and experimentally obtained drag polars for the Opt5 model. A good agreement can be seen between all three data sets. It can be seen in the aeroelastic solution that the aeroelasticity of the outboard wing causes a reduction in the lift coefficient for a given angle-of-attack (since both data points near C_L=0.115 are at the same angle-of-attack), but also a corresponding reduction in drag coefficient for a given angle-of-attack. The net effect is a negligible effect on the predicted drag polars (< 0.1 count) where aeroelasticity appears to cause a shift along the rigid polar rather than a shift to the left or right of the rigid polar.

Aeroelastic Study, Drag Polars

M2.4-7A Opt5 1.675% Model, W/B Configuration

CFL3D N-S, Baldwin-Lomax, M_∞=2.4, Re=4x10^6/ft

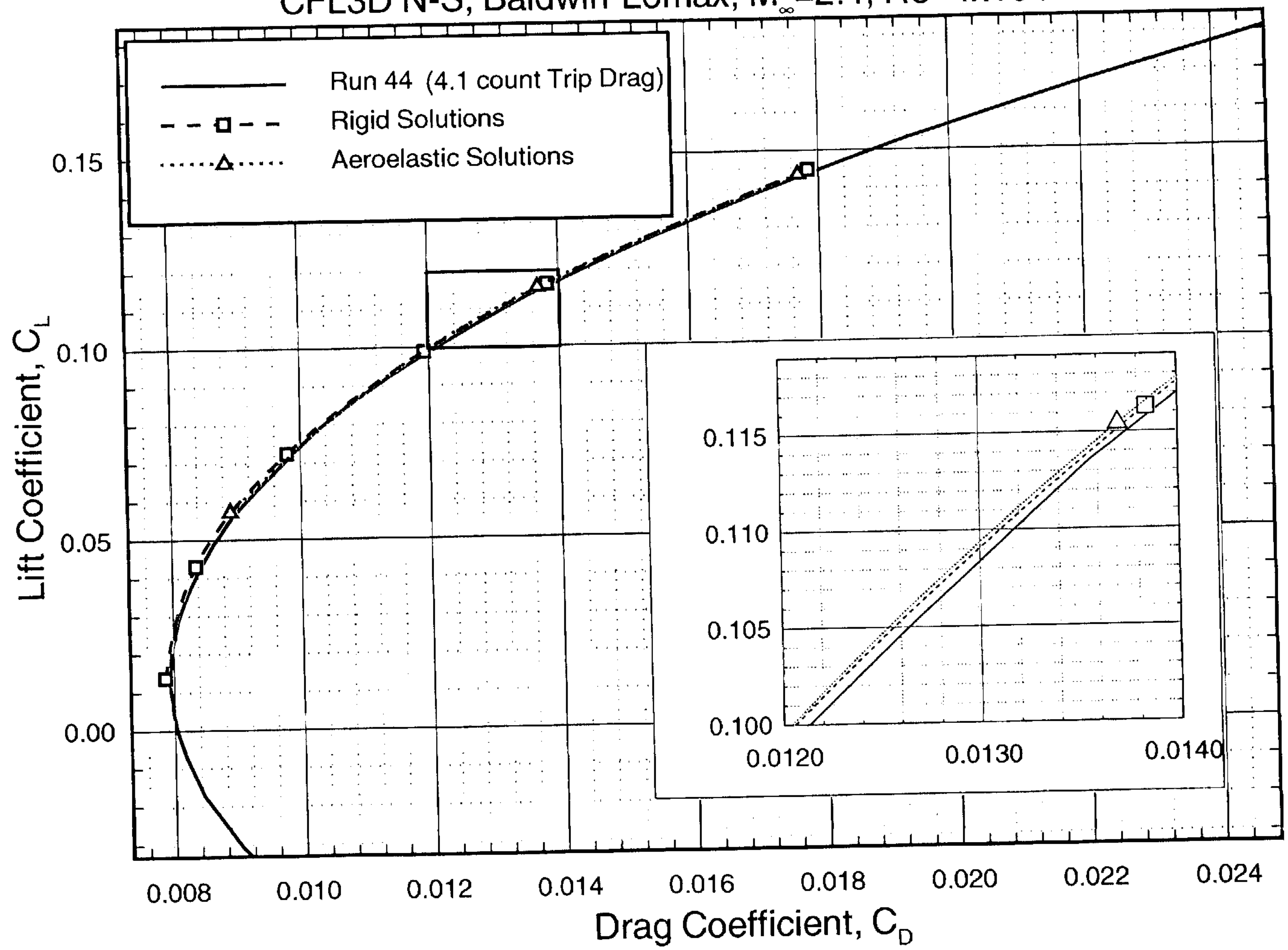

Effect of Reynolds Number on Pressure Drag

The pressure drag values obtained from CFL3D Navier-Stokes solutions (Baldwin-Lomax turbulence model) for the TCA at M_∞=2.4 for the wind-tunnel Reynolds number (Re_c=6.36x10^6) and the flight Reynolds number (Re_c=212x10^6) are presented. For the wing/body configuration, the pressure drag difference between the two conditions is 1.2 counts whereas for the wing/body/nacelle/diverter configuration the difference is 0.8 counts.

Effect of Reynolds Number on Pressure Drag
CFL3D-NS (Baldwin-Lomax), $M_\infty = 2.4$, $C_L = 0.1$

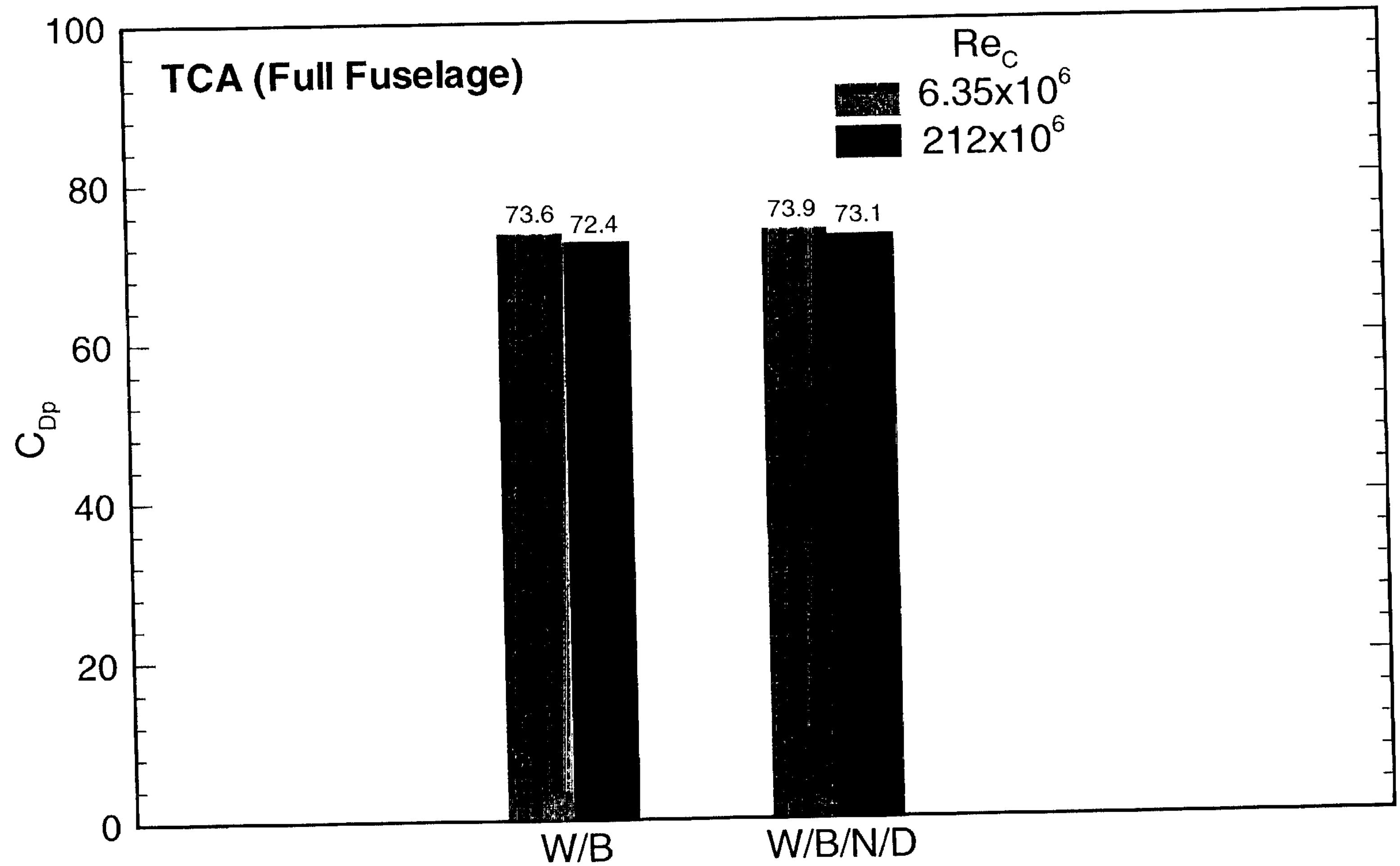

gk970221

Effect of Reynolds Number on Pressure Drag at C_{D_min}

The minimum pressure drag values obtained from CFL3D Navier-Stokes solution (Baldwin-Lomax turbulence model) for the TCA at M_∞=2.4 for the wind-tunnel Reynolds number (Re_c=6.36x10^6) and the flight Reynolds number (Re_c=212x10^6) are presented. For the wing/body configuration, the pressure drag values at the two conditions are very close and for the wing/body/nacelle/diverter configuration they are nearly identical.

Effect of Reynolds Number on Pressure Drag at C_{D_min}
CFL3D-NS (Baldwin-Lomax), $M_\infty = 2.4$, $C_L \approx 0.01$

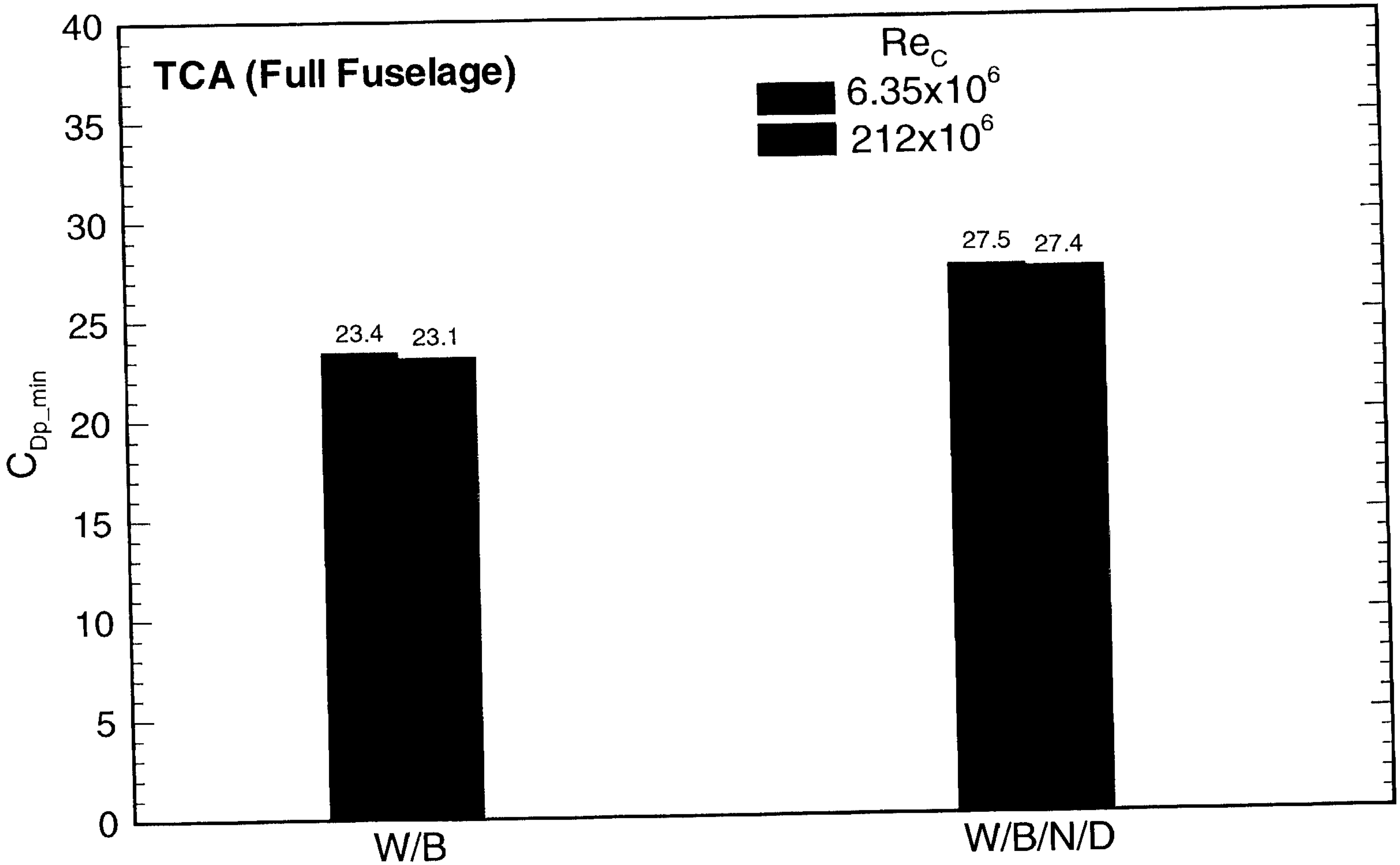

gk970221

Effect of Reynolds Number on Pressure Drag

The pressure drag values obtained from TLNS3D Navier-Stokes solution (Baldwin-Lomax turbulence model) for the 2.2% Ref. H wing/body configuration at M_∞=0.9 are shown for Reynolds numbers of 10, 30 and 80 million. At this condition, the pressure drag values are nearly identical.

Effect of Reynolds Number on Pressure Drag

TLNS3D (Baldwin-Lomax), $M_{\infty} = 0.9$, $C_L = 0.18$

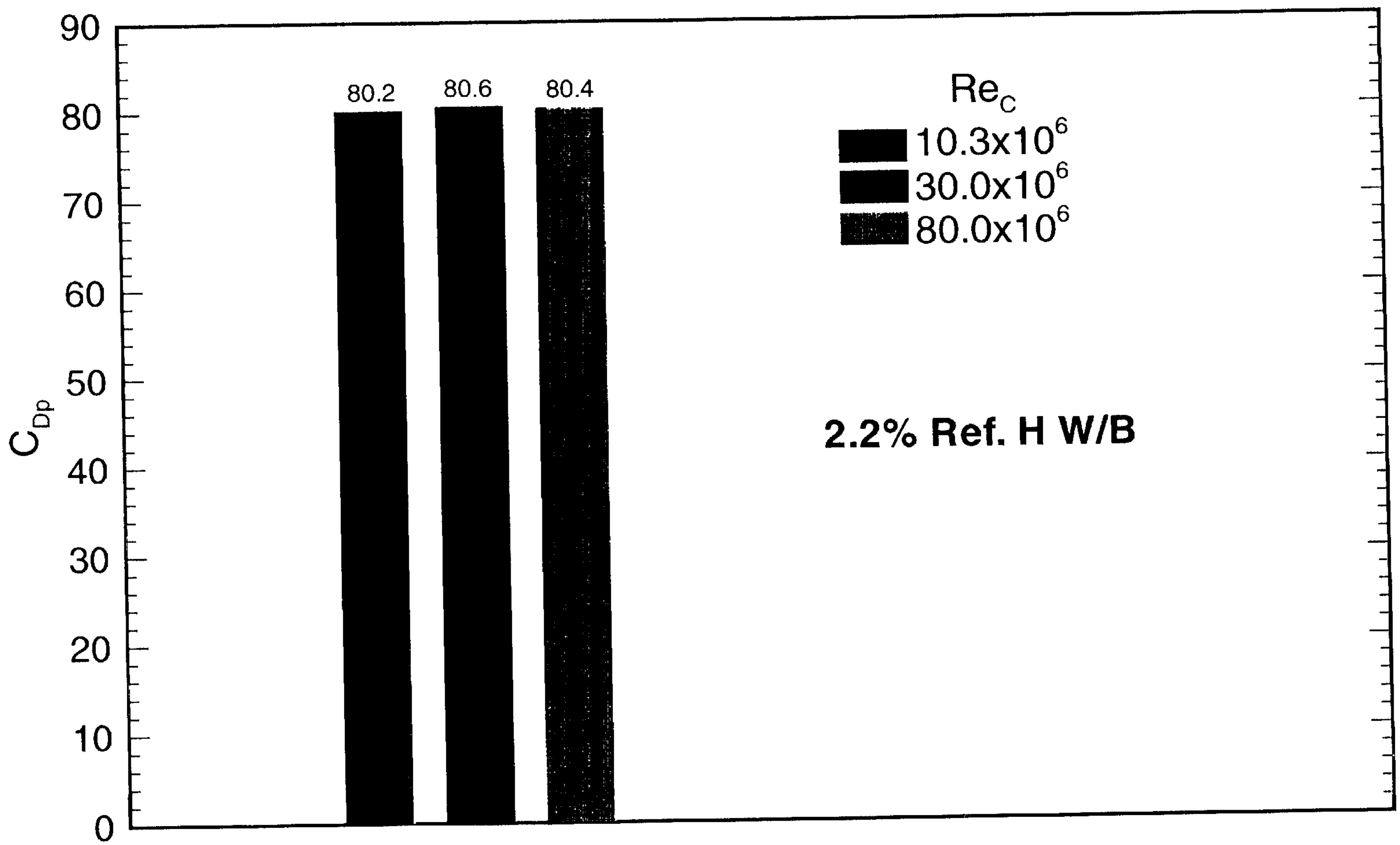

gk970221

Reynolds Number Effects on Pressure Distributions TCA Wing/Body/Nacelle/Diverter Configuration

Streamwise pressure cuts of the CFL3D Navier-Stokes predicted pressure distributions on the TCA wing/body/nacelle/diverter configuration are presented in the following figure. This figure shows that although the pressure drag values appear to be relatively unchanged between the $Re_c=6.36x10^6$ and $Re_c=212x10^6$ solutions, the flow undergoes quite a transformation. Reynolds number is defined as the ratio of inertial to viscous forces and that definition is very evident in the figure. The stronger viscous effects of the $Re_c=6.36x10^6$ solution create a very different shock pattern in the vicinity of the nacelles. The flight Reynolds number sees a pair of reflected shocks and expansions in addition to the shock off of the diverter while at the wind-tunnel Reynolds number these secondary shocks and expansions are much more "smeared out". Likewise, at the 41.3% semi-span station, the flight Reynolds number solution shows a much stronger pair of shocks as well as a stronger expansion. This figure certainly shows that Reynolds number does have an effect on the flow even if it isn't obvious from examination of the drag coefficient.

Reynolds Number Effects on Pressure Distributions

TCA Wing/Body/Nacelle/Diverter Configuration

CFL3D Navier-Stokes (Baldwin-Lomax)

$M_\infty=2.4$, $\alpha=3.5^\circ$

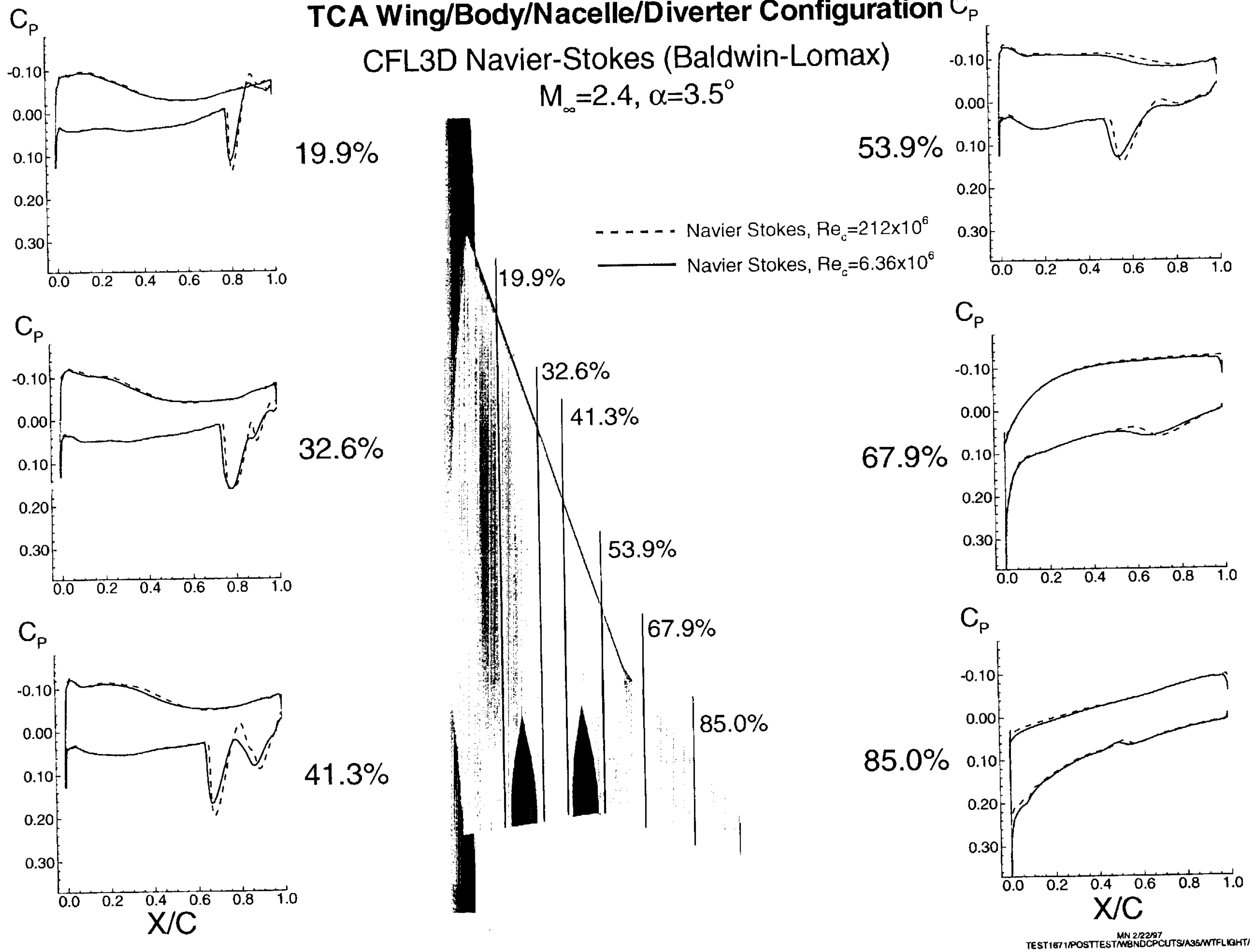

Overall Uncertainties in M_∞ =2.4 Drag Prediction

This is a summary of the various uncertainties discussed during this presentation. As can be recalled, the largest uncertainties are in the skin-friction and boundary layer trip drag predictions. Other contributing factors such as aeroelastic effects, Reynolds number effects, excrescence drag, etc., are difficult to quantify very well as the database is insufficient.

The drag of the full TCA configuration is also shown in this chart. The build-up of this drag will be shown after the next slide.

Overall Uncertainties in M_∞=2.4 Drag Prediction

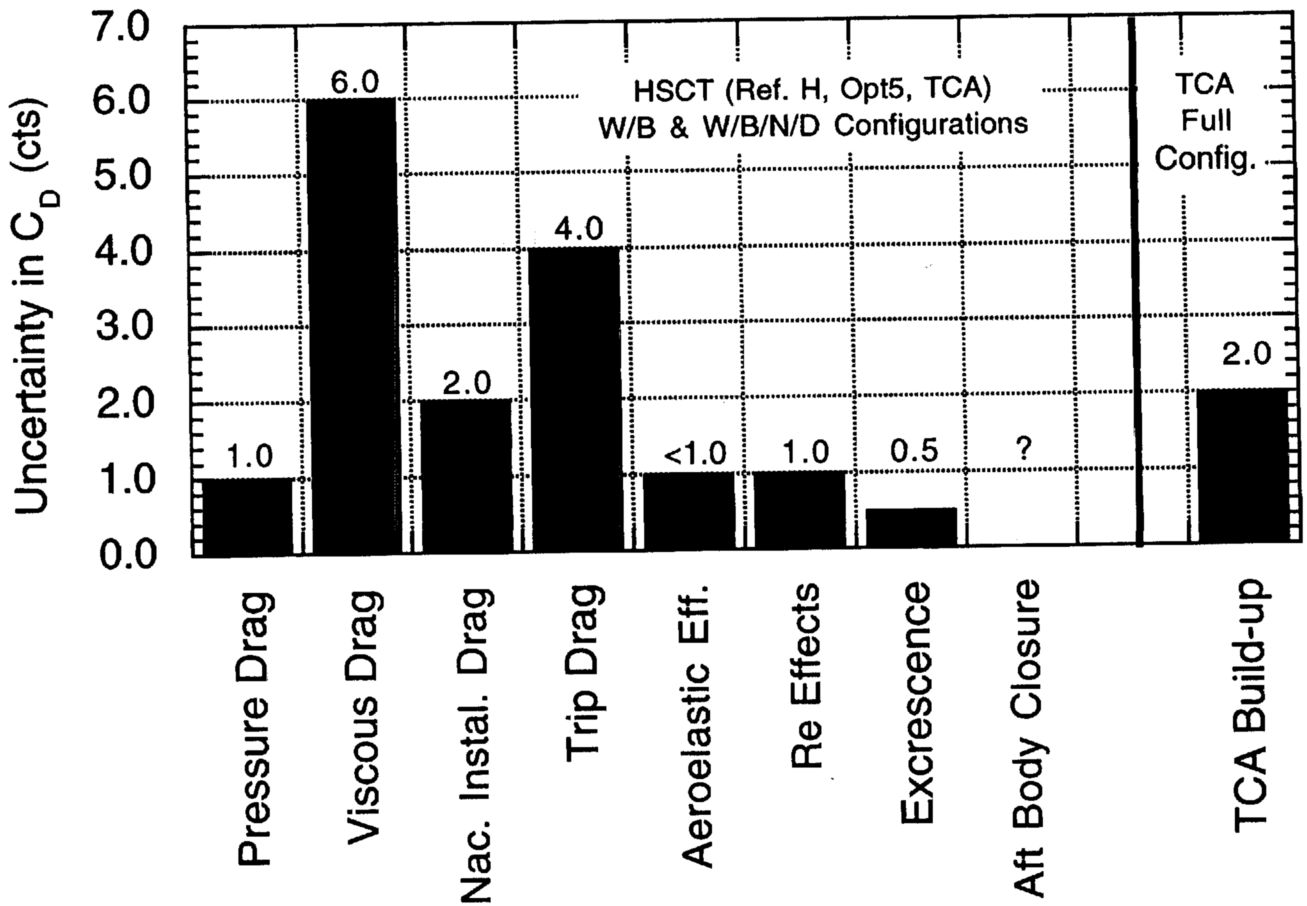

Overall Uncertainties in M_∞ =0.90 Drag Prediction

This is a summary of the various uncertainties discussed during this presentation. As can be recalled, the largest uncertainty is again in the skin-friction predictions. Other contributing factors such as aeroelastic effects, Reynolds number effects, excrescence drag, inlet bleed, inlet bypass, inlet spillage, etc., are again difficult to quantify as the database is insufficient.

Overall Uncertainties in M_∞=0.9 Drag Prediction

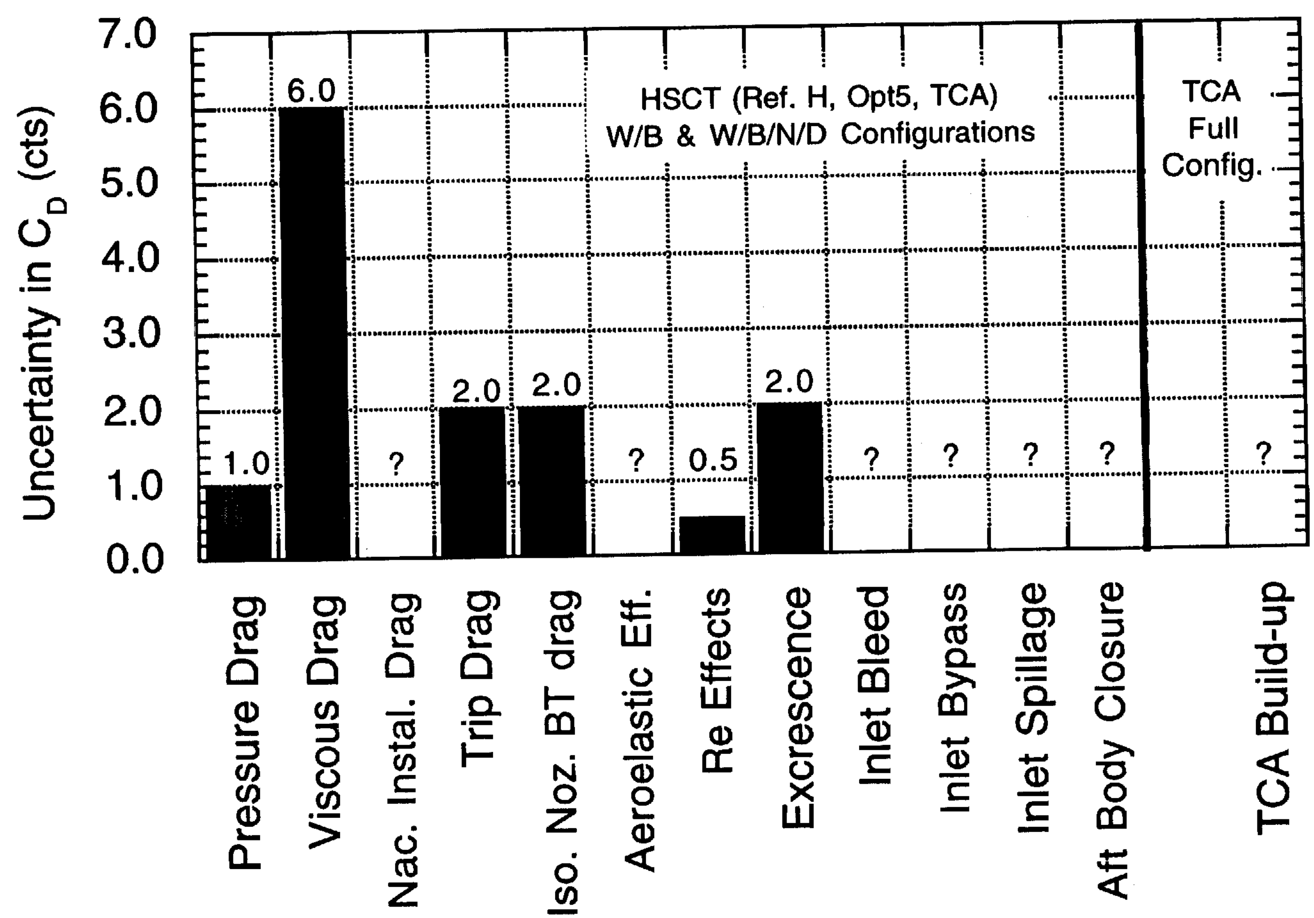

Drag Build-up from CFD to Flight Condition

The following figure presents the components of a drag build-up from the CFL3D Navier-Stokes solution for the full fuselage TCA wing/body/nacelle/diverter configuration to the flight TCA aircraft with the technology projections applied. The difference in the build-up values is surprisingly small at 0.9 counts. It is cautioned that this result may be more a result of cancellation of the various uncertainty components than a solution capability with an excellent confidence level.

Drag Build-up from CFD to Flight Condition

- **TCA Drag Build up Components ($M=2.4$, $C_L=0.1$)**

Item	C_D (counts)	Notes
CFL3D W/B/N/D solution	114.69	Navier-Stokes (B-L) at flight Re # with full fuselage
tail pressure drag	+2.2	calculation. from TI design methods
excrescence (7.1% of C_{Dv})	+2.95	assumed
trim drag	-1.03	calculation from TI design methods
predicted current technology	118.81	
technology projection	-11.9	same as the one used by TI

TCA CFD with Tech. Projection **106.9 counts**

TI Database w/ Tech. Projection **107.8 counts**

Drag Build-up from Wind-Tunnel to Flight Condition

The following figure presents the components of a drag build-up from a wind-tunnel test of the TCA performance model all the way to the flight TCA aircraft with the technology projections applied. The wind-tunnel data is modified to account for a laminar run in front of the trip disks, the change in viscous drag at flight Reynolds number, and the truncated aft-body of the wind-tunnel model. The remaining steps add the remaining components that would yield the full-flight vehicle. The difference in the TI database and TCA buildup values is somewhat surprisingly small at only 1.3 counts. Again, it is cautioned that this result can be considered somewhat serendipitous as apparently the various uncertainties in the build-up components tended to cancel each other out.

Drag Build-up from Wind-Tunnel to Flight Condition

- **TCA Drag Build up Components (M=2.4, C_L=0.1)**

Item	C_D (counts)	Notes
wind-tunnel test (W/B/N/D)	138.96	UPWT Test #1671, run 41
laminar run on model	+1.71	correction for 2.5% laminar run on flat plate
wind-tunnel skin friction	-68.51	equivalent flat plate at wind-tunnel Re#
full-scale skin-friction drag	+43.93	equivalent flat plate at flight Re#
aft body pressure drag	+0.6	TI estimate
tail pressure drag	+2.2	calculation. from TI design methods
excrescence (7.1% of C_{Dv})	+3.12	assumed
trim drag	-1.03	calculation from TI design methods
predicted current technology	120.98	
technology projection	-11.9	TI calculated projection

TCA with Tech. Projection	**109.1 counts**
TI Database w/ Tech. Projection	**107.8 counts**

- CFD and wind-tunnel testing help to check the TI data base and provide data for refinement of assumed drag components and the technology projection

Summary and Conclusions

Conclusions are summarized in the next two slides.

Summary and Conclusions

- Uncertainties in the prediction of
  - pressure drag **very small**
  - viscous drag **very large**
  - boundary layer trip drag **very large**
  - nacelle installation drag **large enough** to cause concern
  - isolated nozzle boattail drag **small**
  - aeroelastic effects **small at w.t. Re**
  - Re effect on pressure drag **relatively small** (still insufficient database), flow physics somewhat altered
- Insufficient database to quantify uncertainties in
  - Aftbody closure drag
  - Excrescence drag
  - Inlet bleed, bypass, spillage effects
  - Aeroelastic effects at flight Re

Summary and Conclusions (cont'd)

- Must minimize uncertainties in
  - wind-tunnel data measurements
  - predictions from various CFD methods
- CFD methods not yet validated at high Reynolds numbers (lack of data)
- Must achieve greater confidence in the full configuration drag prediction

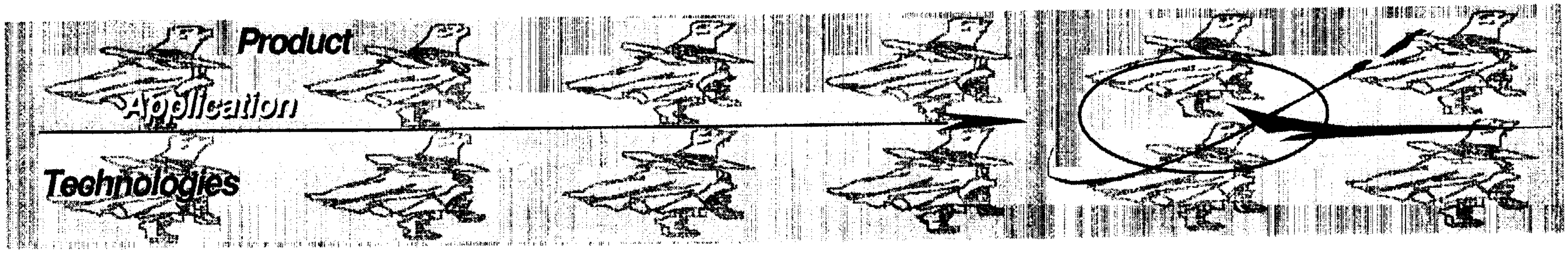

Reference H Cycle 3 Stability, Control, and Flying Qualities Batch Assessments

February 25, 1997

Dr. Dennis Henderson
(310) 982-9269
dhenderson@c17m.mdc.com

High Speed Research
Contract NAS1-20220 Task 32/36

STABILITY, CONTROL AND FLYING QUALITIES TECHNOLOGY

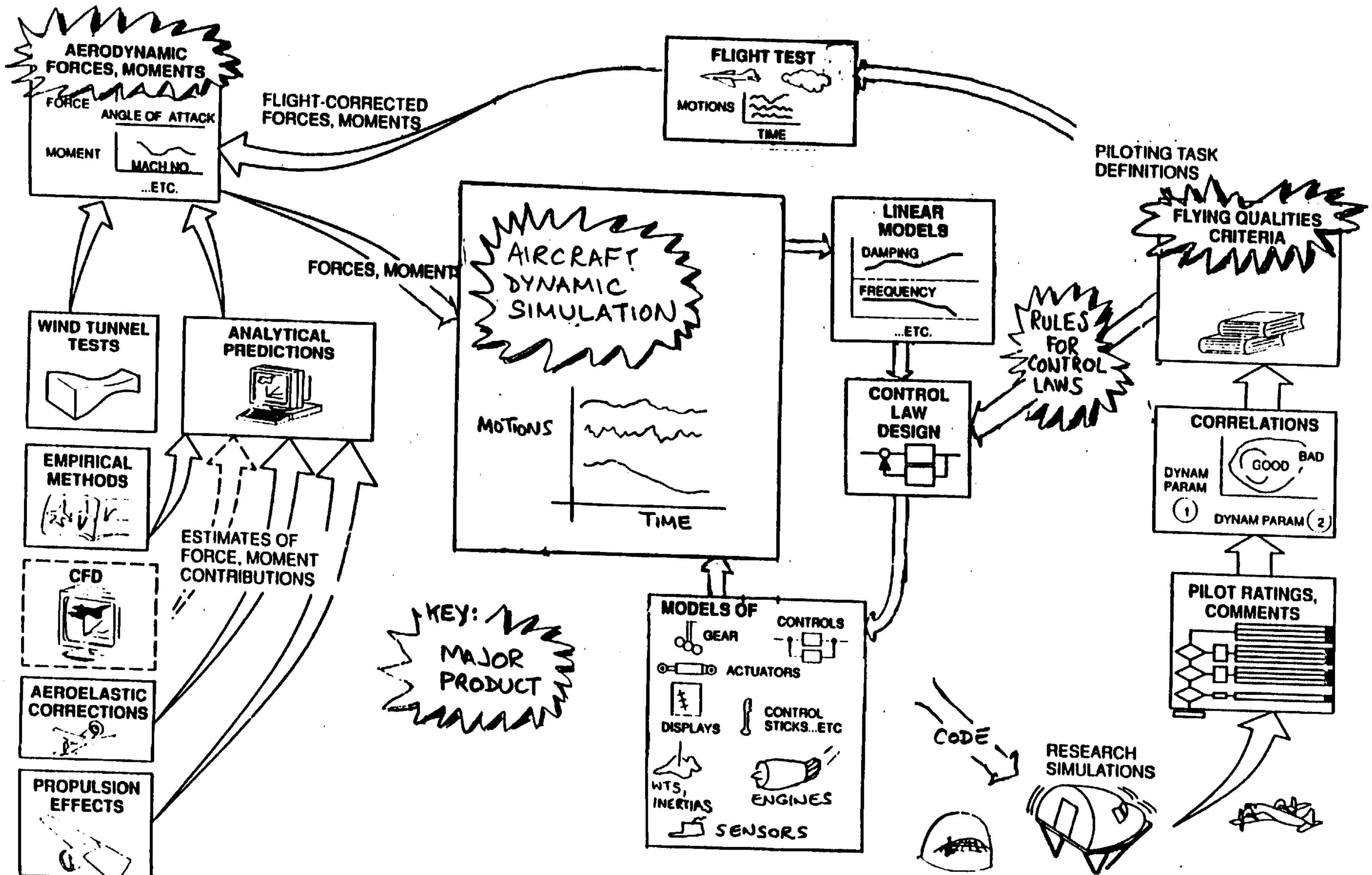

OVERVIEW

The chart shows a top level view of how airplane design is approached in the Stability, Control and Flying Qualities group. The overall design procedure surrounds a dynamic aircraft simulation. The simulation comes from writing equations of motion based on analytical predictions as well as wind tunnel tests. The simulation is used for designing control laws, evaluating the control laws with piloted simulations, and iterating the design process until flying qualities criteria are satisfied. There are three reasons why it is important to perform unaugmented assessments. 1). It is important to understand the characteristics of unaugmented airplane to provide guidance in the control system design, 2). Because of the remote possibility of failure of the flight control system, and 3). It is often found that the open loop criteria impose the greatest constraints on stability and control requirements.

Outline

- Introduction
- Un-augmented batch assessments
- Summary
- Recommendations

Introduction

Goal: Update S&C assessment with Cycle 3 evaluation

Batch Assessments:

- Evaluate unaugmented A/C against FCS req'ts
- Identify impacts of changing flight condition
- Non-real time
- Many points in envelope

Funded By:

- Flight Controls (Task 36)
- Configuration Aerodynamics (Task 32)

Dennis Henderson

INTRODUCTION

This work is an update of the assessment completed in February of 1996, when a preliminary assessment report was issued for the Cycle 2B simulation model. The primary purpose of the final assessment was to re-evaluate each assessment against the flight control system (FCS) requirements document using the updated model. Only a limited number of final assessments were completed due to the close proximity of the release of the Langley model and the assessment deliverable date. The assessment used the nonlinear Cycle 3 simulation model because it combines nonlinear aeroelastic (quasi-static) aerodynamic with hinge moment and rate limited control surface deflections.
Both Configuration Aerodynamics (Task 32) and Flight Controls (Task 36) were funded in 1996 to conduct the final stability and control assessments of the unaugmented Reference H configuration in FY96. Because the two tasks had similar output requirements, the work was divided such that Flight Controls would be responsible for the implementation and checkout of the simulation model and Configuration Aerodynamics for writing Matlab "script" files, conducting the batch assessments and writing the assessment report.

Additionally, Flight Controls was to investigate control surface allocations schemes different from the baseline Reference H in an effort to fulfill flying qualities criteria.

Introduction

Reference H Cycle 3 analytic model:

- Boeing aero, mass, engine, actuator models
  - '96 wind tunnel data: rigid aero, aeroelastic increments
  - control surface hinge moments
  - TCA engine model

- NASA Langley Simulink model
  - flap scheduling
  - V_{min} protection
  - surface lockout with Vcas
  - rate limited control surfaces

Dennis Henderson

INTRODUCTION - Continued

The assessment was conducted using the Reference H Cycle 3 Matlab and Simulink model provided by NASA Langley. The model build-up includes aero, engine, mass, and actuator models developed by the Boeing Company. The simulation uses a simple landing gear model which was not suitable for on-ground assessments.

Updates and Revisions

The Reference H Cycle 3 simulation model used for the assessment is an updated version of the Cycle 2B simulation model. The following items represent the significant updates to the Cycle 2B model:

The aero model was improved over the entire Mach range with the inclusion of experimental data from the Langley 14'x22' low speed wind-tunnel test (LaRC-437), the Langley 16' transonic test (LaRC-469), and the Langley supersonic unitary tests (UPWT 1812/1647). Flap effectiveness and flap interference were modified extensively as a result of these tests.

The Cycle 3 engine model incorporates engine dynamics provided by Pratt & Whitney for the Technical Concept Airplane (TCA). The documentation provided by Boeing (Reference 2) states "the engine data available were limited to low altitude and low speed, which is sufficient for approach. However, the same engine data were used for the entire envelope, so caution should be used when analyzing results at other points in the envelope." For the purposes of the final assessment, it is assumed that the engine model delivers the actual available thrust throughout the envelope.

A number of elements were added to the Cycle 3 Matlab simulation model by NASA Langley for full functionality. These included automatic flap scheduling, including V_{min} protection, control surface lockout with calibrated airspeed, and hinge moment limiting through the actuator model.

S&C Assessments

Assessments Completed:

- Trim in level flight
- Flight path stability
- Descent capability
- Go around
- High alpha recovery
- Diving pullout
- Roll performance
- Inlet unstart

Weight Case	cg
649,914	48.1%
614,864	52.5%
501,324	54.8%
384,862	53.2%
279,080	54.6%

Dennis Henderson

S&C ASSESSMENTS

Assessments were completed for four gross weight cases, each at their nominal center of gravity location. The operating empty weight (OEW) case was not considered. Primary emphasis was placed on those assessments that are of particular interest to Configuration Aerodynamics - at the transonic and supersonic speed regimes and the three cruise weights.

Flight Condition	Weight	Nominal c.g.
Take-off Weight	649,914	48.1%
Start-of-Cruise	614,864	52.5%
Mid-Cruise	501,324	54.8%
End-of-Cruise	384,862	53.2%
Operating Empty Weight	279,080	54.6%

Trim in Level Flight

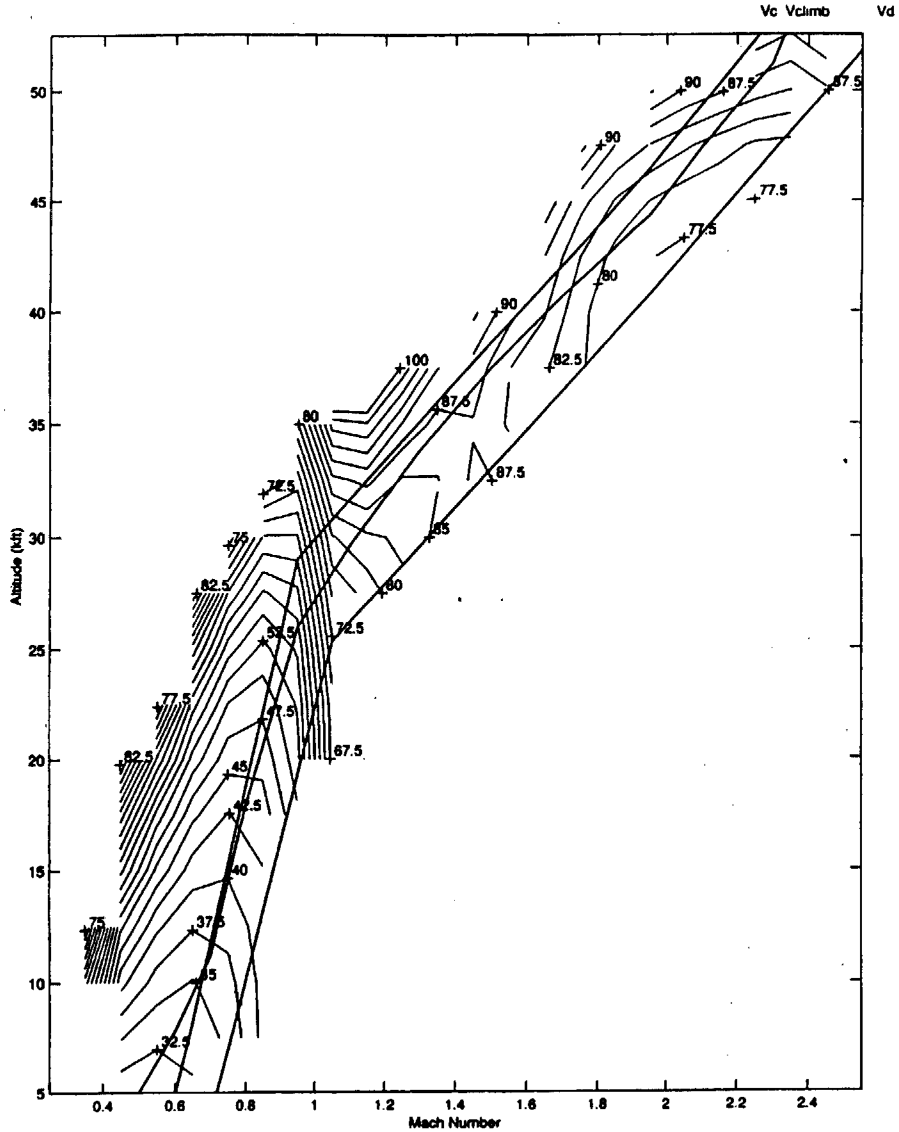

PLA for Gamma=0

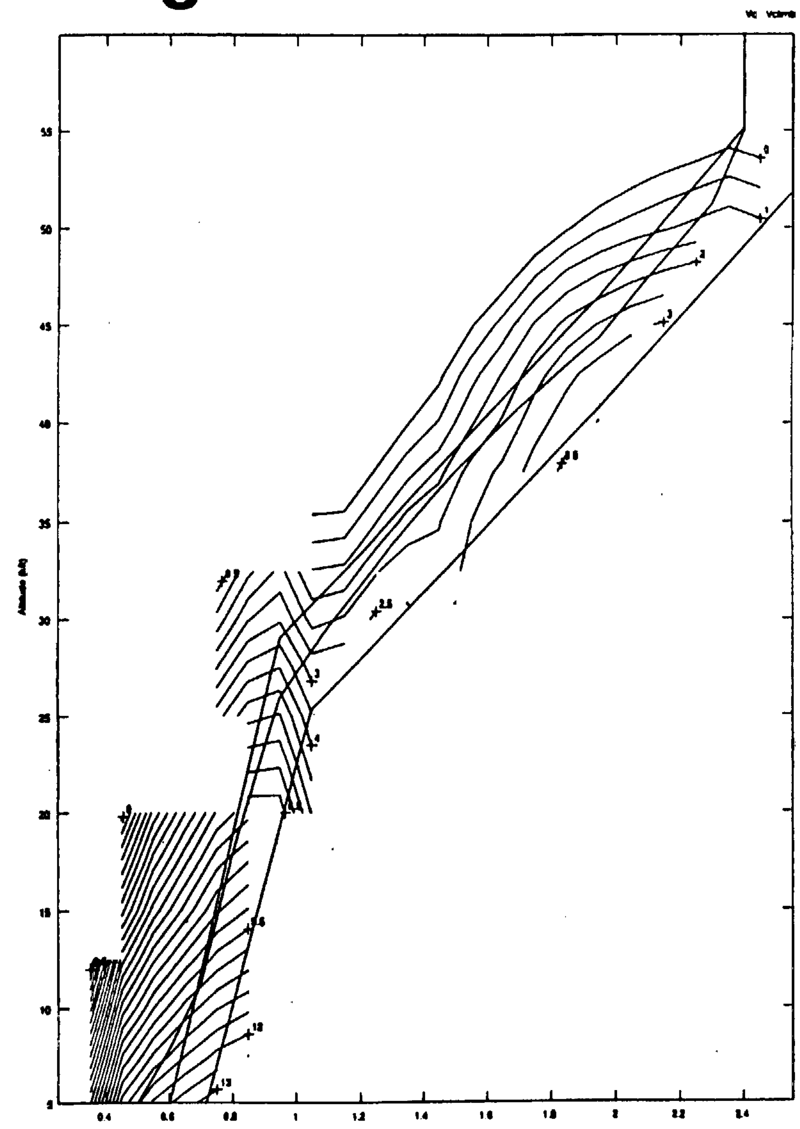

Gamma for PLA=100%

Dennis Henderson

Trim in Level Flight

The plot shows the flight envelope for the start-of-cruise weight case, 614,864 lbs. Altitude is represented on the y axis, and Mach number on the x axis. The contour labels represent PLA as a percentage, where 100% is equal to full thrust. The high speed end of the flight envelope is defined by the cruise velocity (V_C) and dive velocity (V_D) limits. V_{climb} represents the Reference H climb schedule. The low speed end is defined by V_{min}, which is artificially set to fix the approach speed at maximum landing weight to 155 knots. As altitude increases, however, V_{min} represents the speed at which 1g level flight was attainable at full thrust. This is apparent in the trim plots which show the Power Lever Angle (PLA) positions when the flight path angle is constrained to zero. Also of interest are the trimmed angle-of-attack and stabilizer position at each point in the flight envelope. For this weight case, the trim alphas are between about 2 and 11 degrees throughout the envelope and the stab deflections range from about -1 to +2 degrees.

Because the plots show that PLA is the limiting trim variable, the second plot shows flight path angles possible with PLA=100%. Zero flight path angle is seen at the low speed end of the plots, indicating thrust-limited flight. The thrust limit also defines the operational ceiling for each gross weight case. For the start-of-cruise weight plotted here, the ceiling is about 54,000 ft. As weight decreases, the ceiling increases to 65,000 ft. at the end-of-cruise weight.

Flight Path Stability

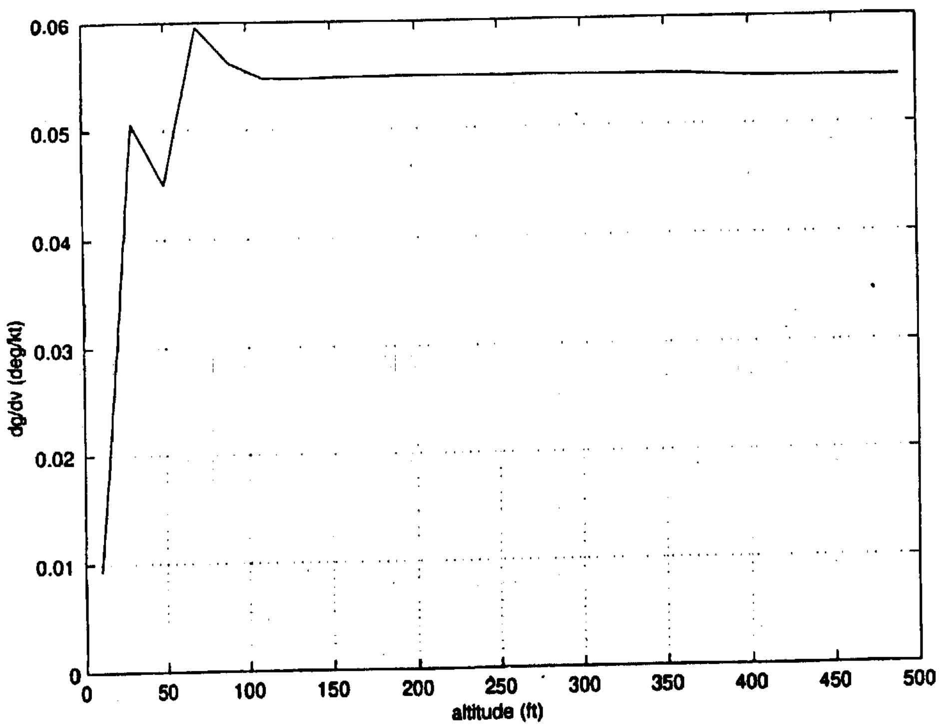

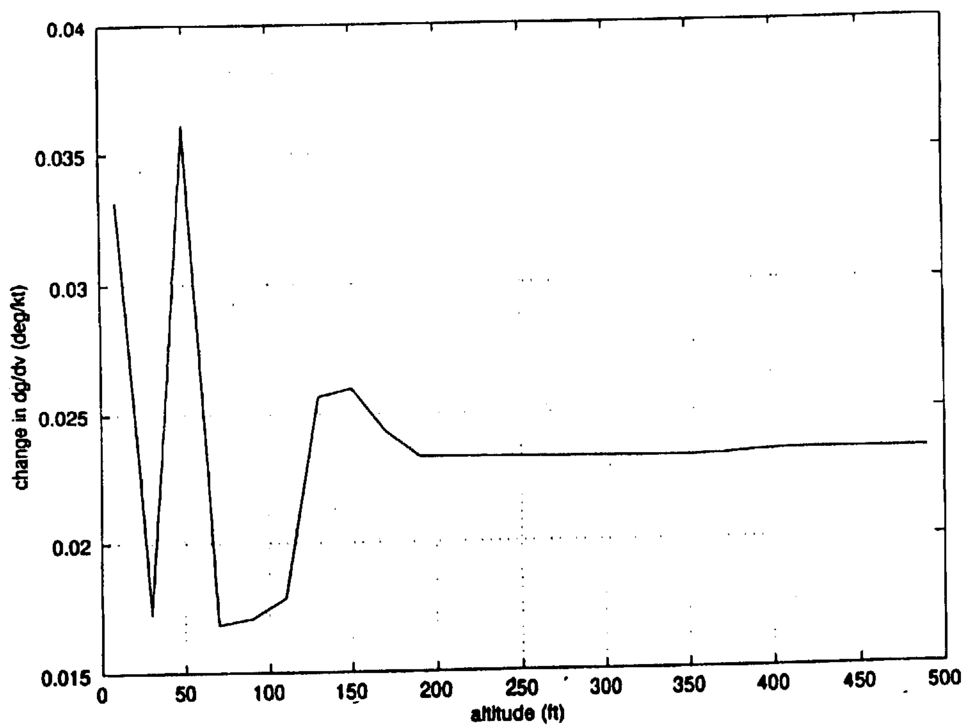

$d\gamma/dV < 0.24$ deg/kt

change in $d\gamma/dV < 0.05$ deg/kt

Dennis Henderson

Bare Airframe Flight Path Stability

The FCS Requirements document states that "The curve of flight path angle versus true airspeed for the unaugmented aircraft shall have a local slope ($d\gamma/dV$) at $V_{trim} = 1.23V_{min-1g}$ +5 kts. which is either negative or no greater than 0.24 degrees/kt. The slope of the flight path angle versus true airspeed curve at 5 knots slower than V_{trim} shall not be more than 0.05 degrees per knot more positive than the slope at V_{trim}".

Flight Path Stability plots for the approach condition were generated for altitudes from 20 ft. to 500 ft. The slope of the flight path angle, $d\gamma/dV$, was plotted on the vertical axis with altitude on the horizontal axis. The figure shows that $d\gamma/dV$ is approximately equal to 0.055 degrees/kt. at altitudes above 50 feet. Some discontinuities are apparent at lower altitudes presumably due to problems encountered with the dynamic ground effect. Work was done at Boeing to resolve that problem, but at the time of the assessments it was not complete.

Next, the incremental change in $d\gamma/dV$ was evaluated by calculating the slope at speeds 5 kts. slower than V_{trim} at the same altitudes and plotting the difference. The figure shows that the difference in $d\gamma/dV$ is less than 0.05 degrees/kt. at all altitudes analyzed.

The final result is that Reference H meets the flight path stability requirement.

Descent Capability

- 10,000 ft/minute descent required
- Analyze with 200 drag count speed brake
- Transonic - Supersonic descent
  - Satisfied for all weights.
- Subsonic descent
  - Satisfied for start-of-cruise weight above 10,000 ft. only.
  - Satisfied for mid-cruise weight above 6,000 ft. only.
  - Satisfied for end-of-cruise weight at all altitudes.

Dennis Henderson

Descent Capability

The HSCT must have the ability to descend rapidly from cruise altitude to minimize injury to passengers in the event of a depressurization or emergency. The requirement is stated as "A speed brake function shall have sufficient authority to achieve a descent rate of 10,000 fpm at maximum operating speed, V_{MO} and flight idle thrust".

The Cycle 2B assessment showed that emergency descent capability was satisfied at transonic and supersonic speeds. It was verified that this is still the case with the Cycle 3 model and this analysis focused on descent capability in the subsonic regime. The baseline configuration studied previously in the Cycle 2B assessment used only the spoiler-slot-deflectors as speed brakes. Because subsonic drag data is not available in the simulation for those devices, they do not contribute to improving the emergency descent capability at subsonic speeds. This may have been an oversight of the previous work, and as a result of discovering the lacking data, the spoiler-slot-deflectors were not used in this analysis.

An alternate speed brake configuration was investigated, which used a combination of trailing-edge surface deflections. Experimental data from the LaRC-480 wind-tunnel test conducted in June 1996 gave the incremental increase in drag by taking the difference between an alternating trailing-edge flap deflection configuration from the baseline. This configuration had alternating spanwise trailing-edge flap deflections of + and - 20 degrees. The report showed that incremental drag increases with Mach number and is also a function of angle-of-attack. For simplicity, a conservative average of 200 incremental drag counts was chosen as the speed brake capability.

Thus, with an additional 200 drag counts, and at flight idle thrust, the descent capabilities were evaluated. Descent capability was examined by simulating the maximum rate of descent at V_{MO} with speed brakes deployed for three cruise weight cases. The results are presented as descent rate versus altitude. For the start-of-cruise weight, the requirement is met at altitudes above 10,000 ft. For the mid-cruise weight case the requirement is met above 6,000 feet, and for the end-of-cruise weight case the requirement is met at all altitudes in the flight envelope.

Descent Capability

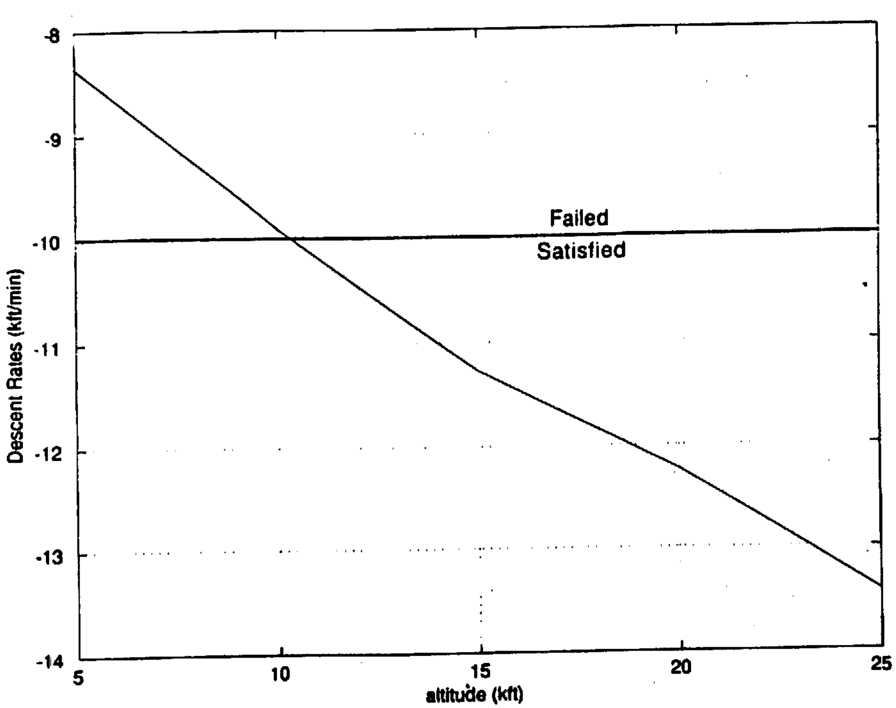

Emergency Descent 614K

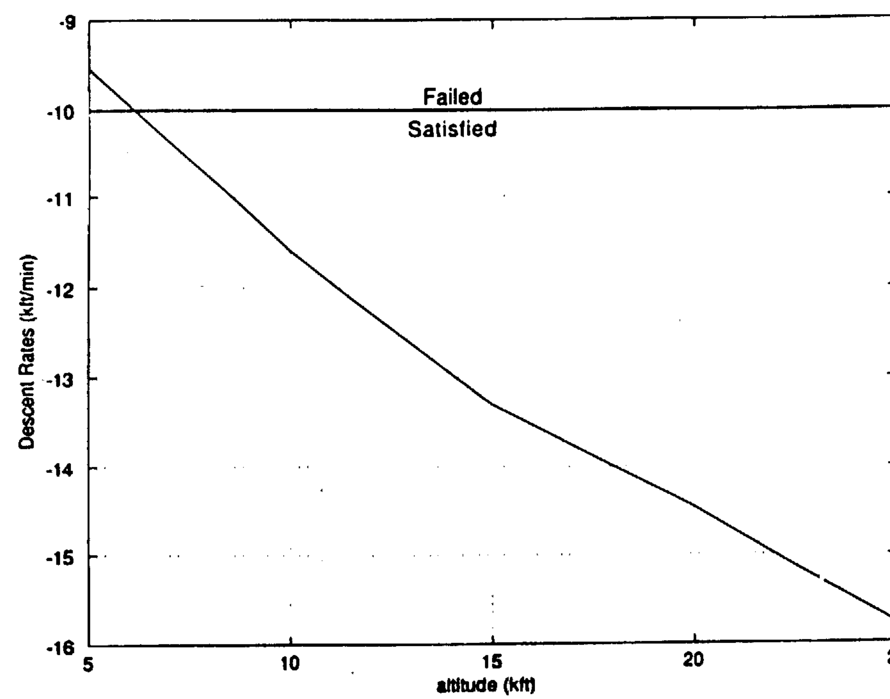

Emergency Descent 501K

Dennis Henderson

Go Around

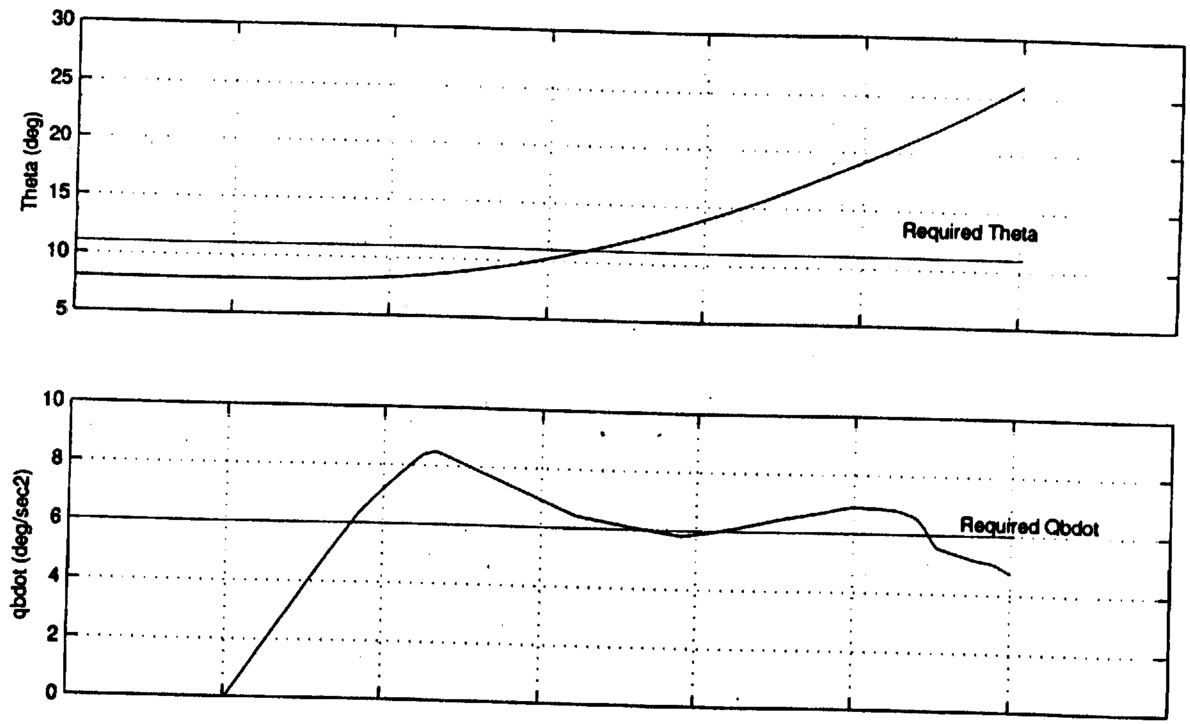

Requirement Satisfied

+ 6 deg/sec^2 pitch acceleration satisfied.

+ 3 degree pitch change in 1 sec. not satisfied

Dennis Henderson

Go Around

Go Around Control Power was evaluated starting from a trimmed landing condition at approach velocity (V_{trim} = $1.23V_{min1\text{-}g}$ + 5 kts.) and -3 degree glideslope. With a full nose up step input command, the simulation time history shows that the Reference H satisfies the requirements of reaching +6 degree/sec^2 pitch acceleration in 1 second. However, the 2.3 degree pitch attitude change in one second observed, fails to meet the second part of the requirement which requires a 3 degree pitch attitude change. Because the requirement allows for either part of the requirement to be satisfied, the Reference H meets the go around requirement.

High α Recovery

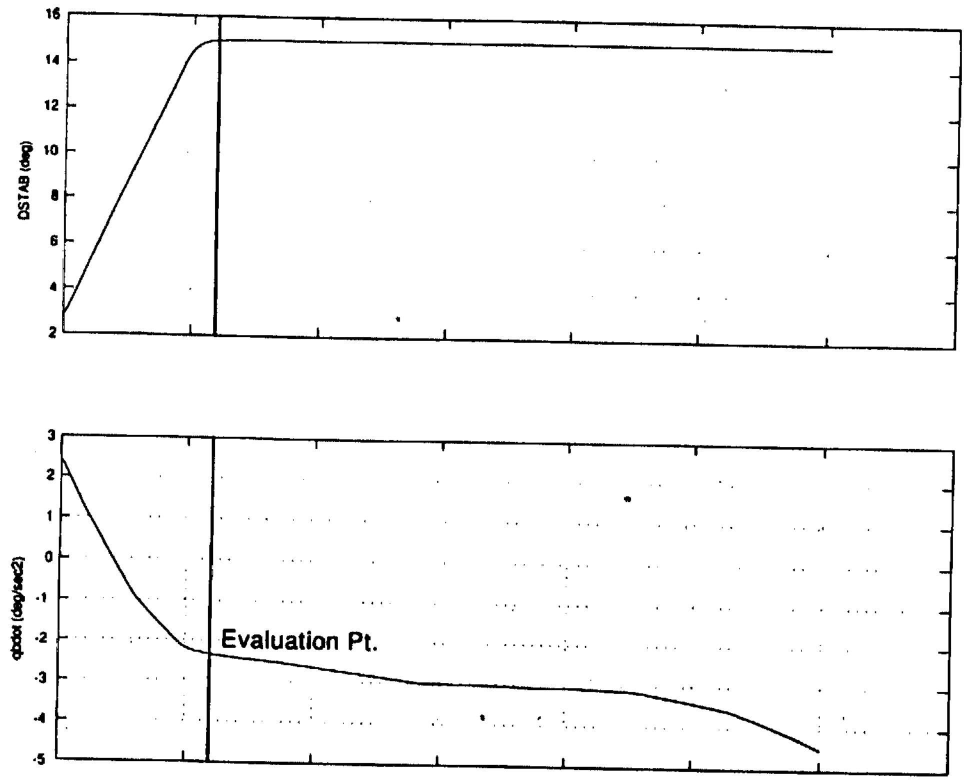

Requirement of -4.0 deg/sec^2 **NOT** satisfied

Dennis Henderson

High Angle-of-Attack Recovery

The High Alpha Recovery requirement was assessed at the end of cruise weight as a two step process. First, the airplane was trimmed at the maximum angle-of-attack, α_{max}, in the landing configuration as defined by the V_{min} speed with PLA set at 0%. Secondly, the angle-of-attack was increased by ten percent (referred to as alpha exceedance, α_{dem}) and with full forward column and full throttle, the dynamic simulation was started. The requirement was evaluated at the instant when the stabilizer reached full deflection, and pitch acceleration (qbdot) was determined to be 2.2 deg/sec^2 nose-down. The requirement states that a pitch acceleration of at least -4 deg/sec^2 must be obtained. The Reference H does not meet the High Angle-of-Attack Recovery requirement. It should be noted, however, that tests in piloted simulations suggest that this requirement may be too conservative, as the pilots still rate the aircraft as Level 1. There are multiple efforts currently underway to investigate improvements to the pitch criteria.

Diving Pullout

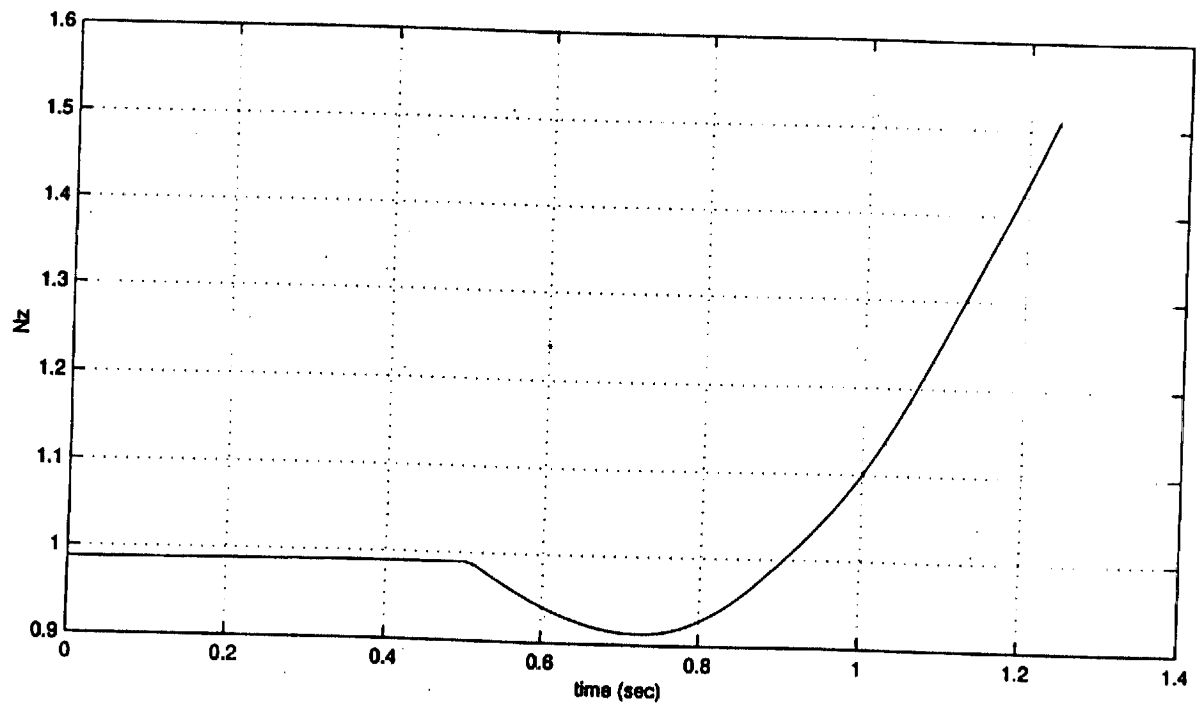

Diving Pullout at 50,000 ft. Altitude: 614 klb.

Requirement written for partial failure, but model does not allow. Satisfied for healthy A/C.

Dennis Henderson

Diving Pullout

The diving pullout requirement states "It shall be possible to effect a 1.5g pull-out at the V_D/M_D boundary with one actuator power supply channel inoperative". Currently, the Simulink model does not have the capability of partial hydraulic system failures; therefore, this assessment was conducted with full hydraulic power available. Diving pullouts were simulated for a heavy cruise weight of 614.9 klbs. and a 1.5g pull-up was attainable throughout the envelope. The figure illustrates time histories for a diving pullout at 50,000 ft.

Roll Performance

- Start-of-cruise weight, alt. range from 5,000 to 50,000 ft.
- 2 Configurations Studied
  - Baseline, TE 1/8, 3/6, and SSDs
  - Alternate, TE 1/8, 2/7, and 3/6

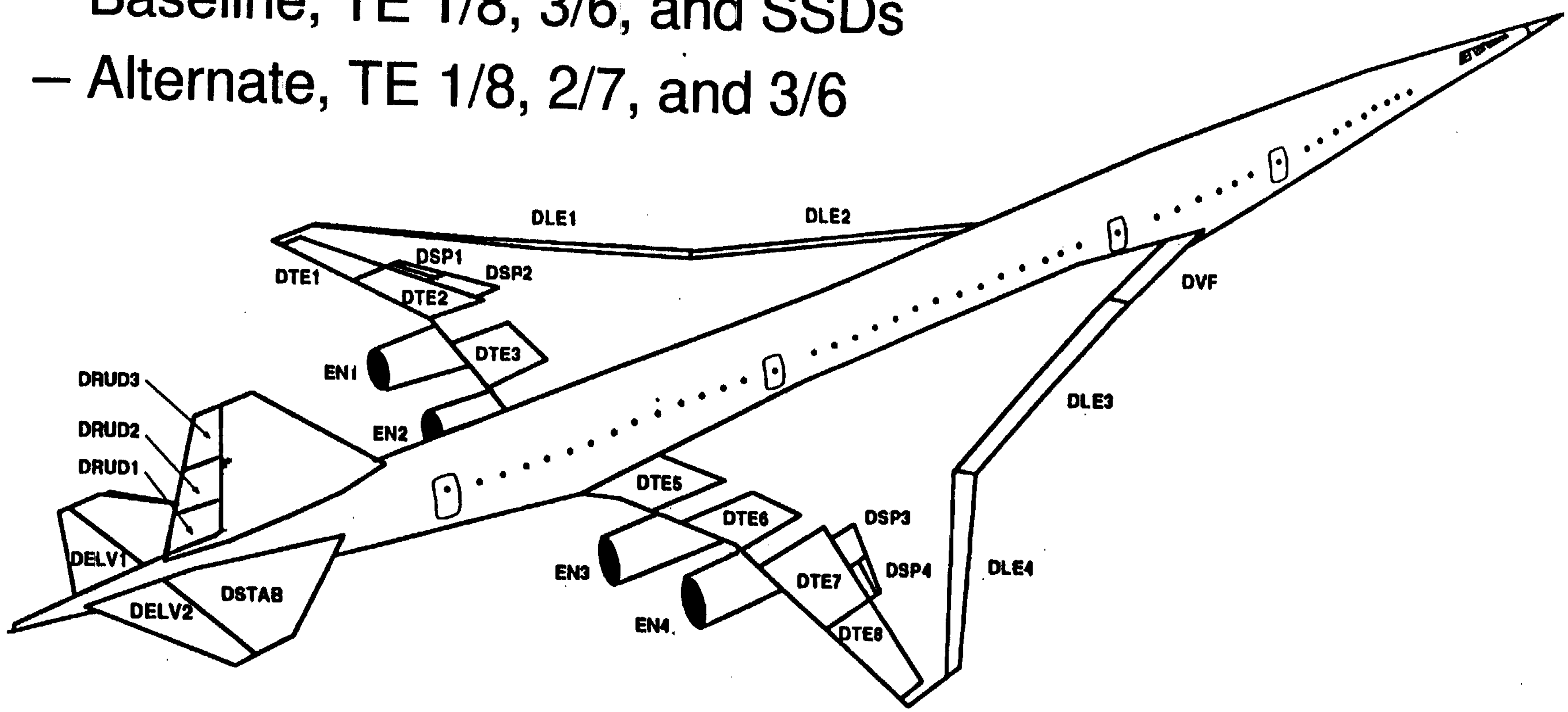

Dennis Henderson

Roll Performance

Roll control power was examined by simulating a roll from a 15 degree left banked turn to a 15 degree right banked turn using full lateral control input. To evaluate the effectiveness of different control allocation schemes, the wheel was used to drive varying configurations of lateral control surfaces including trailing-edge flaps 1/8, 2/7, 3/6, and spoiler-slot-deflectors 1/3. Trailing-edge flaps 1 and 8 are only used for lateral control at speeds below 250 kts. Roll performance was first evaluated using the Reference H baseline lateral control allocation of trailing-edge flaps 1/8, 3/6 and the spoiler-slot-deflectors. Then, roll performance was evaluated using trailing-edge flaps 1/8, 2/7, and 3/6. The intent of studying the various control allocation schemes was to identify the most effective link between the wheel and roll control surfaces.

Time to roll 30 degrees is presented for changing altitude and speed for the heavy initial cruise weight. The figure shows the time-to-roll results for the baseline combination of lateral control surfaces 1/8, 3/6, and spoiler-slot-deflectors 1/3. The figure shows that Level 2 flying qualities result at speeds around V_C and V_{climb} at Mach numbers greater than 1.6.

For the second analysis, three sets of trailing-edge flaps were used for lateral control, 1/8, 2/7, and 3/6. This configuration satisfied Level 1 flying qualities throughout the envelope. Thus, this configuration should be considered desirable as a lateral control allocation scheme.

Roll Performance

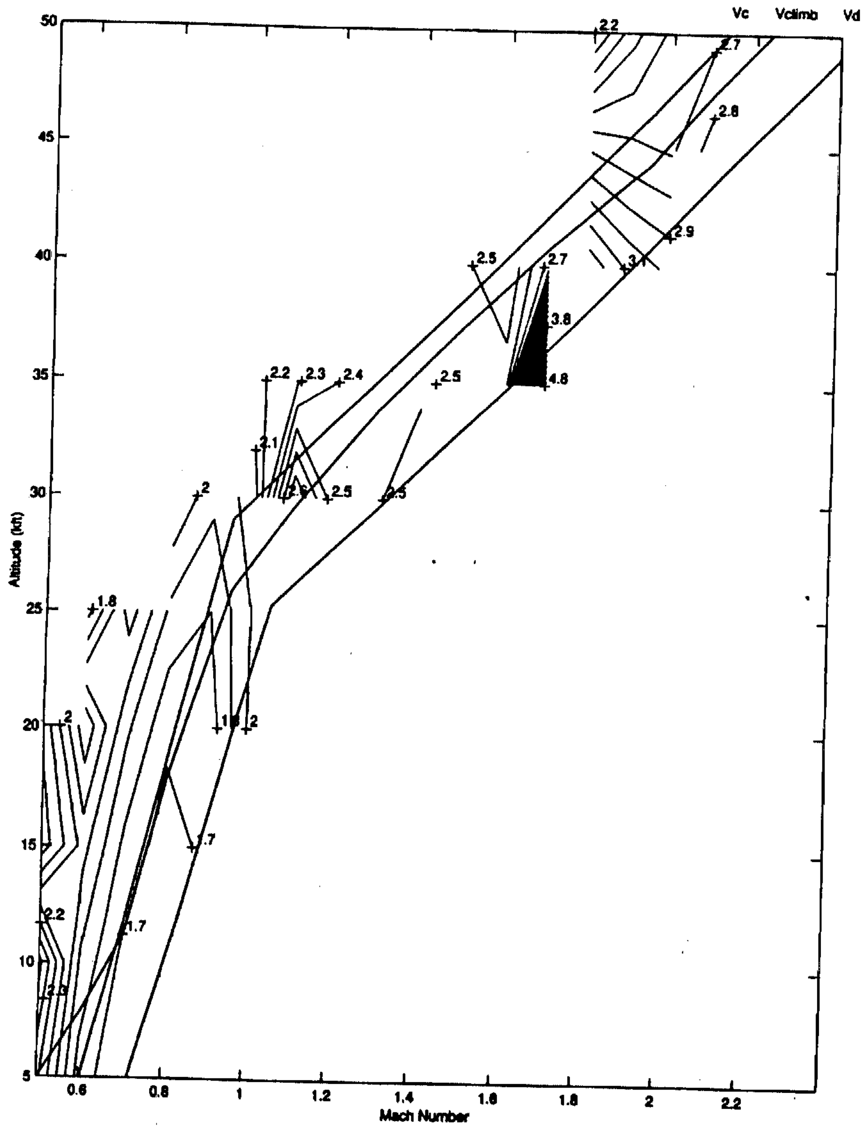

- Configuration 1: Baseline, TE 1/8, 3/6, and SSDs
  - Level 1 FQ **NOT** satisfied

Dennis Henderson

Roll Performance

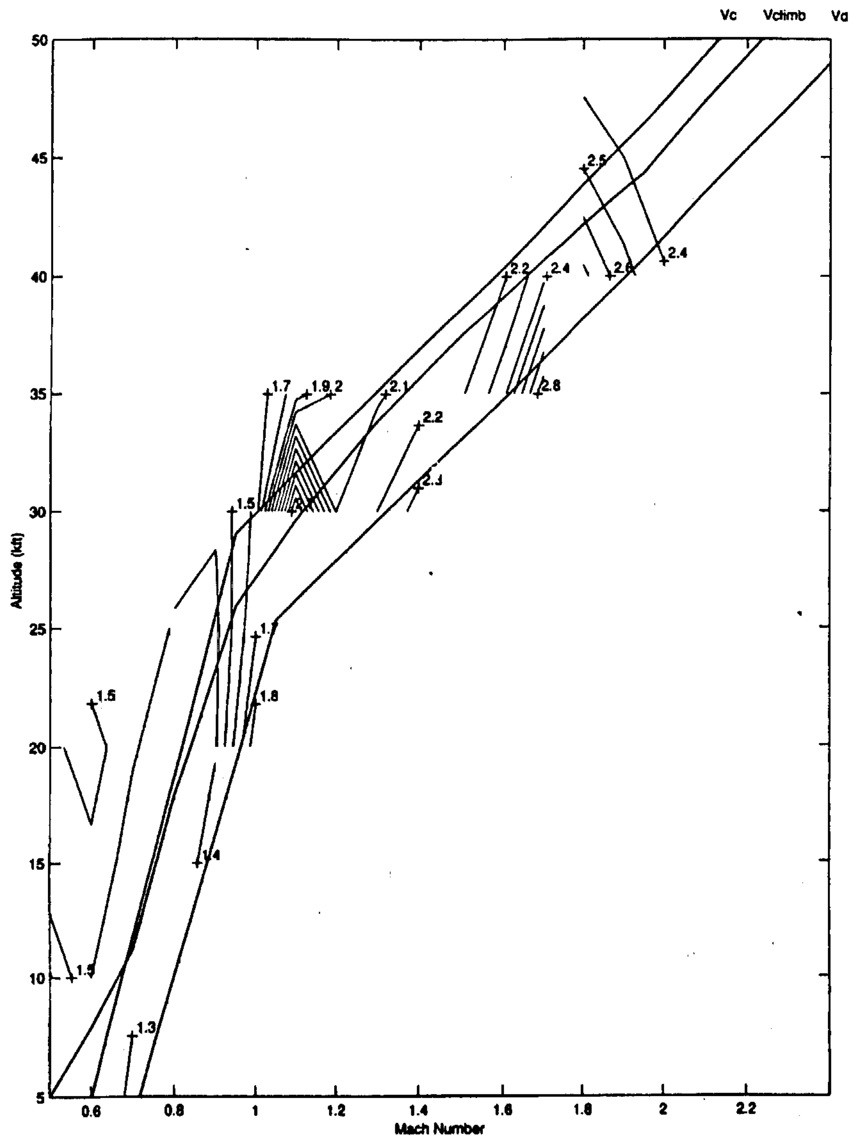

- Configuration 2: TE 1/8, 2/7, and 3/6
  - Level 1 FQ **SATISFIED**

Dennis Henderson

Inlet Unstart

- Start-of-cruise weight, Mach >1.6, two engines out.
- "Desired" Lateral control configuration used 1/8, 2/7, 3/6

Dennis Henderson

Inlet Unstart

The requirement is that the aircraft must be able to attain a 5 deg/sec roll rate during unstart.

Dual Inlet Unstart of engines 3 and 4 was examined for Mach numbers greater than 1.6, the regime where an unstart condition can occur. The assessment was performed for the start of cruise weight case, 614.9 klbs. and the control allocation was that from the previous roll performance assessment. That is, the wheel was connected to trailing-edge flaps 1/8, 2/7 and 3/6. With 100% PLA on the two remaining "started" engines, a zero flight path angle was not achievable as shown in the flight path angle contour plot. Plots of the stabilizer, rudder, and wheel deflection required to maintain wings-level flight showed that the surfaces were able to balance the aircraft easily with small deflections.

A representative transonic condition was chosen (Mach 1.9 at 47,000 ft.) to perform a dynamic simulation to determine if the requirement could be met with the lateral controls remaining after accounting for wings-level trim following a dual inlet unstart. The figure shows that for a full left or full right wheel input, a roll rate of 5 degrees/sec. is easily attainable, satisfying the requirement. Because of the ease with which the requirement was satisfied for this representative case, it is reasonable to assume that the requirement would be satisfied at the remaining flight conditions.

Inlet Unstart

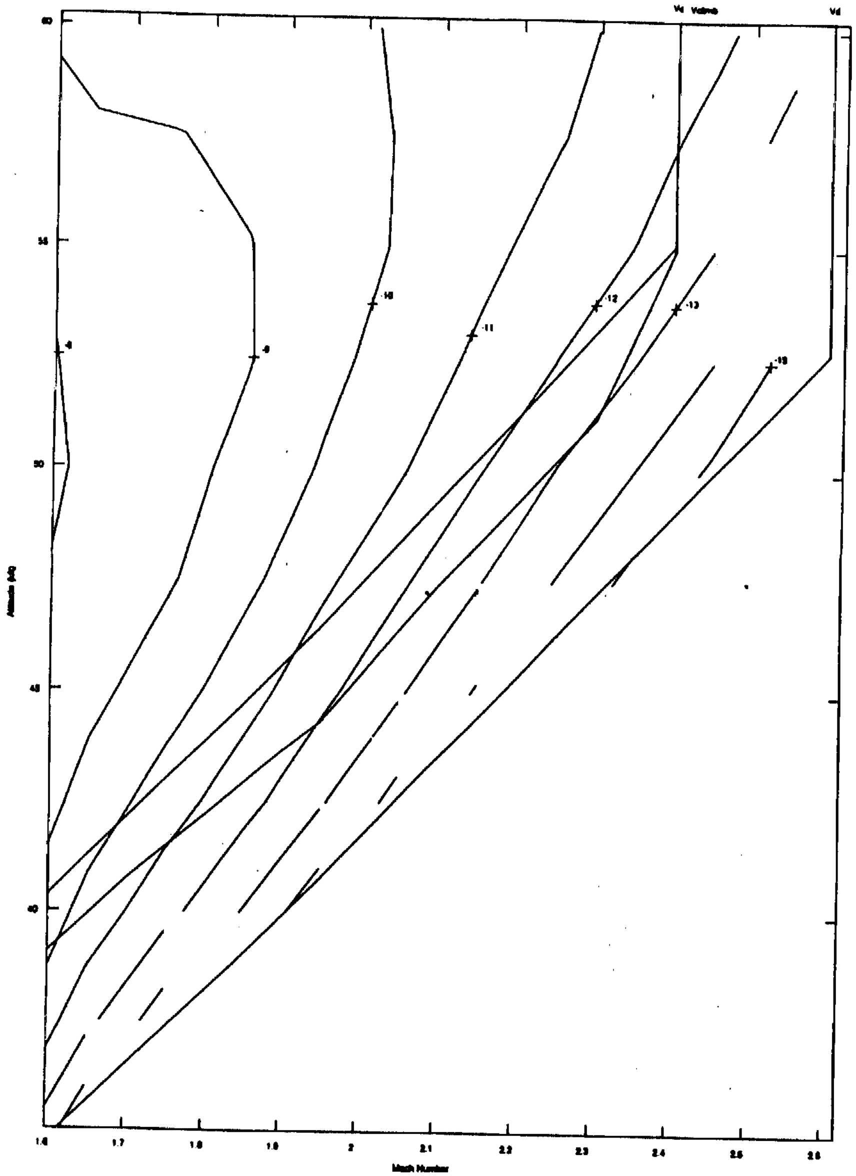

- Can trim at wings level, but not $\gamma = 0$

Dennis Henderson

Inlet Unstart

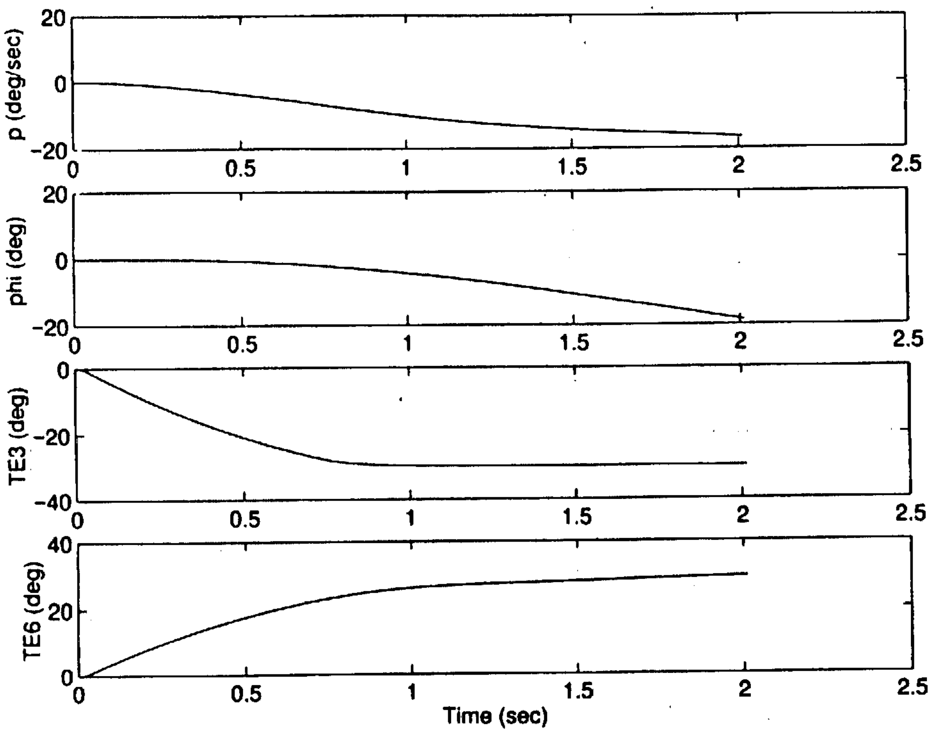

Full Left Wheel Input

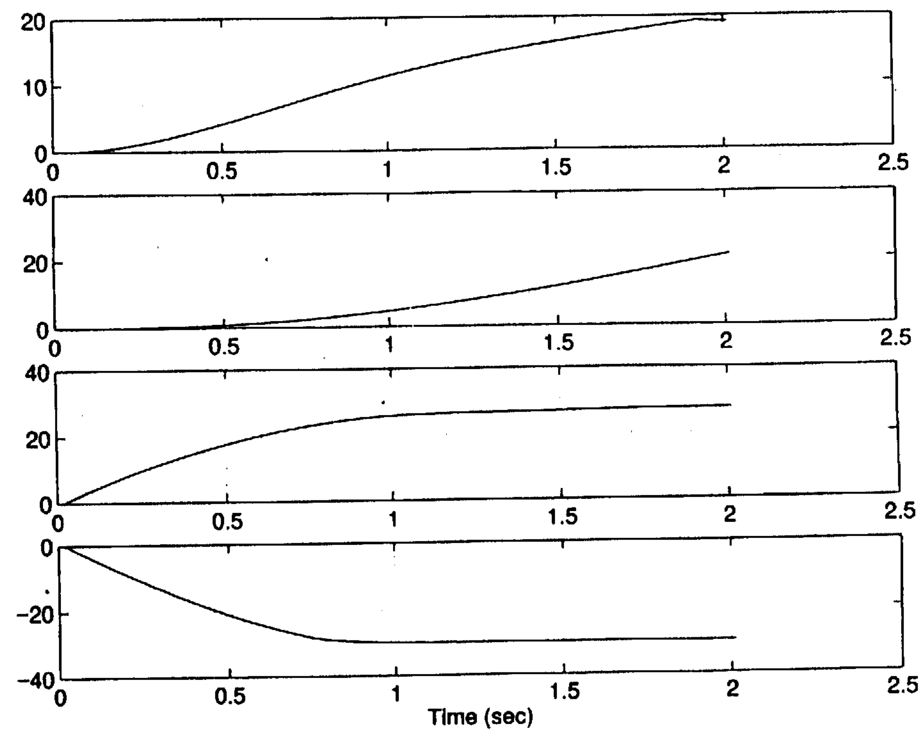

Full Right Wheel Input

- Roll rate of 5 deg/sec easily attainable - reqt. satisfied

Dennis Henderson

Summary

- Trims at straight and level flight throughout a realistic flight envelope due to updated engine models and modifications to Matlab optimization analysis tools.

Requirements Satisfied:

- Flight Path Stability
- Go-Around
- Diving Pullout for a heavy cruise weight case and with full hydraulic power
- Roll Performance requirement with Level 1 flying qualities throughout the flight envelope for a heavy cruise weight case using flaps 1/8, 2/7 and 3/6
- Inlet Unstart roll performance requirement
- Emergency Descent rate requirement for all weight cases in the transonic and supersonic regimes. In the subsonic regime, the requirement is met at end of cruise weight, but is **NOT** met at mid-cruise weight and heavier.

Dennis Henderson

SUMMARY

An assessment of the Reference H configuration using the Cycle 3 simulation model has been conducted and the results have been compared to the FCS requirements. Primary consideration was given to evaluating those requirements that pertain to the HSR Configuration Aerodynamics task. Assessments currently indicate that the Reference H aircraft:

Trims at straight and level flight throughout a realistic flight envelope due to updated engine models and modifications to Matlab optimization analysis tools.

Requirements Satisfied:

Flight Path Stability

Go-Around

Diving Pullout for a heavy cruise weight case and with full hydraulic power

Roll Performance requirement with Level 1 flying qualities throughout the flight envelope for a heavy cruise weight case using trailing-edge surfaces 1/8, 2/7 and 3/6

Inlet Unstart roll performance requirement

Emergency Descent rate requirement for all cruise weight cases in the transonic and supersonic regimes. In the subsonic regime, the requirement is met for altitudes of 10,000 ft. and higher for all cruise weight cases.

Requirements <u>Not</u> Satisfied:

Does **NOT** meet the High Angle-of-Attack Recovery requirement.

Requirements not analyzed:

Minimum Control Speed

Gust Recovery

Maneuvering Performance

Crosswind Landing

Tameness

Summary - cont.

Requirements Not Satisfied:

- Does NOT meet the High α recovery requirement

Requirements not analyzed:

- Minimum Control Speed
- Gust Recovery
- Maneuvering Performance
- Crosswind Landing
- Tameness

Recommendations

- Drag devices on the HSCT must be carefully sized and configured: 200 incremental drag counts over baseline did not satisfy emergency descent req't. at heavier weights.
- Pitch control must be increased to satisfy the High α Recovery requirement.
- The simulation model should be modified to allow partial failure capabilities needed for certain assessments such as diving pullout.
- Plot time histories of surface deflections during roll maneuvers for several Mach numbers at a fixed altitude to study relationships between hinge moments, surface rates and surface deflections.
- Matlab optimization tools used for trimming the aircraft are sensitive to the "initial guess". Alternative schemes should be investigated.

Dennis Henderson

RECOMMENDATIONS

Drag devices on the HSCT must be carefully sized and configured, as it was shown that 200 incremental drag counts over the baseline configuration were required for emergency descent capabilities.

Pitch control must be increased to satisfy the High Angle-of-Attack Recovery requirement.

The simulation model should be modified to allow partial failure capabilities needed for certain assessments such as diving pullout.

It would be interesting in future work to plot roll performance time histories of surface deflections for several Mach numbers at a fixed altitude to determine the relationship between hinge moments, surface rates and surface deflections and how those relationships change with speed.

The Matlab optimization tools used for trimming the aircraft are particularly sensitive to the choice of an "initial guess". Alternative tools, or modifications to current tools should be investigated.

REFERENCES

Henderson, D. and Cameron, D., “Reference H Assessment Summary Report,” NASA Contract NAS1-20220, Task 32, November 18, 1996.

Forced Transition Techniques on HSCT Configurations

Richard A. Wahls
Steven X. S. Bauer
Lewis R. Owens, Jr.
NASA Langley Research Center
February 25, 1997

1997 HSR Aerodynamic Performance Workshop

Outline

- Objectives
- Background
  - description of transition, location of trips, and trip drag
  - supersonic vs subsonic issues
- Approach
  - multiple tests, multiple trip types, patterns, heights
  - low and high Rn, transition detection
- Low Rn Supersonic Testing (UPWT)
- High Rn Supersonic Testing (PSWT)
- High Rn Subsonic & Transonic Testing (NTF)
- Concluding Remarks

As outlined above, this presentation describes the general objectives of the project, followed by background information which led to the initiation of the study, and the approach taken to meet the objectives. Next, experimental studies in the LaRC Unitary Plan Wind Tunnel, the MDA Polysonic Wind Tunnel, and the National Transonic Facility will be discussed. Concluding remarks will close the presentation.

1997 HSR Aerodynamic Performance Workshop

Objectives

- Determine the best method (grit vs dot) of tripping the boundary layer
- Determine the best method for assessing trip effectiveness
- Determine the best method for quantifying trip drag
- Determine any advantage of testing at slightly higher Rn_{∞}/ft available in industry blowdown facilities
- Determine the Reynolds number for fully turbulent flow

The objectives of this effort were to determine (if possible) the best method: 1) for forcing the boundary layer to transition, 2) for assessing trip effectiveness, 3) for quantifying trip drag, 4) for testing at Reynolds numbers per foot from 5 million to maximum available rather than 1 to 5 million, and 5) for boundary layer state determination.

Subsonic vs Supersonic Issues

- Subsonic
  - Rn_k=600
  - possible to size for no/minimal trip drag ---trip usually inside b.l.
  - works in small alpha range --- sized and located based on a given attachment line location
- Supersonic
  - Rn_k =1000
  - possible to size for minimal trip drag ---trip usually outside b.l.
  - works in small alpha range --- sized and located based on a given attachment line location
- Trip Verification Methods
  - flow visualization --- time-consuming
  - Reynolds number sweeps --- less of impact on schedule, in general

It has been shown (Braslow, Hicks, et. al.) that for subsonic through low supersonic conditions, the trip drag can be considered negligible and doubling the effective trip height (as long as the trip does not stick into the freestream) will add an indiscernible amount of drag. However, at supersonic conditions, this is not the case. In order to transition the boundary layer, the trips must be sized larger than the boundary layer thickness. Now, the portion of the trips that stick out into the freestream do produce measurable amounts of drag.

Subsonically, Braslow et al. have shown that trip drag (in the plateau region, which is the region where the boundary layer has transitioned and the trips are not sticking out into the freestream) can be calculated by testing several trip heights and plotting the associated drag versus the trip height. A linear curve can be drawn through the data in the plateau region and extrapolated to k=0 (no height). The trip drag then is equal to the slope of the curve multiplied by the specific trip height in question. Braslow et al. also have shown that supersonically, the best method is to use drag versus k^2. A slope is then found in a similar fashion, however, due to the fact that drag on an object in a freestream is not linear with height (it is closer to quadratic) a much lower drag is estimated.

Finally, sublimation and other flow visualization techniques take a lot of time, whereas running Rn sweeps takes a relatively short time. By accurately reducing the data, a very good understanding of the boundary layer state can be made.

CD vs Rn

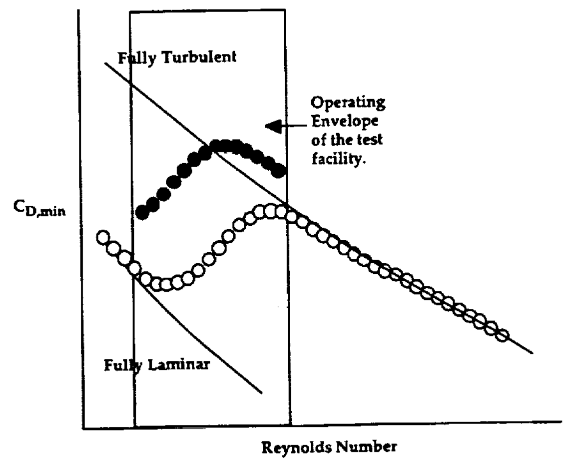

The ideal method of insuring that turbulent boundary layer conditions are met is shown above (open circles). The technique would require that the test be run at Rn conditions that would insure that one would have fully laminar b.l. conditions at the low end of the Rn capability to fully turbulent b.l. conditions at the high end. This technique can be done in some facilities (NTF, 20-Inch Mach 6, PSWT, etc.). However, for most tunnels, the operating Rn range lies completely in the transition region (shown above as the location that the data does not lie on the fully laminar nor the fully turbulent curves). Therefore, one must trip the boundary layer.

The figure above also illustrates the effect of a transition trip on the values of $C_{D,min}$. In the same operating range, fully turbulent boundary-layer conditions can be achieved and the value of trip drag is equal to the difference in the forced-transitioned and the free-transitioned, fully-turbulent b.l. $C_{D,min}$. However, if one can not ever reach free-transitioned, fully-turbulent b.l. conditions in the tunnel, how can one determine the trip drag? Note, it is always a good practice to run through a Rn sweep in the facility at $C_{D,min}$ conditions, just to determine that the transition trips are working (and this usually can be done with minimal impact on the test schedule). Why is this important and what useful data can you get? First, as shown by the solid circles above, $C_{D,min}$ increases until fully turbulent conditions are reached as Rn is increased. As Rn is increased further, the $C_{D,min}$ values will decrease (and the data will fall on a curve that is parallel with the fully turbulent b.l. curve). Thus, while $C_{D,min}$ is still increasing or has reached a plateau, transitioning b.l. conditions are occurring. If the $C_{D,min}$ values decrease at a fairly "constant" rate with Rn (same local slope as that for fully turbulent flow found for free transition), then fully turbulent b.l. conditions have been reached.

1997 HSR Aerodynamic Performance Workshop

Determination of Trip Drag

- Trip Drag may be determined by calculating the slope of the curve for drag (at a specific lift condition) versus k or k^2.

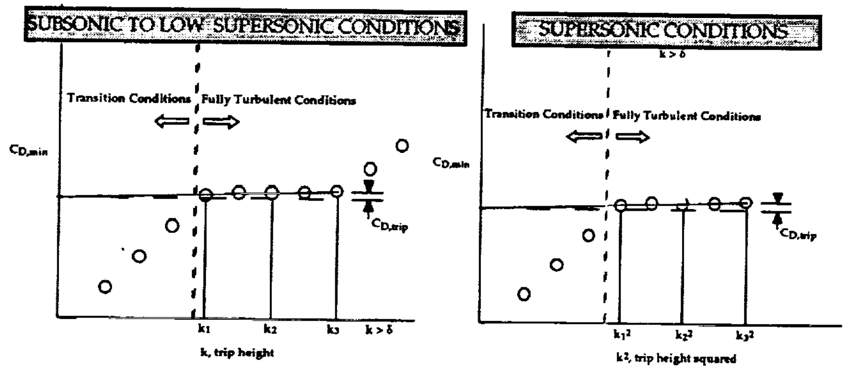

There are several methods of determining trip drag. When a large Rn capability is achievable in the facility, the technique described previously is preferred. However, the reduced capability test facility is usually the norm. In such a facility, one can test the model with different sized trips. Whether the trips are smaller or larger than the boundary layer determine how the trip drag is calculated.

In subsonic to low supersonic flow conditions, the grit particles when sized and located properly on the wing for the freestream conditions, can allow a doubling of the size of the trip to have very little effect on the drag.

Note, once the boundary layer is fully turbulent and as long as the trip height, k, is not greater than the boundary-layer thickness, δ, then the values of CD,min are not overly affected by the trip. Therefore, a trip drag can be calculated by extrapolating a linear curve fit (of the CD,min data for the $k< \delta$ conditions) back to k=0. This will define a CD,min that should be equivalent to fully turbulent flow with no trip drag. Then the trip drag for any k value can be calculated by subtracting the CD,min value for k=0 from the value of CD,min for a given k. Also, note that when $k> \delta$, the CD,min values for those k values increase rapidly. Thus, for conditions that require the size of the trip, k, to be greater than the boundary layer, a similar method can be employed, however, one must use k^2 instead of k to get an accurate extrapolated curve to k or $k^2 = 0$ and thus, CD,min conditions for fully turbulent b.l. with no trip drag.

1997 HSR Aerodynamic Performance Workshop

Streamline Issue

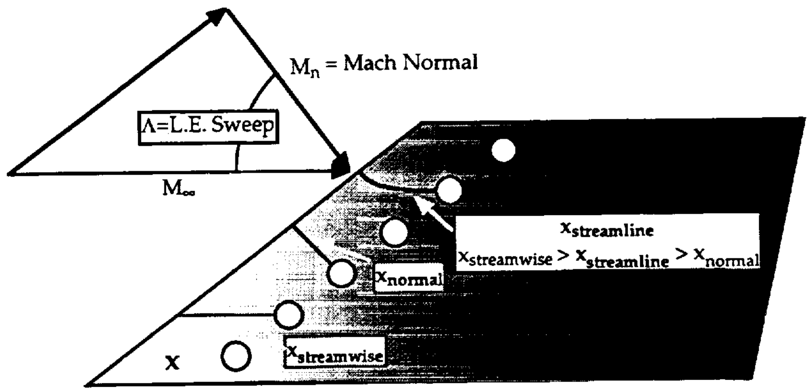

The figure above shows how the actual distance, $x_{streamline}$, that the flow covers from the leading edge to the trip dot (by following the streamline rather than the axial or "streamwise" direction behind the leading edge) can change the height, k, required to transition the boundary layer. For highly swept wings, $x_{streamline}$ can be much less than x and thus, the $Rn_{k,cr}$ is never reached and the trip dot does not have any effect on the boundary layer state.

Transition Detection Methods

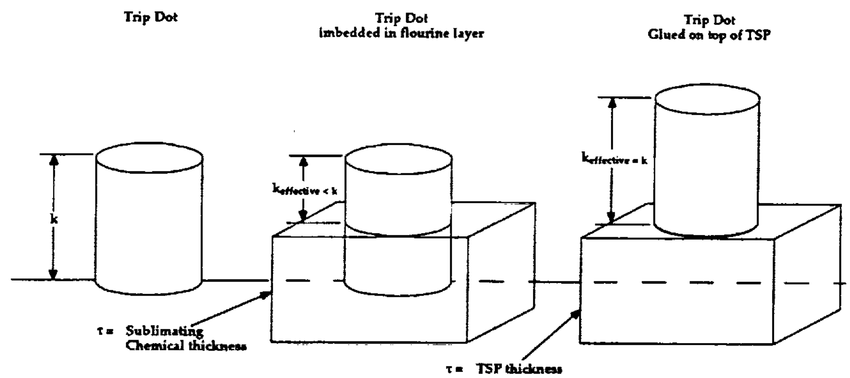

The figure above shows the effective height, k_{eff}, after the sublimating chemical is applied to the surface. Since k_{eff} is smaller than k, the value of $Rn_{k,cr}$ is never reached and the trip dot does not have any (or very little) effect on the boundary-layer state. Thus, a method of applying sublimating chemicals that does not cover the leading edge up to the trips may be required.

Shown to the right (above) is a sketch of the same trip dot glued onto a surface with TSP (Temperature Sensitive Paint). Note, here the effective height of the trip dot is the same as that specified. In addition, the paint surface is hard, thin, smooth, and consistent throughout a series of runs. Note that paint does not have to be reapplied for each angle-of-attack.

Approach

- The M2.4-7A Arrow Wing was tested in UPWT and generated a data base at M_∞=2.4 and Rn_∞ = 1 to 5 million/foot with free (natural) and fixed (grit & dot of various size) transition
- Test the M2.4-7A Arrow Wing in the MDA-E Polysonic Wind Tunnel (PSWT) at Rn_∞ greater than 5 million/foot foot with free (natural) and fixed (grit & dot of various size) transition
- Obtain force and image data for free (natural) and fixed transition

The M2.4-7A Arrow wing configuration was chosen because it was a clean model, had no "planned" entries in the near term, and needed a trip drag analysis at the cruise condition.

The model is slightly larger than ideal for testing in the PSWT due to its large projected area relative to start-up and ending conditions. The model is of typical size for supersonic testing in the HSR program, and results in the PSWT were very promising.

BOUNDARY LAYER HEIGHT AT TWO X-LOCATIONS
LAMINAR FLAT PLATE CALCULATION
$M_\infty = 2.40$

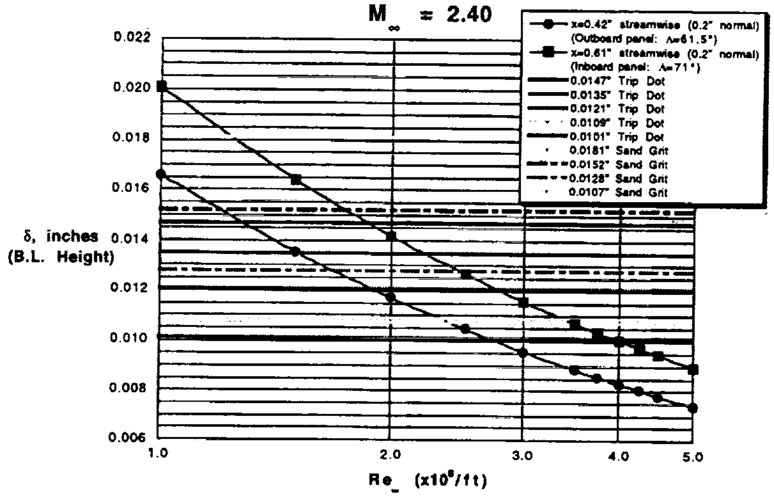

Shown above is a plot of the predicted laminar, flat-plate, boundary-layer height at x = 0.42" and 0.61" from the leading edge in the streamwise direction (outboard panel trip location and inboard panel trip location, respectively). Since the free stream Mach number is 2.4, the required trip height would have to be greater than the boundary layer thickness to be effective. Thus, the plot also includes the sand grit sizes and trip dot heights that were tested on the M2.4-7A configuration in the NASA LaRC UPWT.

1997 HSR Aerodynamic Performance Workshop

TEST 1667 SAND GRIT DRAG DATA
Baseline M2.4-7A Configuration
M_∞ = 2.4, $C_{D,min}$

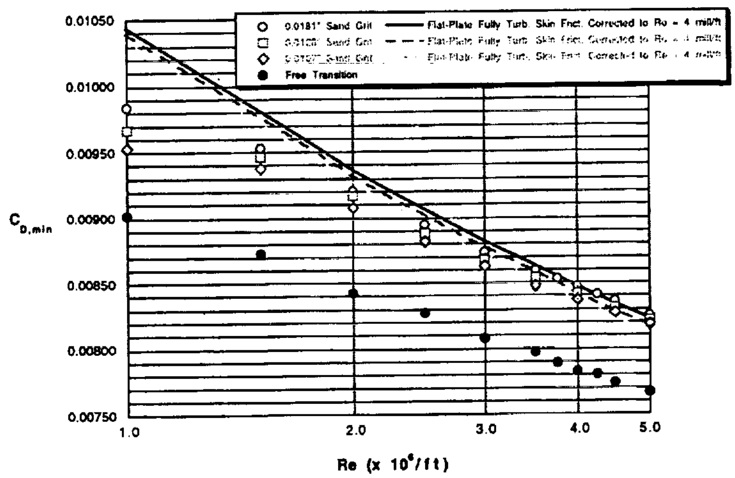

The plot above shows the $C_{D,min}$ values plotted versus Reynolds number for the three sand grit sizes tested as well as the free transition values. Also plotted are the flat plate fully turbulent skin friction drag estimates corrected to the Reynolds number 4 million/foot condition.

The results show that for Reynolds numbers less than 2 million/foot, a transitional stage of the boundary layer is occurring.

1997 HSR Aerodynamic Performance Workshop

TEST 1667 TRIP DOT DRAG DATA
Baseline M2.4-7A Configuration
M_∞ = 2.4, $C_{D,min}$

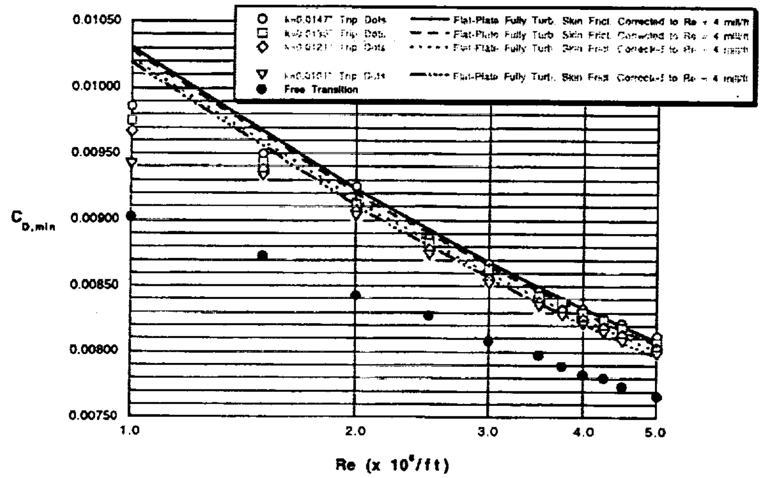

The plot above shows the $C_{D,min}$ values plotted versus Reynolds number for the five trip dot heights tested as well as the free transition values. Also plotted are the flat plate fully turbulent skin friction drag estimates corrected to the Reynolds number 4 million/foot condition.

The results show that for Reynolds numbers less than 2 million/foot, a transitional stage of the boundary layer is occurring as was seen with the sand grit runs.

1997 HSR Aerodynamic Performance Workshop

Baseline M2.4-7A Configuration
(Free Transition)
M_∞ = 2.40, Re_∞ = 1 to 5 x10^6/ft

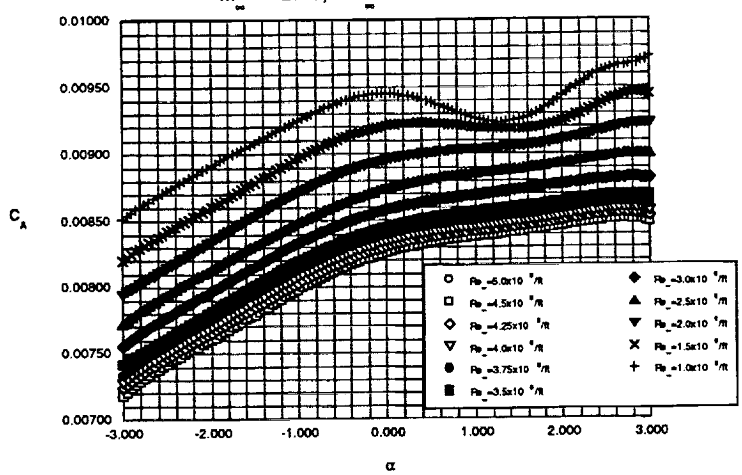

The data above shows the curve fit values of the Axial Force Coefficient (C_A) versus angle of attack, α, for the baseline M2.4-7A configuration at a Mach number of 2.40 and Reynolds numbers varying from 1 to 5 million per foot for the free transition condition. The C_A data is very valuable in determining if a "laminar bubble" occurs at any conditions in the polar as can be clearly seen for the lowest Reynolds numbers tested. As seen above for all Reynolds number conditions, the curves are not continuous. By examining the local slope of the curves ($dC_A/d\alpha$), this effect can more readily be observed.

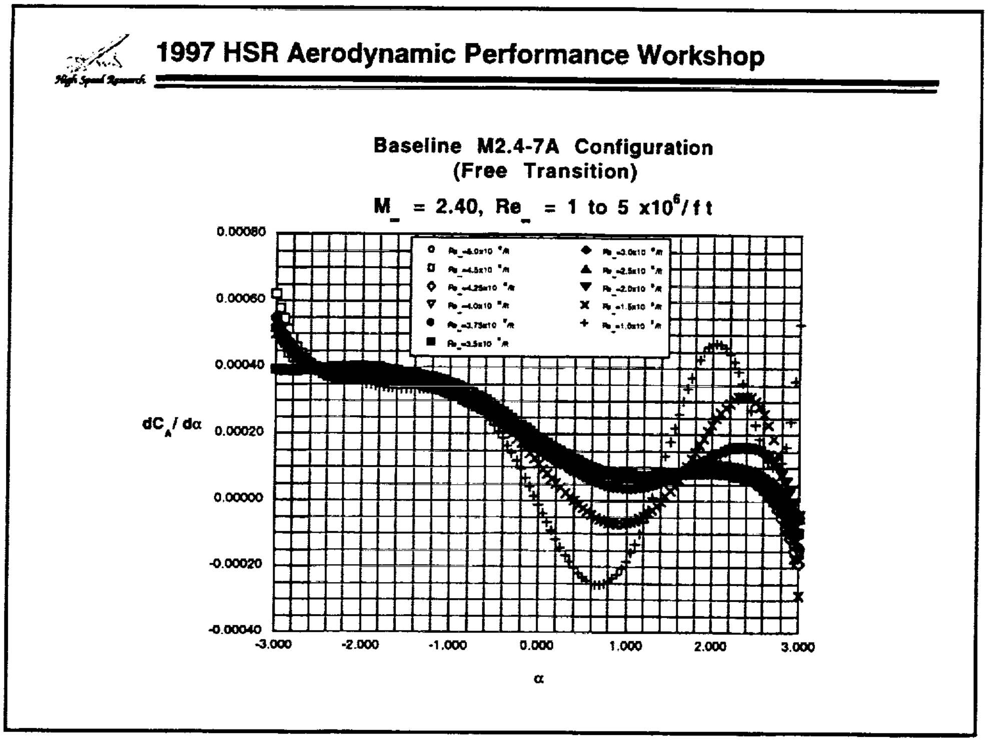

The above plot illustrates how the derivative of C_A ($dC_A/d\alpha$) varies with angle of attack for the free transitioning boundary layer over the Reynolds numbers tested. The data clearly shows changes in the derivative for the lowest Reynolds number conditions and fairly large variations for the higher Reynolds numbers as well.

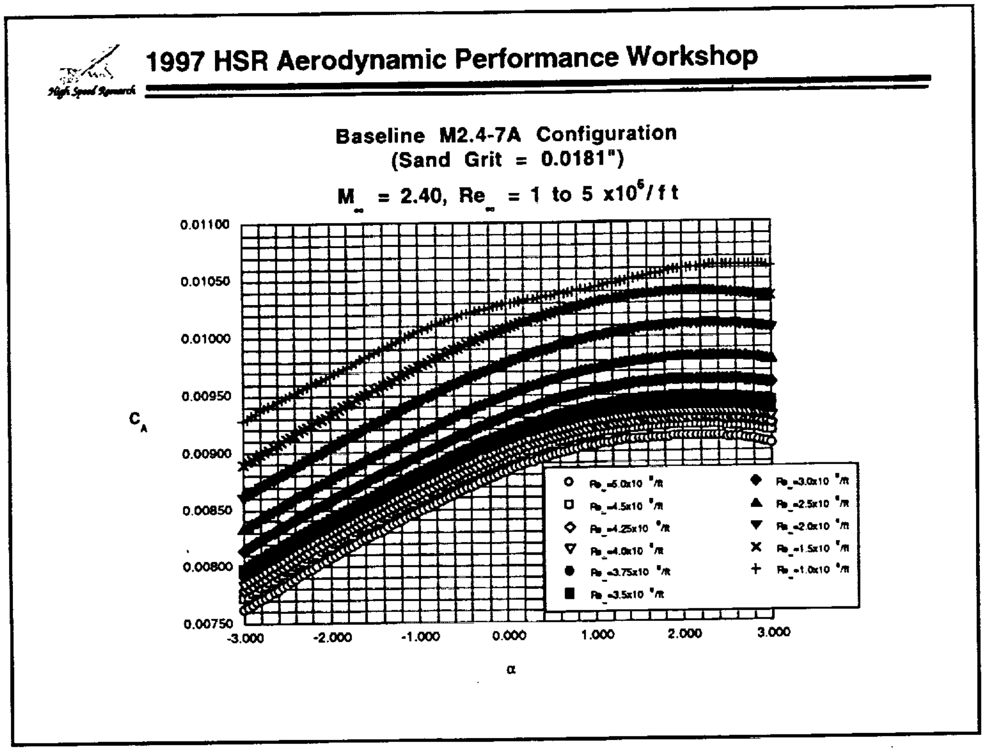

The data above shows the curve fit values of the Axial Force Coefficient (C_A) versus angle of attack, α, for the baseline M2.4-7A configuration at a Mach number of 2.40 and Reynolds numbers varying from 1 to 5 million per foot for forced b.l. transition using sand grit of nominal size 0.0181". The C_A data above show that at a Reynolds number of 1 million/foot the curve does not look smooth (implying that the boundary layer has not fully transitioned).

Baseline M2.4-7A Configuration
(Sand Grit = 0.0181")
M_∞ = 2.40, Re_∞ = 1 to 5 $x10^6$/ft

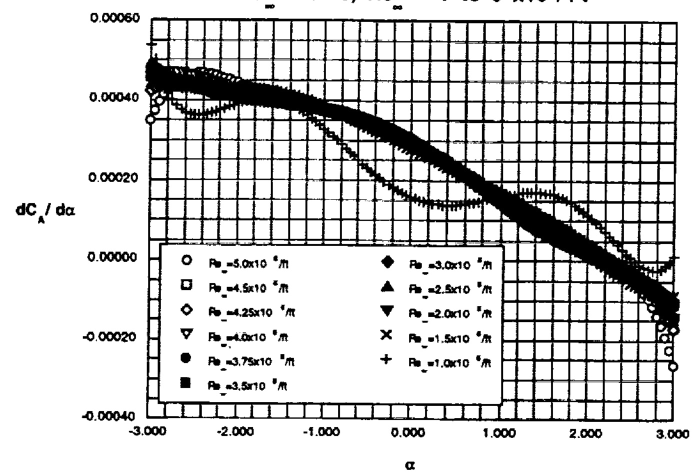

The above plot illustrates that the derivative of C_A ($dC_A/d\alpha$) for the Reynolds number of 1 million/foot appears wavy implying transitioning is occurring.

1997 HSR Aerodynamic Performance Workshop

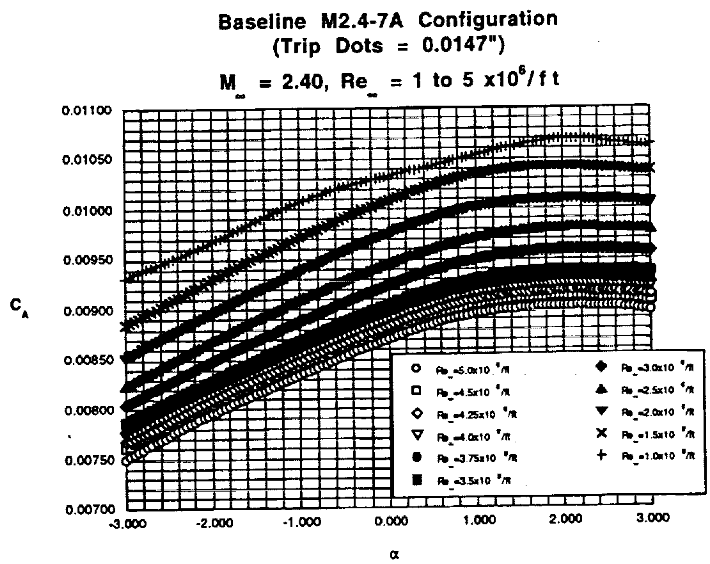

The data above shows the curve fit values of the Axial Force Coefficient (C_A) versus angle of attack, α, for the baseline M2.4-7A configuration at a Mach number of 2.40 and Reynolds numbers varying from 1 to 5 million per foot for forced b.l. transition using trip dots of nominal height 0.0147". The C_A data above show that at a Reynolds number of 1 million/foot the curve does not look smooth (implying that the boundary layer has not fully transitioned).

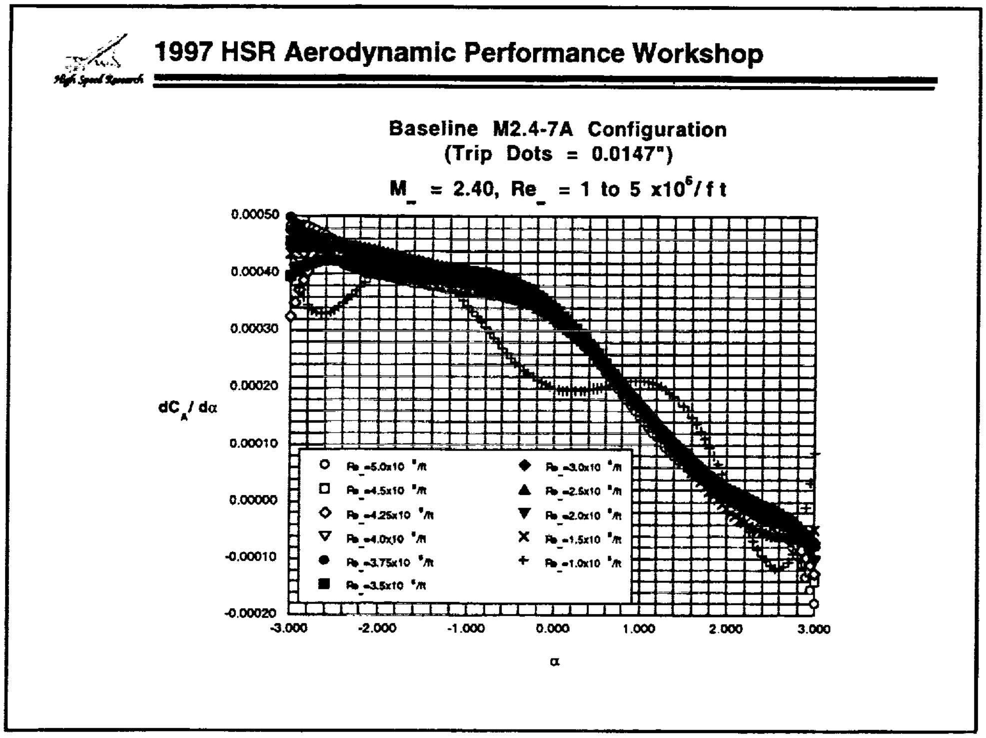

The above plot illustrates that the derivative of C_A ($dC_A/d\alpha$) for the Reynolds number of 1 million/foot appears wavy implying transitioning is occurring.

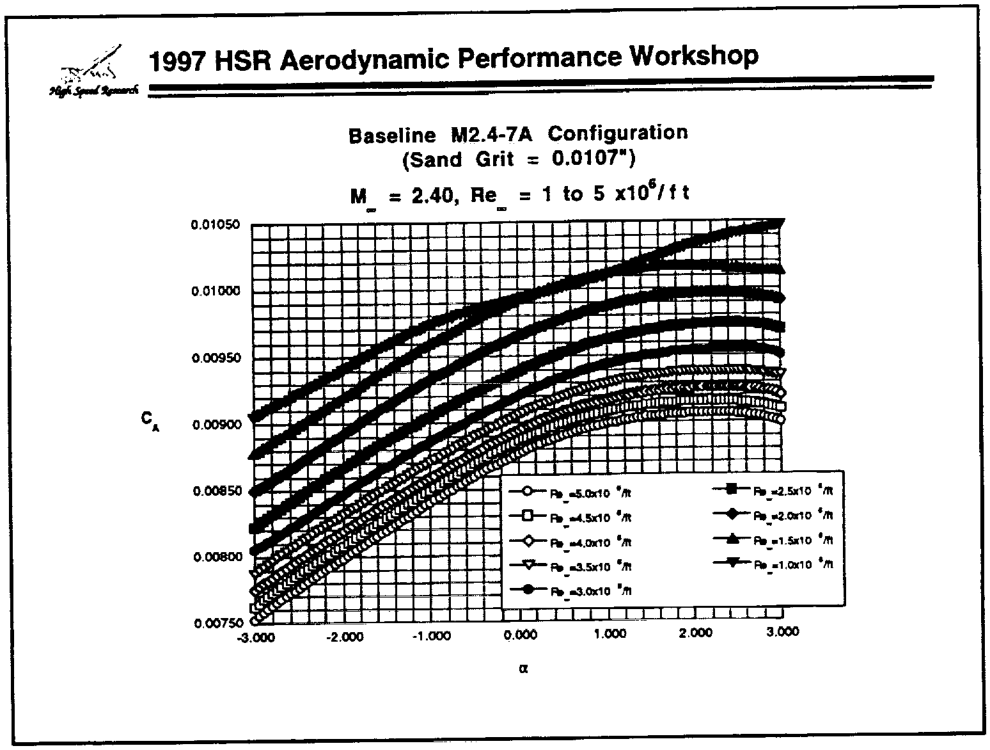

The data above shows the curve fit values of the Axial Force Coefficient (C_A) versus angle of attack, α, for the baseline M2.4-7A configuration at a Mach number of 2.40 and Reynolds numbers varying from 1 to 5 million per foot for forced b.l. transition using sand grit of nominal size 0.0107". The C_A data above show that at a Reynolds number of 1 million/foot the curve does not look smooth (implying that the boundary layer has not fully transitioned).

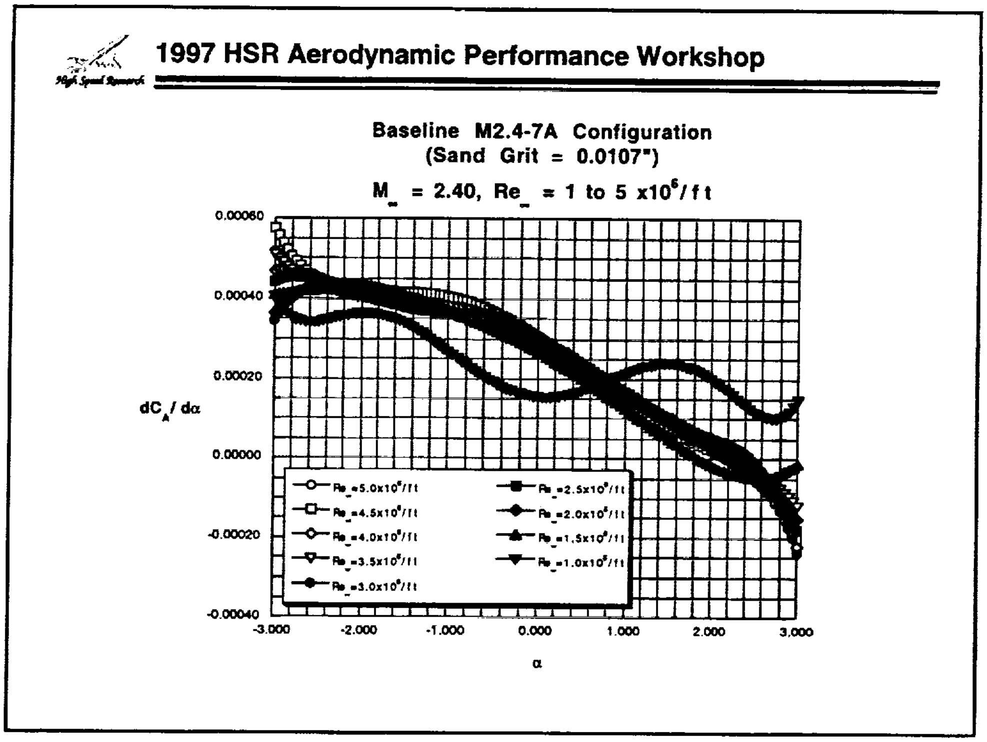

The above plot illustrates that the derivative of C_A ($dC_A/d\alpha$) for the Reynolds numbers of 1 and 1.5 million/foot appear wavy implying transitioning is occurring.

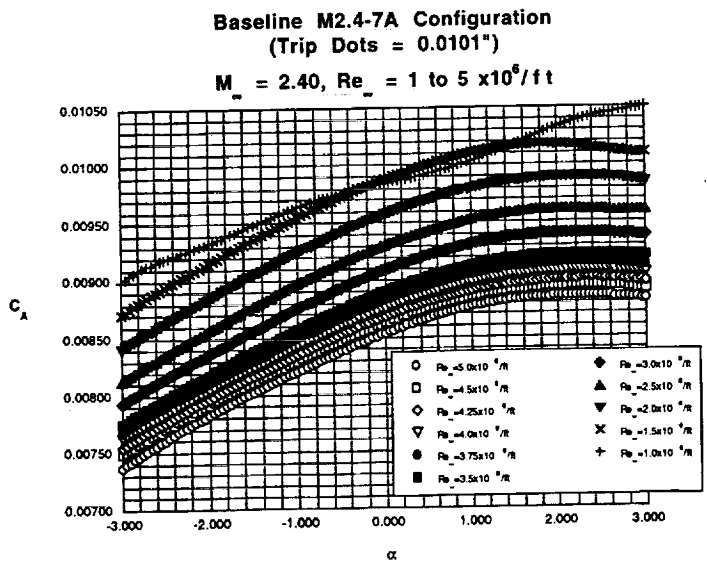

The data above shows the curve fit values of the Axial Force Coefficient (C_A) versus angle of attack, α, for the baseline M2.4-7A configuration at a Mach number of 2.40 and Reynolds numbers varying from 1 to 5 million per foot for forced b.l. transition using trip dots of nominal height 0.0101". The C_A data above show that at Reynolds numbers of 1 and 1.5 million/foot the curves do not look smooth (implying that the boundary layer has not fully transitioned).

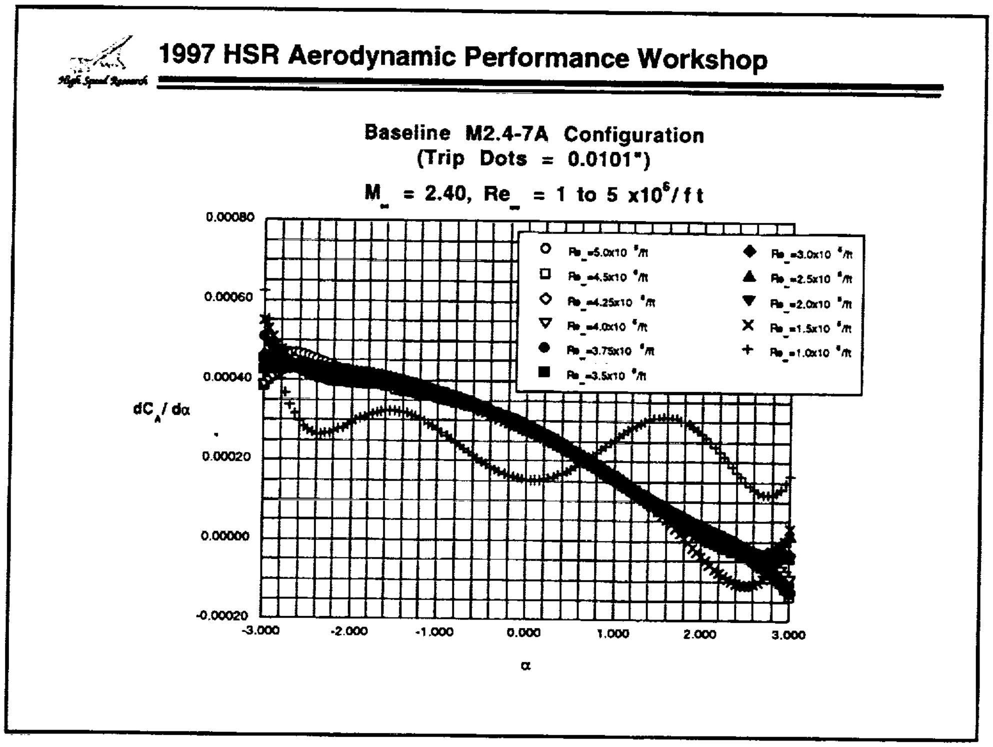

The above plot illustrates that the derivative of C_A ($dC_A/d\alpha$) for the Reynolds numbers of 1 and 1.5 million/foot appear wavy implying transitioning of the boundary layer is occurring.

1997 HSR Aerodynamic Performance Workshop

M2.4-7A UPWT TRIP DRAG ESTIMATES
METHOD COMPARISON

$M_\infty = 2.40$, $Re_\infty = 4.0X10^6/ft$

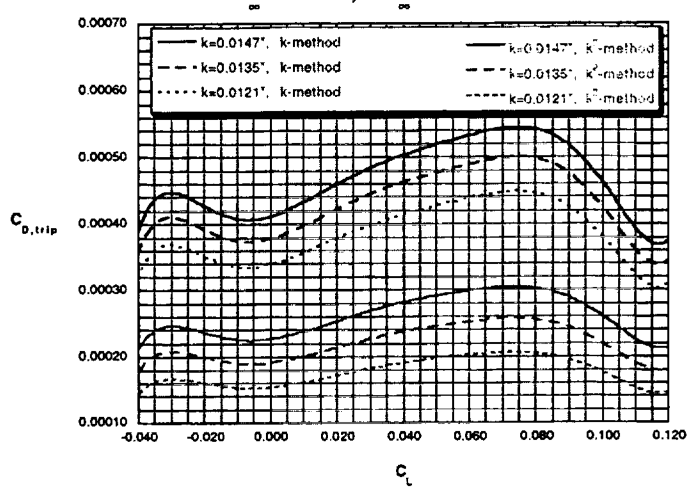

The above plot utilizes the two methods of calculating trip drag described earlier (either calculating a slope for C_D at a given C_L versus k or k^2). The estimated drag using the "k^2" method tends to provide values of $C_{D,trip}$ that are about half those found using the "k" method. Both methods predict rather large variations with differing lifting conditions.

High Rn Supersonic Testing I

- Objectives
  - extension of HSR experimental database to higher Rn at supersonic Mach
  - fully turbulent, free transition data for improved trip drag assessment at low Rn
- Background
  - existing HSR experimental database has Rn,mac max of approx. 7-8 million; cruise flight Rn,mac ~ 150-200 million
  - disagreement in HSR community as to best trip drag assessment methodology; partially due to questions of boundary layer state

In order to further understand forced transition issues, it is valuable to acquire test data with naturally occurring, fully turbulent flow. The importance lies in the ability to anchor data on fully turbulent skin friction drag predictions which can then be extrapolated to flight conditions without the uncertainty of trip drag. On the other side, fully turbulent trip free data provides a target for low Rn data with trip drag corrections.

To date, the existing HSR supersonic experimental database has an Rn,mac maximum in the range of 7 to 8 million; thecruise flight Rn,mac is approximately 150 to 200 million. The high Rn supersonic testing effort set out to extend the HSR supersonic data base to high Rn, and address low Rn forced transition methods and trip drag calculation methods.

High Rn Supersonic Testing II

- Approach
  - Test free & fixed transition configurations from low to high Rn in highest Rn supersonic facility available
    - free transition from low Rn to highest Rn attainable
    - fixed transition at low Rn (variable trip heights, types, patterns)
    - apply transition detection methods to assess boundary layer state
- MDA-E Polysonic Wind Tunnel has highest Rn capability in the US
  - calibrated at M = 2.48 (close to design cruise Mach for HSCT)
  - 4 FT test section (same as LaRC UPWT)
  - blowdown facility (starting/ending loads are an issue)

The approach taken was to test a representative HSCT configuration with both free and fixed transition from low Rn to the highest Rn available in the US. It was planned to evaluate several trip types, patterns, and locations, and several transition detection approaches.

The facility in the US with the highest supersonic Rn capability is the MDA-E Polysonic Wind Tunnel (PSWT) located in St. Louis, MO. The PSWT has a 4 ft test section allowing existing models sized for the LaRC UPWT to be tested. Start-up & ending loads are however larger than experienced at the UPWT due to the fact that the PSWT is a blowdown facility. At present, the PSWT is not calibrated for Mach = 2.4 (HSCT nominal cruise), but is calibrated at Mach = 2.48. For the purposes of this investigation, this difference is not significant.

High Rn Supersonic Testing III

- Status
  - Test 1 (PSWT 689) completed November 25 1996
  - Model Tested: 1.675% scale M2.4-7A baseline wing/body
  - Rn,mac from 8.3 to **20.7 million**, at Mach = 2.48
  - Good shakedown test
    - experience gained in the facility, largest model tested in facility
    - HSR cruise data quality issues addressed
      - questions remain about flow dew point
    - good balance/sting combination; currently in post-test inspection
    - temperature sensitive paint used for transition detection
- Plans
  - Complete data reduction & analysis from test 1
  - 2nd test currently scheduled for 3QFY97

The model chosen for testing in the PSWT was the M2.4-7A baseline configuration (same model as used in UPWT 1667). The initial test in the PSWT was conducted in November, 1996, and was designated PSWT689. Data were obtained from Rn,mac = 8.3 to 20.7 million (5.3 to 13.2 million per foot) at Mach = 2.48 over a nominal angle of attack range from -3 to + 3 deg.

PSWT689 was a good shakedown test. Experience was gained relative to testing in the facility with an HSR model, and data quality requirements. The 1.675% scale model tested was the largest ever tested in the facility, and accordingly, significant time and attention was given to monitoring start-up and ending loads. In fact, half way through the test the balance/sting combination was changed to a stronger system. The second system consisted of LaRC balance 756 and a 2000 lb. normal force sting. This combination worked well, and is currently in post test inspection.

TSP was used for transition detection. At this point, the results are inconclusive. Analysis of the images continues, as does development of the system for application in a blowdown facility.

Force data from the test is to be reduced again to correct several errors discovered in post test analysis. It should be noted that cavity pressures lagged during the 1st run of most "blows", and that the dew point was not known.

1997 HSR Aerodynamic Performance Workshop

High Rn Supersonic Testing IV

- Drag plot vs Rn using available data & accounting for the cavity pressure lag
- Forced Transition runs appear to follow flat plate predicted trend.

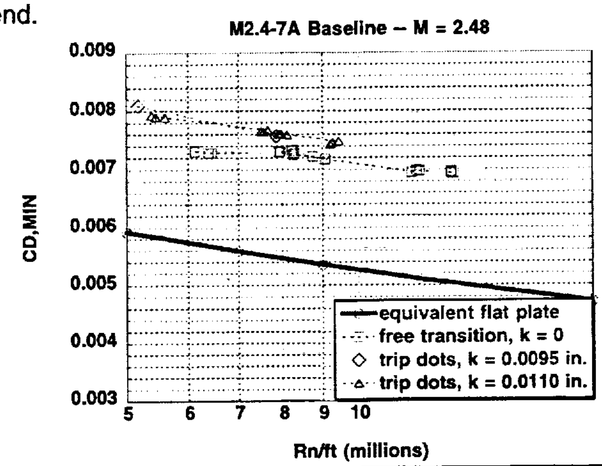

The above chart shows minimum drag data with and without forced transition as compared to an equivalent flat plate prediction. Experimental data is that available prior to a final data reduction (as discussed previously), but has been adjusted manually to account for the cavity pressure lag.

Forced transition data appear to follow the predicted trend, as do the free transition data above Rn/ft ~ 8.5 million. Note also that the trip increment above Rn/ft ~ 8.5 million is on the order of 2-3 drag counts which is similar to that determined in the UPWT tests using the k^2 trip drag assessment method.

This analysis will be updated upon final data reduction, and it is expected to be repeated and extended in a follow on test. Balance and sting limitations should allow extension of data to approximately 15 to 16 million per foot. The limiting factor at this point is sting divergence.

High Rn Subsonic/Transonic Testing I

- Objectives
  - develop the Temperature Sensitive Paint (TSP) test technique
  - detection of free & fixed transition on the 2.2 % HSR Ref. H wing
  - grit drag assessment at subsonic & transonic conditions with & without flaps
- Background
  - TSP technique identified as most promising approach for "global" transition detection in a cryogenic environment
  - joint NASA/Industry/University team formed to develop system
  - risk reduction experiments executed in the 0.3m TCT prior to NTF test to evaluate issues such as paint chemistry & camera requirements

Considerable testing of the HSR Ref. H model has been conducted in the NTF. The primary purpose of these tests, and of all tests in the NTF, is the assessment of Rn effects. Key to understanding Rn effects is the understanding of the boundary layer state at all conditions, both with free and forced transition. Several methods for transition detection in the cryogenic environment of the NTF have been identified; TSP has been identified as the most likely candidate to be successful in providing a productive, high-quality, global assessment of boundary layer state.

A joint NASA/Industry/University team was formed to develop all aspects of such a system. Risk reduction experiments were conducted, including one in the 0.3m TCT at LaRC, prior to application in the NTF.

1997 HSR Aerodynamic Performance Workshop

High Rn Subsonic/Transonic Testing II

- Approach
  - Apply the TSP system in a test of the 2.2% Ref. H model in the NTF
  - Evaluate free transition boundary layer state
  - Confirm boundary-layer fixing with grit trip
  - Assess trip drag
  - Realize that the TSP test was high risk with potentially high pay-off

Once confidence in the technique was gained through the risk reduction activities, the system was ready for the NTF. The initial test was still considered to be high risk in the sense that successful integration of a complex system with a complex tunnel would be difficult on the first try. However, success would bring high pay-offs in terms of flow field understanding.

The first part focussed on applying the TSP system to acquire images showing the free transition boundary layer state. In addition, grit was then applied and images acquired to assess the trip effectiveness. Gaps were intentionally placed in the trip to aid in the assessment. Several results are shown on the following charts. Additional analysis is presented in a paper entitled: "Use of Boundary Layer Transition Detection to Validate full-scale Flight Performance Predictions," by Hamner, Owens, Wahls, and Yeh (presented in High Lift session of this workshop).

The second phase of the test addressed subsonic and low transonic trip drag. Details are not presented here, but as expected, conventional trip location and sizing forced transition in the usual manner without significant trip drag.

1997 HSR Aerodynamic Performance Workshop

High Rn Subsonic/Transonic Testing III

- TSP images showing natural transition at Mach = 0.9, $\alpha \sim 1°$

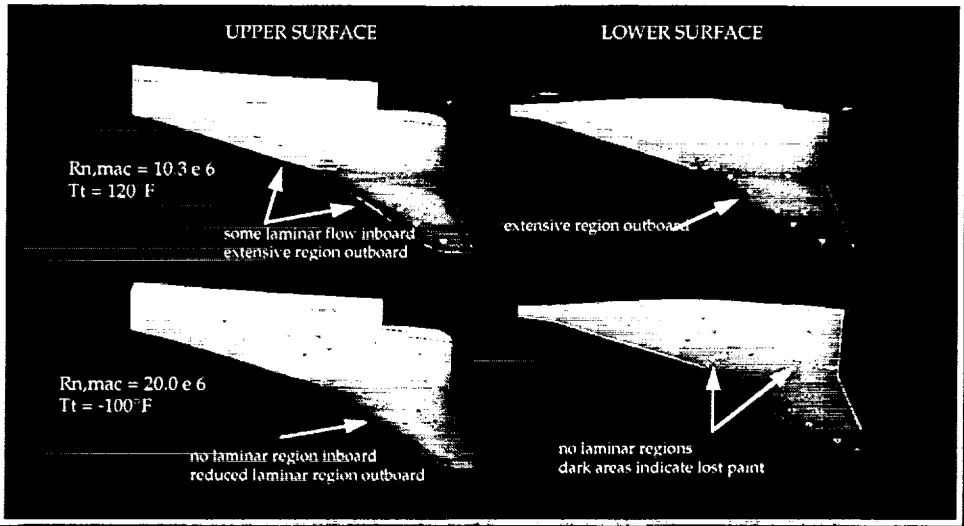

The chart above shows several typical images for Mach = 0.9 and undeflected flaps near the minimum drag condition. Images were acquired across a wide temperature range.

As noted on the chart, the amount of laminar flow decreased with increasing Rn. Although, not shown here, laminar flow did exist on the transonic cruise configuration at Mach = 0.9 and the cruise angle of attack.

1997 HSR Aerodynamic Performance Workshop

High Rn Subsonic/Transonic Testing IV

- 10/3 outboard flaps w/ grit strip
- Mach = 0.9, $R_{n,mac}$ = 10.3 million, α = 2 deg, Tt = 120°F

upper surface

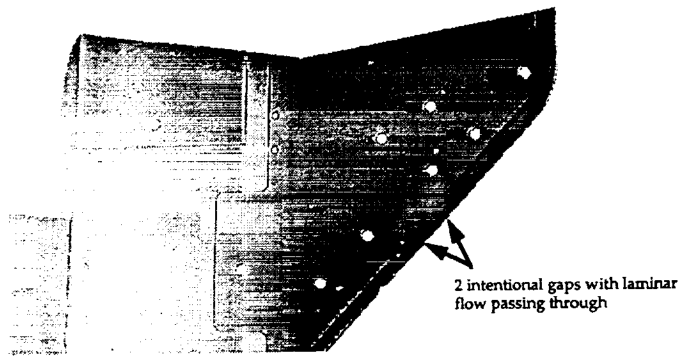

The chart above demonstrates the effectiveness of the conventional grit trip at forcing transition. Laminar flow is clearly shown progressing through the intentional gaps in the trip.

The TSP transition detection technique was considered very successful. Many lessons relative to its application were learned and work on the technique will continue.

Concluding Remarks

- Trip dots and grit performed equally well. (Existing sand grit at UPWT was mislabeled and not well "screened" to ensure consistent size.)
- Reynolds number sweeps backed up with flow visualization techniques worked well.
- Trip drag appears to be best calculated by C_D (at a given C_L) versus k^2 (However, the HSR community has not come to consensus on this!)
- Testing in high(er) Reynolds number facilities should be limited due to the restrictions caused by higher loads, shortness of run times, cost, etc.
- Free-transitioning, fully turbulent flow appears to have been reached in the Polysonic facility.
- Temperature Sensitive Paint for transition detection is viable and worth further development.

The tests showed that the boundary layer could be forced to transition equally well using either grit or trip dots. The trip dots still appear to send small vortices downstream through the boundary layer whereas the vortices generated on the grit seem to combine and not travel all the way to the trailing edge without mixing with the neighboring disturbances).

Very large differences in the value of trip drag estimates are obtained whether using C_D vs k or k^2. Follow on tests in the Polysonic facility should help understand which method is more acceptable. The "k-method" does appear to predict levels of trip drag that can cause fully turbulent drag levels that would fall below free transition values (found experimentally) implying that free transition has higher drag than fully turbulent flow which is clearly incorrect.

Future testing in the Polysonic facility should produce results that will benefit all supersonic testing done in the HSR program.

Finally, initial application of temperature sensitive paint for transition detection has shown it to be a viable test technique, and worth the support for further system development to improve its routine use.

Pressure-Sensitive Paint and Video Model Deformation Systems at the NASA Langley Unitary Plan Wind Tunnel

G. E. Erickson
A.W.Burner
R. DeLoach

25 February 1997
NASA Langley Research Center
Hampton, Virginia

Pressure-Sensitive Paint and Video Model Deformation Systems at the NASA Langley Unitary Plan Wind Tunnel

G. E. Erickson
A. W. Burner
R. Deloach

NASA Langley Research Center
Hampton, Virginia 23681-0001

Pressure-sensitive paint (PSP) and video model deformation (VMD) systems have been installed in the Unitary Plan Wind Tunnel at the NASA Langley Research Center to support the supersonic wind tunnel testing requirements of the High Speed Research (HSR) program. The PSP and VMD systems have been operational since early 1996 and provide the capabilities of measuring global surface static pressures and wing local twist angles and deflections (bending). These techniques have been successfully applied to several HSR wind tunnel models for wide ranges of the Mach number, Reynolds number, and angle of attack. A review of the UPWT PSP and VMD systems is provided, and representative results obtained on selected HSR models are shown. A promising technique to streamline the wind tunnel testing process, Modern Experimental Design, is also discussed in conjunction with recently-completed wing deformation measurements at UPWT.

Presentation Overview

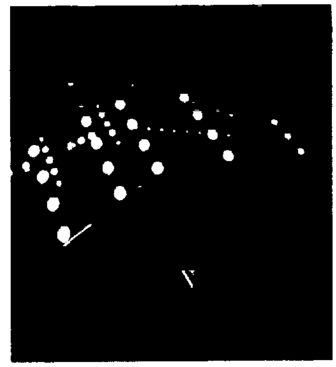

- Review of UPWT PSP system and selected results obtained on HSR models
- Review of UPWT VMD system and selected results from recently-concluded HSR testing
- Discussion of a Modern Experimental Design method for improved wind tunnel productivity
  - -- recently applied at UPWT in conjunction with the VMD system to predict HSR model deformation

A comprehensive facility enhancement program is underway at the NASA Langley Research Center Unitary Plan Wind Tunnel to provide state-of-the-art test techniques to support the supersonic testing requirements of the High-Speed Research program. This paper provides a review of the UPWT pressure-sensitive paint system for global surface static pressure measurements and the UPWT video model deformation system to measure wing local twist and deflections. In an effort to improve wind tunnel productivity, a Modern Experimental Design technique was used in parallel with the model deformation system to determine its effectiveness in predicting wing twist at supersonic speeds. Representative results obtained with the PSP, VMD, and Modern Experimental Design techniques in recent HSR wind tunnel model testing at UPWT are presented.

PSP and VMD Systems at UPWT

- PSP and VMD systems established at UPWT in 1996 to support HSR experimental programs
- Strong cooperative efforts involving Aero-Gas Dynamics Division and Experimental Testing Technology Division (ETTD)
- PSP system evolved from previous installation in the NASA Langley 8-Foot Transonic Pressure Tunnel in 1994 in cooperation with NASA Ames and ETTD
- VMD systems established at the National Transonic Facility and Transonic Dynamics Tunnel in 1994 provided foundation for UPWT installation
- PSP and VMD systems are now operated by UPWT personnel after extensive training with ETTD (setup, operation, image acquisition and processing, and data analysis and plotting)

Cooperative efforts involving personnel from the NASA Langley Aero-Gas Dynamics Division and the Experimental Testing Technology Division have led to the establishment of PSP and VMD deformation systems at UPWT. A PSP system previously installed in the NASA Langley 8-Foot Transonic Pressure Tunnel was upgraded and installed in UPWT in early 1996. This system was modeled after a similar setup currently in use at the NASA Ames Research Center. The VMD systems established by ETTD at the National Transonic Facility and the Transonic Dynamics Facility served as models for the UPWT installation, which was initiated in 1996. Experience gained from several HSR-sponsored tests has provided resident expertise at UPWT in all aspects of the PSP and VMD systems.

UPWT Description

- **Closed-circuit, continuous-flow, variable-density tunnel**
- **Two 4-ft by 4-ft test sections**
- **"Low Mach" test section has a design Mach number range from 1.5 to 2.9**
- **"High Mach" test section has a design Mach number range from 2.3 to 4.6**
- **Both test sections use asymmetric sliding-block nozzles that allow continous variation in Mach number**
- **Maximum Reynolds number/foot varies from $6x10^6$ to $11x10^6$, depending on Mach number**

The NASA Langley UPWT is being extensively used in the HSR program to provide aerodynamic performance and stability and control characteristics at supersonic speeds. The ranges of Mach number and Reynolds number, the control of the dewpoint and stagnation temperature, the optical access to the test section, and the benign environment for the installation of digital and video imaging equipment are factors that render UPWT well-suited to the application of PSP and VMD techniques. The PSP and VMD systems are portable between the "low Mach" and "high Mach" number test sections. In addition, the present facility scheduling features one "active" test section while the "idle" test section is available for PSP and VMD system set-up, check-out, and test technique enhancements.

UPWT PSP System

- Method is based on oxygen sensitivity of photoluminescent material in the form of a "paint" (University of Washington formulation)
- PSP sprayed onto model surface after application of white undercoat
- Purge air is applied through model surface pressure orifices during painting process via electronic pressure scanner modules installed in the wind tunnel model
- Registration marks applied to model using overlay template
- PSP excitation source is 250-W lamps that emit ultraviolet light in a broadband centered around 360 nm and a cutoff filter to block emission in the visible wavelengths
- All other illumination sources are eliminated by installing "light-tight" enclosures on both sides of the wind tunnel test section

The UPWT PSP technique is based on a system developed by the NASA Ames Research Center and the University of Washington. The photoluminescent paint chemistries developed by the University of Washington have been used in all of the NASA Langley UPWT PSP tests and have proved to be very robust for the supersonic experiments. Approximately one shift is required to the application and curing of the white base and PSP coatings. Specially modified ESP scanners, when operated in a purge mode, route air through the wing surface pressure lines to prevent the paint from clogging the orifices. Registration marks are applied to the painted surfaces using an overlay template and a black marking pen. The marks are tyically 0..125 to 0.188 inches in diameter and are positioned along the edges of the model and at selected other locations on the wing. UV lamps are mounted to the webbing of the the test section side wall to provide a continuous illumination source. Manual shutters are used to block the UV light between runs. The large image areas that are typically mapped on HSR models requires at least two UV lamps. Photodegradation of the PSP is a concern because of the proximity of the UV light source to the model (approximately 2 feet), so double and triple filters are applied to the lamps to reduce the UV intensity at the model. A hand-held digital radiometer is used to measure the effectiveness of the UV lamp positioning and filtering arrangements. Wooden enclosures have been built that are bolted/clamped to the test section side walls to eliminate all extraneous light sources.

UPWT PSP System (continued)

- PSP imaging is conducted using 2 scientific-grade, cooled CCD digital cameras (12-bit and 14-bit intensity resolution, 512x512 and 1024x1024 spatial resolution) installed in the "webbing" of the test section side wall
- Optical filters are installed on the camera lenses to permit the passage of the luminescence emission wavelengths while blocking other wavelengths
- Model is rolled 90^0 for best optical access and the model pitch angle is varied using the support system yaw mechanism
- Camera integration time and image acquisition are controlled by host computers located in the UPWT Data Room, about 125 feet from the camera positions

The high CCD performance, low noise, linear response, and good signal-to-noise ratio of scientific-grade digital cameras provide high-precision, quantitative light measurements. Two digital cameras are available at UPWT for PSP image acquisition. In a typical installation, both cameras are mounted inside the webbing of the test section side wall with lenses that are selected to provide a detailed view of an area of particular interest on the model and a global view of the wing surface. Special optical filters are mounted to the front of each lens so that the camera detects only the luminescence emission spectra. Optical access to the test section is available through the schlieren windows in the side walls, so the model is rolled 90° to be roughly orthogonal to the cameras. Variation in the model pitch angle is obtained using a mechanized yaw mechanism. The camera exposure, or integration, time and image acquisition are remotely controlled via a Windows 95-based PC and a UNIX-based workstation that are located in the UPWT Data Room. The integration times are selected to provide high image intensity while avoiding local saturation. Typical integration times are 1 to 1.5 seconds. PSP imaging has not been compromised by the relatively minor model dynamics that are encountered at the supersonic speeds.

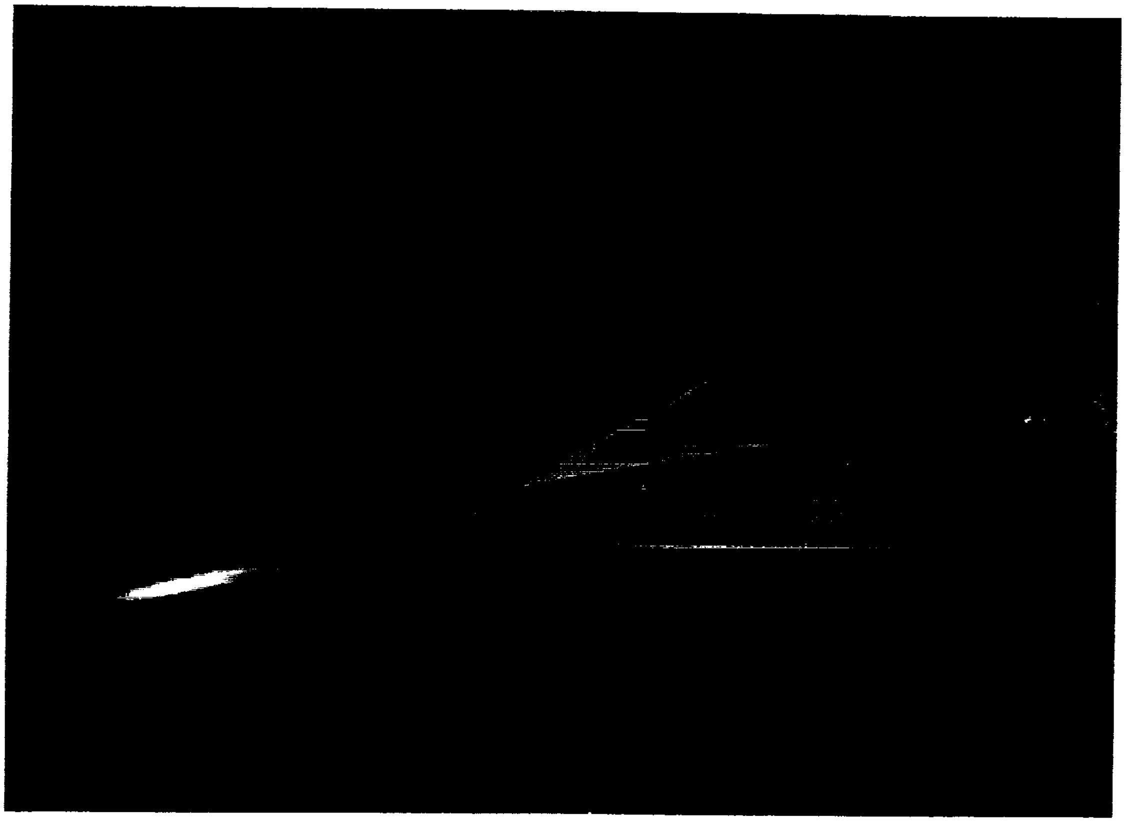

This photograph shows a 1.675%-scale HSR arrow wing model installed in UPWT test section 1. The model is rolled -90^0 for this photograph, although the model was rolled in the opposite direction for the testing. The right (upper) wing surface is coated with pressure-sensitive paint, while the left (lower) wing features an application of temperature-sensitive paint.

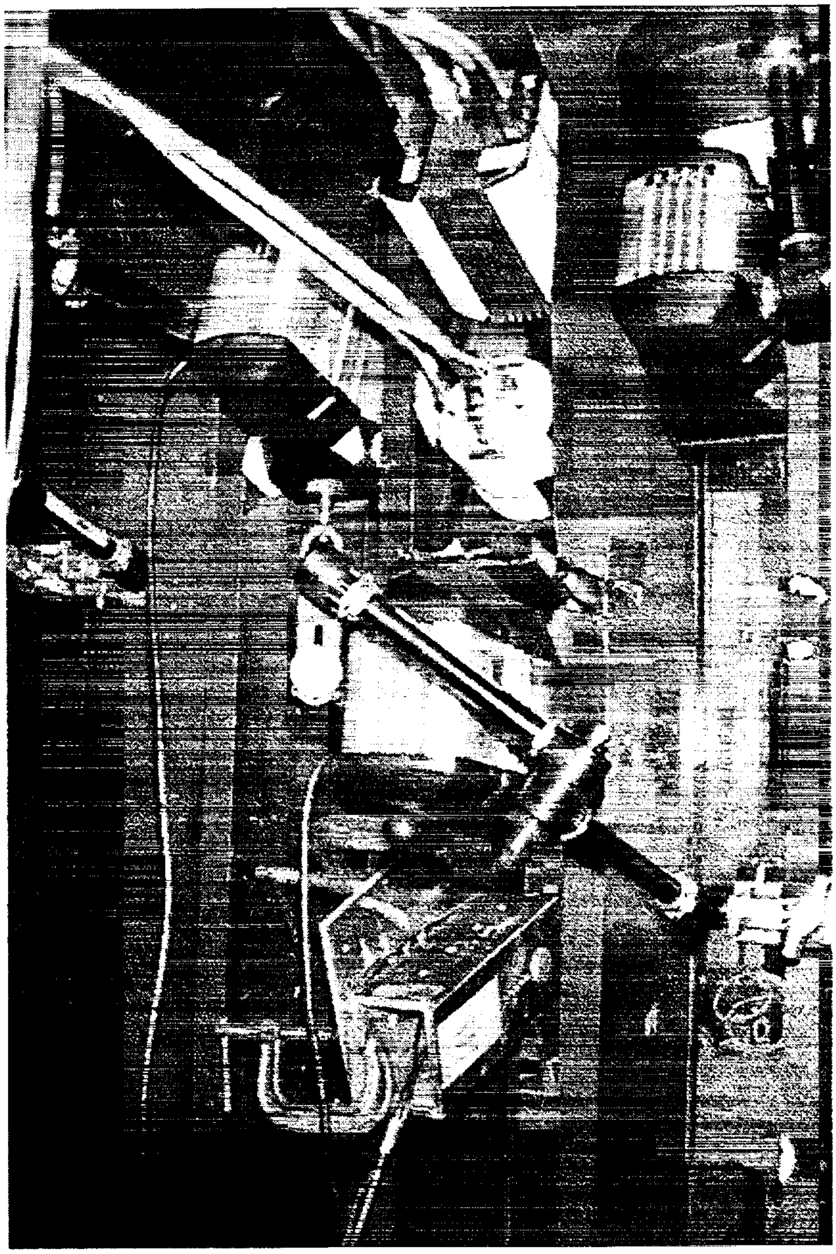

The photograph shows a close-up view of a PSP hardware installation in the webbing of UPWT test section 2. Two scientific-grade CCD digital cameras, one standard video CCD camera, and three 250W UV lamps are installed using articulated mounting arms or C-clamps. The webbing provides a stable, virtually vibration-free mounting surface for the PSP imagers and light sources.

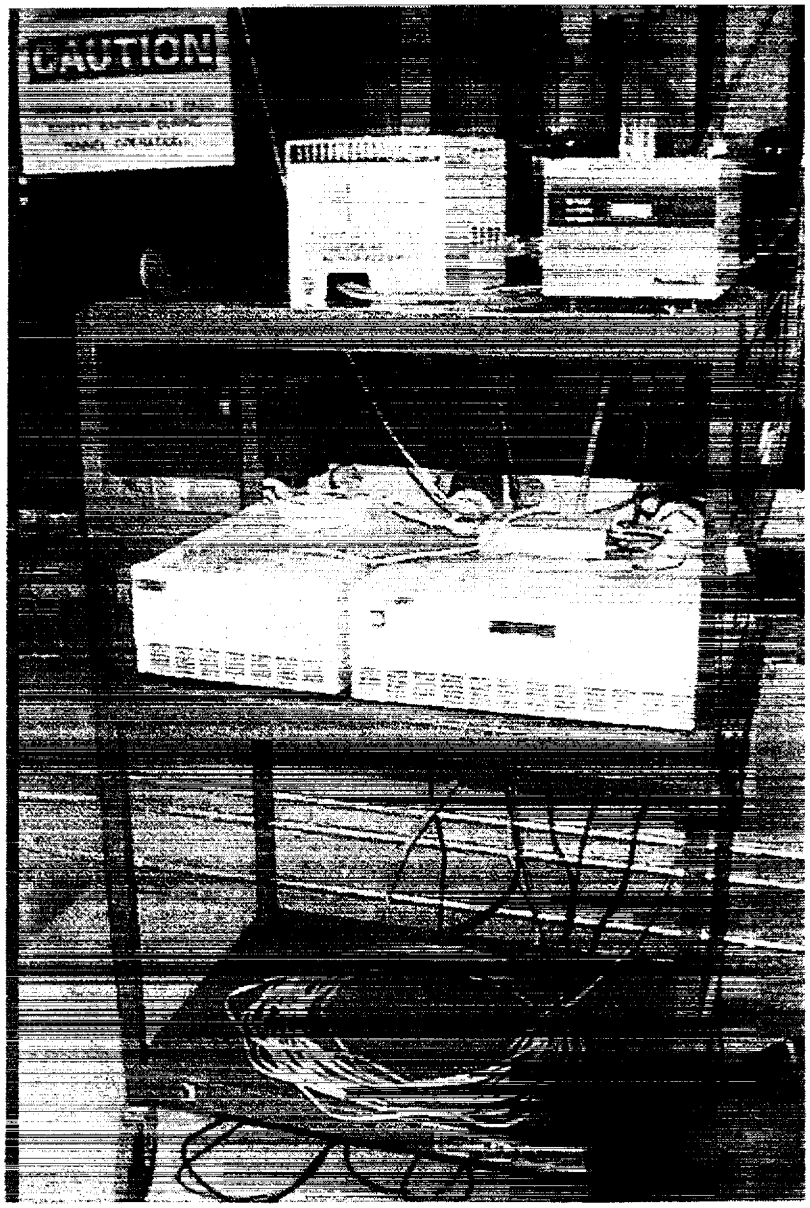

The PSP digital camera electronic control units and chiller units are shown in this figure. Excess length of a 200-foot fiber optic cable is shown at the bottom of the mobile cart, which is positioned adjacent to the test section.

UPWT PSP System (concluded)

- Personal computer controls the 14-bit camera via a proprietary interface card and electronics cable, while a UNIX-based workstation controls the 12-bit camera using a separate interface and a fiber optic-based SCSI link
- Video camera with optical filter provides real-time PSP response
- Wind-off and wind-on images are processed on the UNIX machine using the NASA Ames-developed "paintcp" software package, which performs the image ratio, registration, and paint calibration operations
- PSP is calibrated via an "in-situ" method using surface static pressures obtained from discrete orifices on the model surface connected to internally-mounted ESP scanners
- Image processing, analysis, and plotting are performed on-site and results posted on WWW site established for each UPWT test

The 14-bit digital camera with 512x512 pixel array is controlled by a personal computer and camera interface card. A camera electronics cable extends from the interface card to an electronics control unit and camera chiller unit assembly located adjacent to the test section. The 12-bit digital camera with 1024x1024 pixel array is controlled by a high-end workstation that features a fiber optic-based SCSI bus extender from the workstation to the camera control unit/chiller unit assembly, also positioned in proximity to the test section. Electronics cables and fiber optics cables are permanently routed from the Data Room to both test sections. A separate video CCD camera with optical filter is mounted to the test section webbing to provide real-time display and recording of the paint response, which can include the footprints, or signatures, of shock waves and vortices. An extensive disk array has been assembled to accommodate the image storage requirements of PSP testing. All images are transferred to the workstation, where the image ratioing, image registration, and PSP calibrations are performed using a software package developed by NASA Ames Research Center. An "in-situ" calibration is performed whereby the paint is calibrated using the static pressures measured at discrete locations with internally-mounted pressure scanners. All image processing operations and data analysis and plotting are done on-site. World Wide Web sites are typically established for each UPWT test to allow posting of the processed PSP images.

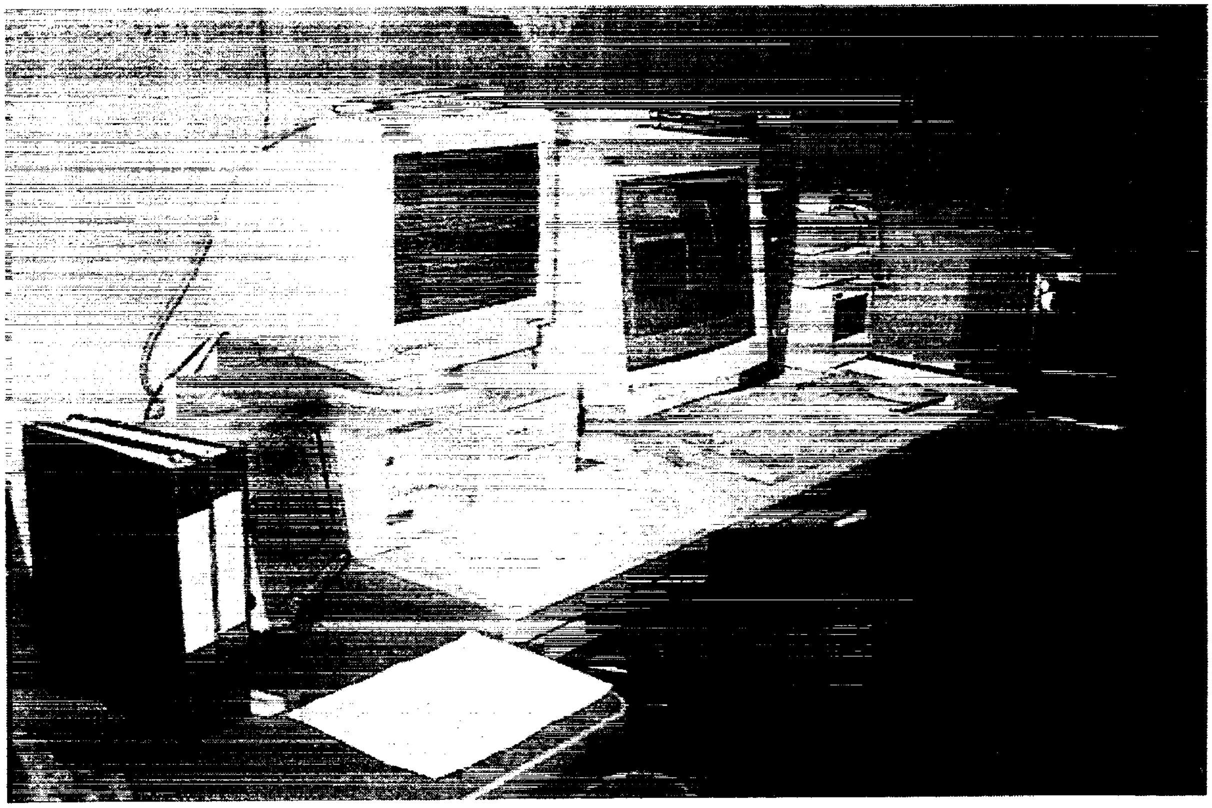

The host computers that control the two PSP digital cameras are shown in the photograph above. The PC (Windows 95 OS) and UNIX workstation are situated side-by-side along with high-capacity disk drives and color postscript printer. Additional magneto-optical hard drives and recordable CD drives have recently been acquired to augment the UPWT PSP system.

UPWT PSP Applications to Date

- 1.675%-scale HSR arrow wing model
- 1.675%-scale HSR TCA 2a model
- Test sections 1 and 2
- M=1.6 to 2.7, Re/ft=3, 4 million
- $\alpha = -2^{o}$ to 8^{o}
- Attached flow, separated (vortex) flow, shock waves

The UPWT PSP system has been applied to several HSR models, including a 1.675%-scale HSR arrow wing model in test sections 1 and 2 and a 1.675%-scale model of the HSR TCA2a model in test section 2. PSP results have been obtained for a wide range of Mach number and angle of attack that encompass flow regimes dominated by attached flow, vortices, and shock waves. Time required to set up the PSP system and acquire all wind-on and wind-off images is approximately 2 shifts. Additional time is required at the outset of the wind tunnel entry to acquire flow angle corrections (upflow and sideflow) to provide accurate determination of the model angle of attack. Runs are also made of the unpainted model at the same test conditions to quantify any obtrusive effects of the paint thickness on the wing surfaces.

Arrow Wing PSP Image at M=1.65, α=8°

UPWT Test 1836 Re/ft = $3(10^6)$ June 1996

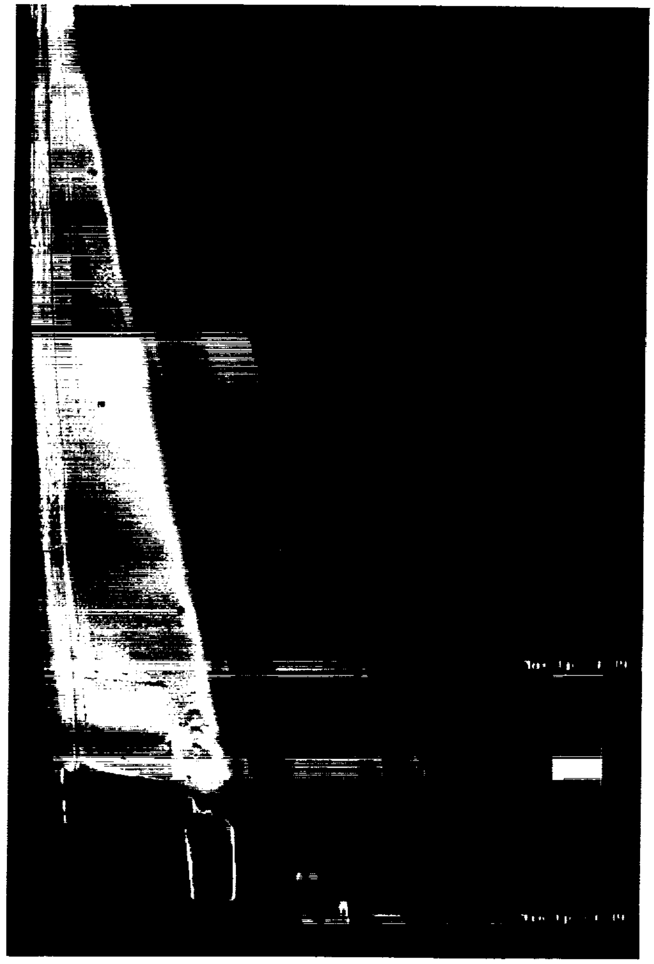

The photograph shown above is a false-colored, ratioed and registered image of the wing upper surface pressure field on a 1.675%-scale model of an HSR arrow wing configuration. The test conditions correspond to a free-stream Mach number of 1.65, Reynolds number per foot of $3(10^6)$, and angle of attack of 8°. Free-stream stagnation temperature is 125 °F. The PSP image clearly shows the signatures of leading-edge vortices that develop from the inboard and outboard wing regions. The inboard wing vortex passes over the outboard nacelles, and the effect of the vortex passage can be correlated with the nacelle base pressure measurements. The paint was calibrated using pressure measurements obtained at discrete ports with two ESP modules. This test was conducted in June 1996 and was the first application of the UPWT PSP system in UPWT test section 1.

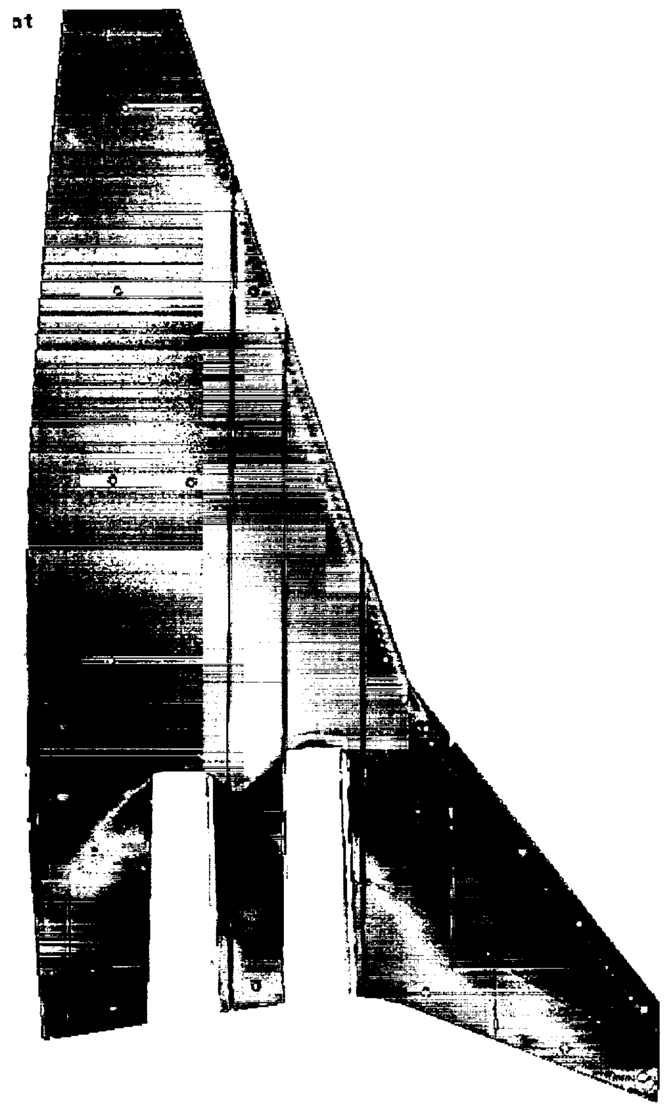

A processed PSP image of the wing lower surface on a 1.675%-scale model of the HSR TCA 2a in UPWT test section 2 is shown above. The test conditions correspond to a Mach number of 2.4, Re/ft = $4(10^6)$, $T_{stag}=125^0$, and $\alpha = 3.5^0$. The inboard and outboard nacelles were installed for this run, but were painted flat black to eliminate the effect of reflected light from the sides of the nacelles on to the wing surface. Of particular interest in this application was the character of the interacting shock waves developed by the nacelle diverters. Reflected shocks from the diverters are also discernible in the original image and in the PSP-derived static pressure distributions. Several streamwise rows of wing lower surface static pressure orifices were plumbed to an ESP module without the purge air capability. As a result, thin strips of masking tape were applied to these rows during the painting process. These unpainted strips are visible in the image above. The in-situ paint calibration required the selection of pixel locations outside of these regions.

Pressure- Sensitive Paint Results on HSR TCA 2 Wing Lower Surface

M=2.40 α=3.5° Re/ft=4(10^6) UPWT Test 1671 (PXL Camera)

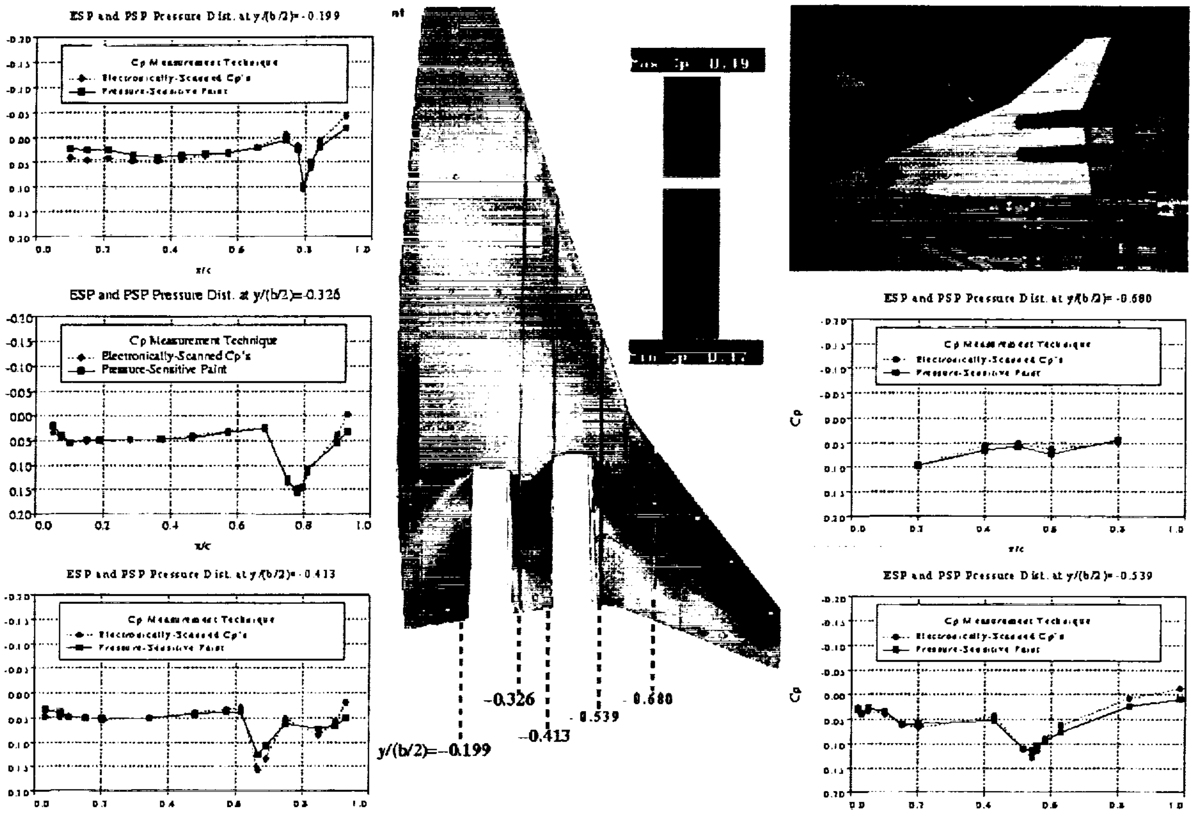

This composite plot compares the streamwise distributions of the wing lower surface static pressure coefficient obtained with the PSP technique and the electronically-scanned pressure modules at Mach=2.4, Re/ft=4(10^6), and α = 3.5° (same case as on previous page). The ratioed and registered PSP image and a model installation image are also included. The PSP and ESP pressure data compare very well, and the maximum difference in the coefficients obtained with the two methods is within approximately 5% of full-scale range of the ESP transducers . The abrupt pressure rise across the shocks is apparent in the first four pressure distribution plots. Note that the PSP data plots are restricted to values obtained at a single pixel in proximity to each pressure orifice. The advantage of the PSP method is that all image pixels are "pressure tap" locations, and the corresponding hundreds of thousands of pixels (depending on the camera resolution) can provide much higher resolution of the C_p distribution, particularly across the shock waves.

UPWT VMD System

- **VMD technique is based on a single video camera photogrammetric determination of two-dimensional coordinates of wing targets with a known fixed third dimensional coordinate (spanwise location)**
- **Primary application of UPWT VMD system is to determine local wing twist, while secondary applications include wing deflection (bending) and model angle of attack measurements**
- **Retroreflective dots with adhesive backing are applied in several chordwise rows from the wing root to the wing tip to provide high-contrast targets**
- **Images are acquired using a standard RS-170 CCD video camera with 752 horizontal by 240 vertical pixel resolution**
- **Illumination source is a fiber optic-based ring light mounted to the front of the camera's 10 to 100mm focal length remote zoom lens**

A unique aspect of the video model deformation system developed by NASA Langley ETTD is the photogrammetric determination of two-dimensional wing targets using a single video camera. A requirement is that the third dimensional coordinate be known and fixed, namely, the spanwise location of the targets. The primary application of the VMD system is to measure the wing local twist angle, although the wing deflection (bending) and model angle of attack measurements may be equally significant depending on the experimental objectives. Targets in the form of retroreflective dots with an adhesive backing are applied at precisely known locations in chordwise rows at several wing span stations. The inboard row of targets is placed in a region of the wing that may be considered rigid. This row serves as a reference to all other target rows and provides an "onboard" angle of attack measurement. The dots provide extremely high-contrast targets for image acquisition, and any glints or other undesired sources of high contrast on the model surface are eliminated by applying a thin coat of flat black paint to these regions (Note: This is not a standard practice at all facilities.) The thickness of the targets is somewhat instrusive and may cause drag coefficient increments of a few counts at the supersonic speeds; as a result, the VMD measurements are generally made in a separate run series in a manner similar to the PSP technique. A standard CCD video camera with characteristics that have been well-documented by ETTD is used to acquire images of the targeted region. Uniform illumination of the model is provided by a fiber optic-based ring light that easily attaches to the front of the camera's remote zoom lens.

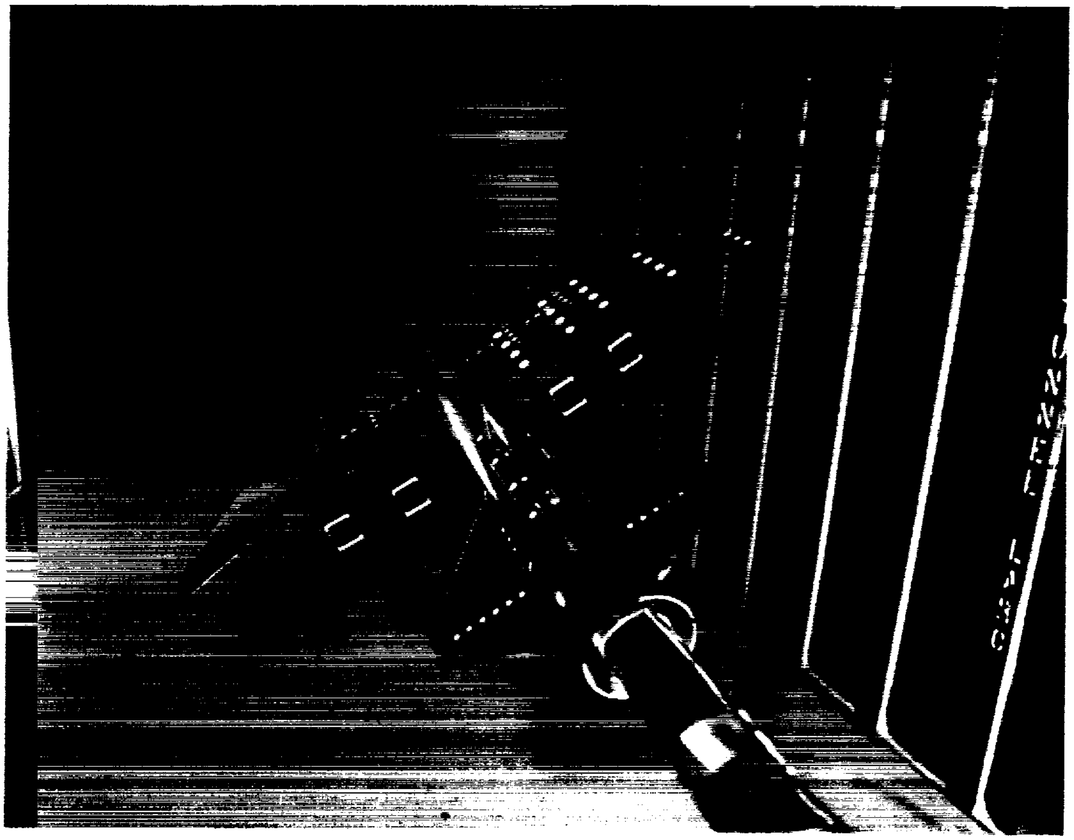

The 1.5%-scale HSR TCA 20 model installed in UPWT test section 1 is shown in the above photograph, taken at the conclusion of a recent video model deformation experiment. The 5 chordwise rows of retroreflective targets are visible on the right wing upper surface.

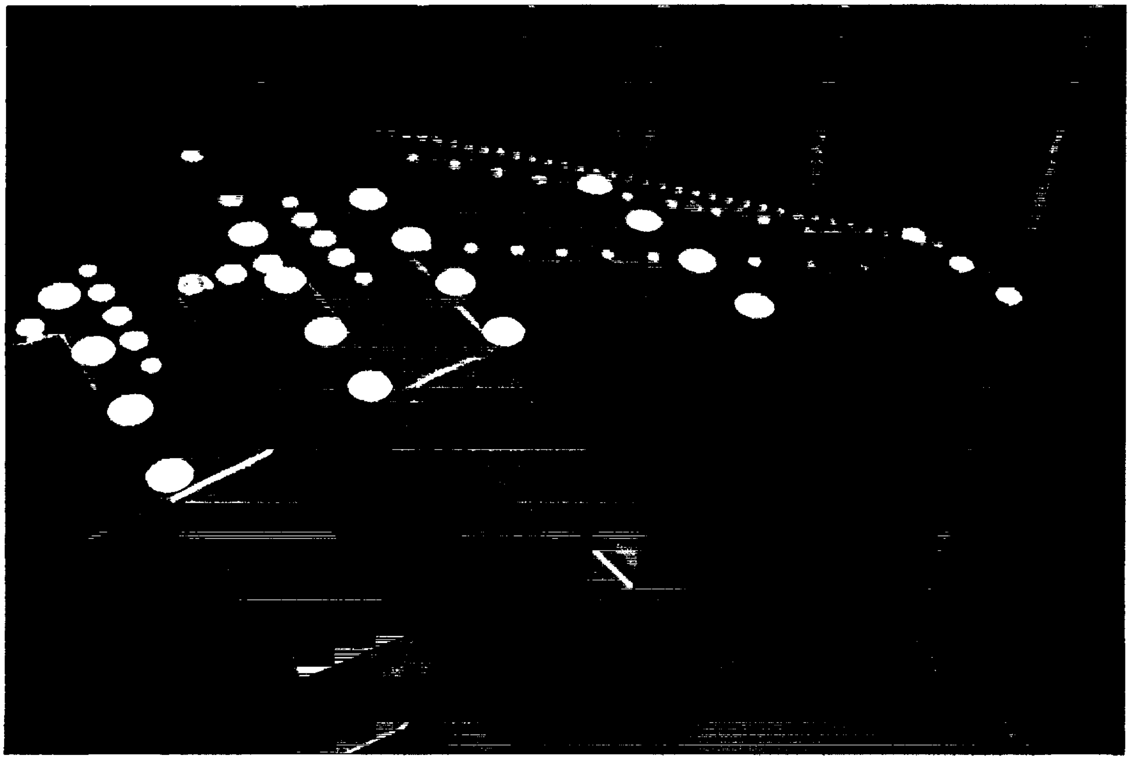

The figure above shows a close-up view of the right-hand wing upper surface on the 1.5%-scale HSR TCA model 20 installed in UPWT test section 1. Five rows of retroreflective targets are visible; the first four chordwise rows (starting from the wing root region) feature four 0.188-inch diameter targets while the fifth row (at the wing tip) has three 0.125-inch diameter targets. The wing twist and deflection measurements that are presented in following figures correspond to the row near the wing tip. Note that several smaller screw holes in the wing surface are filled with dental plaster, and these holes can be miscontrued in the photograph as VMD targets. These holes are not visible during the image acquisition process.

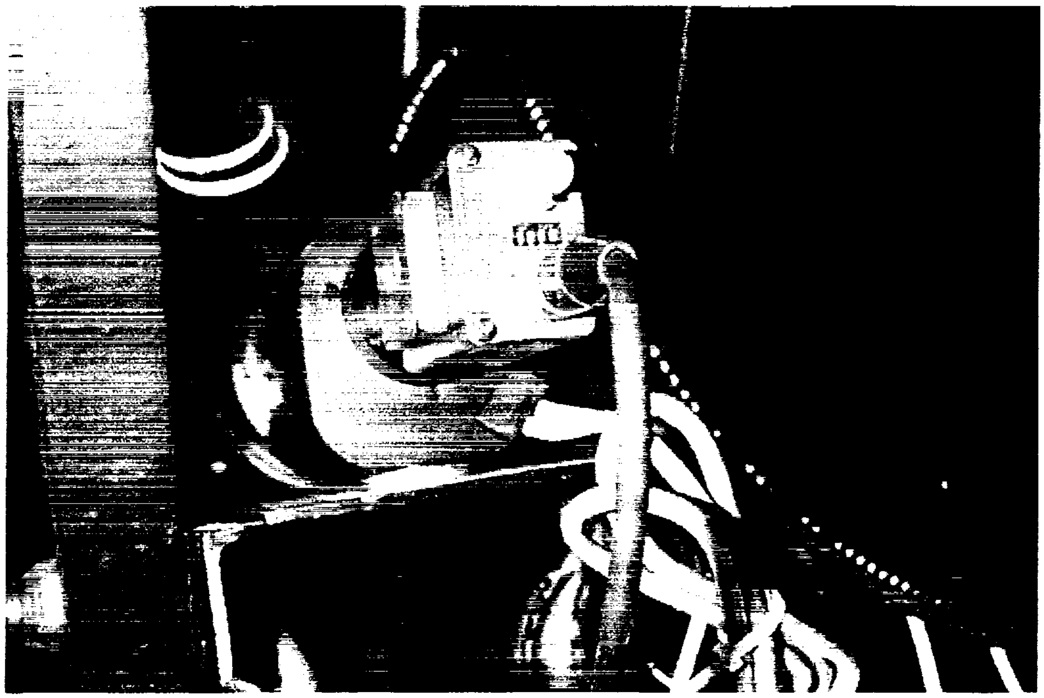

A close-up view of the VMD system camera installed in the webbing of the test section is shown in this photograph. The standard video CCD camera is mounted to the remote zoom lens which, in turn is bolted to an angle plate that is C-clamped to the webbing. The fiber optic link to the lens-mounted ring light is also discernible in the figure. Considerable care is required to ensure that that the focal length and camera position are not changed once the camera calibration is completed. The video signal from the camera is routed to the Data Room via an RG-59 cable to a video distribution amp and to the video framegrabber board in the PC image acquisition system. Set-up of the VMD camera equipment is very straightforward and requires less time than the PSP hardware installation.

UPWT VMD System (concluded)

- **The video signal is routed to a frame grabber controlled by a 120 MHz Pentium PC in the UPWT Data Room**

- **Detailed in-tunnel static calibrations are performed using a target plate to determine the camera position and pointing angles**

- **Wind-off pitch sweeps of the model (in the upright position) and retroreflective targets installed are then conducted**

- **Automated system analyzes several digitized video images at each angle of attack during the wind-off and wind-on pitch sweeps and displays "raw" values of the wing local angle of attack and vertical ("z") coordinates**

- **Commercially-available numeric computation and visualization software package is used to compute and plot final wing twist and wing bending results**

Images are acquired from the video CCD camera using a frame grabber board installed in a Windows 95-based PC. Acquisition of digitized video images is triggered by a "pickle switch" or a keyboard command, and the automated system identifies the model targets and analyzes several video images at each angle of attack. Tunnel test condition information is also acquired at this time from the wind tunnel data acquisition system via an RS-232 interface. The tunnel test conditions, test point information, and the values of the uncorrected local angle of attack and vertical displacement at all target rows are then displayed on-screen, at which point the system is ready for the next data point. Target plate calibrations and wind-off and wind-on data are acquired in the same manner. The calibration of the camera is a detailed procedure which uses a target plate rig constructed for the UPWT system and yields the camera location, pointing angles, and effective focal length. Wind-off pitch sweeps of the model in the upright position are conducted to verify the camera calibration and to provide static "tares" that are subtracted from the wind-on data. Post-run processing of the VMD data is done using a commercially-available software package that computes and plots the corrected wing twist and deflection results.

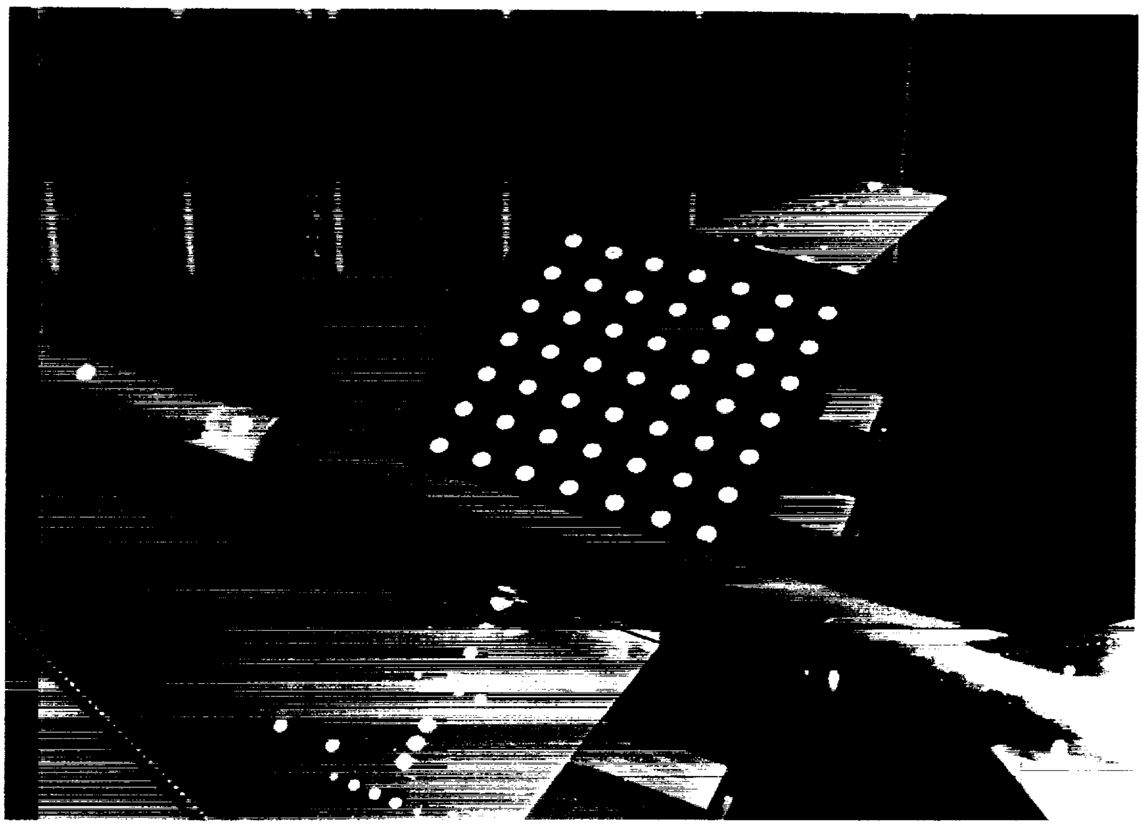

This is a close-up view of the 1.5%-scale HSR TCA 20 model with a VMD system calibration target plate placed on the right wing upper surface. The target plate consists of 49 targets with precisely known x- and y-coordinates measured on a NASA Quality Assurance validator. In practice, the target plate is mounted to a platform that has precise control of the y- and z-position of the plate relative to the model centerline. The target plate is a critical element in the determination of the VMD system camera position and pointing angles.

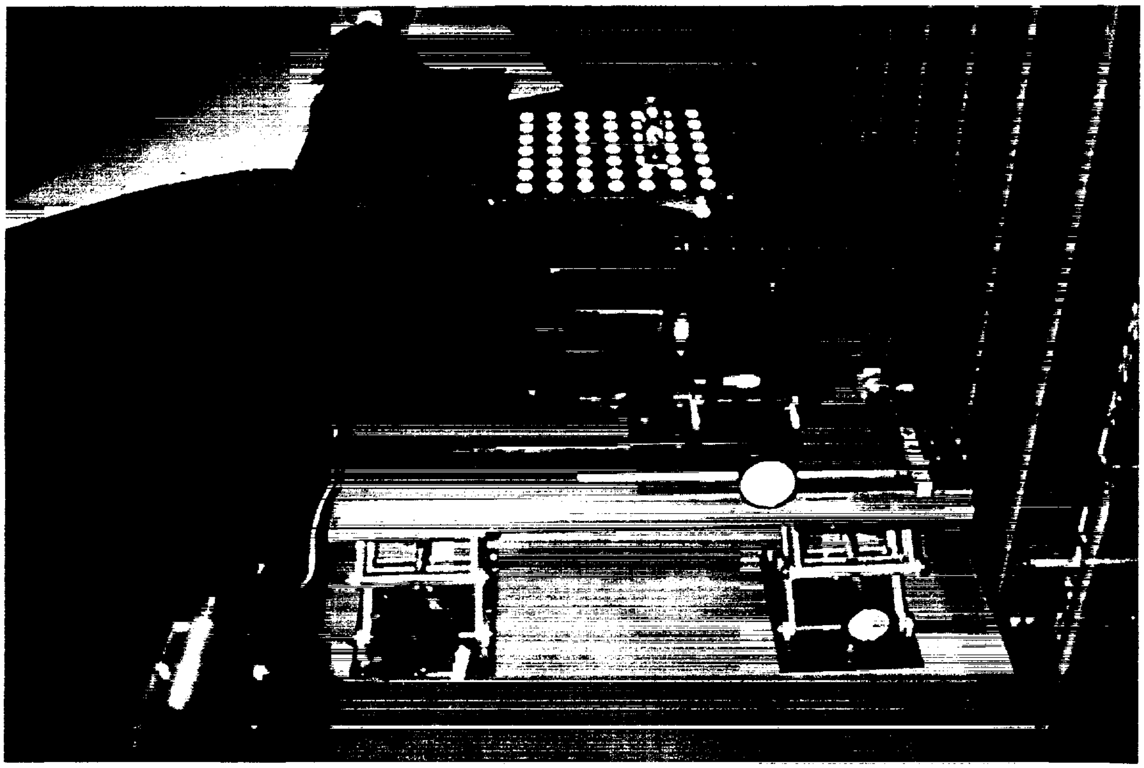

The calibration rig that is used to determine the camera constants (location, pointing angles, effective focal length) is shown in this photograph. The target plate is situated atop the rig and slides over the top of the wing surface. The x-position of the calibration assembly is set to provide a satisfactory image from the video CCD camera, and the y- and z-positions of the plate are varied using optical rail and lab jack arrangements. The y- and z-displacements of the target plate are measured using dial gauges (only one gauge is shown installed in the present photograph). As the calibration progresses, the calibration rig displacements measured with the dial gauges are compared to similar measurements obtained with the VMD system.

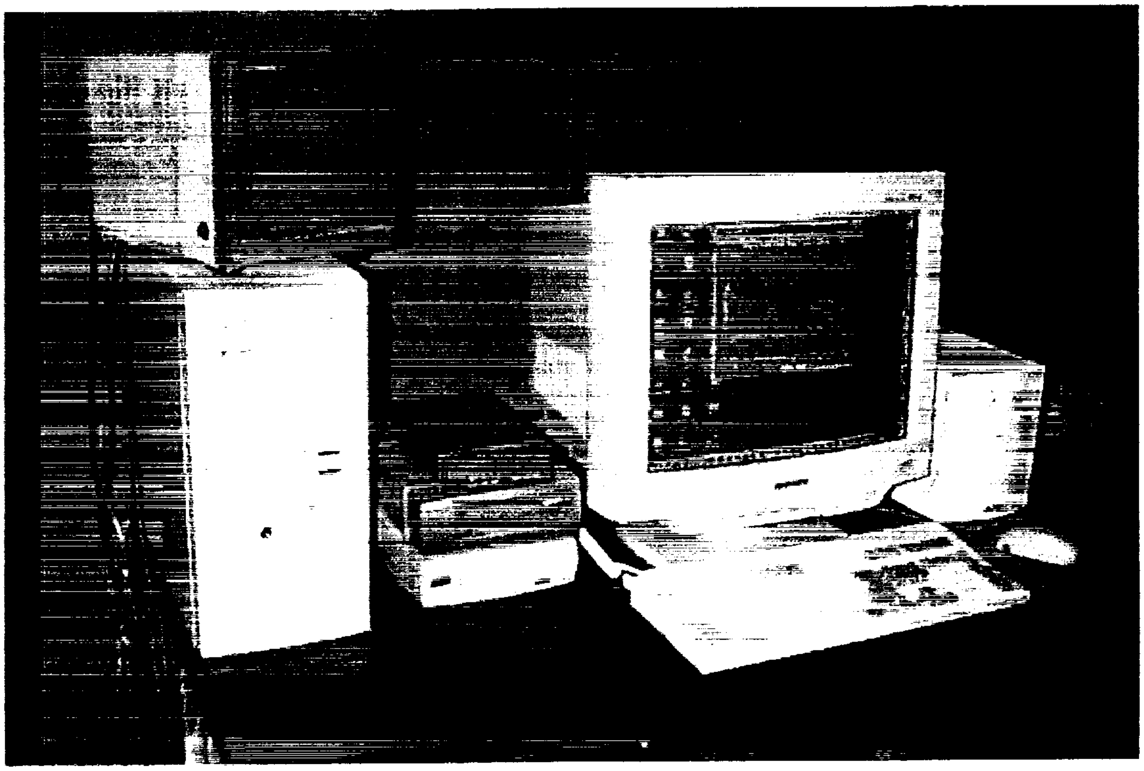

The host computer for the VMD system is illustrated in the above photograph. The mini-tower case contains the video frame grabber board that acquires, stores, and analyzes the digitized images. All image acquisition, processing, analysis, and plotting of the VMD results can be performed from this site.

VMD Applications to Date

- 1.675%-scale HSR Reference H model
- 1.675%-scale HSR TCA 2a model
- 1.675%-scale HSR TCA 20 model
- Test sections 1 and 2
- M=1.6 to 2.7, Re/ft=1-5 million
- $\alpha = -4^\circ$ to 12°

An early proof-of-concept test of the VMD system applied to a 1.675%-scale HSR Reference H model focused on the measurement of the wing twist at supersonic speeds. Each subsequent test led to enhancements of the UPWT VMD system. Primary improvements include additional target rows across the wing span to provide wing twist, deflection, and secondary model pitch angle measurements; improved method of "spatially mapping" the wind-off and wind-on results; and development of an effective target rig that significantly streamlined the camera calibration process. UPWT provides an excellent environment for this test technique, which has been successfully applied in both test sections over wide ranges of Mach number, Reynolds number, and angle of attack.

Mach Number Effect on Wing Twist
HSR TCA 20, Re/ft=3(10^6), UPWT Test 1844

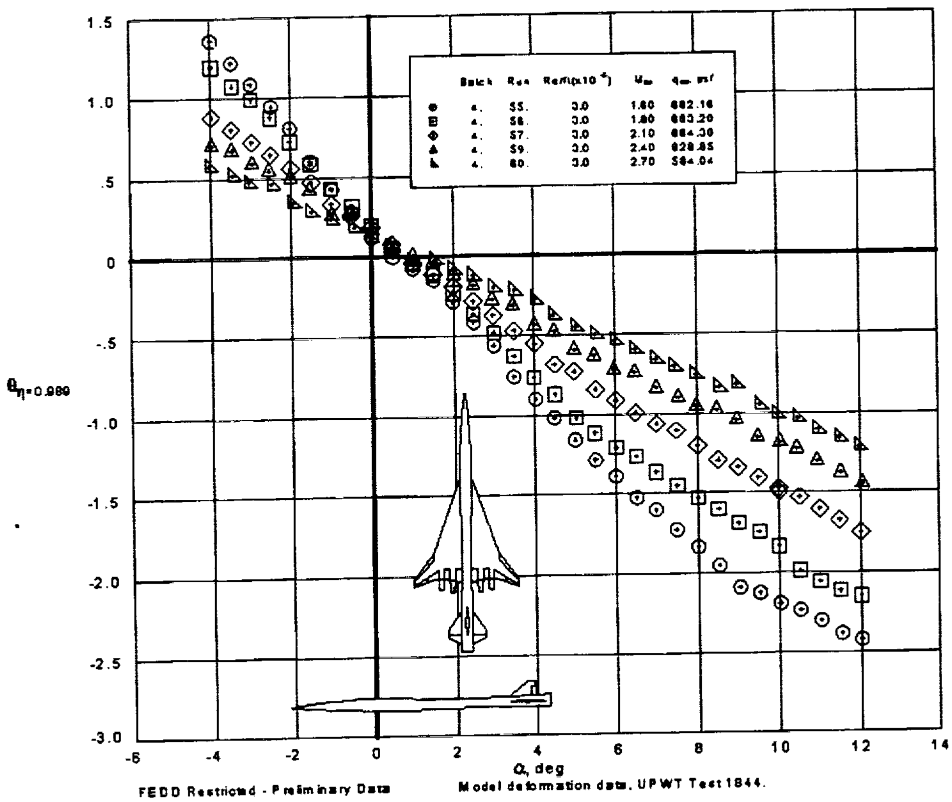

The effect of the free-stream Mach number on the wing twist at the y/(b/2)=0.989 span station is presented above. The Mach number varies from 1.60 to 2.70 at a constant Reynolds number per foot of 3(10^6). Increasing the Mach number decreases the wing twist (washout) at a given angle of attack. This effect is caused by the reduced wing lift as the Mach number is increased. A maximum twist angle of approximatly -2.9^0 was obtained at Mach=1.60 and $\alpha = 12^0$; at the same angle of attack, the twist angle was about -1.2^0 at Mach=2.70.

Mach Number Effect on Wing Deflection
HSR TCA 20, Re/ft=3(10^6), UPWT Test 1844

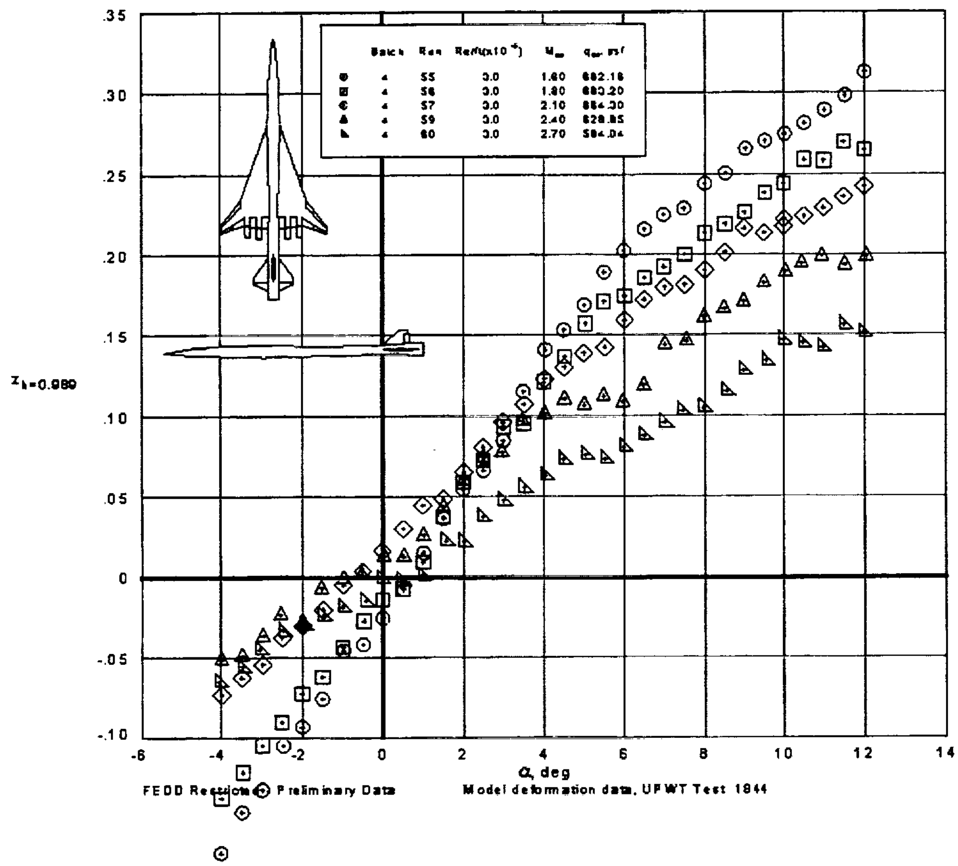

The Mach number effect on the wing deflection (bending) at the y/(b/2)=0.989 span station is shown in this figure. Increasing the Mach number decreases the deflection in the z (vertical) axis at a given angle of attack (less upward bending at the wing tip). The maximum deflection of approximately 0.31 inches was obtained at Mach=1.60 and $\alpha = 12^0$; the z displacement was 0.15 inches at Mach=2.7 and the same angle of attack.

Reynolds Number Effect on Wing Twist
HSR TCA 20,   Mach=2.10,   UPWT Test 1844

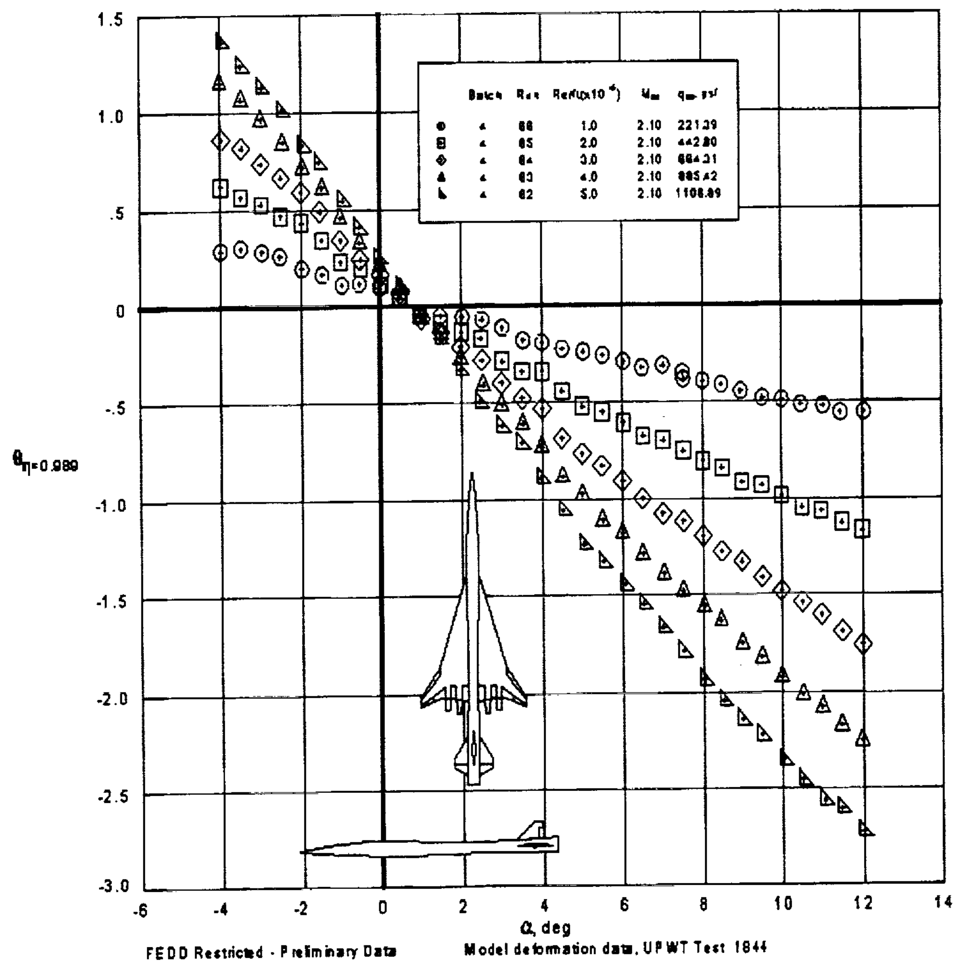

The Reynolds number effect on wing twist at the y/(b/2) = 0.989 span station and a constant Mach number of 2.10 is shown in the data plot above. The Reynolds number per foot varies from 1.0 (10^6) to 5.0(10^6) in increments of 1(10^6). The trend in the data plot is more of a free-stream dynamic pressure ("q") effect than Reynolds number, since q varied from approximately 221 psf at Re/ft = 1(10^6) to 1100 psf at Re/ft = 5(10^6). The twist angle is approximately a linear function of the Reynolds number ("q"); for example, a five-fold increase in the Reynolds causes a corresponding increase in the twist angle near the wing tip. For the range of angle of attack tested, a maximum twist of -2.75^0 occurs at a Reynolds number of 5(10^6)/ft and α = 12^0, while the corresponding twist at Re/ft= 1(10^6) is -0.55^0.

Reynolds Number Effect on Wing Deflection HSR TCA 20, Mach=2.10, UPWT Test 1844

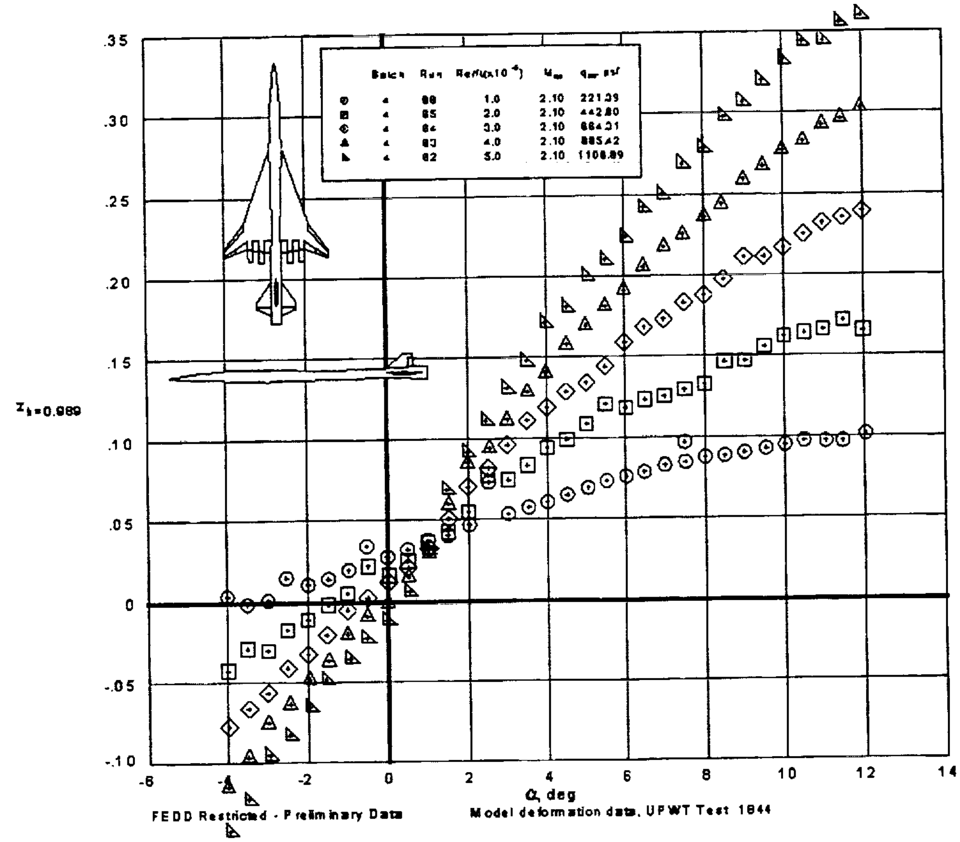

Wing deflection measurements obtained during a Reynolds number "sweep" at constant Mach number (Mach=2.10) are shown in this data plot. The Reynolds number per foot varies from 1.0 (10^6) to 5.0(10^6) in increments of 1(10^6). The z-displacement is approximately a linear function of the Reynolds number. Similar to the results shown in the previous figure, the primary factor affecting the wing displacement is the free-stream dynamic pressure. For the α -range in the present test, a maximum deflection of 0.36 inches occurs at a Reynolds number of 5 (10^6)/ft and $\alpha = 12^0$, while the corresponding displacement at Re/ft= 1(10^6) is 0.10 inches.

Two Experiment Design Types

- **"Classical" designs**
  - Change *one* variable at a time
  - Control errors by "holding all else constant"
  - Goal: Maximum data points for fixed resources
- **"Modern" designs**
  - Change *all* variables each data point
  - Errors controlled by balance and randomization
  - Goal: Specific objective with min. resources

The term "Classical Design" is used to describe an approach to experimentation in which one variable is changed at a time while all other variables are held constant. Classical designs have been used in wind tunnel research at Langley since the earliest days of flight, and are widely used in wind tunnel testing elsewhere as well.

Today, important aircraft design decisions can turn on fractional drag count results, and practitioners of an alternative experiment design philosophy called "Modern Design" recognize the futility of "holding everything constant" which might affect results at this level. Instead, they exploit their knowledge of the stochastic nature of experimental variables to control error through balance and randomization. Modern and classical design philosophies also differ in their approach to productivity enhancement. Classical designers attempt to maximize the data volume for a given resource budget while modern designers attempt to achieve a specific technical result at a prescribed level of confidence with the smallest expenditure of resources possible.

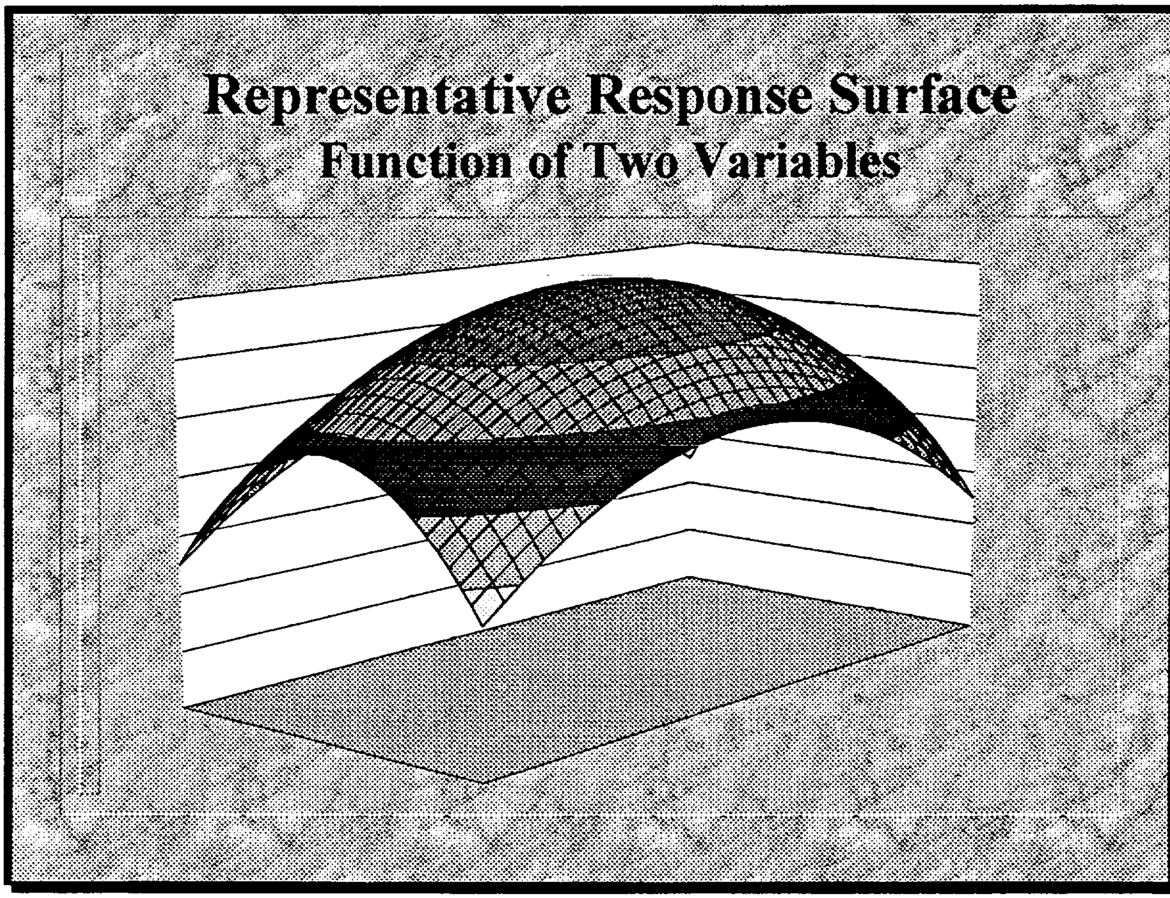

Classical designs divide a given inference space into a "grid" or "matrix" of test conditions at which response variables of interest are measured (forces, moments, etc.) The extent of this grid and the size of the cells which comprise it are influenced by the amount of resources available for a given test.

Modern design practitioners use the concept of a "response surface" to guide their design efforts. A response surface is a logical extension of the simple one-variable line graph in which the dependence of the response variable on all relevant independent variables is simultaneously considered in a small region of interest in the inference space. The extent of this region is purposely limited to that in which the response variable can be approximated adequately by a low-order Taylor series. Methods such as regression and contrast analysis are used to elucidate the response surface. Various curvature tests and optimization procedures are then used to quickly identify regions in the inference space which are the most interesting (peaks, ridge systems, etc.), which reduces resources that would otherwise be spent in less profitable regions.

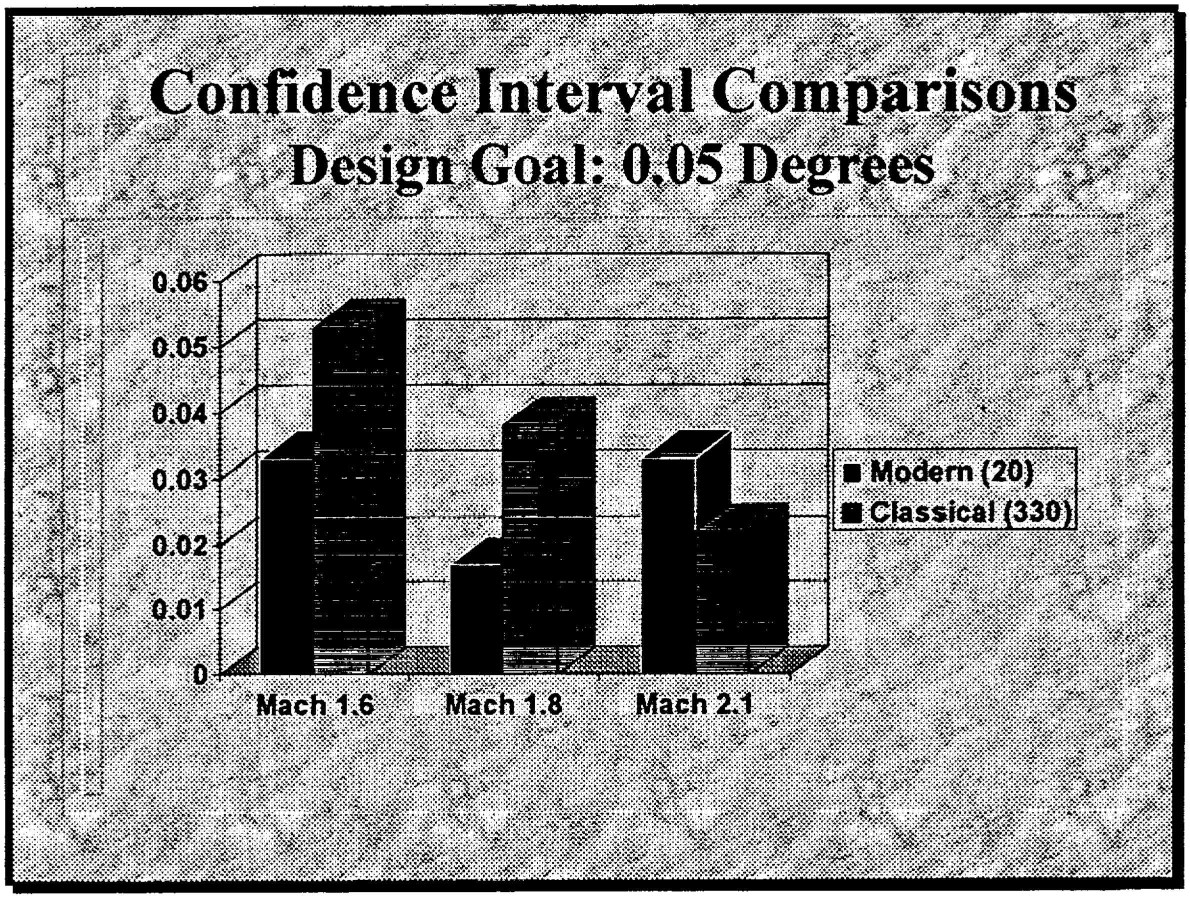

The aerodynamically-induced increase in wing twist for an HSR stability and control model has been measured for a range of angles of attack, Mach numbers, and Reynolds numbers as described elsewhere in this paper. A classical design requiring 330 data points was initially conducted, followed by a modern design to likewise quantify the wing twist change for the same model. The modern design required only 20 data points to define wing twist as a second-order response function in 3 variables with a design-goal precision of 0.05° at a prescribed 95% confidence level, given the 0.04° standard deviation in measured wing twist that was anticipated. The figure above compares 95% confidence intervals for the classical and modern designs. Both methods generated results with a precision that met the 0.05° design goal.

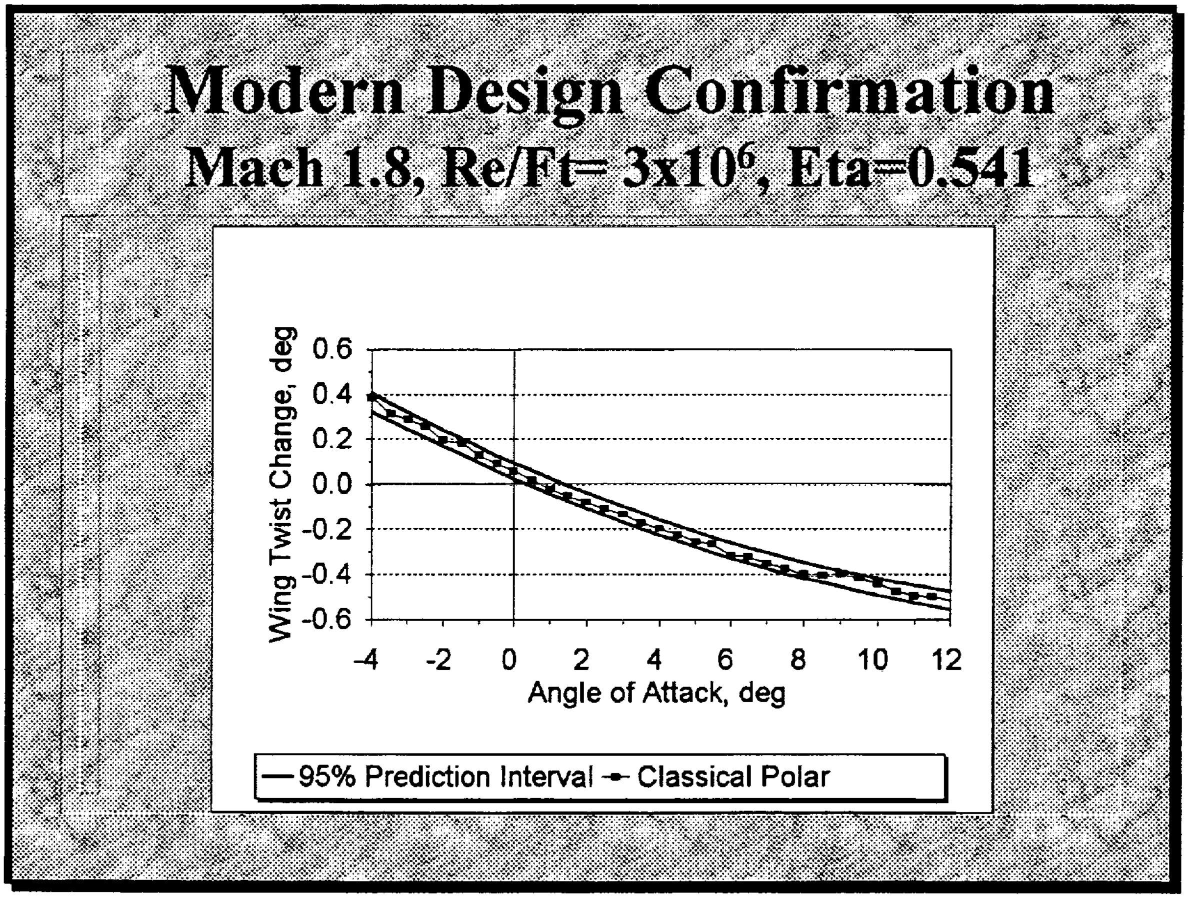

The two solid curves in the above figure mark the upper and lower limits of the 95% prediction interval for the modern design results at a given Mach number, Reynolds number, and normalized semi-span location. This modern design prediction was confirmed by plotting the 33 data points acquired on a different day at the same conditions, using the classical pitch-sweep method. Similar results were obtained at other combinations of Mach and Reynolds number.

Note that the above combination of Mach number and Reynolds number was never actually run in the modern design. This figure simply represents a slice through the modern design response surface in a direction parallel with the "angle of attack axis" at the specified values of Mach number and Reynolds number. This illustrates the fact that modern design response surface methods, once the response surface is adequately defined the response can be quantified for other combinations of the independent variables besides those measured directly.

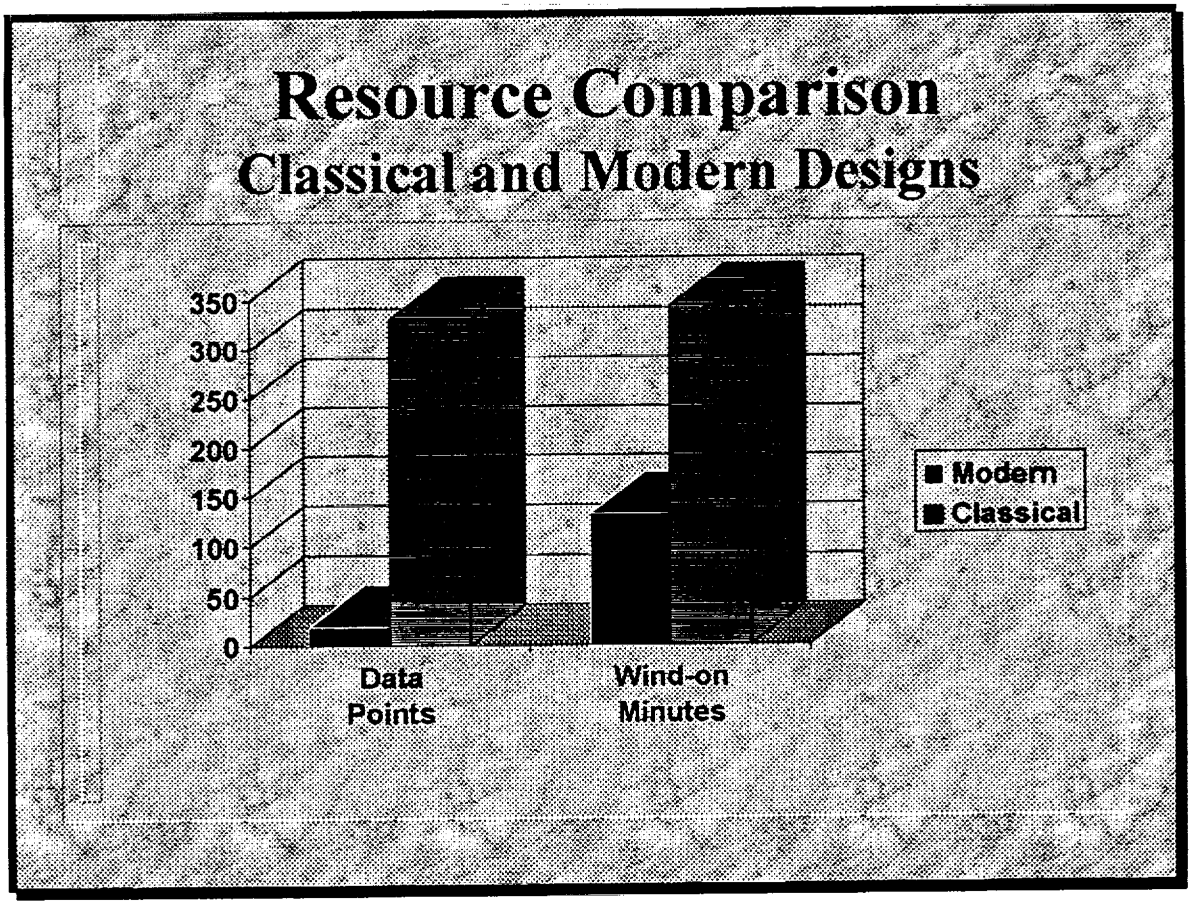

The modern design method only requires enough data to fit a low-order (typically first or second order) function of the independent variables in regions of interest, plus sufficient additional data points to insure that design precision goals are met with a prescribed level of confidence. A Central Composite Rotatable Design (CCRD) was employed in this test which could accomplish these objectives with only 20 data points. This resulted in considerably fewer wind-on minutes than the classical design (approximately one third in this test.)

Additional comparison tests involving other response variables, other independent variables and different ranges of variables, and other facilities, must be conducted before a body of practical tunnel-testing experience will have been accumulated which is sufficient to warrant a general implementation recommendation. However, modern design methods have been shown in this test to have some promising potential for wind tunnel research in an era in which external pressures continue to dictate that more be accomplished with less.

Summary

- PSP and VMD systems are installed and operational at UPWT
- Test techniques provide global surface pressure mapping, qualitative surface flow visualization, and model deformation measurements (twist and bending) at supersonic speeds
- Expertise has been developed at UPWT that allows autonomous operation of both systems
- PSP and VMD systems are "works in progress" that will be subject to continued enhancements
- Modern experimental design technique was effective in capturing wing twist characteristics and may provide a means of streamlining the wind tunnel test process

Pressure-sensitive paint and video model deformation systems are installed in the NASA Langley Unitary Plan Wind Tunnel and have been operational since early 1996. The PSP and VMD systems has been effectively used in support of HSR supersonic wind tunnel testing to provide global surface pressure mapping, qualitative surface pressure field response to shock waves and vortex flows, and measurements of the wing local twist angle and deflections (bending). Time to set up and calibrate the PSP and VMD systems is one shift (each), while one shift for each technique is necessary to acquire a typical set of wind-on runs. Simultaneous installation of the PSP and VMD systems has been done, although the images from each system were acquired in a concurrent, rather than simultaneous, manner because of system conflicts. Future enhancements to these systems that may lead to a "turn-key" operation include the ability to remotely control all illumination sources, including mechanized shutters for the UV lamps to reduce the effects of photodegradation, and full automation of the image acquisition process. The experience gained from PSP and VMD testing in cooperation with ETTD has resulted in resident expertise at UPWT regarding virtually all aspects of the system operations (application of the PSP coating continues to be performed by ETTD). A Modern Experimental Design technique was used during a recent VMD test where all critical test parameters were varied at each of 20 data points. The resultant response surface proved effective in predicting the wing twist over ranges of Mach number, Reynolds number, and angle of attack.

Analysis and Multipoint Design of the TCA Concept

Steven E. Krist
Steven X. S. Bauer
Pieter G. Buning

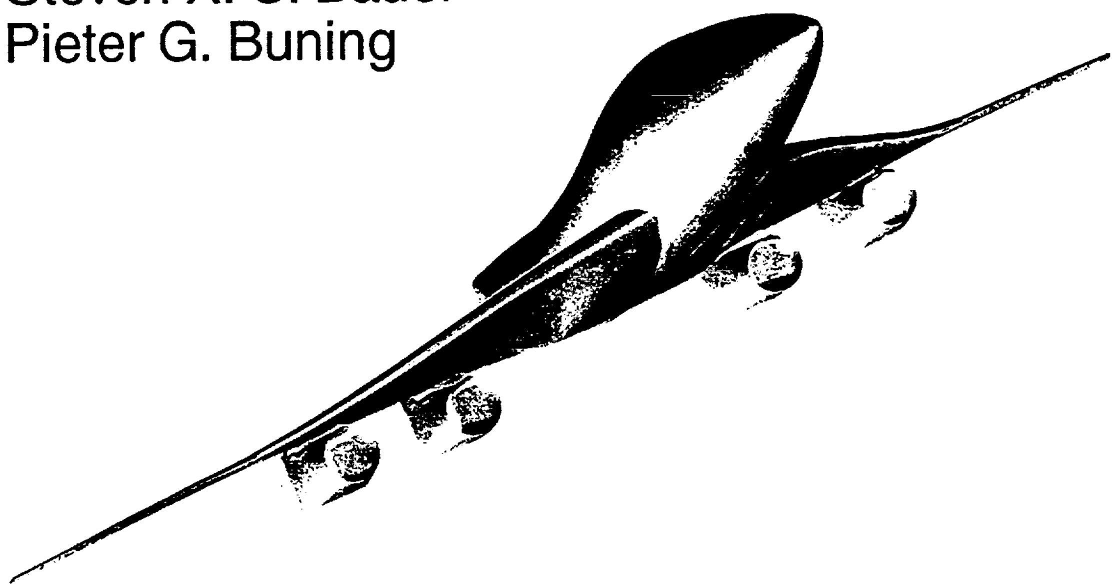

Analysis and Multipoint Design of the TCA Concept

The goal in this effort is to analyze the baseline TCA concept at transonic and supersonic cruise, then apply the natural flow wing design concept to obtain multipoint performance improvemnts. Analyses are conducted with OVERFLOW, a Navier–Stokes code for overset grids, using PEGSUS to compute the interpolations between the overset grids.

Grid Generation and Codes

The initial 20 block overset grid for the TCA baseline configruation, Mach 2.4 cruise condition, was developed by Boeing

Slight topology changes were made to the nacelles to permit the use of PEGSUS41_45 (7 times faster than PEGSUS41_36)

Grids for transonic cruise at Mach 0.95
- 1/3 smaller wall–normal spacing
- 10% more grid points

OVERFLOW version 1.7t

Grid Generation and Codes

The initial overset grids utilized in this effort were developed by Steve Chaney and Steve Ogg at Boeing. The grids were sized for Mach 2.4 supersonic cruise conditions, maintaining a y+ value on the order of one. The grids were modified for the Mach 0.95 transonic cruise condition by decreasing the wall–normal spacing to a third of its original value, thereby maintaining a y+ value of one. A slight change to the topology was also made to the nacelles, using two grids for the external and internal surfaces rather than three. This change permits the user of PEGSUS version 41_45, which is roughly seven times faster than version 41_36, which was required for the successful interpolation of the initial set of overset grids.

The version of OVERFLOW utilized is over1.7t. This version contains upgraded treatments of the multigrid and mesh sequencing boundary conditions.

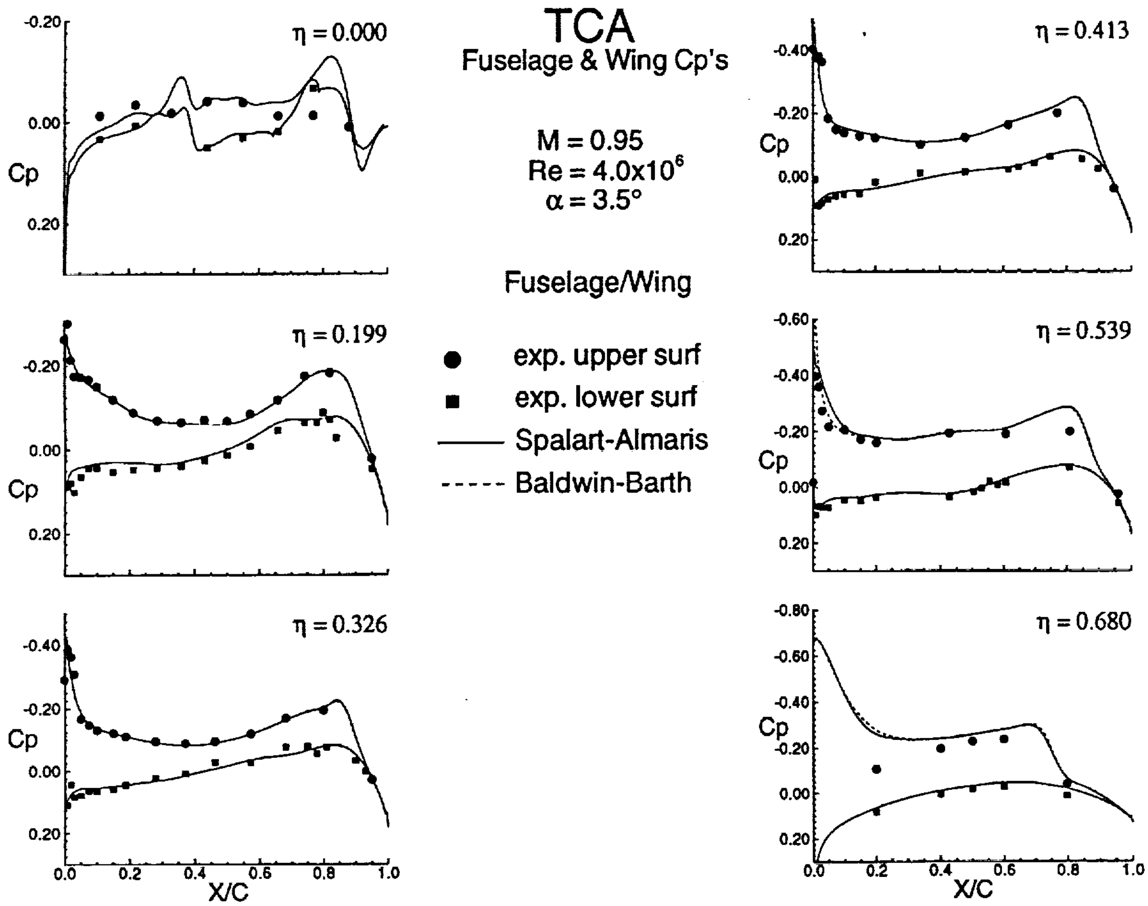

Wing/Body Pressure Coefficient at Mach 0.95

Results using the Spalart–Almaris and Baldwin–Barth turbulence models for the baseline wing/body configuration at Mach 0.95, $\alpha = 3.5$, are compared against the experimental results. While the pressure distributions are virtually identical inboard, by 53.9% span the Spalart–Almaris solution shows a slower recovery from the acceleration over the wing leading edge. This result is consistent with OVERFLOW results for transonic transport configurations, where the transonic shock is typically further aft of the data for the Spallart–Almaris model than for Baldwin–Barth. Forces from the two solutions are compared against data in the following table:

	Cl	Cd	Cm
experiment	.12712	.01184	.00370
Splart–Almaris	.13106	.01256	.01007
Baldwin–Barth	.13161	.01202	.00071

In order to investigate reports suggesting that a y+ of roughly 0.5 is required for the Spalart–Almaris turbulence model in some cases, the wall-normal spacing was halved and the grid refined by 10%. No significant difference was seen in either solution.

Since discrepancies with the data are larger for Spalart–Almaris than for Baldwin–Barth, all subsequent transonic solutions utilize the Baldwin–Barth turbulence model.

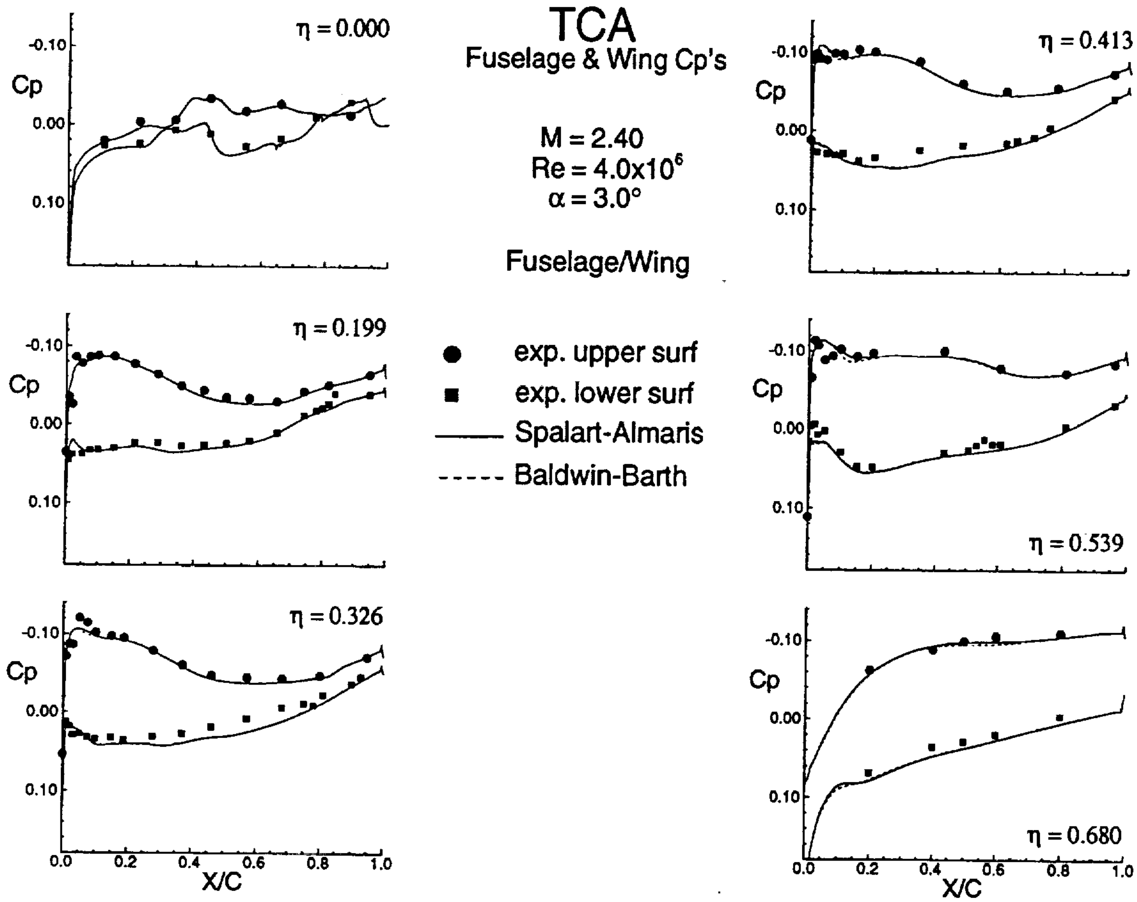

Wing/Body Pressure Coefficient at Mach 2.40

Results using the Spalart–Almaris and Baldwin–Barth turbulence models for the baseline wing/body configuration at Mach 2.40, $\alpha = 3.0$, are compared against the experimental results. In this case the pressure distributions are virtually identical accept at the leading edge. Once again, Spalart–Almaris recovers somewhat more slowly than Baldwin–Barth, but in this case the Spalart–Almaris solution shows better agreement with the data. Forces from the two solutions are compared against data in the following table:

	Cl	Cd	Cm
experiment	.07452	.01080	.00457
Splart–Almaris	.07414	.01047	.00421
Baldwin–Barth	.07394	.01037	.00420

Since discrepancies with the data are larger for Baldwin–Barth than Spalart–Almaris, all subsequent supersonic solutions utilize the Spalart–Almaris turbulence model.

While the solutions generally agree with experiment quite well, a noticable discrepency occurs on the lower wing surface at 32.6% and 41.3 % span.

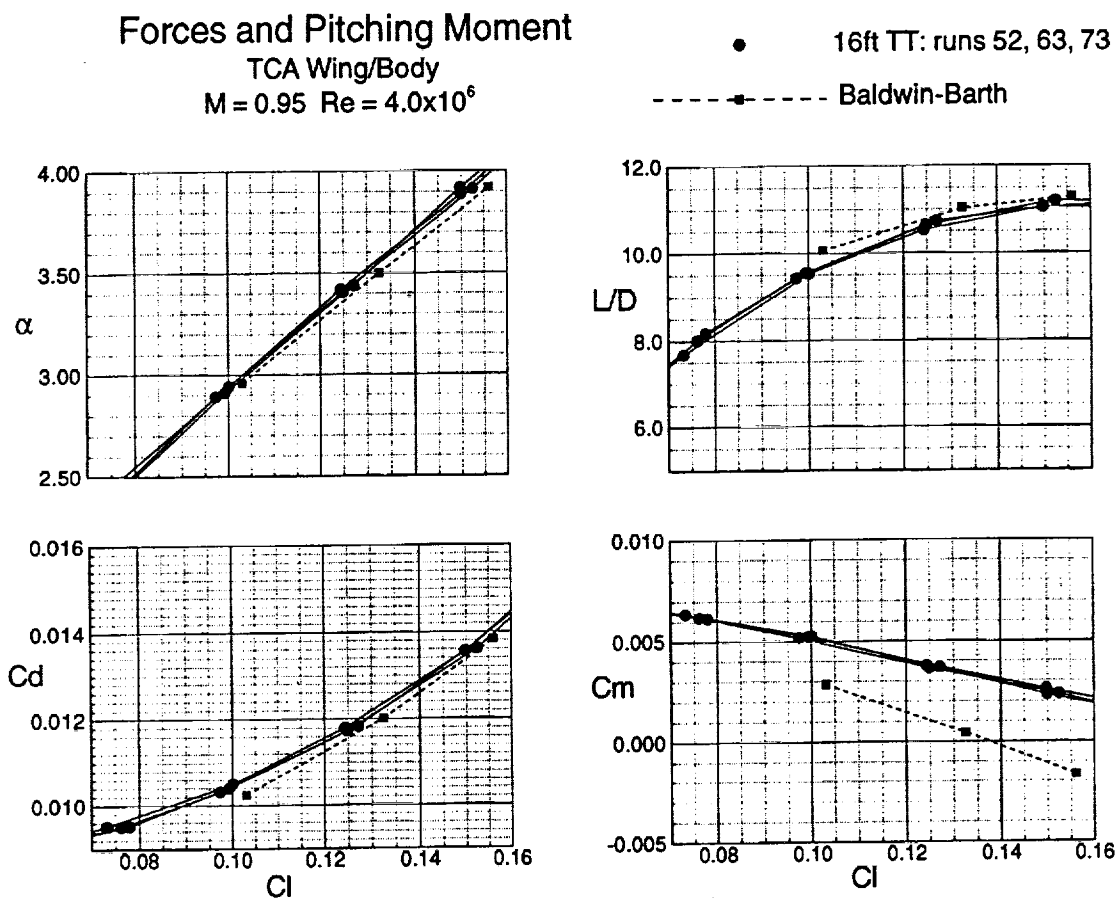

Wing/Body Forces and Moments at Mach 0.95

Solutions with the Baldwin–Barth turbulence model were generated for the baseline wing/body configuration at Mach 0.95 , α = 2.96, 3.5, and 3.92. The results are compared against experiment in the figures. The lift vs. angle of attack curve shows the slight difference in slope which is typical of aeroelastic deformation effects. The lift vs. drag polars also have sligtly different trends , with the discrepency in drag being around 4 counts at the lower Cl's and from 1 to 2 counts at higher Cl's.

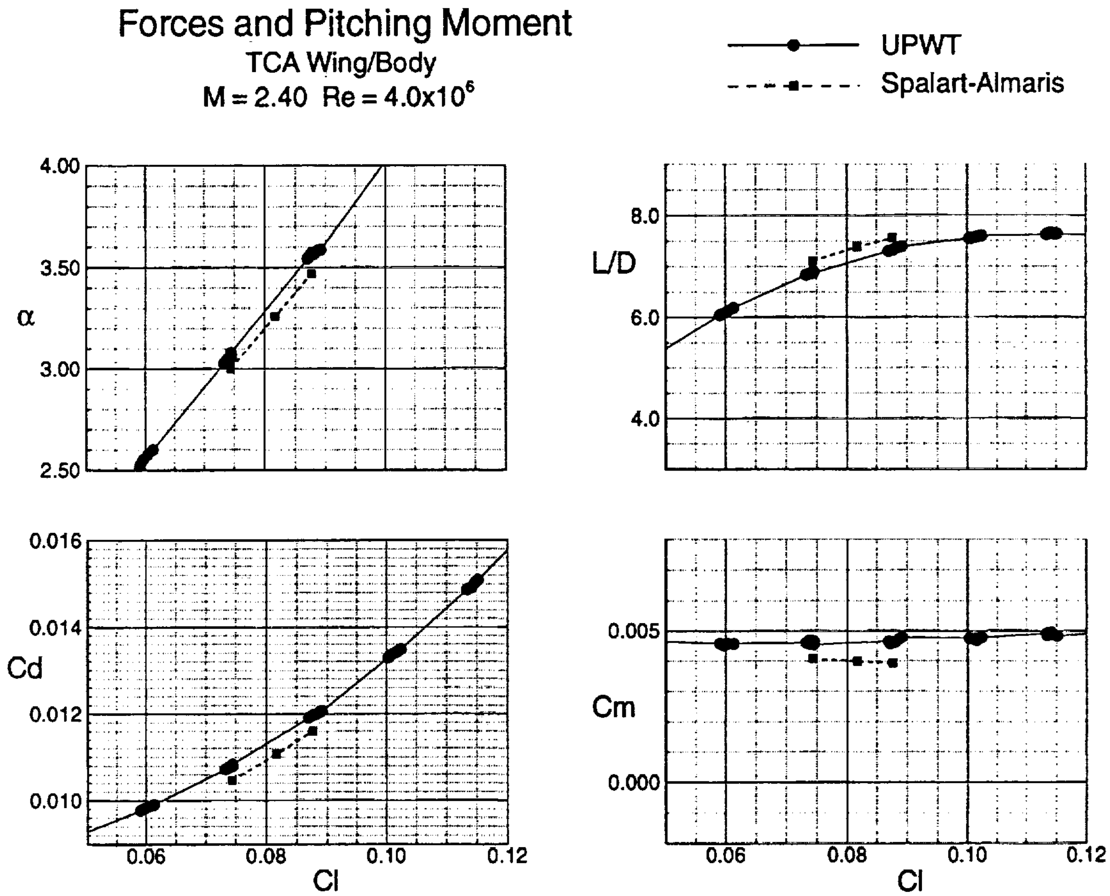

Wing/Body Forces and Moments at Mach 2.40

Solutions with the Spalart–Almaris turbulence model were generated for the baseline wing/body configuration at Mach 2.40 , α = 3.0, 3.26, and 3.47. The results are compared against experiment in the figures. Once again the lift vs. angle of attack curve shows the slight difference in slope which is typical of aeroelastic deformation effects. The lift vs. drag polars show the same trend, but the discrepency in drag is around 4 counts.

The Effect of Trailing Edge Spacing

The initial grid has a trailing edge spacing on the order of 0.5% of chord. The sufficiency of this was checked by decreasing the spacing to 0.05% of chord and refining the streamwise resolution by 10%. Results for transonic and supersonic flow are tablulated below.

Mach	T.E. Spacing	α	Cl	Cd
0.95	0.5%	3.5	.13205	.01204
0.95	0.05%	3.5	.13106	.01256
2.40	0.5%	3.0	.07414	.01047
2.40	0.05%	3.0	.07415	.01051

Effect of Trailing Edge Spacing

In transonic transport problems, solutions from OVERFLOW have been found to be sensititve to trailing edge spacing, particularly in terms of shock location. To determine the sensitivity for HSR configurations, the streamwise spacing at the trailing edge was decreased from 0.5% of chord to 0.05% of chord and the grid was refined with 10% more grid points. The results at both supersonic and transonic conditions indicate that drag increases by about half a count with the grid refinement. However, no significant differences in pressure distributions are seen.

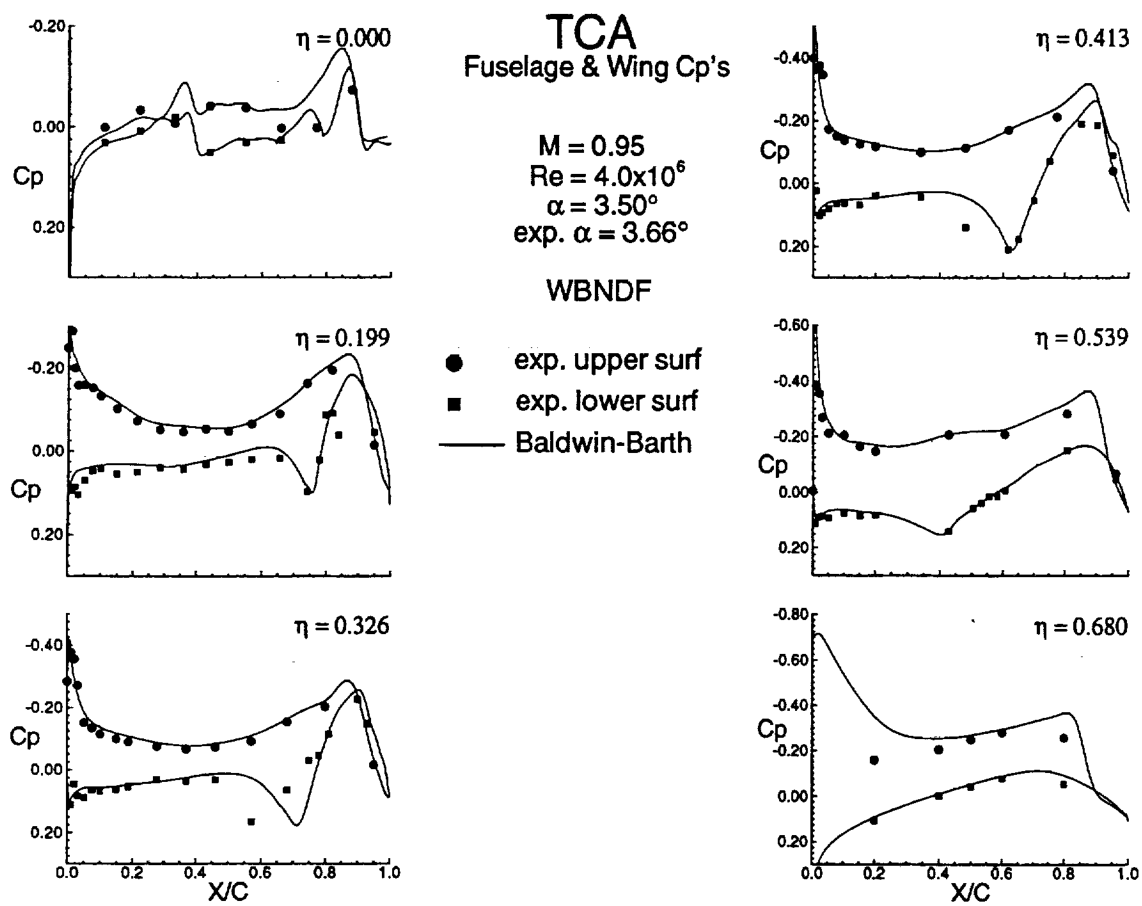

Wing/Body/Nacelle/Diverter Pressure Coefficient at Mach 0.95

Results using the Baldwin–Barth turbulence model for the baseline wing/body/nacelle/diverter configuration, including the fairing where the nacelle protrudes through the upper surface of the wing, at Mach 0.95, $\alpha = 3.5$, are compared against the experimental results. While the computed and experimental distributions are comparable inboard and immediately outboard of the diverters, a large discrepency is seen in the location of the compression between the diverters, at both 32.6% and 41.3% span. Further outboard,at 68% span, the effects of aerolastic deformation are seen with the unloading of the leading edge.

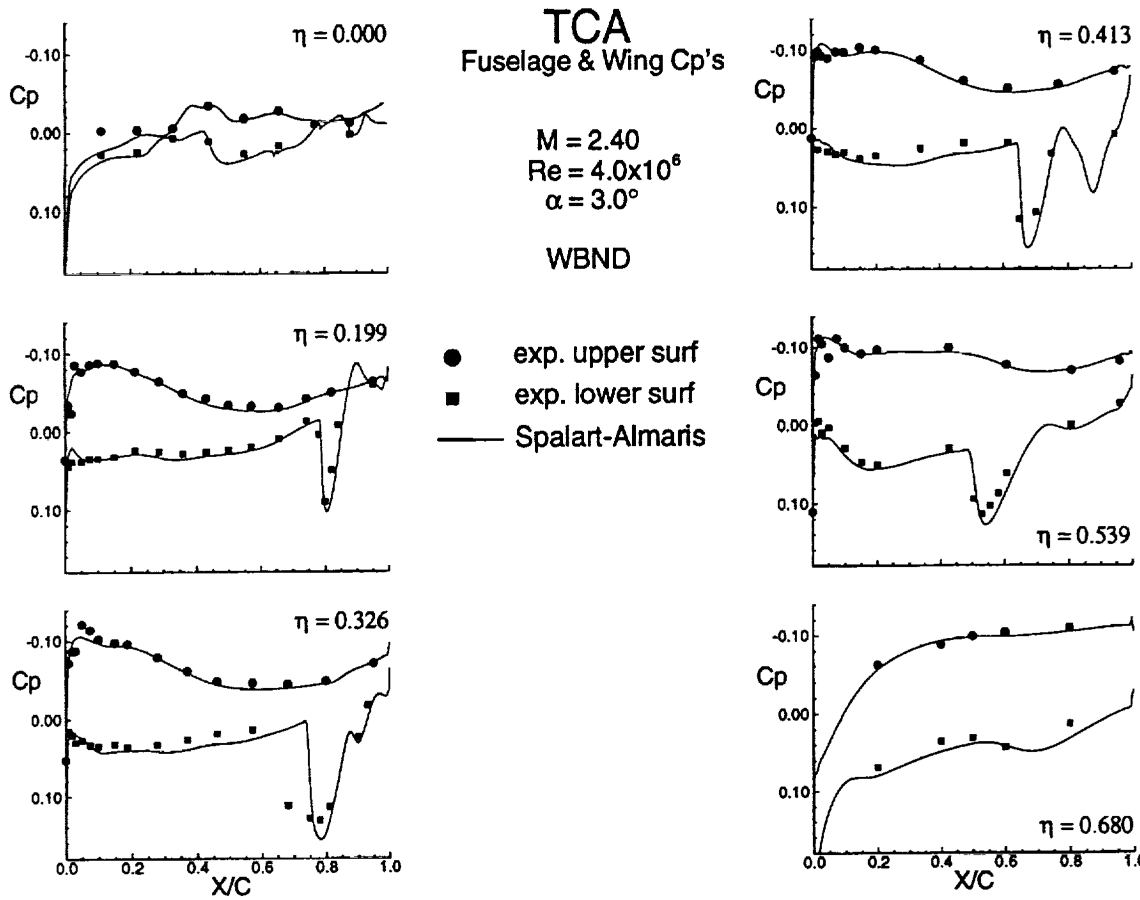

Wing/Body/Nacelle/Diverter Pressure Coefficient at Mach 2.40

Results using the Spalart–Almaris turbulence model for the baseline wing/body/nacelle/diverter configuration, including the fairing where the nacelle protrudes through the upper surface of the wing, at Mach 2.40, $\alpha = 3.0$, are compared against the experimental results. Once again, the computed and experimental distributions are comparable inboard and outboard of the diverters, but a large discrepency is seen in the shock location at 32.6% span.

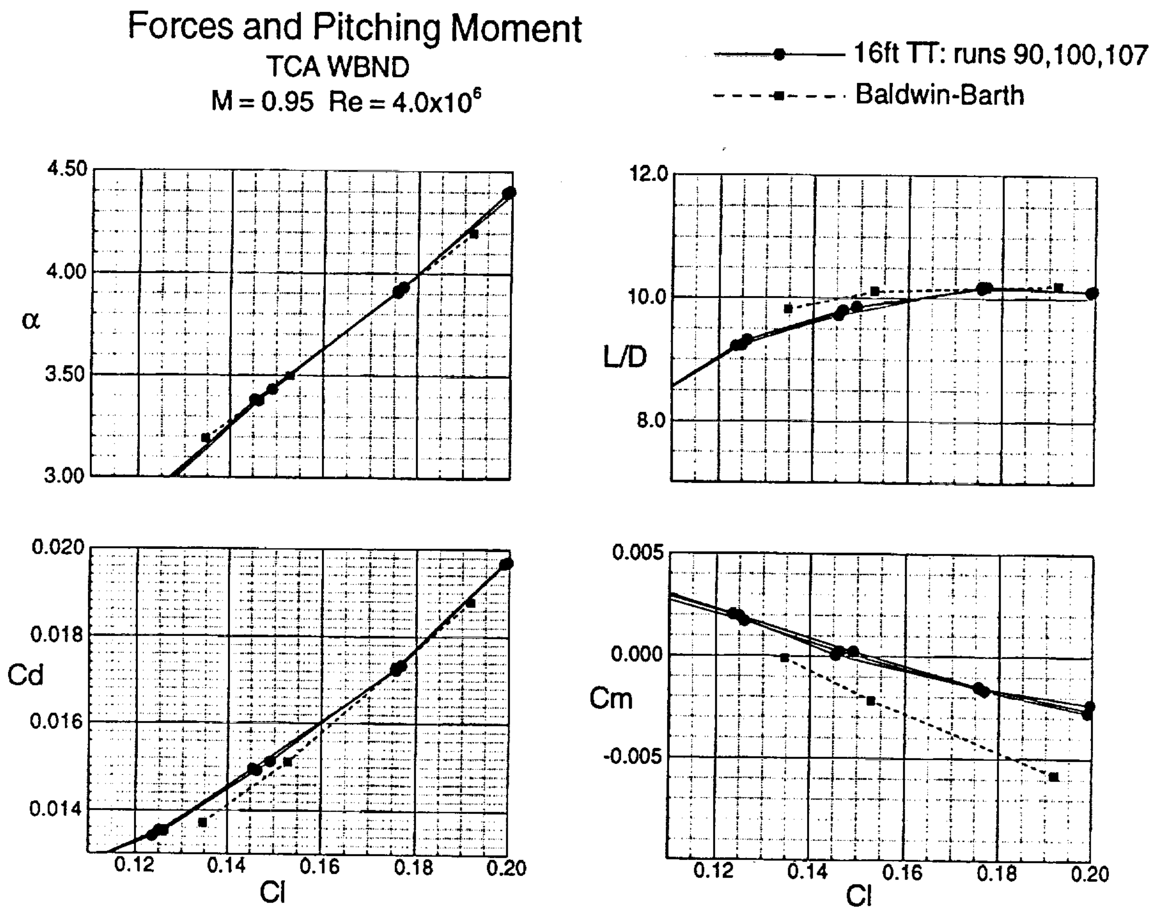

Wing/Body/Nacelle/Diverter Forces and Moments at Mach 0.95

Solutions with the Baldwin–Barth turbulence model were generated for the baseline wing/body/nacelle/diverter configuration at Mach 0.95 , $\alpha =$ 3.2, 3.5, and 4.2. The results exhibit the same trend the wing/body solutions, with the discrepancy in drag varying from 2 to 4 counts.

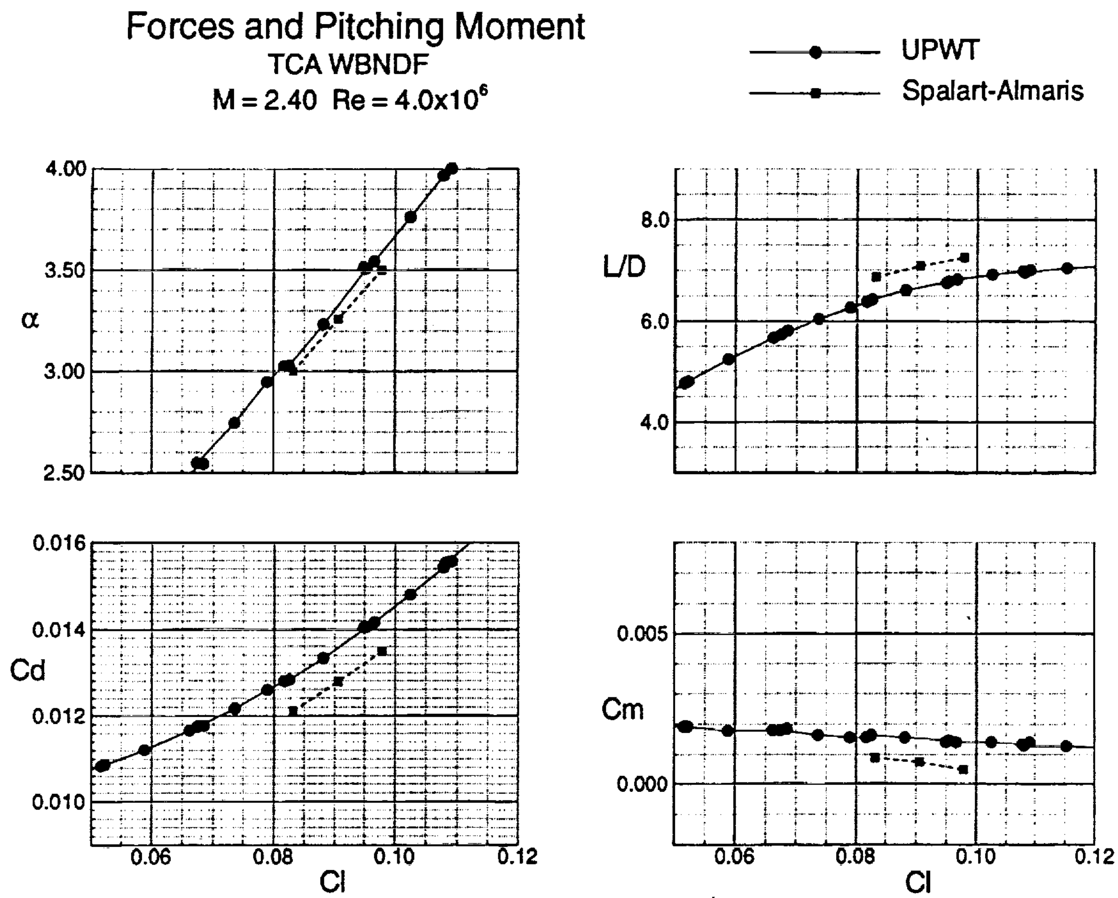

Wing/Body/Nacelle/Diverter Forces and Moments at Mach 2.40

Solutions with the Spalart–Almaris turbulence model were generated for the baseline wing/body configuration at Mach 2.40 , $\alpha =$ 3.0, 3.26, and 3.5. The results exhibit the same trend as for the wing/body, with the drag descrepancy being on the order of 8 counts.

Natural Flow Wing Design

Based on Wing/Body Euler Analyses
- Maintain leading edge thickness constraint
- Blunt leading edge outboard of leading edge break
- Design upper surface for strong conical flow
- Use lower surface to satisfy spar constraints

Regridding for NFW Designs
- Given fuselage and wing definitions
- Wing/Body Script
- Automatic installation script to place nacelle/diverter grids from baseline configuration on redesigned wing.

Natural Flow Wing Design

Designs are based on the Natural Flow Wing Design philosophy developed by Rick Woods and Steve Bauer, as reported in the 1996 HSR workshop proceedings under the title "Application of the Natural Flow Wing Design Philosophy to the HSR Arrow Wing Configuration". An additional aspect of the current design is to maintain a blunt leading edge outboard of the leading edge break for transonic performance.

Wing body grids for the redesigned configruation are generated using a modified form of the wing/body script developed in the AST program. Nacelle/diverter grids for the installed configuration are generated through use of a script file to translate, rotate and project the diverter/nacelle component grids from the baseline configuration onto the new fuselage/wing surface definition. Constraints imposed on the installation are to keep the same inboard diverter/wing trailing edge intersection point, intersect the same point on the outboard diverter with the wing trailing edge, and maintain a constant distance between the nacelle lip and wing surface.

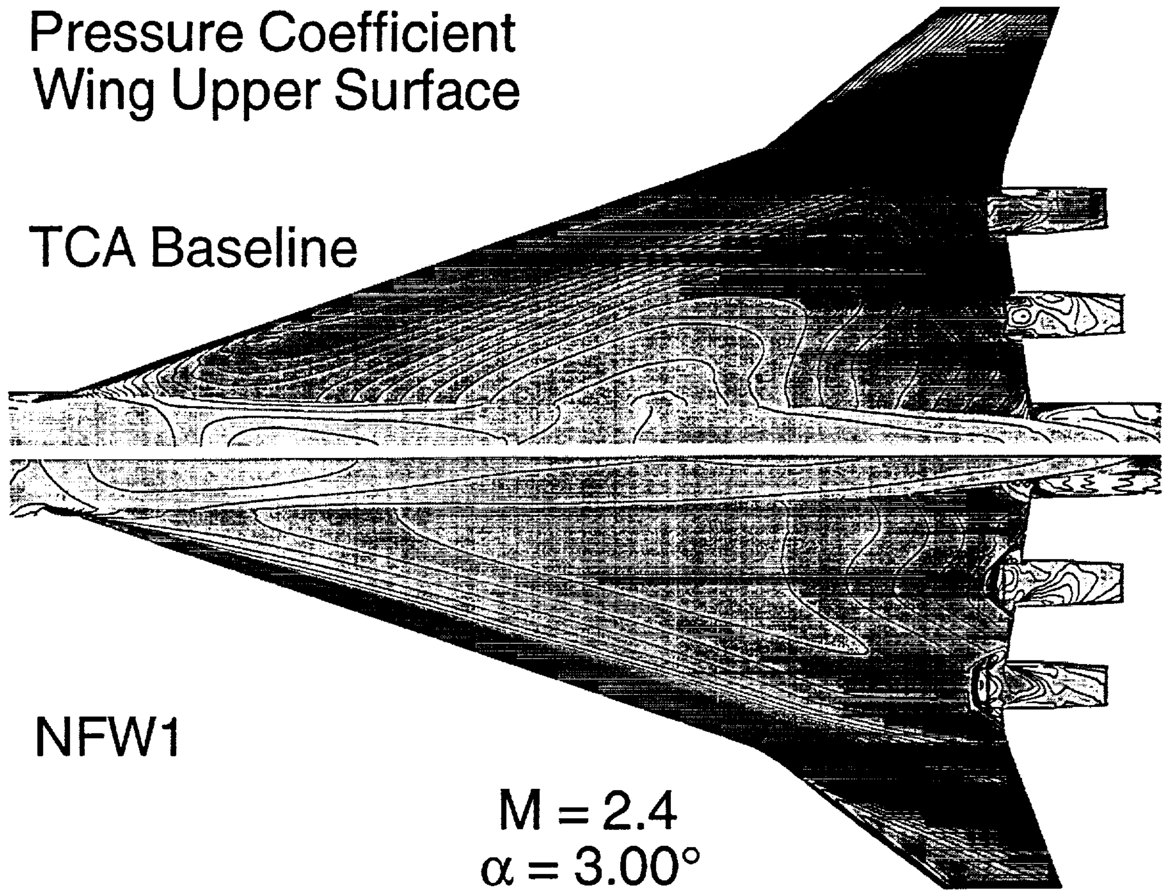

Upper Surface Pressure Coefficient on the Baseline and Design NFW1 at Mach 2.40

The first redesign of the TCA baseline configuration using the Natural Flow Wing design philosophy is designated as NFW1. Pressure distributions on the wing upper surface for the two configurations at Mach 2.4 are illustrated in the figure. In the NFW design, a strong conical expansion is enforced over the leadiing edge. In addition the compression seen on the outboard section of the baseline is eliminated. The compressions seen at the front of the nacelle fairings are due in part to the fact that the nacelles protrude through the upper surface to a greater extent than the baseline. However, it also indicates an inadequate regridding process in the automatic installation of the nacelles.

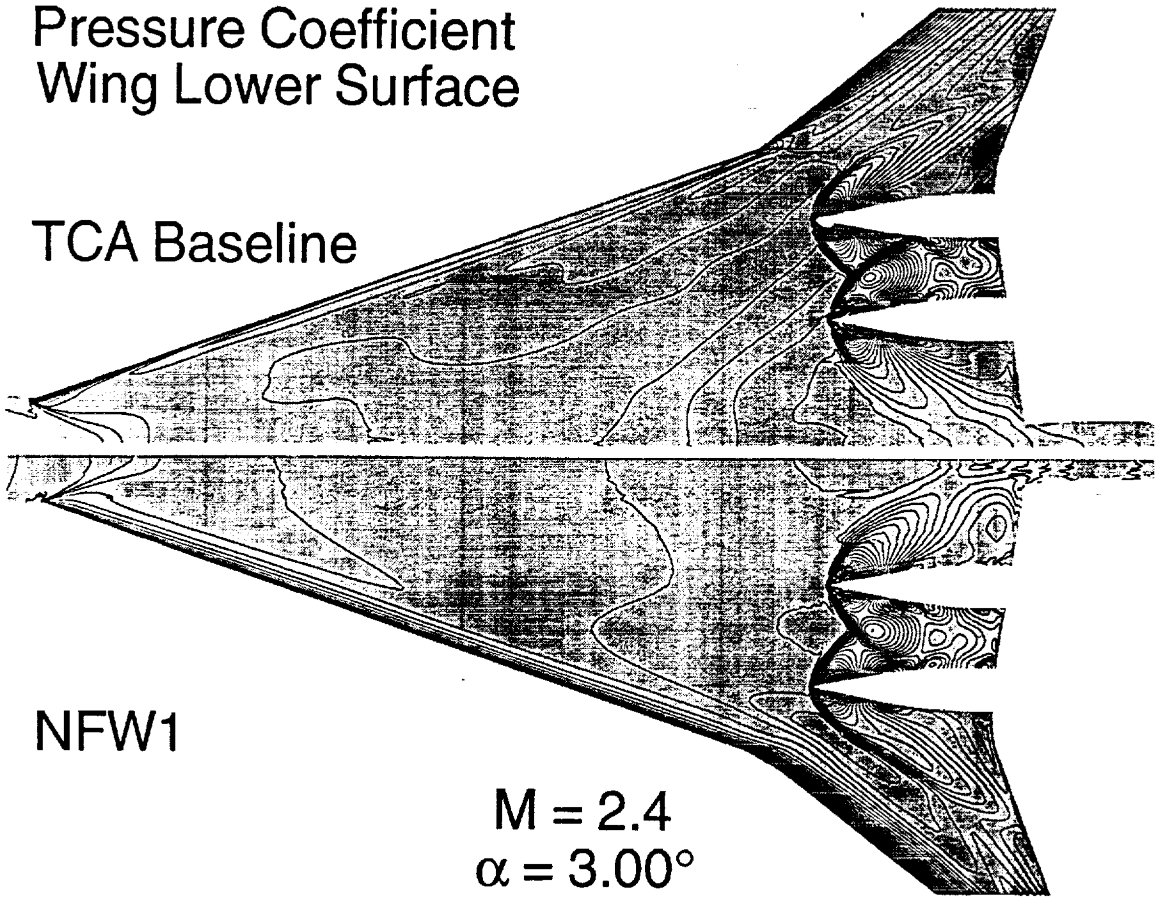

Lower Surface Pressure Coefficient on the Baseline and Design NFW1 at Mach 2.40

Pressure distributions on the wing lower surface for the two configurations at Mach 2.4 are illustrated in the figure. The NFW design exhibits a much stronger shock interaction between the diverters, as well as a larger expansion over the outboard leading edge due to the bluntness.

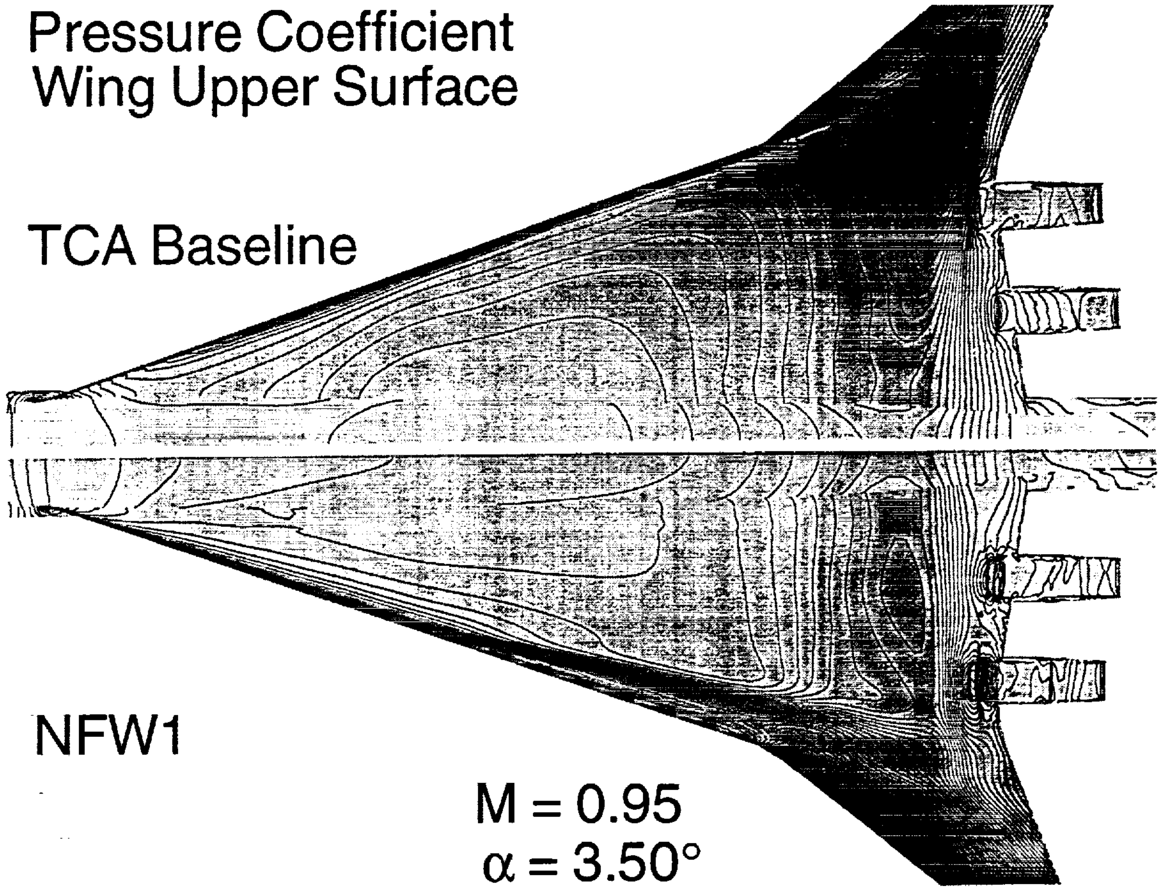

Upper Surface Pressure Coefficient on the Baseline and Design NFW1 at Mach 0.95

Pressure distributions on the wing upper surface for the two configurations at Mach 0.95 are illustrated in the figure. Once again, the NFW design exhibits a much stronger expansion over the leading edge, as well as a shock at the nacelle fairing.

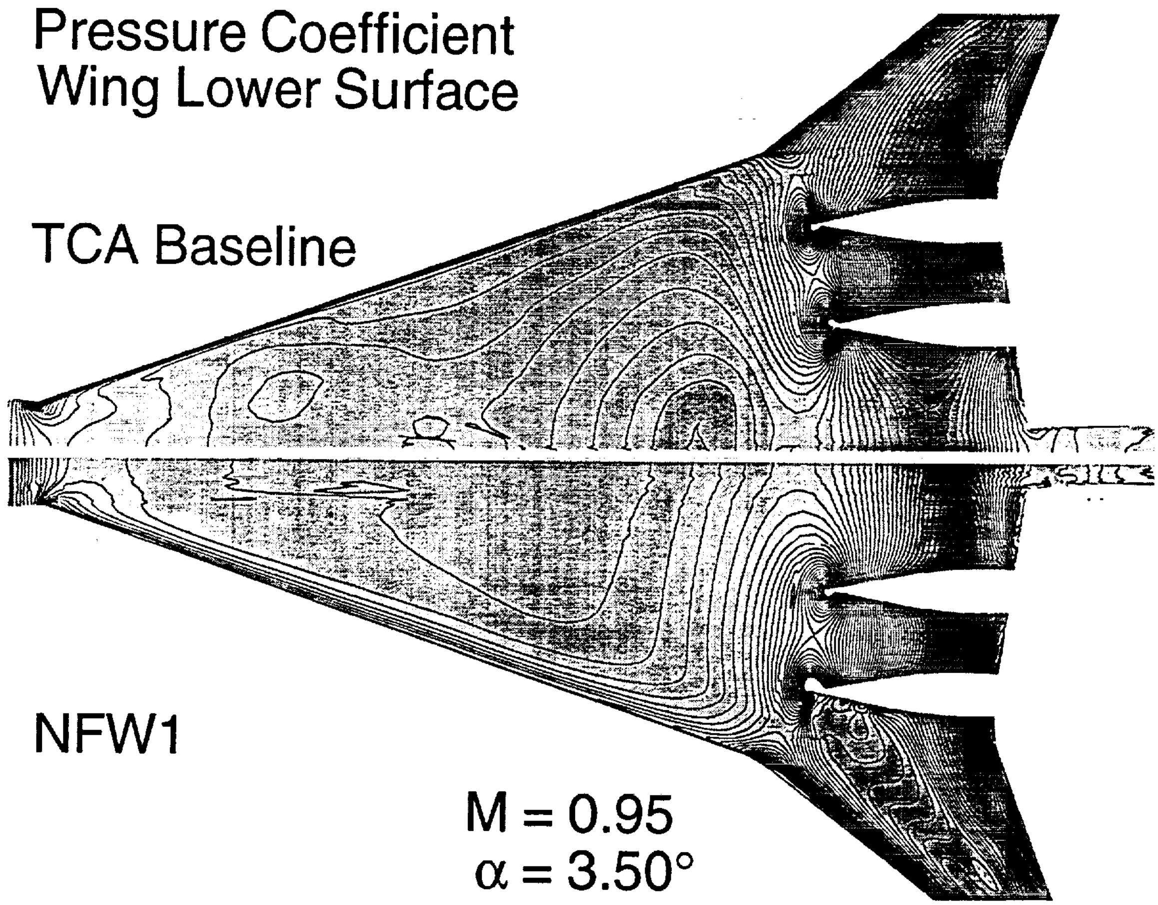

Lower Surface Pressure Coefficient on the Baseline and Design NFW1 at Mach 0.95

Pressure distributions on the wing lower surface for the two configurations at Mach 0.95 are illustrated in the figure. The NFW design exhibits a much stronger shock at the nacelle and diverter leading edges, as well as a stronger expansion between the diverters.

Summary

NFW1 has poor performance
- Drag is 3 counts higher than the baseline at Mach 2.4
- Drag is 23 counts higher than the baseline at Mach 0.95

The wing/body script is fast and robust

The nacelle rerigging script is fast but incomplete
- 2 hour turnaround on grid generation for NFW2
- a sophisticated nacelle fairing treatment is required

Further investigation of the Spalart–Almaris turbulence model is required at transonic conditions

Summary

The first redesign of the TCA Baseline Configuration using the natural flow wing design has poor performance, with the drag 3 counts higher than the baseline at supersonic cruise and 23 counts higher at transonic cruise. A portion of the drag increment can be attributed to the poor installation of the fairing in the automatic installation of the nacelles and diverters.

The wing body and nacelle rerigging scripts are fast and robust. Turnaround time for generating grids for the second design was on the order of 2 hours (this does not include the time to get PEGSUS through the que). However, the nacelle/wing fairing treatment is incomplete, requiring a more sophisticated treatment to ensure captruing the nacelle outer boundary.

While Baldwin–Barth is the preferred method for transonic OVERFLOW solutions at this time, further investigation of the Spalart–Almaris turbulence model is warranted.

TLNS3D/CDISC MULTIPOINT DESIGN OF THE TCA CONCEPT

Richard L. Campbell and Michael J. Mann

1997 HSR Aerodynamic Performance Workshop
NASA Langley Research Center
February 25-28, 1997

This paper presents the work done to date by the authors on developing an efficient approach to multipoint design and applying it to the design of the HSR TCA configuration. While the title indicates that this exploratory study has been performed using the TLNS3DMB flow solver and the CDISC design method, the CDISC method could have been used with any flow solver, and the multipoint design approach does not require the use of CDISC. The goal of the study was to develop a multipoint design method that could achieve a design in about the same time as 10 analysis runs.

OUTLINE OF PRESENTATION

- Review of CDISC design method
- Single-point designs
- Multipoint design approaches
  - weighted average of geometries (WAG)
  - transonic flap
- Concluding remarks

This paper will begin with a review of the Constrained Direct Iterative Surface Curvature (CDISC) design method, then look at its application to design of the TCA configuration at a supersonic and a transonic cruise point. Two approaches to the multipoint design problem will then be considered: a new method that uses a weighted average of the geometries from the previous point designs (referred to as the WAG method), and a second approach that involves the use of a flap on the supersonic point design geometry to improve the transonic performance. The concluding remarks will summarize the lessons learned so far and present the future plans for application of the multipoint design methods.

CDISC DESIGN METHOD

- Efficient constrained design with Navier-Stokes codes (design run time ≈ analysis run time)
- Target pressures automatically generated based on flow constraints
- Geometry constraints allow design to be impacted by requirements from other disciplines
- "Optimization" available through constraint specification and relaxation
- Modular coupling of CDISC and flow solvers

This chart gives a description of some of the key features of the CDISC design method. It is a knowledge-based design approach that uses rules and guidance obtained from analytical, experimental, and computation sources to allow new designs to be obtained in about the same time as a single flow analysis. The target pressure distributions required by the basic DISC method are automatically generated based on flow constraints, and a suite of geometry constraints are available that allow requirements from other disciplines such as structures and manufacturing to be included in the design process. In addition to the TLNS3DMB Navier-Stokes code already mentioned, the CDISC design module has also been coupled with the CFL3D, OVERFLOW, and USM3D flow solvers to allow a variety of options for viscous design of complex configurations.

FLOWCHART OF CDISC DESIGN SYSTEM

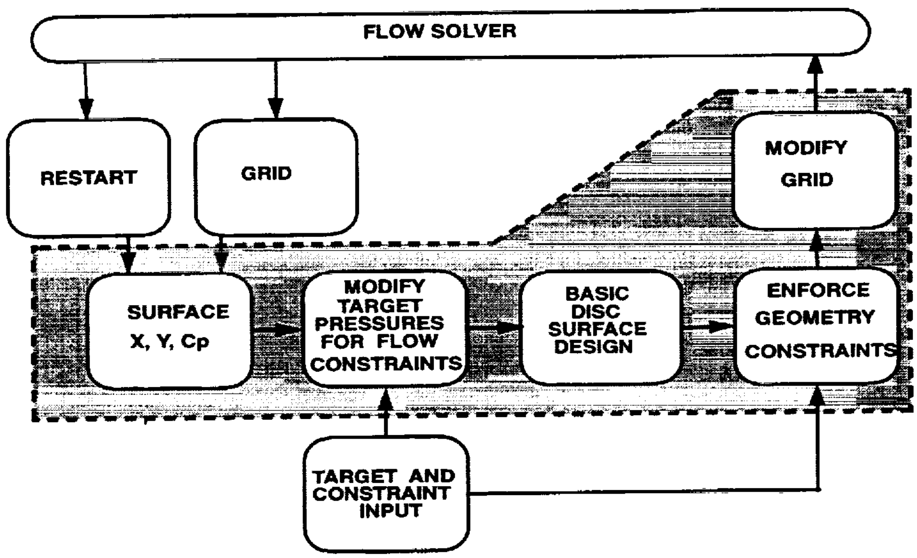

This flow chart shows the components of the CDISC design module and how it is coupled with a flow solver. The design process begins by obtaining a partially-converged flow solution for the initial configuration. The CDISC method then extracts the surface geometry and pressure information that it needs from the grid and restart files. Initial target pressure distributions are defined from the current analysis pressures, then modified as required to meet the flow constraints. After the basic DISC method is used to alter the surface geometry based on these target pressures, the geometry constraints are applied and a grid perturbation scheme is used to modify the volume grid to accommodate the new surface shape. This new grid is then returned to the flow solver for further analysis.

SINGLE POINT DESIGN USING CDISC

- Flow solver: TLNS3DMB (Euler)
- Grid: 117x25x25 C-H
- Objective: reduce drag
- Constraints:
  - twist and camber changes on wing only
  - maintain original lift and spanload distribution
- Design variable: chordwise loading parameter

Since the primary focus of this study was the development and evaluation of a multipoint design method, a simplified approach has been used for the single point designs. A coarse wing/body grid has been used with TLNS3DMB run in an Euler mode to allow rapid flow analysis and the design was limited to twist and camber changes on the wing only. The objective was to reduce the drag at the design point while maintaining the original lift and spanload distribution. For these initial designs, the only design variable was the chordwise loading parameter.

CDISC DESIGN STATIONS ON TCA6 PLANFORM

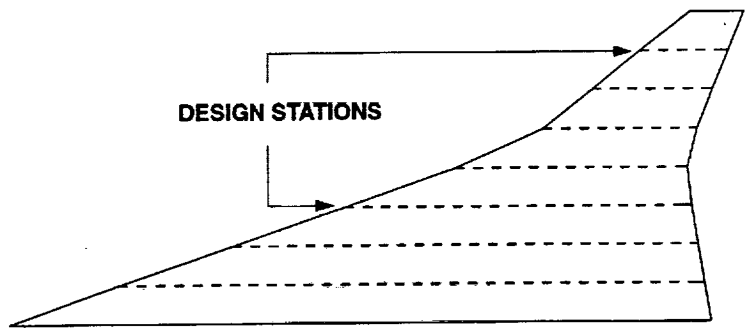

Nine wing stations are used for design in all cases, with the locations indicated by the dashed lines in the figure, along with the root and tip stations. The root station is fixed in order to maintain the fuselage geometry, but is used to interpolate changes from the second station onto grid lines located between the first two design stations. The changes at the tip are aliased to the changes at the changes at the station just inboard of it. The arrows indicate design stations at which sectional pressures and airfoils will be shown in later figures.

SUPERSONIC DESIGN USING CDISC

- **Conditions:**
  - $M = 2.40$
  - $C_L = 0.0896$
- **Results:**
  - $\Delta C_D = -.00002$

The supersonic point design was performed at a Mach number of 2.40 and a lift coefficient of 0.0896 (this value corresponds to lift of the baseline TCA configuration at an angle of attack of 3.5 degrees). A number of combinations of chordwise loading parameter were tried, but little drag reduction was obtained. This was consistent with previous studies that indicated that most of the potential for drag improvement involves wing root design and thickness changes.

SUPERSONIC DESIGN PRESSURES AT η=0.43
M=2.40 C_L=0.0896

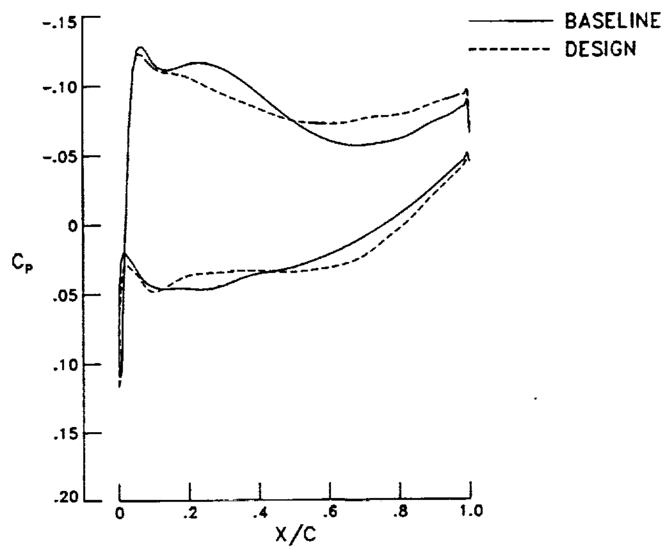

The resulting pressure distributions for the supersonic design are compared with the pressures for the baseline configuration at a station on the inboard portion of the wing. The leading edge expansion is similar for both configurations, but the CDISC design pressure distribution is smoother and somewhat more aft-loaded. It should be noted that the loading could be shifted slightly more forward without a significant drag increase if pitching moment is a constraint.

SUPERSONIC DESIGN AIRFOIL AT η=0.43
M=2.40 C_L=0.0896

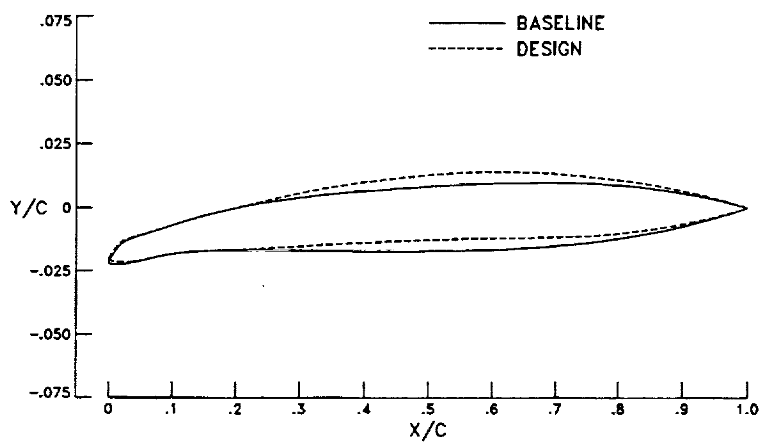

A comparison of the design and baseline airfoils at the same inboard station shows that the angle of attack is nearly the same, but the design airfoil has more camber, which may be helpful at the transonic design point.

SUPERSONIC DESIGN PRESSURES AT η=0.89
M=2.40 C_L=0.0896

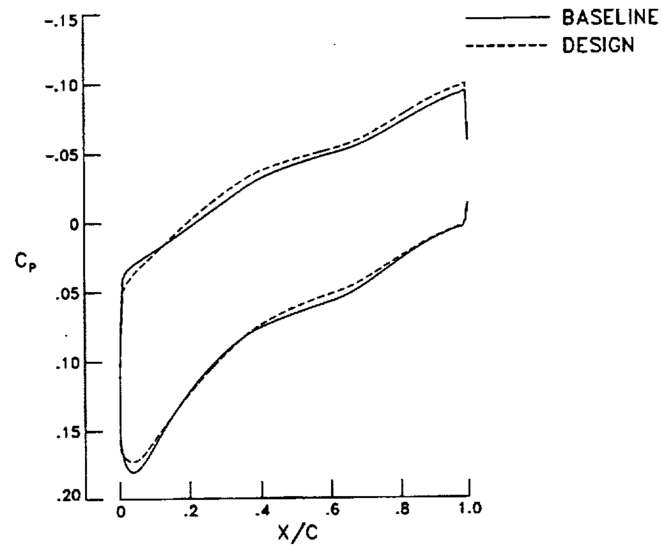

The pressure distributions for the baseline and design airfoils at a station on the outboard portion of the wing are very similar. Both have the nearly uniform chordwise loading that appears to be optimal for airfoils on a wing with a supersonic leading edge.

SUPERSONIC DESIGN AIRFOIL AT η=0.89
M=2.40 C_L=0.0896

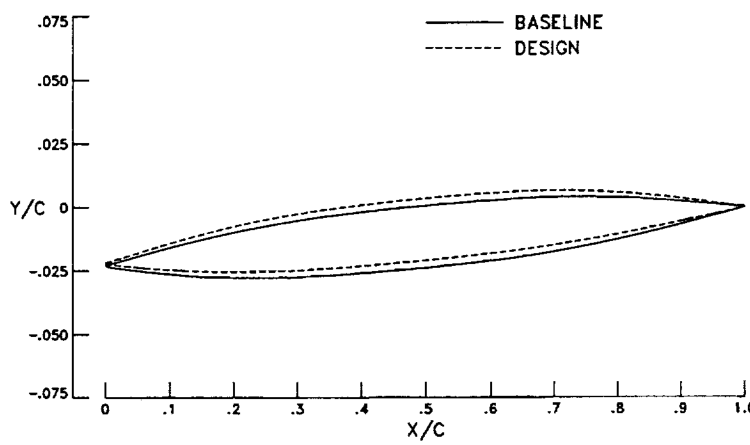

As with the inboard station, the baseline and design airfoils are at a similar angle of attack, with the design airfoil having slightly more camber.

TRANSONIC DESIGN USING CDISC

- **Conditions:**
  - $M = 0.95$
  - $C_L = 0.1438$
- **Results:**
  - $\Delta C_D = -.00137$

The transonic design was performed at a Mach number of 0.95 and a lift coefficient of 0.1438 which, as with the supersonic design, was the lift of the baseline configuration at an angle of attack of 3.5 degrees. Again, several values of the chordwise loading parameter were tried, with the best case producing a drag reduction of almost 14 counts relative to the baseline.

TRANSONIC DESIGN PRESSURES AT η=0.43
M=0.95 C_L=0.1438

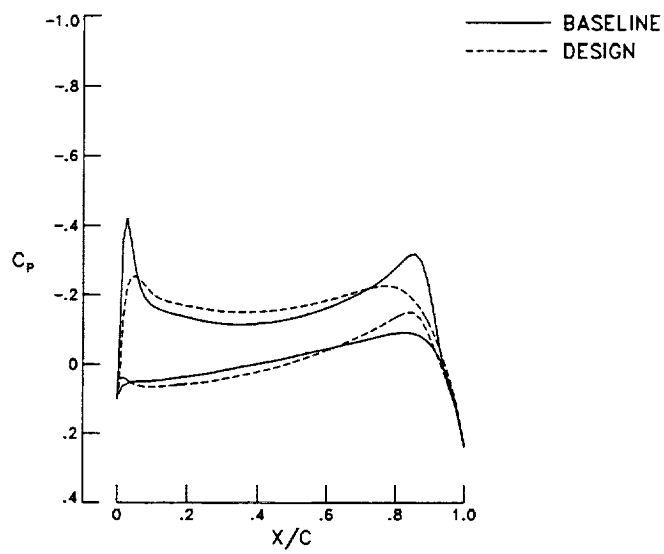

The baseline pressure distribution at the inboard station has a moderate leading-edge peak and an aft re-expansion that creates a fairly steep gradient as the trailing edge is approached. The design pressures soften both of these features. At this Mach number, the sonic pressure coefficient is about -0.1. Although the leading edge peak as well as the aft expansion reach supersonic speeds, there is probably not much wave drag associated with them because of the sweep of the isobars (not shown).

TRANSONIC DESIGN AIRFOIL AT η=0.43
M=0.95 C_L=0.1438

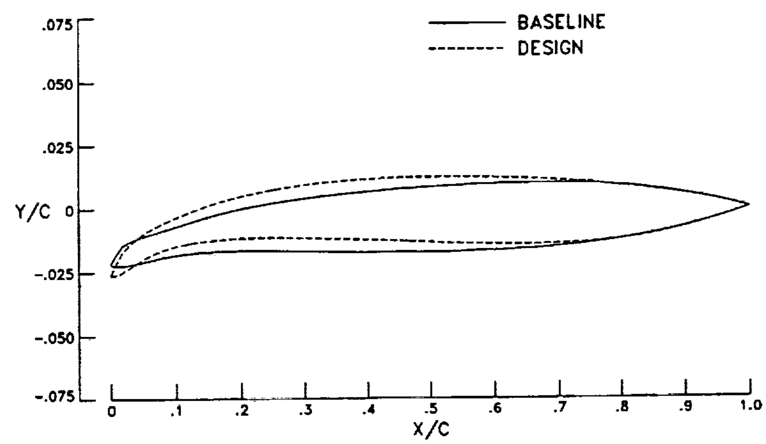

The airfoils that correspond to the pressures in the previous figure are shown in this figure. The angle of attack is nearly the same for the two configurations, but the design airfoil has quite a bit more camber, especially near the leading edge. This suggests that a leading-edge flap could be used to obtain much of the benefits of the transonic camber design at this station.

TRANSONIC DESIGN PRESSURES AT η=0.89
M=0.95 C_L=0.1438

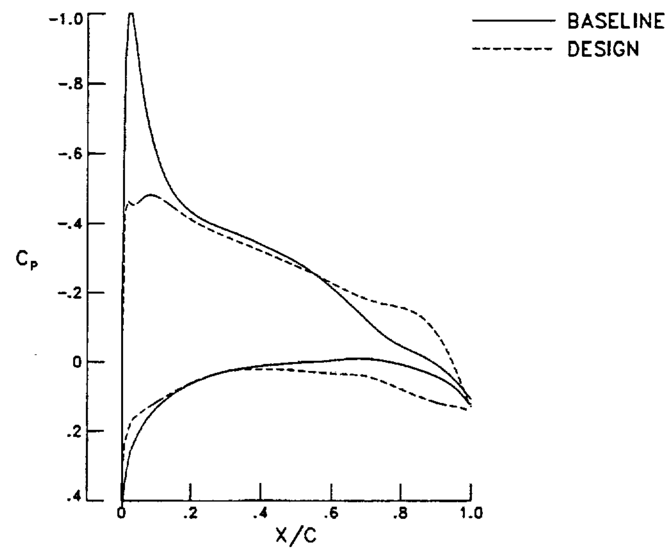

At the outboard design station near the tip, the baseline pressures indicate that a strong leading-edge shock is present. The design has eliminated this shock while recovering the lift through increased aft loading, although the aft recovery gradient is still mild. The leading-edge shock was probably the source of most of the wave drag for the baseline configuration at these conditions, and its elimination is the likely cause of the drag reduction for this case.

TRANSONIC DESIGN AIRFOIL AT η=0.89
M=0.95 C_L=0.1438

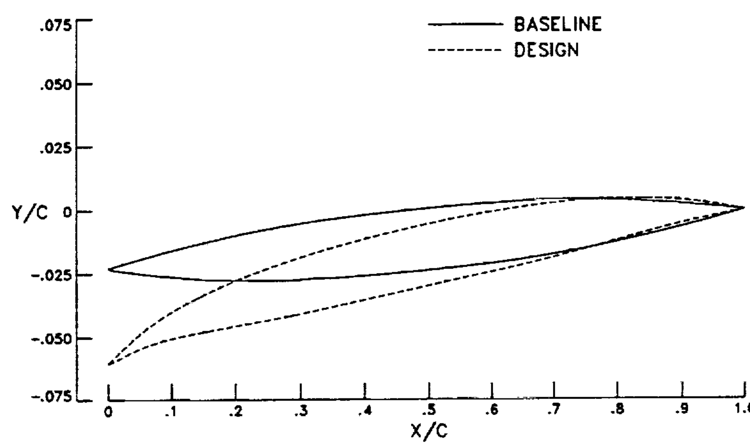

The comparison of the baseline and design airfoils at the outboard station indicates that the reduction in the leading-edge pressure peak was achieved by a combination of twist and camber, with again a noticeable increase in camber near the leading edge. This suggests that only some of the benefit of the transonic design could be achieved by simply deflecting a leading-edge flap.

MULTIPOINT DESIGN APPROACHES

- **Weighted Average of Geometries (WAG)**
  - **single point grids used as design variables**
  - **drag estimation for improved convergence with combined-drag objective function**
  - **drag constraint option also available**
  - **procedure is fully automated**

- **Transonic flaps**
  - **l.e. flap deflected for M_{peak} constraint**
  - **t.e. flap deflected for c_l constraint (not used)**

Having completed the initial single-point designs at supersonic and transonic cruise conditions, the problem of obtaining good performance for a mission that includes flight at both design points was then addressed. Two approaches to this multipoint design problem were considered: a new method that employed a weighted average of the point design geometries (WAG method), and a second approach that used a leading-edge flap to improve the transonic performance.

The WAG method automatically determines a grid weighting factor that will be used to blend the grids from the two point designs in a manner that will minimize a combined-drag objective function (this process will be described in detail in the next figure). A drag estimation procedure is used to help improve the convergence of this process. For this study, the supersonic and transonic drag coefficients are arbitrarily assigned factors of 0.8 and 0.2, respectively, for computing a combined-drag coefficient. The WAG method also has the option of minimizing the drag at one point subject to a drag constraint at the other point.

For the transonic flap approach, a leading-edge flap is simulated on the supersonic point design geometry to reduce the drag at transonic speeds. In this case, a maximum Mach number constraint is imposed, and the flap is automatically deflected in an attempt to meet the constraint.

FLOW CHART FOR WAG MULTIPOINT DESIGN METHOD

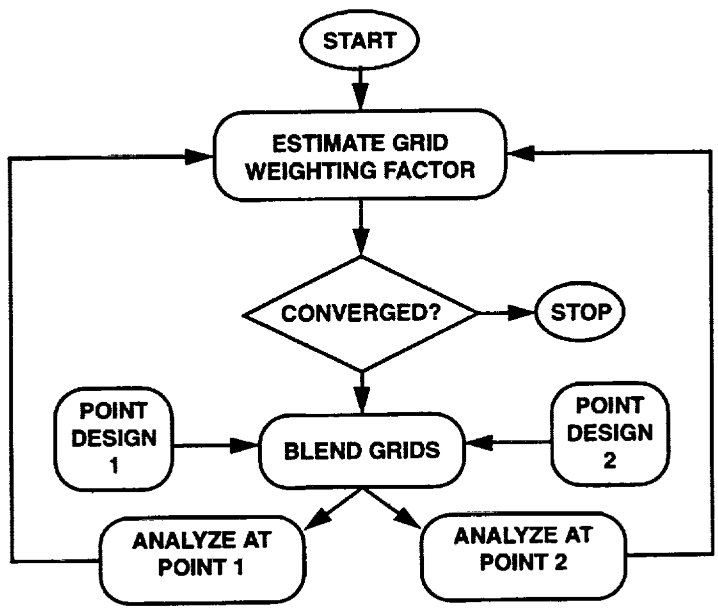

A flow chart of the WAG multipoint design method is shown in this figure. The procedure begins with a program that estimates a grid weighting factor for use in the grid blending program. For the first two passes through the procedure, weighting factors of 1.00 and 0.00 are specified in order to obtain flow analyses at the two design points for each of the initial point designs. For the third pass, the drag is assumed to vary quadratically between configurations at a given design point (e.g, at the supersonic cruise conditions, a 50/50 blend of the supersonic and transonic point design grids will yield a drag that is higher than the drag of the supersonic design by 25 per cent of the drag difference between the transonic and supersonic designs). On subsequent passes, a weighting factor for the drag minimum is estimated using a curve fit of the previous drag values. Currently, convergence is assumed when the new weighting factor is within 0.05 of a previous value.

MULTIPOINT DESIGN RESULTS FOR A GENERIC FIGHTER AT MILD MANEUVER CONDITIONS

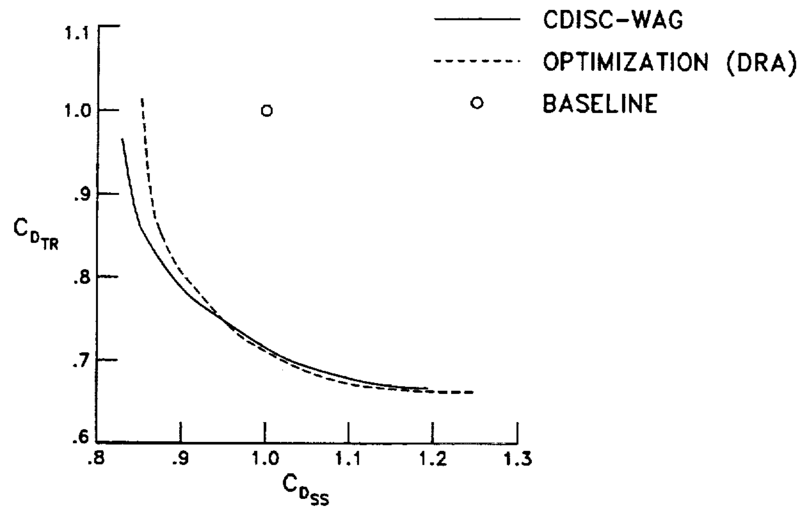

Although the WAG approach is a very simple one, it was shown in one study to produce drag reductions comparable to those achieved from multipoint numerical optimization, but at several orders of magnitude less cost. In this study done cooperatively with the Defense Research Agency (DRA), a generic fighter wing/body configuration was redesigned to minimize the combined-drag coefficient for a number of mission (i.e., relative drag) weighting factors. The two design points were transonic and supersonic mild maneuver conditions. Since different grids and flow solvers were used for the WAG design and the numerical optimization, the design results have been normalized by the drag of the baseline configuration at each design point as predicted by the flow solver used by each design method (the circle symbol on the plot). The lines represent a series of multipoint optimizations performed by each method, where the left end is a purely supersonic mission and the right end is a purely transonic mission. Both methods were effective at reducing drag relative to the baseline, with the CDISC-WAG method showing slightly greater drag reductions for the missions dominated by the supersonic drag point. Each multipoint numerical optimization required several hundred flow analyses, while the WAG method required 6-8 for the first mission and typically only two additional analyses for each new mission after that.

INITIAL MULTIPOINT DESIGN RESULTS USING WAG METHOD

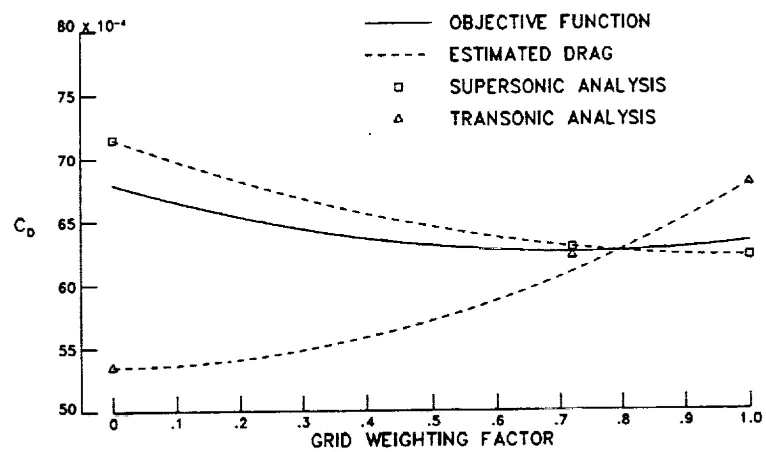

This figure shows the initial results from applying the WAG design method to the TCA configuration. A grid weighting factor (GWF) of 0.0 corresponds to the initial transonic point design while GWF=1.0 corresponds to the initial supersonic point design. The first two cycles generated the four data points at the ends of the dashed lines, with the dashed lines generated by the quadratic drag increase assumption mentioned earlier. Using these assumed drag distributions, the variation of the combined-drag objective function is computed (solid line) and a minimum is found to occur at GWF=0.72. The symbols at this value of GWF indicate the computed supersonic and transonic drag values for this new blended grid. The estimated supersonic drag is nearly identical to the computed value, while the estimated transonic drag is slightly below the computed value.

FINAL MULTIPOINT DESIGN RESULTS USING WAG METHOD

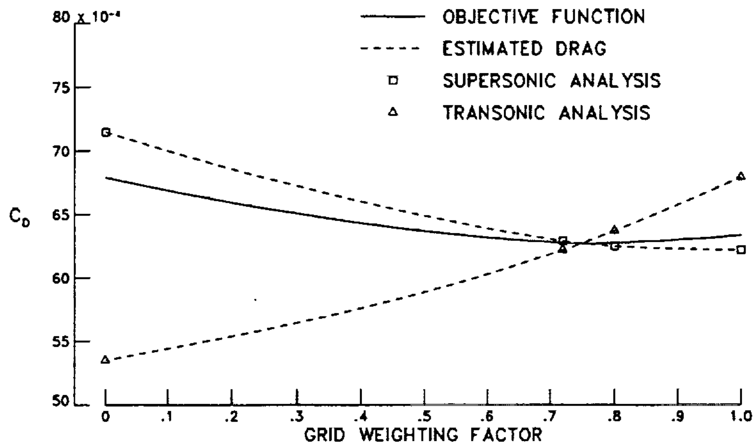

Using curve fits through the computed values of drag, a new estimate of the minimum of the objective function is obtained (GWF=0.80). A new blended grid is generated using this value of GWF and analyzed at the two design points. The resulting drag values are nearly identical to the estimated values. Updating the drag curve fits with the new values changes the minimum of objective function by less than 0.1 count of drag. Thus the WAG method required eight analysis runs to achieved a converged multipoint design.

TRANSONIC FLAP DESIGN

- **Conditions: M = 0.95, CL = 0.1438**
- **Geometry: η = 0.66-1.00, hinge line x/c = 0.15**
- **Constraints: $M_{peak} < 1.3$, $M_{hl} < M_{peak}$**
- **Results: ΔC_D = -.00077**

As an alternative to a single geometry that compromises the performance at the two design points, the design at the dominant design point (supersonic in this case) is maintained and a flap is used to improve the performance at the other design point. Since most of the wave drag at the transonic design point appeared to result from the leading edge shock on the outboard portion of the wing, a flap was defined from the leading-edge planform break to the tip, with a hinge line at x/c=0.15. (This hinge line location was selected based on a brief study of several locations). The CDISC flap constraint was used with a peak Mach number limit of 1.3 which, with the shock sweep considered, gives a normal Mach number of slightly over 1.0. Also included in the flap constraint is a requirement that the hinge-line Mach number not exceed the leading-edge peak Mach number. The flap deflection quickly converged to a value of 5.84 degrees, with a resulting drag reduction of about 8 counts relative to the baseline.

TRANSONIC DESIGN PRESSURES AT η=0.89
M=0.95 C_L=0.1438

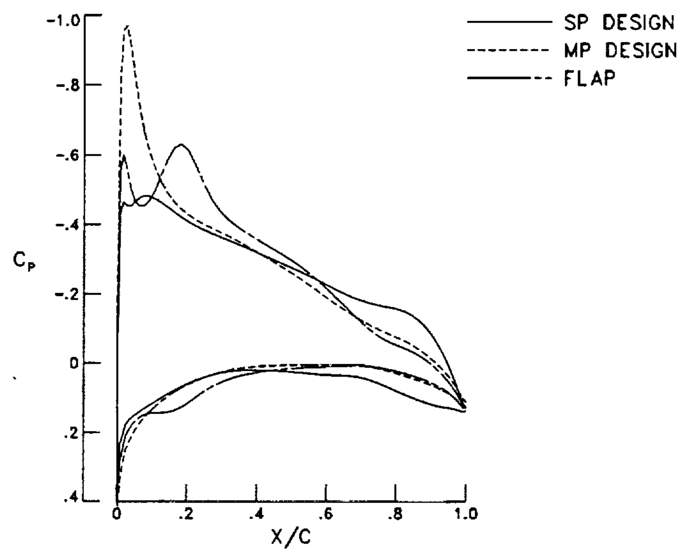

The resulting pressure distribution is compared with the pressures from the transonic single point design (solid line) and the WAG multipoint design (dashed line) at the outboard wing station shown before. The peak Mach number limit corresponds to a pressure coefficient of about -0.56. The flap design did not quite obtain this value because of the limitation also imposed on the hinge-line Mach number. While the flap design did not eliminate the shock as was the case with the single point design, the shock strength was greatly reduced relative to the WAG multipoint case. (It should be noted that the WAG case did, however, reduce the shock strength relative to the baseline).

TRANSONIC DESIGN AIRFOILS AT η=0.89
M=0.95 C_L=0.1438

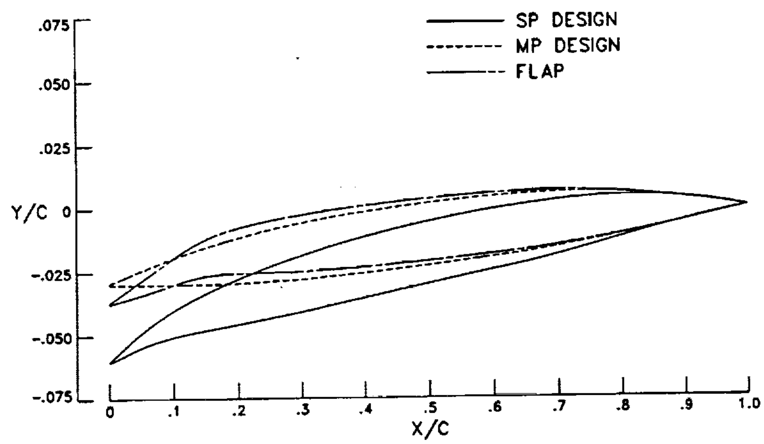

The resulting flap geometry at the outboard station is compared with the airfoils from the single point and multipoint designs in this figure. While there is an obvious twist difference between the single point design and the flap design, the camber lines in the region of the flap are very similar. The large surface curvature that can be seen at the hinge line is the source of the secondary Mach number peak shown in the previous figure.

SUMMARY OF MULTIPOINT DESIGN DRAG COEFFICIENTS

	Baseline	WAG	Flap
Supersonic	0.00624	0.00625	0.00622
Transonic	0.00672	0.00637	0.00595
Combined	0.00634	0.00627	0.00617

A summary of the drag results for the two multipoint design approaches is given in the table above. At the supersonic design point, the WAG design is only slightly worse than the baseline, while the flap design retains the small improvement of the single point supersonic design. At the transonic design point, both designs have improved performance relative to the baseline, with the flap approach providing about twice as much drag reduction as the fixed geometry WAG design. The variation in the combined drag coefficient is small, reflecting the dominance of the supersonic portion of the mission, but the WAG and flap multipoint design approaches do provide about 1 and 2 counts, respectively, of overall drag improvement. On this basis, the flap approach would be preferred, but other systems issues such as weight or safety may affect this conclusion.

CONCLUDING REMARKS

- An efficient automated multipoint design approach (WAG) has been developed
- CDISC camber/twist design at supersonic design point produced no significant drag benefit
- CDISC camber/twist design was effective at reducing drag at the transonic design point
- Flap design was less effective than camber/twist design at reducing drag at the transonic design point, but produced a slightly lower combined drag value than the WAG approach

In conclusion, an efficient, fully-automated multipoint design approach, referred to as the WAG method, has been developed. It combines single point design geometries (developed in this study using the CDISC design method) in a systematic fashion to reduce a combined-drag objective function. For the limited camber/twist designs performed in this initial study, CDISC did not produce an appreciable drag reduction at the supersonic design point, but did significantly reduce the drag at the transonic design point. A transonic flap approach to multipoint design was also evaluated in this study. While the flap was not as effective as the CDISC point design at reducing transonic drag, it did produce a lower combined drag value than the WAG method.

FUTURE PLANS

- Include thickness and fuselage/wing-root design changes (within TCA constraints) in CDISC point designs
- Apply WAG and/or transonic flap multipoint design approaches to promising designs on finer viscous grids, including full-configuration cases

Based on the results of this initial study, it is recommended that future design work with CDISC allow for changes in wing thickness (within the TCA constraints) and also include wing root and fuselage design changes, especially for supersonic point designs. While this relaxed set of design constraints should initially be evaluated using the coarser grids from this study, the efficiency of the CDISC and WAG methods should allow the methods to be practically used for viscous design on fine grids for even full-configuration cases.

1997 HSR Aerodynamic Performance Workshop

Prediction and Assessment of Reynolds Number Sensitivities Associated with Wing Leading-Edge Radius Variations

Richard A. Wahls
Melissa B. Rivers
Lewis R. Owens, Jr.
NASA Langley Research Center
February 25, 1997

The primary objectives of this study were to expand the data base showing the effects of LE radius distribution and corresponding sensitivity to Rn at subsonic and transonic conditions, and to assess the predictive capability of CFD for these effects. Several key elements led to the initiation of this project: 1) the necessity of meeting multipoint design requirements to enable a viable HSCT, 2) the demonstration that blunt supersonic leading-edges can be associated with performance gain at supersonic speeds , and 3) limited data. A test of a modified Reference H model with the TCA planform and 2 LE radius distributions was performed in the NTF, in addtion to Navier-Stokes analysis for an additional 3 LE radius distributions. Results indicate that there is a tremendous potential to improve high-lift performance through the use of a blunt LE across the span given an integrated, fully optimized design, and that low Rn data alone is probably not sufficient to demonstrate the benefit.

Outline

- Objectives
- Background
- Approach
- Model Geometry
- NTF Results
- Navier-Stokes Results
- Concluding Remarks

As outlined above, this presentation will begin with a statement of the general objectives of the project, followed by background information which led to the initiation of the study, and the approach taken to meet the objectives. Next, the wind tunnel model is described including its relationship to both the Reference H and Technology Concept Airplane (TCA) geometries. Finally, preliminary analysis of results from both the experimental and computational portions of the study will be discussed. Concluding remarks will close the presentation.

Objectives

- Expand subsonic/transonic data base of Rn sensitivities associated with LE radius variations, including the supersonic LE of an outboard wing panel
- Obtain data for CFD code validation

The general objectives of the project are shown above. The primary goal was the expansion of the data base showing the effects of LE radius distribution and corresponding sensitivity to Rn at subsonic and transonic conditions. Particular emphasis was placed on the under exploited supersonic LE of the outboard wing panel. The experimental data generated meets the goal of data for CFD validation.

Additional objectives addressed in the course of this study, but not presented herein, included preliminary assessments of the Rn effects associated with the planform change from the Reference H to the TCA and of the corresponding change to the high-lift, inboard LE flap configuration. These topics were addressed in the experimental portion of the study, and results are described in a separate paper in this workshop (High-Lift Session) entitled "Testing a 2.2% HSR Ref. H Model with Modified Wing Planform in the NTF," by Owens, Wahls, and Hamner.

1997 HSR Aerodynamic Performance Workshop

Background I

- Multipoint Design Requirements
  - Take-off, Approach, Transonic Cruise, & Supersonic Cruise
  - High-lift needs quieter engines and/or more L/D to be viable
- Supersonic Issues
  - wave drag increase with LE bluntness for supersonic LE?
  - reduced drag supersonic airfoil design w/ blunt LE reported by Wilby
  - NFW success on M2.4-7A configuration
  - improved multipoint design incorporating a blunt supersonic LE is possible
- Existing Data
  - AST 210 configuration tested in the NTF
    - Mach = 0.3, LE radius variation inboard only: "sharp" vs "blunt"
  - Generic 65 deg delta wing tested in the NTF
    - Mach = 0.4 → 0.9, 4 interchangeable LE's w/ various radius distributions

Several key elements led to the initiation of this project: 1) the necessity of meeting multipoint design requirements, 2) the demonstration that blunt supersonic leading-edges can be associated with performance gain at supersonic speeds , and 3) limited data.

In addition to supersonic cruise, the mission of an HSCT also includes transonic cruise, take-off and landing requirements. Currently, high-lift success requires quieter engines and/or more L/D. Blunt LE geometry can enhance performance at these conditions, particularly if the less swept, outboard portion of the wing is allowed to contribute.

Can improved subsonic performance be realized without adversely affecting supersonic performance? Yes. Wilby (Aeronautical Research Council, CP-921) shows a reduced drag airfoil at supersonic speeds incorporating a relatively blunt LE. The Natural Flow Wing (NFW) design philosophy as applied in the redesign of the M2.4-7A configuration (NASA/CP-1999-209690, Bauer and Krist) demonstrates the possibilities for an HSCT. The key to success is an integrated design; that is, the LE geometry cannot be changed independent of overall geometry.

Data addressing LE radius effects over a large Rn range are limited. Two sources are NTF tests of the AST 210 (73/60 arrow wing) with sharp and blunt inboard LE radi (outboard LE remained sharp)(NASA/TP-1999-209695, Williams, et al.), and of a generic 65 deg delta wing with 4 interchangeable LE sections (NASA TM 4645, Chu and Luckring).

Background II

- HSR Program
  - Baseline configuration changed from Ref H to TCA
  - Timing issues
    - affect next downselect to Tech. Configuration
    - material availability, new vs. modified model, NTF shutdown
    - want to demonstrate that a blunt supersonic LE design is worth pursuing when considering multipoint design requirements

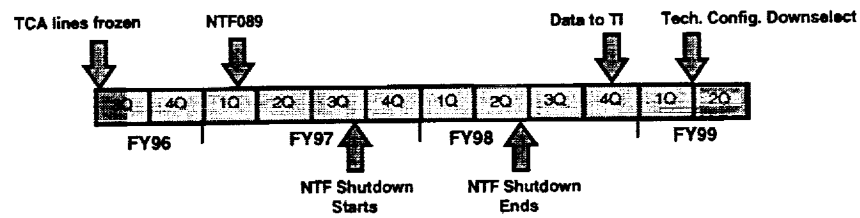

The HSR program is currently in a 3 year phase centered around the evaluation and redesign of the TCA configuration. It was desired to generate Rn effects data on the TCA planform, examine the high-lift LE flap configuration, and demonstrate that a blunt supersonic LE design is worth pursuing in time to provide input to the definition of the follow-on baseline configuration. Given the NTF schedule and major shutdown for upgrade, model material availability, and insufficient funds/support for a new model, the decision was made to target a test window in the NTF in the 1st quarter of FY97 prior to the NTF shutdown.

1997 HSR Aerodynamic Performance Workshop

Approach

- Modify 2.2% Ref H model to TCA planform
  - include alternate LE radius distribution & high-lift flaps
- Execute NTF test
  - Rn effects assessment & CFD validation data
- Execute transonic Navier-Stokes analysis
  - prediction assessment for Rn and LE radius effects

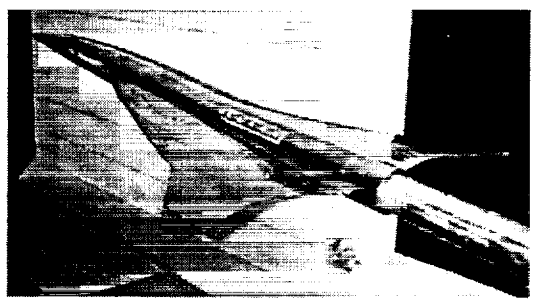

Image 1: 12/6/96

The approach to meet the objectives within the program and facility availability constraints was as follows. First, modify an existing model suitable for the NTF test environment. The obvious choice was the 2.2% HSR Reference H model. Second, execute a test in the NTF at high-lift and transonic conditions to provide a wide range of Rn conditions to allow experimentally based assessments and provide data for CFD validation. Finally, and concurrent with the experimental testing, execute a complementary CFD study to assess predictive capability and to expand the study to geometries not tested experimentally.

1997 HSR Aerodynamic Performance Workshop

Model Geometry I

- Comparison of Modified Ref H and Ref H Models
- Geometric Constants at 2.2% scale

	S,ref ft^2 (gross)	mac in.	span in.	AR	LE sweep deg
Ref. H	3.674	22.71	34.23	2.21	76/68.5/48
Modified Ref. H.	4.114	25.07	34.65	2.03	71/52

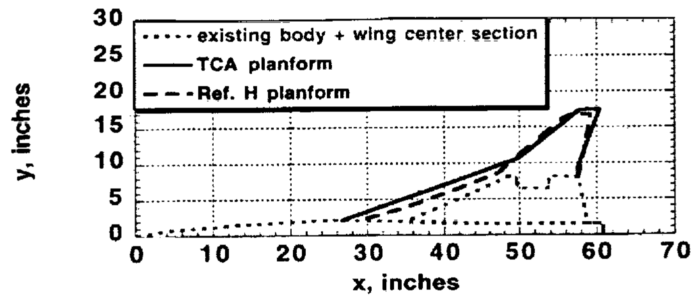

The first step was the modification of the existing 2.2% HSR Ref. H model to represent the TCA wing as closely as possible. Geometric constants are shown above; the Modified Ref. H values are identical to the TCA. Note, that the reference area for the Ref. H is the gross wing area (rather than the wimpress area used during Ref. H testing) to be consistent with the TCA definition. The Ref. H (truncated) body and inboard wing center section and TE (indicated by the dotted lines) were maintained, while the LE and outboard wing panels (indicated by the dashed lines) were not. New LE and outboard wing panels were designed and fabricated to provide the TCA planform while not restricting a return to the Ref. H geometry.

Model Geometry II

- Airfoil modification process was as follows:
  - align TCA & Ref. H TE (inboard sections; existing model)
  - rotate TCA section around TE to align to with existing Ref. H parts
  - blend overlap section between TCA LE and existing Ref. H parts
  - spanwise blending outboard of existing Ref. H parts

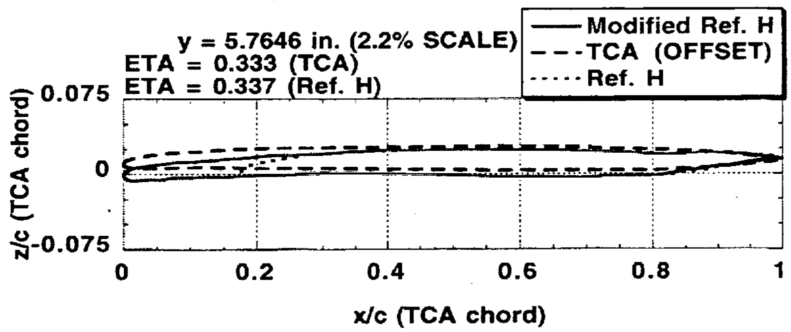

The modification process, or more specifically the blending process, is demonstrated above for a typical inboard airfoil section. First, the TCA section at a given span location is translated to match the TE of the existing Ref. H model hardware. Next, the TCA section is rotated around the TE to align with the existing model parts with emphasis on the upper surface to avoid unwanted surface inflections. Finally, blending occurs over a small region forward of the existing hardware in to the TCA LE region. This sequence was repeated for several airfoils over the span of the existing wing center section/TE hardware; outboard of this point, a small blending region existed in the spanwise direction until the TCA outboard airfoil definitions could be maintained.

1997 HSR Aerodynamic Performance Workshop

Model Geometry III

- Comparison of Modified Ref. H, Ref. H, & TCA Geometries

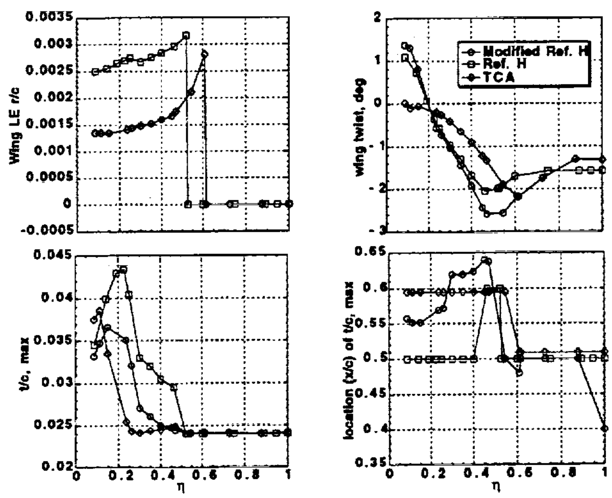

The resulting geometry had the characteristics shown above. Note that wing LE radius distribution of the modified Ref. H is identical to that of the TCA, and that both the TCA and the Ref. H have a sharp LE on the outboard wing panel. Existing Ref. H model hardware inboard drives the differences in wing twist, maximum thickness, and the location of the maximum thickness. Outboard of the pre-existing hardware, the modified Ref. H and TCA geometries more closely match.

The resulting geometry was smooth and sufficient to address the objectives of the study. However, in no way should this geometry be considered optimized aerodynamically.

Model Geometry IV

- Comparison of Modified Ref. H Airfoil Sections
  - Baseline & "Full Blunt" LE's tested in the NTF
  - shown in 2.2% model dimensions
    - y = 13 inches →η= 75%

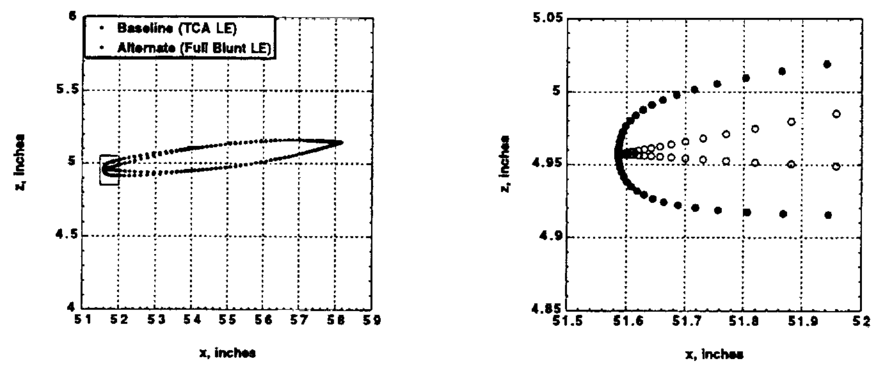

Once the baseline, modified Ref. H geometry was established, several alternative LE radius distributions were quickly assessed using the linear theory code, AERO2S, by Carlson, et. al. Time constraints permitted the selection of one alternative radius distribution for fabrication and testing. The chosen alternative is referred to as the "full blunt" LE, which is characterized by an inboard LE radius identical to the baseline, but a constant LE r/c outboard of the crank and matching that at the crank. Shown above is a comparison of airfoils at the 75% semispan station highlighting the increased LE bluntness of the alternative distribution. The alternative LE blends into the baseline airfoil forward of the maximum thickness location.

Three other alternative LE radius distributions evaluated computationally will be described later.

NTF Test Variables

- Mach = 0.30
- Rn,mac = 9.4 → 100 × 10^6
- α = -3° → 24°
- nacelles on
- 0/0 & 30/10 full-span flaps
- baseline & alt. LE radius

- Mach = 0.90
- Rn,mac = 11 → 89 × 10^6
- α = -2° → 12°
- nacelles off
- 0/0 flaps
- baseline & alt. LE radius

The range of test conditions in the NTF test (designated NTF089) pertinent to this study are shown above. All data shown herein were obtained with natural transition on the wing. A complete set of low Rn data with fixed transition was planned but not obtained due to significant facility downtime associated with a pitch system failure. Force and moment data were obtained. Limited pressure data on the existing Ref. H wing center section were also obtained; LE and outboard wing panel pressures were not obtained due to limited funding and design/fabrication time constraints.

1997 HSR Aerodynamic Performance Workshop

NTF Results Ia

- Comparison of alternate & baseline LE effect on CD
  - Mach = 0.9, 0/0 flaps
  - Generally a small but favorable effect due to the alternate LE

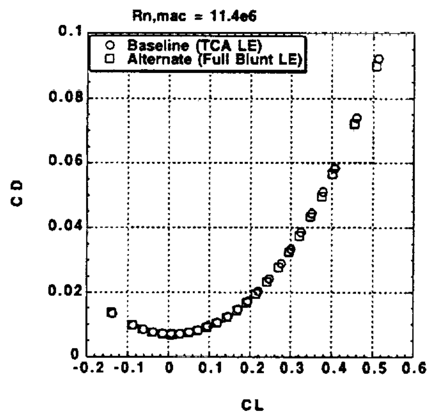

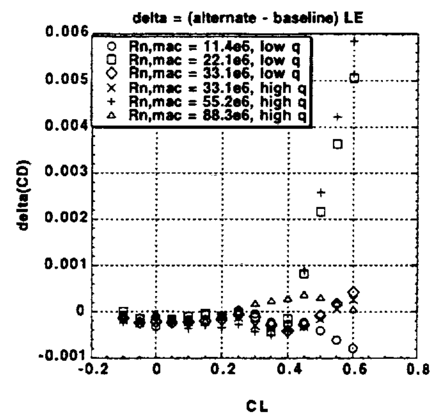

The above chart, and the following chart, show data as a function of LE radius, Rn, and CL at Mach = 0.90 with undeflected flaps. In each chart, the left hand plot shows data for each LE as a function of CL at low Rn. The right hand plot shows the increment due to the alternate LE radius for each Rn as a function of CL. Data has not been corrected for aeroelastic effects (wing twist and bending differences due to two significantly different dynamic pressures needed to span the Rn range).

The incremental drag data above generally show a drag reduction due to the alternate LE, particularly below CL = 0.3. The large, adverse increment in the 22e6 and 55e6 data at high CL are currently attributed to curve fitting uncertainty due to sparse data in this range. This explanation will be further investigated.

1997 HSR Aerodynamic Performance Workshop

NTF Results Ib

- Comparison of alternate & baseline LE effect on L/D
  - Mach = 0.9, 0/0 flaps
  - Generally a small but favorable effect due to the alternate LE

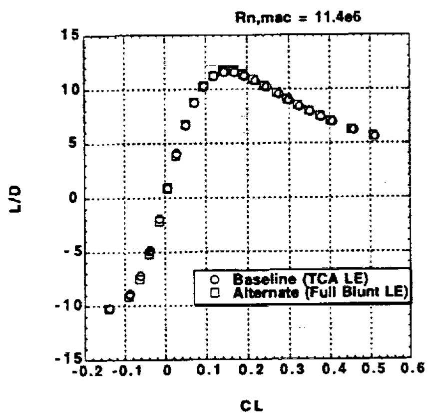

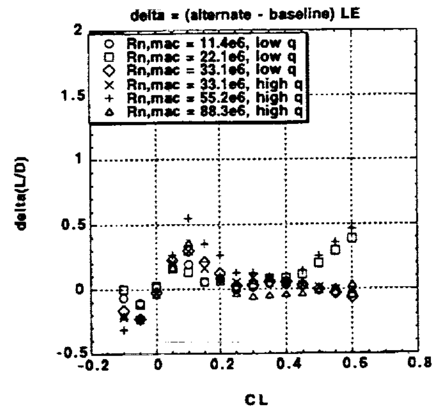

The L/D incremental data are consistent with the CD data of the previous chart, indicating generally small, favorable effects due to the alternate LE. Results are particularly favorable at CL's near L/Dmax.

1997 HSR Aerodynamic Performance Workshop

NTF Results IIa

- Comparison of alternate & baseline LE effect on CD
  - Mach = 0.3, 0/0 flaps
  - Generally a significant favorable effect due to the alternate LE below CL = 0.5

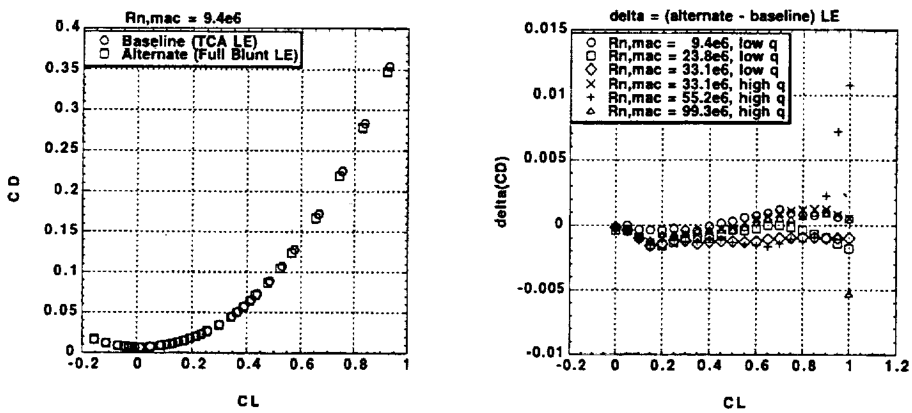

The above chart, and the following chart, show data as a function of LE radius, Rn, and CL at Mach = 0.30 with undeflected flaps. In each chart, the left hand plot shows data for each LE as a function of CL at low Rn. The right hand plot shows the increment due to the alternate LE radius for each Rn as a function of CL. Data has not been corrected for aeroelastic effects (wing twist and bending differences due to two significantly different dynamic pressures needed to span the Rn range).

The incremental drag data above generally show a significant drag reduction due to the alternate LE, particularly below CL = 0.5. The large, adverse increment in the 55e6 data at high CL are currently attributed to curve fitting uncertainty due to sparse data in this range. This explanation will be further investigated.

1997 HSR Aerodynamic Performance Workshop

NTF Results IIb

- Comparison of alternate & baseline LE effect on L/D
  - Mach = 0.3, 0/0 flaps
  - Generally significant favorable effect due to the alternate LE, but decreasing with increasing CL above L/Dmax

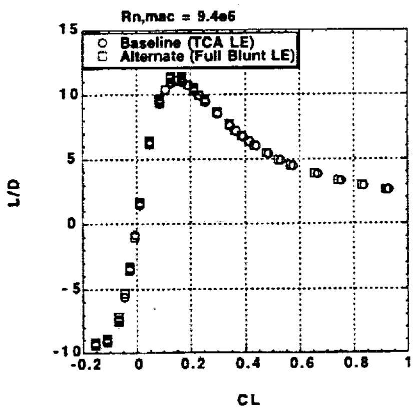

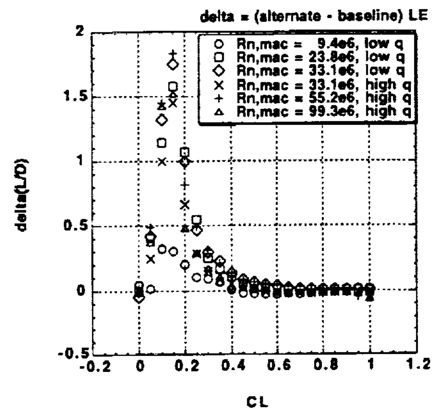

The L/D incremental data are consistent with the CD data of the previous chart, indicating significant, favorable effects due to the alternate LE. Results are particularly favorable at CL's near L/Dmax, but decrease with increasing CL.

1997 HSR Aerodynamic Performance Workshop

NTF Results IIIa

- Comparison of alternate & baseline LE effect on CD
  - Mach = 0.3, 30/10 flaps
  - Significant drag reduction due to the alternate LE in the vicinity of CL= 0.5 (~design)

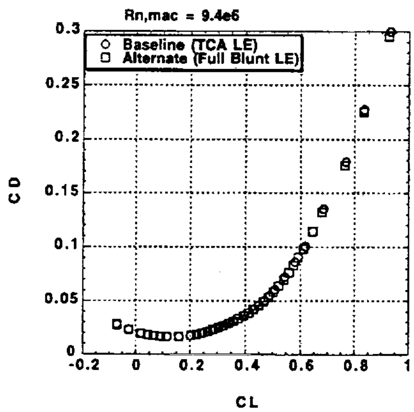

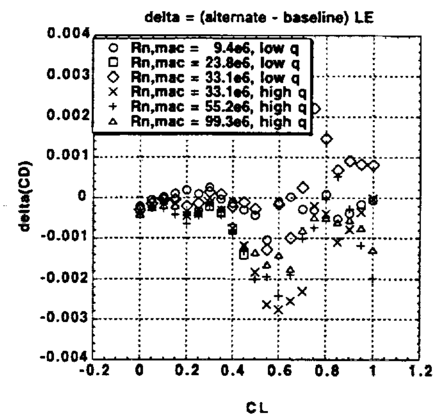

The above chart, and the following chart, show data as a function of LE radius, Rn, and CL at Mach = 0.30 with leading and trailing edge flaps deflected 30 and 10 degrees, respectively. In each chart, the left hand plot shows data for each LE as a function of CL at low Rn. The right hand plot shows the increment due to the alternate LE radius for each Rn as a function of CL. Data has not been corrected for aeroelastic effects (wing twist and bending differences due to two significantly different dynamic pressures needed to span the Rn range).

The incremental drag data above generally show a significant drag reduction due to the alternate LE, particularly near CL = 0.5.

1997 HSR Aerodynamic Performance Workshop

NTF Results IIIb

- Comparison of alternate & baseline LE effect on L/D
  - Mach = 0.3, 30/10 flaps
  - Generally a favorable effect due to the alternate LE

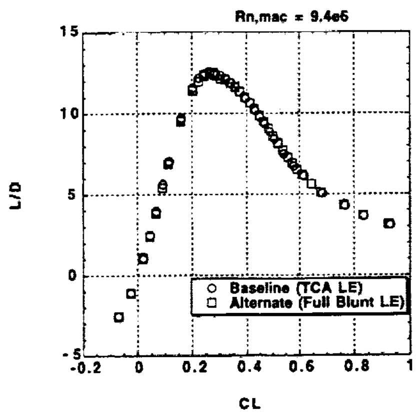

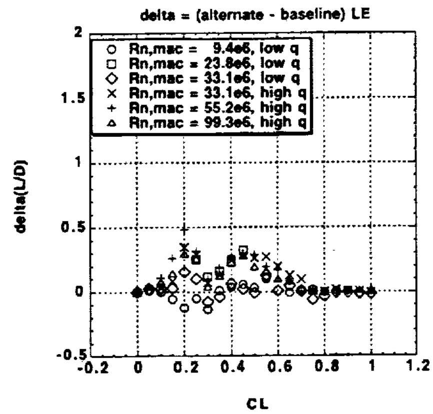

The L/D incremental data indicate favorable effects due to the alternate LE. Results are particularly favorable in the vicinity of CL = 0.5 (~design).

1997 HSR Aerodynamic Performance Workshop

NTF Results IV

- Comparison of CD & L/D increments as a function of Rn
  - positive benefit due to blunt supersonic LE across the Rn range
  - low Rn data alone is not sufficient to demonstrate benefit

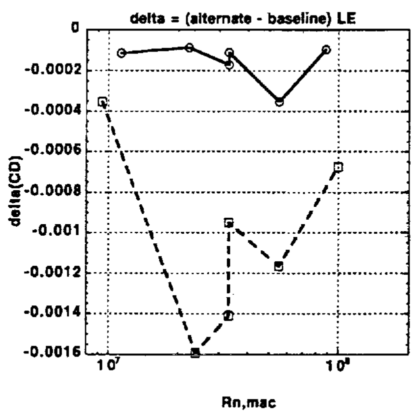

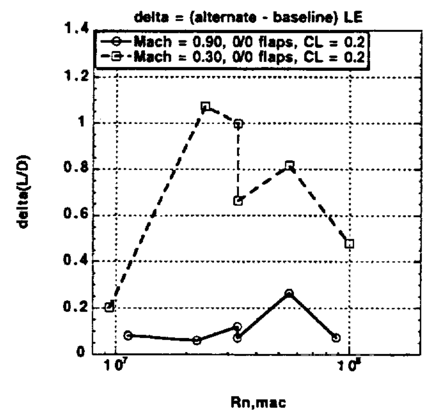

The above chart shows CD and L/D incremental data due to the alternate LE at Mach = 0.3 and 0.9 and CL = 0.2 (near L/Dmax) with undeflected flaps cross plotted against Rn. Jumps in increment values at constant Rn (~33e6) are due to uncorrected aeroelastic effects. Generally, the alternate LE provides a positive benefit across the Rn range as exhibited by reduced CD and increased L/D. The benefits are considerably more significant at the low Mach number, indicating tremendous potential to enhance high-lift performance with an integrated design. Nonmonotonic trends with Rn are not understood at this point, but remain under investigation. Another key element demonstrated above is the fact that low Rn data alone is not sufficient to demonstrate the potential benefit of the alternate LE geometry.

1997 HSR Aerodynamic Performance Workshop

CFD Approach

- Code & Grid
  - CFL3D v4.1
  - BL/DS turb. model
  - C-O grid, single block
  - 141 × 257 × 65

Test Matrix
- Mod. Ref. H w/ 5 LE radius distrib.
- Mach = 0.90
- Rn,mac = 10, 30, 80e6
- α = 1, 3, 5, 7, 10 deg

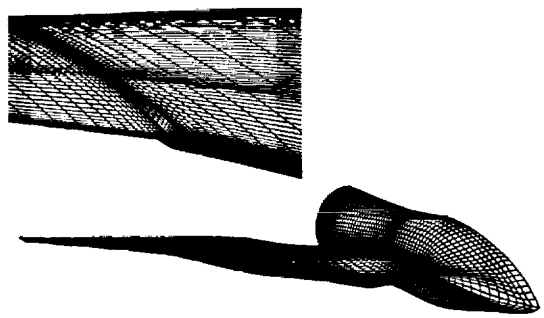

The test matrix for the computational study included 5 geometries (baseline Modified Ref. H and 4 alternate LE radius distributions), 5 angles-of-attack (1,3,5,7, and 10 deg), 3 Rn (10e6, 30e6, and 80e6 based on the mac), and one Mach number (0.90).Navier-Stokes predictions were made using CFL3D, version 4.1, and primarily the Baldwin-Lomax with Degani-Schiff turbulence model. The Baldwin-Barth, Spalart-Allmaras, and Menter's SST turbulence models were also used on the baseline geometry at an angle-of-attack of 5 deg. The single block C-O grid has 141 points streamwise, 257 spanwise, and 65 normal to the surface for total approaching 2.4 million grid points. Normal spacing near the surface was held constant for the Rn = 10e6 and 30e6 cases, and modified for the Rn=80e6 case; in all cases, the average y-plus value is no larger than 1. C90 times for converged solutions ranged from 2 to 11 hours, with angle-of-attack being the dominant factor, followed by the Rn, and finally the LE geometry. Timing for the code was approximately 5 microseconds/grid point/ iteration.

CFD LE Geometry Detail

- Comparison of Modified Ref. H LE Radius Distributions
  - Baseline & "Full Blunt" LE's tested in the NTF

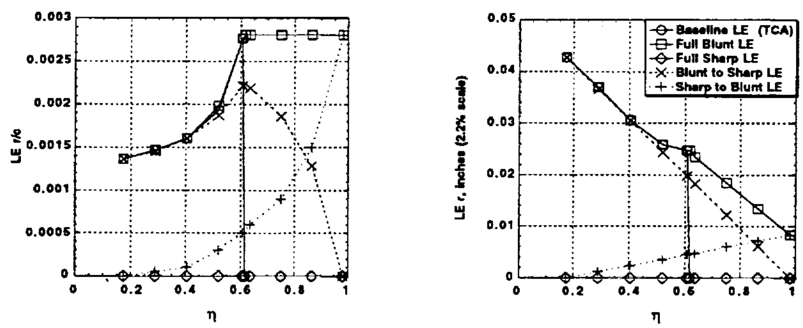

The LE radius detail for the baseline and 4 alternates studied are shown here. Recall that the baseline LE is identical to that of the TCA. The "full blunt" LE matches the inboard LE of the baseline, then maintains the blunt r/c ratio at crank across the entire outboard panel. The "full sharp" LE is identical to the baseline on the outboard panel, in addition to being sharp inboard (r=0). The "blunt to sharp" LE begins with baseline radius at the side of body, then "r" linearly decreases to zero at the tip. Finally, the "sharp to blunt" LE begins as sharp (r=0) at the side of body, then linearly increases to that of the "full blunt" LE at the tip. Recall that the baseline and "full blunt" geometries were tested in the NTF.

1997 HSR Aerodynamic Performance Workshop

CFD Results - Validation

- Comparison of predicted and experimental drag increments
  - Mach = 0.9, 0/0 flaps, no aeroelastic correction to expt. data
- Prediction levels seem optimistic, trends up to Rn,mac ~ 55e6 are similar

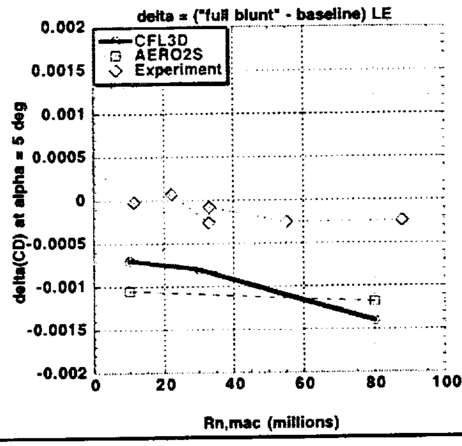

The chart above shows a comparison of drag increments due to the "full blunt" LE at $\alpha = 5$ deg (CL~0.2) between experiment, CFL3D, and AERO2S (AERO2S was used for a quick parametric study to choose the primary alternate LE). Experimental data has not been corrected for aeroelastic effects; the vertical data shift at Rn,mac ~ 33e6 represents the difference between test dynamic pressures of approximately 1000 and 1800 psf. The prediction levels seem optimistic, but the trends with Rn are similar, particularly up to a Rn,mac ~ 55e6. Although not done as yet, correction of the experimental data to that of the rigid geometry shape (q = 0 psf) used in the predictions will shift the experimental results toward the predicted results.

An additional factor not accounted for in this comparison is the fact that the "sharp" LE of the experimental model is in reality a finite thickness on the order of 0.0075 inches while the predictions shown are for a perfectly sharp LE. A quick order of magnitude analysis for this difference was made using AERO2S with a "sharp" LE radius defined as half the finite thickness. The results indicate an effect on the order of 5-6 drag counts in the direction of reducing the disagreement shown above.

CFD Results - Assessment I

- Effect of alternate LE radius distributions
  - Mach = 0.90, 0/0 flaps
- LE bluntness & removal of discontinuity in radius distribution favorable

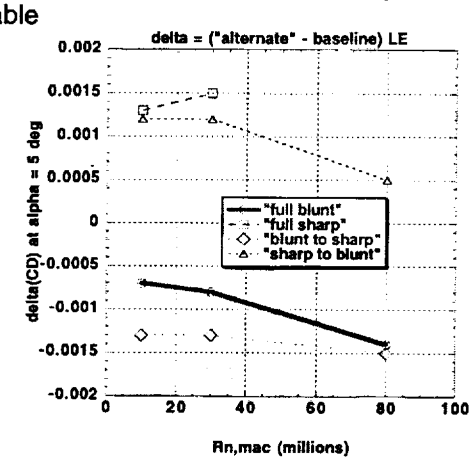

The chart above compares the effects of the 4 alternate LE geometries investigated. The missing point at Rn,mac = 80e6 for the "full sharp" LE is due to the lack of a converged solution. This occurred at angles-of-attack of 1, 5, and 10 deg; angles-of-attack of 3 and 7 deg were not attempted.

The two LE's with the most "sharpness" show degraded performance, while the two LE's with the most "bluntness" show improved performance. The best LE is the "blunt to sharp" which, relative to the baseline, has slightly reduced bluntness just inboard of the crank, but significantly more outboard. The other characteristic of this LE is the smooth, continuous variation of "r" across the crank; this may be why it out performs the "full blunt" LE, which is blunter but still has some geometric discontinuity at the crank.

CFD Results - Assessment IIa

- Upper surface pressure difference due to the "full blunt" LE
  - Rn,mac = 10, 30, and 80 million, Mach = 0.9, $\alpha = 5$ deg
- Relatively lower pressure in the LE region
- Significant differences emanating from the crank

The chart above shows upper surface pressure differences due to the "full blunt" LE on the outboard wing panel. Although somewhat difficult to see, the LE region has increased suction levels due to the bluntness. The more easily seen differences emanate from the crank. The "full blunt" LE has a smoother geometric transition across the crank region than does the baseline, and in turn affects the vortex formation emanating from the crank. The comparisons also show significant differences with increasing Rn as well.

1997 HSR Aerodynamic Performance Workshop

Concluding Remarks

- The Modified Ref. H model tested is in no way aerodynamically optimized
- Smooth, continuous transition from inboard to outboard (at the crank) is important
- Computational modelling of "sharp" LE's vs. physical model geometry may be important
- Positive benefit due to blunt supersonic LE across the Rn range
- Low Rn data alone is not sufficient to demonstrate benefit
- Multipoint designs incorporating blunt supersonic LE's are definitely worth pursuing
  - supersonic improvement (NFW)
  - tremendous potential for high-lift conditions

In conclusion, the following points are reiterated. The modified Reference H model with the TCA planform as tested should in no way be considered an aerodynamically optimized configuration. Rather, it is a test bed for examining sensitivities to localized geometric changes. Results indicate the benefits of a continuous and smooth LE radius distribution across the entire span. Accurate modelling of LE geometries, in particular that of sharp LE's, may significantly affect computational predictions.

Most importantly, the current study demonstrated positive benefit due to the use of a blunt supersonic LE across the Rn range, and that low Rn data alone is not sufficient to demonstrate this benefit. Multipoint designs incorporating blunt supersonic LE's are definitely worth pursuing, both at fundamental and configuration levels of study. The NFW wing design philosophy incorporates this idea by design and has been successful at reducing drag even at supersonic cruise conditions. The tremendous potential for gain at high-lift conditions alone warrants further study be given to LE radius effects, and these studies should include a wide range of Rn.

Preliminary Results of the 1.5% TCA (Modular) Controls Model in the NASA Langley UPWT

Paul Kubiatko (MDC)
Naomi McMillin (NASA LaRC)
Douglas C. Cameron (MDC)

Aero Performance Workshop
February 25-28, 1997

Outline

This slide presents an outline of the major topics covered in this report. The major topics include an overview of the test objectives, model geometry, test highlights, data quality, long-term repeatability, longitudinal, directional, and lateral characteristics, and a summary of the significant results presented.

Outline

- Test Objectives
- Model Geometry / Highlights
- Test Highlights
- Data Quality / Long-term Repeatability
- Longitudinal Characteristics
- Directional Characteristics
- Lateral Characteristics
- Summary

Test Objectives

The primary objective of the test was to obtain an experimental database of the stability and control characteristics for the TCA configuration in order to support the development of the first TCA simulation cycle release (Cycle 1). Additionally, the data obtained will be used to:

- conduct a preliminary full-flight envelope batch assessment of the TCA
- update the preliminary design methods database for control surface sizing
- validate full-configuration force and moment CFD prediction capability

Test Objectives

- Acquire TCA stability and control data to support:
  - TCA simulation (Cycle 1)
  - Preliminary full-flight envelope stability and control assessments
  - Preliminary Design (PD) methods
  - Full-configuration force and moment prediction validation

1.5% TCA Controls Model (#20)

The slide below shows the 1.5% TCA (modular) controls model, also known as model #20.

The model consists of a removable forebody, integral centerbody and main wing, removable outboard wing-tip panels, removable nacelles and diverters, removable horizontal and vertical tails, two interchangeable aftbodies (truncated, extended), and removable forebody chines (built as single piece). Both aftbodies are flared in order to provide the necessary sting-model clearances.

The model was designed to provide control surface deflection capability for the outboard leading-edge flaps, all eight trailing-edge flaps, the horizontal tail, elevator, and rudder.

1.5% TCA Controls Model (#20)

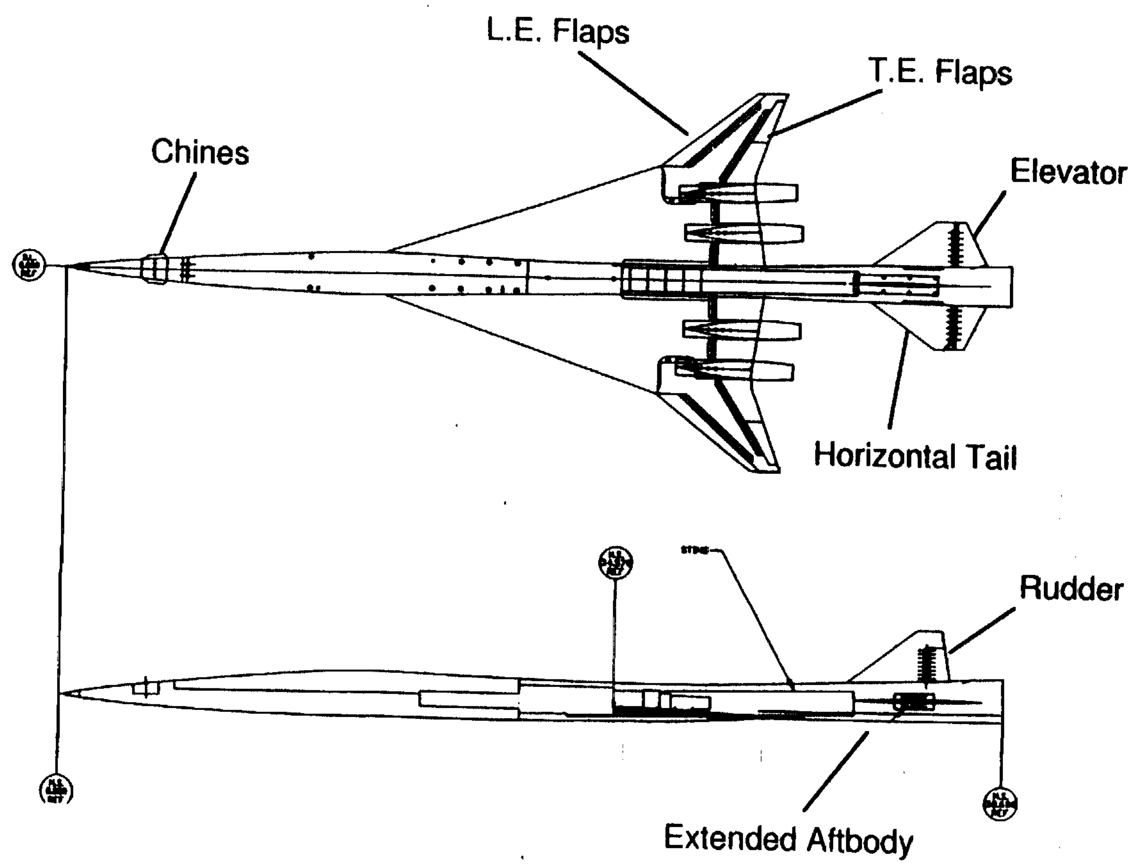

Reference H / TCA Model Comparison

The figure below shows a sketch comparing the TCA and Reference H control models. For comparison, both models are presented at the same scale and aligned at their respective 50% MAC points. This sketch is provided to highlight the significant planform differences between the two models because some of the results presented in this paper draw comparisons between the two models.

At the same scale, the TCA is a longer model. The inboard wing leading-edge sweep is increased and does not have a break. The outboard wing leading-edge sweep is reduced, and significant trailing-edge flap geometry changes have been made. The TCA aftbody is flared, while the Reference H aftbody is a constant radius cylinder. Both the TCA and Reference H horizontal and vertical tails were designed to maintain the correct exposed area for each surface. The rudder for the TCA was built to deflect only the lower two panels compared to all three panels for the Reference H.

TCA / Reference H Model Comparison

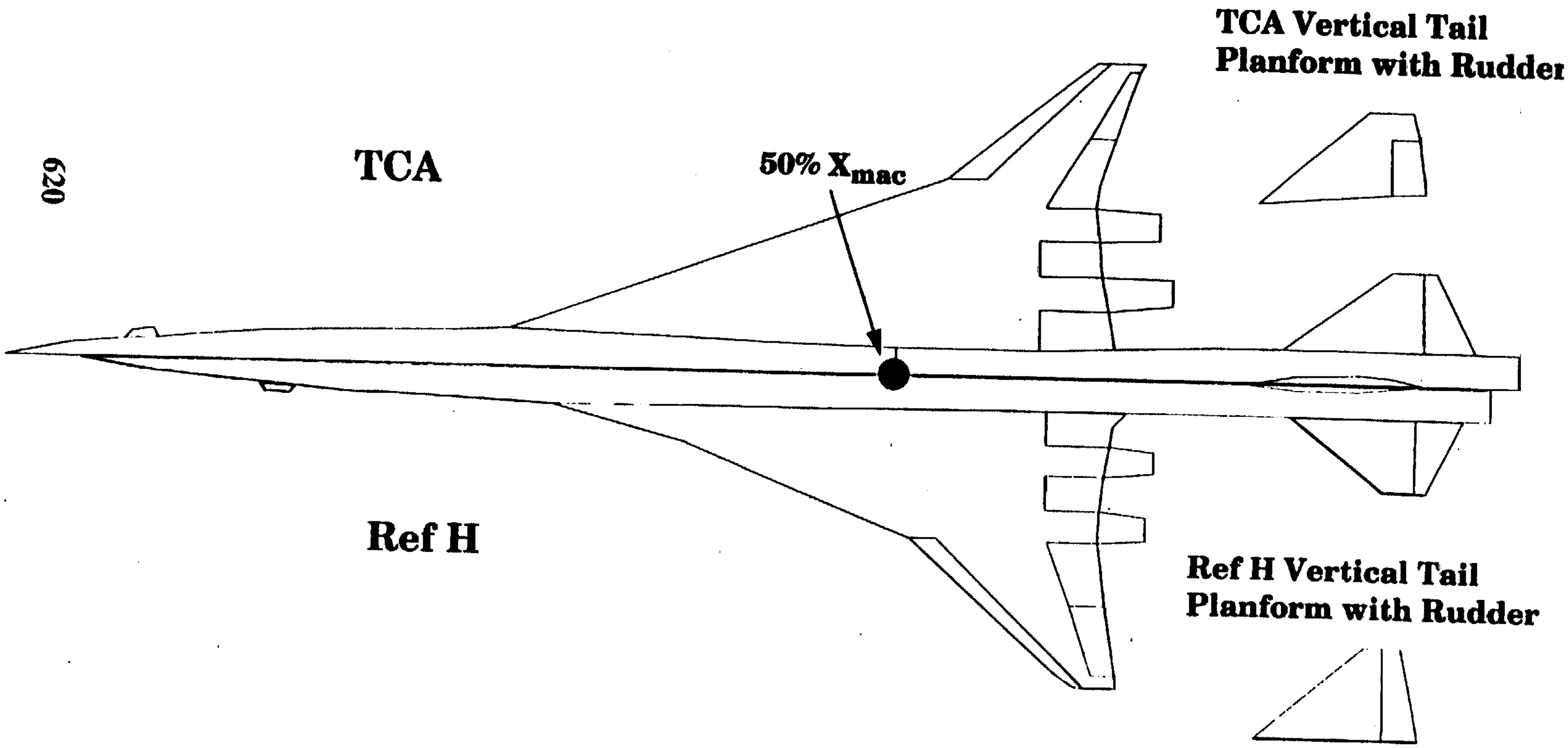

Model Highlights

The significant model geometry highlights for the TCA and Reference H models are tabulated below.

The “gross” wing area was used for the TCA model reference area, while the “Wimpress” area was used for all previous Reference H tests.

Two different trip dot heights were used during the TCA test. A height of 0.010 inches was used in test section #1, and a height of 0.012 inches was used in test section #2. The trip dots were located 1 inch aft of the nose apex and 0.6 inches (streamwise) aft of the leading edge on all other surfaces including the nacelles. Trip dot density was 0.1 inch on the nose, and 0.2 inches on all other surfaces.

Nacelle base pressures for the TCA were obtained for both the inboard and outboard nacelles, with two base pressure taps located on each nacelle. Model chamber pressure measurements were also obtained with two internal pressure taps.

Model Highlights

	TCA	Ref H
Model Scale:	1.5%	1.675%
Model Length:	58.68 in	61 in
Ref Wing Area:	1.913 ft^2 (Gross)	1.992 ft^2 (Wimp)
Ref Wing Span:	23.627 in	26.058 in
Ref Wing MAC :	17.091 in	17.291 in
HTail Volume:	0.09934	0.11318
VTail Volume:	0.03504	0.04180
Trip dot height(T.S.#1):	0.010”	0.0085”
Trip dot height(T.S.#2):	0.012”	0.0085”

TCA Pressures: (2) Inb. and (2) Outb. Nacelle Base
(2) Model Chamber

Test Highlights

The slide below presents a summary of the testing that was conducted at the UPWT with the 1.5% TCA controls model.

A total of 221 runs (41 configurations) were tested in test section #1, and 174 runs (28 configurations) were tested in test section #2. Due to time constraints, fewer configurations were tested in test section #2.

Testing was done at a Reynolds number of 3 million per foot in both test sections. Data was obtained at Mach numbers of 1.8 and 2.1 in test section #1 and at Mach numbers of 2.4 and 2.7 in test section #2.

Pitch polars were done at both 0 and +3 degrees of sideslip angle for most of the configurations and at -3 degrees of sideslip angle for a few selected configurations. The angle-of-attack range was from -4 to +12 degrees in 0.5 degree increments.

Yaw polars were done at angles-of-attack of 0, 4, and 8 degrees. The sideslip angle range was from -6 to +6 degrees in 0.5 degree increments.

Test Highlights

Runs Completed:	221 (Test Section #1)
	174 (Test Section #2)
Configurations:	41 (Test Section #1)
	28 (Test Section #2)
Mach Numbers:	1.8, 2.1 (Test Section #1)
	2.4, 2.7 (Test Section #2)
Reynolds Number :	3×10^6 / ft
Pitch Polars:	$-4^o \leq \alpha_F \leq 12^o$ for $\beta = 0^o, \pm 3^o$
Yaw Polars:	$-6^o \leq \beta \leq 6^o$ for $\alpha_F = 0^o, 4^o, 8^o$

TCA Configurations Tested

The next two slides present an outline of the TCA configurations tested. Note that the order of the configurations shown does not correlate to the actual sequence of configurations tested.

Configuration build-ups were obtained with both the truncated aftbody and the extended aftbody geometry. With the truncated aftbody, the nacelle/diverters were tested both on and off. With the extended aftbody, the horizontal and vertical tails were tested off and on individually and in combination (baseline). The chine was also included as part of the configuration build-up mainly for its effect on the directional characteristics.

Longitudinal control effectiveness was obtained by deflections of the stabilizer and elevator on the baseline configuration. Horizontal tail deflections tested were $\pm$ 6, and $\pm$15 degrees with the elevator undeflected. Elevator deflections tested were $\pm$20 degrees with the horizontal tail undeflected.

TCA Configurations Tested

- **Configuration Build-up (Truncated Aftbody):**
  - W/B
  - W/B/N/D
- **Configuration Build-up (Extended Aftbody):**
  - W/B/N/D
  - W/B/N/D/H
  - W/B/N/D/V
  - W/B/N/D/H/V (Baseline)
  - W/B/N/D/H/V/Chine
- **Longitudinal Control (W/B/N/D/H/V):**
  - $i_H = \pm 6^o$, $\pm 15^o$; $\delta_e = \pm 20^o$

TCA Configurations Tested

Directional control effectiveness was obtained by deflections of the rudder on the baseline configuration. Rudder deflections tested were +10 and +20 degrees. The effect of the chine on directional control effectiveness was also evaluated with the rudder deflect +10 degrees.

Lateral control effectiveness was obtained by deflections of individual and selected combinations of the right-wing trailing-edge flaps. Trailing-edge flaps #6 and #7 were tested individually and in combination at deflections of ±10 degrees for all Mach numbers and at ±20 degrees for Mach numbers of 1.8 and 2.1. Other combinations of trailing-edge flaps were tested at Mach numbers of 1.8 and 2.1 and include #6, #7, and #8 deflected ±10 degrees, #7 and #8 deflected ±10 degrees, and #5, #6, #7, and #8 deflected +10 degrees.

TCA Configurations Tested

- **Directional Control (W/B/N/D/H/V):**
  - $\delta_r = +10^o, +20^o$
- **Directional Control (W/B/N/D/H/V/Chine):**
  - $\delta_r = +10^o$
- **Lateral Control (W/B/N/D/H/V):**
  - $\delta_{TEF\#6}; \delta_{TEF\#7}; \delta_{TEF\#6,7} = \pm 10^o, \pm 20^{o*}$
  - $\delta_{TEF\#6,7,8}; \delta_{TEF\#7,8} = \pm 10^{o*}$
  - $\delta_{TEF\#5,6,7,8} = +10^{o*}$

* Tested at M=1.8 and 2.1 only

Data Quality

Data quality was determined by the repeatability of the longitudinal coefficients for several sets of runs with the baseline configuration, obtained at various times during the test. The slide below shows the data repeatability variation with angle-of-attack for the lift, drag and pitching moment coefficients at Mach 2.4. The data points shown represent the deviation of each individual point from the average of all the repeat points obtained.

Variation of lift coefficient is shown to be within ±0.001(except for a few points), with the majority of the points within ±0.0005.

Variation of the drag coefficient is shown to be within ±0.0001 (except for a few points), with the majority of the points within ±0.00005.

Variation of the pitching moment coefficient is shown to be within ±0.0002.

From these data, it was concluded that the data quality was good and a high confidence level could be placed on the data obtained for the TCA at this Mach number.

Data Quality
TCA Tail-on Baseline, M=2.4

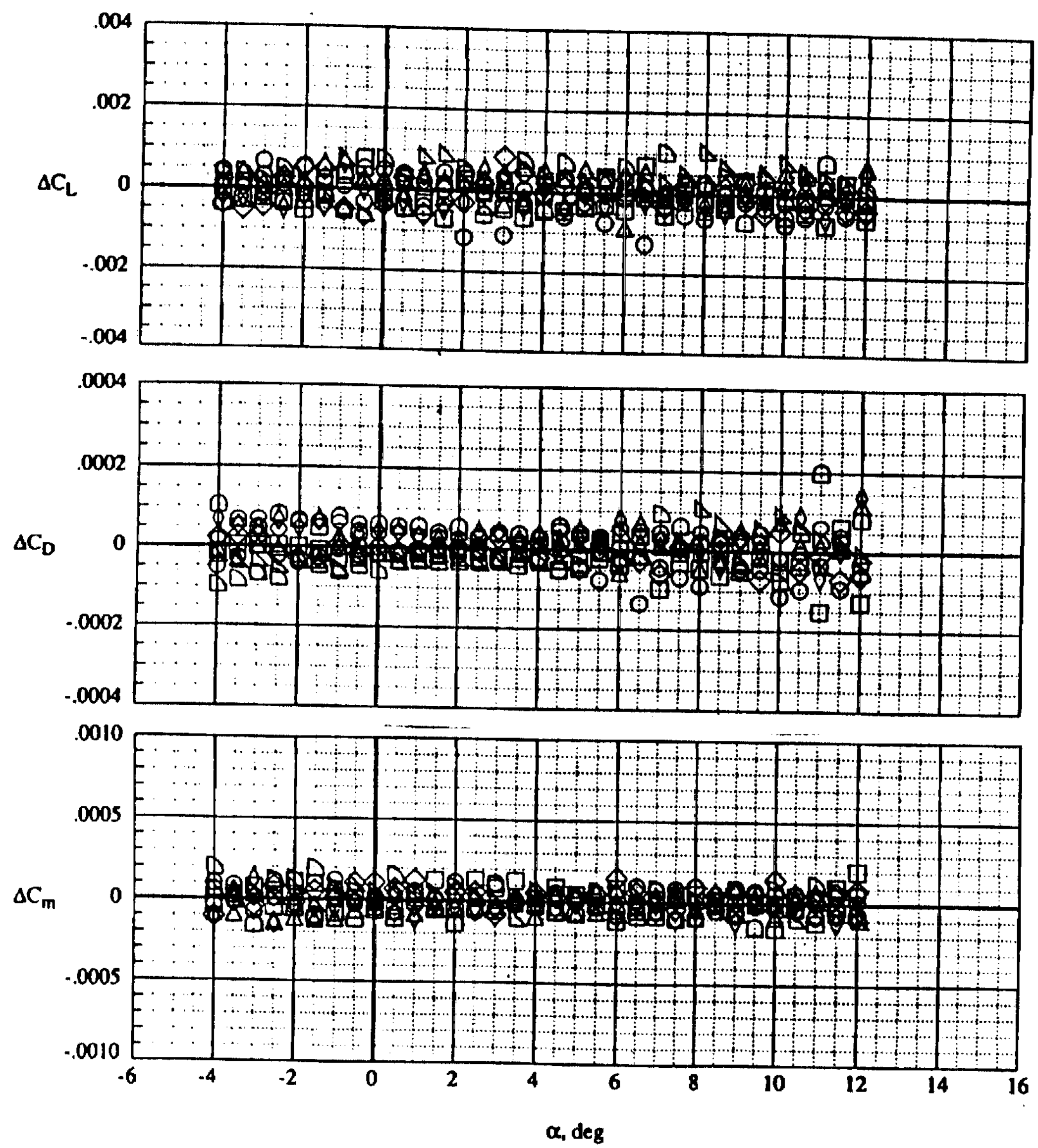

Long-Term Repeatability

Long-term repeatability was determined by comparing the longitudinal coefficients obtained for the Reference H baseline configuration at the start of this test with similar data obtained during a previous Reference H test (UPWT-1647). The slide below shows the data repeatability variation with angle-of-attack for the lift, drag and pitching moment coefficients at Mach 2.4. The data points shown represent the deviation of each individual point from the average of all the repeat points obtained during both tests.

Variation of lift coefficient is shown to be within ±0.001(except for a few points at negative α_F's), with the majority of the points within ±0.0005.

Variation of the drag coefficient is shown to be within ±0.00005 for most of the angle-of-attack range. At the higher α_F's, the divergence between the data for the two tests is in large part due to different sting-bending calibration methods that were used.

Variation of the pitching moment coefficient is shown to be within ±0.0003.

From these data, it was concluded that the long-term repeatability is good at this Mach number.

Long-Term Repeatability
Reference H Tail-on Baseline, M=2.4

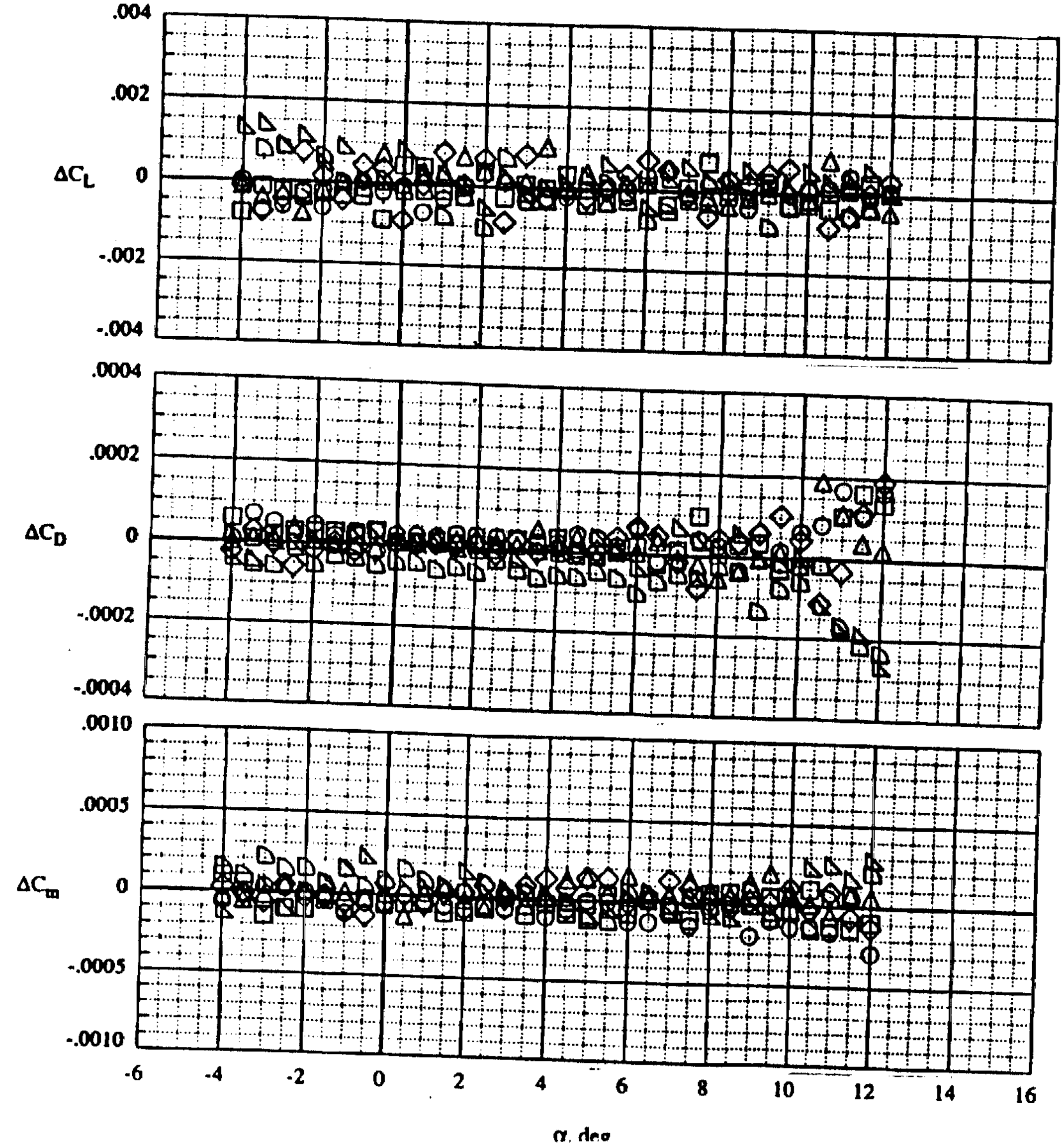

Longitudinal Characteristics Component Build-up

The effect of the model components on the lift coefficient variation with α_F at Mach 2.4 is presented in the slide below. The addition of the chine and vertical tail resulted in no significant change in lift. However, the addition of the horizontal tail increased lift at positive α_F's and decreased lift at negative α_F's. The horizontal tail contributes no lift at approximately $\alpha_F = 1.5$ degrees.

Longitudinal Characteristics
Component Build-up

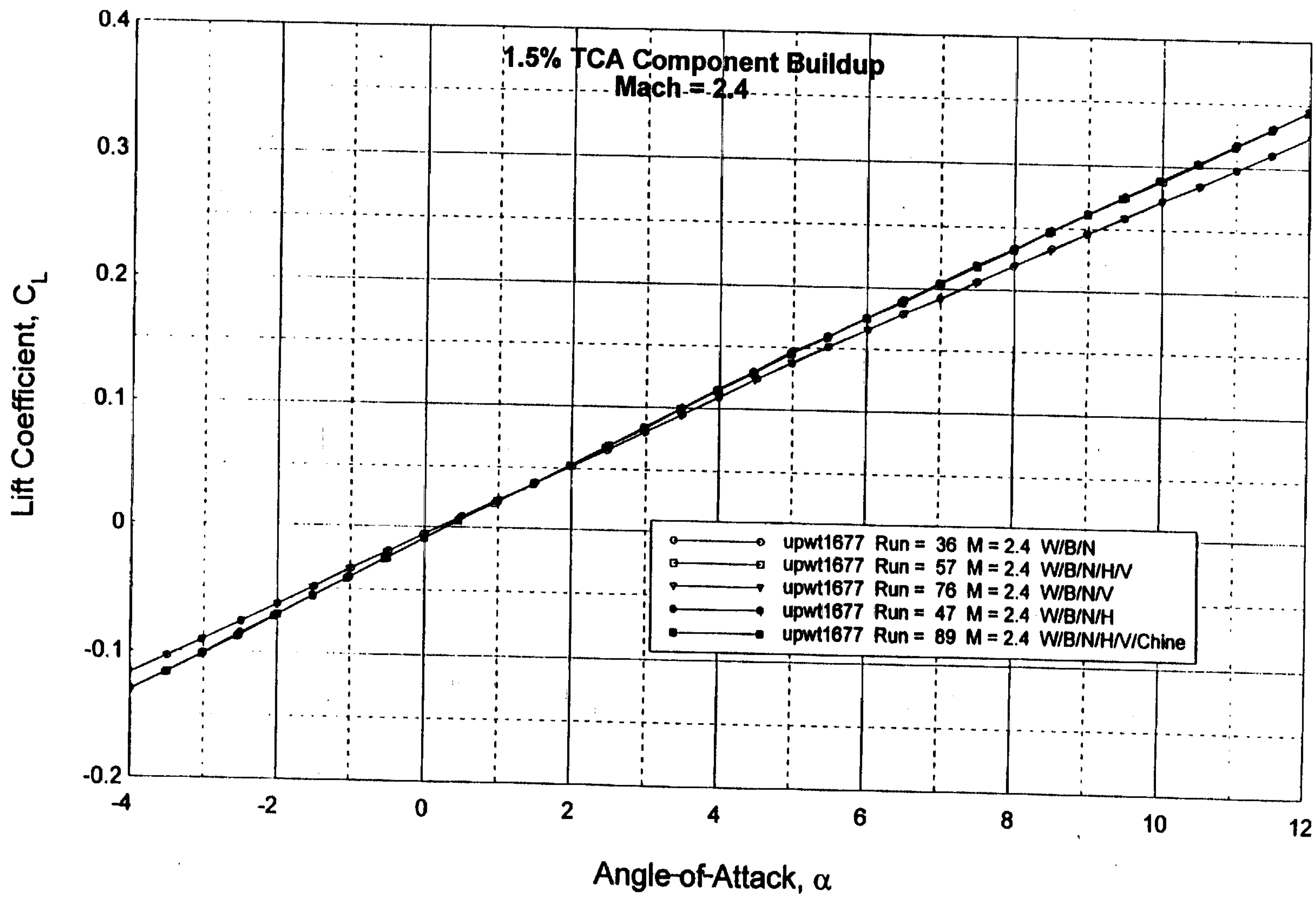

Longitudinal Characteristics Component Build-up

The effect of the model components on drag coefficient variation with lift coefficient (drag polar) at Mach 2.4 is presented in the slide below.

The addition of each component results in increased drag relative to the W/B/N (extended aftbody) configuration near minimum drag. At higher lift coefficients, the horizontal tail-on configurations result in less drag at a given lift. This is because the tail is producing a positive lift increment and, therefore, less α_F is required to obtain a given lift coefficient.

The addition of the chines (Ch) to the baseline configuration results in no noticeable drag change.

Longitudinal Characteristics Component Build-up

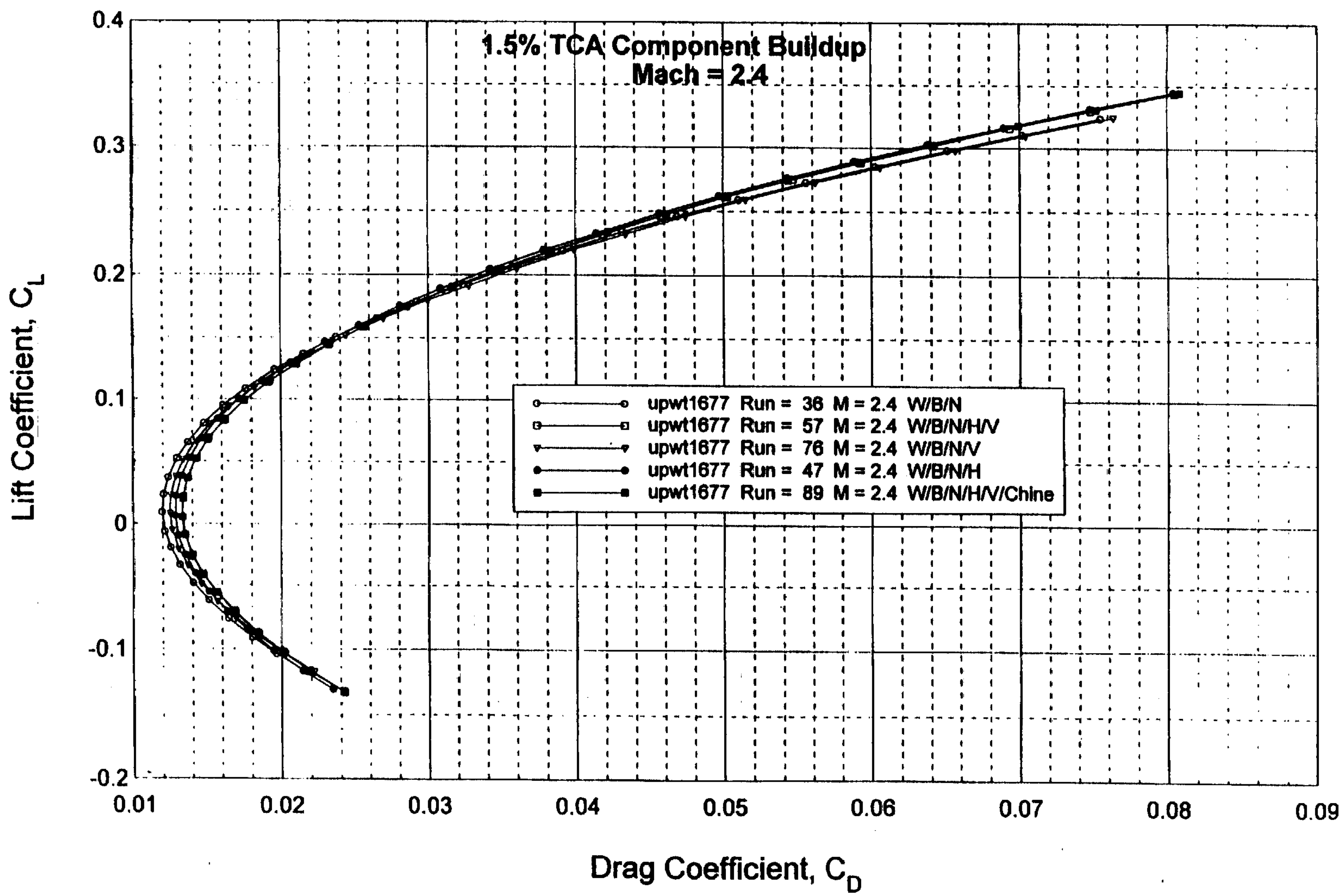

Longitudinal Characteristics
Component Build-up

The effect on the drag polar, at Mach 2.4, of the model components shown in the previous slide is again presented on the slide below. Note that the region around zero lift has been expanded to provide additional clarity.

The vertical tail contributes approximately 5 counts of additional drag for the range of C_L's shown. The increase in drag due to the horizontal tail varies from over 8 counts at minimum drag to only 5 counts near the cruise C_L of 0.1. When both vertical and horizontal tails are added, the resulting drag increase is similar to the sum of each individual contribution.

The forebody chines (Ch) are shown to have a minimal impact on the drag polar for the range of C_L's shown.

Longitudinal Characteristics
Component Build-up

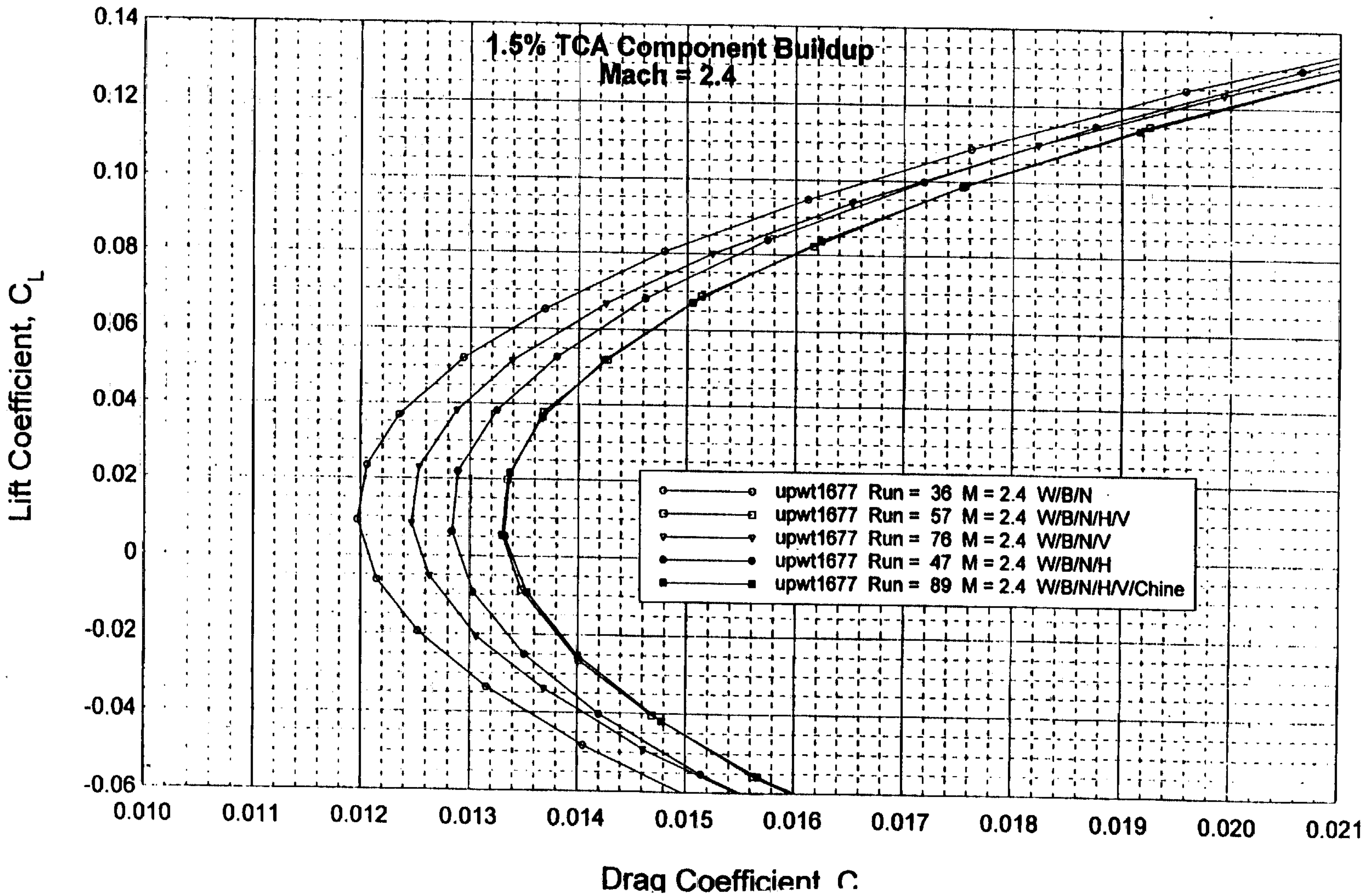

Longitudinal Characteristics
Component Build-up

The effect of the model components on drag, at Mach 2.4, is summarized in the slide below. The incremental drag, in counts, relative to the W/B/N (extended aftbody) configuration is shown at both minimum drag (non-shaded bars) and at a C_L of 0.1(shaded bars). In addition to the data presented in the previous two slides, the incremental drag due to the truncated aftbody (BT) with nacelles and diverters both on and off is included.

The truncated aftbody has approximately 10 counts less drag than the extended aftbody. The removal of the nacelles and diverters resulted in an additional 16 counts of drag reduction.

Longitudinal Characteristics Component Build-up

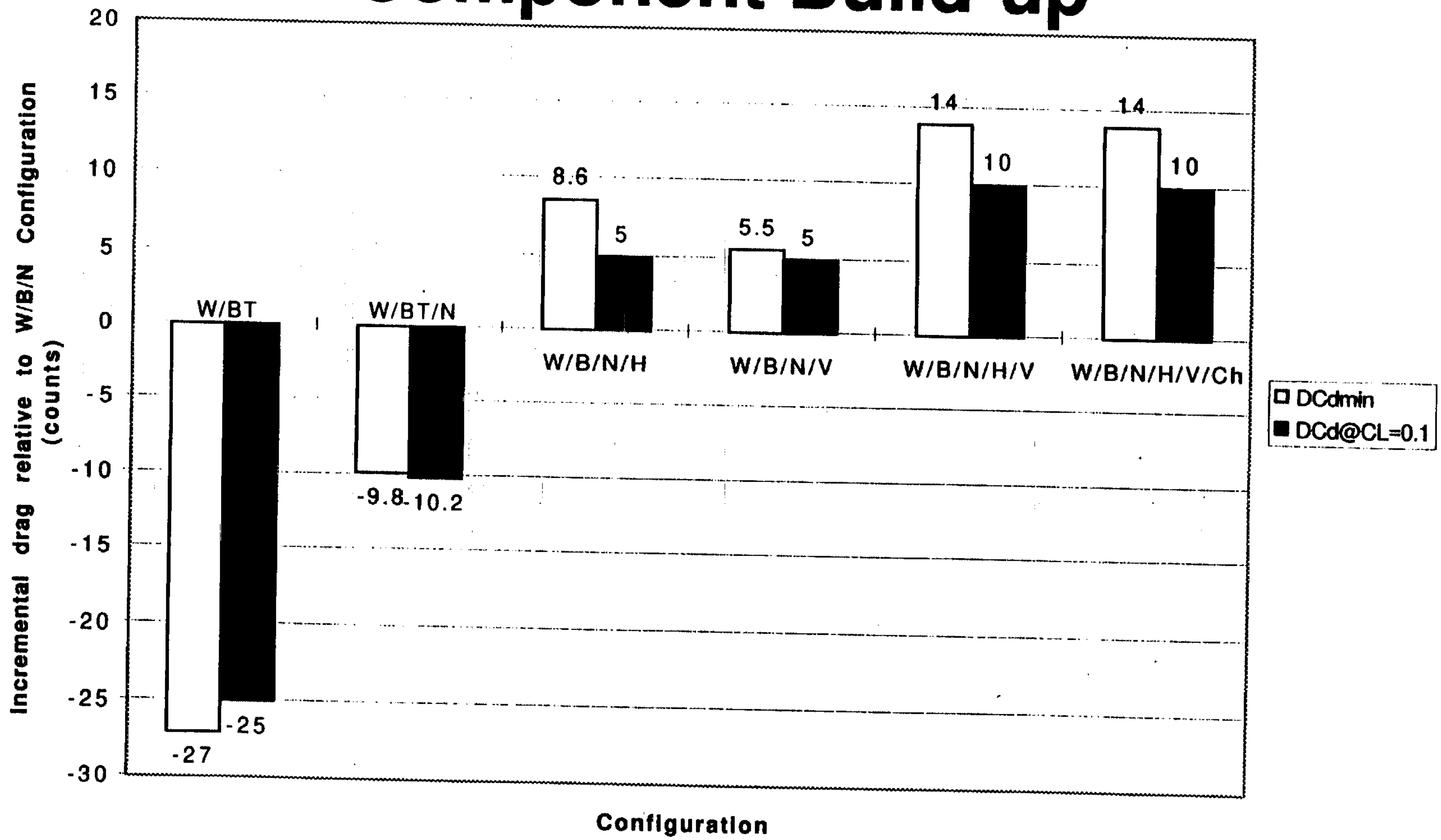

Longitudinal Characteristics
Component Build-up

The effect of the model components on the pitching moment coefficient (about the 50% MAC) variation with lift coefficient (longitudinal stability) at Mach 2.4 is presented in the slide below.

The addition of the vertical tail to the W/B/N (extended aftbody) configuration results in a slight negative pitching moment shift (Cm_o) with no stability change.

The addition of the horizontal tail results in a significant increase in longitudinal stability. When the vertical tail is added along with the horizontal tail, a small negative Cm_o shift occurs relative to the horizontal-tail-only configuration, with no stability change.

The addition of the chine to the tails-on baseline configuration results in a slight longitudinal stability decrease at higher lift coefficients.

Longitudinal Characteristics
Component Build-up

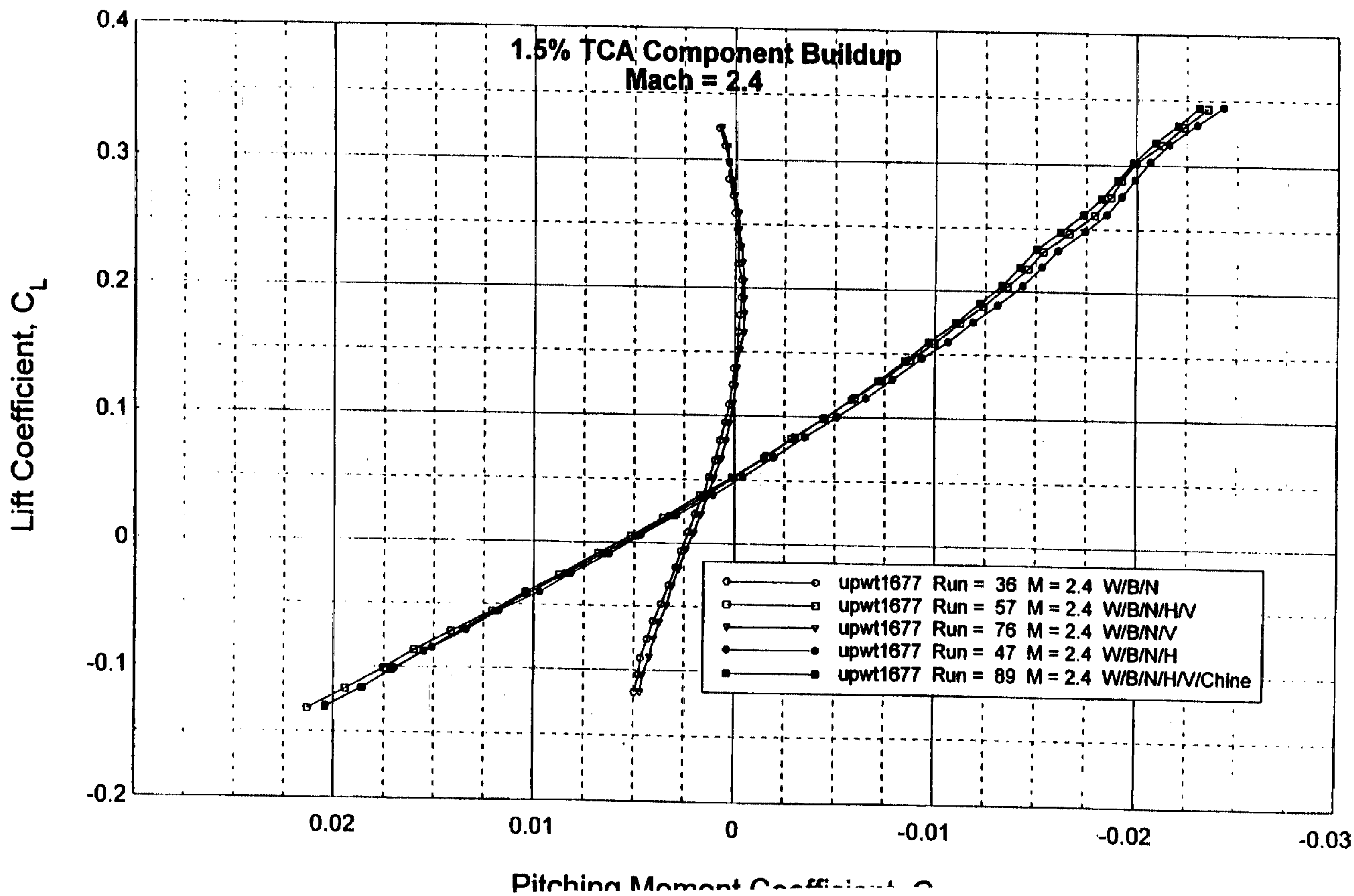

Longitudinal Characteristics
Stability Comparison

The slide below compares the longitudinal stability of the tails-on baseline Reference H configuration with the tails-on baseline TCA configuration at Mach 2.4 about their respective 50% MAC points.

The variation of pitching moment with lift appears very linear for the Reference H configuration. For the TCA configuration, the variation is very non-linear throughout the lift range. The slide also shows the TCA configuration to be more unstable than the Reference H configuration, particularly at higher lift.

Longitudinal Characteristics
Stability Comparison

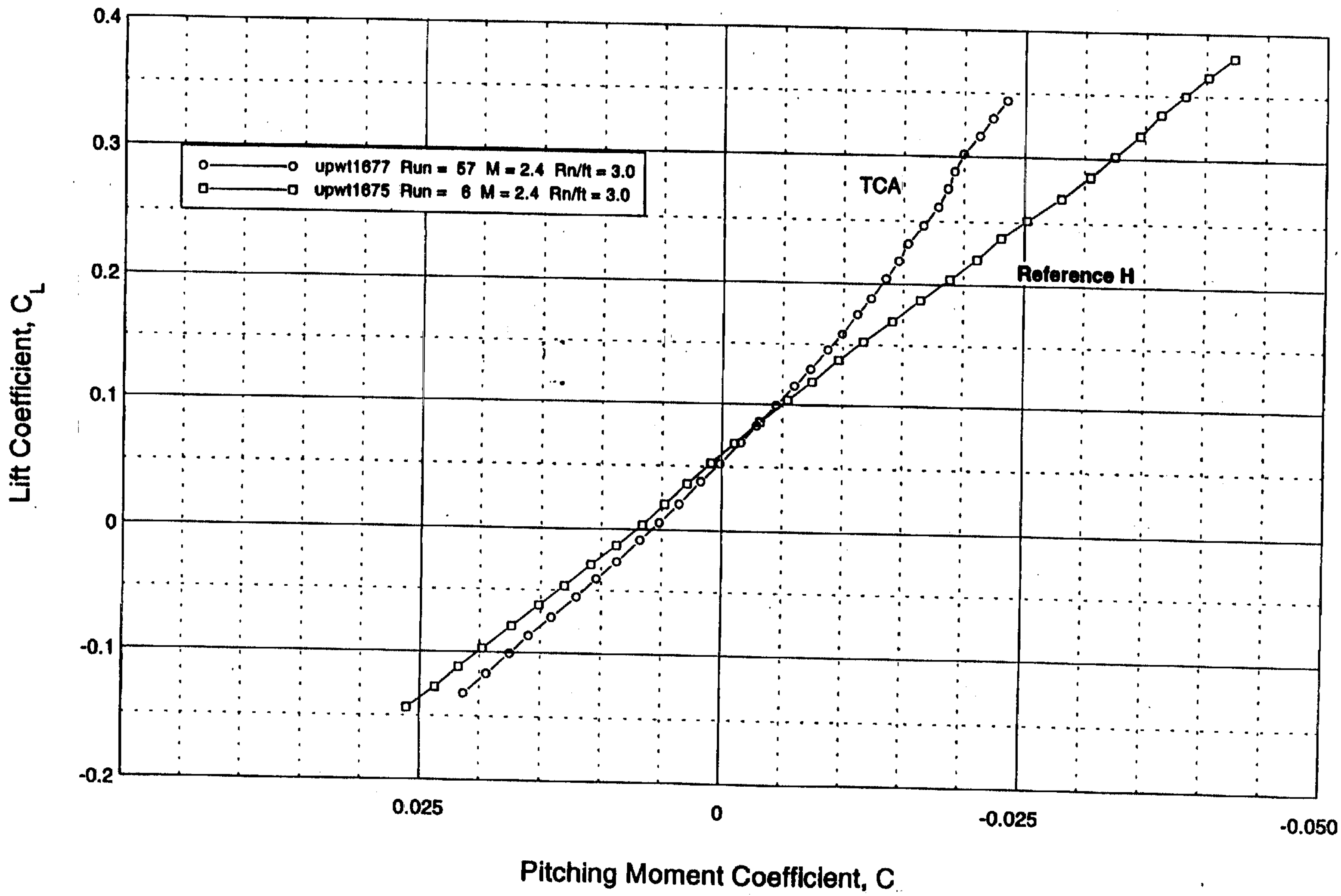

Longitudinal Characteristics
Control Effectiveness

The slide below presents the incremental pitching moment coefficient (control effectiveness) variation with α_F, at Mach 2.4, resulting from various deflections of the horizontal tail and elevator for the TCA configuration. The increment was derived by subtracting the pitching moment coefficient of the deflected configuration from the undeflected configuration. The horizontal tail was deflected with the elevator undeflected, and the elevator was deflected with the horizontal tail undeflected.

The control effectiveness of the horizontal tail appears to be slightly greater (more effective) in the leading-edge down direction (negative deflections) than in the leading-edge up direction. Control effectiveness also decreases at higher α_F's.

The elevator is approximately 1/3 as effective as the horizontal tail, with 20 degrees of elevator deflection being equivalent to 6 degrees of horizontal tail deflection ($\alpha_\delta = 0.3$).

Longitudinal Characteristics
Control Effectiveness

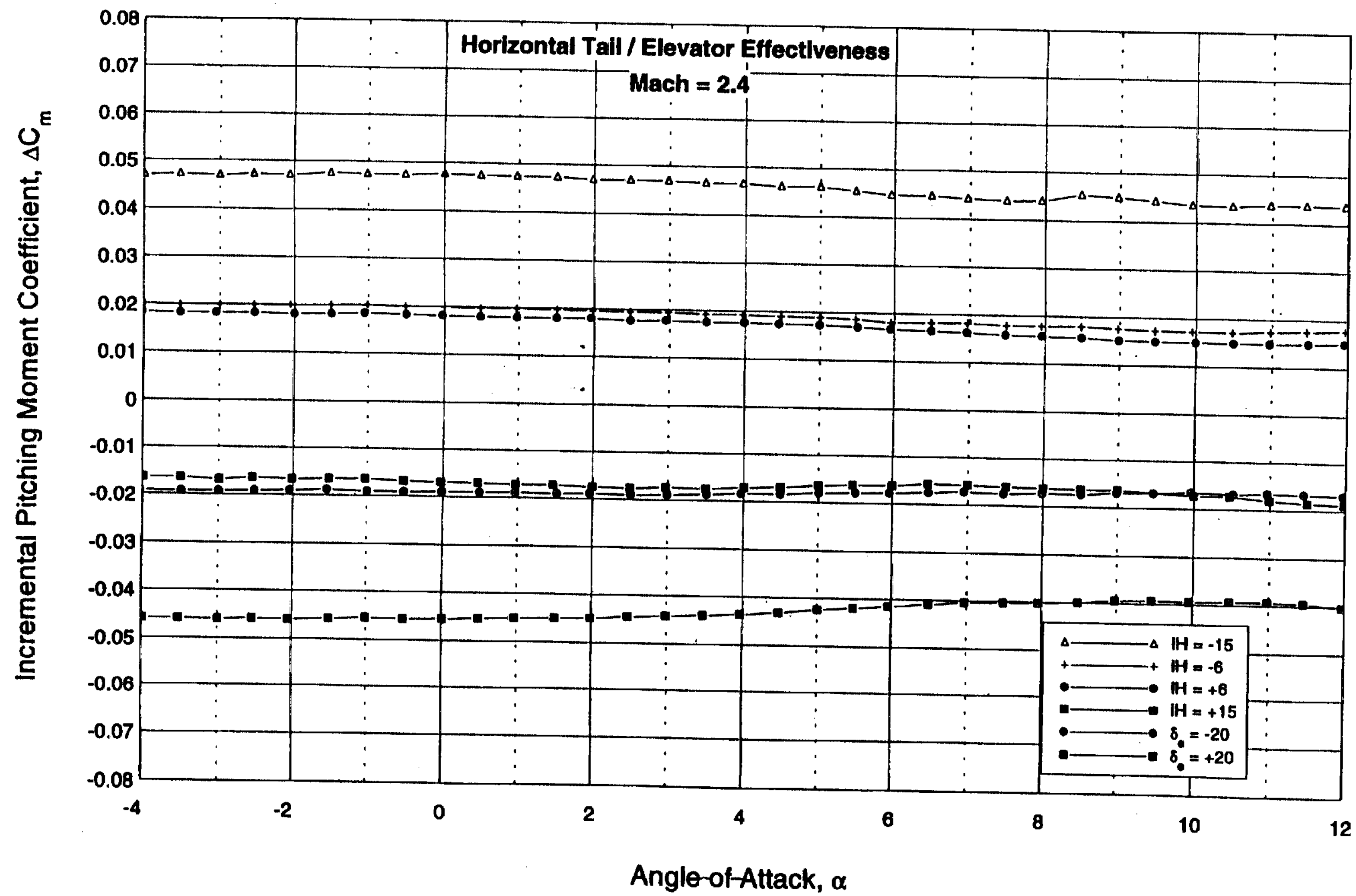

Longitudinal Characteristics
Control Comparison

This slide presents a comparison of the control effectiveness variation with α_F, at Mach 2.4, for the Reference H and TCA horizontal tails.

Per degree of deflection, the Reference H horizontal tail is more effective than the TCA horizontal tail. As shown on the previous slide for the TCA configuration, the control effectiveness also decreases with increasing α_F for the Reference H configuration.

Longitudinal Characteristics Control Comparison

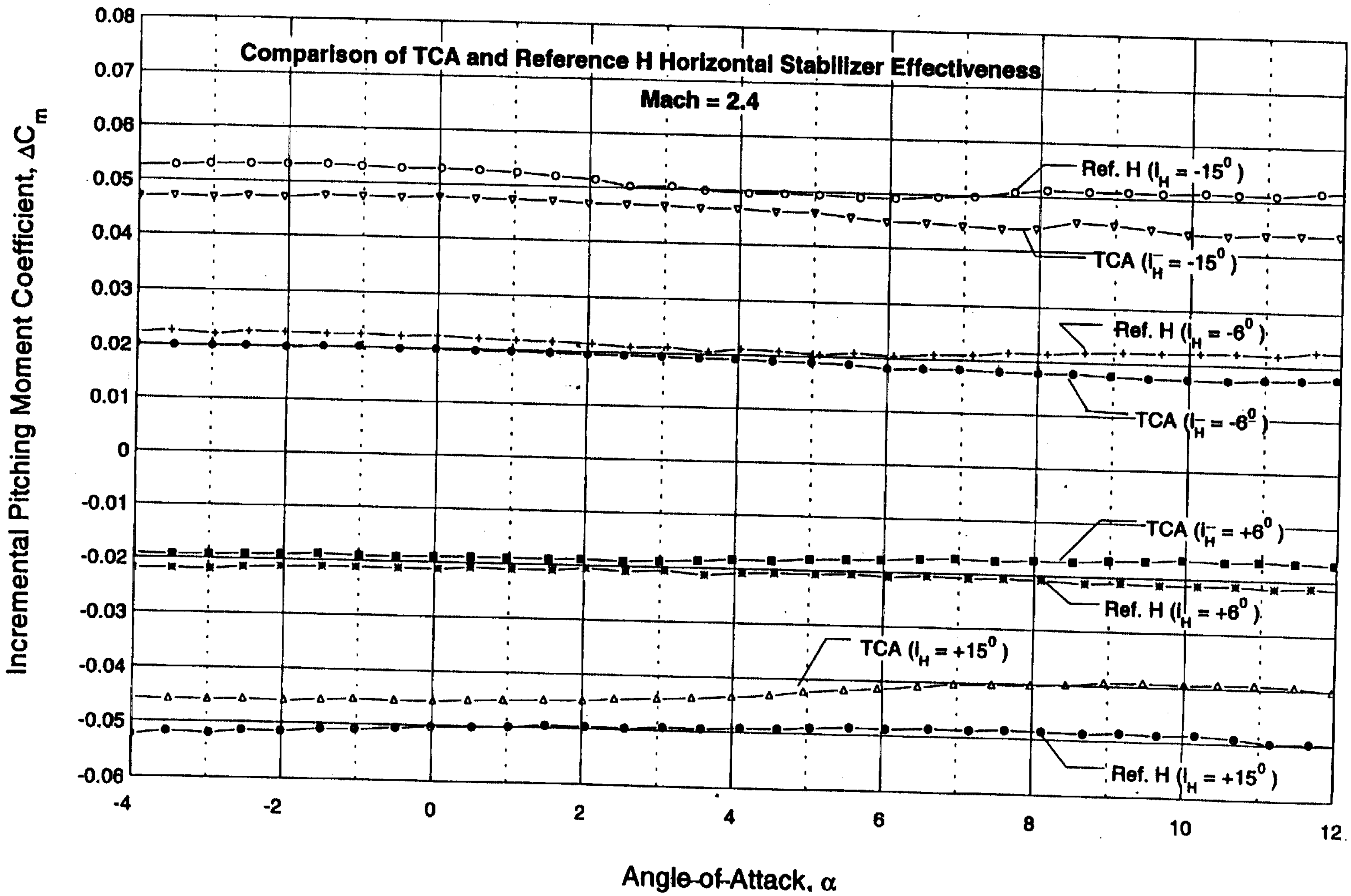

Directional Characteristics
Component Build-up

The next three slides present the effect of the model components on the yawing moment coefficient variation with sideslip angle, at Mach 2.4, for α_F's of 0, 4, and 8 degrees.

Both the W/B/N and W/B/N/H configurations, with the extended aftbody, are directionally unstable (slope of Cn vs. β). The horizontal tail-on configuration is slightly more unstable than the horizontal tail-off configuration.

The addition of the vertical tail results in a stable configuration. The horizontal tail again reduces the directional stability slightly when combined with the vertical tail. The chine has no impact on the directional characteristics at this α_F.

Directional Characteristics
Component Build-up

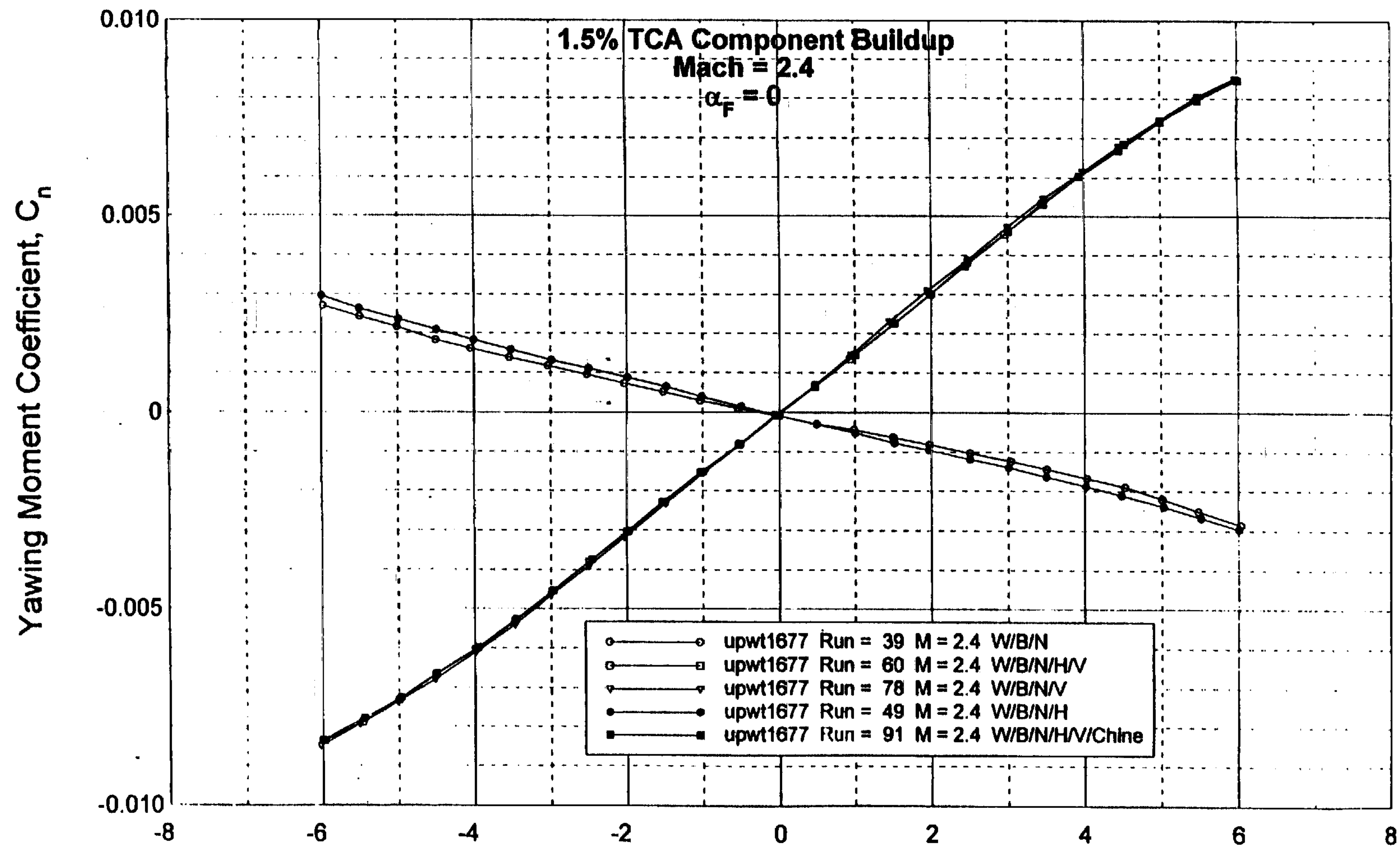

Directional Characteristics
Component Build-up

This slide presents the effect of the model components on the yawing moment coefficient variation with sideslip angle at Mach 2.4 and α_F = 4 degrees.

As shown in the previous slide for $\alpha_F = 0$, both the W/B/N and W/B/N/H configurations, with the extended aftbody, are directionally unstable (slope of Cn vs. β). The horizontal tail-on configuration is slightly more unstable than the horizontal tail-off configuration, particularly at higher β's.

The addition of the vertical tail results in a stable configuration. The horizontal tail reduces the directional stability noticeably when combined with the vertical tail. The chine is shown to increase the directional stability at this α_F.

Directional Characteristics
Component Build-up

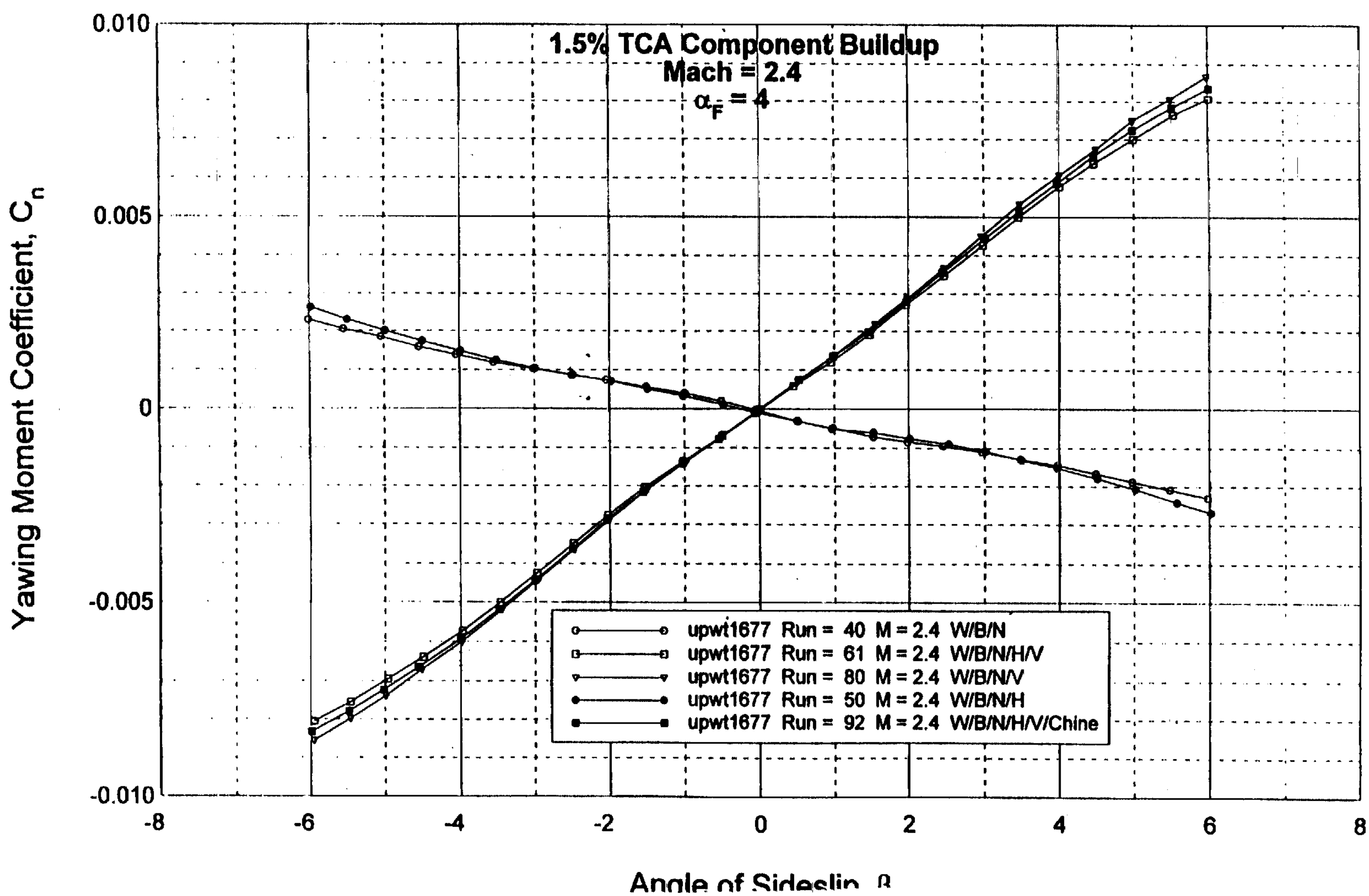

Directional Characteristics
Component Build-up

This slide presents the effect of the model components on the yawing moment coefficient variation with sideslip angle at Mach 2.4 and α_F = 8 degrees.

As shown in the previous two slides for α_F = 0 and 4 degrees, both the W/B/N and W/B/N/H configurations, with the extended aftbody, are directionally unstable (slope of Cn vs. β). The horizontal tail-on configuration is slightly more unstable than the horizontal tail-off configuration, particularly at smaller β's.

The addition of the vertical tail results in a stable configuration, although between $-3 \leq \beta \leq -1$ and $+1 \leq \beta \leq +3$, the stability is affected by flow phenomenon that causes a reduced level of stability. The horizontal tail reduces the directional stability noticeably when combined with the vertical tail, particularly at higher β's. The chine is shown to greatly increase the directional stability at this α_F over the entire β range.

Directional Characteristics
Stability Comparison

This slide shows a comparison, at Mach 2.4, of the variation with α_F of yawing moment coefficient (at β = 3 degrees) between the Reference H and the TCA tail-on configurations. Additionally, the effect of the chine is shown. The directional stability derivative, Cn_β, can be determined by dividing the yawing moment coefficient shown by 3.

Comparing the chine-off baseline configurations, the TCA has less directional stability than the Reference H configuration at angles-of-attack up to α_F = 6 degrees. Beyond α_F = 6 degrees, the TCA configuration has significantly more directional stability than the Reference H configuration. The Reference H configuration becomes directionally unstable beyond α_F = 11 degrees, while the TCA remains stable.

The addition of the forebody chines dramatically improves the directional stability of both configurations at higher α_F's.

Directional Characteristics
Component Build-up

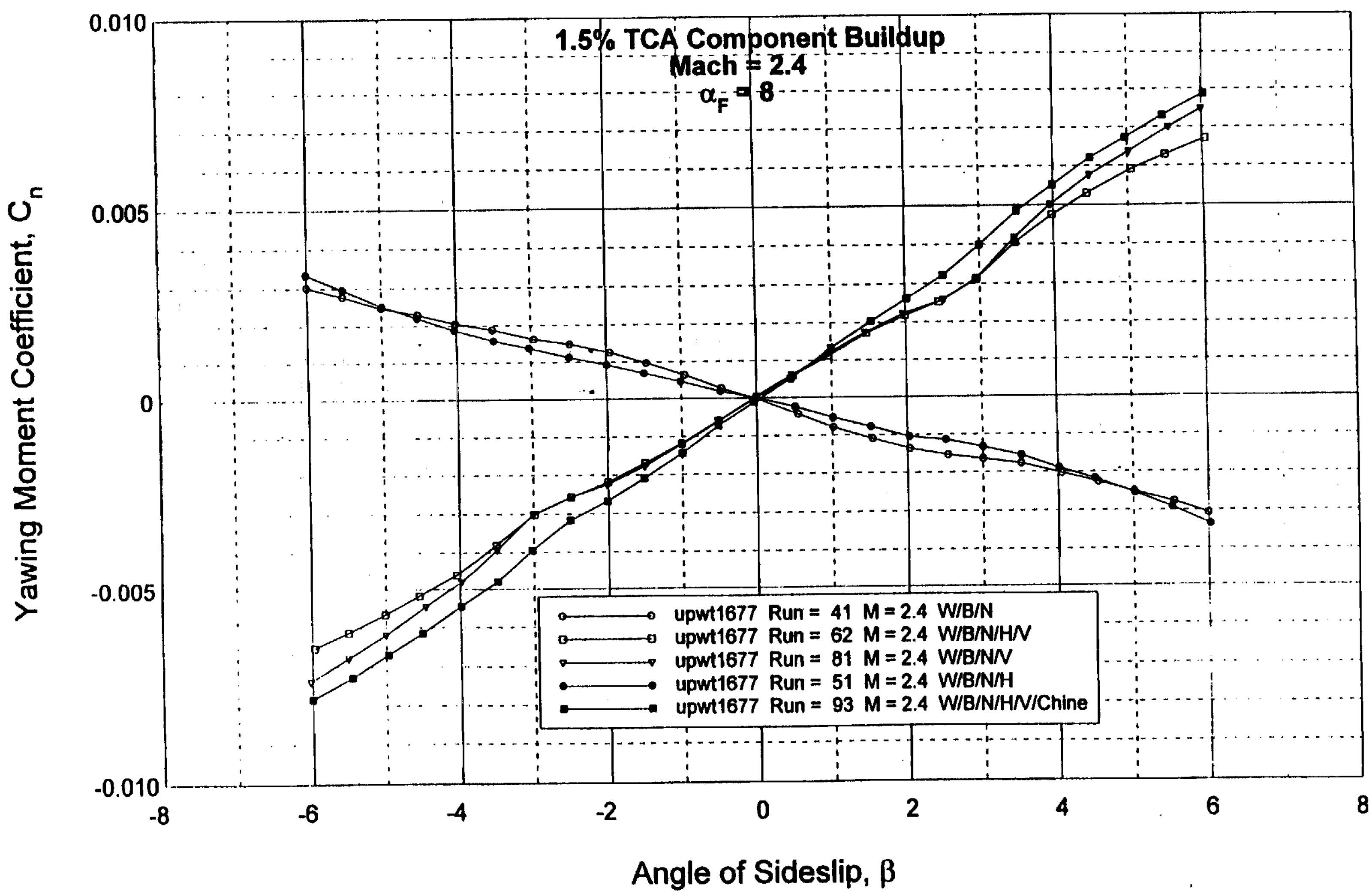

Directional Characteristics Stability Comparison

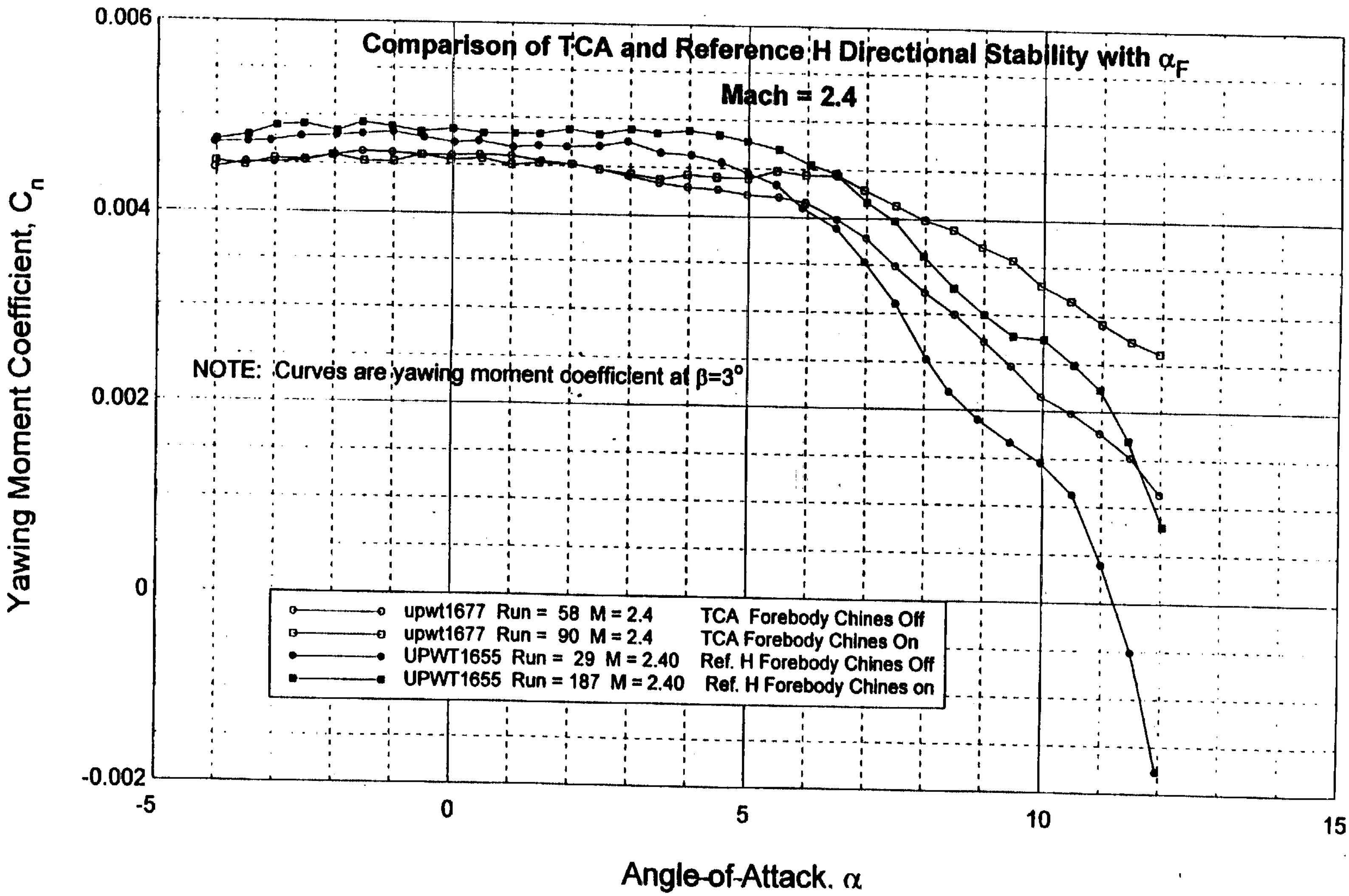

Directional Characteristics
Control Comparison

This slide presents a comparison, at Mach 2.4, of the variation with α_F of incremental yawing moment coefficient due to rudder deflection between the Reference H and the TCA configurations. Additionally, the effect of the chine on rudder effectiveness is shown for the TCA configuration. Note that TCA rudder deflections include only the lower two panels, compared to all three for the Reference H.

The rudder effectiveness of the TCA configuration appears to be approximately linear with respect to rudder deflection, with double the deflection resulting in double the incremental yawing moment. The chines have a small effect on rudder effectiveness, particularly at higher α_F's.

The Reference H rudder effectiveness is nearly constant with α_F, while the TCA rudder effectiveness decreases with increasing α_F. After adjustments for the number of panels deflected and the vertical tail volume, the rudder effectiveness of the TCA and Reference H are nearly identical at low α_F's.

Directional Characteristics
Control Comparison

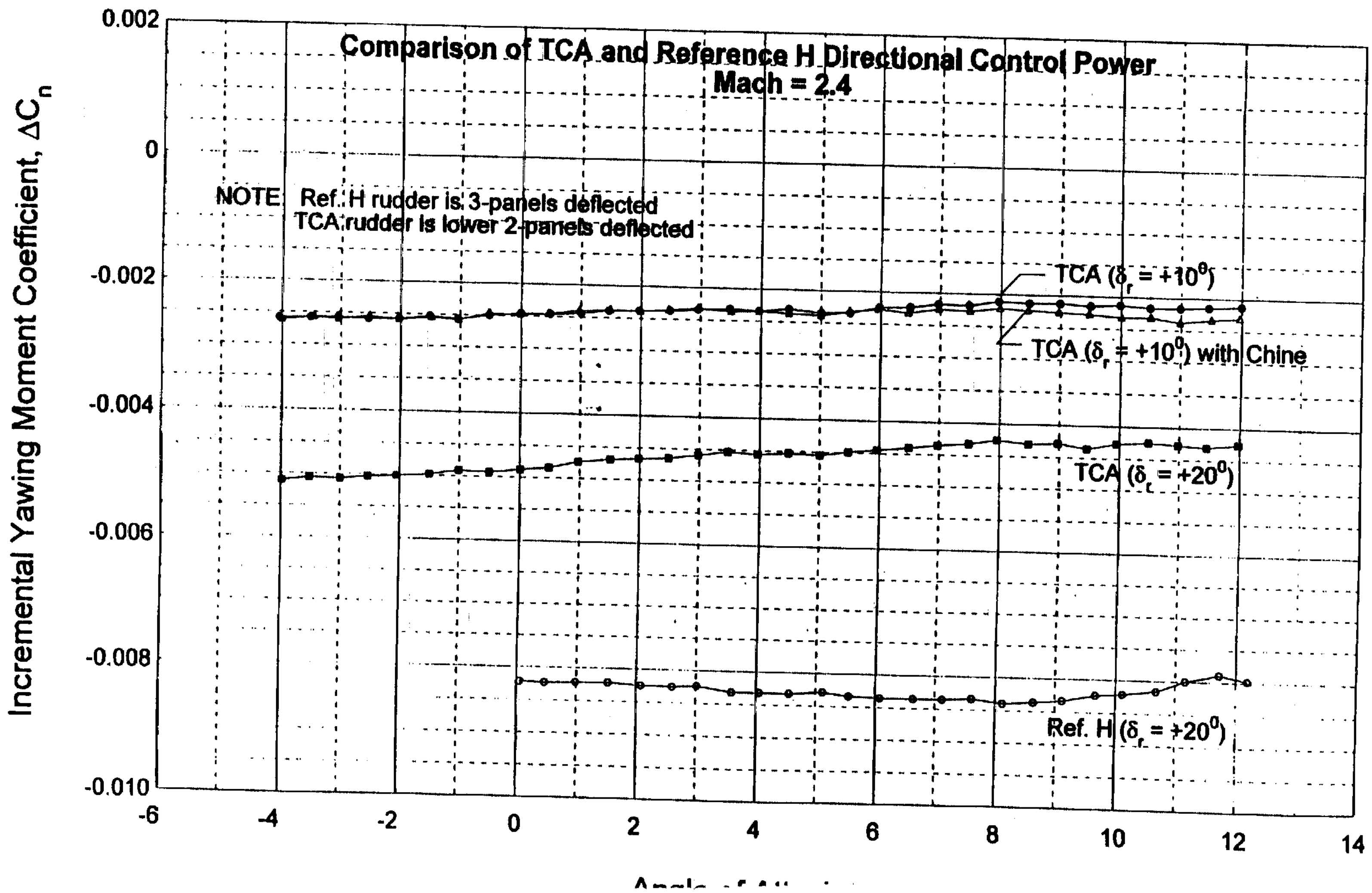

Lateral Characteristics
Stability Comparison

This slide shows a comparison, at Mach 2.4, of the variation with α_F of rolling moment coefficient (at β = 3 degrees) between the Reference H and the TCA baseline tails-on configurations. The lateral stability derivative, Cl_β, can be determined by dividing the rolling moment coefficient shown by 3.

Comparing the two configurations, the TCA has less lateral stability than the Reference H configuration at all α_F's. Both configurations are laterally stable throughout the entire α_F range tested.

The reduced level of lateral stability is beneficial to reducing the lateral control required to offset roll due to sideslip, particularly at low speeds.

Lateral Characteristics Stability Comparison

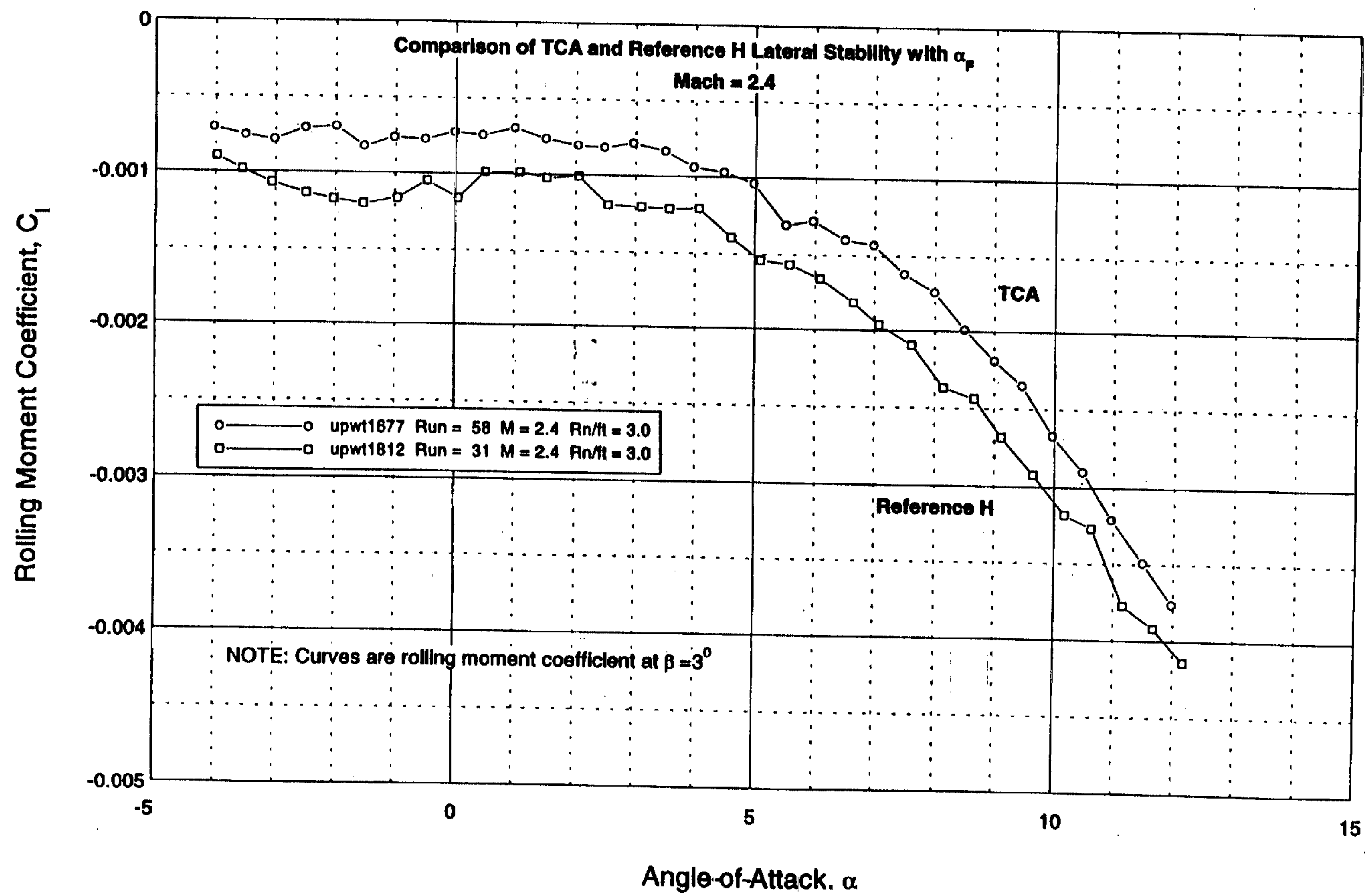

Lateral Characteristics
Control Effectiveness

The slide below presents the incremental rolling moment coefficient variation with α_F, at Mach 2.4, due to trailing-edge flap deflection for the TCA configuration. Trailing-edge flaps #6 and #7 were deflected ± 10 degrees both individually and in combination. The incremental rolling moment coefficient was derived by subtracting the rolling moment of the flap(s)-deflected configurations from the rolling moment of the flaps-undeflected configuration.

At low α_F's, trailing-edge flap #7 is significantly more effective than trailing-edge flap #6 when deflected trailing-edge up. For positive deflections, trailing-edge flap #7 is approximately 30% more effective than trailing-edge flap #6.

At approximately $\alpha_F = 4.5$ degrees, lateral control effectiveness increases suddenly for negative deflections of trailing-edge flap #6, and decreases suddenly for positive deflections of trailing-edge flaps #6 and #7.

The lateral control effectiveness of combined trailing-edge flap deflections is approximately the same as the sum of the lateral control effectiveness of the individual trailing-edge flap deflections. Except at low α_F's, the control effectiveness in either direction is approximately the same in magnitude.

Lateral Characteristics
Control Effectiveness

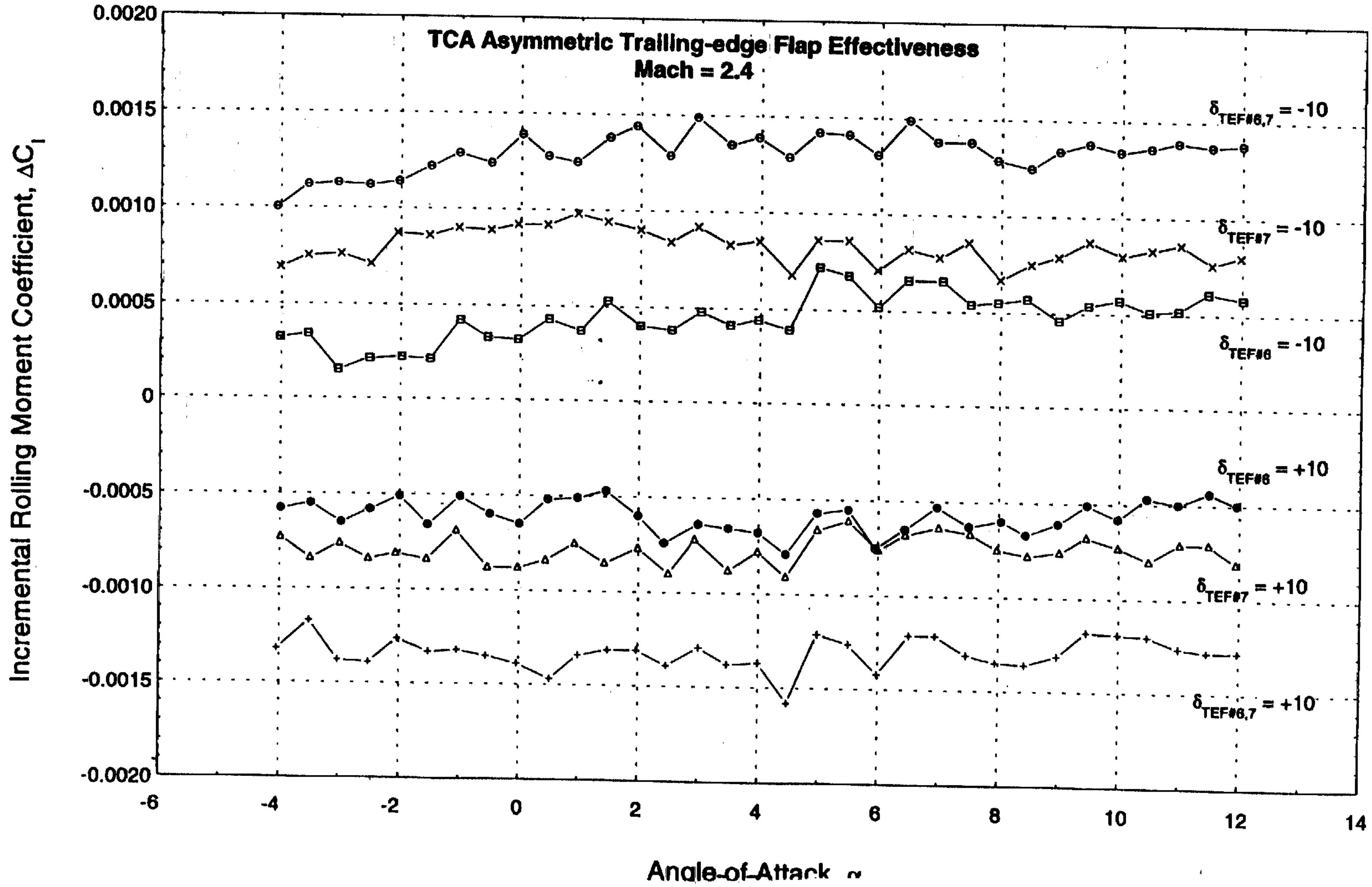

Lateral Characteristics
Control Comparison

This slide presents a comparison, at Mach 2.4, of the variation with α_F of incremental rolling moment coefficient due to trailing-edge flap deflection between the Reference H and the TCA configurations. Lateral control effectiveness is shown for both individual trailing-edge flaps as well as combinations of trailing-edge flaps.

Significant observations include:

(1) For negative deflections of the trailing-edge flaps, the Reference H and TCA have nearly identical control effectiveness.

(2) For positive deflections of the trailing-edge flaps, trailing-edge flap #7 on the Reference H is significantly (25%) more effective than trailing-edge flap #7 on the TCA. In fact, the combination of trailing-edge flaps #6 and #7 deflected on the TCA has nearly the same control effectiveness of only trailing-edge flap #7 deflected for the Reference H.

Lateral Characteristics
Control Comparison

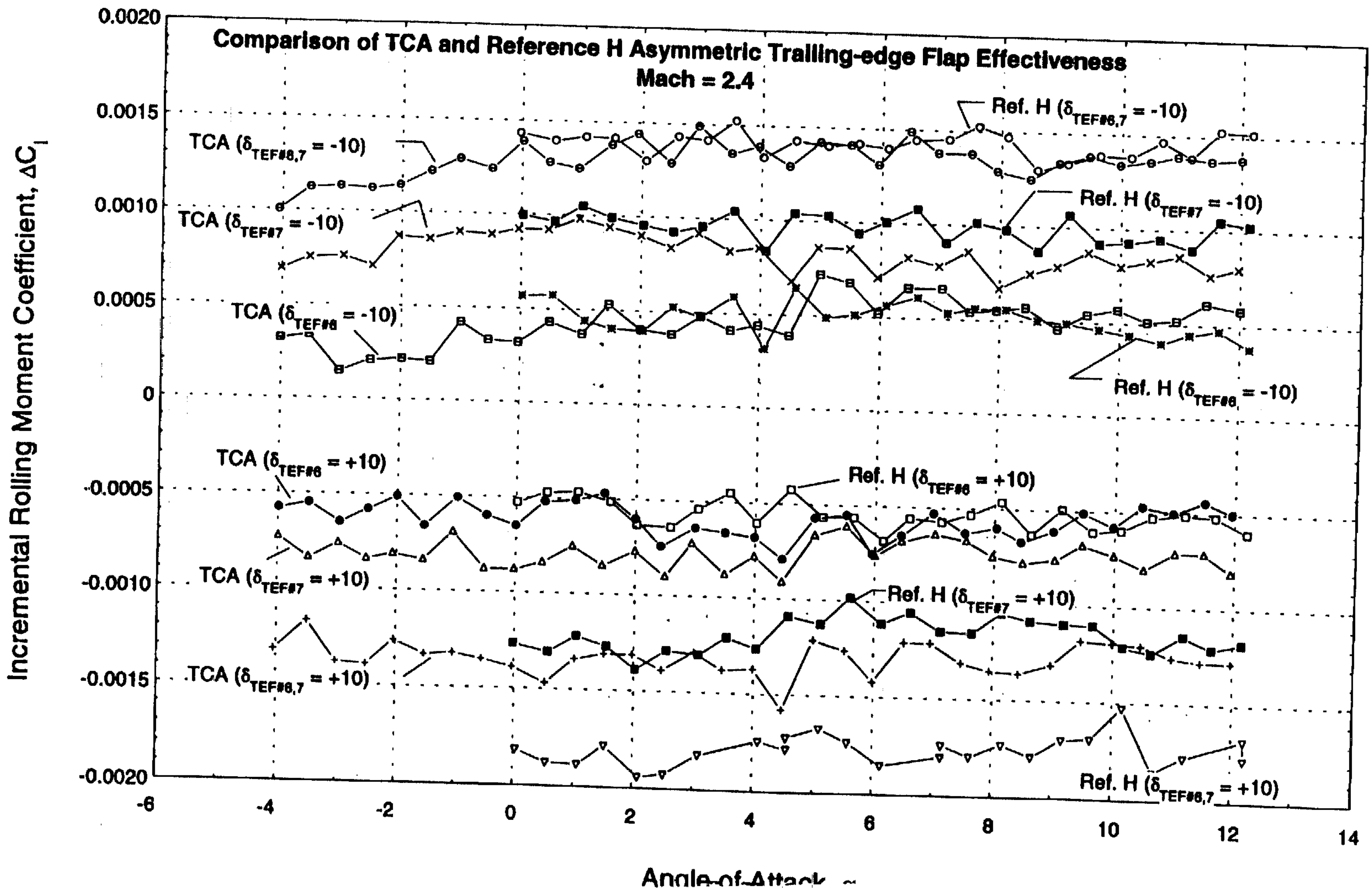

Summary

The following two slides present a summary of the data presented in this report. While all of the data and comparisons to the Reference H have been made at Mach 2.4, similar observations were made during the course of testing at the other Mach numbers tested.

To summarize the significant highlights in this report:

(1) Data quality, determined by multiple repeat runs performed on the TCA baseline configuration, and long-term repeatability, determined by comparing baseline Reference H data from this test to a previous test, have been shown to be good.

(2) The longitudinal stability of the TCA is more non-linear than for the Reference H, and while it is similar at normal lift values, the TCA has considerably more pitch-up at higher lift.

(3) Longitudinal control effectiveness of the TCA is similar to the Reference H and the ratio of elevator effectiveness to horizontal tail effectiveness is approximately 0.3.

(4) The directional stability of the TCA is improved relative to Reference H at higher angles-of attack. The chine is effective for improving directional stability.

Summary

- Data Quality / Long-term Repeatability Good
- Longitudinal Stability
  - Same as Reference H at normal α_F's, more non-linear
  - Increased "pitch-up" at higher α_F's
- Longitudinal Control
  - Similar to Reference H ($\alpha_\delta \cong 0.3$)
- Directional Stability
  - Increased at higher α_F's with and without chines

Summary (Cont'd)

(5) The directional control effectiveness of the TCA rudder is the same as that of the Reference H rudder at low angles-of-attack, after taking factors, such as number of rudder panels deflected and vertical tail volume into account. However, rudder effectiveness was shown to be reduced at higher angles-of-attack.

(6) The lateral stability was shown to be reduced relative to the Reference H, which may be benefitial at low speeds for alleviating lateral control saturation.

(7) Lateral control effectiveness for the TCA was shown to be similar to the Reference H for negative trailing-edge flap deflections and was reduced by approximately 25% for positive trailing-edge flap deflections.

Summary (Cont'd)

- Directional Control
  - Same at low α_F's, reduced at higher α_F's
- Lateral Stability
  - Reduced relative to Reference H at all α_F's (may be good)
- Lateral Control
  - Similar to Reference H for negative trailing-edge flap deflections
  - Reduced ($\cong$ 25%) relative to Reference H for positive trailing-edge flap deflections

HSR - 1997 Aerodynamic Performance Workshop

Effect of Boattail and Sidewall Curvature on Nozzle Drag Characteristics

Francis J. Capone, Karen A. Deere,
Linda S. Bangert and Paul S. Pao

NASA Langley Research Center
February 25, 1997

HSR - 1997 Aerodynamic Performance Workshop

Program Objectives

- **Objectives:**
  - For a representative HSR 2D nozzle, determine the effects of
    - Nozzle external flap curvature and length
    - Sidewall boattail angle and curvature
  - Develop an experimental data base for 2D nozzles with long divergent flaps and low boattail angles
  - Provide validation data for isolated transonic nozzle boattail drag program CFD prediction studies

The NASA-industry team has sponsored several studies in the last two years to address the installed nozzle boattail drag issues. Some early studies suggested that nozzle boattail drag could be as much as 25 to 40 percent of the subsonic cruise. As part of this study tests have been conducted at NASA-Langley to determine the uninstalled drag characteristics of a proposed nozzle. The overall objective was to determine the effects of nozzle external flap curvature and sidewall boattail variations. This test would also provide data for validating CFD predictions of nozzle boattail drag.

HSR - 1997 Aerodynamic Performance Workshop
Model Scale Sizing Criteria

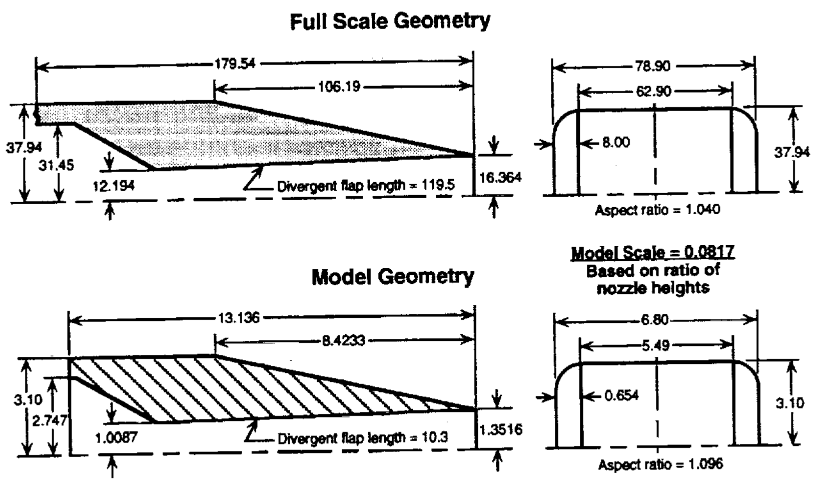

Full-scale geometry of the "Best DSM" nozzle chosen for the installed nozzle drag program is shown in the upper left of this figure. This nozzle, which comprises over 40-percent of the total nacelle is 78.90 by 74.88 inches with an aspect ratio of 1.040. In order to provide data in a timely fashion, tests were to be conducted on an existing propulsion simulation system used in the 16-Foot Transonic Tunnel. Of the three simulators, the on with the smallest aspect ratio was chosen for tests. This simulator is 6.80 by 6.20 inches with an aspect ratio of 1.096. From this, it was decided to use the height of the model for scaling purposes. This dimension was chosen because it gives the best representation of nozzle boattail closure. The resulting scale was 8.17%. From this scale, an appropriate reference area can be obtained for subsequent use in nondimensionalizing drag in order to produce a meaningful drag coefficient in terms of airplane drag counts.

HSR - 1997 Aerodynamic Performance Workshop

Nozzle Flap Definition

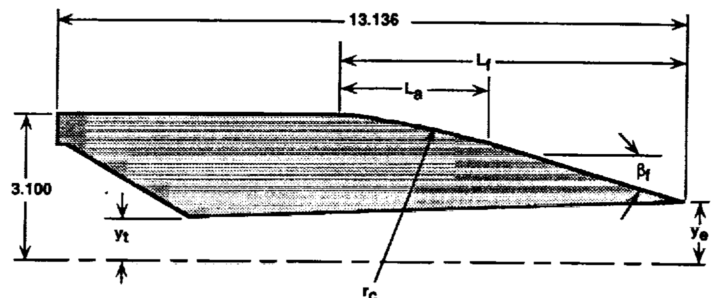

Parameter	Nozzle Flap						
	F1	F2	F3	F4	F5	F6	F7
L_f, in	8.4233	8.4233	8.4233	8.4233	6.7386	6.7386	8.4233
$r_c/r_{c,max}$	0.4	0.1	0.0	1.0	0.4	0.1	0.4
β_f, deg	16.379	12.882	11.719	23.437	20.298	15.974	20.527
y_t, in	1.0087	1.0087	1.0087	1.0087	1.0087	1.0087	0.6641
y_e, in	1.3516	1.3516	1.3516	1.3516	1.3516	1.3516	0.8898
A_t, in^2	11.0791	11.0791	11.0791	11.0791	11.0791	11.0791	7.2973
A_e, in^2	14.846	14.846	14.846	14.846	14.846	14.846	9.7736
A_e/A_t	1.34	1.34	1.34	1.34	1.34	1.34	1.34
A_e/A_{max}	0.36	0.36	0.36	0.36	0.36	0.36	0.36

This chart summarizes the various parameters used to define the nozzle external shape. The term L_f represents the length of the external flap of the nozzle. The baseline nozzle has a flap length of 8.4233 inches. Two nozzles with shorter flap lengths were also tested. Note that the overall length of the nozzle was not changed when nozzle flap length was varied. The boattail curvature parameter is $r_c/r_{c,max}$. Nozzles with curvatures from o to 100% were tested. A nozzle with no curvature would probably be the simplest to build since this flap would have a simple hinge joint. All the nozzles had the same internal contour, throat area and exit area. Thus changes in performance should only be attributed to external flow effects over the nozzle flaps.

The geometry of the sidewalls was defined in a similar manner.

HSR - 1997 Aerodynamic Performance Workshop

Configuration Matrix

Nozzle Config	Nozzle Flaps				Nozzle Sidewall			
	Flap	L_f/h_m	$r_c/r_{c,max}$	β_f, deg	Sidewall	β_{sw}, deg	$r_c/r_{c,max}$	Height
N-3	F-3	1.2	0%	11.719	S-1	4	0%	Full
N-2	F-2	1.2	10%	12.882	S-1	4	0%	Full
N-1	F-1	1.2	40%	16.379	S-1	4	0%	Full
N-4	F-4	1.2	100%	23.437	S-1	4	0%	Full
N-14	F-6	1.0	10%	15.974	S-1	4	0%	Full
N-13	F-5	1.0	40%	20.298	S-1	4	0%	Full
N-5	F-1	1.2	40%	16.379	S-2	6	0%	Full
N-6	F-1	1.2	40%	16.379	S-3	8	0%	Full
N-7	F-1	1.2	40%	16.379	S-4	6	10%	Full
N-9	F-1	1.2	40%	16.379	S-6	6	40%	Full
N-8	F-1	1.2	40%	16.379	S-5	8	10%	Full
N-10	F-1	1.2	40%	16.379	S-7	8	100%	Full
N-12	F-2	1.2	10%	12.882	S-8	4	0%	None
N-11	F-1	1.2	40%	16.379	S-8	4	0%	None
N-1 PSP	F-1	1.2	40%	16.379	S-1	4	0%	Full
N-11 PSP	F-1	1.2	40%	16.379	S-8	4	0%	None

This table summarizes the various nozzle configurations tested. For the first four configurations, nozzle curvature was varied with the nozzle baseline length being held constant. Note that boattail angle varies for these configurations from 11.719° to 23.437°. Nozzle curvature was also varied for the nozzles with the shorter flap length as indicated by the fifth and sixth configurations.

The effect of varying nozzle sidewall boattail angle and curvature were studied with the remaining configurations. Sidewall S-1 with no curvature and 4° boattail was the baseline sidewall. The height of the sidewall denoted "full" was fixed to a distance such that the nozzle flaps would not unport with the nozzle in the supersonic cruise position. In this position the nozzle flaps have a boattail angle of 0°. Some tests were conducted with a reduced height sidewall to determine what the penalty might be for having these large sidewalls. The height of the sidewall labeled "none" followed the contour of nozzle flap N1.

HSR - 1997 Aerodynamic Performance Workshop

Experimental Arrangement

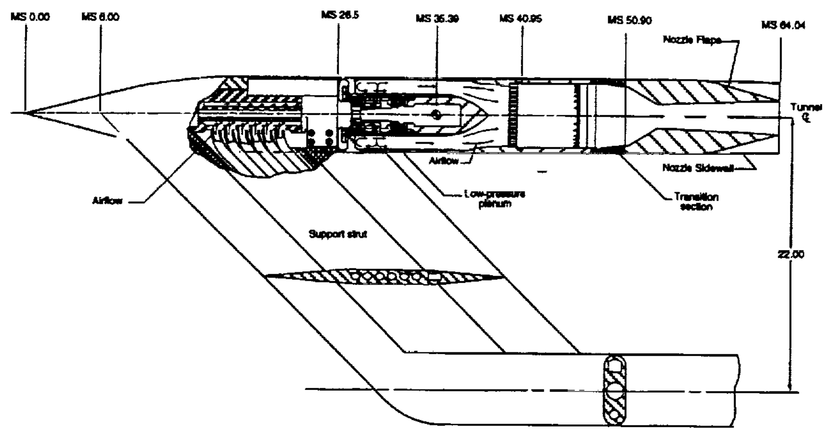

The two-dimensional propulsion air-powered simulation system is shown in this figure. This model is composed of three major components: a nose-forebody section, a centerbody section, and the nozzle. The nozzle connect station is at model station 50.90. The nose-forebody was nonmetric; that is it was not connected to the force balance. This simulation system is equipped with a flow transfer system that is designed to minimize the transfer of axial momentum across the force balance.

The nozzle is shown with the baseline sidewalls. Sidewall height was fixed so that the nozzle flaps would not unport with the nozzle at the supersonic cruise position (no nozzle boattail)

The nozzle upper or lower flaps were each instrumented with two rows of pressure tapes with 25 taps per row. Thus, nozzle pressure drag was determined from integrating 100 pressures. On one of the nozzle sidewalls, there were two rows of pressure taps with 20 taps per row.

For this investigation, nozzle drag is defined over that portion of the model from model station 50.90 to 64.04.

HSR - 1997 Aerodynamic Performance Workshop
CFD - PAB3D (version 13/ASM)

- Code Architecture
  - Modular multi-block structure w/grid sequencing
  - Multiple-to-one and patched interfaces
  - In-code calculations of integrated forces, moments, and flux quantities
- Code Performance Statistics
  - Compact memory requirements: 23 words per grid point
  - 38 m-sec (Cray-YMP) per iteration per grid point
  - Compatible with most workstations

PAB3D solves the three-dimensional Reynolds-averaged Navier-Stokes equations with a finite-volume formulation on structured multi-block grids. A grid sequencing scheme allows for automatic assessment of grid density on flow solutions. In addition to memory management, grid sequencing also allows for quick initial solutions and increased convergence rates.

One-to-one, multiple-to-one and general patching between block interfaces is accepted by the flow solver for the development of complex geometric grids. A conservative patching utility is used to determine the communication between block interfaces.

The in-code performance package supplies the user with integrated forces, moments and flux quantities in output file formats that are compatible with many standard graphics packages.

HSR - 1997 Aerodynamic Performance Workshop

CFD - PAB3D (version 13/ASM)

- Flow Solver Characteristics
  - Mixed Roe and van Leer schemes
  - Local time stepping and upwind biased with user-selected limiter options
  - Two-equation k-e or ASM Turbulence Models

The code allows the user to select between multiple flow solvers, limiters and boundary conditions at code run time. Generally, the Roe and van Leer schemes offer improved accuracy and quick convergence rates.

The flow solver has a robust two-equation k-e turbulence model and several anisotropic algebraic Reynolds stress models (ASM).

HSR - 1997 Aerodynamic Performance Workshop

CFD Solution Run-Times

Nozzle	Condition NPR=5	Hours Cray-YMP	Grid Level
N1	M=0.9	16.4	cut 222
N1	M=0.9	46	base (211 sequence)
N1	M=1.11	15.9	cut 222
N1	M=1.2	12.2	cut 222
N3	M=0.9	13.3	cut 222
N3	M=1.11	7.9	cut 222
N3	M=1.2	7.2	cut 222

This charts illustrates the time required on a Cray-YMP to develop converged solutions with the results in this presentation. This charts also exhibits the benefit of database reduction and grid sequencing.

For example, the first two records represent the solution of nozzle N1 at M=0.9 and NPR=5. A converged solution was developed within 16.4 hours on a cut grid. However, the solution was developed to the base level to quantify the effect of grid density. Nozzle drag decrease a mere 0.2 of a count in another 30 hours of Cray-YMP time. Since the solution appears to be minimally dependent on doubling the grid density beyond the cut 222 level, the remaining solutions were developed by sequencing on the cut grid only. This allowed for quicker solution times due to the substantially smaller memory requirement.

The base grid is a quarter plane representation of the experimental model with 1.57 million grid points in 9 blocks. Using a database reduction scheme, a cut 222 grid is generated by eliminating every other grid point in the i, j, and k directions. This cuts each grid dimension by 2, which decreases the grid count to 207,437 and substantially reduces the memory required to run the flow solver. The grid can be sequenced in each direction for improved convergence rates and for grid assessment. For example, the flow solver uses alternating points in the i direction and every point in the j and k directions in a 211 sequence. Generally, a user would begin sequencing on the cut 222 grid. A pattern of 222, 221, 211, and then 111, or no sequencing might be used to assess solution behavior as more points are utilized in a particular direction. The solution is developed until convergence requirements are met at each level. Once the solution is converged on the cut 222 grid, the solution may be extrapolated to the base grid and sequencing may again be utilized.

HSR - 1997 Aerodynamic Performance Workshop
Residual and Drag Convergence History

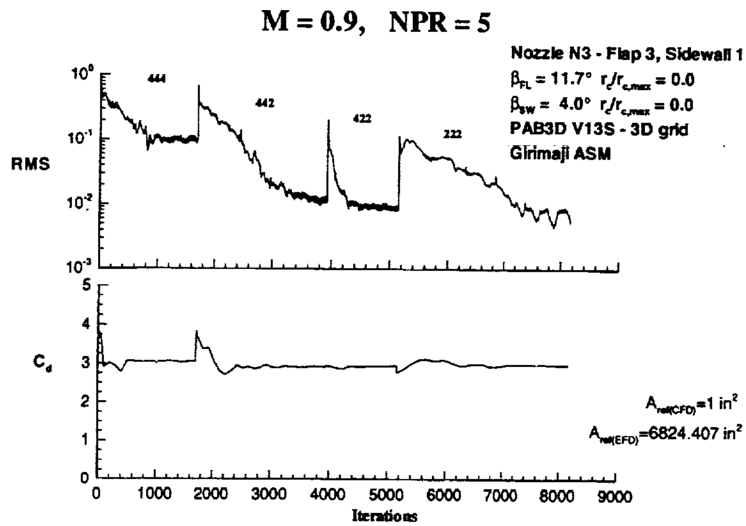

Typical convergence histories for Nozzle 3 are shown in the following three figures. Similar results were obtained for Nozzle 1.

This figure shows the convergence history for Nozzle N3 at M=0.9 and NPR=5. Spikes in the residual history exhibit locations of solution extrapolation to a finer grid level. Accordingly, small adjustments in drag coefficient, C_d, are observed at these locations, also.

The solution converges at the 222 grid level after 6500 iterations, with no further change in drag coefficient as the residual continues to drop. Drag coefficient increased a mere 1.2 percent from the 422 grid level to the 222 grid level.

Computational drag coefficient was calculated with a reference area of 1 in^2. Therefore, a reference area of A=6824.407 in^2 is used to convert to a scale comparable to experimental results.

HSR - 1997 Aerodynamic Performance Workshop
Residual and Drag Convergence History

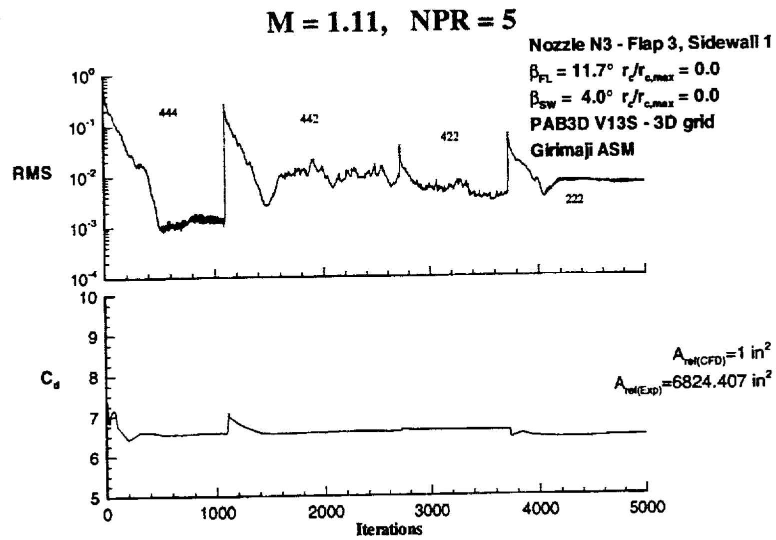

This figure shows the convergence history for Nozzle N3 at M=1.11 and NPR=5. Spikes in the residual history exhibit locations of solution extrapolation to a finer grid level. Accordingly, small adjustments in C_d are observed at these locations, also.

The residual drops 3 orders of magnitude on the 444 grid level. The residual then flattens and C_d remains unchanged after 500 iterations, suggesting convergence at this grid level. The solution converges at the 222 grid level after 4500 iterations. Drag coefficient decreased 2.3 percent from the 422 grid level to the 222 grid level.

HSR - 1997 Aerodynamic Performance Workshop
Residual and Drag Convergence History

M = 1.2, NPR = 5.0

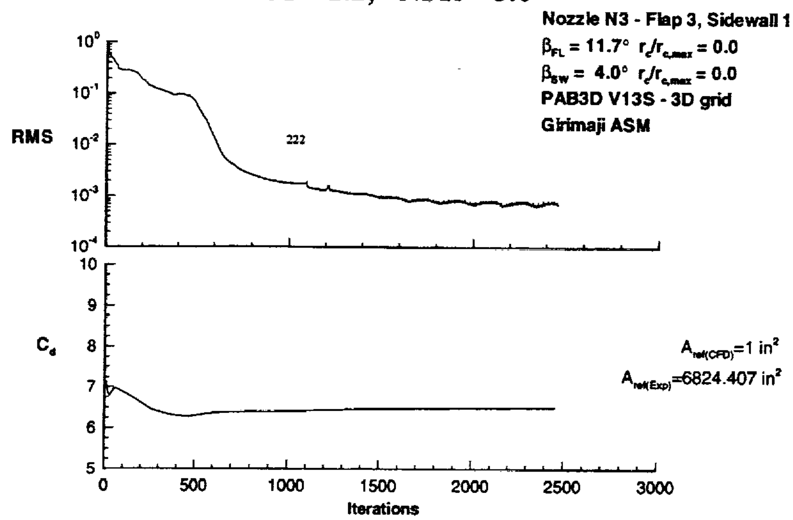

This figure shows the convergence history for Nozzle N3 at M=1.2 and NPR=5. Since minimal change in drag coefficient was apparent from the previous solutions, this solution was developed on the 222 grid level in an effort to minimize resources.

The residual drops 3 orders of magnitude and flattens after 1000 iterations. Drag coefficient remains constant after 1500 iterations. This suggests solution convergence at this grid level.

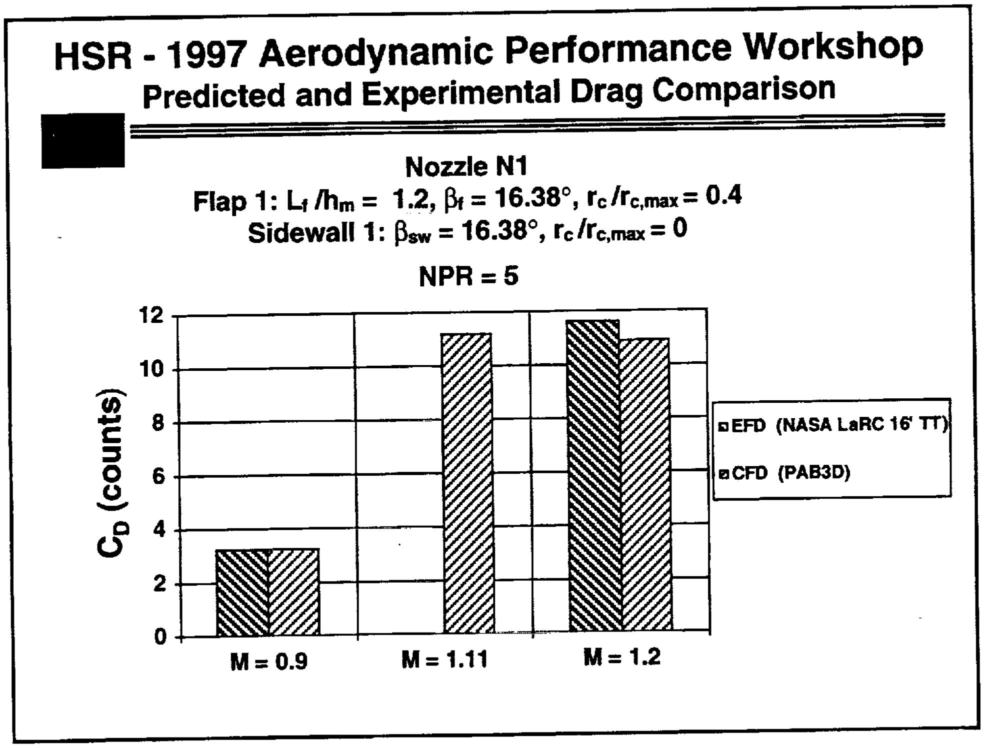

Nozzle N1 has a 40 percent flap curvature along the boattail. The predicted drag is in excellent agreement with experimental drag at M=0.9 and is within 0.7 of a count of experimental drag at M=1.2. PAB3D predicted a nozzle drag of 11.21 counts at M= 1.11.

HSR - 1997 Aerodynamic Performance Workshop
Predicted and Experimental Pressures Along Flap

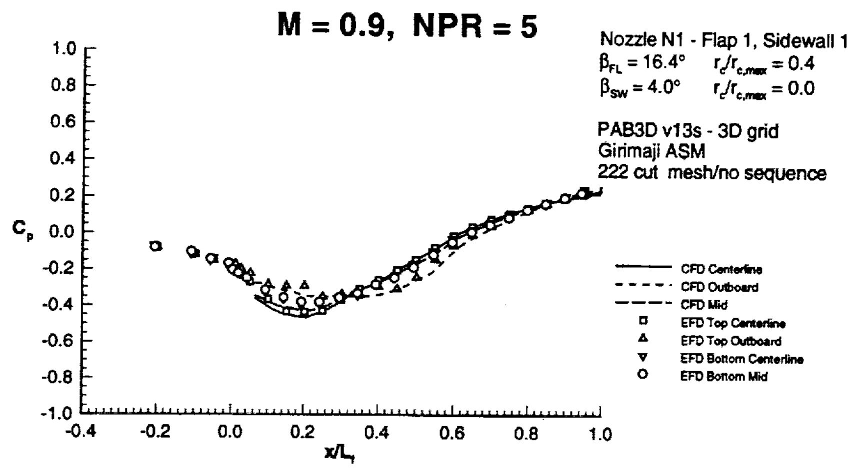

As expected from the agreement between nozzle drag, $C_{d(EFD)}$= 9.8 counts compared to $C_{d(CFD)}$=9.53 counts, the predicted pressures are in excellent agreement with experimental data at M = 0.9 and NPR = 5.

Data is compared along the flap centerline (z=0), at a flap outboard station (z=2.61 in) and at a flap 'mid' station (z=1.373 in) in this and the following pressure charts.

HSR - 1997 Aerodynamic Performance Workshop
Predicted and Experimental Pressures Along Flap

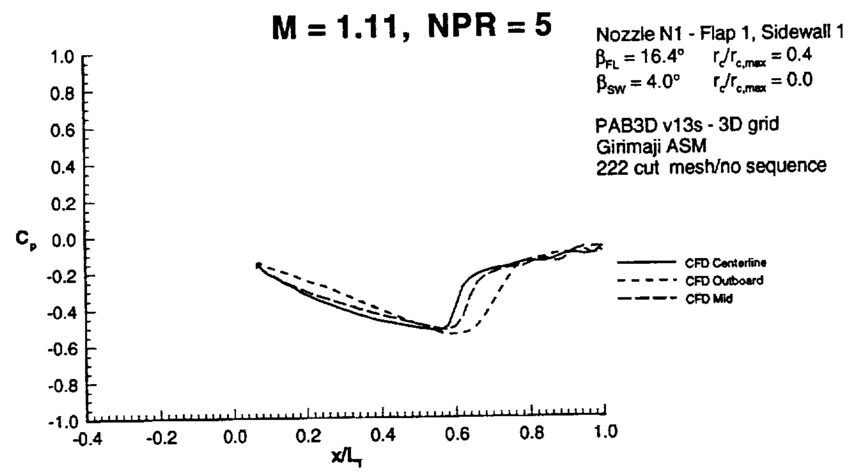

Predicted pressures exhibit the expansion and shock along the flap at three stations. Pressure differences between the stations suggest highly three-dimensional flow along the flap.

HSR - 1997 Aerodynamic Performance Workshop
Predicted and Experimental Pressures Along Flap

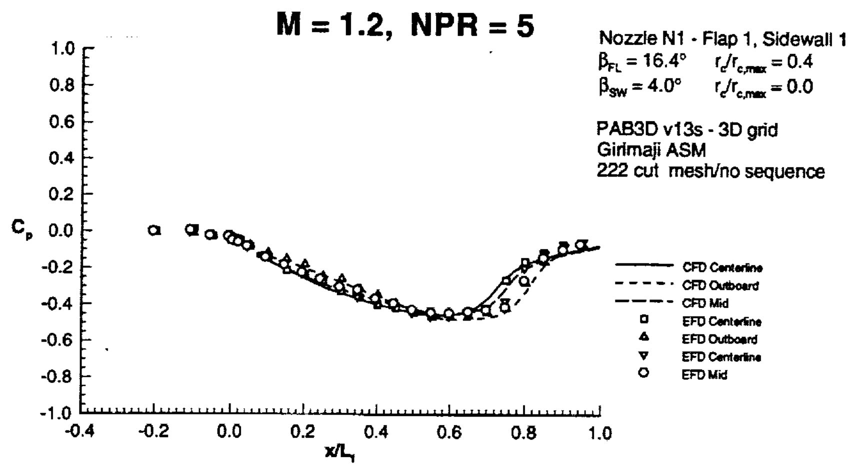

Predicted pressures are in good agreement with experimental data at M = 1.2 and NPR = 5. The largest difference in pressure occurs near x/L=0.8 at the outboard and mid stations.

HSR - 1997 Aerodynamic Performance Workshop
Predicted and Experimental Drag Comparison

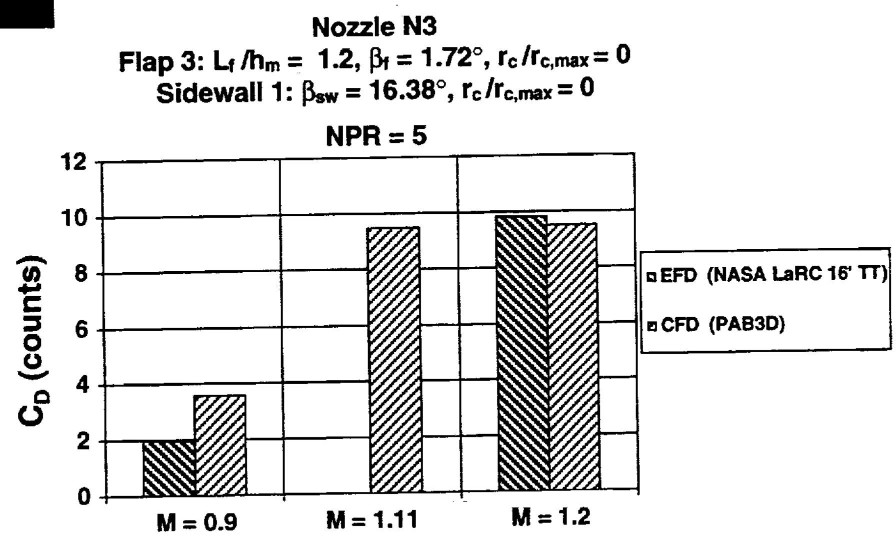

Nozzle N3 has a sharp corner (no curvature) leading into the flap. The predicted drag is within 0.3 of a count at M=1.2 and within 1.6 counts at M=0.9. PAB3D predicted a nozzle drag of 9.5 counts at M= 1.11, which is an improvement compared to Nozzle N1.

HSR - 1997 Aerodynamic Performance Workshop

Predicted and Experimental Pressures Along Flap

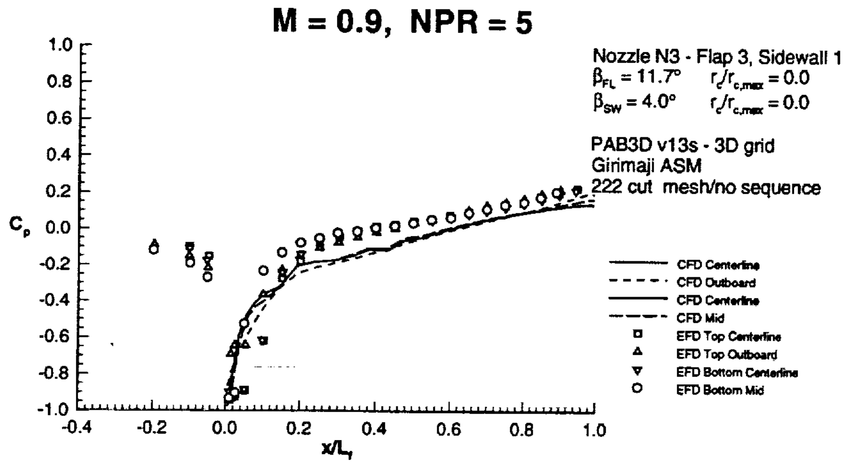

The pressure recovery along the flap is underpredicted compared with experimental data at M = 0.9 and NPR = 5. The higher experimental pressure recovery results in lower drag compared with predicted data, $C_{d(EFD)}$=1.97 counts compared to $C_{d(CFD)}$=3.56 counts.

HSR - 1997 Aerodynamic Performance Workshop
Predicted and Experimental Pressures Along Flap

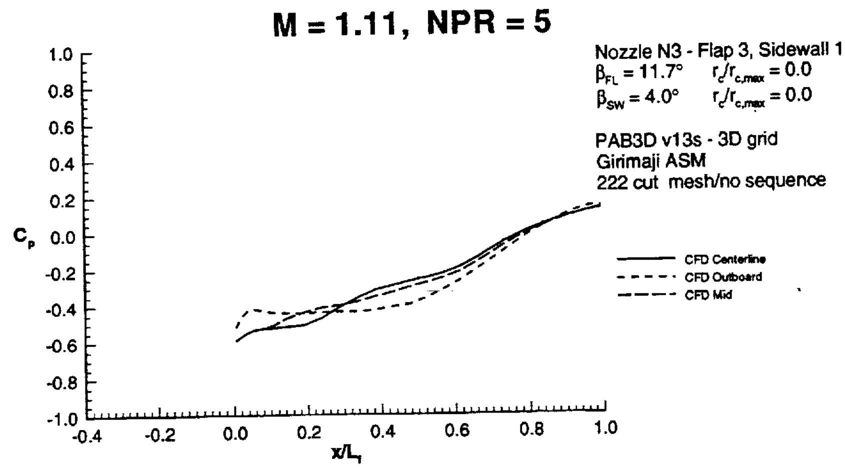

The pressure recovery along the flap corresponds to a drag of $C_{d(CFD)}$=9.49 counts.

HSR - 1997 Aerodynamic Performance Workshop

Predicted and Experimental Pressures Along Flap

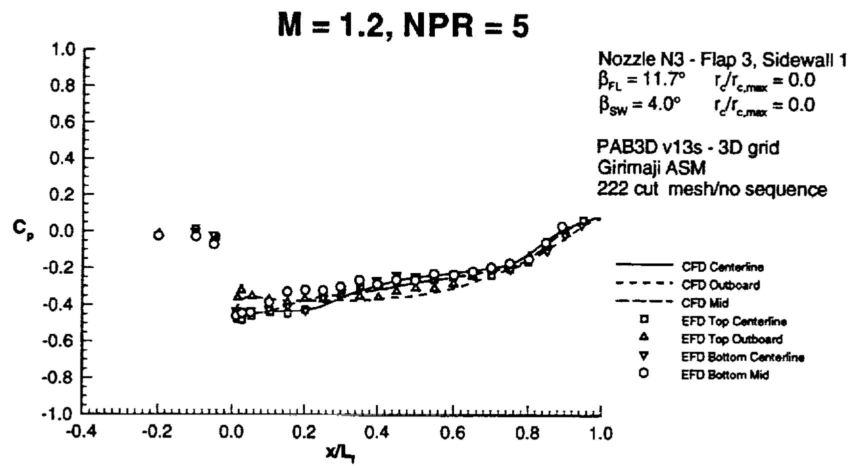

In general, the predicted pressures are in good agreement with experimental data at M = 1.2 and NPR = 5, which is expected with the good correlation between nozzle drag also, $C_{d(EFD)}$=9.8 counts compared to $C_{d(CFD)}$=9.53 counts.

HSR - 1997 Aerodynamic Performance Workshop
Comparison of Pressure Drag

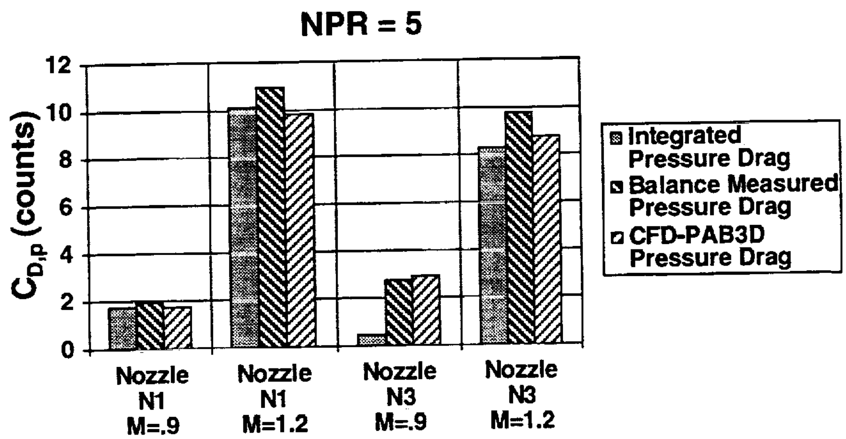

This figure compares pressure drag for each nozzle at M=0.9 and M=1.2, in an effort to understand the larger difference between predicted and experimental drag for Nozzle N3 at M=0.9, compared with the other solutions. Three methods were used for determining pressure drag: integrated pressures, balanced measured and computational fluid dynamics using PAB3D. It appears as though there is a discrepancy using the integrated method compared with balance measured and PAB3D predicted pressure drag methods. Work is in progress to discern the data.

HSR - 1997 Aerodynamic Performance Workshop

Nozzle Pressure Drag Breakdown - Nozzle N1

NASA Langley 16-Ft Transonic Tunnel Test 477

Flap 1: L_f/h_m = 1.2, b_f = 16.38°, $r_c/r_{c,max}$ = 0.4
Sidewall 1: b_{sw} = 16.38°, $r_c/r_{c,max}$ = 0

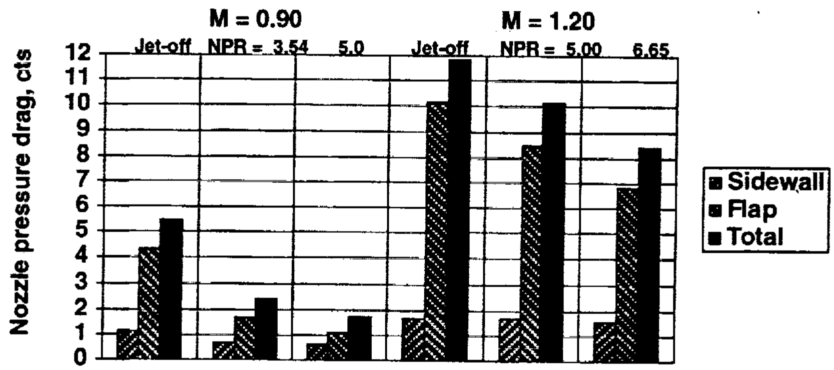

This figure illustrates the breakdown of pressure drag between the nozzle flaps and the sidewalls. Also shown is the effect of the jet on nozzle pressure drag. Note that the jet effects shown are typical for this class of nozzles and the breakdown of the pressure drags are similar for the other nozzle tested.

HSR - 1997 Aerodynamic Performance Workshop

Flap Curvature Effects on Flap Pressure Drag

NASA Langley 16-Ft Transonic Tunnel Test 477

Nozzle Flap $L_f / h_m = 1.2$

NPR = 5

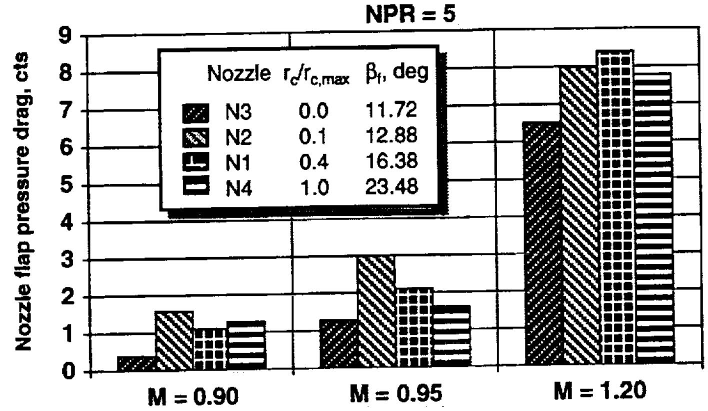

The effect of varying nozzle boattail curvature on the nozzle flap pressure drag is illustrated above for the nozzle with the baseline flap length. As can be seen, the nozzle N3 with no curvature had the least flap pressure drag. This result was somewhat surprising because previous experience has shown that nozzles with a sharp shoulder generally had higher drag. However, these nozzles had shorter external flaps and higher boattail angles (usually greater than 16°). In order to try to understand this result, pressure distributions on these nozzles will be shown in some subsequent figures.

HSR - 1997 Aerodynamic Performance Workshop

Flap Curvature Effects on Nozzle Drag

NASA Langley 16-Ft Transonic Tunnel Test 477

Nozzle Flap $L_f / h_m = 1.2$, NPR = 5

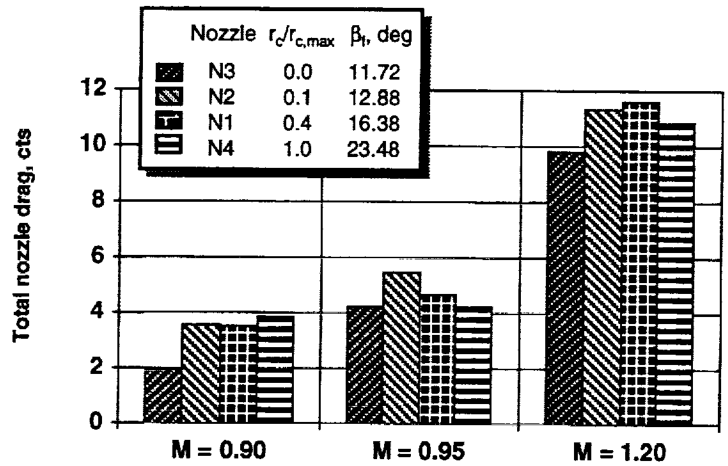

Similar results from the previous figure are also shown above. Total nozzle drag is the sum of the flap and sidewall pressure drags plus a skin friction drag (calculated as a simple flat plate friction drag).

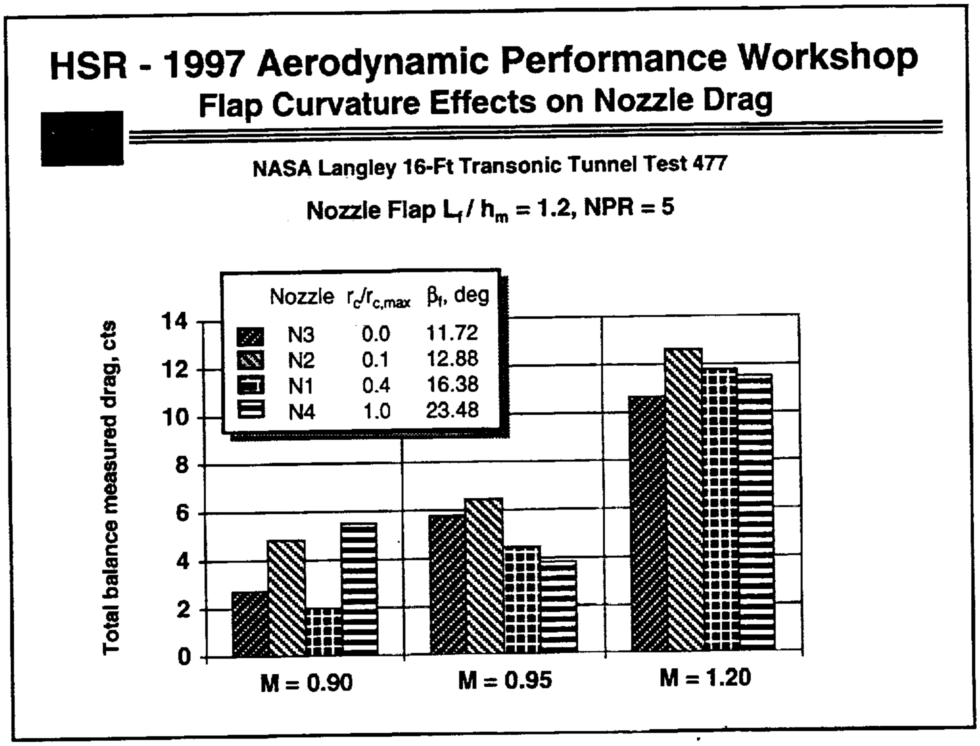

Similar results are obtained when the total nozzle drag measured by the force balance is considered.

HSR - 1997 Aerodynamic Performance Workshop

Flap Pressure Distributions

NASA Langley 16-Ft Transonic Tunnel Test 477

M = 0.90, NPR = 4.97, $\alpha = 0°$

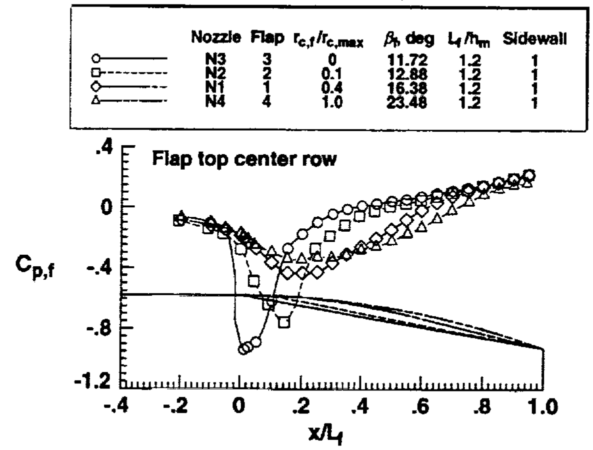

Pressure distributions along the center row of the top flap for nozzle N1, N2, N3, and N4 are presented at M = 0.9 and at a nozzle pressure ratio of 5. An NPR of 5 was used in the CFD installed nozzle study. Basically what is shown is that even though nozzle N3 with no curvature had the greatest expansion of flow about the nozzle shoulder, it had better pressure recovery characteristics than the other three nozzles.

It should be pointed out that these pressure distributions do not show the presence of shocks on the nozzle flap. This result is typical for most of the nozzles tested. This apparent lack of shocks on the nozzle probably results in the low boattail angles that most of the nozzles have.

HSR - 1997 Aerodynamic Performance Workshop
Flap Pressure Distributions

NASA Langley 16-Ft Transonic Tunnel Test 477

M = 0.95, NPR = 5.00, $\alpha = 0°$

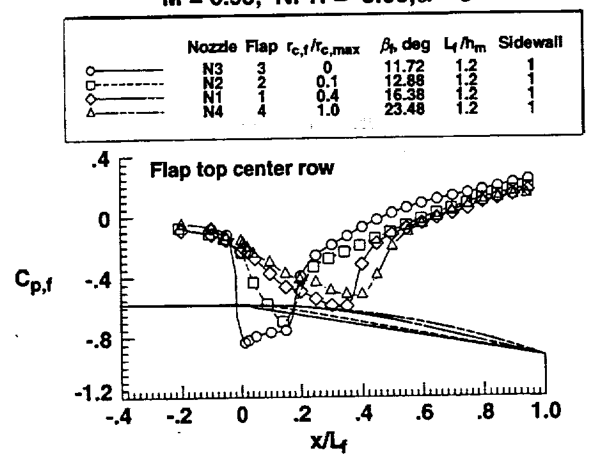

Similar results to those previously show were also obtained at M = 0.95.

HSR - 1997 Aerodynamic Performance Workshop
Flap Pressure Distributions

NASA Langley 16-Ft Transonic Tunnel Test 477

M = 1.20, NPR = 5.01, $\alpha = 0°$

	Nozzle	Flap	$r_{c,f}/r_{c,max}$	β_h deg	L_f/h_m	Sidewall
○	N3	3	0	11.72	1.2	1
□	N2	2	0.1	12.88	1.2	1
◇	N1	1	0.4	16.38	1.2	1
△	N4	4	1.0	23.48	1.2	1

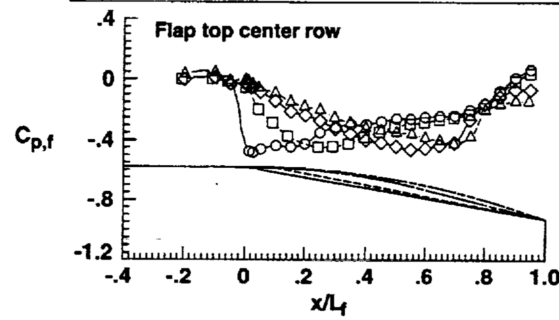

Similar results to those previously show were also obtained at M = 1.20.

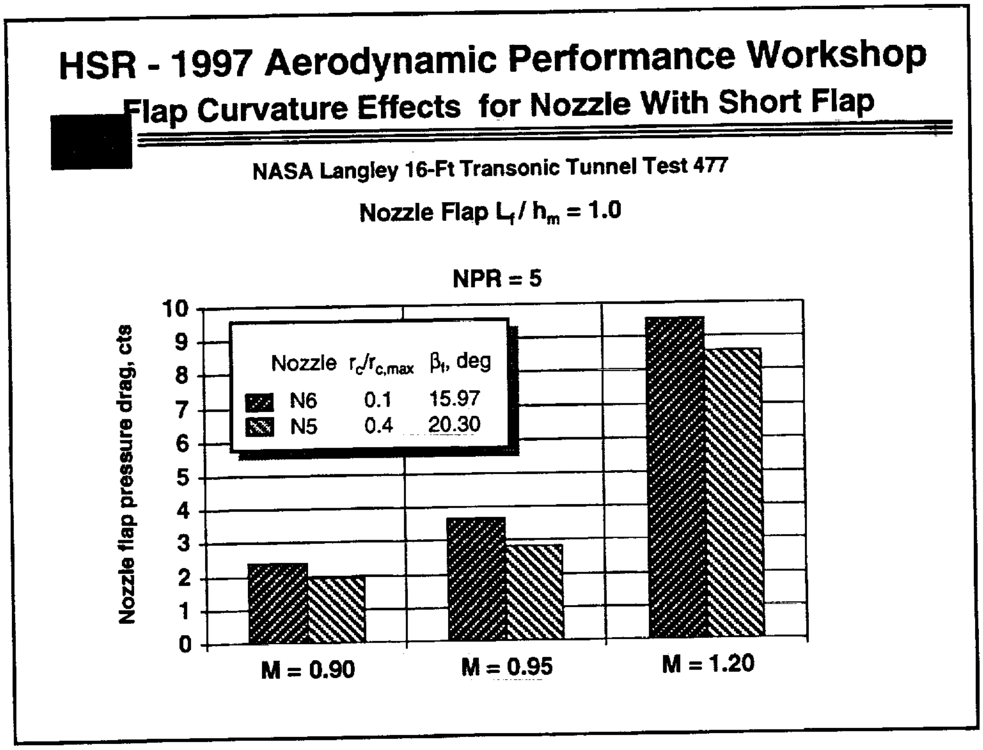

This figure shows flap pressure drag for the two nozzles tested with the smaller flap lengths. In contrast to previous results, lower flap pressure drag was obtained with nozzle N5 which had more curvature.

HSR - 1997 Aerodynamic Performance Workshop
Nozzle Flap Length Effects

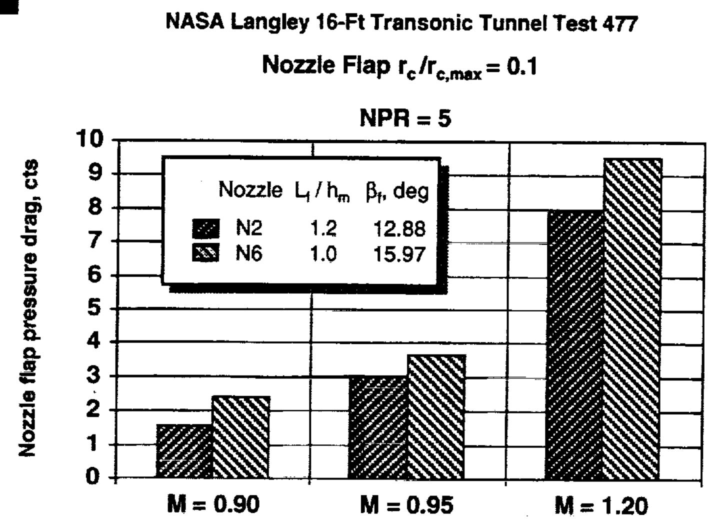

The effect of nozzle flap length is illustrated in this figure where flap pressure drag is compared between nozzle N2 and N6. Each of these nozzles had a curvature ratio of 0.1. As can be seen, the nozzle with the longer nozzle flap had lower drag at all the the Mach numbers tested. This was probably due to the lower boattail angle N2 had.

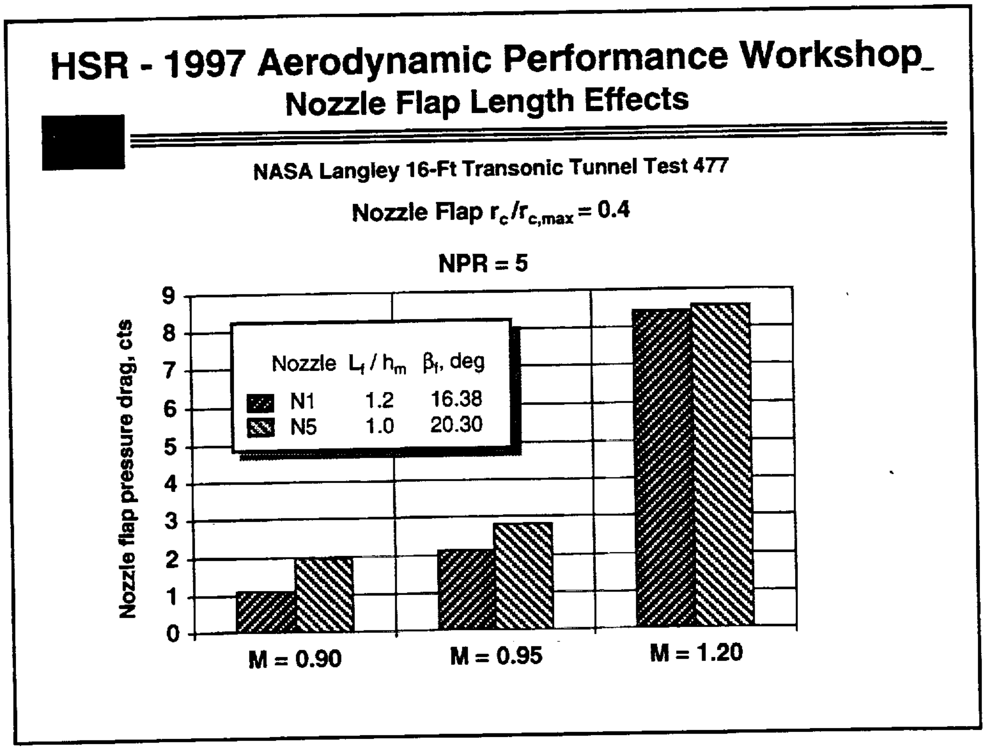

Results similar to those shown in the previous figure were obtained for nozzles N1 and N5. These nozzles had a curvature ratio of 0.4.

HSR - 1997 Aerodynamic Performance Workshop
Nozzle Sidewall Boattail Angle Effects

NASA Langley 16-Ft Transonic Tunnel Test 477

Nozzle Flap $r_c/r_{c,max} = 0.4$

NPR = 5

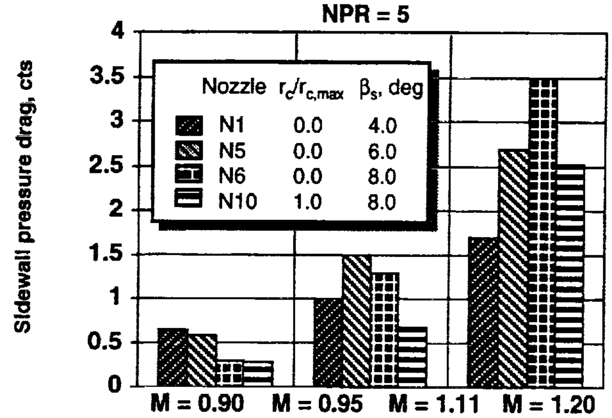

This figure summarizes the effect of sidewall boattail angle and curvature on sidewall pressure drag. At M = 0.90, nozzle N6 with a 8° boattail angle had the lowest sidewall pressure drag. At M = 1.2, just the opposite was true. At this mach number, nozzle N6 had about 2.3 times as much drag as nozzle N1 with the 4° boattail. Although the 4° boattail sidewall was considered to be the baseline, it is probable that the boattail angle will have to ber as much as 8° in order to house nozzle actuation hardware.

Putting full curvature on the sidewall with the 8° boattail resulted in a one count pressure drag reduction. Sidewalls with full curvature are feasible for the full scale aircraft since the sidewalls are fixed.

HSR - 1997 Aerodynamic Performance Workshop
Sidewall Pressure Distributions

NASA Langley 16-Ft Transonic Tunnel Test 477

M = 0.90, NPR = 5.01, $\alpha = 0°$

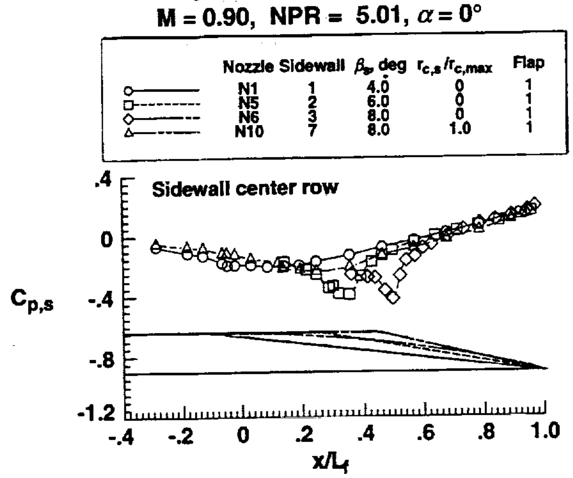

Pressure distributions along the center row of the sidewall for nozzle N1, N5, N6, and N10 are presented at M = 0.9 and at a nozzle pressure ratio of 5. These results are similar to thsose already shown for the nozzle flaps. Even though nozzle N6 with the 8° sidewall boattail had the greatest expansion of flow about the nozzle shoulder, it had excellent pressure recovery characteristics such that sidewall drag was lower.

HSR - 1997 Aerodynamic Performance Workshop
Sidewall Pressure Distributions

NASA Langley 16-Ft Transonic Tunnel Test 477

M = 0.95, NPR = 5.01, α = -0.1°

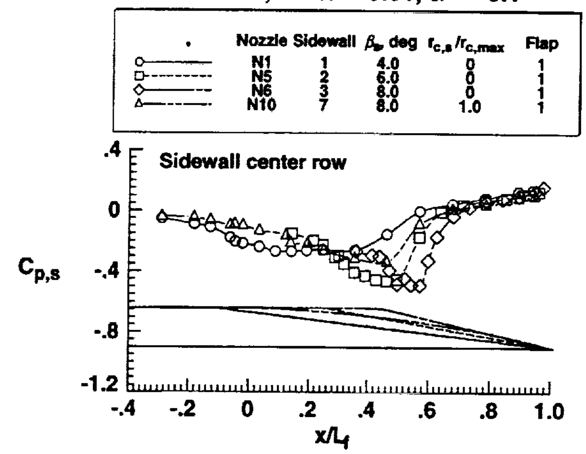

Similar results to those previously show were also obtained at M = 0.95

HSR - 1997 Aerodynamic Performance Workshop

Sidewall Pressure Distributions

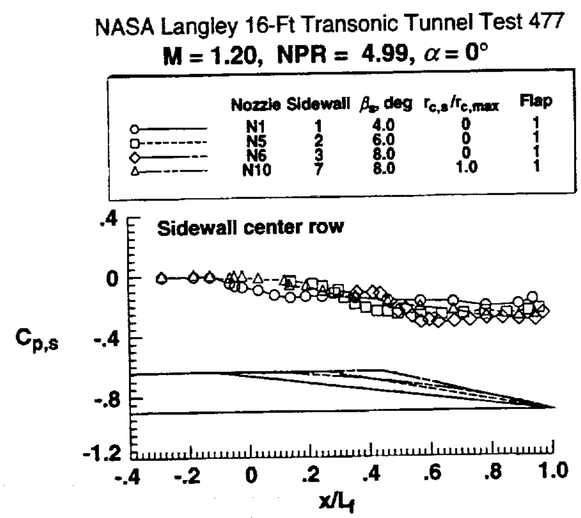

At M = 1.2, it appears as though pressures are lower on nozzle N6 with the 8° sidewall boattail. This lower pressure is acting over most of the sidewall and causing the higher drag.

HSR - 1997 Aerodynamic Performance Workshop

Nozzle Sidewall Curvature Effects

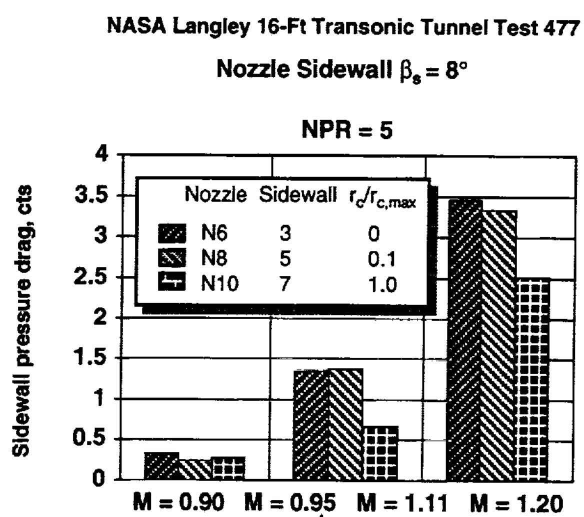

This figure illustrates the effect of sidewall curvature for those sidewalls with 8° boattail angle. At all Mach numbers, the sidewall with a curvature ratio of 1 had the lowest sidewall pressure drag.

HSR - 1997 Aerodynamic Performance Workshop
Nozzle Sidewall Height Effects

NASA Langley 16-Ft Transonic Tunnel Test 477

Nozzle Sidewall $\beta_s = 4°$, $r_c / r_{c,max} = 0$

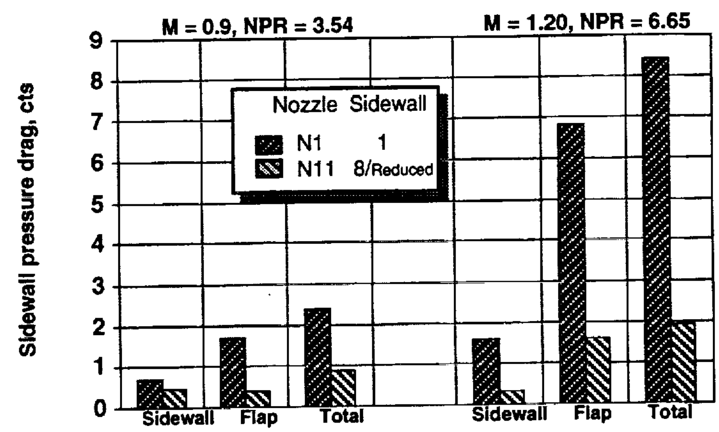

It was previously stated that the height of the sidewall was fixed to a distance such that the nozzle flaps would not unport with the nozzle in the supersonic cruise position. In this position the nozzle flaps have a boattail angle of 0°. Some tests were conducted with a reduced height sidewall just to see what the penalty might be for having these large sidewalls. The reduced height sidewall followed the contour of nozzle flap N1. As can be seen in the above figure, not only was sidewall pressure drag dramatically reduced, so was the flap pressure drag.

HSR - 1997 Aerodynamic Performance Workshop
Summary

- All nozzles exhibited expected pressure distributions. At most test condition, there were no shocks or shock induced separation
- Excellent corelation between experimental and CFD results were obtained
- The nozzle with an external flap with a sharp shoulder (no curvature) had the least pressure drag
- For the nozzle with a sidewall with 8° boattail angle, pressure drag increased from 0.3 to 3.5 counts from M = 0.9 to 1.2.

Development Of TCA Flight Drag Polars For Airplane Performance

Chester P. Nelson
Eric E. Adamson
HSCT Aerodynamics
Boeing Commercial Airplane Group
Seattle, Washington

A

1997 HSR Aerodynamic Performance Workshop
February 25-28, 1997
NASA Langley Research Center, Hampton, VA

Development Of TCA Flight Drag Polars For Airplane Performance

Chester P. Nelson*
Eric E. Adamson**
Boeing Commercial Airplane Group
P.O. Box 3707, MS 6H-FK
Seattle, WA 98124-2207

Abstract:

In early 1996 the NASA-Industry High Speed Research Technical Integration team released the final definition of the HSCT Technology Concept Airplane (TCA). This configuration represents the integration of current inputs from all technical disciplines into a realistic High Speed Civil Transport concept. This paper reviews the development and content of the high speed aerodynamics inputs to the TCA sizing and flight performance predictions. The paper also summarizes subsequent detailed analysis work, CFD, and TCA wind tunnel test data that are now being used to assess the drag levels of the "status" airplane (i.e. without projections). A bottoms-up assessment of the high speed drag technology projection is shown to identify reasonable sources of drag improvements that would meet the target levels. Sources of uncertainty in the current HSCT high speed drag predictions are outlined, and areas for risk reduction in future performance predictions are identified.

* Lead Engineer
**Senior Engineer
HSCT High Speed Aerodynamics
Configuration Development Group

TCA Flight Drag Polars For Airplane Performance

- High speed performance drag polar build-up process
- Relative magnitude of HSCT drag and lift components
- Performance polar technology projection assumptions
- TCA "Status" drag and uncertainty sources
- Summary

Introduction:

In early 1996 the NASA-Industry High Speed Research Technical Integration team released the final definition of the HSCT Technology Concept Airplane (TCA). This configuration represents the integration of current inputs from all technical disciplines into a realistic High Speed Civil Transport concept. The TCA replaces the Boeing "Reference-H" and McDonnell-Douglas "M2.4-7A" designs used previously as parallel HSR baselines (primary and alternate, respectively). The certainty with which the TCA's external lines and aerodynamic parameters correctly reflect the characteristics of a production HSCT is critical for assessing the continued viability of the program, and for correctly down-selecting long lead-time items such as propulsion components.

This paper reviews the development and content of the high speed aerodynamics inputs to the TCA sizing and flight performance predictions. This discussion includes a review of the "technology projection" assumptions and a bottoms-up assessment of potential drag improvements required to meet the target levels. Subsequent detailed analysis work, CFD, and TCA wind tunnel test data that are now being used to assess the drag levels of the "status" airplane (i.e. without projections) are summarized. Sources of uncertainty in the current HSCT high speed drag predictions are outlined, and areas for risk reduction in future performance predictions are identified.

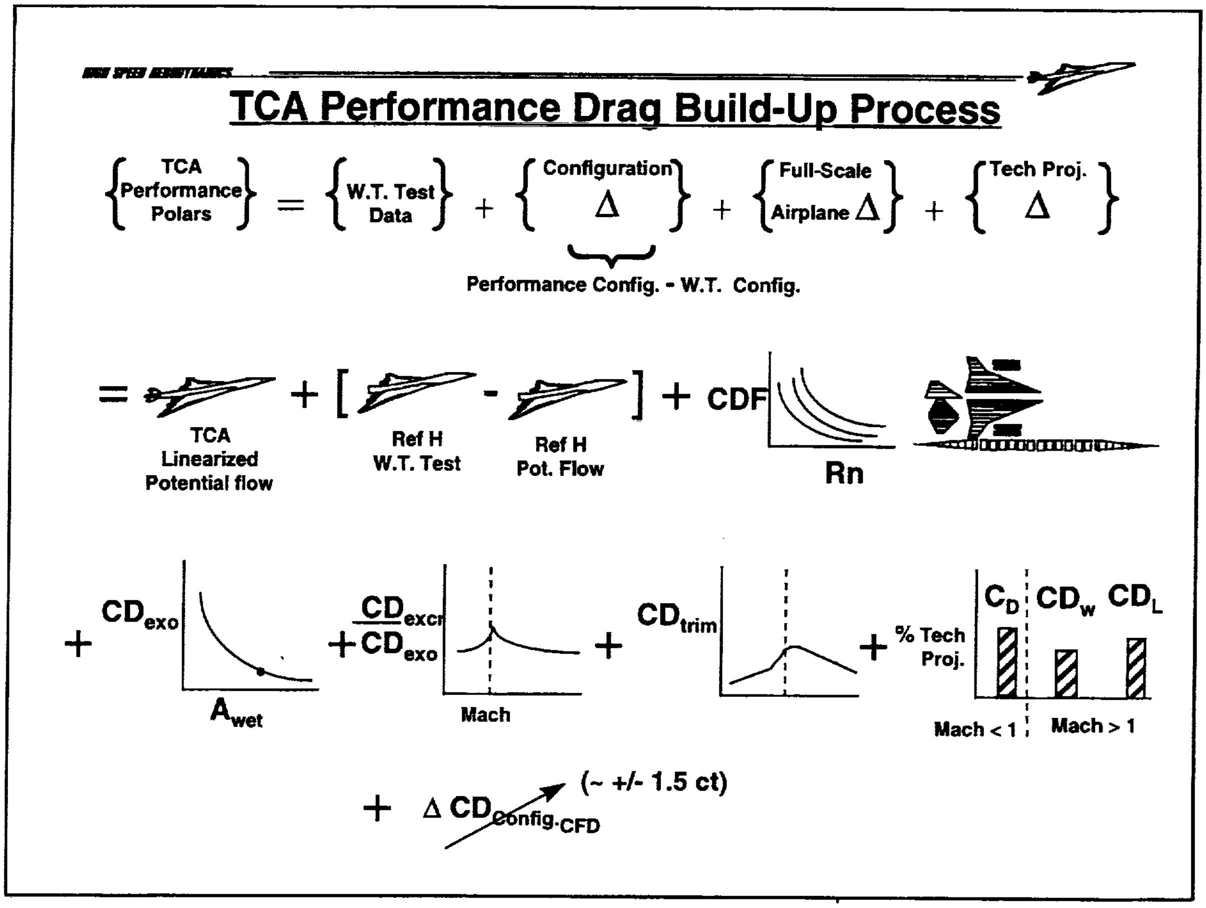

The process followed in building up the high speed aerodynamics inputs for the TCA was essentially identical to that used for airplane level TI trades. This process anchors the drag polars to available wind tunnel test data while accounting for increments between the wind tunnel model and a full scale airplane in flight. These increments include all configuration differences, skin friction changes due to Reynolds number, trim and excrescence drags, and a projection of future drag reduction. It can be seen by rearranging the terms in the first equation above that the geometry related increment is equal to the computed drag of the full TCA plus the difference between the measured and computed results for the reference test model. The wind tunnel data for the TCA polar build-up was from the "Reference-H" model. The skin friction at flight Reynolds number was computed using a strip-wise summation of the Karman-Schoenherr flat plate skin friction with the Sommer-Short compressibility correction, assuming an adiabatic wall. An allowance was made for excrescence ("protuberance drag") approximating that of current subsonic transports at incompressible speeds (7% of skin friction). This incompressible value was scaled versus Mach to account for compressibility. The high speed polars used a normalized trim drag allowance vs. Mach which was based on previous detailed analyses of the Ref.-H and B-2707. Technology projections were added based on a tops-down L/D assessment. CFD was employed as a "numerical wind tunnel" on the final geometry to confirm that additional drag had not inadvertently been incurred in "real flow" during lofting of the linear design. (This generally results in CFD-based adjustment of less than +/- 1.5 counts at Mach 2.4.)

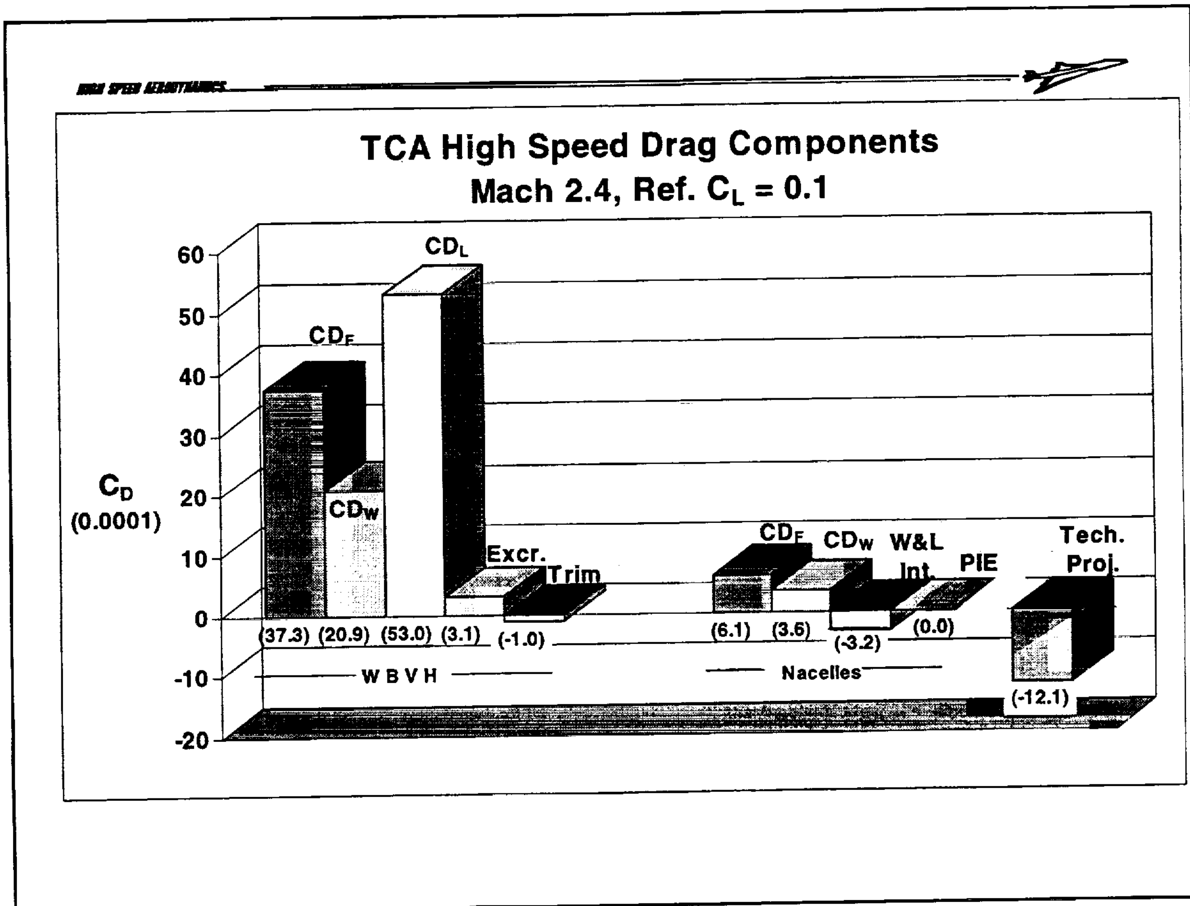

The chart above illustrates the relative magnitudes of the various components of the resulting TCA drag polars used in the configuration sizing and mission performance analysis for the Mach 2.4 cruise condition.

Several facts are immediately noted. One is that the majority of the cruise drag is in the areas of skin friction and drag due to lift. Roughly one third (16 counts) of the drag due to lift is due to ideal incompressible induced drag. The remainder is vortex drag (span load efficiency), and wave drag due to lift. While non-linear optimization can significantly reduce the drag due to lift term, the substantial skin friction level is a result of configuration wetted area and cannot be significantly reduced without the application of laminar flow technologies which are not included in the TCA definition. The large size of the skin friction term relative to the total high speed aerodynamics technology projection means that accurately predicting the skin friction in flight at combined high Reynolds number /Mach number conditions is of enough importance to warrant more attention. That is to say for example that the potential drag error incurred by a 4% uncertainty in the skin friction component alone is equal to a 30% shortfall in the gain projected for direct wing-body non-linear optimization. Differences between the various flat plate skin friction handbook calculation methods, various Navier-Stokes CFD solutions, and wind tunnel measured Cdmin levels easily cover a range of +/- 4 to 5% of the friction drag.

Another fact to take note of is that the successful nacelle installation design of the TCA results in favorable nacelle pressure field wave and lift interference nearly canceling the nacelle's isolated wave drag.

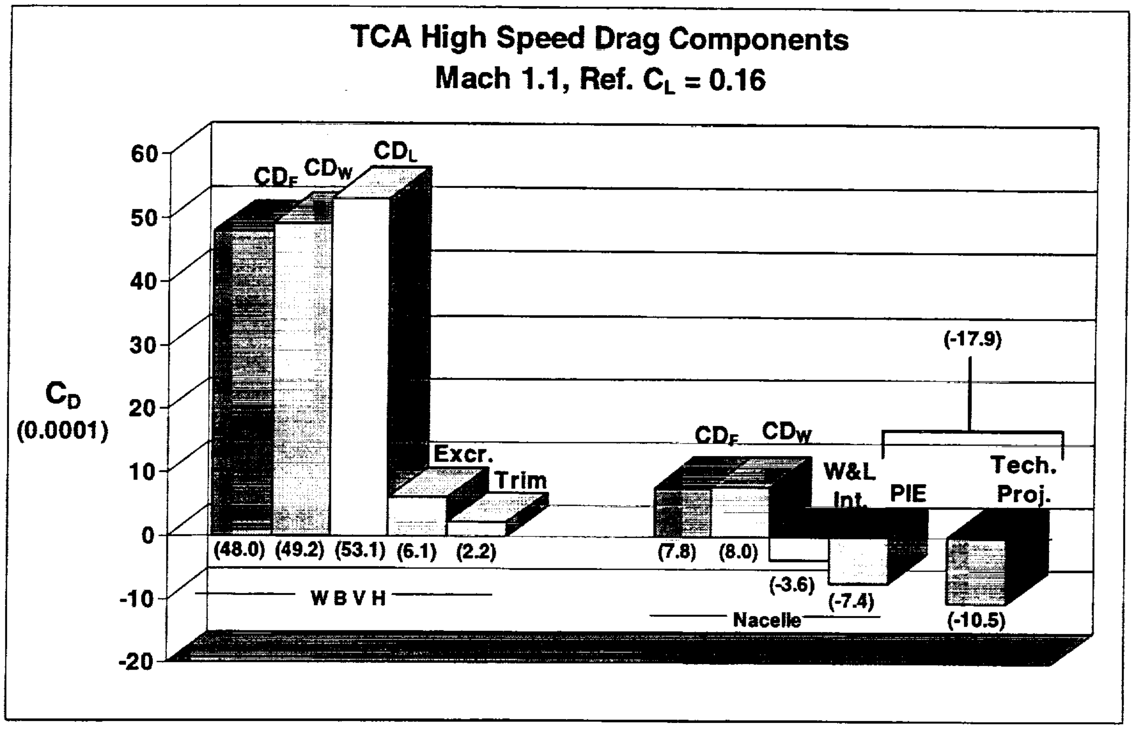

The above charts illustrates the equivalent drag component break-out for the typical transonic acceleration condition at Mach 1.1, CL=0.16. The large rise in the zero-lift wave drag component near Mach one is evident. There is a corresponding increase in the excrescence drag level and the nacelle wave drag. The favorable nacelle interference is only slightly greater than the supersonic cruise value so it no longer calcels out the isolated wave drag of the nacelles.

The technology projection near Mach 1 is scaled up to remain the same percentage improvements in wave drag and drag due to lift as in the supersonic cruise tops-down analysis. While the resulting projection level is very large (about 18 counts) it is believed that a strong favorable spillage/bypass interference term will be able to make up nearly half of this amount. This assumption is based on test data from sting-mounted nacelles under a Ref.H model wing in the ARC 11Ft tunnel. Additional thrust-drag accounting details, CFD validation, and spillage/bypass test data with captive nacelles (I.e. with wing-mount and diverters present) will be required before the potential large favorable effects are understood well enough for them to be bookkept as part of the "status" flight polar. Another potentially favorable Propulsion Induced Effect ("PIE") that is not well enough quantified to justify inclusion in the TI polar build-up is the nozzle boattail and exhaust plume interference pressures on the closing aft fuselage. For the time being all of these PIE effects are lumped in with the transonic drag technology projection.

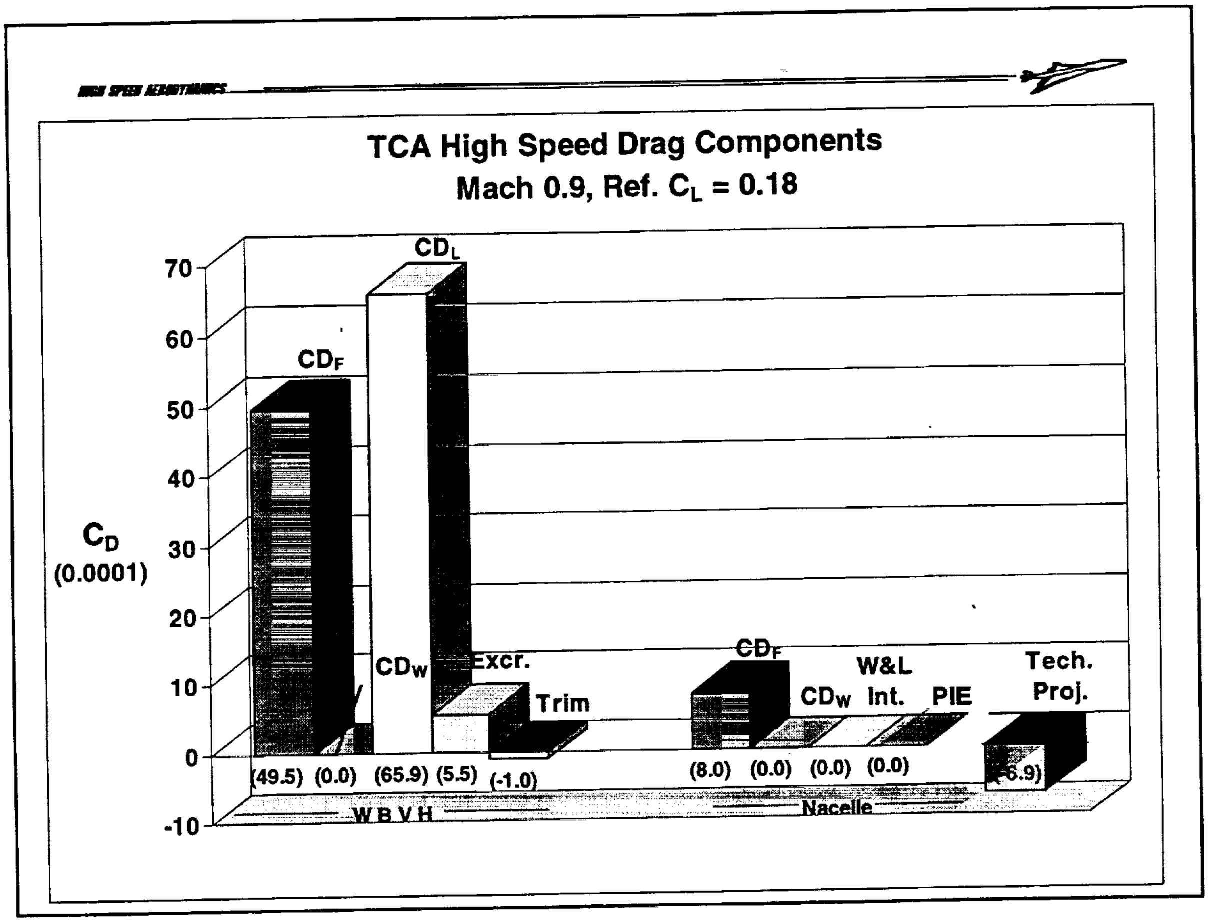

The equivalent drag components for the TCA's subsonic "over-land cruise" condition at Mach 0.9 are shown above. The reference CL of 0.18 was chosen to approximate the average of heavy and light airplane subsonic cruise legs, climbs, and descents. The zero lift wave drag terms, nacelle wave and lift interference terms and PIE terms are all assumed equal to zero at Mach 0.9. Nacelle on/off wind tunnel comparison data on previous configurations has shown that a favorable increment in lift at alpha would probably be present on the TCA but that it may be accompanied by a corresponding increase in pressure drag so there is no net favorable nacelle interference credited to the drag polar.

Theoretically, AERO2S or similar panel method code could be used to obtain preliminary design ("PD") estimates of the drag due to lift at these conditions, but the leading edge suction levels predicted by such codes tend to be less accurate at locally compressible Mach numbers, especially with the significant bluntness of the TCA inboard airfoils. In lieu of a robust calibrated PD drag code for the 0.9 to 1.0 Mach range, drag polars for the TCA were created using Ref.-H's NTF wind tunnel data adjusted for aspect ratio and wetted area differences. The Ref.-H dragrise shape was also assumed up to Mach 1.1, beginning at around Mach 0.95-0.98. The TCA polars were not penalized for the more triangular span load of the TCA relative to the Ref.-H, nor were any possible adverse off-design aeroelastic deflections taken into account. Leading and trailing edge flap effectiveness equal to that of the Ref.-H was also assumed.

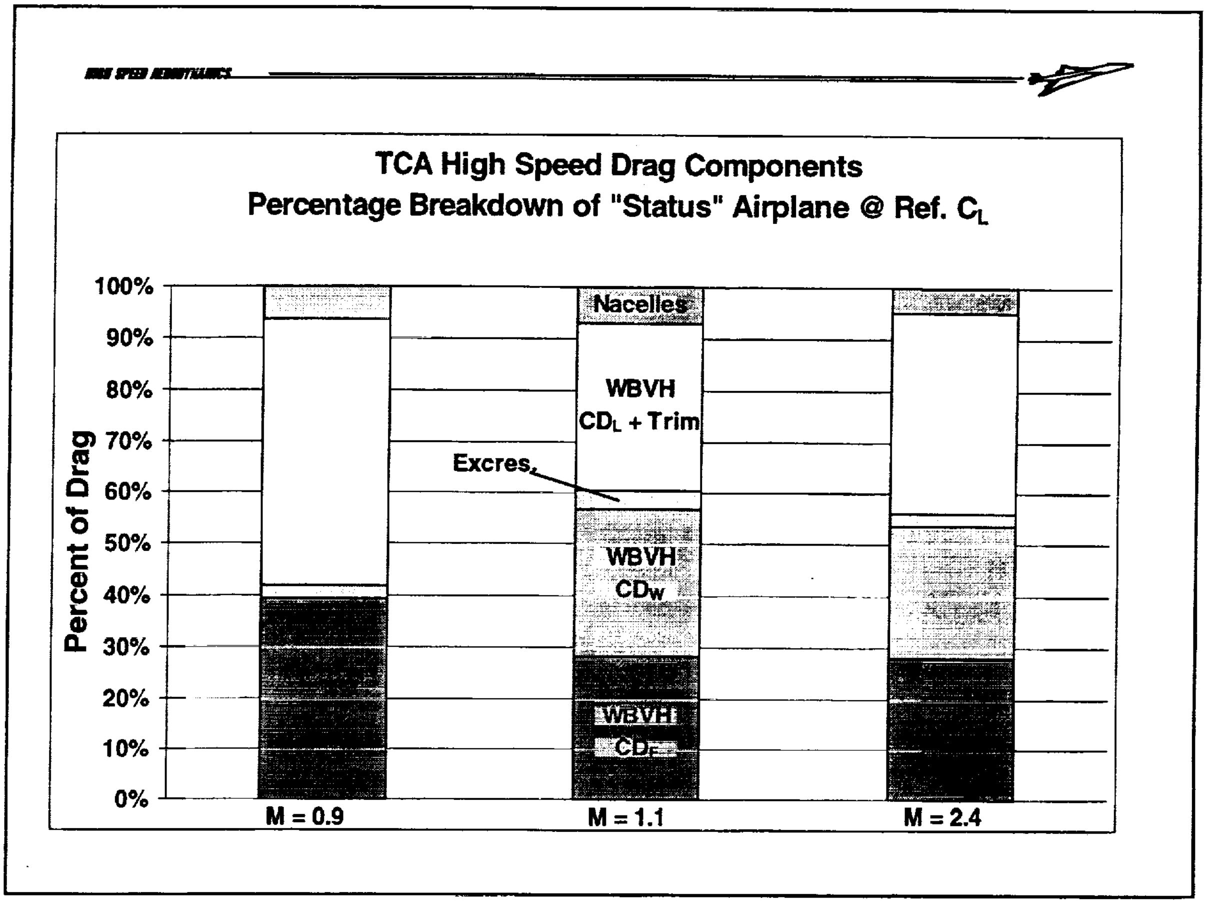

The relative proportion of drag due to each major physical component is shown above at all three Mach numbers. The drop in skin friction and increase in wave drag with increasing Mach is obvious when plotted in this manner as percents of the total drag.

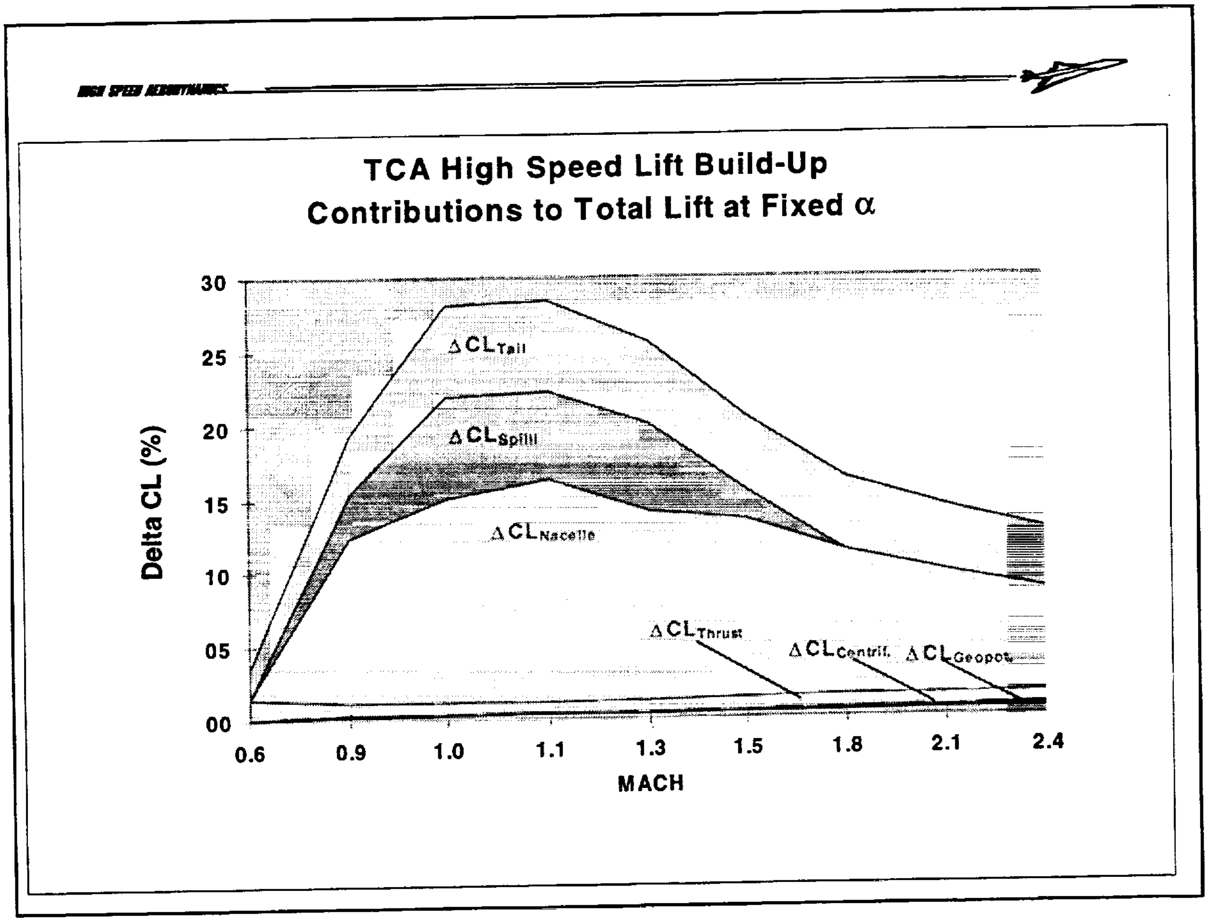

During the preparations for performing non-linear CFD optimizations on the TCA baseline geometry, the choice of a reference CL as the "cruise point" for the optimization was the topic of considerable discussion. Numerous questions were raised about the expected differences between total configuration lift, the wing-body-nacelle lift, and the lift contribution of the TCA wing-body alone. The chart above illustrates the large amounts of lift that may be accounted for by sources other than the wing-body. The performance and size optimization program used to select the final wing area and engine thrust of the TCA was not at the time coded to account for the effects of geopotential altitude, orbital velocity, and the downward component of the nozzle gross thrust vector. The effective "lift" contributions of these terms, while small, are not negligible and have been included in the chart above.

HSCT High Speed Aero Technology Projection

- Objective, Tops-Down Method, Doesn't Depend On "Status"
- "Optimum" Is Linear Theory Physics Based
- Configuration Dependent L/D, Showing CDo and CDL Terms
- "Target" is % of Theory Judged Achievable With...
  - Fixed General Arrangement
  - MDO Geom. Constraints

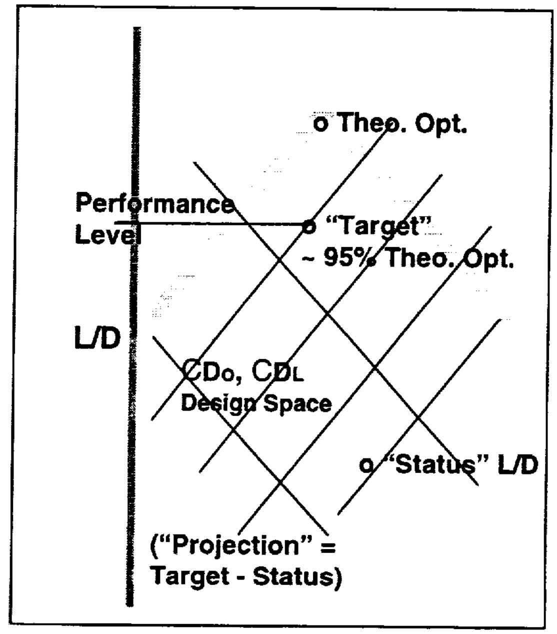

The "aerodynamic technology projection" is a key part of the polars. At supersonic speeds the projection is split between zero lift drag (CDo) and drag due to lift (CDL) improvements. A fixed projection of roughly 6% L/D is applied subsonically, and an excrescence improvement of 20% is assumed at all Mach numbers. The supersonic cruise projection was formulated based on a tops-down method (by R. M. Kulfan) that uses the overall geometric parameters of a given configuration to determine a theoretical "best possible L/D" assuming complete freedom to optimize the aerodynamic shape within the bounds of the wing-body general arrangement. This theoretical optimum is then adjusted downward to account for the fact that additional multi-disciplinary geometry constraints will be required and that some shape changes which could improve cruise drag will be negated by off-design penalties. With input from the HSR Configuration Aerodynamics (CA) team, the TCA's projected performance target level was fixed at a consensus level of about 95% of the theoretical optimum.

It should be noted that using this approach the total projected performance is defined as a specific L/D level that does not depend on knowing the performance of the "status" (unprojected) airplane--only its gross geometric parameters (span, length, volume, cross-sectional area, nacelle size, etc.). The size of the "projection increment" itself is simply the difference between the "target performance" level and the current best assessment of the airplane's status at full scale flight conditions.

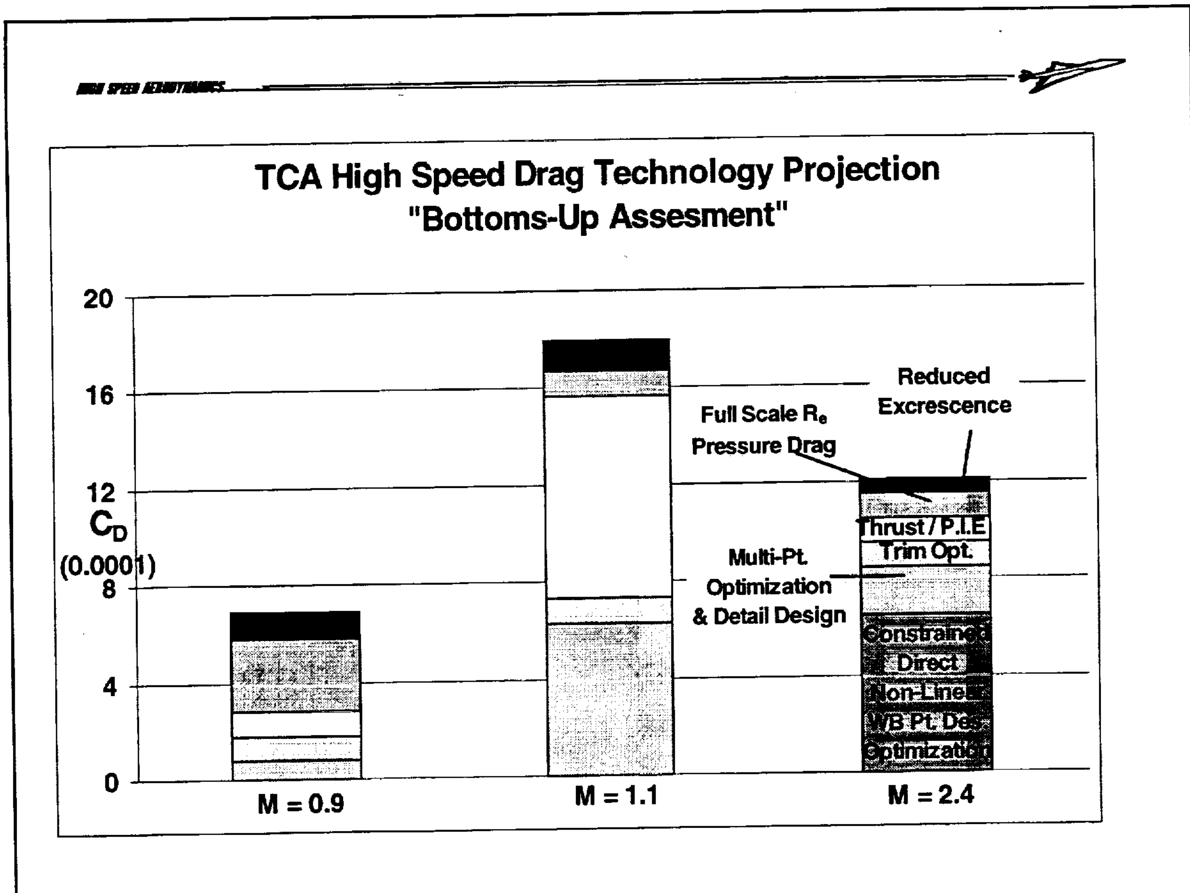

In order to keep a constant check on the assumptions being made in the committed TCA performance levels, TI has maintained a "bottoms-up" check of the reasonableness of the tops-down projections. The projections for the three most critical high speed Mach numbers are shown above. Each bar is divided into identifiable sources of potential drag improvements that would sum up to the total projection at each Mach. In recent months, the CFD non-linear optimization tools appear to be well on their way to providing the 6.5 counts improvement assumed above at the Mach 2.4 cruise design point. It is believed that some combination of viscous and inviscid non-linear optimization, analysis, and flow visualization tools will enable additional improvements of 1.5 to 2.5 counts in detail design at Mach 2.4. CFD-aided detail design integration and multi-point design of body area rule, nacelle shapes and wing camber are believed to account for more than a third of the Mach 1.1 projection. As mentioned earlier, the other large piece of the Mach 1.1 projection will be in understanding the PIE effects well enough to reliably take credit for favorable transonic interference terms (or eliminating adverse effects) wherever possible.

Accounting for thrust and PIE effects, and optimizing the wing-body, nozzle, and tail contributions to trim drag at Mach 2.4 could account for 2 to 3 more counts of the cruise projection. Improved validation of subsonic CFD methods for subsonic Reynolds number effects, leading edge flap optimization and trim including aeroelastics, are assumed to account for most of the subsonic cruise projection. The projection of a 20% reduction in excrescence at all Machs appears to be a reasonable goal making up the remainder of the projections.

HSR Technology Integration
"Airplane Design Process" Study

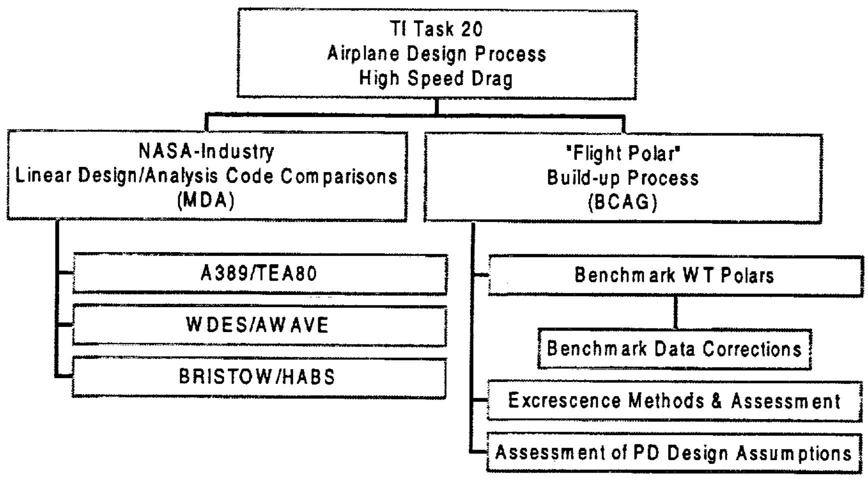

Based on experiences with the downselect to the TCA configuration in 1995, it was recognized that the HSR program would benefit from improved PD prediction methods. A TI "Airplane Design Process" (ADP) task was implemented, directed toward improving the Propulsion, Noise, Weights, and Aerodynamics groups' inputs to airplane level trade studies, metrics, and annual baseline updates. Aerodynamics discipline tasks under this on-going effort were divided into;

1) understanding differences between (and improving) the various linearized potential flow design and analysis codes used by NASA and industry, and

2) improving the accuracy of the build-up from the potential flow analysis results to the full scale flight drag "status" polars.

For the high speed performance regime (Mach >0.6) responsibility for the former task was given to the McDonnell-Douglas, while Boeing (BCAG) undertook the latter, with NASA LaRC contributing to understanding both areas. The BCAG effort includes sub-tasks addressing excrescence drag assessment, aft-body / trim drag, transonic flap predictions, and TI's use of corrected wind tunnel data in the drag polar build-up process. The potential flow analysis methods, excrescence drag, and an alternate approach to wind tunnel trip drag corrections are the subjects of other papers in this Workshop. ADP work planned for 1997 includes updating TI's performance polars for CA's technology projections and TCA wind tunnel test data, as well as improving capability for drag predictions of multi-surface control concepts.

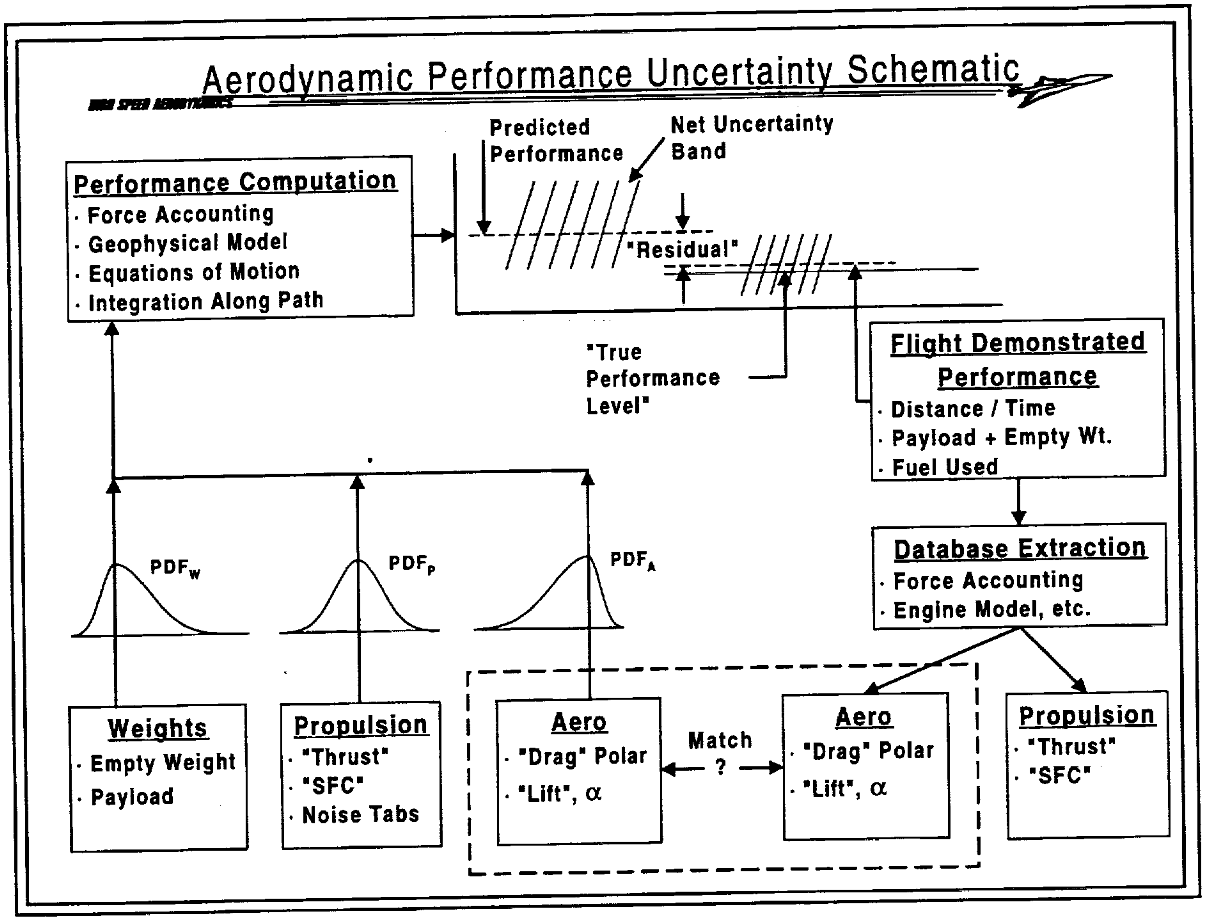

The "ADP" task must take an end-to-end view of the performance prediction process in order to identify sources of uncertainty and prediction improvements. Accurate aerodynamic performance prediction is important for all types of aircraft. For most military aircraft and civil light or utility aircraft, the most critical performance parameters are often those not directly dependent on cruise drag (e.g. thrust-to-weight ratio, turn capability, takeoff distance, roll rate, maximum payload, or range-at-any-cost). On long-range commercial transports where the economic margin for error is very small, the ability to very accurately predict absolute cruise performance is essential for success. The cruise performance parameters that directly impact the commercial viability of a transport are the payload carried, the distance flown in a given time, and the fuel burned to get there ---all of which are relatively easy to measure in flight on a given airplane to within 1% or less. To sell a new airplane type, the manufacturer must typically guarantee that a deviation of no more than a few percent will exist between the predicted performance and that measured in flight tests. Unfortunately, the pre-flight predictions can only be calculated from the constituent lift, drag, thrust, SFC, and mass properties, each of which have their own uncertainties (represented by Probability Density Functions, PDF). The ability of the Aero and Propulsion disciplines to accurately establish their components of performance can only be assessed in "hindsight" by back-calculating the corresponding components from the measurable flight test quantities. (Physical understanding, testing and CFD technologies and accounting methods can then be developed to minimize unpleasant surprises in the future.)

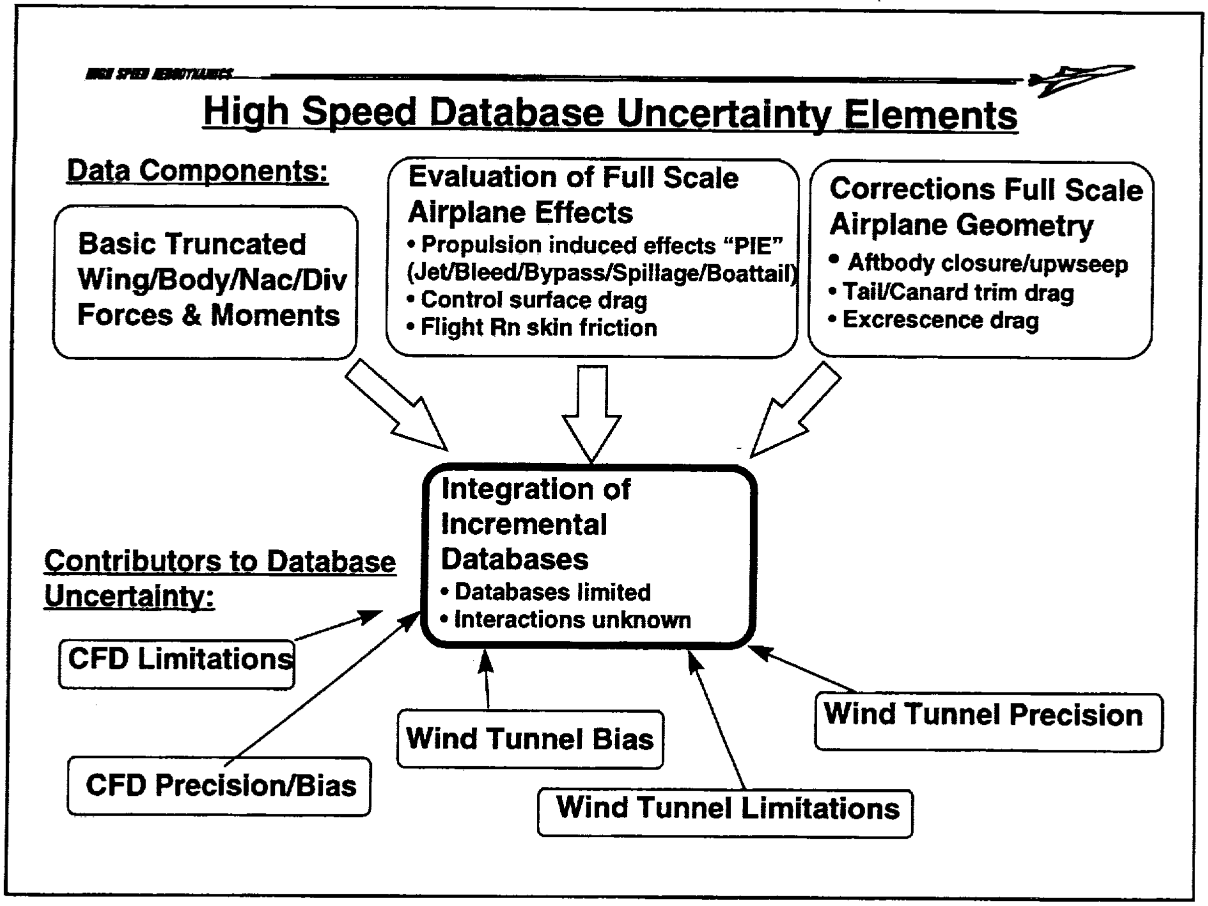

While most aerodynamic technology development and optimization work can focus on incremental CFD and test databases, the importance of establishing accurate absolutes as early as possible is obvious. The net impact of every one count cruise drag miss (Δ CD=0.0001) integrated over a complete flight results in a 10,000 LB increase in the design Maximum Takeoff Gross Weight (MTOW) required to fly the mission. Once the engine size is frozen and MTOW is fixed the airplane must loose 6 seats, or find a one ton savings in structural weight just to break-even with a one count cruise drag increase.

At this early stage of the HSCT program, there are really two main areas where integrated assessments of "absolute" drag levels are needed. One is in defining the conceptual airplane used as a confirmation of continued program viability and a common baseline airplane geometry for all disciplines to use. (The TCA now filling this role, along with periodic baseline concept updates will be the basis of several key program decisions in the next few months and years.) The second is to accurately calibrate the CFD tools and processes that are being developed to enable the design and optimization the future production HSCT.

From the preceding discussion of the TCA drag polar build-up it can be seen that the high speed drag polars for performance modeling are a complex combination of increments and absolutes from different sources. Each of these inputs has its own inherent precision and bias errors --- some easier to determine and control than others. For the purposes of the "flight polar build-up" ADP sub-task, data used in the TCA polar build-up was assessed for potential sources of bias and precision (repeatability) error.

Examples of Uncertainty in TCA High Speed Drag Polars

- Test-to-test, and tunnel-to-tunnel differences (1.5ct)
- Wind tunnel model corrections:
  - Trip drag / laminar run (2.0ct)
  - Model fidelity and aeroelastics (2.5ct)
  - Nacelle internal forces (2.0ct)
  - Installation T&I (~2ct ? trans. / 0 super.)
- "Full scale airplane" drag increments:
  - Excrescence (2ct)
  - Empennage / trim (6ct)
  - Propulsion induced effects (10ct trans. / 2 super.)
  - Reynolds number/skin friction effects (4ct)

Significant sources of uncertainties in the absolute drag levels quoted for performance use were identified based on existing discrepancies between various semi-empirical, CFD, and wind tunnel sources. Uncertainties in the ability to obtain improvements with non-linear optimization technology, and any biases related to the basic linearized potential flow design and analysis tools were not considered.

Depending on the exact data sources compared, varying uncertainty levels can be assessed. Those shown in the chart above are believed to be the most representative relative to the specific components in the TCA polars. All quantities are +/- the value shown.

As part of BCAG's portion of the ADP task in 1996, the areas of excrescence drag, empennage drag (upsweep, closure, tail trim), and wind tunnel database corrections and averaging were chosen for more detailed investigation. CFD solutions (Overflow and TLNS3D-MB) were used to get a better assessment of the the empennage drag terms and Reynolds number effects. It should be noted that the wind tunnel database uncertainties generally get incorporated into the status polars both directly through the "test-theory increments", and indirectly through the CFD-based geometry increments as the CFD codes were validated using wind tunnel data.

(The potential uses of CFD data in the assessment of excrescence drag and wind tunnel trip drag are the subject of additional BCAG papers.)

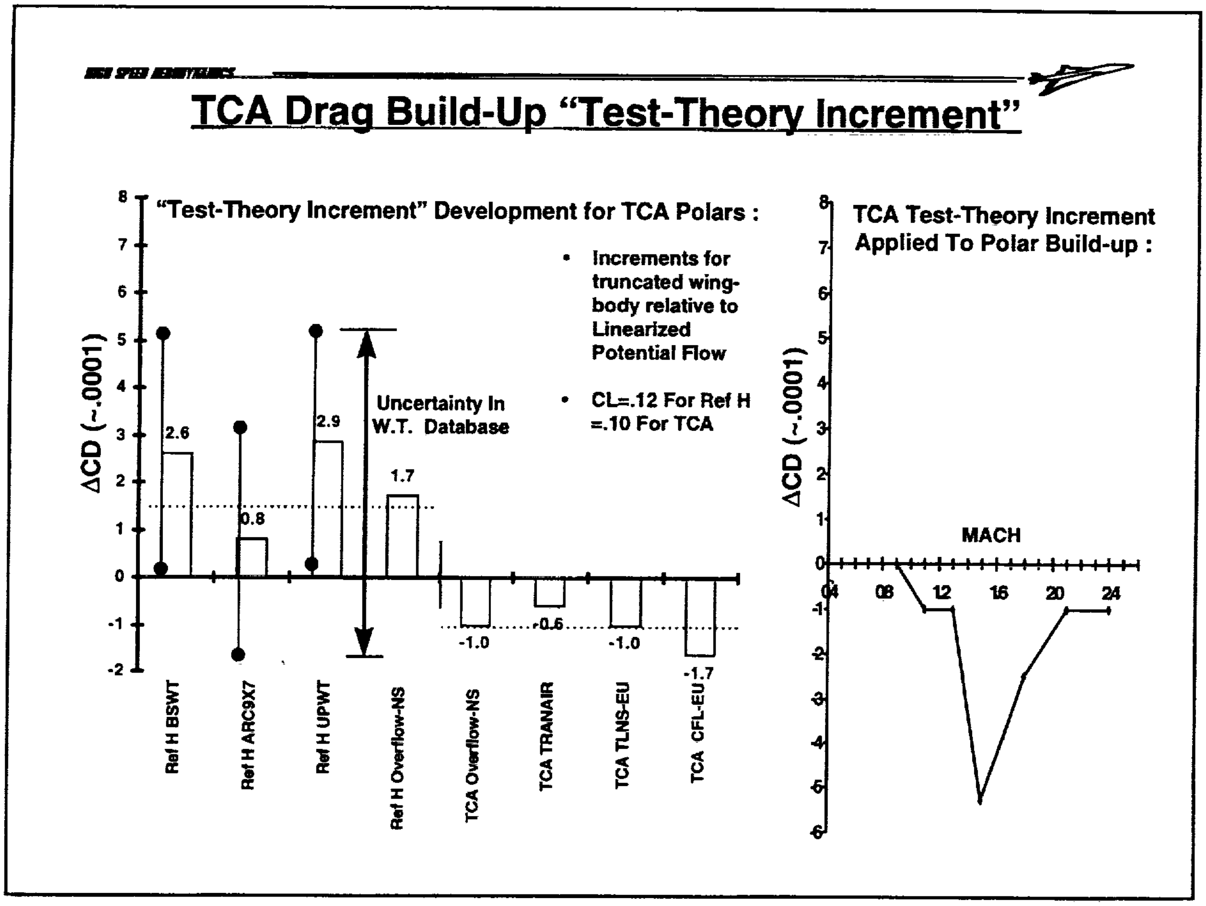

The tunnel-to-tunnel repeatability as seen on the Reference-H configuration (roughly +/- 1.5 count) has been a concern for several years. The "Benchmark Models Program" co-op testing program begun by BCAG and NASA prior to HSR-2 was intended to uncover and resolve such discrepancies to reduce uncertainty in absolute level drags. (The Ames Unitary tunnel was unavailable to complete the model-to-model portion of the program and the remainder of the study was out-prioritized by HSR-2 and BCAG activities.) "Test-theory increments" to be applied to linearized potential flow results are shown in the above left bar chart based on various Ref.-H wind tunnel sources. Error bands about the individual wind tunnel levels are shown representing 80% confidence levels for measurement repeatability and uncertainties in the data corrections (primarily trip drags and model fidelity). Using just the Ref.-H wind tunnel database would have indicated that the TCA drag prediction would need an average 1.5 count test-theory increment at Mach 2.4. As shown, this was confirmed by the Ref.-H Overflow Navier-Stokes results. Pre-test CFD results for the TCA however, indicated a level about 1count below the uncorrected potential flow results. As it was believed that the higher sweep angles and more slender body of the TCA might have more favorable "real flow" effects than the Ref.-H, a test-theory increment of -1count was chosen for the TCA performance polars. The Ref.-H wind tunnel database test-theory increments was still used as a guide in fairing out the TCA's -1count across the Mach range (see upper right graph). TCA transonic/subsonic test results from LaRC 16T are still being analyzed.

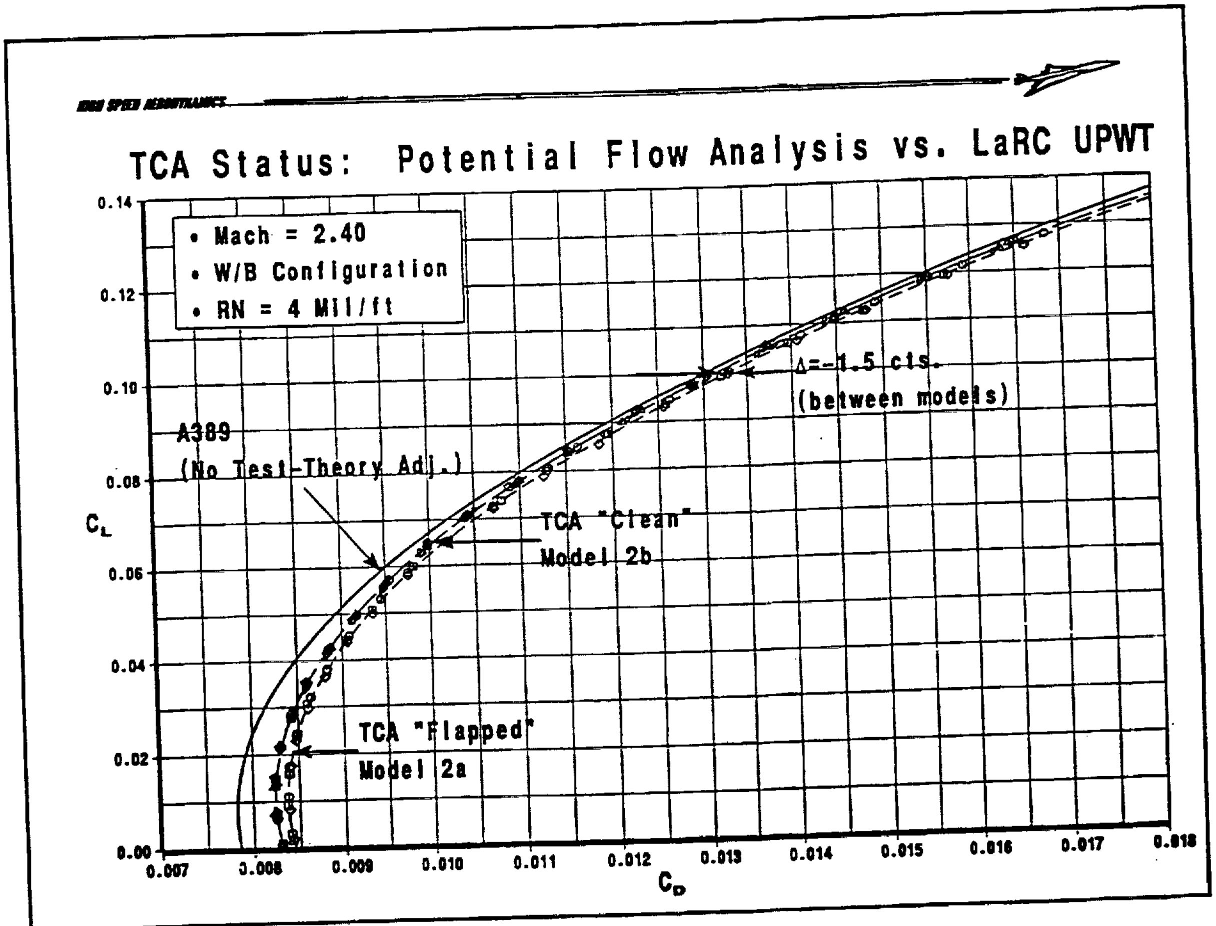

Initial TCA test results show that the -1 count test-theory increment agrees with the measured drag polar of the "clean wing" model if one assumes that the net adjustment for trip drag+laminar run should correctly be 2.5 to 3.0 counts.

Unfortunately the statistical uncertainty in trip drag correction due to curve fit questions, basic data scatter, and laminar run correction unknowns, is significantly larger than the test-theory correction so a definitive answer is impossible at this time. A method using CFD results and excrescence drag calculation methods to reduce these correction uncertainties shows promise but requires calibration with additional very high quality wind tunnel data.

The other fact that can be gathered from the above test data plot is that the impact of model fidelity (including model excrescence) cannot be ignored. While the test-to-test repeatability of the TCA wing which included flap cut-outs was excellent (fractions of a count), it clearly has a 1.5 count model fidelity penalty relative to the second model which was built with a "clean" wing. The model fidelity penalty grows to nearly 2 counts for the nacelles-on case.

Subsonic and transonic TCA force data obtained recently in the LaRC 16Ft transonic tunnel are still being analized at the time of this writing. No off-design supersonic data (i.e. Machs from 1.3 - 2.1) were taken on the TCA performance model so the large test-theory increment predicted from the Ref.-H data cannot be confirmed.

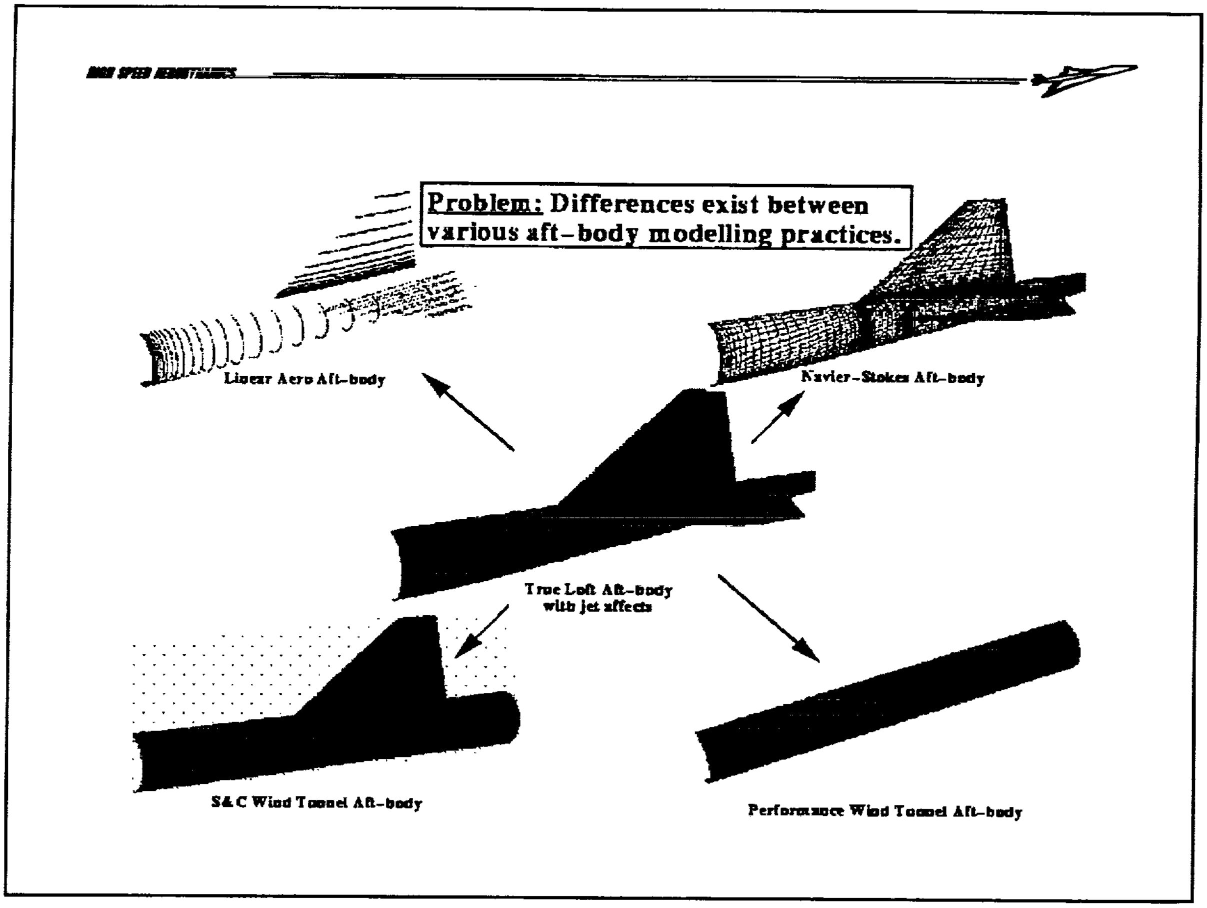

Several areas were identified where viscous CFD analysis might provide additional data to reduce the uncertainty levels in HSCT performance polars. The use of Navier-Stokes results in the resolution of trip drag corrections and excrescence drag estimates has already been mentioned. Navier-Stokes results were also used to provide an assessment of empennage drag and possible Reynolds number effects not capytured by the simplified PD methods used in the current polar buildups.

Considerable time and effort went into using TLNS3D-MB for empennage analysis. Seven different aft-body/ vertical tail geometries were run, plus three tail angles on the baseline TCA body. While the results of the trim drag portion were encouraging, the aft-body upsweep and closure increment study was inconclusive. Grid problems with viscous flow continuity at block boundaries and the unexpected complexity of the aft-body viscous flow caused significant errors in both the skin friction and viscous pressure drag of the various bodies. This problem is currently being investigated further.

CFD Assessment of Empennage Drag and Rn Effects

- TLNS3D-MB study of empennage drag:
  - 7 aft-body / tail geometries
  - 3 tail angles on baseline TCA aft-body
  - Horiz. is unported at best trim angle
  - Status trim o.k. (+1ct downwash, -1ct vert-horiz. interf.)
  - Upsweep / closure drag results inconclusive
- Ref. H and TCA wing-body @ w.t. and flight Rn
  - Overflow (dense grid, Bladwin-Barth)
  - Both showed dCD/dRn slope 2ct less than flat plate calc.
  - -1ct visc. pressure drag at flight on Ref.-H
  - +2% visc. CL at flight on TCA

The trim drag results showed that the baseline tail is unported at the optimum tail angle. If the tail is "resealed" to the body wiping surface, the large effective downwash (4 degrees) and poor installed tail polar cause a one count trim penalty. The total status tail drag is about equal to that predicted using the normalized trim approximation as there is also about one count favorable horizontal-vertical tail volume interference. Similar results were obtained across the Mach range. The tail polar and sensitivity to downwash and body shape indicate that the projected additional reduction of 1 to 2 counts is probably achievable with non-linear optimization. Of course wind tunnel data is still needed to validate the empennage CFD results for future designs and predictions.

Overflow solutions on the TCA and Ref.-H wing-bodies were studied to identify trends in skin friction and viscous pressure drag at cruise Mach conditions. Both geometries showed a CDf trend from wind tunnel to flight Reynolds number that is about 2 counts less than predicted from standard falt plate skin friction methods. In addition, the Ref.-H showed a potential 1 count pressure drag reduction in flight. The TCA showed a potential 2% increase in lift at flight Reynolds number. Again, test data and additional CFD-to-flat-plate theory comparisons are needed to reduce uncertainty in this area.

Summary Of Drag Polar Build-Up For High Speed Performance

- "Performance Polars" = Projected Level from tops-down method

  "Tech. Projection" = (Projected Level) - (Status polars @ flight)

  "Status" =(W.T. database) + (potential flow, PD, CFD-based Δ's)

- Uncertainty bands around Status can add significant program risk (e.g. viability assessment, technology metrics, downselects)

In addition to CFD analysis and optimization tools, HSCT testing and accounting methods must be validated to a high confidence level before production go-ahead, e.g. ...
- Empennage drag
- Propulsion induced effects (PIE)
- Rn effects on supersonic pressure drag and skin friction

This paper has reviewed the various components of the TCA high speed drag polars used for airplane sizing, mission performance analysis, and Technical Integration (TI) airplane level trade studies. The level of cruise L/D in the TCA polars has been set equal to the target cruise performance determined by concensus of the joint NASA-industry Configuration Aerodynamics (CA) team. An unprojected "status" level TCA polar was developed based on a combination of available wind tunnel data, geometry changes, and "real airplane" details. The "technology projection" is the drag improvement required to cover the difference between the concensus "tops-down" based performance L/D and the status polar. A projection formula based on the percent change in cruise wave drag, and drag due to lift was then applied at all supersonic Mach numbers. A 20% excrescence reduction at all Machs and a 6% improvement at subsonic conditions are also applied.

Potential errors in the absolute level of predicted drag can have an adverse impact on the determination of program viability or major concept downselects. Several sources of uncertainty in the current polars have been described. Some efforts under the TI "ADP" task to further quantify or reduce several uncertainty elements have been shown. The use of calibrated CFD solutions appears to offer benefits in several areas. Future wind tunnel tests to extend the existing wind tunnel databases and provide CFD validation must be carefully planned to obtain maximum data quality if significant progress is to be made in eliminating uncertainty sources.

References:

High Speed Civil Transport (HSCT) Technology Concept Airplane Outer Mold Line (OML) Definition, Mc Donnell Douglas and Boeing Commercial Airplane Group, Rev.A March 13, 1996.

High Speed Civil Transport (HSCT) Technology Concept Airplane Configuration Description Document, Mc Donnell Douglas and Boeing Commercial Airplane Group, April, 1996.

Acknowledgments:

The authors wish to thank Tsong-Jhy Kao of Boeing and Ross Sheckler of Dynacs Engineering Inc. who provided CFD grids and solutions for the HSR Technology Integration Task-20 Airplane Design Process (ADP) study outlined in this paper.

Task 2.1 - Technology Integration

Sub-task 2.1.5 Aircraft Design Processes

Sub-Sub-task 2.1.5.1 High Speed Aerodynamic Processes

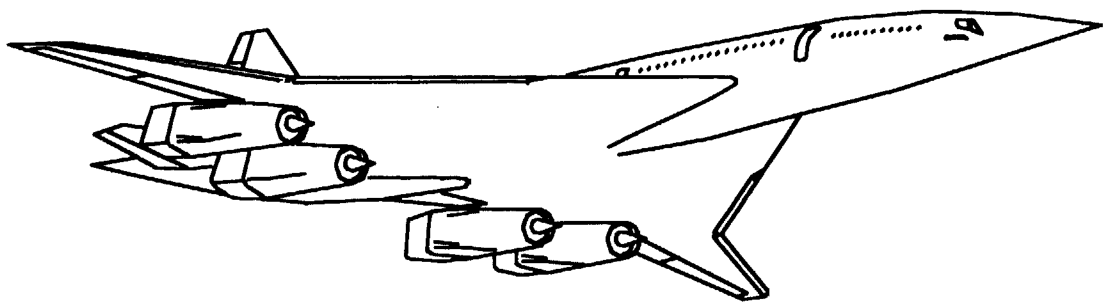

Comparison of Linearized Potential Flow Design and Analysis Codes

John Morgenstern
McDonnell Douglas

Aerodynamic Performance Workshop
February 25-27, 1997

Outline

- **Drag Bookkeeping**
- **CD Induced**
    - Goal - TRENDS
- **CD Induced Codes**
    - WINGDES
    - SDAS/A389
    - BRISTOW
- **Mach 2.4 Flat Wing Comparisons**
- **Mach 2.4 Design**
    - Qualitative Assessments
- **Mach 2.4 Analysis**
    - BRISTOW Designs
    - TCA Prediction Comparisons
- **Mach 1.1 Analysis of BRISTOW Designs**
- **CD Induced Summary**
- **Preliminary Conclusions and Future Plans**
- **References**

The purpose of this task is to compare high speed aerodynamics design methods to find the most accurate and consistent methods for use in HSR Technology Integration studies.

In order to compare design methods for Technology Integration, we first separate drag into the components that each method predicts. CD Friction process differences have been quantified and should not affect drag trends between designs; therefore, the differences are considered acceptable. Based on previous work, differences in CD Wave were relatively small and probably due to differences in the geometry analyzed and the number of cuts used--process improvements are still under investigation. CD Induced and ΔCD Nacelles were known to have the largest differences, so the most effort has been concentrated in those two areas. This paper discusses only the CD Induced results.

DRAG BOOKKEEPING

	Method	Status	Conclusion
CD Friction	Flat Plate	Results Close	Acceptable
CD Wave	Far-Field	(in progress)	*pending*
CD Induced	Vortex Lattice	Differences in: • Design for LET • Fuselage Interference and Thickness	*pending*
ΔCD Nacelles	NFWD vs CFD/FP	Differences in: • Diverter and Footprint • Local Conditions	*pending*
ΔCD Trim	-1 Count	Assumption	*tbd-time*
ΔCD Techno.	f(CD,LE Break)	Assumption	*permitting*

For Technology Integration studies, all methods will be corrected with a test to theory increment, calculated from a common database developed by Boeing's parallel task. Therefore, getting the correct change in drag between designs is more important than getting the correct drag level. To understand the differences between induced drag methods, the modeling was made very consistent between codes. Empirical corrections were dropped, the fuselage was modeled as a flat plate without thickness, and the panel density in BRISTOW was increased. NASA's continuing sponsorship of method improvements has been put to good use. Work by Carlson, et. al., developed enhancements in leading edge thrust calculation methodology used in WINGDES, as documented in reference 3. Under IRAD funding, the attainable thrust limiting routines in BRISTOW were revised to match the enhanced method. SDAS/A389 thrust limiting is based on the previous method in reference 7.

Additionally, since trends are of greatest importance, the predicted drag difference between a 2.4-7 Arrow Planform and Ref. H Planform were compared.

CD Induced

The #1 goal is correct TRENDS between designs

Comparisons were started from the simpliest cases:

Flat Wing and Body Trends

And modeling changes were made that reduced inconsistency (like not using BRISTOW fuselage interference) and reduced interpolation error between codes before proceeding to:

Wing Design

Wing/Warped-Plate-Body Analysis of Best Designs

Before this task, the drag of a design could vary 2 to 7 counts at Mach 2.4 and was different by as much as 10 counts at Mach 1.1. Modeling and interpolation processess were made more consistent, and paneling density was increased. With these updates, the no thrust vortex lattice methods for similarly modeled, uncambered designs, the were shown to predict between 0 and 1 count of difference--a very consistent comparison.

FLAT WING AND BODY - NO THRUST
Mach 2.4, CL=0.10

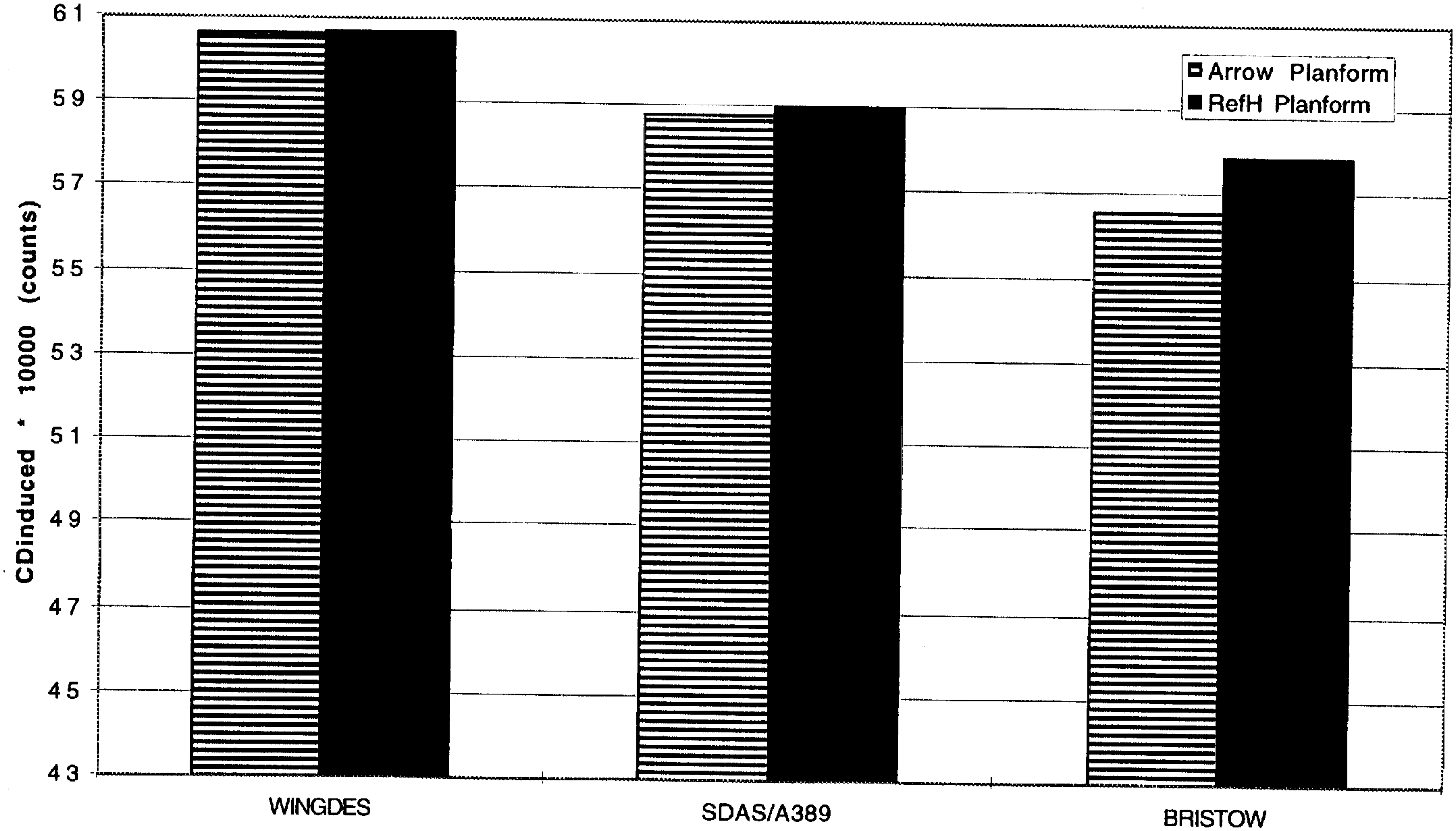

All three codes use the same method to calculate full leading edge thrust, so the differences in thrust increments are due to differences in the pressures used to extrapolate the leading edge pressure. The consistent drag increments, within 1 count at a CL of 0.10, demonstrate agreement in these flat wing thrust predictions.

FLAT WING AND BODY - FULL THRUST
Mach 2.4, CL=0.10

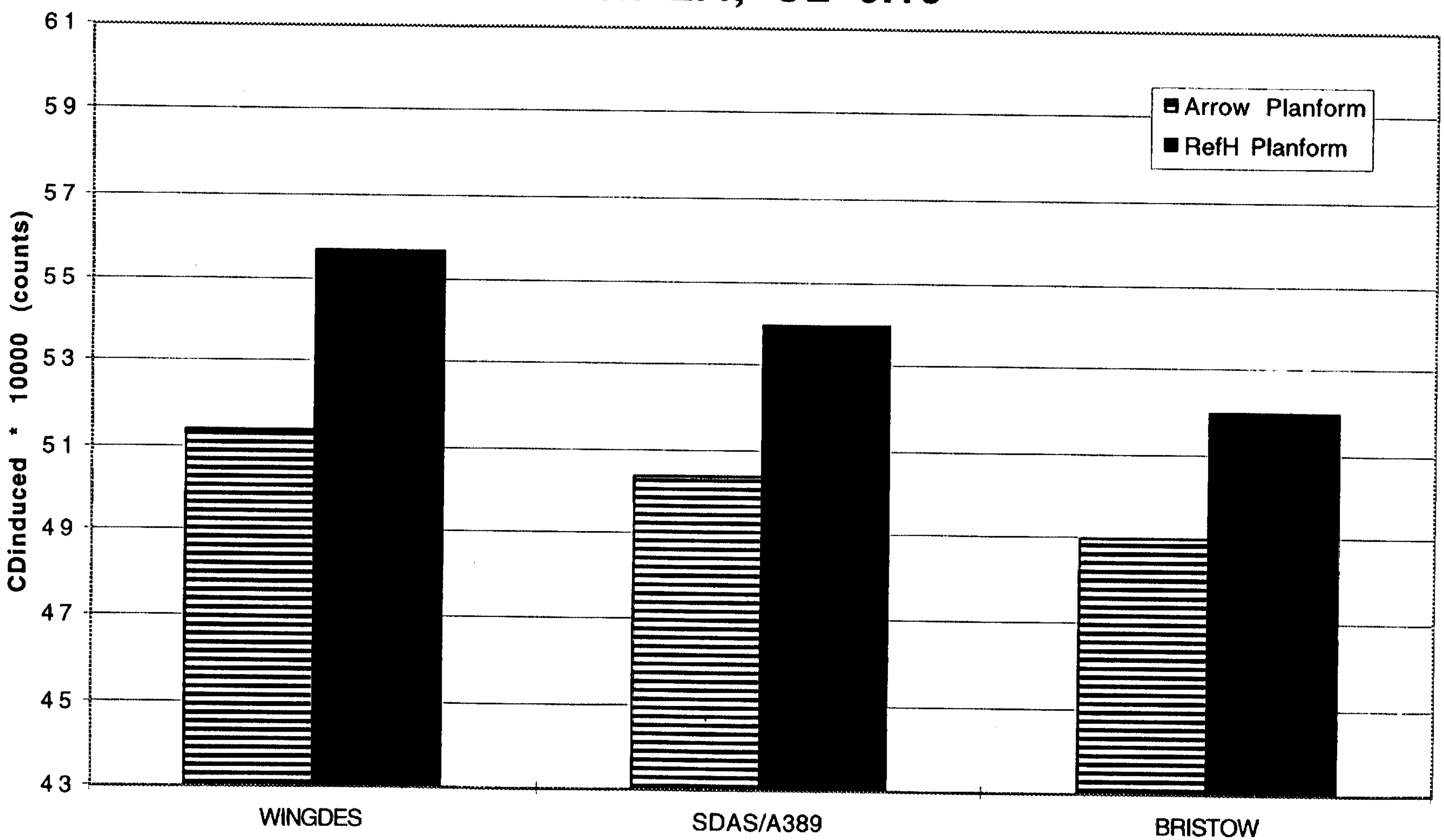

Attainable thrust increments also agree within 1 count, but notice that the SDAS/A389 attainable thrust is less limiting--relative to WINGDES and BRISTOW. Probably due to differences in the reference 7 versus reference 3 methods.

FLAT WING AND BODY - ATTAINABLE THRUST
Mach 2.4, CL=0.10

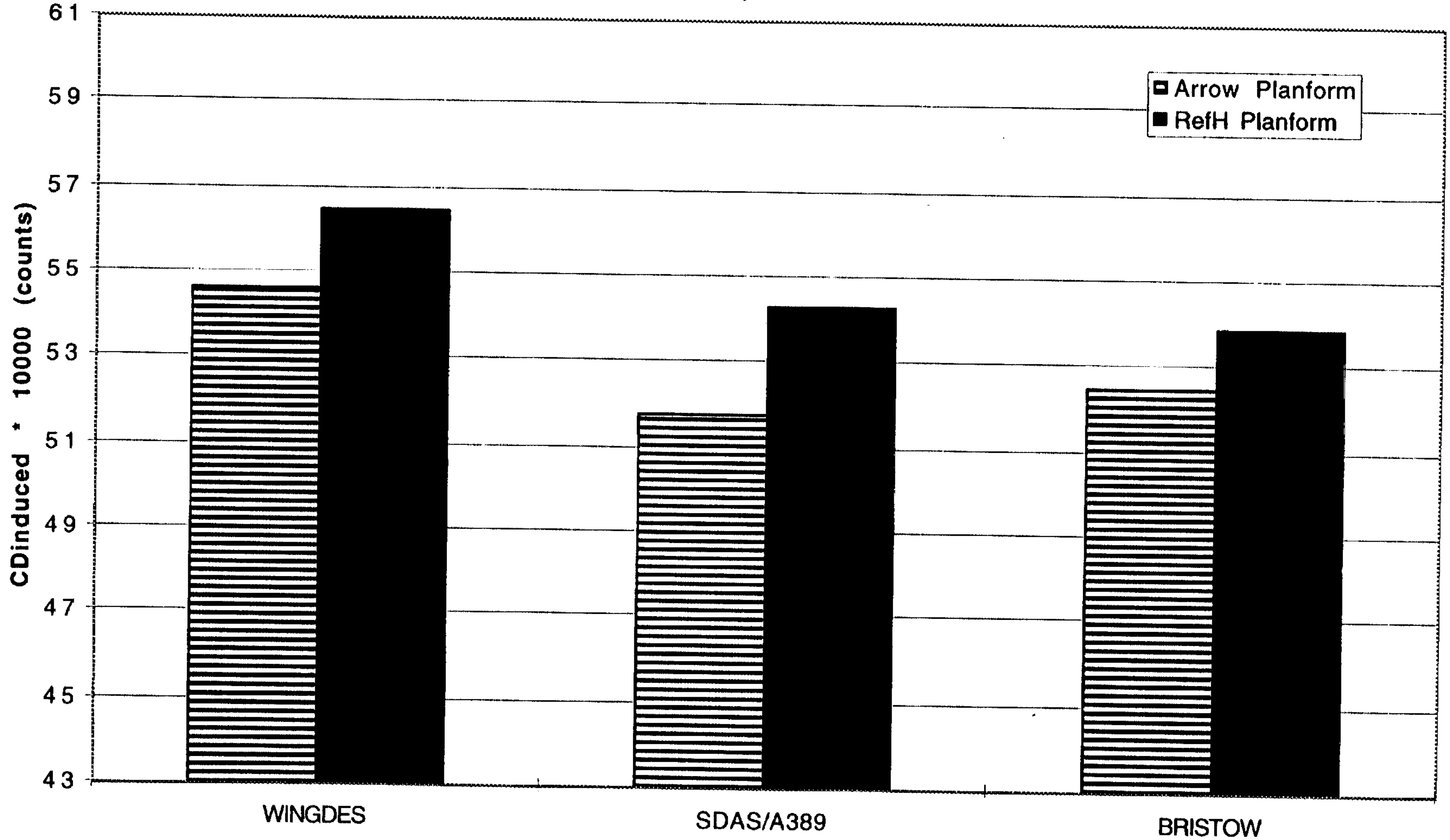

NASA, Boeing, and MDC each use different codes that calculate linearized potential flow using a vortex-lattice. Even though all codes employ the same theory, each code uses a different method to design optimally cambered wings. WINGDES (refs. 1-3) uses 8 shape functions plus up to 40 leading edge shape functions, SDAS/A389 (refs. 4-7) uses 5-17 loading functions, and BRISTOW (refs. 3, 8-11) uses 432 panels' camber slopes as shape functions.

Further, each code has unique capabilities not found in the other codes. WINGDES is the only code that designs for leading edge thrust (LET). According to our linear analyses, LET designs have lower camber and 1 to 2 counts lower induced drag. SDAS/A389 has a Near-Field Wave Drag (NFWD) method for rapidly estimating nacelle effects and reflexing the wing during camber optimization for improved performance with nacelles. BRISTOW includes fuselage interference and wing thickness effects.

CD Induced Codes

Three Vortex-Lattice Codes

WINGDES (NASA)

Planer formulation, rectangular panels

- 8 shape + 40 LE shape functions in design
- Design for leading edge thrust

SDAS/A389 (NASA/Boeing)

Planer formulation, rectangular panels

- 5 to 17 loading functions in design
- Wing design and analysis with nacelles

BRISTOW (MDC)

Non-planer with cylindrical fuselage interference, swept/tapered panels

- 432 camber slopes in design
- Analysis with circular fuselage and wing thickness effects

In FY95, a great deal of effort was expended to understand what the induced drag increment should be between consistent, well optimized Arrow and Ref. H planform designs. Wind tunnel data of CFD optimized designs were considered. Linear designs were analyzed using CFD. And finally, CFD re-optimization and analyses were performed on a series of consistent configurations in reference 11, resulting in a final increment of 7 counts.

CD Induced
Mach 2.4 Wing Design

A ΔCD Induced trend of 7 counts between the Arrow and Ref. H planforms was established in earlier planform studies and was verified by CFD.

All codes' designs are within 1 count of the established trend.

Substantial differences exist in drag level, pressure loading smoothness, and shape smoothness

Drag levels are shown below for designs optimized and analyzed by their own code. Since WINGDES is the only code that can design for Leading Edge Thrust, two sets of WINGDES designs are shown: with LET and without (without is comparable to SDAS/BRISTOW). The WINGDES designs have been updated from the 1996 ADP report, using NASA's help, to correct the design inputs. All methods match the established trend when analyzed with or without leading edge thrust.

MACH 2.4 DESIGN OPTIMIZATION COMPARISON - NO THRUST

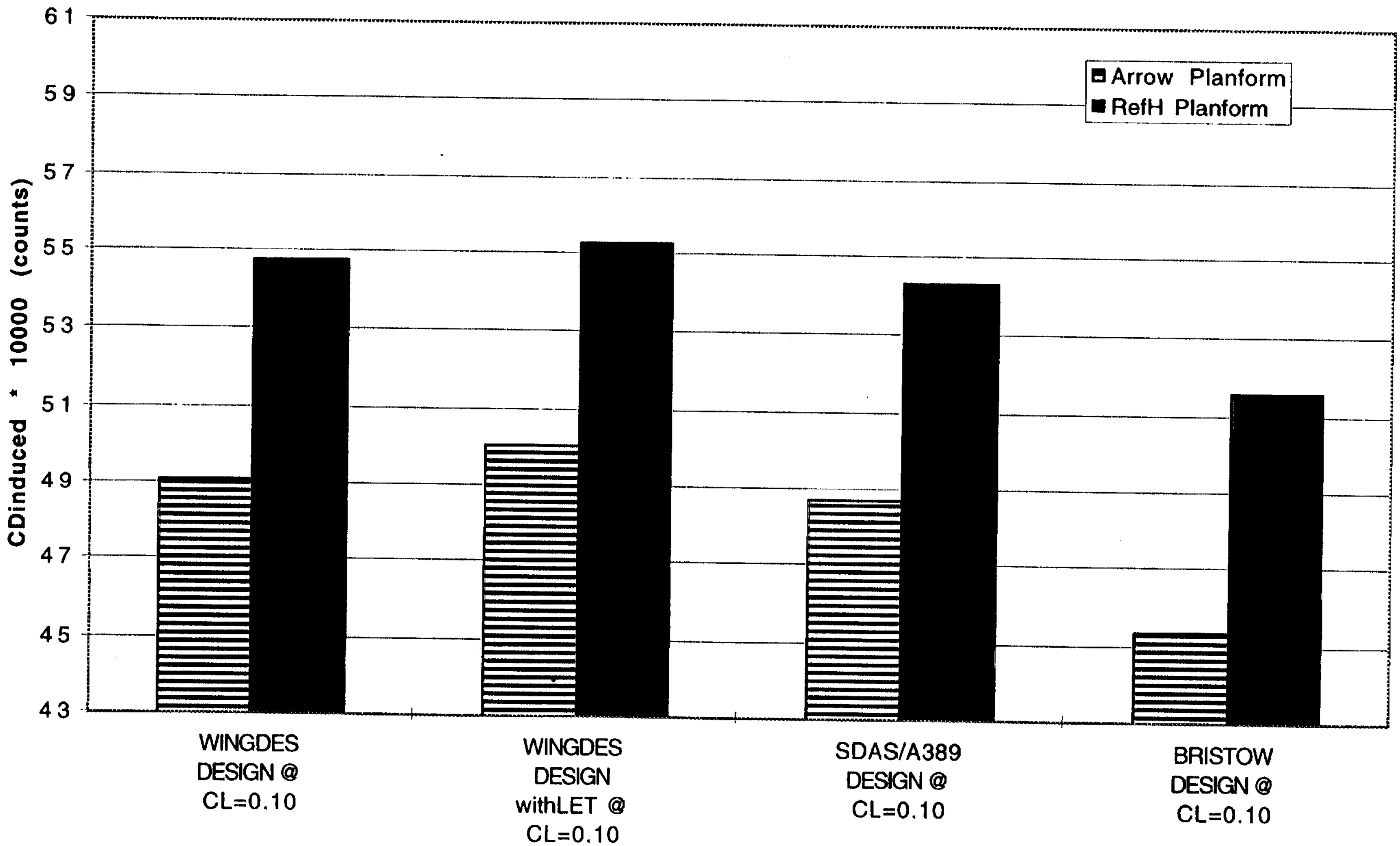

MACH 2.4 DESIGN OPTIMIZATION COMPARISON - FULL THRUST

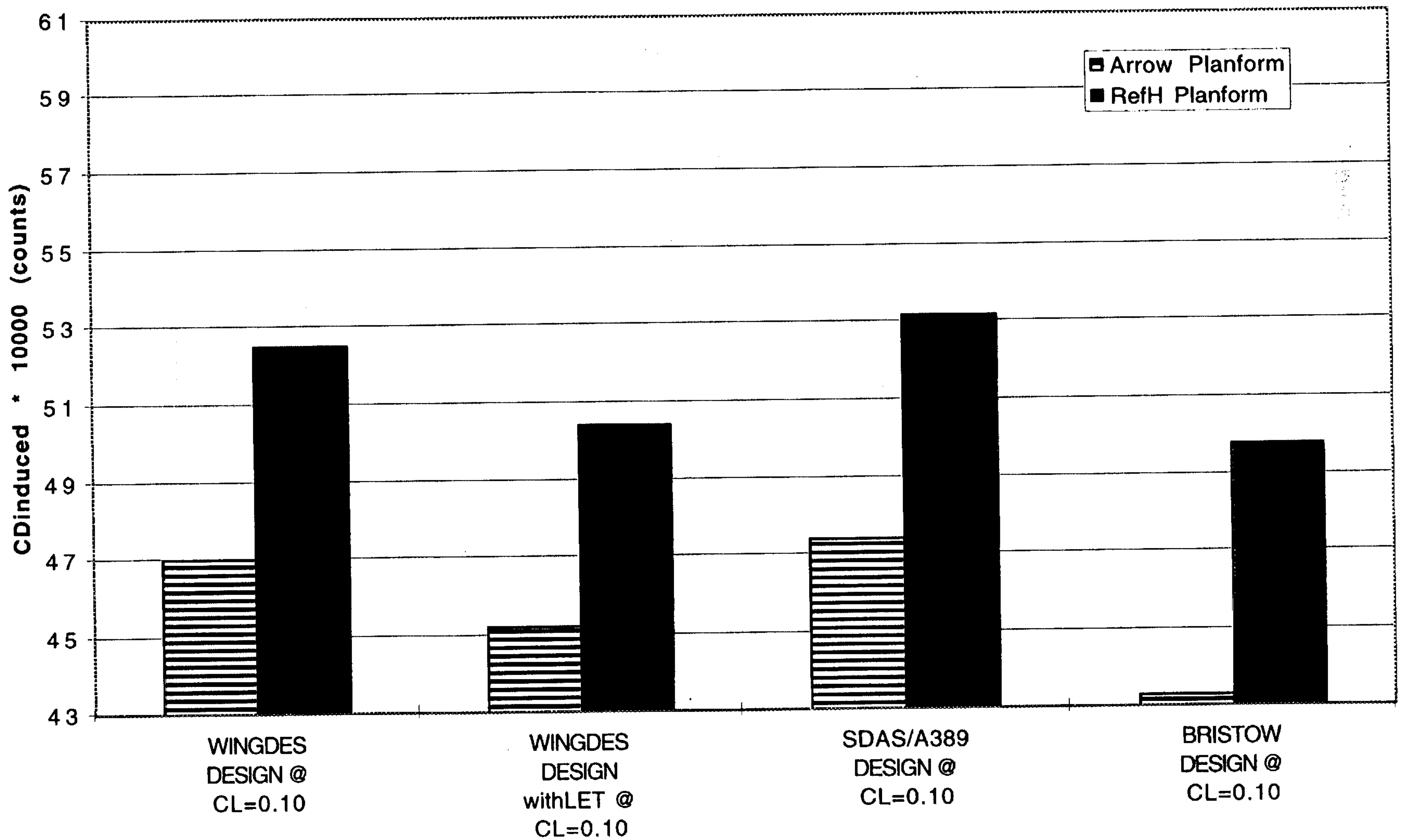

MACH 2.4 DESIGN OPTIMIZATION - ATTAINABLE THRUST

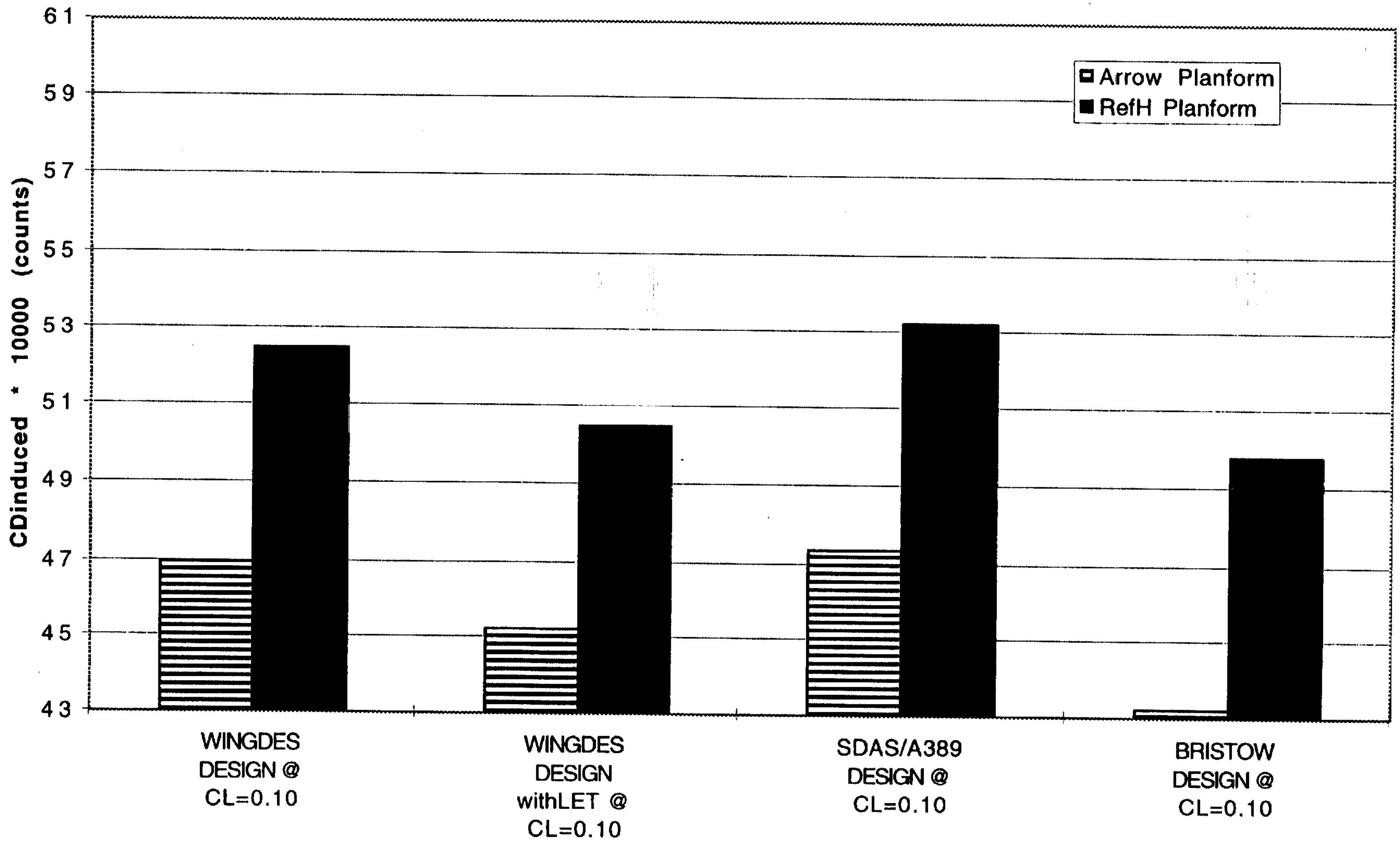

WINGDES, SDAS/A389, and the BRISTOW design trends are within 1 count of each other and are within 1 count of the established trend when the CD induced tech. projection is included (tech. projection = -7.3 counts for Arrow and -6.4 counts for Ref. H. The tech. projection increases the linear increment by 0.9 counts because non-linear optimization results indicate that a linear Arrow wing design will benefit more from non-linear optimization because of its larger amount of subsonic swept leading edge.)

MACH 2.4 DESIGN TREND COMPARISON - ATTAINABLE THRUST

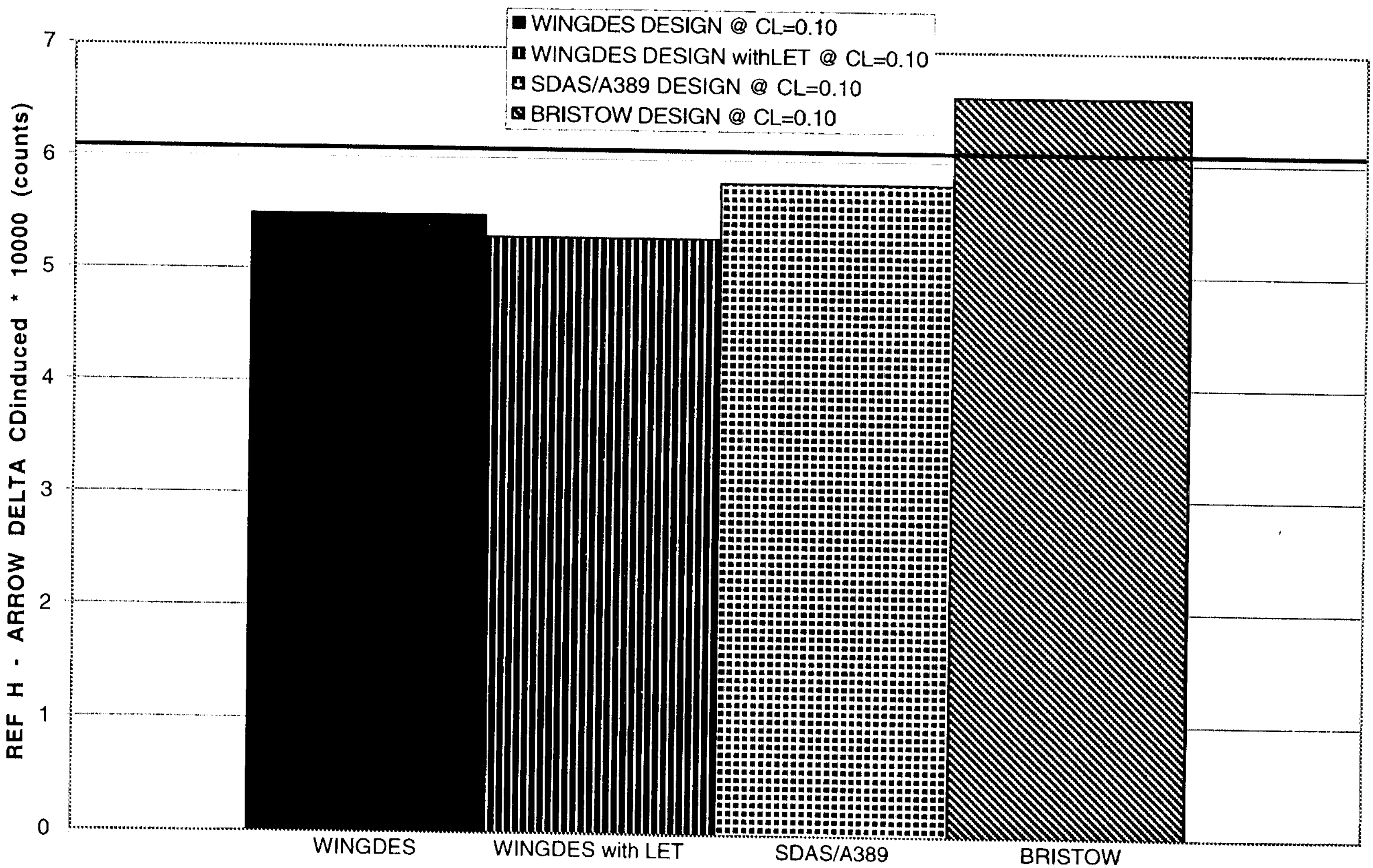

Qualitative Assessment:

In the following comparisons, all codes agree that the BRISTOW designs have the lowest drag. However, the BRISTOW designs also have high upper surface peak suction levels, which CFD analyses have shown to yield higher drag than linear predictions indicate. SDAS can reduce this problem by limiting the loading functions to smooth shapes (or constraining loads). However, planform break points cause spikes in the SDAS twist distribution when smooth loads are proscribed, requiring hand tailoring to create a more practical final shape (causing some increase in drag). Since WINGDES uses smooth shape functions to begin with, its wings are generally the smoothest. It also tends to have smooth load distributions for low drag in higher order analyses. However, WINGDES has the least capability for modeling fuselage, thickness and nacelle effects.

There is no clear advantage of one code's design over another, using consistent modeling; but there are some substantial differences. Final comparisons, using the LET, nacelle and fuselage/thickness effects unique to each code, will be investigated in future studies.

Ref. H Planform Optimization

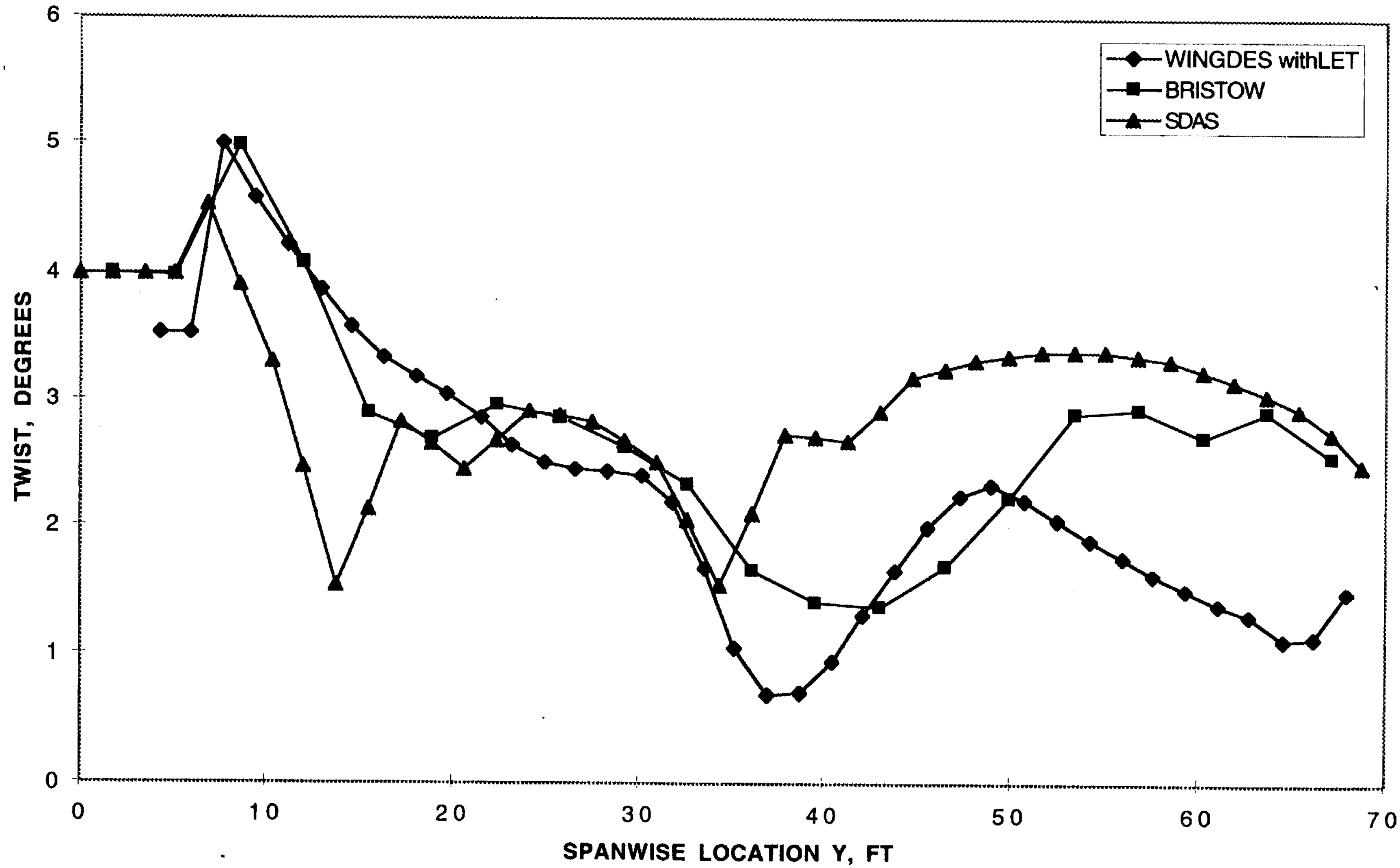

Of course, these trends were based on each code analyzing its own designs. To ensure consistency, the lowest drag BRISTOW designs were choosen to be analyzed by the other codes to see if their results would match the BRISTOW results. Using consistent modeling, the results were consistent for all codes at the cruise condition.

CD Induced
Mach 2.4 Analysis
Wing/Warped-Plate-Body BRISTOW Designs

Analysis of the same design by different codes yields the same trends and very similar drag levels with and without LET.

BRISTOW DESIGN: ANALYSES COMPARED - NO THRUST
Mach 2.4, CL=0.10

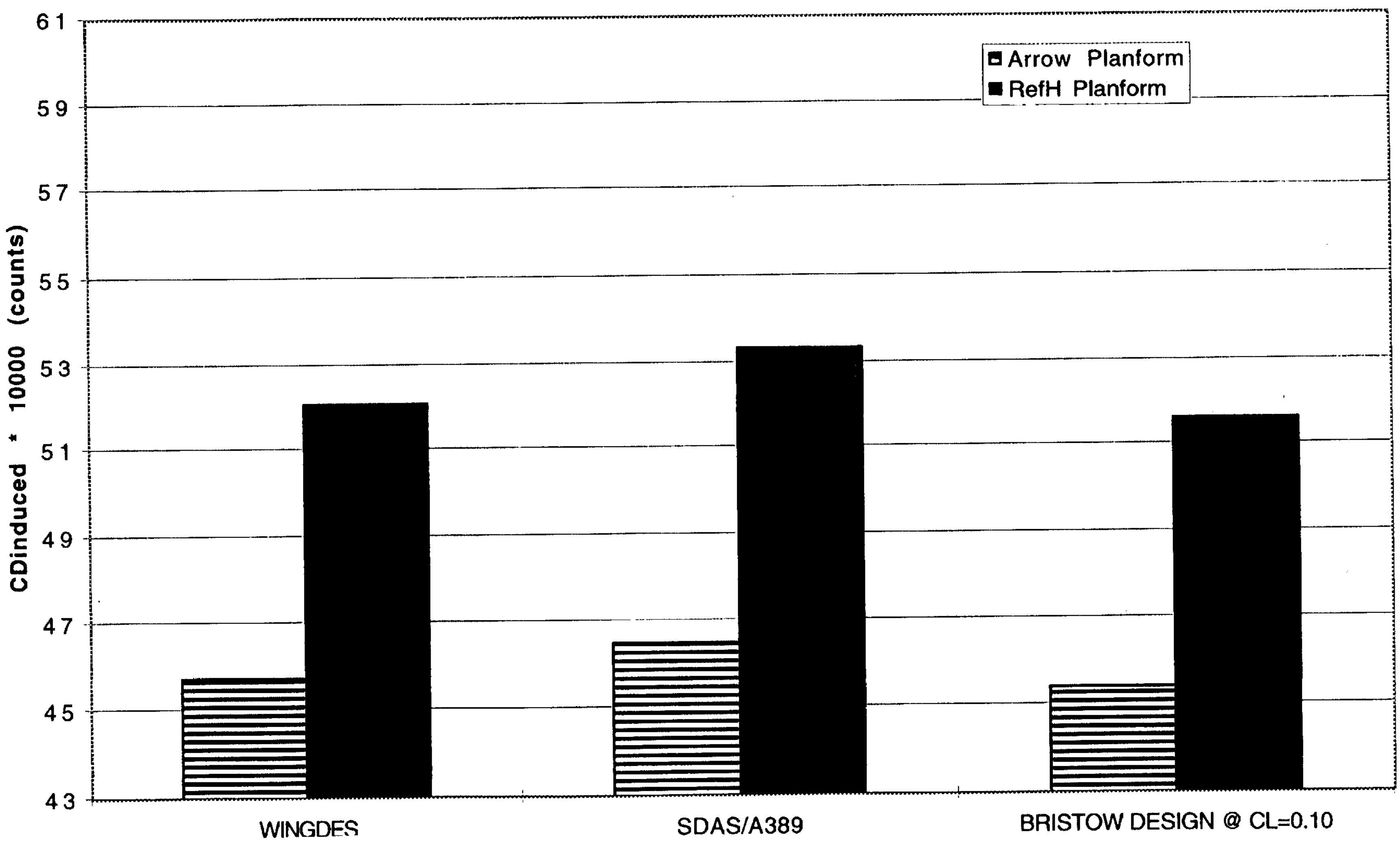

BRISTOW DESIGN: ANALYSES COMPARED - ATTAINABLE THRUST
Mach 2.4, CL=0.10

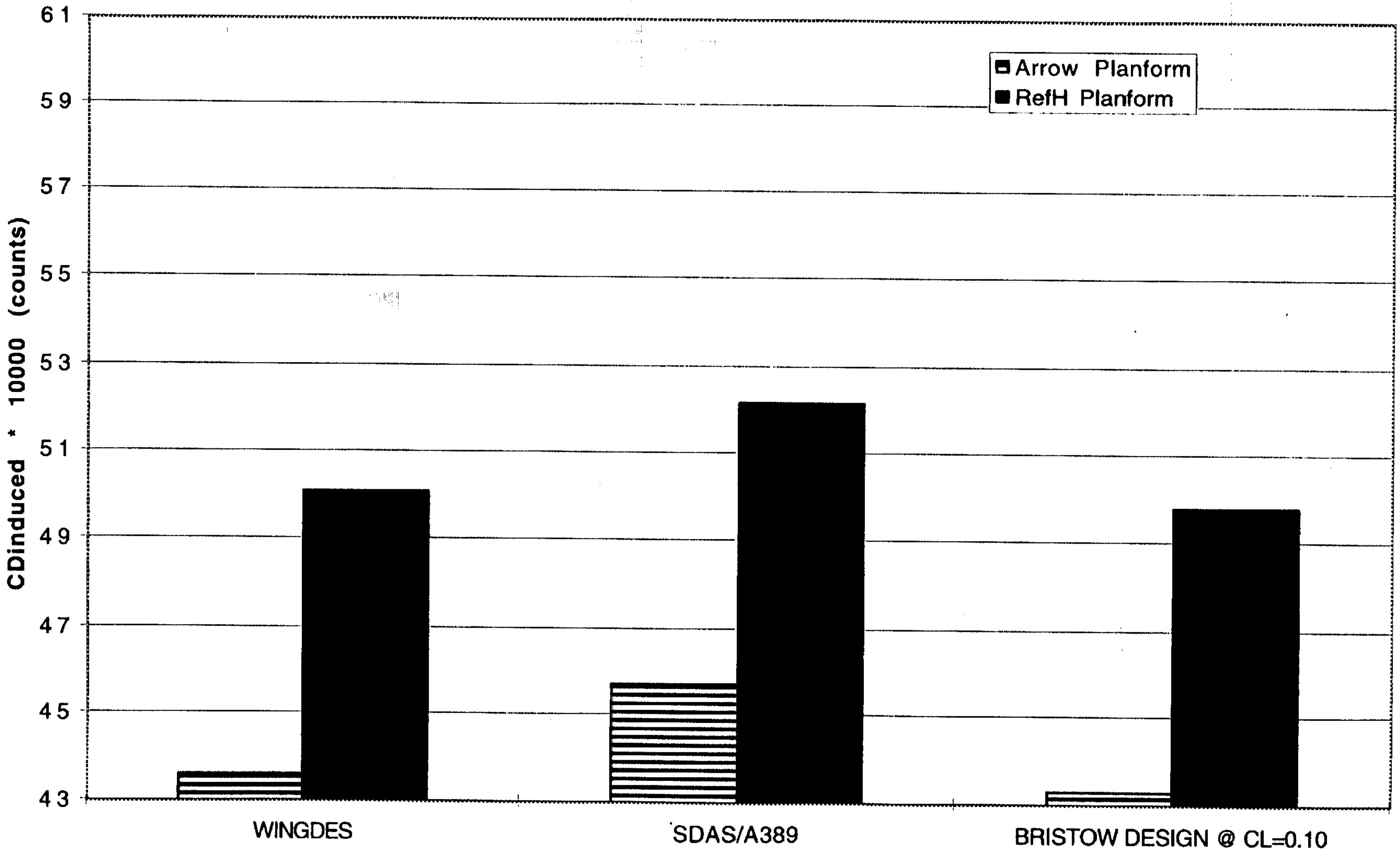

Predictions compare well with and without thrust estimates at CL=0.10; however, at the minimum drag CL, SDAS/A389 predicts several counts more thrust--resulting in negative drag (at Mach 2.4 and 1.1). Further, SDAS/A389 thrust predictions of the TCA show a 1/2 degree disagreement in alpha for zero thrust at Mach 2.4 (but no disagreement for TCA at Mach 1.2) compared with WINGDES and BRISTOW. Boeing takes a conservative approach by not using any LET predictions from A389 above Mach 1.5.

BRISTOW DESIGN: ANALYSES TREND - ATTAINABLE THRUST

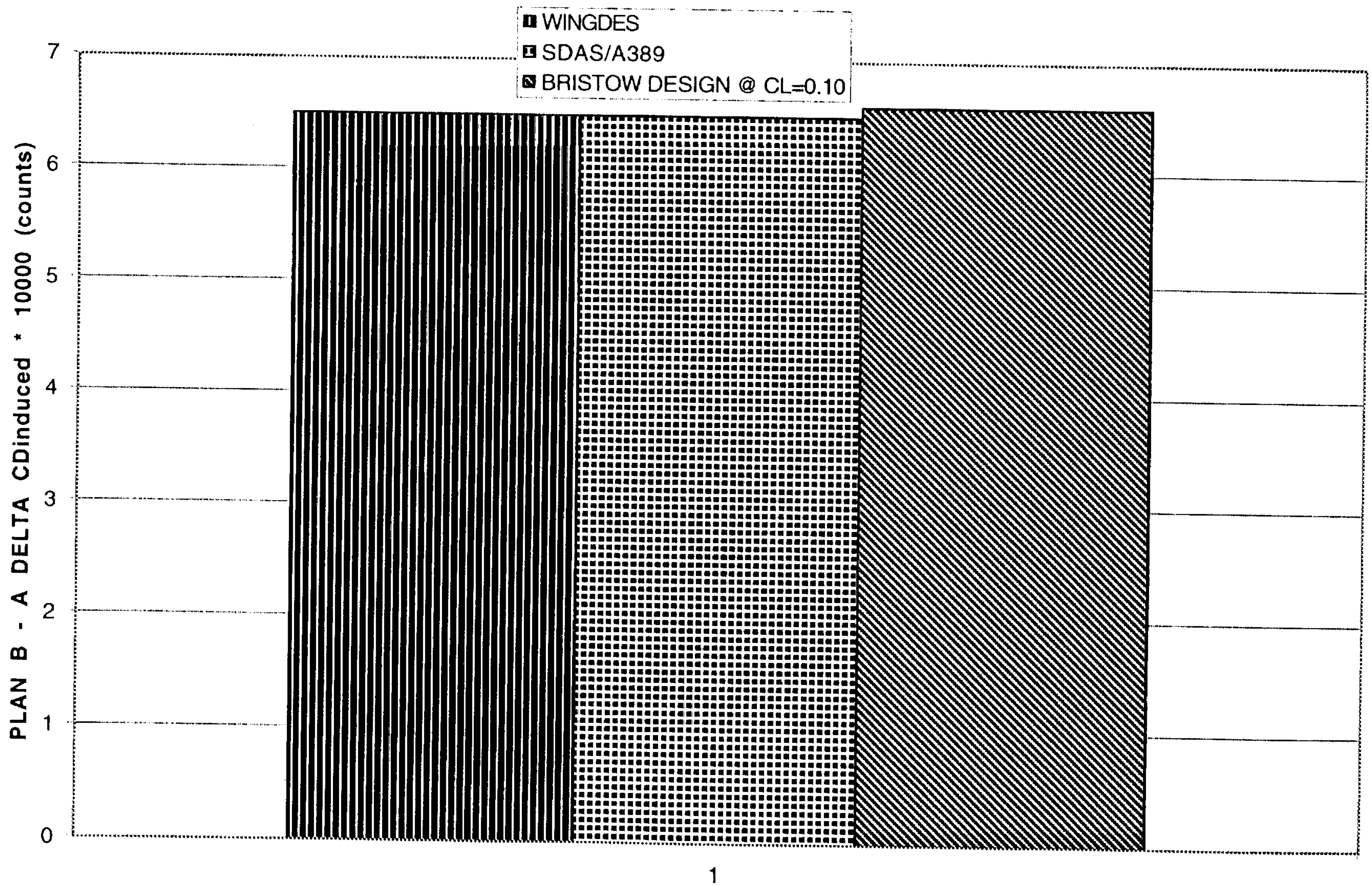

Mach 2.4 Analysis of BRISTOW Designs - Full Thrust

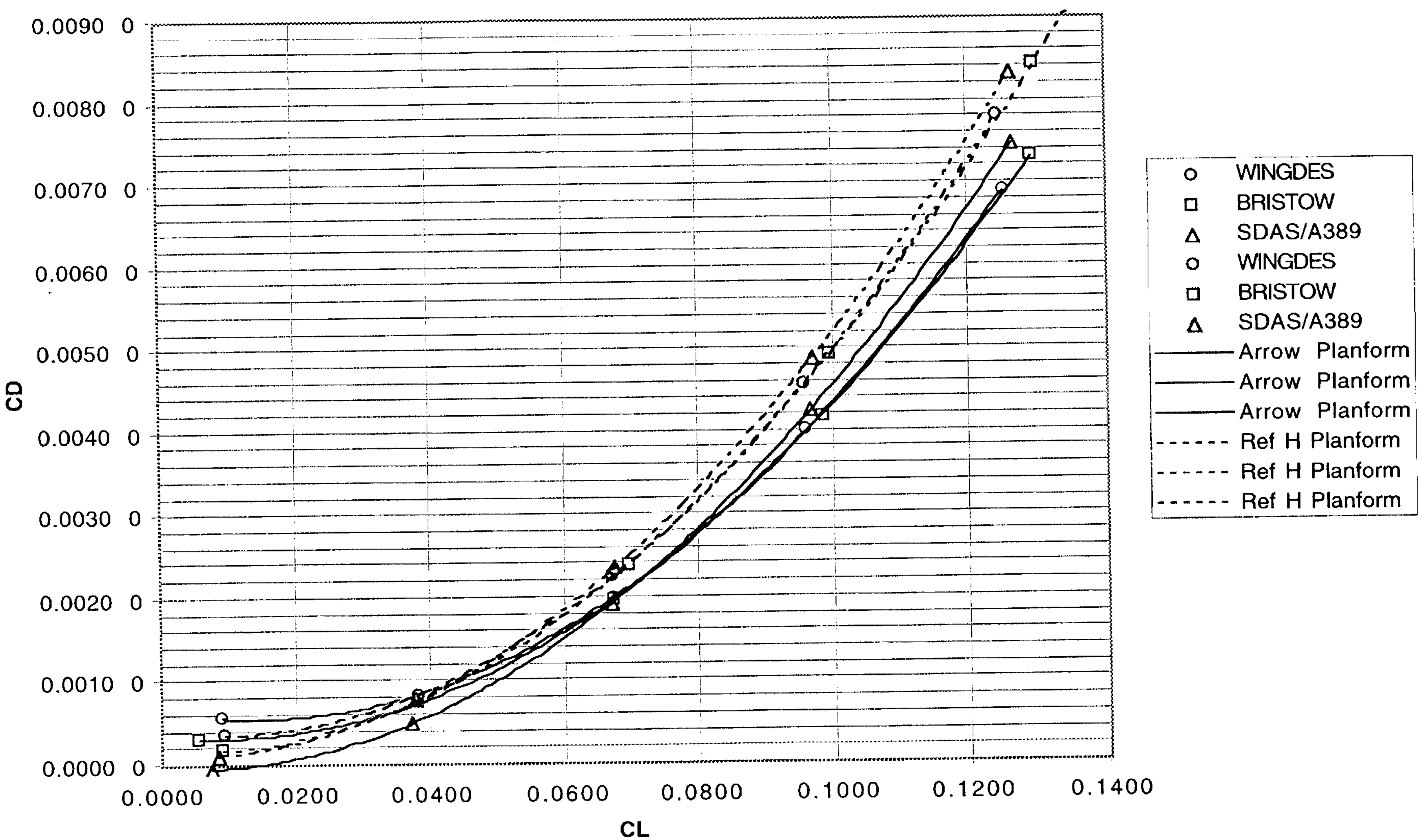

TCA6 LET Prediction Comparison at Mach 2.4

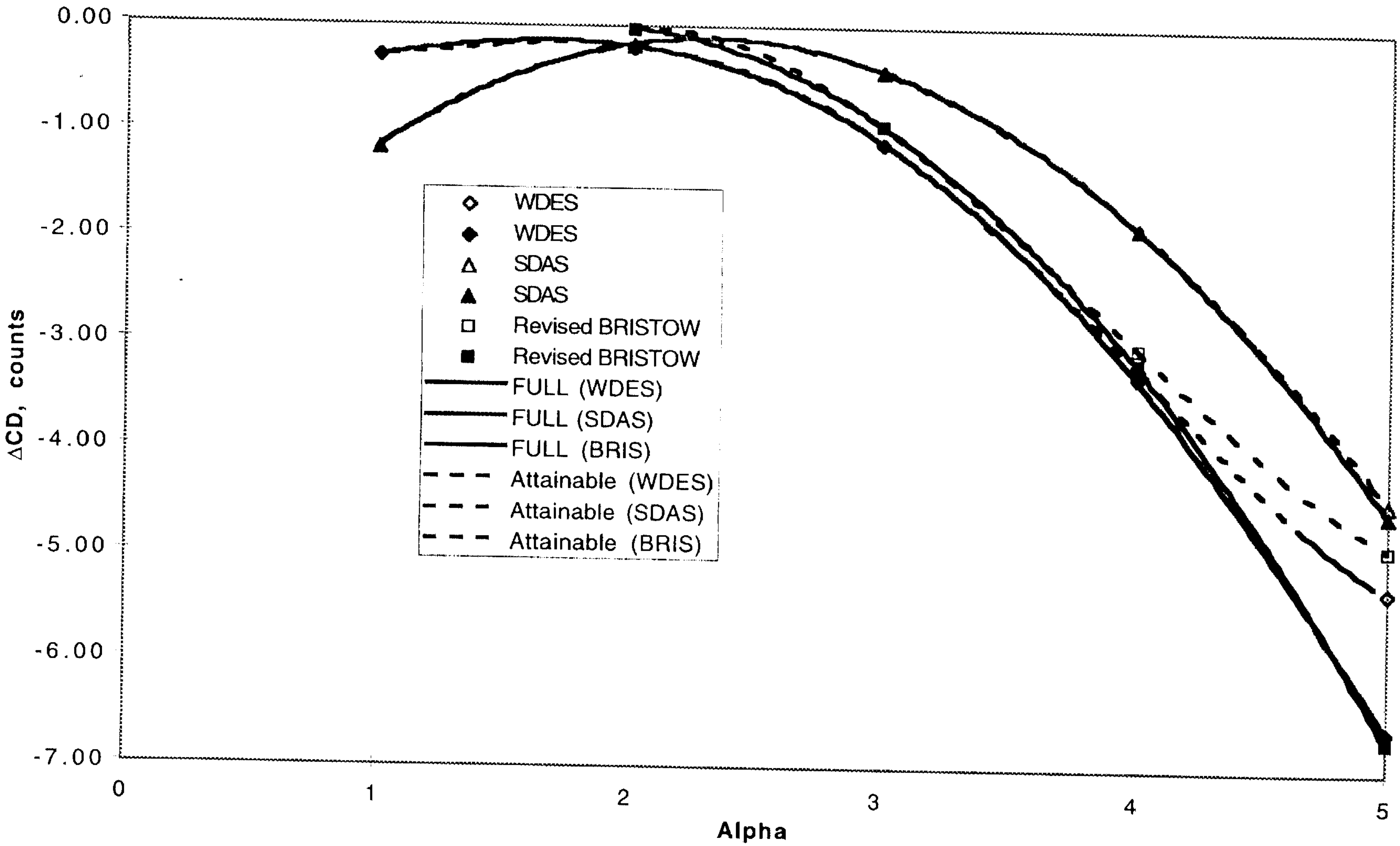

TCA Prediction Comparisons

In addition to comparing the linear methods to one another, a comparison was made against a CFL3D Euler calculation of the TCA configuration. Pressure predictions near the side-of-body show good agreement with a BRISTOW wing-body prediction. Only BRISTOW pressures are shown since WINGDES only calculates delta Cps and SDAS TCA decks from Boeing did not include fuselage effects in the lift analysis. (The oscillations in the BRISTOW predictions are due to a slight influence instability in the body paneling which dies out quickly, farther from the body, and does not seem to affect force predictions since the flow is isentropic.)

TCA WING-BODY Cp at MACH 2.4 and CL=0.09

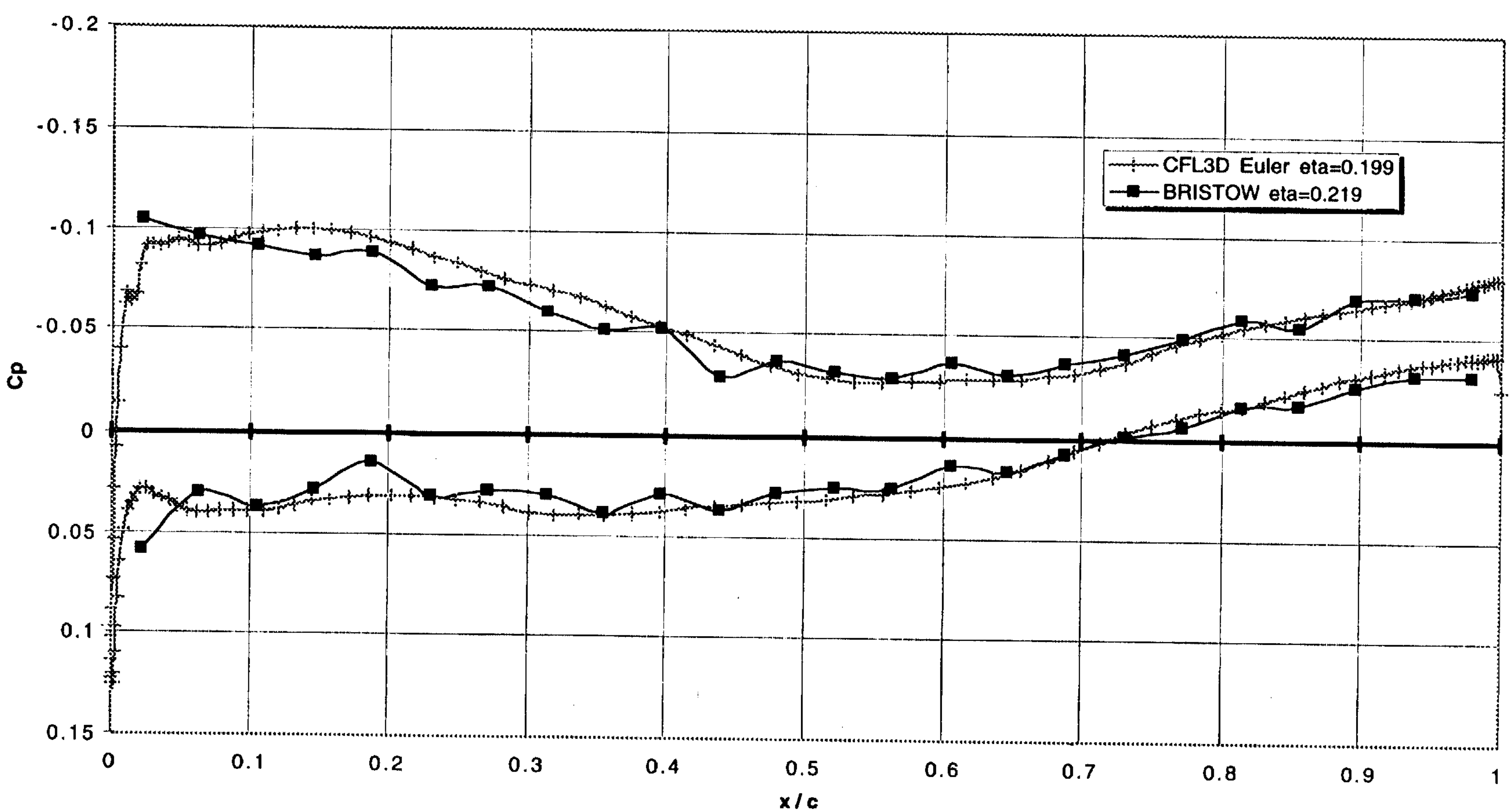

Just inboard of the leading edge break, the lower surface pressure comparison still looks good. But contrary to the lower surface, the linear method predicts too much leading edge suction and not enough suction on the upper surface following the peak. This is believed to be a failure caused by the linearization of the potential flow equations. The lower surface pressure coefficients are much closer to zero, therefore, non-linear terms are smaller. The acceleration of the flow on the upper surface changes the local Mach number; and therefore, the influences of the panels on one another. The peak local Mach number on the upper surface is around 2.6--enough of an increase in the Mach cone angle to more than halve the number of inboard leading edge panels creating upwash at this midspan leading edge location. As you can see, this definitely affects leading edge thrust results and all force predictions. More examination of the consequences of this result are needed.

TCA WING-BODY Cp at MACH 2.4 and CL=0.09

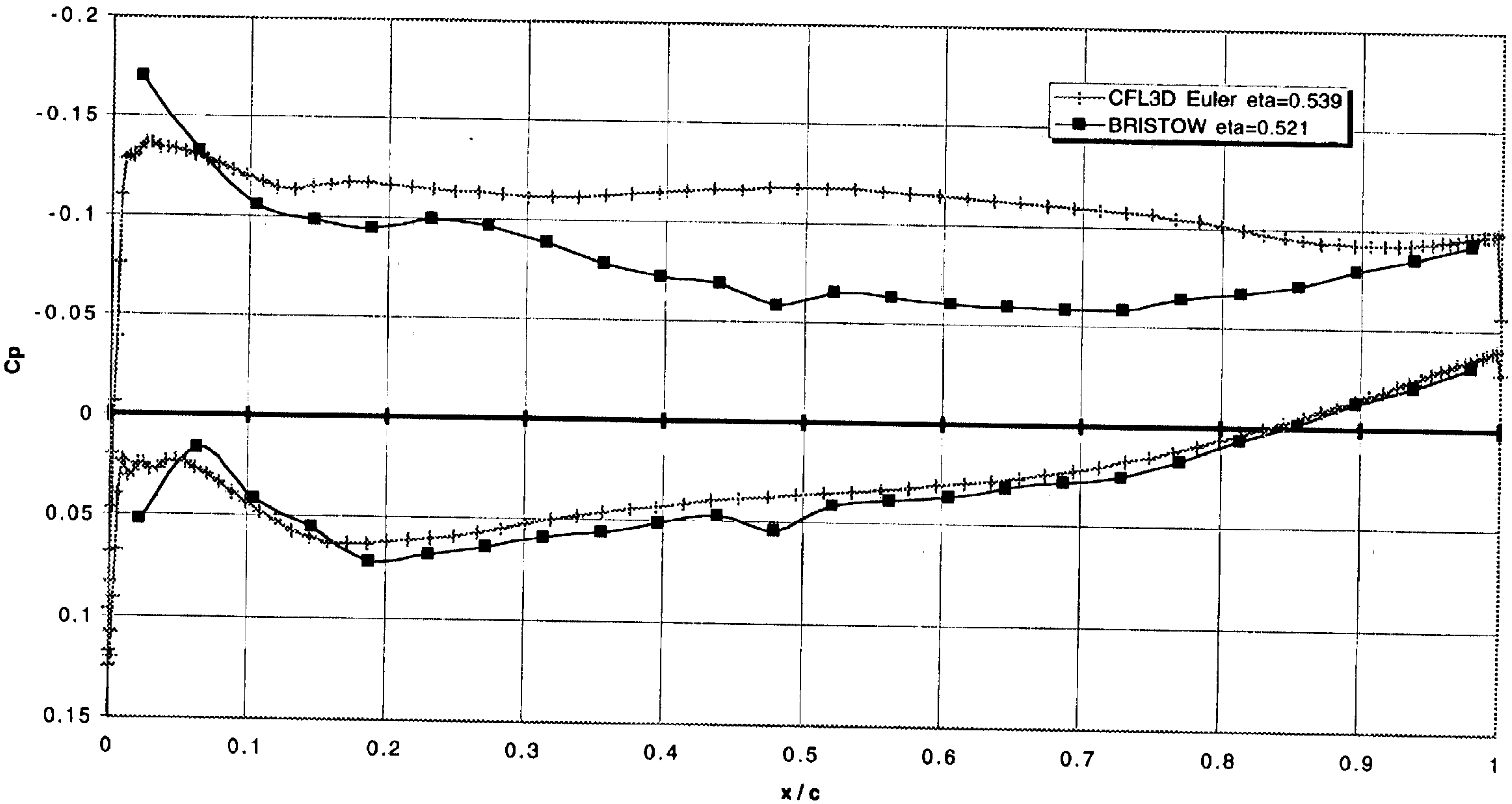

Since these are induced drag codes, they are designed to predict changes in drag versus CL. To compare their accuracy, a plot was made of the difference between TCA wind tunnel data and each codes' prediction. A CFL3D Euler prediction was added for comparison. To be a good induced drag method, the difference plotted should be a zero slope line. All three linear methods plot as parabolas, with good accuracy at, or a little below, cruise CL and worsening predictions beyond that. BRISTOW is shown with and without fuselage and wing thickness effects. The BRISTOW prediction including fuselage and wing thickness effects shows a substantially better trend versus CL, much closer to the Euler trend.

TCA6: METHOD minus TEST at Mach 2.4 - ΔDRAG VERSUS CL
Linear CDwave = 0.00187

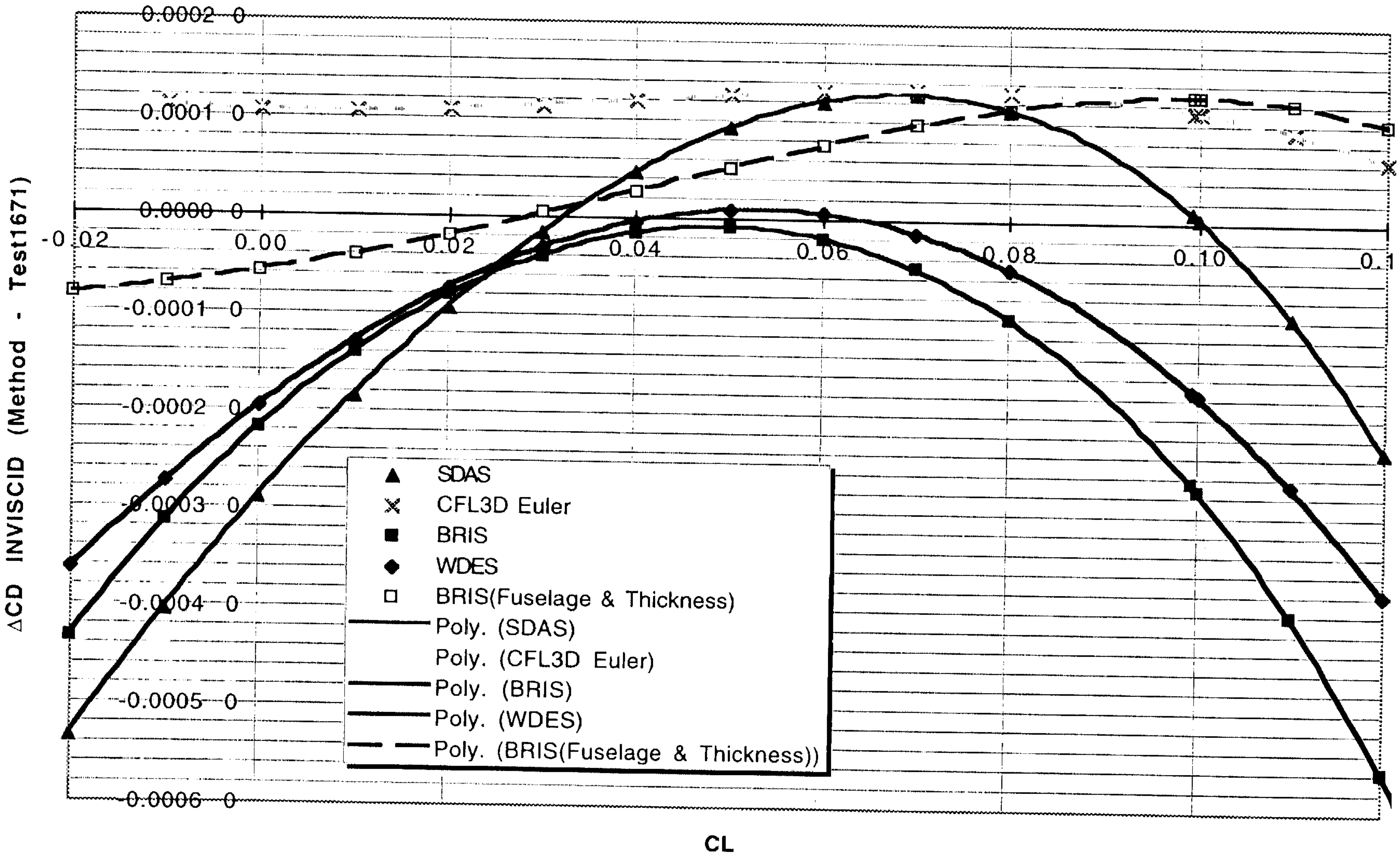

Here SDAS is shown without its LET estimate, since that is the way Boeing uses the code at Mach 2.4. Interestingly, the trend is a better--much flatter--comparison versus CL. (The trend mimics the BRISTOW fuselage and thickness effects, but the cause is unrelated.) However, when SDAS/A389 predictions without LET are used to analyze WINGDES designs with and without thrust, the predicted increment would say the design with LET is 1 count worse (the no thrust result) instead of 2 counts better. Analysis without LET estimates should not be used on wings designed for LET.

TCA6: METHOD minus TEST at Mach 2.4 - ΔDRAG VERSUS CL
Linear CDwave = 0.00187

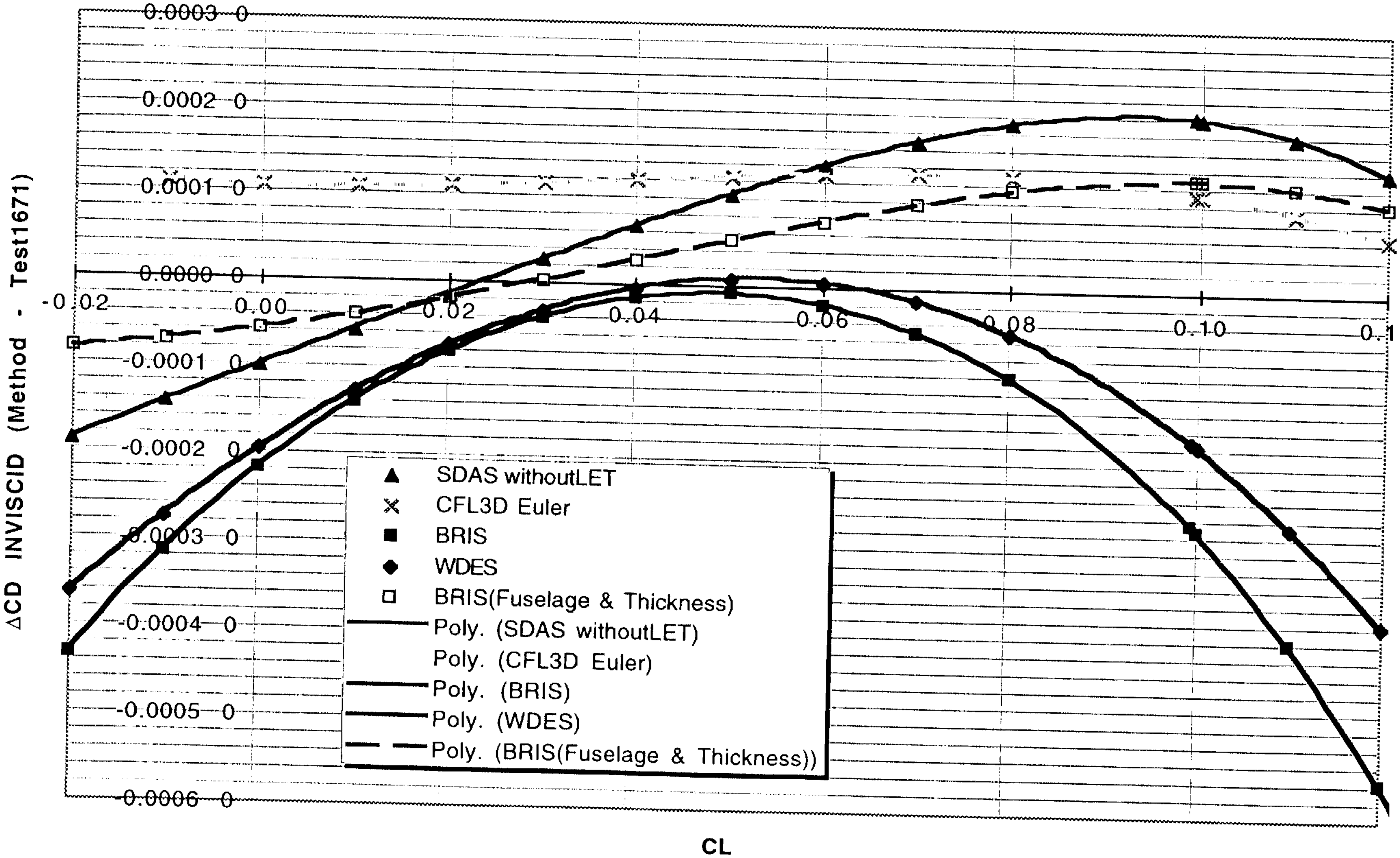

CD Induced
Mach 1.1 Analysis
of BRISTOW Designs

All codes yield no thrust and thrust results within 2 counts of each other for the same Wing/Warped-Plate-Body design, which is considered acceptable at Mach 1.1.

BRISTOW Designs: Mach 1.1 CDinduced at CL=0.15

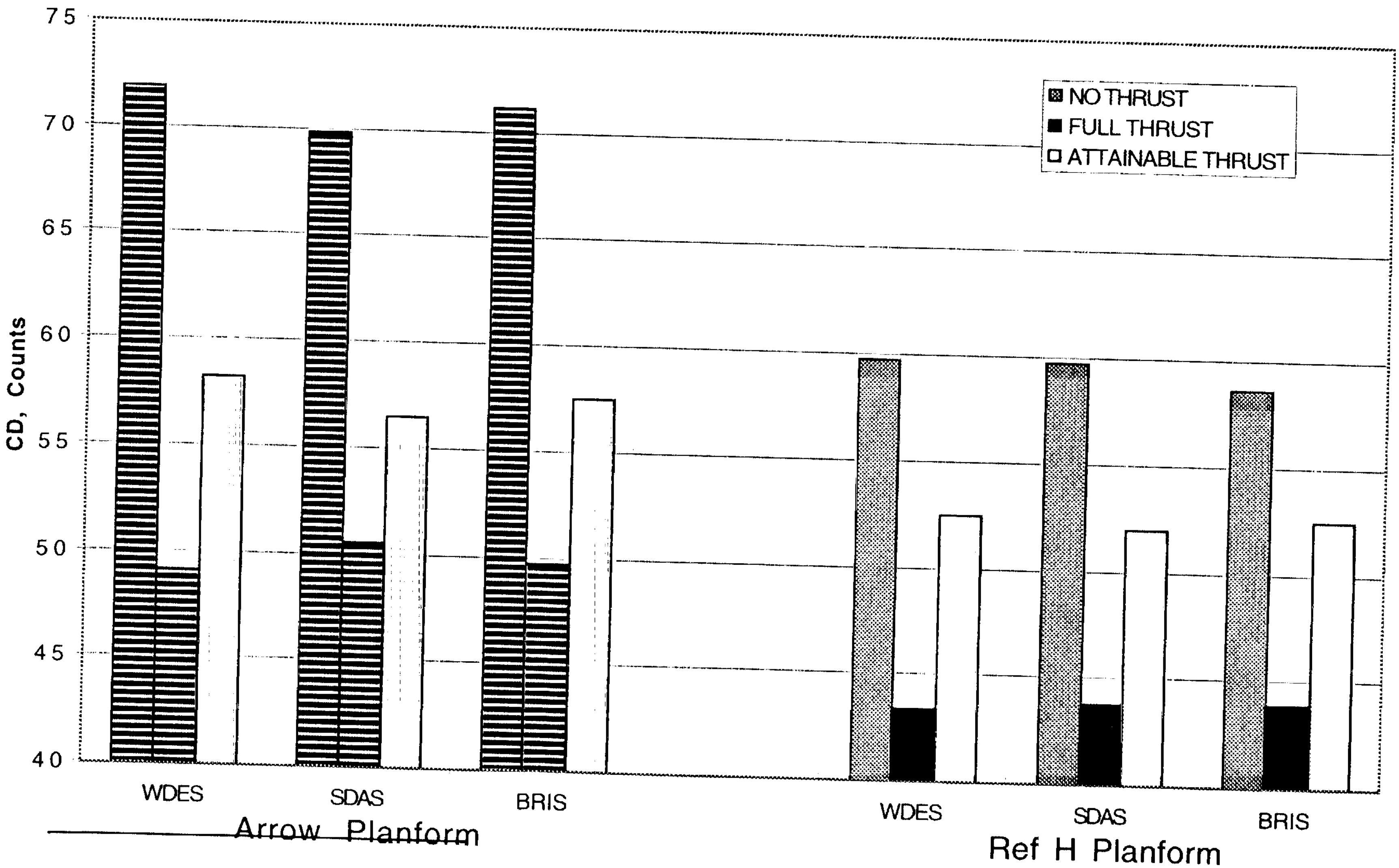

A plot of the spanwise leading edge thrust prediction from WINGDES and BRISTOW were compared to examine why thrust predictions differed. WINGDES had to reduce is paneling to 19 columns at Mach 1.1. BRISTOW used 18 columns but spline fits the leading edge pressure and integrates on 1% intervals. BRISTOW pressures yield a much smoother distribution (except for the discontinuous sweep break) and a more conservative prediction on the outboard sharp leading edge, but there is no way to tell which is more correct. Fortunately, sharp leading edge prediction differences are minimized when attainable thrust limiting is applied. Since transonic drags levels have less of an effect on the design, the inconsistency magnitude is considered acceptable.

SPANWISE THRUST DISTRIBUTION--ARROW at MACH 1.1

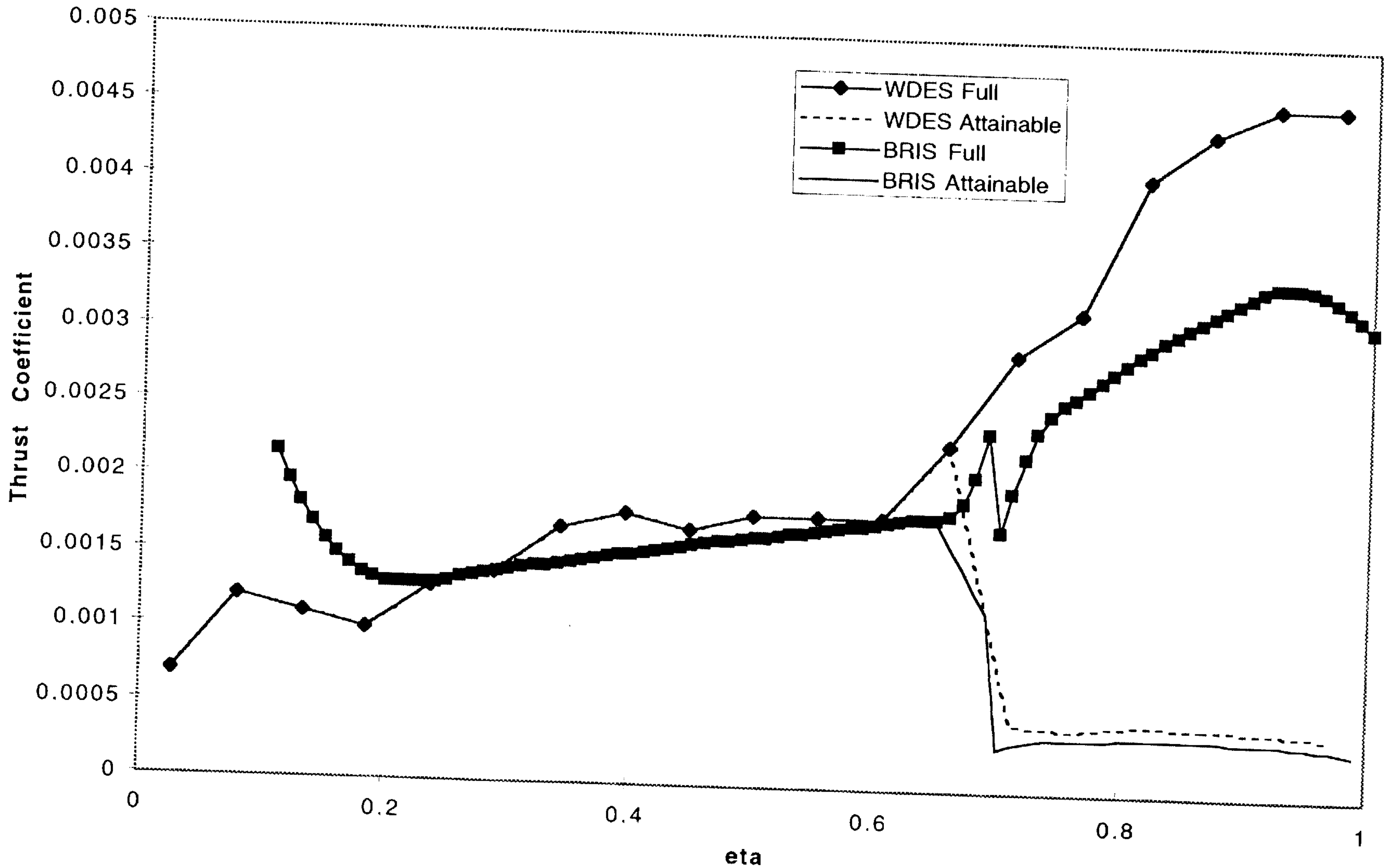

CD Induced Summary

Status	Conclusion
Mach 2.4 Design	
Design	All codes produce similar trends
Only WDES has LET design	Should include in other codes
Mach 2.4 Analysis	
Wing/Warped-Plate-Body	All Codes have similar trends
LET of SDAS not useable	?
Fuselage interference/Thickness only in BRISTOW	?
Inaccuracies outboard	?
Mach 1.1 Analysis	
Wing/WP-Body	All Codes have similar results
SDAS LET predicts negative CD at low CL	?

PRELIMINARY CONCLUSIONS AND FUTURE PLANS

CD Induced Methods

Drag differences were eliminated by improving modeling processes.

All codes now match in design and analysis trend predictions.

WINGDES is the only code to design with LET.

SDAS is the only code with rapid nacelle prediction and design, but data comparisons are needed to validate the benefits.

SDAS is unable to use LET at Mach 2.4.

BRISTOW is the only code calculating fuselage interference and wing thickness, but more data comparisons are needed to validate the benefits.

Need to improve understanding of linear pressure prediction inaccuracies.

References

1. Carlson, H. W. and Walkley, K. B. "Neumerical Methods and a Computer Program for Subsonic and Supersonic Aerodynamic Design and Analysis of Wings With Attainable Thrust Considerations." NASA CR-3808, Aug. 1984.

2. Carlson, H. W. and Darden, C. M. "Validation of a Pair of Computer Codes for Estimation and Optimization of Subsonic Aerodynamic Performance of Simple Hinged-Flap Systems for Thin Swept Wings." NASA TP-2828, Nov. 1988.

3. Carlson, H. W.; McElroy, M. O.; Lessard, W. B. and McCullers, L. A. "Improved Method for Prediction of Attainable Wing Leading-Edge Thrust." NASA TP-3557, Apr. 1996.

4. Middleton, W. D. and Lundry, J. L. "A System for Aerodynamic Design and Analysis of Supersonic Aircraft. Part 1 - General Description and Theoretical Development." NASA CR-3351, Dec. 1980.

5. Middleton, W. D. and Lundry, J. L. "A System for Aerodynamic Design and Analysis of Supersonic Aircraft. Part 2 - User's Manual." NASA CR-3352, Dec. 1980.

6. Middleton, W. D. and Lundry, J. L. "A System for Aerodynamic Design and Analysis of Supersonic Aircraft. Part 3 - Program Description." NASA CR-3353, Dec. 1980.

7. Carlson, H. W.; Mack, R. J. and Barger, R. L. "Estimation of Attainable Leading-Edge Thrust for Wings at Subsonic and Supersonic Speeds." NASA TP-1500, Oct. 1979.

8. Woodward, F. A. and Larsen, J. W. "A Method of Optimizing Camber Surfaces for Wing-Body Combinations at Supersonic Speeds--Theory and Application." Document D6-10741--Part 1, Sept. 1965, The Boeing Co; also available as NASA CR-69181.

9. Woodward, F. A.; Tinoco, E. N. and Larsen J. W. "Analysis and Design of Supersonic Wing-Body Combinations, Including Flow Properties in the Near Field - Part I - Theory and Application." NASA CR-73106, Aug. 1967.

References (cont.)

9. LaRowe, E. and Love, J. E. "Analysis and Design of Supersonic Wing-Body Combinations, Including Flow Properties in the Near Field - Part II - Digital Computer Program Description." NASA CR-73107, Aug. 1967.

10. Bristow, D. R. "Computer Program to Solve the Three-Dimensional Mixed Boundary Condition Problem for Subsonic or Supersonic Potential Flow." MDC A3190, Dec. 1974, McDonnell Aircraft Co, St. Louis, MO.

11. Kuruvila, G.; Hager, J. O.; Unger, E. R.; Arslan, A. E.; Bruns, D. B.; Sundaram, P.; Martin, G. and Agrawal, S. "Technology Integration CFD Planform Study of the 1400 Series. [1404-1407]" Contract NAS1-20220, Task 11 Report, Nov. 15, 1995; McDonnell Douglas Aerospace-Transport Aircraft, Long Beach, CA.

REPORT DOCUMENTATION PAGE

Form Approved
OMB No. 0704-0188

1. AGENCY USE ONLY *(Leave blank)*

2. REPORT DATE
December 1999

3. REPORT TYPE AND DATES COVERED
Conference Publication

4. TITLE AND SUBTITLE
1997 NASA High-Speed Research Program Aerodynamic Performance Workshop
Volume I—Configuration Aerodynamics

5. FUNDING NUMBERS
WU 537-07

6. AUTHOR(S)
Daniel G. Baize, Editor

7. PERFORMING ORGANIZATION NAME(S) AND ADDRESS(ES)
NASA Langley Research Center
Hampton, VA 23681-2199

8. PERFORMING ORGANIZATION REPORT NUMBER
L-17916B

9. SPONSORING/MONITORING AGENCY NAME(S) AND ADDRESS(ES)
National Aeronautics and Space Administration
Washington, DC 20546-0001

10. SPONSORING/MONITORING AGENCY REPORT NUMBER
NASA/CP-1999-209691/VOL1/PT1

11. SUPPLEMENTARY NOTES

12a. DISTRIBUTION/AVAILABILITY STATEMENT
Unclassified–Unlimited
Subject Category 02 Distribution: Nonstandard
Availability: NASA CASI (301) 621-0390

12b. DISTRIBUTION CODE

13. ABSTRACT *(Maximum 200 words)*

The High-Speed Research Program and NASA Langley Research Center sponsored the NASA High-Speed Research Program Aerodynamic Performance Workshop on February 25–28, 1997. The workshop was designed to bring together NASA and industry High-Speed Civil Tranport (HSCT) Aerodynamic Performance technology development participants in area of Configuration Aerodynamics (transonic and supersonic cruise drag prediction and minimization), High-Lift, Flight Controls, Supersonic Laminar Flow Control, and Sonic Boom Prediction. The workshop objectives were to (1) report the progress and status of HSCT aeroydamic performance technology development; (2) disseminate this technology within the appropriate technical communities; and (3) promote synergy among the scientist and engineers working HSCT aerodynamics. In particular, single- and multi-point optimized HSCT configurations, HSCT high-lift system performance predictions, and HSCT Motion Simulator results were presented along with executive summaries for all the Aerodynamic Performance technology areas.

14. SUBJECT TERMS
High-Speed Research; High-Speed Civil Transport

15. NUMBER OF PAGES
803

16. PRICE CODE
A99

17. SECURITY CLASSIFICATION OF REPORT	18. SECURITY CLASSIFICATION OF THIS PAGE	19. SECURITY CLASSIFICATION OF ABSTRACT	20. LIMITATION OF ABSTRACT
Unclassified	Unclassified	Unclassified	UL